Cranfield University

M. FÁTIMA O. VALES SILVA

MULTILAYER TiB₂/X HARD COATINGS BY SPUTTERING DEPOSITION

School of Industrial and Manufacturing Science

Ph.D. Thesis

Cranfield University

School of Industrial and Manufacturing Science

Ph.D. Thesis

Academic Year 1997/1998

Maria de Fátima Oliveira Vales da Silva

MULTILAYER TiB$_2$/X HARD COATINGS BY SPUTTERING DEPOSITION

Supervisors:
Professor Peter Hancock
Professor John R. Nicholls

OCTOBER 1998

ABSTRACT

ABSTRACT

Titanium diboride has been investigated as a potential candidate for aerospace structures, cutting tools, surface coatings of first-wall components and diffusion barriers in integrated circuit metallization. Titanium diboride is a very stable hard refractory compound but its brittleness is the main drawback. It was possible to lessen the TiB_2 brittleness by producing TiB_2/X coating designs by the multi-target RF magnetron sputtering process. X is the metal layer (Al, Ti, NiCr, Mo) in the composite system.

The influence of the composition wavelength and volume fraction of ceramic has been studied over a range of sputtering conditions. The most suitable multilayer coating design (TiB_2/NiCr) on steel substrate, for maximum hardness (18.81GPa) and elastic modulus (304.6GPa) was found to be with a composition wavelength of 50nm and volume fraction of ceramic of 75%. The greatest improvement of the elastic modulus measured by nanoindentation was found to be for a TiB_2/Al two-layer coating design either on steel or on aluminium substrate, giving 36.2% and 40% improvement above the rule of mixtures respectively, when compared with TiB_2 coatings deposited under the same sputtering conditions.

Several pieces of three-point bent apparatus were designed for measuring the in-plane elastic modulus of the coatings. The three-point bent test by nanoindenter shows promise as a method for measuring the in-plane elastic modulus on uncoated beams.

A comparison between traditional and non-traditional methods of measuring mechanical properties of the coatings was performed in this study. The nanoindentation technique was found to be an appropriate method to measure the mechanical properties of multilayer coating designs.

ACKNOWLEDGEMENTS

Acknowledgements

LIST OF CONTENTS

PREFACE

List of Contents

1. INTRODUCTION

High technology applications are so demanding in terms of power/weight ratio and lifetime that components of bulk materials cannot deliver the required performance. Consequently, surface engineering has been and will continue to be a key technology in the development of improving wear, fatigue, corrosion and bio-compatibility of the materials.

Attempts to improve the operating performance of hard coatings have been centered on the development of the new types of matrix alloys, complex composition and metastable structures and multilayer coating design.

The general concept of multilayer coating design is nowadays well accepted and provides the ability to synthesise such materials for both Science and Technology with Industrial applications.

The motivation for using a multilayer coating design in the field of hard coatings is mainly to improve adhesion between film and substrate, to obtain wear-protective films with a low chemical reactivity and low friction, to increase the strength and hardness of the deposited film.

Multilayer coating design characterization has been focussed either on a parametric relationship between some property and multilayer period or specifically directed to synthesis process-structure-property relationships.

PVD techniques are very competitive for synthesising superlattice structures and multilayer coatings. The PVD sputtering method is capable of depositing dense and adherent thin films at low substrate temperature for amorphous structures but it is possible to deposit crystalline structures on heated substrates.

2. OBJECTIVE

Titanium diboride is a potential candidate material for aerospace structures and is a possible new ceramic for other applications because of its exceptional properties such as: high hardness, oxidation resistance, strength retention at high temperature and stability. However, its brittleness has postponed its use as a potential hard coating.

The aim of this project was to produce a new type of hard coating of TiB_2/metal composite design in order to lessen the brittleness of the titanium diboride. The composite was produced using R.F. Magnetron Sputtering in a sequential manner.

The parameters which varied within the composite were a combination of the composition wavelength and the volume fraction of ceramic in order to optimise the mechanical properties of the coating.

The mechanical properties of the coatings were measured either by traditional methods or by non-traditional methods such as nanoindentation.

3. STRUCTURE OF THE THESIS

The thesis is divided into four chapters which address the following aspects:

Chapter 1: Limited technical review of subjects related to hard materials, hard coatings, thin film technology, sputtering process, structural characterisation, mechanical properties of thin films by traditional and non-traditional methods.

Chapter 2: Description of the experimental procedure.

Chapter 3: Experimental results and discussion are presented for single-layer, two-layer and multilayer coatings and respective short summaries.

Chapter 4: General conclusion, limitations of this work and guidelines for further research are given in this chapter.

LIST OF SYMBOLS

LIST OF SYMBOLS *

T_s - Substrate temperature (°C)

t_c - Thickness of the composite (coating/substrate) (mm)

t_f - Thickness of the coating (μm)

t_s - Thickness of the substrate (mm)

l - Length of the beam (mm)

b - Width of the beam (mm)

σ_f - residual stresses in the film (GPa)

E_s - Elastic modulus of the substrate (GPa)

E_f - Elastic modulus of the coating (GPa)

$(E_f)_{1a}$ - Elastic modulus of the the coating based on γ_c from δ/P, for E_s=207GPa, from equation 2.11 (GPa)

$(E_f)_{1b}$ - Elastic modulus of the the coating based on γ_c and γ_s from δ/P, from equation 2.11 (GPa)

$(E_f)_{2a}$ - Elastic modulus of the the coating based on γ_c from δ/P, for E_s=207GPa, from equation 2.23 (GPa)

$(E_f)_{2b}$ - Elastic modulus of the the coating based on γ_c and γ_s from δ/P, from equation 2.23 (GPa)

d - Deposition rate (μm/h)

R_0 - Distance between target and substrate

H - Hardness (GPa)

E_r - Reduced elastic modulus (GPa)

υ - Poisson's ratio

C - Compliance of the nanoindenter machine (nm/mN)

$(\gamma_s)_1$ - slope from the ratio of the δ/P for each load, for uncoated beams

$(\gamma_c)_1$ - slope from the ratio of the δ/P for each load, for the composite

$(\gamma_s)_2$ - slope from a linear curve fit (Least square) of the δ versus P curve, for uncoated beams

$(\gamma_c)_2$ - slope from a linear curve fit (Least square) of the δ versus P curve, for the composite

R^2 - Correlation factor of the fitting δ versus P curve

λ - Composition wavelength (nm)

V_c - Volume fraction of the ceramic

*List of symbols only for the experimental work.

ABBREVIATIONS

ABBREVIATIONS

ARE – Activated reactive evaporation

AES – Auger electron spectroscopy

BARE – Biased activated reactive evaporation

CDS – Cathode dark space

CEEXAPS – Conversion electron extended X-ray adsorption fine structure

CIP – Chemical ion plating

CVD – Chemical vapour deposition

DIM – Dynamic ion mixing

dpa – Displacement per atom

EBDIM- Electron beam evaporation dynamic ion mixing

EDS – Energy dispersive X-ray spectroscopy

ESEM – Environmental scanning electron microscopy

ISE – Indentation size effect

MFC – Mass flow controllers

mfp – Mean free path

NG – Glow region

PACVD – Plasma-assisted CVD

PC – Positive column region

PECVD – Plasma-enhanced CVD

PVD – Physical vapour deposition

RBS – Rutherford backscattering spectroscopy

RIP – Reactive ion plating

SAD – Selected area diffraction

SCCM – Standard cubic centimeter per minute

SEM – Scanning electron microscopy

SIMS – Secondary ion mass spectroscopy

SIP – Sputter ion plating

SPDIM – Sputtering beam evaporation dynamic ion mixing

TEM – Transmission electron microscopy

XPS – X-ray photoelectron spectroscopy

XRD – X-ray diffraction

STATE OF THE ART

1. STATE OF THE ART

1.1. BRIEF REVIEW OF HARD MATERIALS

LAYOUT
⇓
Material Performance
⇓
Factors Which Determine Material Properties
⇓
Main Group of Hard Materials
⇓
Chemical Bonding of Hard Materials for Coatings
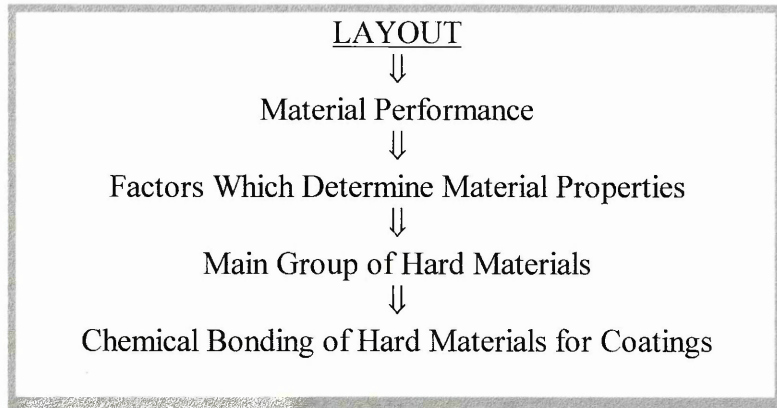
The material performance pyramid in figure 1.1 illustrates the path that should be followed in the future to guarantee hard material performance. Going from the top of the pyramid (Macroprocesses: Functional quality) to the bottom (Microprocesses: Theory of dislocations) it should be possible to develop materials for specific industrial applications, thus reducing industrial and research costs. The factors that affect the parameters, which control corrosion and wear, are the material and the environment. Both of them must be considered in the material′s performance. The people factor (designers, procurement, manufacturers, engineers...) plays an important role in materials management. This determines the successful relationship between material performance and functional quality.
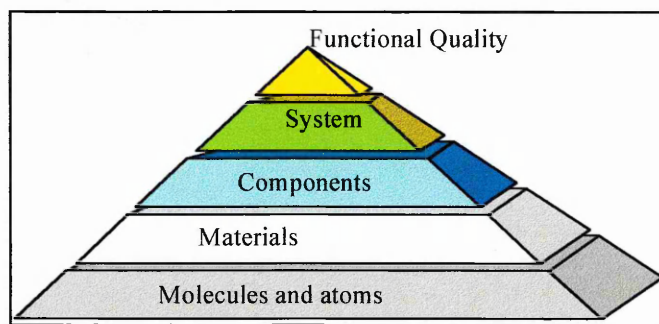
Figure 1.1. The material performance pyramid.

Two important factors in determining material properties are the constitution of the materials and fabrication conditions. Equally important is the optimisation of the material properties that could interfere with the application characteristics and with future developments [1]. This is illustrated in figure 1.2.
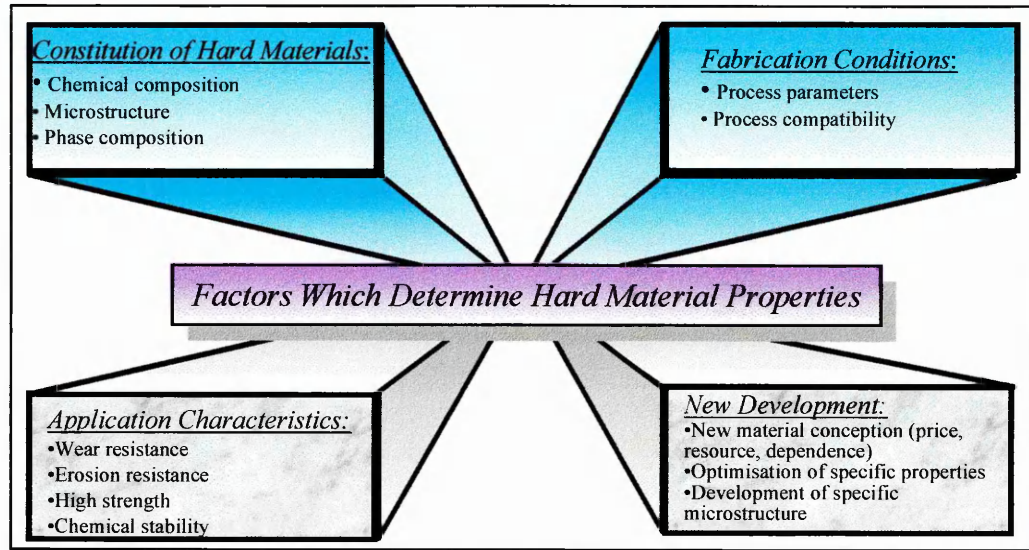
Figure 1.2. Factors which determine hard material properties.

The main groups of hard materials are illustrated in figure 1.3 as a function of their hardness and transverse rupture strength [1,2]. The fields of materials in order of decreasing hardness are: Superhard materials, hard carbides, ceramic materials and hard metals. The field of hard metals is subdivided into hard metal I (carbide-rich) and hard metal II (metal-rich). Each group of hard metals is subdivided into the TiC-based materials at lower strength and WC-based materials at higher strength. The strength of the materials increases on going from TiC to WC in both metal I field and metal II. The main features of the material of each field are described below [1,2,3,4,5,6].

SUPERHARD MATERIALS: Diamond-metal composites have been reported with hardness of 107.9GPa (11000HV) and a transverse rupture strength of 21GPa ($2100Nmm^{-2}$). Cubic boron nitride is the second hardest material that keeps its hardness up to 1370°C. c-BN has been used as a material for cutting tools. Also B_4C has excellent hot hardness, about 39.2GPa (4000HV), over the range of 200-1400°C. The hardness of the hardest carbide (BC) ranges from 29.4 to 68.6GPa (3000 to $7000Kgmm^{-2}$).

CARBIDES: The transition metal carbide field is limited by TiC on the high hardness but low strength side and by WC on the higher strength but lower hardness side. SiC is available in two allotropic forms; the cubic has a hardness of 27.5GPa (2800 $Kg.mm^{-2}$) while the hexagonal is higher at approximately 44.1GPa ($4500Kg.mm^{-2}$). The wear resistant elements in steels and hard metals are supplied by carbides. Wear resistance is their main application, owing to the fact that pure carbides are too brittle for tool applications.

CERAMICS: The most common ceramic material is the alumina based ceramic. The multicomponent ceramic system could offer many such new compositions, such as TiC-TiB_2 hardness of 23GPa (2350HV) at 25°C and 8.3GPa (850HV) at 600°C.

HARD METAL I : This field is formed by adding to the carbides a binder metal of the group VIII such as: Fe, Co, Ni. As a result, the hard metal I field is extended in the direction of high strength.

HARD METAL II: This field is formed by replacing the heavy, expensive transition metals with cheaper, abundant and light, iron and nickel based alloys.

COATINGS: Improvements through the use of coatings result in an increase in abrasion resistance (hardness) and transverse rupture strength of the composite. However, their lack of toughness leads to limited fatigue strength and adherence. Over the last few years attempts have been made to overcome these restrictions with multilayer coatings or multicompound coatings and this is the subject of this thesis. This subject is going to be treated in detail later in this chapter.

Figure 1.3. Developments in the field of wear resistant materials [1].

The nature of chemical bonding of the hard materials has a strong influence on adherence to the substrate, adhesion to other materials and on the hardness/toughness ratio. In terms of the chemical bonding, the hard materials for coatings can be divided into three groups [4,7]:

1. Metallic hard materials (Borides, carbides and nitrides of the transition metals).

2. Covalent hard materials (Borides, carbides and nitrides of Al, Si, B and diamond).

3. Ionic hard materials (Oxides of Al, Zr, Ti and Be).

Each group has restrictions in respect of applications as hard coatings. The main properties of the three groups are outlined in the table 1.1.

3

Properties	*Hardness*	*Brittleness*	*Melting Point*	*Stability (-ΔG)*	*Thermal expansion coefficient*	*Adherence to metallic substrate*	*Interaction tendency*	*Multilayer stability*
High	c	i	c	i	i	m	m	m
↓	m	c	m	m	m	i	c	i
Low	i	m	i	c	c	c	i	c
m-metallic; c-covalent; i-ionic								

Table 1.1. Properties and behaviour of the different groups of hard materials [7].

The information in table 1.1 leads to the following conclusions:

1. All the compounds stand out for their high hardness and high melting point.

2. The metallic materials are suitable for layered composites.

3. The ionic hard materials are suitable for surfaces because of high stability and low interaction tendency. However, their modulus of elasticity is lower.

4. In terms of hard materials, for example, the optimum wear resistance can only be achieved by sequential phases or layers.

Finally, when dealing with these structures, Hägg's rule is a useful guide for determining the structure of transition-metal carbides, nitrides, borides and hybrids [5,8,9]. The rule states that the structure of these materials is determined by the ratio of the atomic radius of the interstitial element and the transition metal ($R = R_x/R_{mc}$). If R<0.59 then simple structures such as NaCl or simple hexagonal structures will be formed. If R>0.59 the transition-metal and the interstitial atoms form very complex structures.

1.1.1. PROPERTIES OF THE BORIDE MATERIALS

```
                        LAYOUT
                           ⇓
          Composition and Structure of Borides
                           ⇓
               Main Properties of Borides
                           ⇓
     Comparison of Properties of Borides, Nitrides and
                        Carbides
                           ⇓
        Main Properties and Applications of $TiB_2$
```
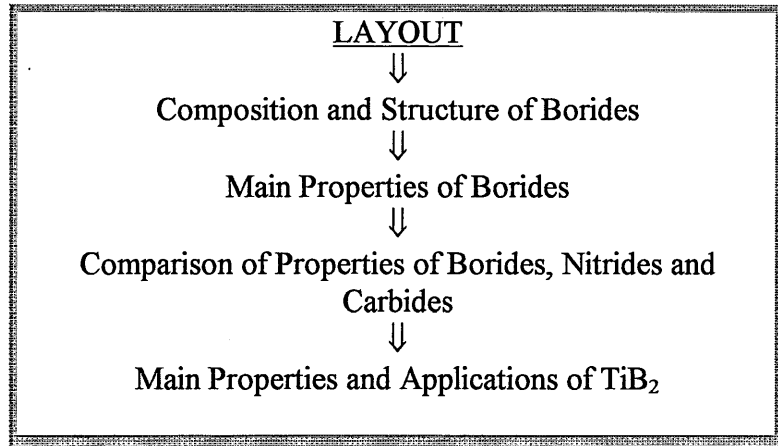
Borides stand out due to a unique combination of thermal, mechanical, electrical and chemical properties. It is expected that the further development of ceramics for industrial applications will continue to overcome their limitations (brittleness, for example) and expand the use of these compounds. In this chapter, titanium diboride is reviewed in detail, focussing on its properties compared to other borides.

Borides belong to the group of interstitial phases (or interstitial alloys or Hägg compounds) that were identified more than 60 years ago. They are interstitial compounds of metals with boron and can form a great range of structures and compositions from M_5B-MB_{12} and sometimes $MB_{66\text{-}100}$. Several metals can form six or seven distinctive boride phases, but none will form all the types of boride phases, as will be explained below. For example, titanium can only form TiB, TiB_2 and Ti_2B_5 [5,10,11,12,13].

Three main factors control the composition of the borides. These are the ratio of atomic sizes of the boron to metal atoms, the electrochemical factor linked with electronic transitions and electron concentration determined by degree of localisation and delocalisation of electrons, ie, the distribution of the electrons around the boron atom [12].

The redistribution of the outer electrons during the formation of the borides, results in the electron configuration of sp^2 and sp^3 that are characteristics of strong covalent bonds. It is the various combinations of s^2p, sp, sp^2 and sp^3 electron configurations that explain the various boride structures. On the other hand, the various valence states linked with overlapping d, f, p and s orbitals account for an enormous number of different boride phases which occur in transition metal borides [12].

Nevertheless, the atomic size of boron rather than the electron valence is the principal factor governing the boride structures. The interstitial substitution of boron in the undistorted octahedral site is very unlikely because of the large atomic size of B ($\cong 0.091$nm) compared to C ($\cong 0.077$nm) or N ($\cong 0.071$nm). Then the result is the formation of B-B bonding. Furthermore, the boron size sites the borides on the borderline of Hägg's rule. This rule, valid for carbides and nitrides, begins to fail for the borides due to the development of direct boron linkages. However, it is still valid for the

metal-rich borides [5,14]. The radii of the boron atoms vary with the co-ordination number and environment, giving a possible radius range of at least 0.087 ± 0.01nm [14].

On a crystallochemical basis, the borides may be classified into two groups[12,13,14]:

1. Metal-rich borides: M_4B, M_3B, M_2B, M_3B_2, MB, M_3B_4
2. Boron-rich borides: MB_2, MB_4, MB_6, MB_{12}, MB_{49}, $MB_{66\text{-}100}$

In metal-rich boride the boron atoms are so diluted that they are considered as isolated atoms and, therefore, predominantly the M-B bonds. As the boron concentration increases or the size of metal atoms decreases then the boron atoms could form pairs, then single zigzag chains, then double chains, then two dimensional networks and finally a three-dimensional framework as illustrated in figure 1.4 [11,12,14].
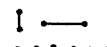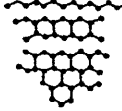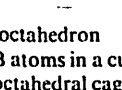
Unit	Atomic ratio	Examples	B–B (nm)	Boron units
Isolated B atom	M_4B	Mn_4B	<0.21	
	M_3B	Co_3B, Ni_3B	<0.21	
	M_2B	Be_2B	0.330	
Pairs of B atoms	M_3B_2	V_3B_2	0.179	
Single chains	MB	FeB	0.177	
Double chains	M_3B_4	Ta_3B_4	—	
		Cr_3B_4		
Layer networks	MB_2	TiB_2	0.175	
		YB_2	0.190	
Three-dimensional	MB_4	UB_4	0.170	
frameworks	MB_6	CaB_6	0.174	B_6 octahedron
	MB_{12}	ZrB_{12}	0.175	24B atoms in a cubo-octahedral cage

Figure 1.4. Boron atom configuration in borides [11].

The metallic lattice structures in the metal-rich borides determine their structure, whereas the covalent B-B bonds determine the structure of the boron-rich borides. The composition of metal-rich borides, between M_3B and MB_2 is one of distorted trigonal prisms, while boron-rich borides consist of rigid covalent boron lattices.

In monoborides and diborides non-stoichiometry originates from either boron chains or lattice vacancies, not from metal-boron links, while in boron-rich borides non-stoichiometry arises from vacancies on the metal sub-lattice due to the strong covalent bonding.

Some conclusions can be drawn from the structural and composition analyses of the borides [5,11,12,14]:

1. The principal new peculiarity of borides compared with other interstitial compounds is the existence of B-B linkages. The radius-ratio criterion is less significant when the B-B bond becomes established. The B-B bond becomes very important in MB compounds and above because of its strong covalent nature.

2. As the degree of covalent bonding increases in the borides, beneficial properties include for instance: high hardness, high melting point, high elastic modulus.

3. The high electrical conductivity of some borides is due to the boron bond formation being through covalent chains and nets. This implies that electrons are free to transfer from boron to metal lattice.

4. The main chemical bonding forces in most borides are ionic, covalent or mixed bonding. However, alloying can cause them to lose their brittleness.

5. The thermal conductivity of borides results from both a lattice and an electronic contribution to electron transport.

The main properties of the borides are mentioned below [10,11,12,15]:

MELTING POINT: The melting point of all borides except iron boride (1390°C) are high (1950-3100°C). The borides formed by group IV elements of the periodic table seem to be the most stable. When the structure is dominated by the boron lattice, the melting point is often identical, for example, CaB_6 (2230°C), LaB_6 (2230°C).

DENSITY: The density of the borides ranges from 2.5 to 16.7g.cm^{-3}.

THERMAL EXPANSION: The thermal expansion values are around 5 to 8×10^{-6} K^{-1} at temperatures from 20 to 1000°C. This property is usually anisotropic for the borides. Linear thermal expansion of 2% or less is reported for the borides in the range of 21 to 2204°C.

THERMAL CONDUCTIVITY: The thermal conductivity of the borides is relatively high with average values of 138.8W/m.K at 295K (80Btu./ft.hr.F at 70F) and 26W/m.K at 1920K (15Btu./ft.hr.F at 3000F). This property gives the borides high thermal shock resistance.

THERMAL STABILITY: The thermal stability of the borides is generally good up to the melting point but there are some exceptions:

$TiB \rightarrow TiB_2 + Ti_2B$ at 2060°C

$ZrB \rightarrow ZrB_2 + Zr$ below 800°C and above 1250°C

$LaB_6 \rightarrow La_{1-x}B_6 + La$ above 1400°C
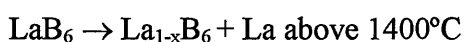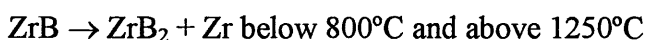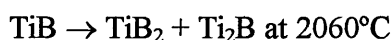
SPECIFIC HEAT: In general, the specific heat of borides is less than 5.7Kg^{-1}K^{-1} up to 2480K (0.35 Btu./lb.F up to 4000F).

ELECTRICAL PROPERTIES: In general, the electrical conductivity of the borides is comparable with many metals and is superior to that of the corresponding carbides. Most borides are excellent electrical conductors with resistivities in the range 5 to 80μΩcm. However, CaB_6 is notable for its high resistivity (1×10^5 μΩcm) due to ionic bonding.

MAGNETIC PROPERTIES: The magnetic properties of borides vary from diamagnetic to strongly ferromagnetic. Most borides are weakly paramagnetic at room temperature. However, ZrB_2, VB and CrB are strongly paramagnetic and the Fe_2B, FeB and MnB are ferromagnetic.

MECHANICAL PROPERTIES: The hardness values for borides range from 12.8 to 32.5GPa (1300 to 3300Kg.mm^{-2}). The modulus of elasticity ranges from 207 to 413.4GPa (30 to 60×10^6 psi) at room temperature.

CHEMICAL PROPERTIES: Borides are known for their resistance to chemical attack and in particular their excellent oxidation resistance. The good stability of the borides, under many conditions, is due to the high negative free energy of formation (see table 1.3). The chemical inertness increases with boron content, depending on the manufacturing process (microstructure, purity...). The borides which stand out by their oxidation resistance are mainly HfB_2, ZrB_2 and Cr_2B. The oxidation resistance of diborides decreases in the order of $HfB_2 > ZrB_2 > TiB_2 > TaB_2 > NbB_2$. The oxidation rate of the borides increases in the presence of water vapour. However, the controlling factor is the surface layer of oxide formed at low temperatures. This layer prevents further oxidation, until B_2O_3 volatilises (above 1500°C), unless the oxide is mechanically removed. A typical boride feature is the possibility that the metal oxide skin may be a glass former with B_2O_3 and this increases oxidation inhibition. TiB_2 and ZrB_2 have good oxidation resistance up to 1400°C and 1300°C respectively. They oxidise parabolically to TiO_2 and ZrO_2. The NbB_2 oxidises rapidly and linearly at 1200°C. The MoB_2 is less adequately protected because MoO_3 is volatile at low temperature. The CrB_2 can endure 1700°C because chromium forms stable borates. All borides are stable to high temperatures in the presence of nitrogen. The TiB_2, ZrB_2 and CrB_2 are all soluble in molten titanium because they form eutectics. Nevertheless, they are very resistant to molten Al, Cu, Mg, Sn, Bi, Zn, and Pb. In general, the borides are strongly wetted by and slightly soluble in Al. All borides are resistant to non-oxidising salts such as molten fluorides and metallurgical slags but they are not resistant to oxidising melts like hydroxides, nitrides, carbonates and peroxides.

Comparing boride, carbide and nitride properties leads to the following conclusions [7,11,12]:

1. The melting point, hardness and electrical conductivity of the borides are comparable to the carbides and nitrides.

2. The inertness to non-oxidising reagents, the resistance to oxidisation at red-heat and the stability of the borides are enhanced when compared to the carbides and nitrides. Thus, the chemical resistance and oxidation resistance are superior to most ceramics.

3. All borides, carbides and nitrides are refractory compounds.

4. The borides and carbides have high hardness, a high melting point, high stability, a low thermal expansion coefficient, better adherence to metallic substrates but also high interaction tendency with other materials compared to the nitrides.

5. The borides have moderate strength and toughness compared to other ceramics.

6. The thermal conductivity of the borides is generally high compared to other ceramics.

Commercially the most important borides are CrB, CrB_2, TiB_2 and ZrB_2. Some of the industrial applications for the borides are outlined below [11,12,13,15,16]:

♦ The diborides are used as coatings on turbine blades, combustion chamber liners, rocket nozzles and rocket nose cones for heat and abrasion resistance.

♦ The TiB_2+BN composites are used to improve electrical resistance and electrical heating, including crucibles for the evaporation of Al in the vacuum metallising industry.

♦ Pump parts are made from CrB_2 or CrB_2-Fe composite to resist molten Zn, Cu, Al and Mg at 600°C.

♦ The hexaborides in particular LaB_6 are used as electron sources for the SEM.

♦ The hexaborides and a variety of borides are used as additives in both ferrous and non-ferrous metal industries.

♦ The ZrB_2 platelet-reinforced ZrC-Zr cermets are used as rocket engine components, wear parts and bio-materials.

♦ The ZrB_2-based composites have been used in components of supersonic aircraft.

The most attractive borides are the diborides of the transition metals. Their attractive properties are high specific strength, high specific modulus, high hardness and high melting point with good oxidation resistance up to 1400°C.

A review of the literature has resulted in table 1.2 for physical and mechanical properties of the diborides. The scatter in the values for different sources could be due to different loads or different grain size and porosity within materials of a given composition.

Physical Properties of the Diborides							
Boride	Composition (wt% Boron)	Structure	Lattice Parameters (Å)	Melting Point (°C)	Electrical Resistivity ($\mu\Omega$cm)	Thermal Conductivity (cal/cm/sec/°C)	Thermal Expansion Coefficient ($10^{-6}K^{-1}$)
HfB_2	10.81	HCP	a=3.14 c=3.48 c/a=1.11	3250	12 (25°C)	0.138 (1600°C) 0.310 (2000°C)	6.3 (27-1027°C)(a) 5.5 (25-1000°C)
TaB_2	10.68	HCP	a=3.08 c=3.23 c/a=1.05	3100	68 (25°C) 14-68(b) 14(c)	0.276 (260°C) 0.103 (2200°C)	8.2 (27-1027°C)(a) 5.72 (25-2200°C)
ZrB_2	19.17	HCP	a=3.17 c=3.53 c/a=1.11	3060 3245(c)	9-16(25°C) 7-10(b) 6(c)	0.104 (260°C) 0.060 (1920°C)	5.9 (27-1027°C)(a) 7.5 (25-1350°C)
CbB_2	18.89	HCP	a=3.09 c=3.30 c/a=1.07	3000	32 (25°C)	0.040 (25°C) 0.047-0.062 (200°C)	
TiB_2	31.12	HCP	a=3.03 c=3.23 c/a=1.07	2980 3225(c)	10-30(25°C) 60 (1000°C) 9-15(b) 7(c)	0.141 (50°C) 0.107 (1000°C)	4.6 (27-1027°C)(a) 7.8 (c) 6.4 (25-1250°C)
CrB_2				1950(b) 2188(c)	21-56(b) 18(c)		10.5 (27-1027°C)(a)
MoB_2				2250(b)	20-40(b)		
VB_2				2747(c)	13(c)		7.6 (c)
NbB_2				3036(c)	12(c)		8.0 (27-1027°C) (a)
a-Ref.12; b-Ref.11; c-Ref.7							

Physical and Mechanical Properties of Diborides (Cont.)						
Boride	Density $(g.cm^{-3})$	Hardness $(Kg.mm^{-2})$	Modulus of Rupture (GPa)	Modulus of Elasticity (GPa)	Compressive Strength (GPa)	Poisson's Ratio
HfB_2	11.2			500GPa (a)		0.12(a)
TaB_2	12.6	$2530K_{100}$ (25°C) 2100(c)		252 (37×10^6psi) (25°C) 680 $(680KNmm^{-2})$ (c)		
ZrB_2	6.1	$1915K_{100}$ (25°C) 2250(b) 2300(c)	$0.20(29\times10^3psi)$ (25°C)	$340(50\times10^6psi)(25°C)$ $540(540KNmm^{-2})$(c) 343GPa (a)	$1.14(230\times10^3psi)$ (25°C) $0.2(29\times10^3psi)$ (25°C-tensile)	0.11(a)
CbB_2	7.2	$1820K_{200}$ (25°C) $1260K_{200}$ (900°C)		163-299 $(29\text{-}44\times10^6psi)$ (25°C)		
TiB_2	4.5	$3370K_{100}$ (25°C) $860K_{100}$ (900°C) 3000(c) 3350(b)	$0.24(35\times10^3psi)$ (25-2000°C)	$408(60\times10^6psi)$ (25°C) $560(560KNmm^{-2})$(c) 530GPa (a)	$0.7(97\times10^3psi)$ (20°C) 1.3GPa (a)	0.11 (a,d)
CrB_2	5.20(b) 5.58(c)	1800(b) 2250(c)		$540(540KNmm^{-2})$(c) 211GPa (a)	1.3GPa (a)	
MoB_2	7.70(b)	1200 (b)				
VB_2	5.05(c)	2150 (c)		$510(510KNmm^{-2})$(c) 268GPa (a)		
NbB_2	6.98(c)	2600 (c)		$630(630KNmm^{-2})$(c) 637GPa (a)		
a-Ref.12; b-Ref.11; c-Ref.7; d-Ref.17						

Table 1.2. Physical and mechanical properties of refractory diborides [15]. Properties determined on polycrystalline material prepared by powder metallurgy techniques with 5-15% porosity and 2-5% impurity.

The thermodynamic results for diborides are shown in the table 1.3. The enthalpies of formation are strongly correlated with Gibbs´ free energies because the entropy is small. This also means that the free energy is relatively insensitive to temperature. The stability of the diborides decreases in the order HfB_2>TiB_2; ZrB_2>>TaB_2; VB_2>>>CrB_2 [12].

Borides	Heat Capacity at constant pressure, Cp (J/mol.K)			Enthalpy of Formation ΔHf at 1 atm. (KJ/mol.)			Gibbs' Free Energy of Formation, ΔGf at 1 atm (KJ/mol.)		
Temperature	298 K	1000 K	2000 K	298 K	1000 K	2000 K	298 K	1000 K	2000 K
CrB_2	53.59	85.07	-	-94.14	-94.02	-	-91.37	-85.52	-
HfB_2	49.45	81.67	-	-335.98	-334.9	-	-332.20	-324.49	-
TaB_2	48.19	76.77	96.71	-209.20	-209.77	-208.02	-206.53	-200.18	-191.02
TiB_2	44.28	76.89	94.54	-323.84	-326.59	-347.87	-319.69	-308.34	-347.87
VB_2	46.98	80.85	160.28	-203.76	-203.69	-202.02	-200.60	-193.19	-183.20
ZrB_2	48.37	71.99	82.66	-322.59	-326.65	-309.99	-318.16	-306.34	-279.60

Table.1.3. Thermodynamic data for diborides [12].

Refractory diborides are potential candidates for aerospace structural materials and are a possible new ceramic for other applications because of their unique combination of oxidation resistance and strength retention at high temperatures, as mentioned earlier. For all these reasons, considerable research has been done in this area. This is particularly the case for TiB_2 as a very stable hard refractory compound that offers a unique combination of exceptional and useful properties as summed up in figure 1.5 [11,15,16,18,19,20,21]. In the scope of this project the TiB_2 will receive particular attention.

THE TITANIUM DIBORIDE STRUCTURE
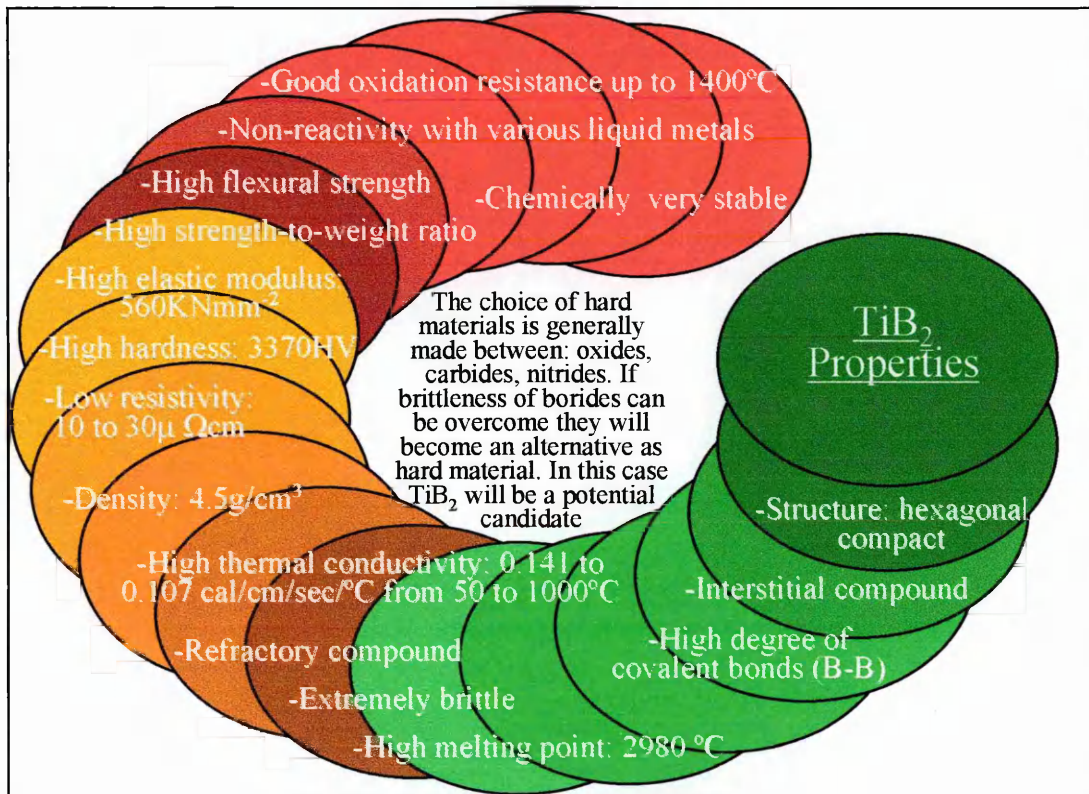
Figure 1.5. The main properties of titanium diboride.

11

The titanium diboride structure is dominated by the two-dimensional network boron configuration with covalent B-B bonds. The TiB_2 crystal structure shows properties of high hardness, brittleness, high electrical conductivity and good chemical stability [18]. The fracture toughness values for bulk TiB_2 that have been reported range from 4.9 to 6.0MPa$\sqrt{m}$. However they are lower than indentation or single-edge notched beam values which are in the range 6.7 to 8.0MPa$\sqrt{m}$ [12].

A coefficient of friction of 0.4 for TiB_2 has been quoted in reference 12. The counter face was not stated. This study was for TiB_2 with grain size of 0.8μm and has been reported at room temperature as having a linear decrease to 0.2 at 1000°C.

The yield strength of TiB_2 is greater than any other ceramic compound except high purity SiC. A high-temperature plastic yielding mechanism was observed and a Hall-Petch dependency on grain size resulted in an activation energy of 308kJ.mol⁻¹, in vacuum, for temperatures between 1750 to 2000°C [12].

The thermal conductivity as a function of temperature for TiB_2 makes TiB_2 an excellent choice for heat dissipation at high temperature as referred to in figure 1.6. The hexagonal structure of TiB_2 causes a thermal expansion anisotropy. The expansion along the c-axis is greater than along the a-axis. This difference is about 42% from 25 to 930°C and increases for T>930°C. The thermal expansion anisotropy causes internal stresses and microcracking during cooling. The microcracking occurs within the grains and at grain boundaries causing a degradation of mechanical properties [21].

Chemical dissolution could become the main wear mechanism at high temperatures for cutting tools. As TiB_2 is very soluble in iron, then it is not an option for machining steels. One can envisage the wear-protective coatings based on TiB_2 could be successful in cutting Al and its alloys because its solubility in Al is very low [18].

TiB_2 can be used in air up to 1400°C, but above this temperature the oxidation rate increases rapidly. It is resistant to graphite up to 2200°C. The maximum working temperatures in reducing or inert atmospheres is above 2000°C [16,22].

The TiB_2 is illustrated in the Ti-B phase diagram in figure 1.7. It has a narrow homogeneity range. This means that the non-metal to metal ratio does not allow the control of properties. However, the twin reactions $Ti_2B \rightarrow TiB+Liq.$ and $TiB \rightarrow Ti_2B+TiB_2$ should be noted as this implies that, over a certain limited temperature range, the structure changes rapidly from isolated to chain to network types [7,12,14].

The main research on TiB_2 is directed toward assessing its potential as a future high-temperature material. Nevertheless, TiB_2 is an attractive candidate in various technological engineering applications where erosion, corrosion, high temperature and electrical conductivity are required [11,12,16,20,21,22], for example:

◆ Cutting tools, wear parts and mechanical seals

◆ Valve trim for erosive environments

◆ Armour plating due to high Young's modulus

◆ Thermocouple protection tubes in Al reduction cells

♦ Sliding electrical contacts

♦ Electrodes in metal extraction

♦ Cathodes in Hall-Heroult reduction cells for processing molten aluminium

♦ Corrosion and wear resistant coatings in metallurgical and chemical industries

♦ TiB_2 films as diffusion barriers between ohmic metallic contacts and the semiconductor substrate (silicon or GaAs)

♦ Aerospace structural materials

♦ Surface coatings of first-wall components

♦ Electrodes in polycrystalline silicon thin film solar cells

♦ Magnetic recording industry.
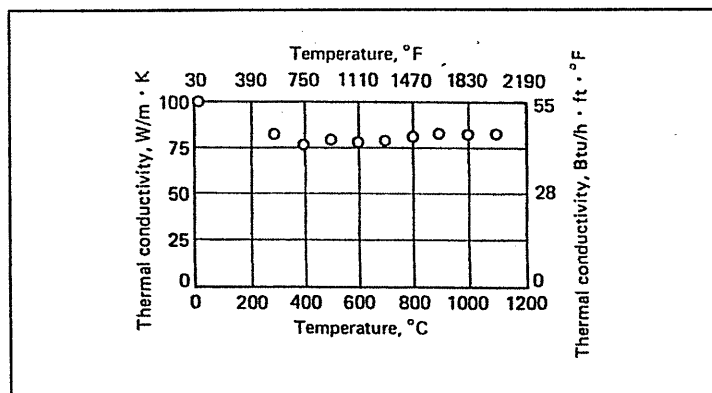
Figure 1.6. Thermal conductivity versus temperature for TiB_2 [12].
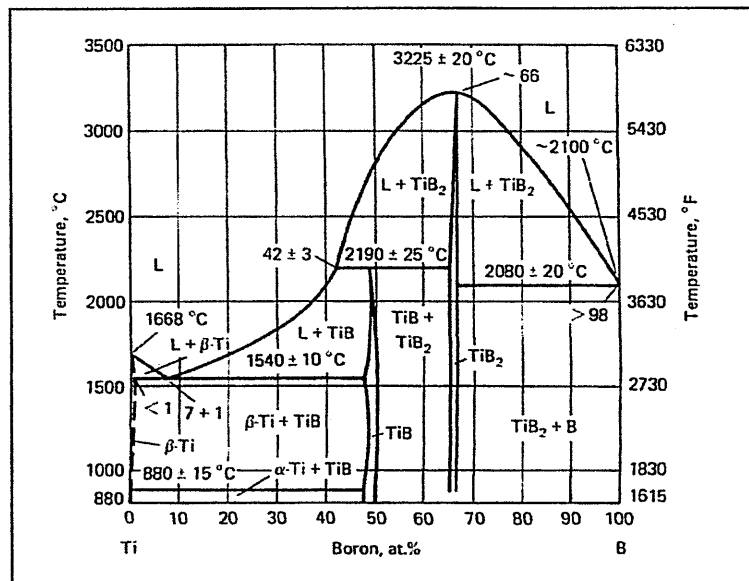
Figure 1.7. Binary phase diagram of Ti-B [12].

1.2. BRIEF REVIEW OF HARD COATINGS

```
LAYOUT
⇓
Surface Engineering Definition and Advantages
⇓
Factors Which Determine Coating Properties
⇓
Criteria of Material Selection: Analysis of Interface
Composites
⇓
Advantages of Multilayer Coatings
⇓
Key Points in Manufacturing Multilayer Coatings
⇓
Main Group of Hard Coatings
```
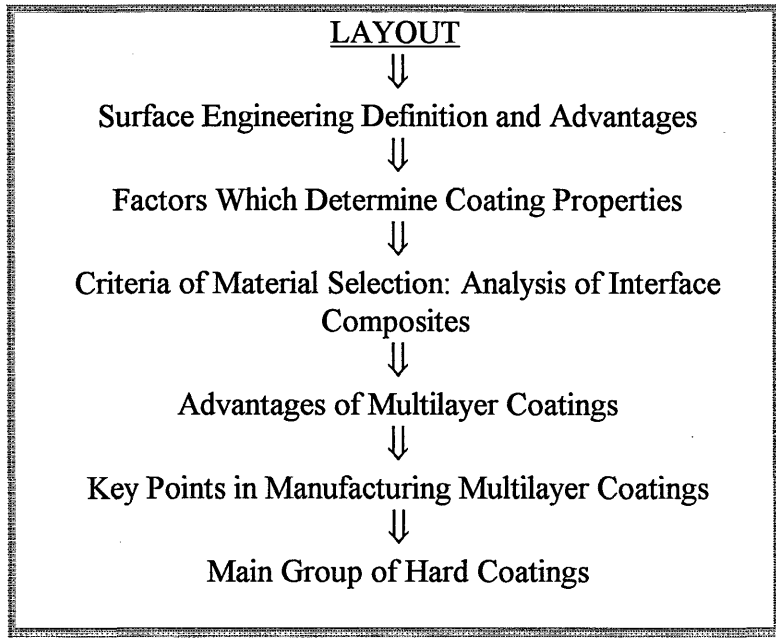
Nowadays, operating conditions in some systems, for high technology applications are so demanding in terms of power/weigh ratio and lifetime that bulk material components do not have the required properties. To minimise some of these situations, three approaches have been reported, namely: to develop new types of matrix alloys or to use surface treatments or to apply hard coatings. The decision is determined by the specific application [5].

Of these approaches, the use of surface engineering, for example, the protection of materials by hard coatings, has been proved to be one of the most important and versatile routes to improving component performance over the last two decades. The trend is towards moving from single coatings to coatings of complex composition or multilayer coatings and so custom-design the performance of the coating system [23,24].

Surface engineering has been defined by Strafford et al [24] as a field encircling techniques or processes used to induce, modify and enhance the performance of surfaces regarding wear, fatigue, corrosion and bio-compatibility. The following examples emphasise certain improvements in the area of wear resistant coatings [24,25]:

♦ A thin layer of hard refractory compound such as TiC, TiN, or Al_2O_3 could prevent microweldings between workpiece and cutting tools (high-speed steel or cermet carbide) and also improve the tool life by a factor of 300 to 800%.

♦ Thin hard coatings of borides, carbides, nitrides and oxides, both in single or in combination or multilayer design are now available commercially, e.g. cutting tools coated with TiN, TiAlN, TiC/Al_2O_3/TiN.

♦ Erosion resistance has been another area for hard coatings applications such as: the erosion in energy conversion device components due to the interactions with

gases or liquid particles; the erosion in compressor blades in gas turbine engines that results in loss of power, loss of surge margin and increased fuel consumption; reduction in operating lifetime of coal gasification plants and slurry pipelines due to the erosion of various valves, seals, bearings and fittings.

The constitution of the material system and fabrication parameters determine the microstructure of the coating [7,24,26]. All these factors are reflected in coating properties and consequently, influence the performance of the coated component, as illustrated in figure 1.8.
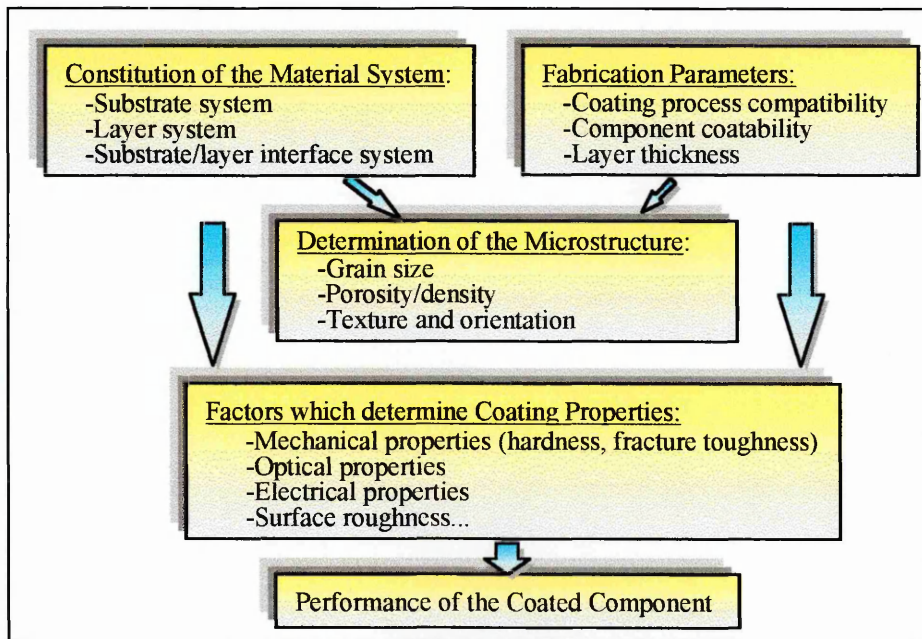
Figure 1.8. Factors which determine performance of the coated component.

The full knowledge and understanding of the interrelations between the three elements of coating technology - constitution of the material, fabrication parameters and microstructure - and the capability of manufacturing new materials and microstructures will certainly go one step further in the optimisation of coatings for specific applications. This will lead to further major developments in advanced and guaranteed material performance [7,27].

The hard coating area has seen rapid development and the number of applications and types of coating have grown sharply over the last decade. Nevertheless, the fundamental understanding of coating microstructures and properties is still lacking, as the following examples show:

♦ The properties and characteristics of coatings are very variable and strongly influenced by processing variables. For example, the processing variables for the sputtering technique include: substrate finish conditions, bias voltage, gas composition, substrate temperature and equipment details. To understand more fully these interactions, in order to generate reproducible properties and characteristics of the coatings requires more systematic research, but can now be

15

aided by computer processing/manufacturing operations, allowing maximum efficiency in manufacturing to be achieved [24].

♦ In many cases, coatings are grown at high rates, low temperatures and under an impinging ion flux resulting in supersaturated or amorphous solid solutions and metastable structures with entrapped noble gas impurities. These coatings often exhibit high internal stress levels and high hardness. Because of the lack of knowledge of nucleation and growth processes in these non-equilibrium structures, as influenced by the processing parameters, it is difficult to correlate microstructure with measured physical properties. This lack of knowledge limits the wide usage of these new metastable materials in hard coating systems [5].

♦ The possibility of predicting the constitution of multicomponent layer or layered materials is lacking and the physicochemical basis of nanostructures in material science is still being researched [27,28].

♦ The erosion response of a material is a complex function of the eroded material properties (hardness, elastic modulus, fracture toughness), the velocity and angle of impingement of the particles and the parameters defining the erosion environment. Understanding why a set of process parameters influences the erosion rate should aid the design of new coatings for erosion resistance and help in the prediction of their lifetime in an erosive environment [7].

♦ The understanding of strengthening mechanisms for multilayer coatings is still not complete [24].

To summarize from the example above; for a coating system to be successful and functional, it should be designed ab initio rather than as a last recourse to fix an inadequately performing component or tool [24].

The key point in designing successful coating technology is to pinpoint the material selection. From a microanalysis point of view, the factors that influence the material selection are: life time, which is directly interrelated with the service environment, and function, risk, material, design, data and cost, although each of these factors has different parameters to be considered as outlined in figure 1.9.
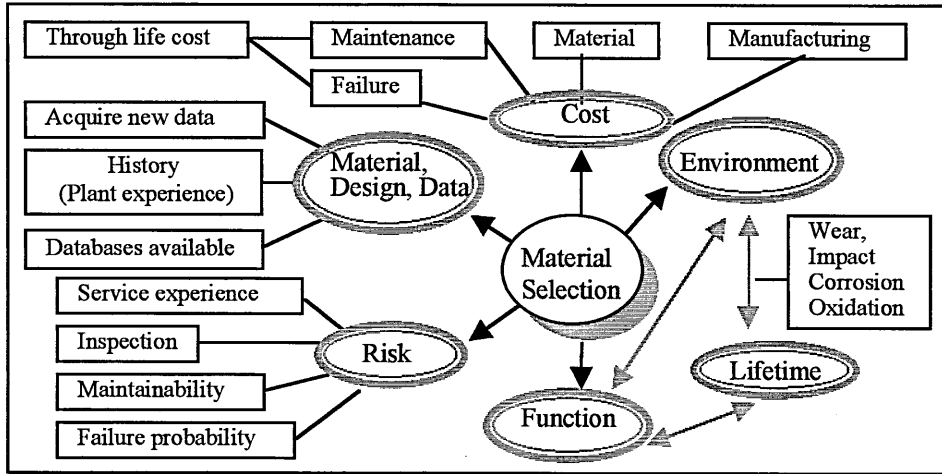
Figure 1.9. Factors that influence material selection.

When considering materials for advanced, and often expensive, industries like nuclear, aerospace and bio-materials, material selection could become very complex. A criterion is needed for selecting the most suitable material for specific applications. This is a difficult task because the requirements for the composite substrate/layer/environment are often stringent and clashes often require many compromises to be made.

For example, increasing hardness, strength, with no surface interactions of the coating are concomitant with decreasing toughness and adherence to the substrate/layer interface. Thus high hardness/strength and good toughness cannot be obtained at once in a single layer of material. In this case, then, a monolayer coating cannot match these differing requirements. However, multilayer coatings may achieve this compromise and therefore, seem to be the best option.

A criterion for a composite coating/substrate system is described in figure 1.10, in which are identified three sub-systems, each one providing a different property requirement [7,24,26]:

1. *Layer surface/environment system*: Interface between the coating and the environment or work material.

2. *Layer system*: Single or multilayer coatings.

3. *Substrate/layer interface system*: Interface between the coating and the substrate.

Considering the main characteristics of the scale of hard materials against the criteria outlined in figure 1.10, it may be possible to design coatings with different property requirements. However, one must be aware when designing substrate/coating composite systems that the system involves two types of solid interface: substrate/coating interface and multilayer coating interfaces. The properties of these interfaces are a critical influence on coating performance.

System	General Features	Main Properties	Interactive damage Mode/Process
Working Environment	Liquid / Gas / Solid → Metallic Inorganic Organic; Ambient / Operating → Temperature Pressure ...	•Chemical •Physical •Mechanical	Corrosion / Wear → Abrasive Adhesive Erosive Fretting
Interface Surface Layer / Environment			
Coating	Solid → Ceramic Metallic Polymer	• Chemical, physical, mechanical • Reduction in surface temperature: low thermal conductivity, low radiative heat transfer, high emittance • Oxidation resistance: thermodynamically stable with slow growth rates • Erosion resistance: hard, dense material	Loss of coherency
Interface Coating / Substrate			Interdiffusion
Substrate	Solid → Metal Ceramic Plastic	•Chemical •Physical •Mechanical	Loss of adhesion

Layer Surface System:
•Interaction layer/workpiece.
•Interaction layer/environment.

Coating System:
• Composition of the layer or layers
• Microstructure of the layer or layers.
• Mechanical compatibility: hardness, strength, toughness, internal stresses.
• Strain accommodation mechanisms.
• Coating cohesion.
• Thermal conductivity.
• Thermal stability.

Substrate/Coating System:
• Adhesion.
• Strain by thermal expansion misfit.
• Interaction or reaction of substrate/coating.

SUBSTRATE

Figure 1.10. Main features of a working substrate/coating composite system.

SUBSTRATE/COATING INTERFACE:

The thermal expansion coefficient of the coating and substrate material are of concern when high temperatures are reached during manufacturing or service. The thermal expansion coefficient of coating and substrate materials seems to be a function of their bonding character, for example whether covalent, ionic or metallic, which also determines their hardness [7].

Severe constraints apply to the coating/substrate composite. For wear applications, the adherence of the substrate/coating interface should withstand the high forces and high temperatures developed near the cutting tip.

The coating adhesion must be sufficiently high that the stresses do not result in delamination at the substrate/coating interface [29]. Both the thermal stresses and those caused by the difference in elastic properties between the coating and substrate should be made as low as possible up to the point that the stress levels do not cause failure. The intrinsic stresses generated during growth of the film can also be detrimental to adhesion. The chemical and metallurgical compatibility between coating and substrate is of importance to avoid excessive interdiffusion and chemical reaction during service [5,26].

18

MULTILAYER COATING INTERFACES:

Cracking generated in the coating may cause crack initiation in the substrate and thus a complete failure of the component. In spite of this, the mechanical strength and toughness of the multilayer coating itself should be as high as possible. Also, the toughness of hard coatings influences the flank wear in metal cutting. The mechanical strength depends upon the number of layer boundaries which influence the dissipation of crack energy and crack deflection. Nevertheless, annealing treatment of hard coatings deposited at low temperature can provide an increase in strength and resistance to crack propagation in the layered material, because the annealing treatment results in reduced internal stress [5,26].

A knowledge of the composition of the layer boundaries is important for the interpretation of the mechanical properties and the wear behaviour of sequential coatings. The effect of both extrinsic and intrinsic stresses within the layers on the internal strength and hardness of the coatings, must also be considered [5].

Many of the relations between constitution and properties known for bulk materials can be used to optimise coating materials [7,25,30]. Research on solid bulk materials suggests three possibilities of interface, illustrated in figure 1.11 [4,7]:

1. Coherent

2. Partially coherent interface with a boundary phase

3. Uncoherent interface, i.e., interaction-free phase boundaries

Interfaces between metallic hard materials and metals or other metallic hard materials are often able to form coherent or semi-coherent bonding. As a result low interfacial energy with optimum adherence can be obtained (e.g. TiC/TiB_2). Interfaces between metallic and ionic hard materials often show intermediate regions of variable composition (e.g. TiC/Al_2O_3). Interfaces between covalent hard materials seem to be quasi-interaction free with the consequence of detrimental adherence of the phases (e.g. B_4C/Al_2O_3) [7].

| (partially) coherent boundaries | phase boundary-(mixed) phase | interaction-free phase boundaries |
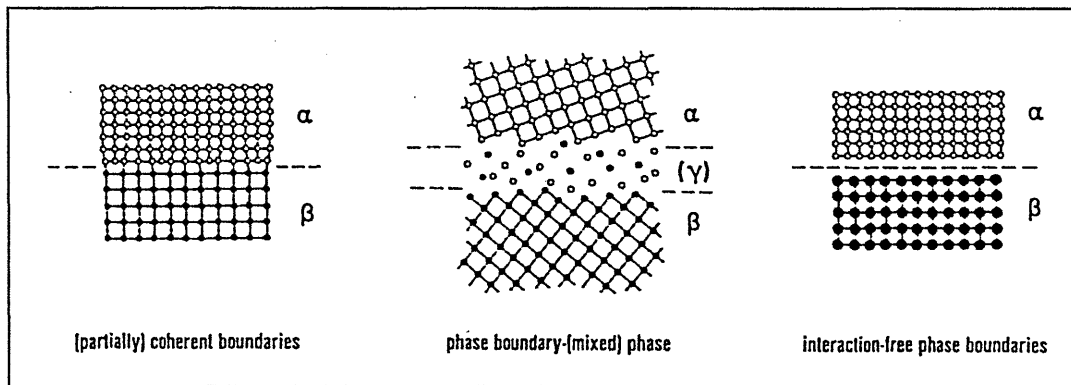
Figure 1.11. Different natures of phase boundaries [4,7].

The benefits of producing multilayer coatings have been recognised for some time. The phenomenon of increased strength by producing a laminate substrate of alternating thin layers of two metals was first proposed by Köhler in 1970 and

experimentally verified on Al/Cu and Al/Ag multilayer structures by Lehoczky in 1978[31,32,33]. The Composite of the two materials was proposed in order to have a shear modulus that was widely different for the two materials. The individual layers should be very thin (in terms of superlattice structures) in which case the Frank Read source cannot operate in either material and the dislocations become trapped at the interface. In this case the strength of the composite could be much greater than predicted by the rule of mixtures. This strengthening mechanism results from the difference in the dislocation-line energies of the two materials. Some considerations, in respect of interfacial stability for long term application, should be taken into account such as that the interfaces should remain sharp and interfacial reactions between layers should be avoided to maintain their strength [31].

Not all scientists agree with this theory and so no universal explanation of this phenomenon has yet been reached. However, it is generally agreed that multilayer films are beneficial in comparison with alloyed and monolayer films for many applications[7,27]. The main advantages offered by producing multilayer coatings are referred to in figure 1.12. Interstitial phases like nitrides, carbides and borides, including compositional or multilayer (superlattice) films, have shown outstanding properties such as hardness and wear resistance. This has been demonstrated in several systems: TiC/TiB_2, SiC/TiC, B_4C/TiB_2, TiN/ZrN, TiN/NbN, TiN/CrN, TiN/VN, TiN/NbN, $TiN/(Nb,V)N$, $TiN/(Ti,Nb)N$, TiN/Si_3N_4, TiN/CN_x [13,28].
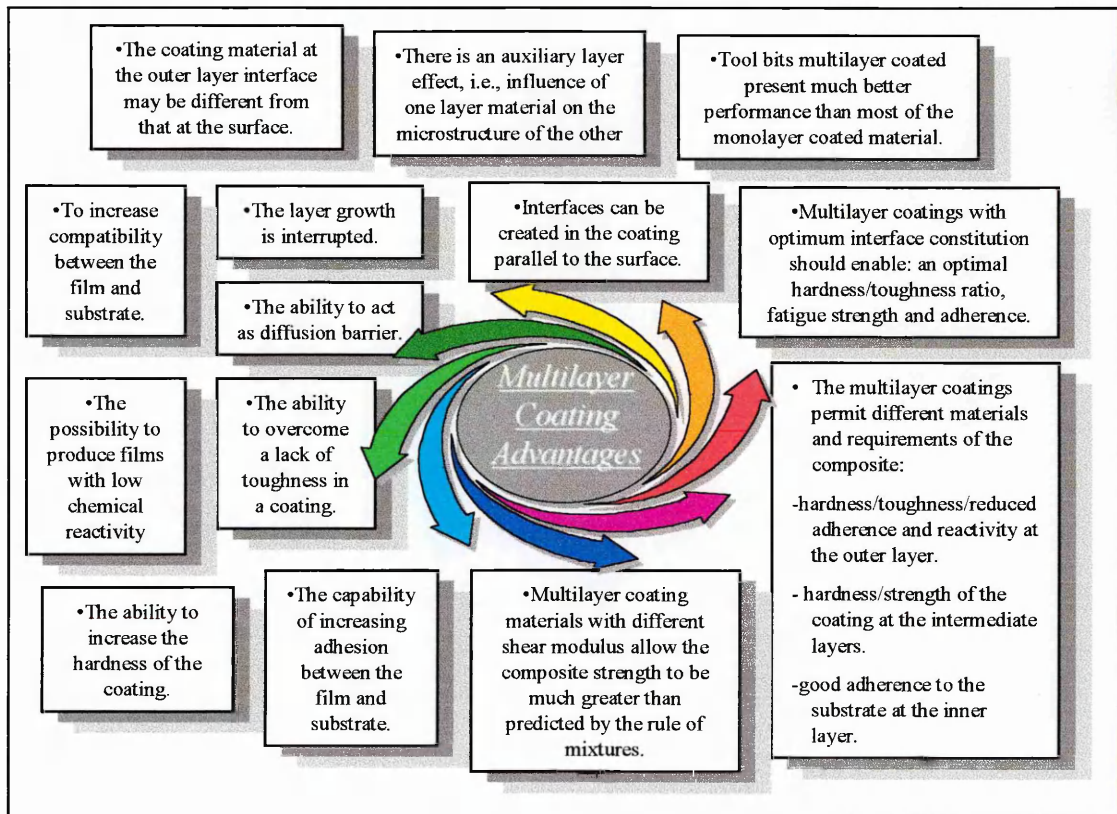
Figure 1.12. Multilayer coating's advantages.

Producing multilayer coatings requires special attention to material selection and manufacturing due to the factors outlined in figure 1.13 [7,31].
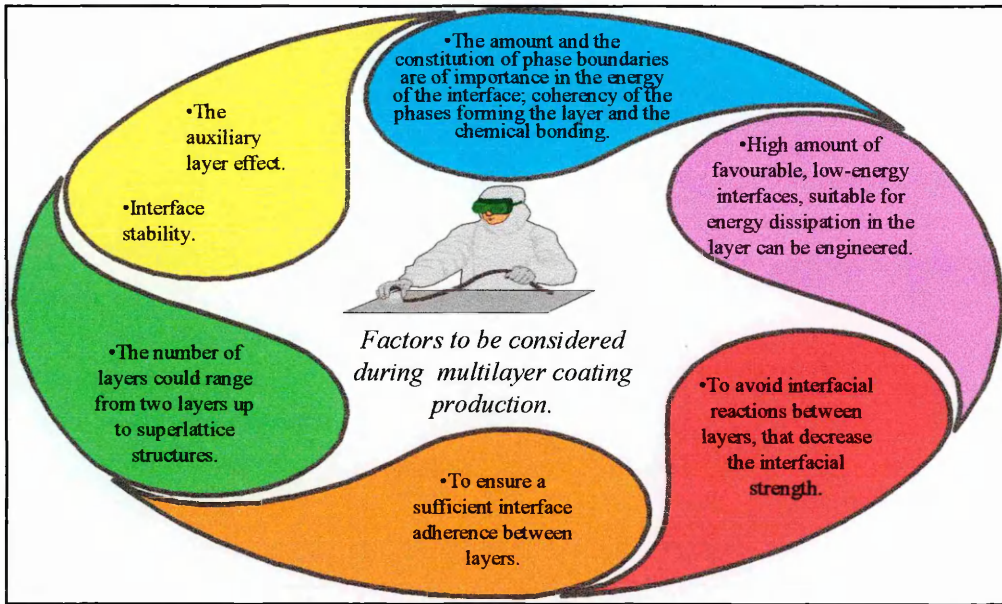
Figure 1.13. Factors to be considered during multilayer coating production.

Over the last few years ceramic coatings have been considered for a wide range of technological applications such as high temperature and wear resistance - in particular hard coatings as well as protective films for corrosion or thermal oxidation, owing to their chemical stability. However, hard coatings are not only made from ceramics. They can range from ultrahard materials such as diamondlike carbon through refractory compounds to alloys. The transition-metal carbides and nitrides, mainly titanium carbide and titanium nitride, have so far achieved the highest level of commercial success. However, other refractory compounds, such as oxides and borides, are being increasingly considered and used [5].

The main features of each group of hard coatings are described below[5,24,34,35,36,38]. The table 1.4 allows a comparison of key properties of many potential coating materials.

DIAMONDLIKE CARBON FILMS: These diamond films have been deposited by ion-assisted deposition techniques with a hardness range from 58.8 to 68.6GPa (6000 to 7000Kg.mm^{-2}) with a metastable structure. Owing to the fact that diamond at room temperature and atmospheric pressure is in a metastable state, operating conditions are very limited. The thermal stability limits working temperatures to 400°C.

NITRIDES: The transition metal atom nitrides, especially group IV (Ti, Zr, Hf) have been used extensively. The main applications range from wear-protection films in cutting or forming tools to optical films and diffusion barriers in integrated circuits. The groups IV and V have either a B$_1$-NaCl structure (TiN, ZrN, HfN, VN) or hexagonal structure (NbN, TaN). TiN films grown by PVD techniques have improved oxidation resistance at 500°C to 850°C if Al is incorporated in the structure, giving a TiAlN coating. This is produced by a reactive co-sputtering process. The cubic boron nitride (c-BN) is, next to diamond, the hardest material known and has been grown by CVD and PVD techniques with hardness in the range from 19.6 to 46.1GPa (2000 to 4700Kg.mm^{-2}). However, the

i-TiN coatings have been reported with a hardness range from 39.2 to 68.6GPa (4000-7000Kg.mm^{-2}) depending on the deposition conditions.

CARBIDES: The transition metal carbides from group IV (TiC, ZrC, HfC) are used mostly. In addition, the group V (VC, NbC, TaC) and group VI (CrC, MoC, WC) carbides as well as boron silicon carbide are being used. All mono-carbides in groups IV and V have a B_1-NaCl structure, while group VI carbides have more complex structures. The hardness of the carbides is in general higher than the corresponding nitrides due to a more pronounced covalent bonding.

OXIDES: Several oxides are used as hard coatings due to their extreme chemical stability. The low transverse rupture strength is a limitation for them as hard wear-protective coatings. Oxides grown from the vapour phase are Al_2O_3, ZrO_2 and TaO_2. Most oxide coatings are used because of their specific optical or electrical properties.

BORIDES: Boride coatings have not been studied as much as carbides and nitrides due to their inherent brittleness. However, they exhibit similar properties to the carbides and nitrides but these are somewhat greater, like hardness, due to the higher degree of covalent bonding in the boride structures. Borides are very inert and chemically stable and this explains their use in some applications such as protective coatings of TiB_2 and ZrB_2 for wear resistant coatings. Most boride coatings are prepared by CVD and PVD, such as TiB_2, ZrB_2, HfB_2, TaB_2. The ZrB_2 coatings are softer than TiB_2 but have higher corrosion resistance.

MIXED COMPOUNDS: The utilisation of mixed compounds is a continuing challenge where different requirements can be established in a coating for specific applications. Coatings that not only have the same chemical stability as oxides but also a considerably higher strength can be achieved by mixed compounds such as oxynitrides or carboxynitrides (TiC_xN_y) or oxycarbonitrides ($TiC_{0.34}O_{0.32}N_{0.24}$). The latter has a maximum hardness of 43.2GPa (4400Kg.mm^{-2}). TiAlN films have been reported with maximum hardness around 34.3GPa (3500Kg.mm^{-2}), depending on N_2 flow rate.

METALS AND ALLOYS: The most commonly used metals are Cr, Mo-Ta, NiFe, M-Cr-Al-Y. Metal and alloy coatings never reach the same hardness values as compound coatings do. In addition, as the substrate temperature is increased, the hardness of the metal and alloy coating decreases, in contrast to the behaviour of most of the refractory compound coatings over normal temperature ranges for component operation.

In conclusion, the research on ceramic, interstitial phases and hard coatings, either as mono or multilayer thin films, is still not complete. This is in part a result of the lack of methods for producing reproducible, high quality films. The extended studies of such hard films that are currently ongoing, have only been possible over the past 10-15 years following the development of advanced technology techniques for deposition of these coatings such as: electron-beam evaporation, magnetron sputtering, plasma-assisted CVD (PACVD), plasma-enhanced CVD (PECVD) [28].

Materials	CARBIDES											BORIDES								
	B_4C	SiC	TiC	ZrC	H_fC	VC	NbC	TaC	Cr_3C_2	Mo_2C	WC	TiB_2	ZrB_2	H_fB_2	VB_2	NbB_2	TaB_2	CrB_2	MoB_2	W_2B_5
Crystal Structure	Rhom.	Cubic	Cubic	Cubic	Cubic	Cubic	Cubic	Cubic	Ostho.	Hexa.	Hexa.	Hexa.	Hexa.	Hexa.	Hexa.	Hexa.	Hexa.	Hexa.	Hexa.	Hexa.
Melting Point (K)	2700	2200-2700	3340 ±15	3693 ±20	4203 ±20	2972 ±50	3772 ±75	4152 ±28	2166	2777 ±16	3050	3144	3311	3522	2700	3272	3366	2422	2747	2638
Density (g/cc)	2.52	3.14	4.92	6.56	12.67	5.48	7.82	14.50	6.68	9.12	15.80	4.52	6.09	11.02	5.10	7.21	12.60	5.60	7.78	13.10
Specific Heat (J/Kg.K)		670										963								
Thermal Conduc. (W/m.K)	31	87.1	33									25.3								
Thermal Exp. Coeff. (10^{-6}/°C)	4.5	4.02	7.4-8.6	7.0-7.4	6.6	6.5	6.6	6.3	10.3	10.3	4.3	8								
Elastic Modulus (GPa)	289-454	406	447	358	316-461	268-420	330-537	241-722	385	227	688	480			260					
Hardness (Kg/mm²)	3200	2800	3200	2600	1900-2100	2000-3000	1900-2600	1600-2400	1350-2280	1500-1800	1700-2400	3370			2800	2500-2900	2000			
Poisson's ratio	0.19	0.24	0.19	0.19	0.18	0.22	0.22	0.24			0.19									

Materials	NITRIDES											OTHERS					
	BN	Si_3N_4	TiN	ZrN	H_fN	VN	NbN	TaN	CrN	MoN	WN	Al_2O_3	Diamond	HSS	Cemented carbide	Cast Iron	SiAlON
Crystal Structure	Cubic	Hexa	Cubic	Cubic	Cubic	Cubic	Cubic	Hexa.	Cubic	Hexa.	Hexa.	Hexa.	Cubic				
Melting Point (K)	1770		3223 ±50	3253 ±55	3660 ±43	2450 ±139	2477	3366 ±44	1772	1022	873	2300	>3550	1300		1500	
Density (g/cc)	2.08	3.20	5.44	7.35	13.94	6.10	8.36	14.36	6.14	9.18	12.10	3.90		7.90	15.0	7.20	3.25
Specific Heat (J/Kg.K)		710							711	293		1070			210	500	620
Thermal Conduc. (W/m.K)	188.3	18.0	24.0	12.6	12.6	12.6	4.2		12.0	17.0		8.0	1004	50.2	75	50	21
Thermal Exp. Coeff. (10^{-6}/°C)	4.8	3.2	8.0	7.9	6.9	8.1	10.1	3.6	0.7-3.1	1.8		6.9	1.0	12.0	4.5-6.0	12.0	3.0
Elastic Modulus (GPa)	41-65	220	251									400			580	150	280
Hardness (Kg/mm²)	4700	2200	2000	1500	1640	1500	1400	2400	1093			2500	8000-10000	850	1400	200	2000
Poisson's ratio		0.25										0.23			0.26	0.27	0.23

Table 1.4. Main properties of various coating materials such as: Borides, Carbides, Nitrides and others[24].

1.2.1. SINGLE-LAYER OR MULTILAYER DIBORIDE COATINGS

<div style="border: 2px solid black; padding: 10px;">

LAYOUT
⇓

Chronological review of single and multilayer TiB₂ or TiB₂-based coatings by CVD and PVD techniques:

- ◆ CVD: TiB_2; TiC/TiB_2; TiN/TiB_2
- ◆ Evaporation: TiB_2; TiB_2/Cu; TiB_2/TiN
- ◆ Sputtering: TiB_2; TiB_x; $TiB(N)$; TiB_2+Ni; TiC/TiB_2; TiB_2/TiN; SiC/TiB_2; B_4C/TiB_2; $(TiB_2+Ni)/Ni$; $(TiB_2+Ni)/Ni/Ti$; $(TiB_2+Ni)/Cr$
- ◆ Ion-plating: TiB_2

⇓

Other Diboride Coatings: ZrB_2; TaB_2; HfB_2

</div>
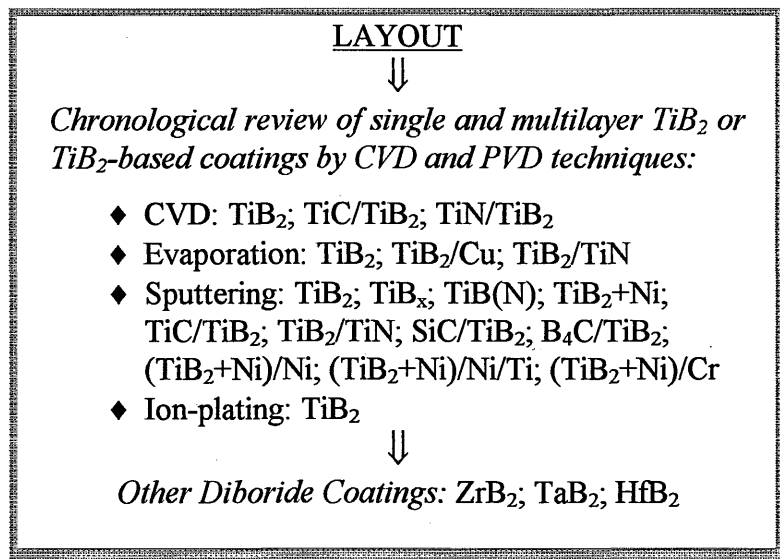
A review of the literature of recent years shows that some effort has been made to produce and also to improve the properties of, diboride coatings such as TiB_2 ZrB_2, TaB_2 and HfB_2. Most the research has been focussed on TiB_2.

Different techniques have been reported for producing diboride coatings, including: CVD, direct evaporation, reactive or non-reactive sputtering and magnetron sputtering. With specific regard to TiB_2 deposition a wide range of methods is reported and includes: vacuum plasma spraying, electrodeposition from a molten alkali metal borate bath [37], CVD from diborane, laser-induced CVD, direct evaporation from compact billets, electron-beam evaporation from a sintered TiB_2 target, ion-beam enhanced evaporation, magnetron sputtering, ion mixing.

Some attempts have been made to overcome their brittleness by multilayer coatings, reactive sputtering (N, C, BF_3, B_2H_6), or co-sputtering (Ti+B; Ti+B particles) and heavy ion bombardment (Kr, Ar, Xe). These approaches will be reviewed latter in this chapter, particularly focussing on the production of TiB_2.

TITANIUM DIBORIDE OR TITANIUM DIBORIDE BASED COATINGS (TiB₂):

A chronological review follows of titanium diboride based coatings for different methods of deposition.

1. CVD Techniques

H. O. Piersson et al [5,38] in 1980 reported amorphous and overstoichiometric TiB_2 films on graphite produced by CVD from diborine at $T_s < 500°C$. However, increasing the temperature, the films become crystalline at $T_s \cong 600°C$. The grain size increased from about 6nm at $T_s \cong 600°C$ to 110nm at $T_s \cong 1000°C$. A maximum hardness of 44.1GPa (4500Kg.mm^{-2}) was reported, which varied with process parameters such as:

deposition rate, amount of reactant, chlorine impurities, etc. The deposition temperature can cause stress relief, sublattice or vacancy rearrangements and atom mobility, which can explain the TiB_2 coating property variations with deposition temperature.

M. Kaminsky et al [39], in 1982 also used a CVD technique to deposit TiB_2. They reported that TiB_2 coatings are suitable for erosion resistance and plasma purity control for first wall components in fusion devices, owing to the total sputtering yield values of these coatings being lower than those for stainless steel. Moreover, the fusion plasma could be maintained with an atomic number close to 1 and thus reduce power loss, instability and improve plasma purity. This is due to the fact that the partial sputtering yield for B (low Z) is larger than for Ti (high Z) for the study range of energy. For example, at 10KeV the partial yield of B is 3.0×10^{-2}atoms/ion for Ti 2.4×10^{-2}atoms/ion, while for TiB_2 it is 4.0×10^{-2}atoms/ion. In this work stoichiometric TiB_2 coatings onto graphite were prepared by CVD for film thickness of 10-25μm. The coatings, after deposition, were bombarded by $^4He^+$ irradiation of 3 to 60KeV at room temperature. The ion beam current dose varied from 2×10^8 to 8×10^{20} ions/cm^2. The sputtered material was collected onto Al foils and analysed by RBS and AES. The partial yield of resputtered material for both polished and unpolished coating substrates shows a decrease with increasing ion energy. The partial and total sputtering yields for the as-deposited films are larger for the unpolished than those for the polished surface. This implies that the sputtering rate increases with the surface roughness due to charges in the incident angle.

Since 1969, TiB_2 has been selected as a diffusion barrier in integrated circuit metalization. The high-temperature processing of the CVD technique, in conjunction with good step coverage, are the reasons ensuring that this application is undertaken using a CVD process. PVD techniques have not been used because of problems with poor step coverage. Furthermore, L. M. William [40] in 1985 reported that TiB_2 can also be formed by plasma enhanced CVD (PECVD) producing coatings with resistivity of 200μΩcm. The glow discharge operates at 39Pa (0.3Torr) pressure and 20WRF power in $TiCl_4$, BCl_3 and H_2 gases mixture atmosphere. These films are smooth, shiny and crack-free at moderate temperature (480-650°C), with good step coverage. Previous reports have also mentioned that TiB_2 films deposited by evaporation and sputtering can reach lower resistivities but these had to be annealed. The resistivity of TiB_2 by evaporation and annealing (950°C) is 30μΩcm, by sputtering as-deposited 500μΩcm and after annealing (1050°C) is 150μΩcm. Nevertheless, the author suggests that the resistivity of PECVD films could be improved by high-temperature annealing and by optimisation of the deposition conditions.

In the same year, 1985, G. L. Platonon et al [23] reported that TiB_2 film on hard metal could be deposited from $BCl_3(BBr_3)+TiCl_4$ gas mixtures over a range of temperatures from 700-1100°C. The reaction between the substrate and the coating results in the formation of the compounds TiB and Ti_3B_4. The same author next concentrated on improving the wear-protective potentiality of TiB_2 using CVD techniques by producing TiC/TiB_2 and TiN/TiB_2 coatings of 4-8μm thickness. The TiC or TiN layer acted as a diffusion barrier between the substrate and the TiB_2 outer layer. As a result, the lifetime of hard metal tools coated with TiC/TiB_2 was improved from one and a half to twice that of a tool with a single layer of TiC. This is because of the much higher hardness and chemical stability of TiB_2 compared with TiC, both at room

temperature and at a working temperature of 1100°C (6GPa for TiB_2 and 2GPa for TiC). The TiB_2 composition in the range of 900-1100°C was close to stoichiometric. In the carbide/substrate interface a transition layer was formed of η-phase (Co_6W_6C) 2μm thick. The TiB_2 was found to adhere better to TiC than to TiN. The texture of the TiB_2 layer was found to be independent of the texture in the intermediate layer. The resultant stress, by X-ray diffraction was found to be compressive with a value range from -250 to -370MPa for deposition temperatures between 750 to 1100°C for TiC/TiB_2 coatings and range from -270 to -360MPa for deposition temperatures between 800 to 1000°C for TiN/TiB_2 coatings.

Elders et al [41] in 1991 produced TiB_2 films by laser-induced CVD (LCVD) and reported the hardness of the TiB_2 films to be higher than 29.4GPa (3000Kg.mm^{-2} for HV_{N25})

From the above, one can conclude that not only single layers but also multilayer coatings like TiC/TiB_2 can be deposited by CVD techniques and enhanced CVD processes [23,28]. The CVD processes have a major drawback when compared to PVD processes; they need to be processed at high temperatures because the chemical reaction occurs at a high temperature of about 927°C (1200K) and they use toxic gases [42].

J.-E. Sundgren et al, in a review published in 1986 [5] state that the hardness of TiB_2 films grown either by CVD or PVD increased with temperature up to a maximum value and then approached the bulk value of 33GPa (3370Kg.mm^{-2}). He also reported that films deposited by CVD seem to be somewhat harder than those deposited by PVD. Nowadays, it may not be wise to draw the same conclusion, as will be evident from the literature review on PVD deposited coatings.

2. Evaporation Techniques

Some attempts have been made to produce TiB_2 films by electron-beam or ion-beam enhanced evaporation processes. Electron beam and ion-beam evaporation sources are used instead of direct resistance and radiation, owing to the high melting temperature of the borides.

R. F. Bunshah et al in 1978 [43] reported that they were able to produce microcrystalline TiB_2 films at 600°C by activated reactive evaporation using an electron-beam source (ARE) from compact billets. The structure and composition of the films were observed to be dependent on the deposition rate. Increasing the temperature up to 1300°C the X-ray peaks became sharper and the films exhibited preferential orientation (001) for deposition rates of 0.2μm/min. At this rate the hardness increases with the deposition temperature (600-1150°C) from 24 to 29.4GPa (2445 to 3000HV). At a higher deposition rate of 6.3μm/min the film becomes boron deficient, especially at high temperature and at these high temperatures the films developed a fibrous morphology. The hardness varies from 12.5 to 32.2GPa (1275 to 3285HV) for temperatures in the range from 690°C to 1300°C. In conclusion, the deposition temperature had a strong influence on structure, preferred orientation, composition and cross-section microhardness over deposition rate. The same authors have studied the synthesis of mixed compounds using electron beam evaporation from multiple sources, producing

26

coatings such as 50TiC-50TiB$_2$ and 90(TiC-TiB$_2$)-10Co. The TiC-TiB$_2$ coatings developed a strong preferred orientation of (220) for TiC, which may explain the hardness value of 33GPa (3365HV) at 1040°C. The TiC-TiB$_2$-Co coatings showed two layer structures. Near the substrate the structure was smooth and recrystallized, while at the top layer it became smooth and fine. The preferential orientation was (111) for TiC with maximum hardness of 25.5GPa (2600HV) at 1090°C.

In 1981 C. Feldman et al [44], reported that evaporated TiB$_2$ films show values of resistivity lower than 30μΩcm after heating. Two layers of B/Ti onto Al$_2$O$_3$ were deposited by ion beam evaporation at T$_s$=500°C. The sputter ion beam used 10KeV Ar$^+$ ions at 5.3×10^{-5} Pa (4×10^{-7}Torr) pressure. A post heating of the films produces crystalline TiB$_2$. B/Ti films have excess boron following deposition when they form stoichiometric TiB$_2$ films during a post heating treatment.

S. N. Basu et al in 1990 [31] reported the production of TiB$_2$/Cu multilayer coatings on silicon by electron beam evaporation. The 24 layers of TiB$_2$/Cu were deposited at room temperature for a total thickness of 200nm starting with TiB$_2$. The substrate was previously coated with two layers: SiO$_2$ (250nm thick) and Ti (10nm thick) on top. This coating seems to fulfil the criteria of a large difference in the shear modulus, hence ensuring composite strength. No interfacial mixing was found due to the positive free energy change for any interfacial reaction in this layered system. The composite proved to be extremely stable against radiation damage and was suggested as an ideal candidate for high stability Köhler strengthening.

K. M. Hubbarad et al [32] undertook a similar project, conducting an investigation into hardness and tribological properties of Cu/TiB$_2$ multilayer coatings on steel with an intermediate layer of Ti. The system provides a combination of a high-strength but brittle ceramic, with a ductile metal for enhanced fracture toughness. Furthermore, thermodynamic analyses of Cu-Ti-B systems suggest that the formation of Ti-Cu compounds at the interfaces is negligible. This implies stability of the composite against ageing and thermal-induced interdiffusion. The films were deposited at T$_s$±200°C by electron-beam evaporation with 12 pairs of TiB$_2$/Cu layers. The Cu layer thickness was about 10% less than those of TiB$_2$ layers. The films were irradiated by 400KeV Ne ions to doses of 1.0, 6.0 and 12×10^{15}ion/cm^2, which resulted in an increased hardness and stability against radiation damage. X-ray diffraction analyses show that the Cu films were polycrystalline with a strong preferred orientation <111> while the TiB$_2$ was amorphous. The Cu/TiB$_2$ interfaces were found to be sharp without mixing, indicating that the stability against radiation damage is also good. However, significant ion-mixing was observed at the TiB$_2$/Ti interface. The hardness of the coating increased from 14 to 16.5GPa with the radiation damage. This may be due to the coalescence of point defects in the structure and dislocation mobility in the Cu layer. The composite has a hardness 18% greater than that predicted by the law of mixtures applied to the reference standard. However, the wear properties of the film were found to be poor because of the lack of adhesion at or near the substrate/coating interface. Thus, failure occurred at the substrate/multilayer interface and not in the Cu/TiB$_2$ layers.

In 1996, Yunjie Yang et al [45], reported the production of TiB$_2$ films and TiB$_2$/TiN or TiN/TiB$_2$ double-layer coatings, of 1μm thickness, by ion-beam-enhanced

deposition at ambient temperature. The coating design associates hard TiB_2 and relatively tough TiN to improve wear resistance. TiB_2 films were deposited from a sintered TiB_2 source by electron beam evaporation and xenon gas as ion bombardment. The evaporation rate was 0.6nm/sec and the ion-beam current density was $32\mu Acm^{-2}$. The ion energy was varied from 25KeV to 85KeV. The sub-layer thickness of the double-layer coating was 0.5μm. The AES analyses show an overstoichiometric TiB_2 film (B/Ti=2.1) and a uniform composition through the thickness. The HRTEM analyses demonstrated that the TiB_2 film microstructure is mainly composed of TiB_2 hexagonal nanocrystallites with an average size of several nanometers, except that the part close to the substrate is also amorphous. The TiB_2 structure without ion bombardment is amorphous. Increasing the ion energy of bombardment increases the hardness of TiB_2 film measured by nanoindentation up to a value of 39GPa for 85KeV Xenon ion bombardment. The corresponding elastic modulus was 230GPa. The high hardness may be due to the nano-crystallites formed in the coating. The tribological properties of the TiB_2 films were also improved with ion bombardment. The properties of both double-layer TiB_2/TiN and TiN/TiB_2 films do not exhibit significant differences from the single-layer TiB_2 films. Both, however, show an improved tribological behaviour (wear, adhesion) compared with the TiB_2 single-layer film.

As stated earlier in this section, low erosion yield and impurity release yield are required for plasma-facing material and coatings for some parts of a Tokamak fusion reactor. TiB_2 coating has been investigated by T. Nenadovic et al for this propose. They reported in 1996 [46], that the sputtering yield of crystalline TiB_2 coatings depends on the state of the surface (porosity and roughness), when bombarded with Ar^+ ions and a laser beam. Moreover, the sputtering yield values for TiB_2 were found to be lower than those for Ti. These values for TiB_2 are higher than those reported in earlier studies by M. Kaminsky et al. These TiB_2 coatings were prepared by electron-beam evaporation from TiB_2 billets at temperatures up to 3500°C. The film thickness ranged from 40nm to 1μm. The Ar^+ ion energy for sputtering yield ranged from 3 to 12KeV and the bombardment dose from 3.6×10^{17}-1.3×10^{19}ions/cm^2.

3. Sputtering Technique

The sputtering process has been the main PVD technique to produce TiB_2 films with controlled composition and structure at temperatures slightly lower than CVD processes [42], i.e. at about 600°C (870K).

K. R. Padmanabhan & G. Sørensen [47], in 1981 reported that heavy ion bombardment with an inert gas may improve the mechanical properties of TiB_2 films, but with some formation of blisters and flaking. Films of TiB_2 on stainless steel and silicon were deposited by RF sputtering at 500WRF in an argon (2.5×10^{-2}mbar) and Ar-BF$_3$ mixture (2×10^{-3}mbar BF$_3$ partial pressure). After deposition the films were implanted with B^+ and Kr^+ ions at 600KeV. The RBS spectrum has shown that TiB_2 films sputtered in argon have a ratio of Ti/B=0.66, whereas the reactively sputtered films showed a ratio of Ti/B=0.5 but because of fluorine contamination these films deteriorated after production. The stoichiometry of non-reactive sputtered films could be adjusted by ion implantation of boron. The hardness and adhesion of as-deposited films were improved

by Kr^+ ion implantation, with some films forming blisters. The hardness was found to be about 40-60% higher, depending on the Kr^+ dose. For excessive blister formation no improvement was observed in adhesion and mechanical properties for these implanted coatings.

J. G. Ryan et al [48], in 1987 reported that titanium boride thin films of different composition could be prepared by magnetron sputtering for use as a potential diffusion barrier and as a boron diffusion source. TiB_2 films were prepared by DC magnetron sputtering from a TiB_2 target. Films with B/Ti ratio between 2-1 were also prepared by co-sputtering from Ti and B targets in RF mode. $TiB_{2.1}$ films did not react with the silicon substrate during annealing up to 1092°C but TiB films reacted with silicon at elevated temperatures. Thicker TiB_2 films (485nm) had lower resisitivities than thinner (103nm) films when annealed above 1000°C. The resistivity and film stress exhibited by TiB_2 thin films are comparable to those for refractory metal silicides, with values of 130$\mu\Omega$cm and 1.0GPa ($1.0 \times 10^9 Nm^{-2}$) respectively.

T. Shikama et at [49], in 1988 reported the deposition of $Ti_{1-x}B_x$ films onto Molybdenum by co-sputtering from a Ti target with boron particles. The films were prepared by RF magnetron sputtering with 1000WRF power and 0.5Pa argon pressure. During deposition the target temperature reached 1027°C (1300K) and the coating temperature was 597°C (870K). The film thickness was about 6μm. Various bias voltages were applied to the substrate range from 0 to -230V. The TiB_2 films have a strong preferred crystalline orientation (001) with almost the same chemical bonding as sintered TiB_2 and a hardness around 29.4GPa (3000Kg.mm^{-2}). The TiB_2 films deposited without an applied negative bias voltage have a poorly crystallised structure.

H-O. Blom et al [50] in 1989, observed that the TiB_2 layer acts as a diffusion barrier between silicon and aluminium up to 600°C. TiB_2 films with different compositions were deposited by reactive RF sputtering of a Ti target in a mixture of 6% diborane (B_2H_6) in a total argon pressure of 1.3Pa (10mTorr). The resistivity is shown to vary linearly with the boron content in the as-deposited films. After annealing at 900°C the lowest resistivity of 270$\mu\Omega$cm is obtained for the stoichiometric TiB_2.

E. Matsubara et al [19] in 1990 reported that crystalline TiB_2 films were formed on silicon deposited by magnetron co-sputtering from Ti and B targets in DC and RF mode respectively. The argon pressure was 0.69Pa and the film thickness was about 1.1μm. The grazing incident X-ray diffraction method showed that the coordination number and atomic distance were coincident with those of the crystalline TiB_2.

R. Lohmann et al [51], in 1991 reported that chemical composition and structure of the TiB_2 films on steel deposited by RF magnetron sputtering depends upon the bias voltage. The substrates were initially coated with a Ti film about 0.5μm thick to improve the adhesion. The TiB_2 film thickness was about 4μm. The bias voltage was varied from 0 to -50V in steps of 10V and the sputtering power was held at 750WRF at an argon pressure of 0.5Pa. The AES analyses showed that the B/Ti ratio of the film rises with higher bias voltage up to a value of 2.8. This may be due to the boron being deposited in interstitial sites or at grain boundaries However, the chemical composition is homogeneous with depth in the film. The morphology of the films depends on the bias

voltage and is a result of the preferred direction of crystal growth. The structure varies from a dense fibrous-like structure at low bias voltage to a very dense columnar structure at high bias voltage. The highest crystal size was found for -20V bias voltage based on the width of XRD peaks.

G. Sade & J. Pelleg [52], in 1995 reported that amorphous TiB_2 films were found to be a good diffusion barrier against Cu penetration up to 680°C when deposited with RF bias. These TiB_2 films on silicon and alumina were deposited by magnetron co-sputtering from Ti and B targets in 0.5Pa Ar pressure with 70WDC for Ti and 320WRF for B targets. TiB_2 film thickness was in the range of 250-500nm. The substrate RF bias of about 15W was used, which gives about -200V self-bias voltage. A 100nm layer of Cu was sputtered on top of the TiB_2 film and then annealed at 680°C. The as-deposited amorphous film has a high resistivity of 500μΩcm but after annealing decreases to 50μΩcm, while the structure remains amorphous. The amorphous boride films are stable up to 890°C. The crystallisation temperature can be decreased by RF bias application and microscrystalline TiB_2 films can be formed as low as 400°C. The as-deposited TiB_2 film that was heated in-situ at 400°C with an 15WRF bias showed crystalline $TiB_{1.92}$ with strong preferred (001) orientation. The grain size of this film as-deposited was about 10nm and Ti 2p peaks were observed. After annealing at 1080°C the TiB_2 grain size had risen to 80nm. $TiSi_2$ can also be formed during annealing at low temperatures (>765°C) as a result of the reaction of TiB_2 containing free Ti with the silicon substrate. This layer might be helpful as a barrier between the boride and the silicon. AES and SEM analyses revealed that Cu penetration into amorphous titanium boride is greater in the unbiased film. This may be associated with a non-uniform resputtering from the substrate due to the bias voltage. The bias also makes the growing film more dense and non-porous.

J. Chen & J. A. Barnard [53], in 1995 reported that the microstructure of TiB_2 films depends on the film thickness. Thin hexagonal TiB_2 films on oxidised silicon were deposited using DC magnetron sputtering. The sputtering condition was fixed at 400W power and 0.6Pa (5mTorr) argon. The TiB_2 thickness ranged from 20 to 500nm. Films less than 100nm have randomly oriented fine grains, whereas films with more than 100nm grain size start to develop a (001) texture. The textured crystallite alignment improves when the thickness of films increases. The grain size of the film increases with increasing film thickness. For 35nm thick films, small spherical grains are observed with a size of about 5nm, while 130nm thick films show a grain size of about 50nm. The residual stresses in all films are compressive and increase slightly with increasing film thickness. After 400°C annealing the film stress shifts toward the tensile direction, mainly with the thinner films. This may be attributed to the elimination of structural defects, for example vacancies. Reduction in the density of defects allows a clearer grain growth in thinner films.

C. Mitterer et al [18], in 1990 reported the production of ultrahard TiB_2 based coatings with hardness greater than 39.2GPa (4000HV). The coatings were produced by reactive and non-reactive DC magnetron sputtering with power density of 7Wcm^{-2}. In previous work [54] the RF sputtering did not show such high hardness values. The coatings were deposited onto Mo, Nb and cermet carbide. The substrates were either grounded or biased up to -1500V. The bias voltage during deposition was held at a constant DC potential. The reactive gas was nitrogen and propane. Non-reactive sputtering results in

very fine-columned films attributed to the T zone of the Thornton diagram with (001) orientation TiB_2 phase and B/Ti=2.8. For reactive sputtering in $Ar-N_2$ gas mixtures, an hexagonal $TiB_{2-x}N_y$ phase appears at low N_2 flow. An increase in N_2 flow results in the formation of a phase based on TiN. Reactive deposition in $Ar-C_3H_8$ leads to the existence of mixed-phase structure with phase based on TiB_2 and TiC. Coatings deposited reactively in $Ar-N_2-C_3H_8$ exhibit very fine-grained to amorphous with multiphase structure consisting of phases based on TiB_2, TiC and TiN. The hardness of the coatings ($HV_{0.05}$) on cermet carbide substrate with 3-5µm thickness shows the following values: Ti-B film 51GPa (5200HV); Ti-B-N films 56.7GPa (5800HV); Ti-B-C films 43.2GPa (4400HV); Ti-B-C-N films 50GPa (5100HV). These high values can be explained in part due to structural disorder, intrinsic stresses in the film and formation of mixed phase structure consisting of compounds based on TiB_2, TiN, TiC. The increasing bias voltage enhances the hardness of Ti-B-N much more than that of Ti-B films alone. The stresses were found to be compressive, with values up to 4GPa. The results of scratch tests indicate good adherence onto cermet carbide and the measured values for the critical load lay in the range of 50-90N depending of the thickness.

Herr et al [41], in 1991 reported the highest hardness for TiB_2 films by RF sputtering to be 39.2GPa (4000Kg.mm^{-2}). However, only one data point above 29.4GPa (3000Kg.mm^{-2}) was presented for Ti(B,N) coatings.

T. Friesen et al (*55*), in 1991 produced ultrahard multilayer coatings with hardness values up to 58.8GPa (6000HV). The concentration of Ti, B, N was reported in the ratio of (Ti):(B):(N)=1:0.5:0.4 for Ti=10nm thick and BN=4nm thick. Moreover, a mixture of two solid solutions of $Ti(B_xN_x)$ and $TiN_{1-x}B_y$ was reported. The multilayer coatings of Ti/BN were prepared by reactive or non-reactive magnetron sputtering from a Ti target between 50-300WDC and h-BN target at 1KWRF. The argon pressure was held at 0.5Pa (5×10^{-3}mbar). The film thickness was between 1-3µm. The as-deposited films display hardness values between 2-4GPa (200-400HV). However, after annealing at 400°C for 10h they became very hard (3200HV) and roughly stress free (-0.4GPa up to 0.26GPa). The hardening mechanism was found to be due an interdiffusion at the Ti/BN interfaces and so to phase transformation. The hardness also depends on the thickness ratio of the Ti/BN layer with the maximum at 1.7. Applying bias voltage of 50V during sputtering, the multilayer coatings reached values of hardness of 58.8GPa (6000HV). The films show good adhesion and the scratch tests reveal a critical load of 40N for coatings Ti=8nm thick and BN=4nm thick onto steel.

H. Deng et al [41], in 1995 reported that a small N_2 content added to the TiB_2 films exhibited a crystallised microstructure similar to the pure TiB_2 film and improved the mechanical and tribological properties. The TiB_2 and $TiB_2(N)$ films with small N_2 content may have potential applications as protective coatings in the magnetic recording industry. The $TiB_2(N)$ and TiB_2 films on oxidised silicon were prepared by reactive and non-reactive DC magnetron sputtering in a nitrogen atmosphere. The films were deposited at a fixed power of 400W and a deposition pressure of 0.6Pa (5mTorr) with seven levels of nitrogen flow rates: 0, 5,15, 30, 45, 60 and 80sccm. The thickness of these films was about 550nm. Grazing angle X-ray diffraction and TEM analyses indicate two groups of very different microstructures. The pure TiB_2 and $TiB_2(N)$ films with small N_2 content exhibit on (001) textured well-crystallised microstructure, while more

N_2 results in a $TiB_2(N)$ amorphous microstructure. When the N_2 flow rate increases from 0 to 5 sccm (standard cubic centimetres per minute), both the hardness and Young's modulus of the film are significantly improved. Nanoindentation hardness is increased from about 34 to 40GPa and Young's modulus changes from 280 to 390GPa. However, further increases in N_2 resulted in a sharp decrease in these properties. The tribological properties follow the same path. A solid solution strengthening mechanism, believed to be nitrogen solution in TiB_2, may be the explanation for these improvements at low nitrogen flow rates.

As far as I am aware, H. Holleck et al have done research into ceramic hard coatings for improving wear resistance, since 1985 [2,7]. They suggested that the toughness of the TiC/TiB_2 coating is influenced by the number and constitution of phase boundaries. In this work, multilayer coatings were deposited by RF magnetron sputtering from the TiC and TiB_2 target alternatively. The deposition conditions are: turning speed up to 1.6rpm, 650WRF power for TiB_2 target and 500WRF for TiC target, cathode diameter of 15cm, deposition time between 7-15h and 1.2Pa (1.2×10^{-2}mbar) argon pressure. A single layer thickness of 4nm leads to about 10^3 TiC/TiB_2 phase layers for a coating thickness of 4μm. These have been deposited onto steel and hard metal substrates. They reported the wear of the composite to be about half that of the single-layer coatings due to the improvement in adherence and toughness of the multilayer coatings. The Ti close-packed planes in the TiB_2 and TiC structures form partly coherent phase boundaries which give the explanation for high toughness of the composite. The adherence as evaluated by a scratch test resulted in critical loads of 10N for the TiC layer, 20N for the TiB_2 layer and 38N for the TiC/TiB_2 layer.

Later in 1987, H. Holleck & H. Schulz [27], concluded that TiC/TiN, TiB_2/TiN, and TiC/TiB_2 coatings of 5μm thickness exhibit the optimum properties and performance with 100-250 layers. Sequential sputtering was used to fabricate multilayer coatings on hard metal with composition wavelength (λ) of 5, 50, 125, 250, and 500nm. The single layer thickness varied from 500nm (10 layers) to 5nm (1000 layers). An increase in the width of the interface was observed from the TiN/TiB_2 interface, (about 0.6-1nm), the TiC/TiB_2 interfaces (about 2nm) to TiC/TiN interface (about 3nm). For λ=250 and 500 the structure of the single layers was strongly influenced by the preceding layer, so that as the number of layers increased, an increasing lattice distortion was observed.

The same authors [57], later in 1988, reported an investigation focussed on mechanical and tribological properties. The sequential magnetron sputtering coatings onto cermeted carbides were deposited at 0.2Pa argon pressure, 1000WDC power, the cathode diameter of 150mm and the same composition wavelength as before. The hardness of the sequential coatings was influenced by the amount of phase boundaries. The peak of hardness for TiC/TiB_2 with 250 layers is around 31.9GPa (3250HV); for TiC/TiN with 100 layers it is around 27.5GPa (2850HV) and for TiB_2/TiN with 500 layers it is around 27.4GPa (2800HV). Cutting tests with TiC/TiB_2 coated inserts were produced under continuous and interrupted cutting of low carbon steel. The coating with 100 phase boundaries shows the lowest flank wear, which is about four times less than TiB_2 and half the TiC coating. This can be explained by the optimised toughness of the coating, by introducing a large number of phase boundaries. The crack resistance of the coating is due to the dissipation of crack energy and crack deflection at the phase

boundaries. Another factor is the different composition of the phase transition in these sequential coatings, reflected in the microstructure of the coating.

Keeping to the same system, G. Hilz & H. Holleck [58], in 1991, reported that in contrast to former investigations with AES, TEM showed no clear evidence for interfacial zones between TiC and TiB_2 in multilayer coatings. However, TEM examinations of single-layer TiB_2 coating indicate a change of texture and grain size with distance from the substrate/coating interface. In multilayer coating a similar change of texture can be found and could be the reason for the change in properties and X-ray diffraction peaks as a function of the amount of phase transformed. This time, the TiC and TiB_2 single-layer and TiC/TiB_2 multilayer coatings onto cermeted carbide inserts including 10, 100, 1000 individual layers with a total thickness of 5μm were prepared by magnetron sputtering, at an argon pressure of 1Pa and 500WDC power.

Later in 1996 the same authors [59] added SiC and B_4C to the other systems. They reported that the maximum values of hardness for the following systems are: TiC/TiB_2 with 10 layers 36.1GPa (3685HV); SiC/TiC with 100 layers 37.7GPa (3842HV); SiC/TiB_2 with 10 layers 37.6GPa (3831HV); B_4C/TiB_2 with 100 layers 39.9GPa (4071HV); B_4C/SiC with 10 layers 35.6GPa (3627HV). All the systems were prepared by magnetron sputtering for a total thickness of 5μm. The constitution of single layers in SiC/TiC, SiC/TiB_2, B_4C/TiB_2 and B_4C/SiC multilayer coatings fits the microstructure of single phase coatings of the same thickness. However, for the TiC/TiB_2 coating the texture of the individual layers is influenced by the texture of the previous layer, as they had concluded in previous research. The occurrence of mixing zones between the layers depends on the materials, and the crystallinity of the previous layer.

As far as I know, research into the $Ni+TiB_2$ system commenced in 1987 when R. H. Parrish et al [30] reported deposition of 10%$Ni+TiB_2$ films on Ti-6Al-4V and Inconel 718 by sputtering, for film thickness of 25μm. The effects of the surface preparation parameters were reflected in the morphology of the film. Substrates prepared by liquid vapour honing with 1250 grit Al_2O_3 particles developed a finer nodule size compared to that of a 180 grit bast and the hardness was 20% greater.

Using the same system, J. J. Wert & S. J. Oppliger [25,60] in 1992, reported that $Ni+TiB_2$ coatings may protect Ti-6Al-4V and Inconel 718 from an erosion environment. However, the growth morphology of these coatings is dependent on the substrate preparation. The coatings were produced by DC magnetron sputtering and were 30μm thick. The substrate was prepared by two methods: liquid vapour honed and grit bast. Liquid vapour honed substrates produced coatings having a zone T-type growth morphology (dense close-packed array of nodules with poorly defined boundaries), whereas grit-blasted substrate produced coatings with a zone 1-type (tapered nodules having domed tops separated by boundaries containing voids). The nodule diameter was also found to be dependent on the substrate preparation. Coatings deposited on Inconel 718 tend to be more adherent and more effective as an erosion barrier than coatings deposited on Ti-6Al-4V, due to the differences in the coefficient of thermal expansion of the two substrate materials. Coating properties like: hardness and elastic modulus were found to be independent of the substrate material. For the same sputtering deposition and

substrate parameters the addition of 10%Ni+TiB$_2$ reduced the erosion resistance of the coating. The TiB$_2$ coating is appreciably softer 24.2GPa (24.2GNmm^{-2}) and has a lower elastic modulus 264GPa (264GNmm^{-2}) than 10%Ni+TiB$_2$ coating that has hardness of 43.9GPa (43.9GNmm^{-2}) and elastic modulus of 365GPa (365GNmm^{-2}). Replacing some of the TiB$_2$ with 10%WC (10%Ni+10%WC+TiB$_2$) significantly increased both the hardness and elastic modulus.

D. L. Chambers et al [61], in 1991, reported that TiC+Ni and TiB$_2$+Ni coatings with Ni and Ti interfacial layers could be a potential coating for erosion resistance. The films were deposited on carbon steel substrate by DC magnetron sputtering at 0.4Pa argon pressure. The Ti coatings were deposited at a power density of 4.1W/cm^2 and the others at 7.2W/cm^2. The substrates were sputter etched before deposition at a power of 130W and 3.3Pa argon pressure. The substrate temperature during deposition was about 135°C. The thickness of the coating range from 2.5 to 12.0µm and the intermediate layer from 2.5 to 9µm. The ratio of the T$_s$/T$_m$ for TiB$_2$, TiC, Ti and Ni coatings deposited ranges from 0.12 to 0.24 siting these structures in the T region where they should have a dense fibrous structure in which high levels of intrinsic stress can form. The TiC+Ni and TiB$_2$+Ni coatings were in a state of compressive stress. When interfacial layers are included in the coating, the intrinsic stress in Ni interface coating assumes a positive value and a negative value when the Ti layer is added. The addition of an Ni interfacial coating improved the erosion resistance of the TiB$_2$ coatings and a further improvement was observed with a second interlayer (Ti) on top the Ni interlayer. The erosion resistance of the TiC coating was identical to TiB$_2$ coating with a Ni interlayer. However, when the Ti interlayer was added, the erosion resistance decreased significantly. The TiB$_2$ and TiC coatings with 5%Ni binder had a lower erosion rate than those with 10%Ni binder.

Following this last work, K. A. Taylar & A. J. Emrick [62], in 1992, proposed improving erosion resistance of the polymer matrix composite (graphite fiber) with high thermal and mechanical stability for the aerospace industry, by depositing a TiB$_2$+Ni coating with a Cr interface layer to improve adhesion. The films of TiB$_2$+10Ni were prepared by DC magnetron sputtering from Cr and TiB$_2$+Ni targets at a power density of 3.7W/cm^2 and 6.8 or 9.3W/cm^2 respectively and argon pressure of 0.5Pa. The maximum substrate temperature was 260°C. The coating thickness was about 25.4µm and the Cr layer ranged from 5.1 to 12.7µm. The substrate surface was grit blasted. The TiB$_2$+Ni developed a structure of large tapered domelike crystals that are prone to catastrophic failure by brittle fracture. It was concluded that substrate surface roughness must be minimised for an effective erosion resistant coating to be achieved.

R. A. Andrievskii, in a review published in 1997 [9,28], suggested that the mode of deposition process has a strong influence on the hardness, composition and structure of TiB$_2$ coatings such as: substrate temperature, bias voltage, annealing temperature, as illustrated in table 1.5. The superstoichiometry of the TiB$_2$ phase has been attributed to the mobility and collision reactions of the boron and metal atoms leading to vacancies in the metallic sublattice.

Phase	Deposition Process	Film Thickness (μm)	Substrate	Hardness (GPa)
TiB_2	D.C. Magnetron Sputtering	5.0	WC/Co	34.0
TiB_2 (amorphous)	D.C. Magnetron Sputtering	5.0	WC/Co	23.5
$TiB_{\approx2.8}$	D.C. Magnetron Sputtering	4.1	WC/Co	51.0
$TiB_{\approx2}$	R.F. Magnetron Sputtering	5.0	Cr steel	37.2
$TiB_{\approx1.9}$	D.C. Magnetron Sputtering	8.0	HSS	62.5
$TiB_{\approx2}$	Dynamic ion mixing	1.0	WC/Co	27.5

Table 1.5. TiB_2 hardness in function of modes of sputtering process.

4. Ion Plating Techniques

The Dynamic Ion Mixing (DIM) method has been recently developed for depositing adherent TiB_2 coatings of nanocrystalline structure at low temperature. This technique consists of depositing and bombardment by a heavy ion beam of higher energy (100-300KeV) simultaneously. The DIM method can be used either with electron beam co-evaporaton of Ti and B with ion mixing (EBDIM) or sputtering of the TiB_2 target with ion mixing (SPDIM) or co-sputtering of the TiB_2+B target with ion mixing [42,63,64,65].

J. P. Riviere et at [63], in 1991 reported a 1μm thick TiB_2 film, at room temperature, by using EBDIM and SPDIM techniques, using high energy heavy ions of 100KeV Ar^+ and 320KeV Ar^+ or 320KeV Xe^+ respectively. The substrate was steel or silicon. The SIMS analyses showed uniform composition of Ti and B throughout the film. The electron probe X-ray microanalysis gave a ratio B/Ti=2 for EBDIM films with hardness of 27.9GPa (2840HV) and about 1.5 for SPDIM with a hardness range of 21.5-22.5GPa (2190-2290HV).

The structure of TiB_2 films produced by electron-beam evaporation without ion mixing is amorphous up to 1170K, and by sputtering without ion mixing is not completely amorphous with hardness of 1600HV. A hexagonal nanocrystalline structure is formed by EBDIM [63] and SPDIM [42]. A critical damage level of about 1dpa (displacement per atom), is necessary to induce crystallisation. When an efficient interface mixing was achieved, the result was an improvement in the steel substrate adhesion.

A few years later (1995) P. Chartier and J. P. Riviere et at [64] reported that TiB_2 films deposited by EBDIM had been analysed by CEEXAPS (Conversion electron extended X-ray adsorption fine structure), concluding that fine crystalline grains (4-6nm) are formed from stoichiometric TiB_2 and that the excess Ti atoms are located in the intergranular regions of the disordered structure.

To overcome the lack of substoichoimetry of TiB_2 films deposited by SPDIM, J.P. Riviere et at [65], in 1996, reported stoichiometric TiB_2 films at room temperature by SPDIM using a TiB_2 target enriched with boron. The TEM and XPS support the formation of TiB_2 polycrystalline phases with bonding energy of B1s typical of the TiB_2 hexagonal structure.

OTHER DIBORIDE COATINGS

1. ZIRCONIUM DIBORIDE (ZrB$_2$) COATINGS

Evaporation of ZrB$_2$ directly from compacted billets resulted in crystalline films at T_s=600°C. At lower deposition rates ($\cong$0.11μm/min) the cross-section hardness reached a maximum value of 29.9GPa (3050Kg.mm^{-2}) at T_s=850°C and the structure showed preferential orientation of (100) planes. For high deposition rates ($\cong$2.14μm/min) the hardness decreased with increasing temperature from 27.6GPa (2815Kg.mm^{-2}) at 670°C to 12.3GPa (1255Kg.mm^{-2}) at 1300°C. At this deposition rate the structure showed a preferential orientation of (001), with ZrB and B present, at the lower temperature and changed to (100) above 1180°C. The coating morphology changes from domed to columnar as the deposition temperature increases [5].

For films deposited by CVD the hardness values are very close to the bulk material of 22.6GPa (2300Kg.mm^{-2}) [5,43].

The electrical resistivity for ZrB$_{\cong 2}$ films deposited by RF magnetron sputtering at room temperature was reported 250μΩcm and 75μΩcm after annealing. The hardness of ZrB$_{\cong 2}$ films onto stainless steel by DC magnetron sputtering with 5μm thickness was reported to be 21.6GPa [9,28].

2. TANTALUM DIBORIDE (TaB$_2$) COATINGS:

TaB$_2$ coatings have been deposited by CVD processes. The grain size at 500°C is about 5nm, whereas at 700°C is about 10nm. The hardness is from 21.6 to 26.5GPa (2200 to 2700Kg.mm^{-2}) at T_s>600°C. The bulk material value is 24.5GPa (2500Kg.mm^{-2}) [5].

3. HAFNIUM DIBORIDE (HfB$_2$) COATINGS:

The electrical resistivity for HfB$_x$ films by RF co-sputtering of B and Hf was reported to be about 370μΩcm at room temperature. Changing the x values from 1 to 5 was shown to increase the film resistivity by less than a factor of 2. However, an increase in the oxygen impurity content from 0.3% to 0.6% was found to increase the resistivity value by an order of magnitude [9,28].

1.3. THIN FILM TECHNOLOGY: DEPOSITION PROCESSES

```
LAYOUT
⇓
Why Thin Films Have Industrial Interest?
⇓
Definition of Overlayer and Diffusion Coatings
⇓
Classification of Deposition Processes
⇓
Selection of Deposition Processes
⇓
Advantages of PVD & CVD Processes
```
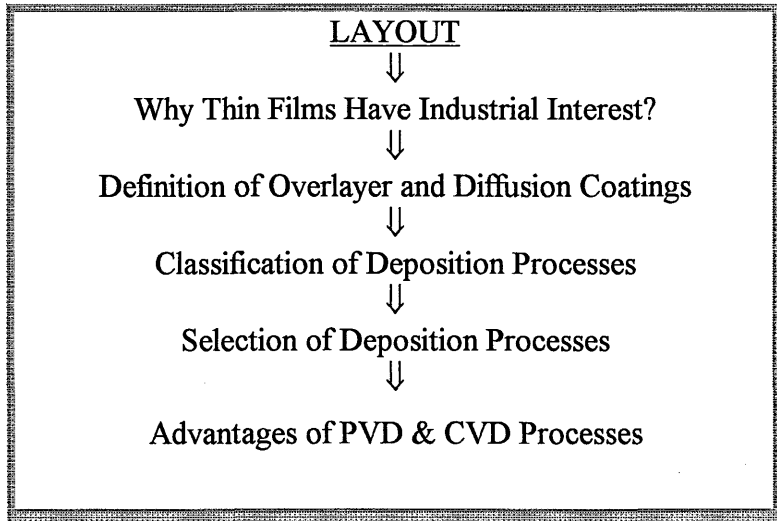
Developments in surface engineering products have been a continuing challenge to achieve increased performance, reduced costs and control of surface properties independently of the substrate. R. F. Bunshah [66], in 1994 reported that Japan was spending $100 to $150 million on R&D in diamond and diamond-like carbon coatings. It was estimated that more than $10 million was spent in the U.S. in thermal barrier coatings for high temperature on turbine blades. Likewise, wear resistant coatings for discs and heads has pulled in more than $10 million in R&D spending throughout the world.

From the available information, it is apparent that the surface engineering area will continue to expand in industrial and academic fields for many decades ahead offering the possibility of research and development in the following areas [66]:

♦ Creation of new products

♦ Solutions to previous engineering problems

♦ Improved product functionality

♦ Development of manufacturing techniques

♦ Conservation of scarce materials

♦ Improvements in ecological matters: reduction in effluent output and power consumption

The benefits of combining two or more of the following properties: high temperature strength, impact strength, specific optical, electrical or magnetic properties, wear resistance, ability to be fabricated into complex shapes, biocompatibility and cost have been recognised for some time. Hence, attempts to deposit a thin layer or layers, of a second material (coating), applied to the component surface have been a continuing challenge in order to achieve the required properties to fulfil the specifications. So, thin film technology is a key point in many areas of industry. For example, a composite material with high surface hardness and a tough core should be ideal for many engineering components. Similarly, high temperature strength provided by the bulk

material and corrosion resistance coming from the coating is a combination suitable for hot stage blades and vanes in a gas turbine.

There are two main ways of depositing films. These can be classified as overlay coatings and diffusion coatings [66,67,68]. Surface modification is also possible by ion implantation. In this case, the surface layer consists of a new material made from both the parent and added material.

Diffusion coatings are produced by depositing a material that alters the composition of the surface region by interdiffusion into the interface. Therefore, the coating forms an integral part of the component. There is also a concentration gradient (various layers) from the surface to the interior of the coating which is dictated by the thermodynamic and kinetic basis of the coating process.

An overlay coating is an add-on to the surface of the substrate by processes such as PVD or CVD. Depending on the process parameters, an interdiffusion layer may or may not be formed. The advantages of overlay coatings, over diffusion coatings including: wide range of deposited compositions, design flexibility, wide range of coating thicknesses. However, the limitations are preferential attack down defects, poor adhesion, if substrate is badly prepared, and increased cost.

A standard definition of thickness of thin film is lacking. However, a thickness of 1μm is often accepted as the boundary between thin and thick films. Recently, it has been suggested that a film can be considered thin or thick depending on whether it exhibits surface-like or bulk-like properties [66].

On balance, coatings are helpful for a variety of reasons, including economics, material conservation, unique properties or design flexibility that can be obtained by separating the surface properties from the bulk properties.

A standard classification of deposition processes has been difficult to achieve because there are a very large number of techniques. On the other hand, depending on the viewpoint, various processes could overlap different categories. P. Furnival [69] grouped the coatings processes as illustrated in figure 1.14, which has been modified to include ion beam assisted deposition (IBAD) as ion implantation is not a cooling process.
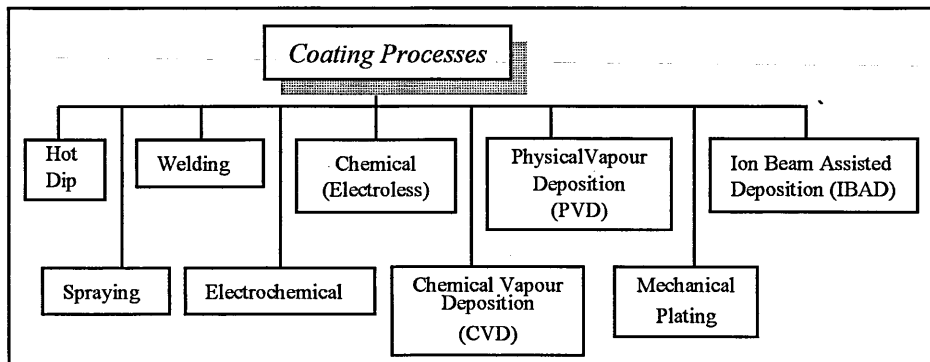
Figure 1.14. Classification of Deposition Processes.

Schiller, Heisig, Goedricke and Weissmantel [66,70] give a brief group survey of vacuum deposition techniques as outlined in figure 1.15.
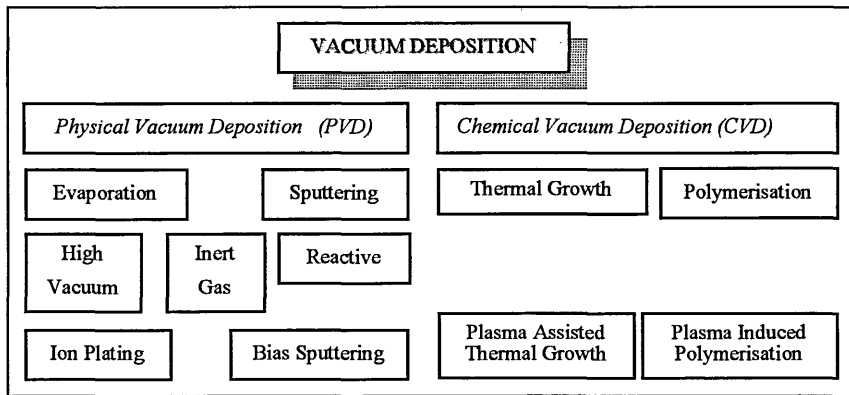
Figure 1.15. Classification of PVD and CVD Processes [66,70].

A different classification for CVD and PVD variants recently developed is shown in figure 1.16.

Source of Deposition Species	High Vavuum $(10^{-4}-10^{-7}\,mbar)$	Soft Vacuum $(10^{-1}-10^{-3}\,mbar)$		Deposition Process
		Plasma (RF or DC)	Bias (self or negative)	
Thermal Energy	*Evaporation *Ion Plating	No	No	Reactive Evaporation
		Yes	No	Activated Reactive Evaporation (ARE)
		Yes	Yes	Reactive Ion Plating Biased Activated Reactive Evaporation (BARE)
Momentum Transfer	*Sputtering *Ion Beam	Yes	No	Reactive Sputtering
		Yes	Yes	Biased Sputtering Sputter Ion Plating (SIP)
Vapour / Gas phase	*CVD	No	No	CVD
		Yes	Yes	Chemical Ion Plating (CIP)
		Yes	No	Plasma Assisted CVD

Figure 1.16. Classification of Vacuum Deposition Processes.

The formation of a deposit, from a vapour phase, takes place according to the three steps outlined below [56,66,70,71,72,73]:

1-Synthesis or Creation of Vapour Phase Species. This step consists of the transition from a condensed phase (solid or liquid) to the vapour phase and also defines the basic class of the coating:

◊ Thermal excitation: Evaporation.

◊ Momentum transfer: Sputtering.

◊ Gas or vapour species: CVD.

2-Transport of the Vapour Phase from Source to Substrate. Three factors should be considered in this step:

◊ Degree of vacuum: type of flow gas, mean free path (average distance traversed by particles between collisions), as seen in table 1.6.

◊ Presence of plasma that can be generated by RF or DC.

◊ Reactivity of the gas environment: reactive processes.

3-Condensation of the Vapour Phase Followed by Film Nucleation and Growth. The factors to be considered in this step are:

◊ The microstructure and composition can be modified either by ion bombardment of the growing film (back sputtering and recombination, enhanced surface atom mobility) or by deposition temperature.

◊ Ion bombardment depends on the degree of bias (no bias, self bias, negative bias, positive bias).

These steps can be independently controlled in PVD process but not in CVD processes. This means that there is much greater flexibility in controlling the structure, properties and deposition rate for PVD processes, over CVD process. The three steps for CVD process can take place simultaneously at the substrate and cannot be independently controlled.

Characteristics of the Various Types of Vacuum			
	Low Vacuum	*Medium Vacuum*	*High Vacuum*	*Ultra-High Vacuum*
Pressure (mbar)	1013-1	$1\text{-}10^{-3}$	$10^{-3}\text{-}10^{-7}$	$<10^{-7}$
Mean Free Path (cm)	$<10^{-2}$	$10^{-2}\text{-}10$	$10\text{-}10^{-5}$	$>10^{5}$
Flow Type	Viscous: *Laminar *Turbulent	Transition from viscous to molecular	Molecular	Molecular
PVD Process Applicability	$\ll\ll\ll\diamond\gg\gg\gg$ Sputtering Evaporation Ion Plating			

Table 1.6. Characteristics of the various types of vacuum [71,74,75].

Some characteristics of the deposition processes are described in the table 1.7[66]. The selection of one specific deposition process to be used depends on the several factors[66,69]:

♦ Vapour Source: material to be deposited, resources, purity

♦ Processing parameters

♦ Apparatus required and availability

♦ Limitations imposed by the substrate: size, shape, sensitivity to heat and plasma irradiation

♦ Coating material: properties required, single-layer or multilayer design, thickness

♦ Cost: cost/benefit analysis by grading the possible options and the risks involved

♦ Ecological considerations

Considering all these factors and an accurate analysis of the characteristics of each process, it should be possible to select a suitable process. Moreover, in some situations adding an appropriate thermal treatment could enable the coating properties to be optimised according to specific application requirements.

	Evaporation	Ion Plating	Sputtering	Chemical Vapor Deposition	Electro-deposition	Thermal Spraying
Mechanism of production of depositing species	Thermal energy	Thermal energy	Momentum transfer	Chemical reaction	Deposition from solution	From flames or plasmas
Deposition rate	Can be very high (up to 750,000 A/min)	Can be very high (up to 250,000 A/min)	Low except for pure metals (e.g., Cu–10,000 A/min)	Moderate (200–2,500 A/min)	Low to high	Very high
Depositing specie	Atoms and ions	Atoms and ions	Atoms and ions	Atoms	Ions	Droplets
Throwing power for:						
a. Complex shaped object	Poor line-of-sight coverage except by gas scattering	Good, but nonuniform thickness distributions	Good, but nonuniform thickness distribution	Good	Good	No
b. Into small blind holes	Poor	Poor	Poor	Limited	Limited	Very limited
Metal deposition	Yes	Yes	Yes	Yes	Yes, limited	Yes
Alloy deposition	Yes	Yes	Yes	Yes	Quite limited	Yes
Refractory compound deposition	Yes	Yes	Yes	Yes	Limited	Yes
Energy of deposit species	Low ≈0.1 to 0.5 eV	Can be high (1–100 eV)	Can be high (1–100 eV)	Can be high with plasma-aided CVD	Can be high	Can be high
Bombardment of substrate/deposit by inert gas ions	Not normally	Yes	Yes or no depending on geometry	Possible	No	Yes
Growth interface perturbation	Not normally	Yes	Yes	Yes (by rubbing)	No	No
Substrate heating (by external means)	Yes, normally	Yes or no	Not generally	Yes	No	Not normally

Table 1.7. Characteristics of Deposition Processes [26,66].

Both PVD and CVD techniques offer a wide variety of advantages that have followed the most important progressions in vacuum engineering, as illustrated in figure 1.17 [2,5,66,28].

Considerable progress has been made in the last decade but the understanding of basic processes and phenomena is still lacking in some areas. Areas for research activities include:

♦ Relationship between microstructure and properties of the coating with process parameters in the nano-scale range. This is particularly important for submicron microelectronics, reflective surfaces, corrosion, etc.

♦ Effect of the energy of the depositing species on interfacial interaction, nucleation and growth of deposit, mainly in multilayer coatings, alloys and compounds.

♦ Effects of substrate surface conditions: contamination, layers, adsorbed gases, surface topography.

♦ Influence of process parameters on the residual stresses and elastic properties of the film.

- The deposition process from vapour phases has been able to produce more than a doubling of the diversity of materials, over liquid phase deposition processes.

- Ecological benefits with certain techniques (sputtering).

- The atomistic processes allow high levels of cleanliness during deposition in order to obtain high quality coatings.

- The possibility of applying analytical tools that allow the growth to be monitored and process parameters that could produce new coatings, higher manufacturing quality and reproducibility, with higher production throughput to give a more profitable process.

- The coating properties produced from the vapour phase can be varied more than the coatings produced from the liquid phase. Owing to the fact that deposition conditions can be chosen to produce coatings either close to or far from thermodynamic equilibrium.

- Flexibility in changing the morphology and crystallography of the coatings that can be grown either from completely amorphous to crystalline or from ultrafine (submicron grains or nano-scale laminate) to single crystal films.

- Hard coatings have been produced either in the form of a monolayer or multilayers for improving wear resistance for cutting tools or wear parts.

- Deposition of thin films or self-standing shapes.

- Overlay coatings can be deposited with properties independent of the thermodynamic basis (PVD).

Figure 1.17. Advantages of PVD and CVD Processes.

1.3.1. PHYSICAL VAPOUR DEPOSITION PROCESSES (PVD)

<u>LAYOUT</u>
⇓
Overview of PVD Process
⇓
Evaporation Process
⇓
Ion Plating Process
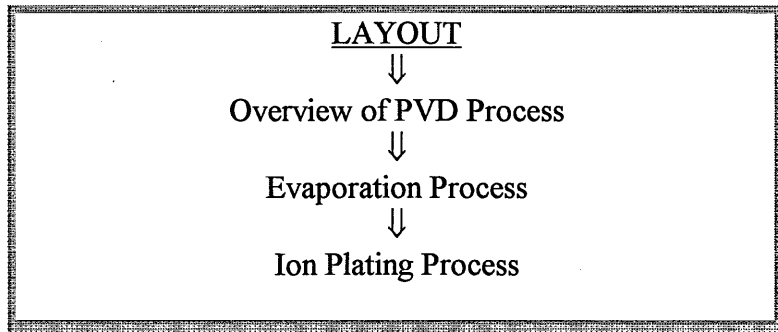
Physical vapour deposition encompasses three deposition processes [70,76]: evaporation, sputtering and ion plating. In the scope of this thesis, the sputtering process is treated in detail. However, an introductory description is given for evaporation and ion plating.

As early as 1877 mirrors were coated with thin films by sputtering deposition[68,77]. Initially, improvements in vacuum technology and electron beam technique allowed vacuum evaporation to largely replace the sputtering process because of the higher evaporation deposition rates. However, as many materials could not be evaporated by resistance heating methods, increased knowledge of sputtering processes plus the invention of RF sputtering brought about renewed interest in sputtering. Hence scientists and engineers, have made continuous progress in both technologies.

Over the last few years, some specialised variants of PVD processes have been developed, for instance: reactive ion plating, activated reactive evaporation, reactive sputtering, unbalanced magnetron sputtering, new heating methods of the vapour sources (by induction or electron beam).

One of the most recent reported variants of the PVD process is the Dynamic Ion Mixing (DIM) [63]. This is an example of ion beam assisted deposition (IBAD). The technique consists of simultaneous deposition and bombardment by a broad heavy ion beam (Ar^+, Xe^+) of high energy (100-300KeV). DIM technique has been used with either electron-beam evaporation (EBDIM) or sputtering (SPDIM). DIM is based on the highly energetic ions that may produce dense displacement cascades inducing an effective collision mixing at the coating/substrate interface during growth of the film. The consequences are: increased adhesion to the substrate by the interface mixing effect; control of the microstructure and phase formation in the growing film. Both could be modified in a reproducible way, independently of the system; relieving the intrinsic stresses of the film; increasing the film density.

The need to develop these techniques will increase their usage, as the high technology applications require multiple and often conflicting sets of engineering material properties.

The wide variety of applications of these techniques ranges from decorative to significant segments of the engineering, chemical, nuclear, microelectronics and related industries [76].

In PVD processes the material to be deposited will be transformed into a vapour phase by a physical process, either thermal evaporation or an impact process. The deposition on the substrate occurs in a vacuum chamber.

The main characteristics of atomistic deposition processes are:

♦ Film formation is by condensation onto substrate

♦ Surface migration of condensed species may occur

♦ Nucleation and growth occur at preferred sites

♦ Nucleation and growth modes determine the crystallography and microstructure of the coating

♦ Adatoms rarely achieve their lowest energy configuration

Consequently, the coatings can contain high concentrations of structural defects which may or may not be beneficial.

The deposition rate limits for PVD processes are indicated in table 1.8 [76]. It is clear that evaporation and ion plating have much higher deposition rates than sputtering. The high deposition rates of evaporation processes occur because the electron beam is much faster and creates a large volume of vapour plasma. However, the sputtering process can be used for substrates that will not withstand high temperature and alloy composition and deposition rates are easier to control in sputtering, as opposed to evaporation processes.

PVD Processes	Deposition Rate (nm/min.)
Evaporation	10-25000 (in special cases to 50000)
Ion Plating	10-25000
Sputtering	2.5-1000

Table 1.8. The deposition rate limits for PVD processes [76].

Some features and drawbacks of evaporation and sputtering methods are summarised in the table 1.9 [70].

There are several advantages and some shortcomings of PVD processes over competitive processes such as: CVD, electrodeposition and plasma spray, as mentioned in figure 1.18 [70,73,76].

Process	Direct Evaporation	Reactive Evaporation	Activated Reactive Evaporation	Direct Sputtering	Reactive Sputtering	Magnetron Sputtering
Operating Pressure Range, torr	10^{-4}–10^{-5}	10^{-3}–10^{-4}	10^{-3}–10^{-4}	10^{-2}–10^{-3}	10^{-2}–10^{-3}	10^{-3}–10^{-4}
Substrate Temperature, °C	500–1000	500–1000	room temp. –500	200–500	200–500	room temp. –500
Source-to-Substrate Gap, cm	25	25	25	5–10	5–10	5–20
Deposition Rate, Å/min	generally low; <300 for compound films	generally low 200	<500–10000	500 for compound films	up to 1000	up to 2000
Compound Dissociation	A major problem			limits dep. rates	Target poisoning	
Comments	Difficult to deposit fully stoichiometric film	High temp. reqd.; low dep.rates	High dep.rates; plasma control indep. pressure & source power.	High temp. due to energetic particle bombardment.	Interdependent reactive gas pressure, source power & surface state of target.	Magnetic confinement restricts substrate bombardment.

Table 1.9. Characteristics of Evaporation and Sputtering Processes [70].

Advantages of PVD techniques

- Extremely versatile in composition of deposit. Virtually every type of inorganic material like: metals, alloys, ceramics, refractory compounds, intermetallic compounds or their mixtures, as well as some inorganic materials can be deposited.
- The substrate temperature may be varied within limits (<-80 to 800°C).
- The PVD techniques produce an overlay coating.
- Excellent bonding can be achieved, mainly with ion plating.
- Possibility to vary the atmosphere environment.
- The structure, purity and adhesion are better controled, compared to CVD methods.
- Unusual microstructures and new crystallographic morphologies can be produced, for example, amorphous deposits.
- Evaporation and sputtering processes have been able to deposit refractory compounds that could provide near full density coatings.
- Deposits can be of high purity.
- Excellent surface finish can be produced. This can be equal to that of the substrate. Thus machining or grinding operations can be eliminated.
- The PVD technique can deposit coatings of free standing shapes at high rates such as: sheets, foils, tubes.
- The film thickness may be varied over wide limits, from angstroms to millimetres.
- A clean process. Elimination of pollutants and effluents from the process. They are ecological friendly.

Disadvantages of PVD techniques

- Inability to deposit polymeric materials with certain exceptions (PTFE).
- High sophistication of the processing equipment gives high capital equipment costs.
- Inability to coat some complex geometries, e.g. re-entrant angles and long, small holes can be difficult.

Figure 1.18. Advantages and disadvantages of PVD processes.

EVAPORATION PROCESS

The metal deposits which Faraday obtained in 1857 were probably the first evaporated thin films. The large scale industrial applications of these technologies had to await the vacuum technique developments and for that reason date from 1946 and onwards [70,76].

In the evaporation process the vapour phases are produced from a material located in a source that is heated by different methods: direct and indirect resistance, radiation, induction, eddy currents, electron beam (thermionic and plasma), laser beam[78] and arc discharge.

The process is usually carried out in a vacuum, typically 1.3×10^{-3} to 1.3×10^{-4} Pa (10^{-5} to 10^{-6} Torr) and consequently the evaporated atoms undergo an essentially collisionless line-of-sight transport before condensation on the substrate. The substrate is usually at ground potential (no bias). For most materials of practical interest, the source operating temperatures range from 1000 to 2000°C [66,70,79].

The transition of solids or liquids into the vapour phase could be considered as a macroscopic or atomistic phenomenon. The atomistic approach is derived from the kinetic theory of gases for nucleation and growth. Both macroscopic and atomistic approaches are of interest in the microstructure of the film [76].

Evaporation equipment consists of the following systems: vacuum chamber, vacuum system, evaporation sources, substrate holders, rate monitors and pressure control system. For high purity coatings ultra-high vacuum is needed and an ion-pump, or turbo-molecular, or cryo-pumped system have been used to produce a low contamination, high vacuum environment [70,76,77]. Substrate holders may be very simple for flat substrates or can incorporate complex motion for planetary or rotating devices.

Evaporation sources are classified by the method of heating them. Difficulties in evaporating all materials from any type of source contribute to many types of source design. The main reasons are [76]:

1. Chemical interactions between source material and evaporant.

2. Reactions between metallic sources and evaporant.

3. The power density varies with the method of heating the sources.

Many factors influence the selection of source material such as [79]:

♦ Material to be deposited.

♦ Required film purity.

♦ The material must have inconsequential vapour and dissociation pressures at the operating temperature to avoid molten droplet ejection from the pool (spitting).

♦ Availability in the desired shape.

♦ Applicable to different methods of heating.

The emission characteristics of the vapour source are very important in the design of the source to ensure thickness uniformity of the film. This problem could be

minimised by either moving the substrate or using multiple sources or sources of special shapes [76,79].

The properties of the film depend upon the processing parameters, such as: surface properties of the substrate, residual gas in the chamber, deposition rate, thickness uniformity, geometrical design between the source and the substrate, heating of both the substrate and source, substrate bias, etc.

The material selection for direct evaporation deposition depends on the melting point, vapour pressure and compatibility with the source material. The process is considered efficient and reliable for metals but difficult for ceramic and compound materials unless electron beam sources are used [77]. To overcome these difficulties, two variants of the evaporation technique have been developed [70,76,79]: reactive evaporation and activated reactive evaporation (ARE).

The reactive evaporation process is identical to the direct evaporation process, apart from the presence of a reactive gas in the chamber. The compound is formed by reaction of the evaporated metal species with the molecules of the reactive gas. The partial pressure of the reacting species is low ($<10^{-5}$Torr) and the mean free path of the reacting species is longer than the source-to-substrate, consequently the reaction between the metal atoms and the gas atoms occurs only on the substrate.

Activated reactive evaporation (ARE) occurs in the presence of a plasma of a reactive gas. The partial pressure of the metal vapour and gas atoms used is above 6.6×10^{-2}Pa (5×10^{-4}Torr). However, the plasma presence influences the kinetic reactions by supplying activation energy to the reactive species. Thereby the synthesis of the compounds with desired stoichiometry at high rates and low temperature has been possible by modifying the growth kinetics and thus the morphology of the deposits. The substrate can be either grounded or positively or negatively biased.

The reactive evaporation and activated reactive evaporation techniques allow a wide range of materials to be deposited by evaporation. Metals, semi-conductors, alloys, intermetallic compounds, refractory compounds and mixtures have been deposited successfully. However, compounds that decompose irreversibly during evaporation cannot be evaporated [70,76,77].

ION PLATING PROCESSES

Ion plating is a vacuum deposition technique that was introduced by Don Mattox in 1964 and has been used since then [68,70,77]. It is a hybrid process linking two techniques: the material to be deposited is evaporated in a similar way to that in evaporation processes and the substrate is biased (similar to the way the cathode behaves in sputtering).

The D.C. diode ion plating configuration consists of an anode and a cathode immersed in a low pressure gas. The material to be deposited onto the substrate is then evaporated from a resistively heated filament (anode). The glow discharge is produced by biasing the substrate to a high negative potential (0.2 to 5KV). The argon pressure, in the chamber, ranges from 1.3×10^{-1} to 1.3×10^{1} Pa (10^{-3} to 10^{-1}Torr). The evaporated

atoms are ionised in the plasma by impact and accelerated towards the substrate by an applied electric field, between substrate and earth [68,76,77].

Applying bias and ion beam simultaneously, leads to the deposit itself being sputtered away (resputtering) and redeposited along with ion bombardment of the growing coating. To minimise this effect, the conditions must be chosen correctly so that the deposition rate is higher than the resputtering rate. Moreover, heating of the substrate occurs due to the intensive gas ion bombardment [77]. The latter problem can be lessened by using an auxiliary heating tungsten filament to generate the plasma [66].

Nevertheless, a constant cleaning of the substrate is occurs. As the arriving ions have a substantial kinetic energy, films with good adhesion, high density, lower residual stresses and low impurity can be produced [66]. If the deposition rate is sufficient to maintain an adequate partial pressure of the evaporatant then the discharge can become self-sustaining. Insulating substrates can be coated by replacing the DC bias by RF and by placing a metal cathode backing plate to avoid a positive surface charge build-up [70].

The most typical configurations to create a plasma are [81]: DC diode discharge, RF discharge, electron emitter sustained discharge, magnetron enhanced discharge, microwave discharge, hollow cathode discharge, vacuum arcs and plasma arcs.

Ion plating can produce metals, alloys, ceramics or metal/ceramic composite coatings. The use of a reactive gas such as O_2, N_2 or hydrocarbon allows a variety of compounds to be deposited by reactive ion plating (RIP) or activated reactive evaporation (ARE) [70]. Recently, ion implantation accelerators have been used to give high energy ion bombardment (50-100KeV) of as-deposited films for mixing the interfacial region [70,81].

The main advantages offered by ion plating techniques and some drawbacks are illustrated in figure 1.19 [68,70,80,81].

There are many features of the ion plating process that are important for applications, such as [68,81]:

♦ Excellent film durability and high deposition rates: turbine engine blades and rotary engine surfaces.

♦ Good adhesion: Ag on steel for mirrors, soft metals on bearing surfaces for space lubrication, Ag on Be for diffusion bonding, Cu and Au on Ta and Mo for subsequent brazing, Cu-on-ceramic metallization.

♦ Metallization: Al, Ag, Au on plastics and semiconductors.

♦ Uniform film on complex shapes: TiN on tool bits, moulds and jewellery items, semiconductor metallization.

♦ Good reaction and stoichiometry: TiN on tool bits.

♦ Corrosion resistance: Al on U, steel and Ti; C and Ta on biological implants.

♦ Abrasion resistance: MgF_2 on plastics.

♦ Diffusion barriers: HfN and TiN on semiconductor devices.

♦ Wear and erosion resistance: HfN and TiC.
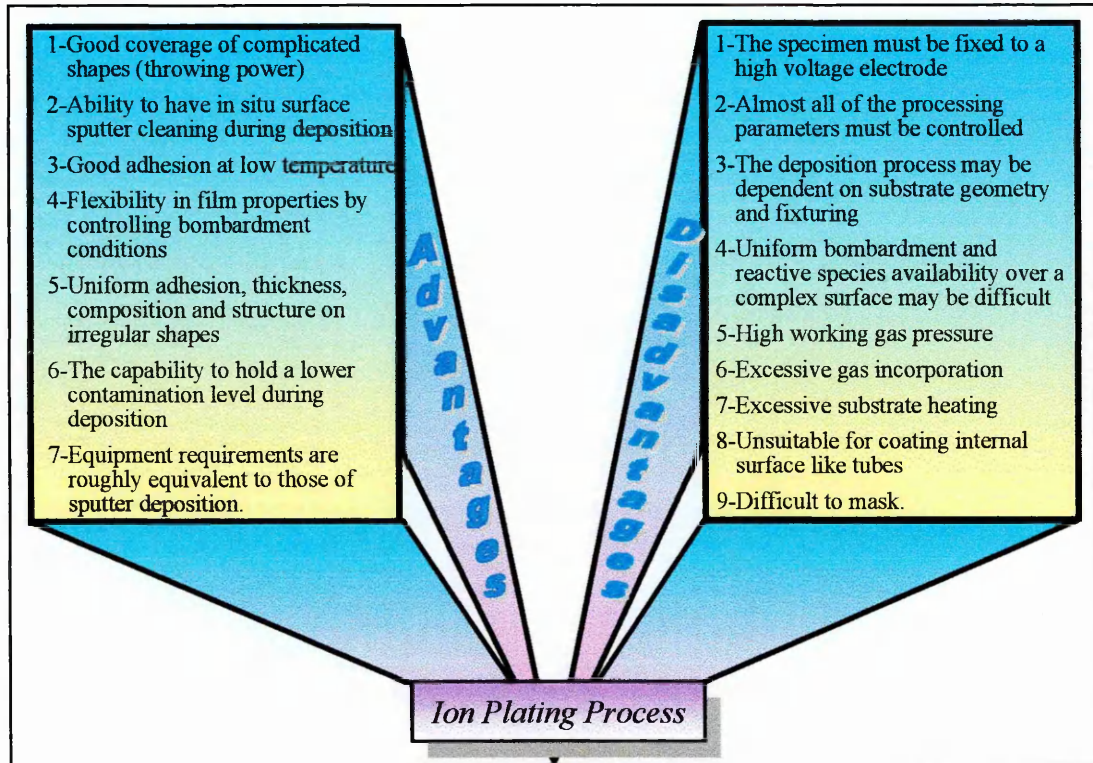
Figure 1.19. Advantages and disadvantages of ion plating techniques.

Advantages

1-Good coverage of complicated shapes (throwing power)

2-Ability to have in situ surface sputter cleaning during deposition

3-Good adhesion at low temperature

4-Flexibility in film properties by controlling bombardment conditions

5-Uniform adhesion, thickness, composition and structure on irregular shapes

6-The capability to hold a lower contamination level during deposition

7-Equipment requirements are roughly equivalent to those of sputter deposition.

Disadvantages

1-The specimen must be fixed to a high voltage electrode

2-Almost all of the processing parameters must be controlled

3-The deposition process may be dependent on substrate geometry and fixturing

4-Uniform bombardment and reactive species availability over a complex surface may be difficult

5-High working gas pressure

6-Excessive gas incorporation

7-Excessive substrate heating

8-Unsuitable for coating internal surface like tubes

9-Difficult to mask.

Ion Plating Process

1.4. THE SPUTTERING PROCESS

LAYOUT
⇓
General Outlook of Sputtering Process
⇓
Processing Parameters
⇓
Sputtering Advantages and Shortcomings
⇓
Sputtering Applications

The advanced concepts of PVD techniques, for hard coatings, involving multicomponent mixed phases, new metastable materials and multilayers have been studied over the last few decades. Therefore, it has been a continuing challenge to develop and control the sputtering process. The trend will be in the direction of optimising and improving the functional behaviour of the film depositions and consequently their properties.

Sputtering is an atom-by-atom deposition process, as illustrated in figure 1.20. Material is dislodged and ejected from a target surface by momentum exchange, associated with surface bombardment by energetic particles and subsequently deposited onto the substrate surface.
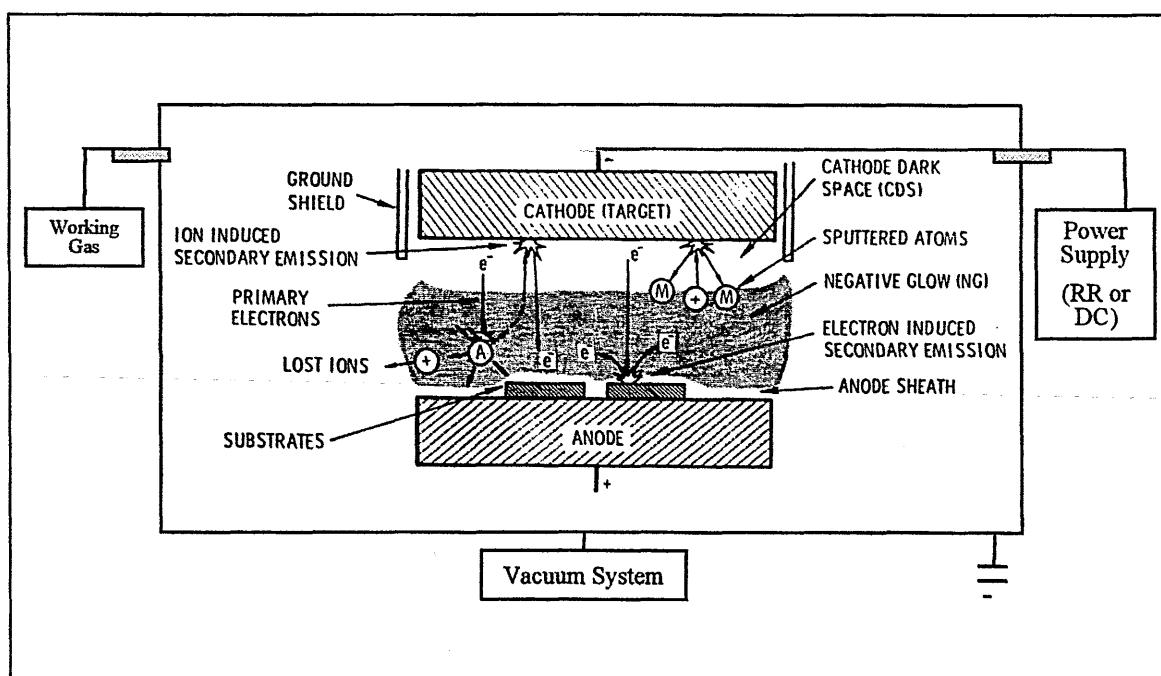

Figure 1.20. Representation of sputtering process.

The energetic particles (positive ions) are produced in a glow discharge, typically at gas pressure between 5 to 5×10^{-1}Pa (5×10^{-2} to 5×10^{-4}mbar). A negative potential, between 0.5-5KV, is applied to the target (cathode) to keep the ion bombardment running, while the counterelectrode (substrate) may be grounded. The sputtering process occurs in a vacuum chamber that is evacuated to a base pressure range from 1.3×10^{-4}-1.3^{-8}Pa (10^{-6}-10^{-10}Torr). The process occurs at deposition temperatures usually lower than 300°C [76,77].

The formulation of a theory which enables prediction of the experimental data has been difficult to achieve as the sputtering mechanism involves several parameters like: kinetic energy of the ions, electronic structure of the collision partners, binding energy of lattice atoms.

However, an adequate understanding of the complex process occurring during ion bombardment of solid surfaces has recently been established, allowing a reproducible and controllable sputter deposition process [68,77,82]. Monte-Carlo simulation tools offer the possibility to study several physical processes, under defined sputter conditions, e.g. the path of the ejected particles from the target. This method has been used to consider the target material, geometry, energy and angle of sputtered particles, gas scattering, particle loss, film thickness, angle and energy distribution [83].

Keeping the sputtering process under control is as meaningful as the understanding of sputtering mechanisms for producing high quality single crystal, complex alloys, compounds, superlattice coatings with suitable known microstructure and properties. Nevertheless, this area requires further research [70].

The process parameters should be established in terms of maintenance, tolerances and material to be deposited. While the controllable parameters should be settled according a systematic control study that includes: deposition rate, pressure monitoring, gas composition measurements, etc. The processing parameters are selected before deposition and should not change. While the controllable parameters may change during the run. Both are listed in the figure 1.21.

The Controllable parameters ask: Why are you looking puzzled?

Deposition rate:
•cycling pressure

Reactive gas:
•composition
•pressure

Sputtering pressure

Bias voltage to the substrate:
•clean substrate
•reduce Ar in the film
•increase film density

Deposition time & turning speed

Voltage & Current

Temperature:
•target
•vacuum chamber
•substrate

Carrier gas:
•getter temperature
•pressure
•flow rate

Sputtering power:
•bombarding target to backing plate
•damage the target itself
•damage the associated seals

The processing parameters reply: How can you fit together like a puzzle

System geometry:
•BI-switch
•Target/substrate spacing

Target:
•Composition
•Cooling system
•Bonding system

Masking:
•Material
• Shape

Process routes:
•RF, DC
•Magnetron
•Bias voltage
•Ion beam
•Reactive sputtering

System clanliness:
•Substrate
•Chamber
•Target
• Initial vacuum

Substrate:
•Material
•Shape

Magnetron sputtering:
•Efficiency of the magnetic field

Deposition rate:
•Clamp target system
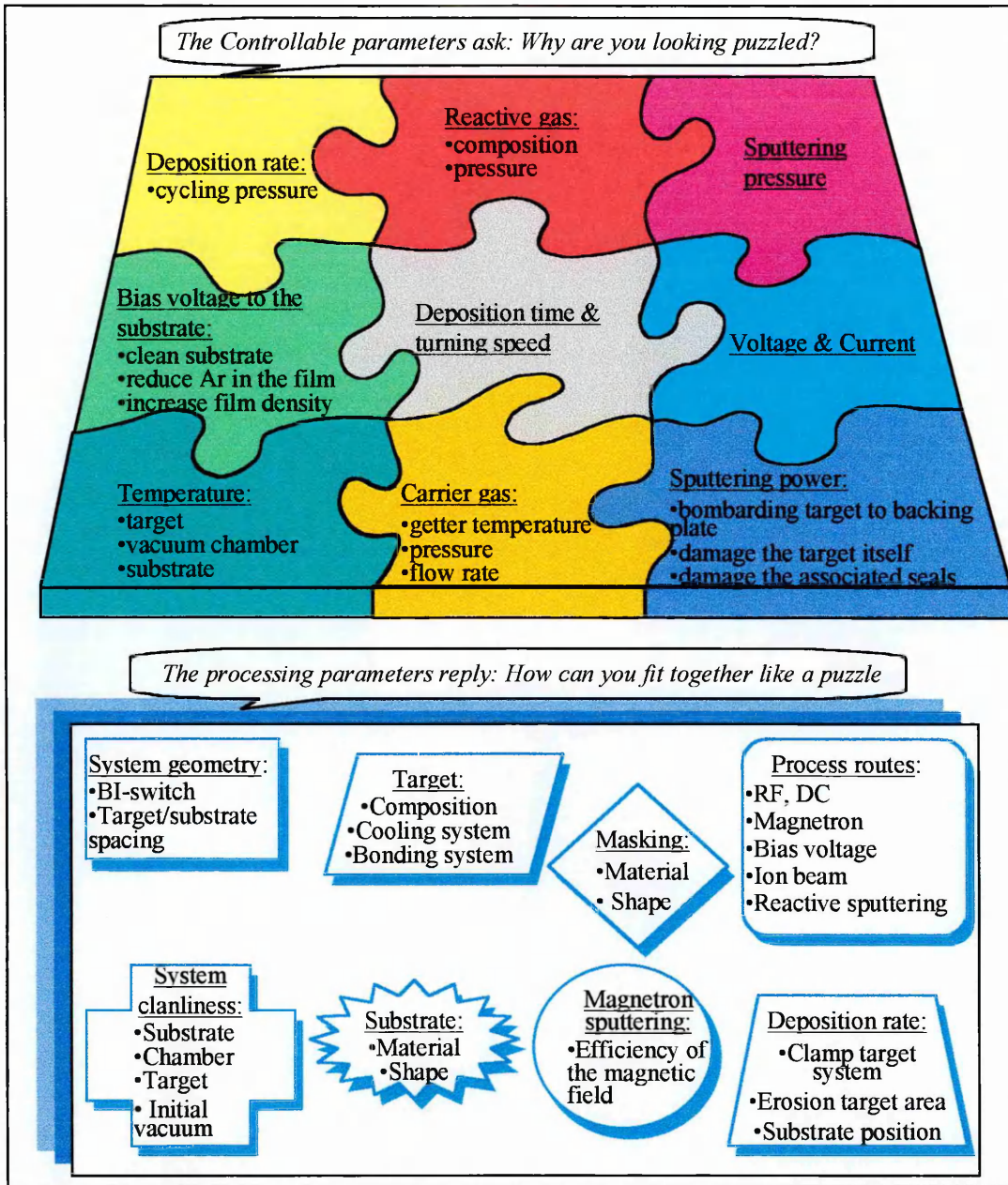•Erosion target area
•Substrate position

Figure 1.21. The processing and controllable parameters of the sputtering process.

Films containing essentially every element in the periodic table have been prepared by also sputtering multicomponent alloys, refractory compounds, insulating materials and PTFE for lubricant films. Alloys, compounds or their mixtures can be prepared from single compound targets or simultaneously from several different targets (co-sputtering), by reactive sputtering or by a combination of these techniques.

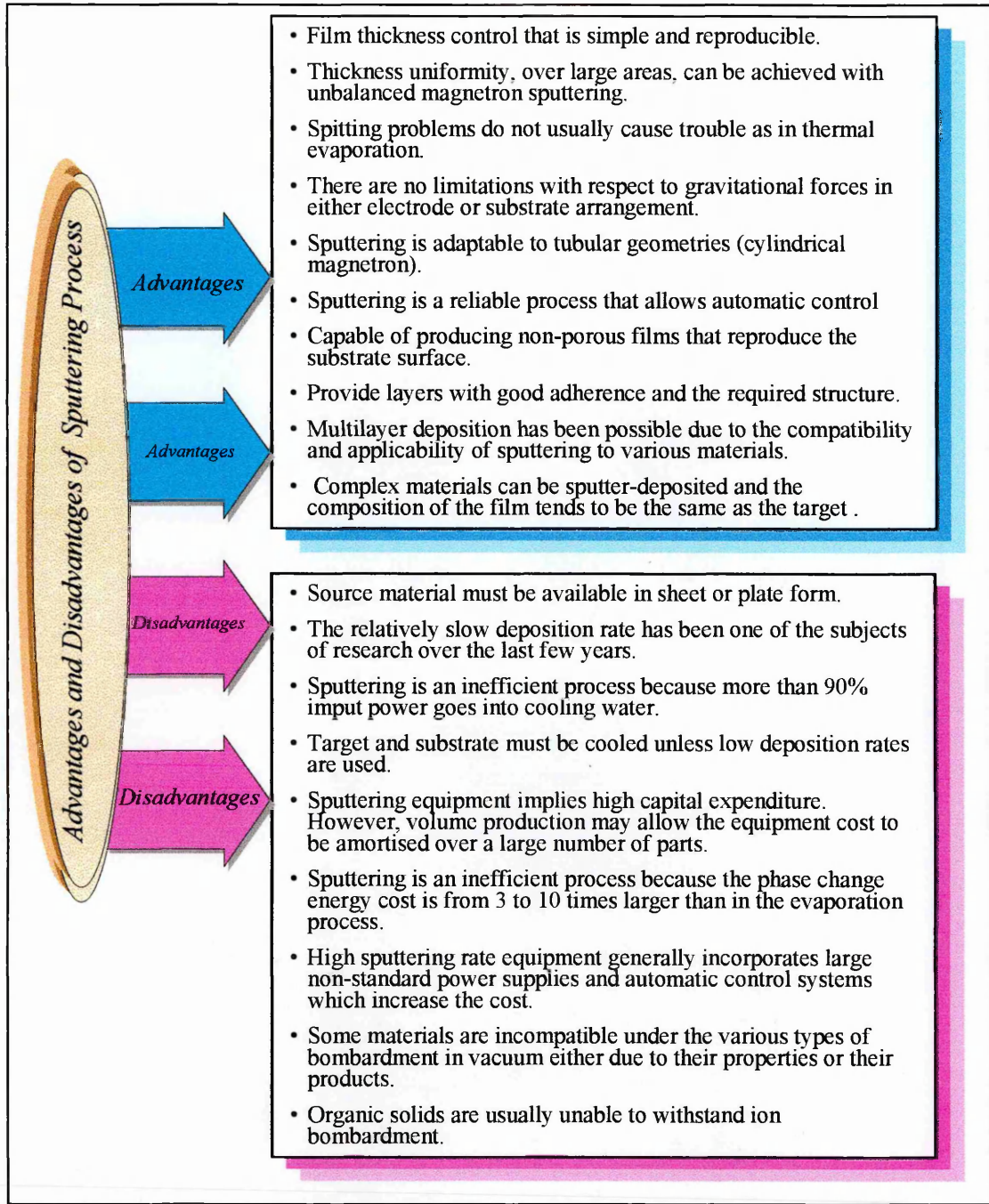Sputtering processes present some advantages and shortcomings, as illustrated in figure 1.22 [68,70,76,77,82,84].

Advantages

- Film thickness control that is simple and reproducible.
- Thickness uniformity, over large areas, can be achieved with unbalanced magnetron sputtering.
- Spitting problems do not usually cause trouble as in thermal evaporation.
- There are no limitations with respect to gravitational forces in either electrode or substrate arrangement.
- Sputtering is adaptable to tubular geometries (cylindrical magnetron).
- Sputtering is a reliable process that allows automatic control
- Capable of producing non-porous films that reproduce the substrate surface.
- Provide layers with good adherence and the required structure.
- Multilayer deposition has been possible due to the compatibility and applicability of sputtering to various materials.
- Complex materials can be sputter-deposited and the composition of the film tends to be the same as the target .

Disadvantages

- Source material must be available in sheet or plate form.
- The relatively slow deposition rate has been one of the subjects of research over the last few years.
- Sputtering is an inefficient process because more than 90% imput power goes into cooling water.
- Target and substrate must be cooled unless low deposition rates are used.
- Sputtering equipment implies high capital expenditure. However, volume production may allow the equipment cost to be amortised over a large number of parts.
- Sputtering is an inefficient process because the phase change energy cost is from 3 to 10 times larger than in the evaporation process.
- High sputtering rate equipment generally incorporates large non-standard power supplies and automatic control systems which increase the cost.
- Some materials are incompatible under the various types of bombardment in vacuum either due to their properties or their products.
- Organic solids are usually unable to withstand ion bombardment.

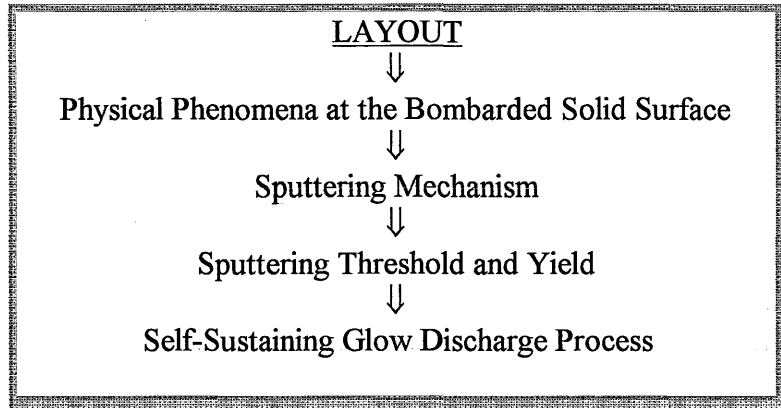*Advantages and Disadvantages of Sputtering Process*

Figure 1.22. Advantages and disadvantages of sputtering process.

The enormous range of sputtering applications reflects the universality of the process due to the relative insensitivity to the properties of the target material. They range from coatings for razor blades to depositing wear-resistant coatings for machine tools. Typical applications are microcircuit metallization layers, microcircuit insulation layers, transport conducting electrodes, amorphous films for integrated optic devices, piezo-electric transducers, photoconductors and luminescent films for display devices, thin film lasers, resistors and capacitors, video-discs [68,82].

1.4.1. SPUTTERING MECHANISM AND GLOW DISCHARGE PROCESSES

LAYOUT
⇓
Physical Phenomena at the Bombarded Solid Surface
⇓
Sputtering Mechanism
⇓
Sputtering Threshold and Yield
⇓
Self-Sustaining Glow Discharge Process

When a solid surface (target) is bombarded by energetic particles (ions, molecules, atoms) several physical phenomena can spring up, as pictured in figure 1.23. The latter are dependent on the bombarding particles (mass, flux, kinetic energy), the flux of non-energetic particles and the bombarded surface (atomic mass, chemical nature).

Several effects of energetic particle bombardment on a solid surface are outlined below [80,82]:

♦ Desorption of weakly bonded surface species (plasma cleaning).

♦ Reflection of the energetic species as high energy neutrals (ion scattering).

♦ Sputter ejection of surface atoms by momentum transfer through collision cascades (physical sputtering).

♦ The impact of the ion may cause the target to eject an electron (secondary electrons).

♦ Sputtering and redeposition of sputtered species by collisions in the gas phase, ionisation and acceleration back to the surface.

♦ Raised chemical reaction of impinging and adsorbed species to produce condensed species (reactive deposition) or volatile species (etching).

♦ The energetic particle may become buried in the surface (ion implantation).

♦ Surface species may be recoil-implanted into the sub-surface lattice.

♦ Mobile species may be trapped at lattice defects.

♦ The energetic particle impacts may also be responsible for structural rearrangements in the target such as: vacancies, interstitials, lattice defects, surface mobilities of atoms (displacement), changes of stoichiometry and changes in electrical charge levels.
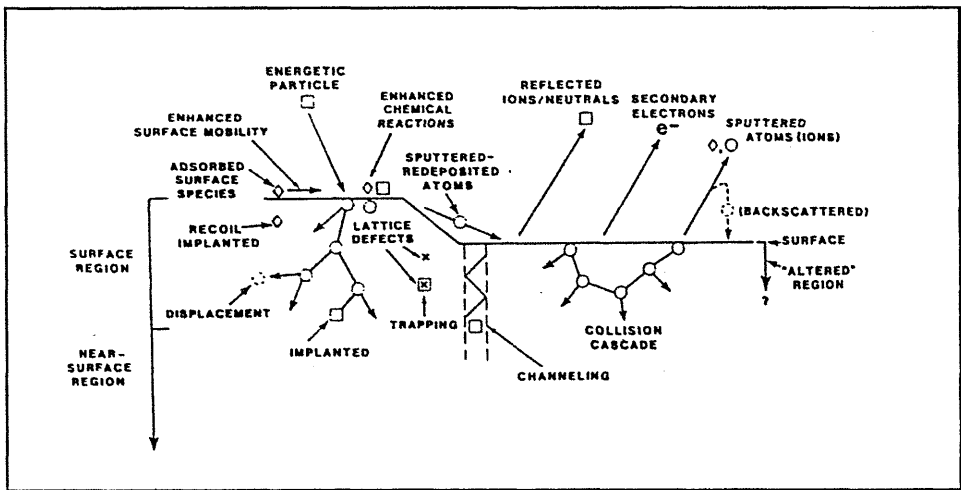
Figure 1.23. Effect of energetic particle bombardment on a solid surface [82].

Sputtering can be considered as a statistical process that occurs as a result of momentum-exchange collisional cascades [82], due to the bombardment of energetic particles on the surface of the target. The so called collision cascade can be explained, on the basis of computer simulation, as a series of binary collisions, as pictured in figure 1.24A. The incident particle strikes the atom 1 (elastic collision) driving it deeper into the target lattice. Subsequently, the glancing collision with atom 2 causes the incident particle to hit atom 3 that is displaced and collides with atom 4. The atom 4 overcomes the surface barrier and can be ejected. The incident particle, atom 1 and atom 2 displace other lattice atoms in subsequent knock-out collisions.

The more practicable simulation of the sputtering process is the comparison with the billiard game break [80], pictured in figure 1.24B. The cue ball (the bombarding ion) strikes the neatly arranged pack (the atomic arrangement of the target), scattering balls (target atoms) in all directions including some back toward the player (out of the target surface). Both approaches have limitations. The dependence of the interactomic forces versus interatomic distance is different from the hard sphere billiard ball model.
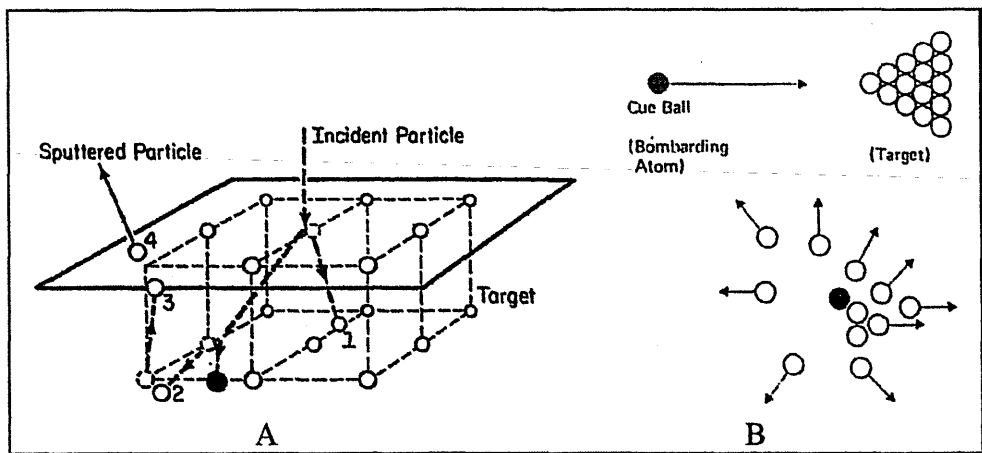
Figure 1.24. Approaches to the sputtering process [80,82].

Summing up, from the approaches above the sputtering process is combined with surface migration of atoms and permanent or temporary damage to the lattice. The kinetic energy of the ions is adsorbed either as electron transitions or goes into the lattice causing atom vibration or displacement and consequently heat. Only less than 1% of the bombardment energy gives sputtered atoms and the remainder causes target heating. The risk of overlapping lattice regions that will be excited simultaneously by individual bombardment is diminished because the interactions in the target are shorter and consequently only interactions between near neighbours should be considered [70,82].

Which energetic particles are used to bombard the target surface? They are mostly ions due to their ability to be accelerated to any desired kinetic energy with any electric field. Using inert gas ions, avoids chemical reactions at the target and substrate. Argon is often used as the working gas, because of its mass compatibility with materials of engineering interest, low cost and it is easily available [84].

The sputtering threshold is the minimum ion energy that is able to dislodge target atoms. The values typically range between 13-35eV. The threshold energy is virtually independent for different ions and for the energy-transfer coefficient but seems to be dependent of the target material which reflects the atomic bonding [68,82].

The sputtering process is quantified in terms of the sputtering yield (S), which is defined as a ratio of the number of emitted atoms per incident ions to the surface. The sputtering yield is determined experimentally. However, in the last few years one of the goals in sputtering has been to be able to calculate yield from atomic or lattice data without adjustable parameters.

M. Kaminsky et al [39], calculated the sputtering yield of compounds and considered that the partial sputtering yield S_v^* of the constituent v of a compound surface is related to the total sputtering yield by the expression $S=\Sigma_v S_v^*$, the partial sputtering yield S_v^* is defined by $S_v^*=N_v/N_i$, where N_v is the number of atoms sputtered of element v and N_i is the total number of ions incident on the compound surface.

The sputtering yield depends on several parameters such as: energy of the incident ion, relative mass of the incident ion, structure and crystallography, target material, incident angle of the ions, surface morphology and sputtering pressure[68,70,77,82,84]. The main features of each one are outlined below:

1. Energy of Incident Ion:

Figure 1.25 shows the variation of sputtering yield for several materials versus argon ion energies. Above the threshold of 20-40eV the sputtering yield rises nearly linearly. The sputtering process in this region is more efficient on the basis of energy consumption. At higher energies, the yield versus ion energy becomes less linear.
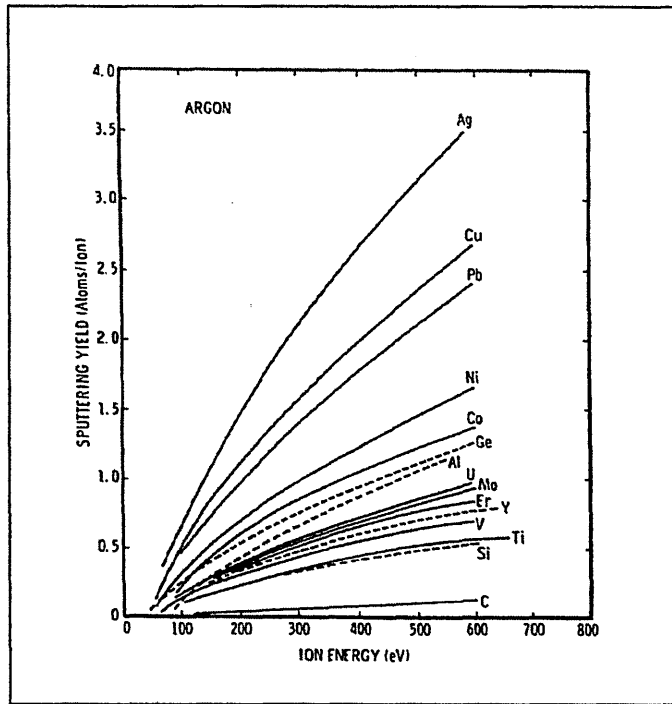
Figure 1.25. Sputtering yield of several materials as a function [82].

2. Relative Mass of Incident Ion:

Sputtering yield tends to increase when the mass of the bombarding particles is of the same order of magnitude or larger than the target atoms. For a given row in the periodic table, the rare-gas ions have the highest yields. The sputtering yield with argon ions is much higher than with He and Ne but only a little less than the more expensive Krypton and Xenon gases. Only when sputtering massive atoms such as uranium is the use of heavier inert gas ions required. The yields vary with ion species much more (factor of 100 or more) than with target atom species.

3. Structure and Crystallography:

The yield depends on the orientation of the crystal with respect to the bombarding ions. Channelling effects in the target near the surface region can modify the sputtering yield.

4. Target Material:

The table 1.10 shows the sputtering yield for various materials under argon ion bombardment. Sputtering yields are of the same order of magnitude for different metals, alloys, insulators and compounds except for carbon and compounds that have a tendency to dissociate. This is why when sputtering alloys it is easier to get the right composition than with evaporation where elemental vapour pressures vary widely. This table also shows the importance of sublimation heat of the target material. The elements from the centre column of the periodic chart (Al, Ti, Zr, Hf and rare-earth series) have the lowest yields.

Target	200	600	Ion Energy (eV) 1,000	2,000	5,000	10,000	Heat of Sublimation
Metal			Sputtering Yields (Atoms/Ion)				(eV/atom***)
Ag	1.6	3.4	-	-	-	8.8	2.94
Al	0.35	1.2	-	-	2.0	-	3.33
Au	1.1	2.8	3.6	5.6	7.9	-	3.82
C	0.05*	0.2*	-	-	-	-	7.39
Co	0.6	1.4	-	-	-	-	4.40
Cr	0.7	1.3	-	-	-	-	4.11
Cu	1.1	2.3	3.2	4.3	5.5	6.6	3.50
Fe	0.5	1.3	1.4	2.0**	2.5**	-	4.13
Ge	0.5	1.2	1.5	2.0	3.0	-	3.98
Mo	0.4	0.9	1.1	-	1.5	2.2	6.88
Nb	0.25	0.65	-	-	-	-	-
Ni	0.7	1.5	2.1	-	-	-	4.45
Os	0.4	0.95	-	-	-	-	8.18
Pd	1.0	2.4	-	-	-	-	3.90
Pt	0.6	1.6	-	-	-	-	5.95
Re	0.4	0.9	-	-	-	-	8.06
Rh	0.55	1.5	-	-	-	-	5.76
Si	0.2	0.5	0.6	0.9	1.4	-	4.68
Ta	0.3	0.6	-	-	1.05	-	8.10
Th	0.3	0.7	-	-	-	-	5.97
Ti	0.2	0.6	-	1.1	1.7	2.1	4.86
U	0.35	1.0	-	-	-	-	5.00
W	0.3	0.6	-	-	1.1	-	8.80
Zr	0.3	0.75	-	-	-	-	6.34
Compound			Sputtering Yields (Molecules/Ion)				
CdS(1010)	0.5	1.2	-	-	-	-	
GaAs(110)	0.4	0.9	-	-	-	-	
GaP(111)	0.4	1.0	-	-	-	-	
GaSb(111)	0.4	0.9	1.2	-	-	-	
InSb(110)	0.25	0.55	-	-	-	-	
PbTe(110)	0.6	1.40	-	-	-	-	
SiC(0001)	-	0.45	-	-	-	-	
SiO_2	-	-	0.13	0.4	-	-	
Al_2O_3	-	-	0.04	0.11	-	-	

Kr ions   **Type 304 stainless steel   ***From Ref. 240

Table 1.10. Sputtering yields of several materials under argon ion bombardment.

5. Incident Angle of the Ions:

Figure 1.26 shows the variation of the sputtering yield versus incident angle of the ions for a constant ion energy. In general the ions approach the target in a direction normal to the target surface. However, when the target surface is irregular, the angle of incident ions can be changed. An ion which is incident on the target surface at an angle θ will have its path length increased by a factor of sec θ before it passes through the depth d. The sputtering yield increases with oblique ion incidence up to 70° and then decreases because the ion reflection dominates.
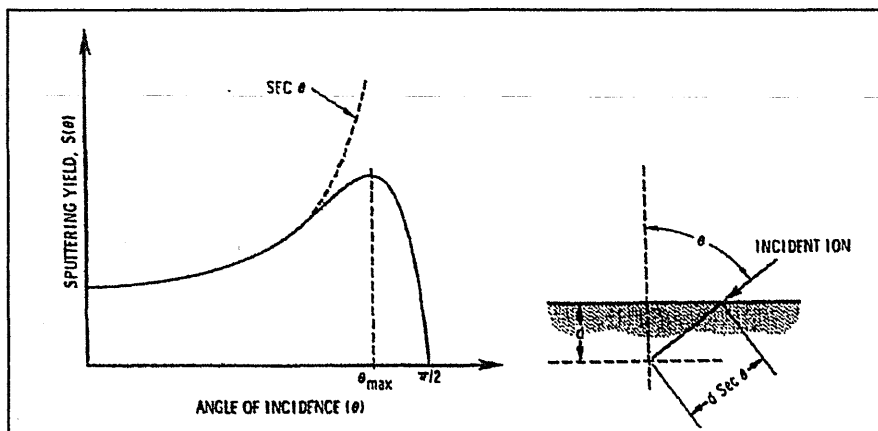

Figure 1.26. Sputtering yield versus ion angle of incidence [82].

6. Surface Morphology:

The roughness of the target surface affects the yield even under normal ion incident conditions because sputtered atoms may not be able to detach from the surface and may become reattached on neighbouring hills.

7. Sputtering Pressure:

The sputtering yield decreases with gas pressure due to backward scattering. The sputtering yield is relatively independent of the target temperature, though at high temperatures evaporation may occur. Moreover, if the bombardment species are ionised or not, this does not affect the yield because the incident ions have a high probability of being neutralised before impact. The erosion rate of the target is given by:

$$R = \frac{(6.23 \times J \times S \times M)}{\rho} \quad \text{(nm/min)} \qquad (1.1)$$

Where J is the ion current density
        S is the sputtering yield
        M is the atomic weight
        ρ is the density of the target material

The life span of the positive ions in the glow discharge at low pressure is defined by the mean free path inside the vacuum chamber. The mean free path of the energetic particles is inversely proportional to the pressure in the vacuum chamber (Torr) [85] as described by:

$$L = \frac{5 \times 10^{-3}}{p} \quad \text{(cm)} \qquad (1.2)$$

An important difference between sputtering and other vapour-phase deposition techniques is that sputtered atoms can have quite high kinetic energies and much greater than thermal. The cosine law describes the energy distribution of sputtered species impinging on the substrate and will also be roughly the same as the ejected species from polycrystalline targets [80]. This dictates the deposition rate, as can be seen in figure 1.44. Likewise, the most probable ejection energy is typically of the order of one half the surface binding energy and in general is found to increase with atomic number of the target. It has been reported that the average energy of the ions emitted from the alloy target was lower than those emitted from the elemental co-sputtering target (the cosine law often do not apply when sputter is from compound targets). The former produce much more uniform film surface morphology and this may be due to the fact that the deposited particles have high surface mobility [86].

The directions of the sputter atoms, from the target, are influenced by the energy and direction of the incident ions. Perpendicular or oblique incident bombardment results in sputtered atoms, from polycrystalline or amorphous targets, in a roughly random direction, owing to the multiple collisions within the target and also the roughness of the target surface [82]. However, collisions between sputtered atoms and the inert gas, change the original direction of the former and decrease their energy. This effect can be greater for high gas pressures due to the mean free path being smaller

compared with the target-substrate spacing. Consequently, the increased number of thermalized particles affects the diffusion process and also the film properties and the thickness distribution [83].

Resputtering may occur during film deposition due to the energetic neutrals, and negative ions created at or near the cathode. But also, for insulating films, the positive ions may be accelerated toward the film surface as a result of a negative floating potential and so produce resputtering.

Some of the effects which can influence the preferential sputtering from a compound material are listed below [39,87]:

♦ The difference in energy transfer between primary ion and the light or heavy elements of the compound.

♦ The difference in the back scattering probability of a light ion from a heavy or light element of a compound for a given ion energy

♦ The difference in the surface binding energies for each element of a compound

♦ Different isotopes of an element may be released preferentially.

THE GLOW DISCHARGE

An undersanding of the self-sustained glow discharge process is fundamental for the design and control of the glow discharge itself. Several analytical methods have been used to study the glow discharge such as: mass spectrometry, electrostatic probes, optical emission spectroscopy [88,89].

The glow discharge is a low pressure gas at low temperature that contain ions, electrons and neutrals. Also, a degree of ionisation is sustained in the glow discharge by energetic particles. Typical glow discharge electron densities are in the range of 10^8 to $10^{12} cm^{-3}$ with average electron energies of 1-30eV, as illustrated in figure 1.27.
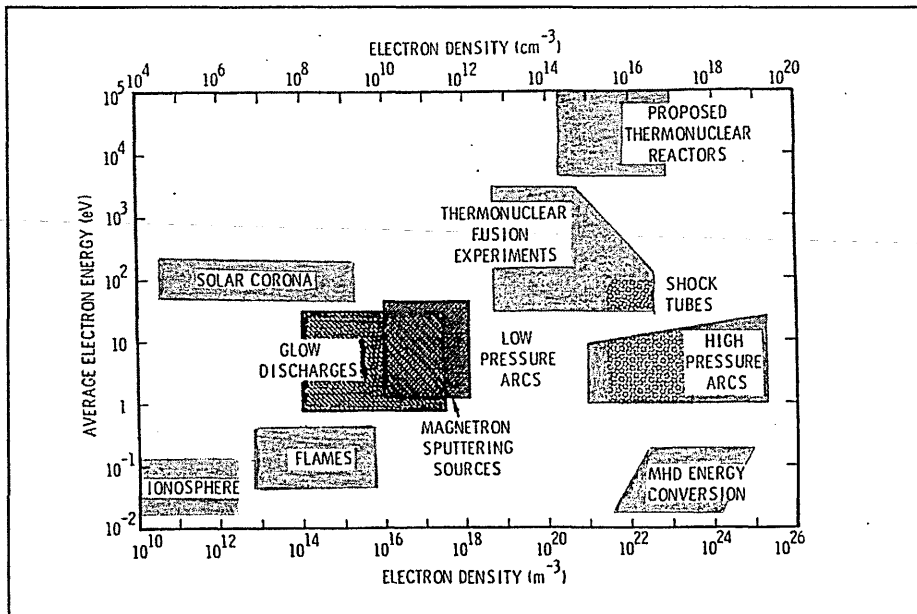

Figure 1.27. Areas of average electron density and energy of several types of plasma [82].

To keep the steady state of electrons and ion density between recombination and ionisation processes requires an external energy source (electric field). The potential variation between the electrode surface and the plasma is mostly confined to a layer called sheaths. The function of the sheaths is to form a potential barrier, so the more mobile species, which is the electrons, except in the case of a strong magnetic field, are electrically reflected.

When an electric field is applied to an ionised gas, energy is transferred more rapidly to the electrons than to the ions. Consequently, at low pressure the electrons can accumulate sufficient kinetic energy to increase the probability of excitation or ionisation during collisions with heavy particles [82]. However, the major factor in sustaining a glow discharge is an electron impact ionisation with argon atoms in the negative glow ($e^- + Ar \rightarrow 2e^- + Ar^+$). Additional contributions come from electron or ion impact ionisation in the cathode sheath and from ionisation of metastables in the glow discharge[84].

The degree of ionisation in a glow discharge depends on the balance between the rate at which ionisation is produced by energetic electrons and the rate at which particles are lost by volume recombination and wall losses. The latter generally dominates over volume recombination. The rate of ionisation depends on the type of gas, the gas pressure and the strength of the electric field.

Several factors determine the occurrence of breakdown voltage (V_b), for a given equipment set up, such as:

♦ Gas pressure
♦ Electric field strength
♦ Ratio of surface-to-volume of the plasma
♦ Mean free path of the secondary electrons
♦ Distance between anode and cathode

The interelectrode breakdown voltage (V_b) as a function of the gas pressure (p) and electrode separation (d) is given by Paschen's law [85] and is illustrated in figure 1.28.
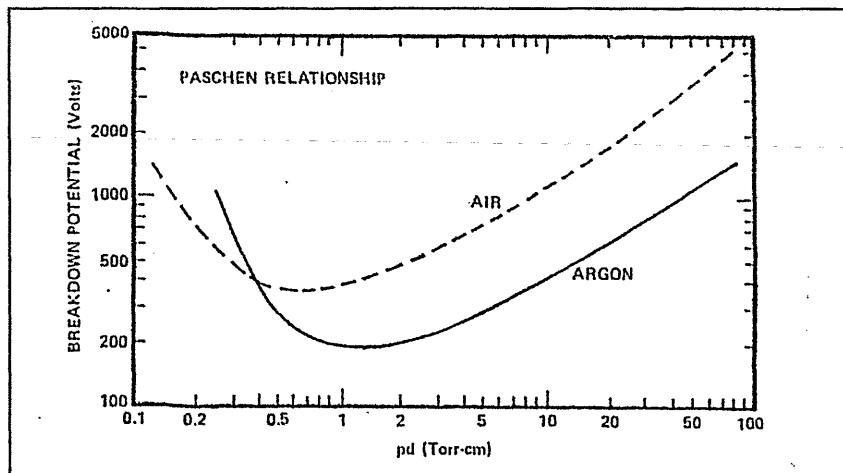

Figure 1.28. Paschen curves for breakdown between plane-parallel electrodes in air and argon at 20°C [85].

From Paschen's curve we can derive the following conclusions:

♦ The curves are useful guides for adjusting the operating conditions for a given piece of equipment in order to produce a plasma discharge.

♦ Increase in breakdown voltage for low values of pd is due to the electrons lost through the walls. This can result either because the sputtering device is small or the gas density is lower.

♦ Increase in breakdown voltage for high values of pd is because the electron energy is too low to produce ionisation. This can occur either at high pressure due to the high frequency of the electron collisions; or at a given applied voltage in a large chamber where the electric field in the plasma is very weak ·

♦ Maintaining the discharge in a small apparatus requires a higher average electron energy to counteract wall losses.

In practice the breakdown voltage occurs at values lower than would be predicted. The ions have lower mobility, due to their mass, compared to electrons. Consequently they tend to gather in front of the cathode to form a space change known as cathode dark space (CDS) or sheath. Then, most the power supply is consumed in that region so the electric field is increased in front of the cathode [82,84]. When the breakdown voltage occurs, the secondary electrons produced at the cathode are sufficient to keep up the discharge, known as a self-sustained glow discharge. The cross-sectional view of the cold-cathode glow discharge is pictured in figure 1.29.
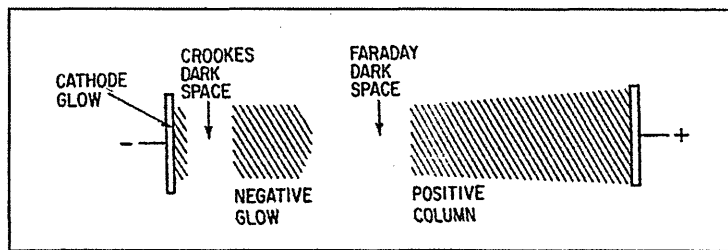

Figure 1.29. Glow discharge cross-sectional view [90].

The glow discharge is maintained during the process basically by secondary electrons emitted from the cathode due to the ion bombardment from the plasma.

The secondary electrons are the important key in maintaining the discharge and also in the growth of sputtered film. These secondary electrons are accelerated and energised in the CDS region and traverse it very rapidly due to the large electric field. Then they enter into the negative glow region (NG), where they are known as primary electrons. The electrons collide with gas atoms and they must produce the necessary volume of ionisation to sustain the discharge. At least each primary electron in the NG region must produce a number of ions to release one further secondary electron from the cathode [82,84].

The NG region of the plasma is where the primary electrons spend their energy in travelling from the target. This region is an ionised gas of nearly neutral charge due to the beam of fast electrons entering from the cathode. The plasma also consists of primary

electrons, thermalised electrons and low-energy ionisation products. The electron energy distribution in the NG is multimodal [82,84].

The Faraday dark space is a region where the electrons have insufficient energy to cause either ionisation or excitation [90]. A positive column region (PC) lies between the NG and the anode. The PC region has enough electric field to transport the discharge current from the NG to the anode.

When two electrodes are moved closer to each other, the CDS and NG regions are unaffected while the PC region reduces and can eventually disappear. The minimum separation is about twice the CDS thickness, otherwise the dark space becomes distorted and then the discharge is extinguished [84]. The target-substrate distance should not be less than a few mean free paths.

The cold-cathode glow discharge operates effectively at low pressures if the electrons are preserved without being lost in the system until they have had a chance to expend their energy in ionisation. To reduce the pressure, the length of the dark space as well as the voltage required to maintain the glow will increase. Ultimately the dark space will extend all the way through to the anode and the available voltage will not be sufficient to start or maintain the glow [90].

At low working pressures the energy of ions bombarding the cathode will be about the difference between the cathode and plasma potential. At higher pressures, where ion collisions become important, the bombardment flux consists of both ions and energetic neutrals due to charge exchange collisions. In this case the average bombardment energies are considerably less than the potential drop across the CDS region.

Sputtering processes are achieved within abnormal glow discharge because the current density and drop voltage in the normal glow discharge are quite low, while the current density in the abnormal discharge increases with increasing voltage, as illustrated in figure 1.30 [90]. The target atoms and argon ions at high pressure collide at a greater rate. The number of bombarding ions tends to decrease with the pressure reduction in the vacuum chamber, but as a consequence their mean free path increases, along with their bombarding energy at the cathode. To sustain the abnormal discharge at high pressure requires a high density of argon collision by primary electrons [85].
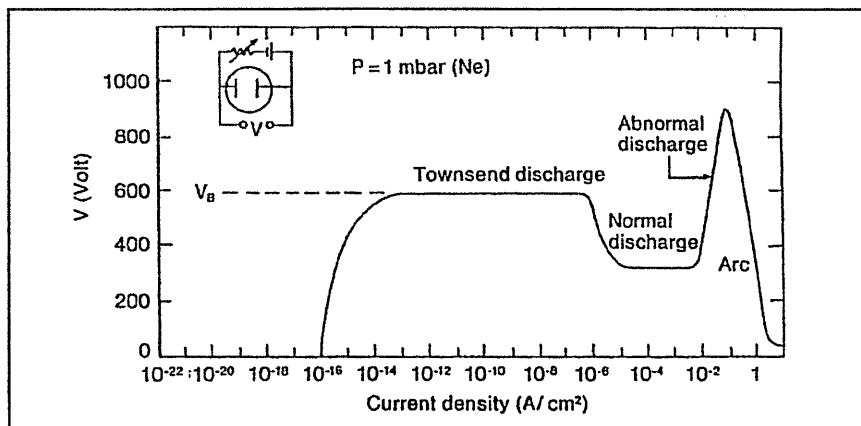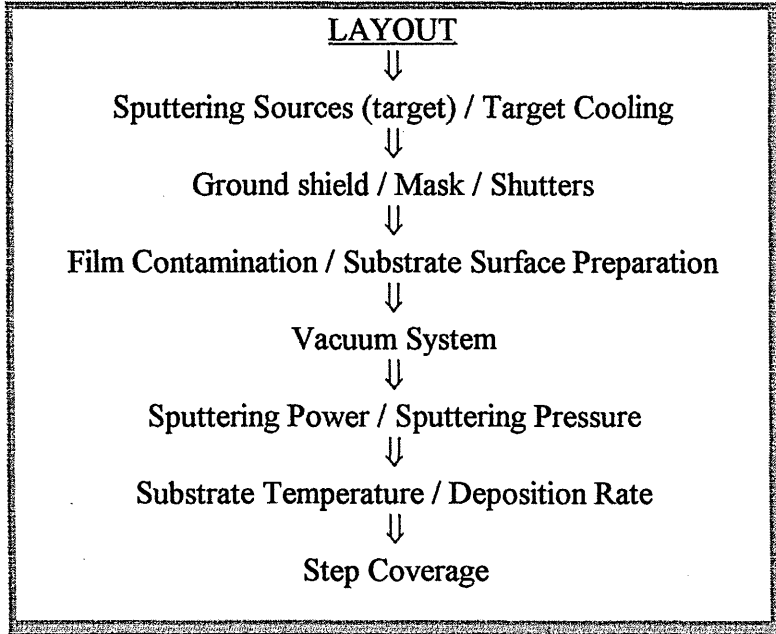

Figure 1.30. The formation of a DC glow discharge [90].

1.4.2. PRACTICAL ASPECTS OF THE SPUTTERING PROCESS

<u>LAYOUT</u>
⇓
Sputtering Sources (target) / Target Cooling
⇓
Ground shield / Mask / Shutters
⇓
Film Contamination / Substrate Surface Preparation
⇓
Vacuum System
⇓
Sputtering Power / Sputtering Pressure
⇓
Substrate Temperature / Deposition Rate
⇓
Step Coverage

The sputtering equipment consists of the following systems: vacuum chamber, vacuum system, sputtering source (target), water cooling system, substrate holders, pressure control system, power supply and gas system. All these systems are illustrated in the figure 1.31.
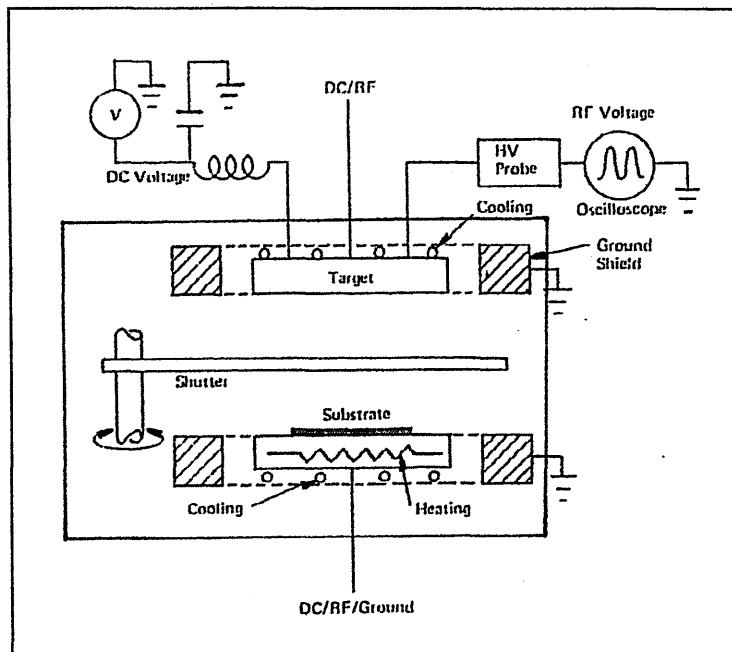
Figure 1.31. Schematic of sputtering system [80].

SPUTTERING SOURCES (TARGET)

Sputtering targets have been used in different shapes, including: flat rectangles, squares or circles, cylindrical, conical, hemispherical, stepped target, etc. Usually, the targets are in the solid state, although powder and liquid are occasionally used. Targets of both single crystal and polycristalline materials are available [77,80].

The wide range of metals, alloys and compounds as well as many different purities, target sizes and tolerances make the target up-to-date. Manufacturing processes for targets used are generally vacuum melting, casting and rolling, cold pressed powder then sintered, hot pressing techniques or vacuum plasma spraying.

Coatings may be formed by using either targets which are a mosaic of several materials (co-sputtering), or several different targets simultaneously to obtain an alloy film, or several targets sequentially to produce a layered coating without breaking the vacuum. Co-sputtering demands a uniform and homogeneous surface to each of the target components in order to obtain stoichiometric films [42,85].

The understanding of source behaviour during deposition and the way it affects film properties and thickness uniformity will undoubtedly improve the design of sputtering sources and apparatus. For example, the film composition tends to be the same as the target if the following aspects occur [82,91]:

♦ Keeping the target cool during the run to avoid bulk diffusion of the constituents

♦ Oxidation effects do not prevail

♦ Resputtering from the film does not occur

♦ The target does not decompose under the operation conditions

♦ Reactive contaminants are not present in the deposition system

♦ The working gas composition does not change during the run

♦ The sticking coefficient or angular distribution for ejected species on the substrate is the same (the sticking coefficient is the ratio of the number of atoms adhering to the substrate to the number of atoms striking the substrate).

For planar diode and triode target systems, it is possible to consume about 70% of the target material before target wear out and less for RF sputtering, while the planar magnetron results in about 35-40% utilisation. Clearly the target utilisation is of prime importance for industrial applications in terms of profitability, as these determine the waste target material and the period of machine downtime for replacing the target and control. The best target utilisation does not give the best thickness uniformity and therefore a compromise has to be made in design between these two factors [91,92]. Nevertheless, most of the targets last for several deposition runs.

TARGET COOLING

Sputtering has been considered an inefficient process because most of the power input to the system appears finally as target heating. For example, the power dissipated as heat into the planar magnetron target, at high sputtering rate, can range from 70-90%

of the power supplied. The remaining energy is carried away by the sputter atoms, secondary electrons, backscattered argon atoms, ions and infrared radiation. The latter leads to heat in the system [68,77,92].

Such heating can become excessive and can lead to severe damage including: the bonding between the target and the backing plate, the target itself (cracks, spalls, composition), the associated vacuum "O-rings". However, this can be minimised or avoided by an efficient direct cooling target system with water or another suitable liquid.

The cooling efficiency of the target, for a given power, depends on several factors, including [92]:

♦ Cooling system efficiency

♦ Thermal impedance of the target and backing plate materials

♦ Thermal and chemical properties of the bonding material between target and backing plate

The cooling efficiency of the target can be estimated by measuring the temperature increase of the cooling water as it passes through the source. With the variation in temperature and the flow rate of the water, the power dissipation can be determined by using the nomograph of the figure 1.32 [77]. However, the calculation accuracy could also be reaffected by secondary electron emission.
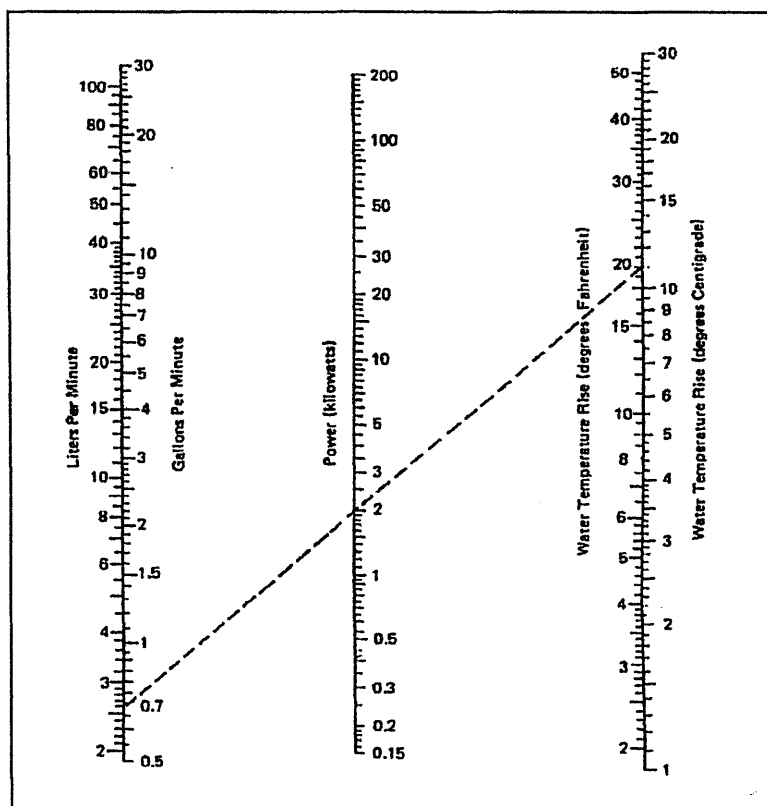

Figure 1.32. Nomograph of the power dissipated in water-cooled sputtering devices [77].

GROUND SHIELD

The target is surrounded by a ground shield. The function of the ground shield is to prevent ion bombardment and sputtering from the target backing plate, mounting clips and mechanical supports that would cause film contamination, and also to promote a uniform erosion rate over the target surface [84,90].

The space between the target and the ground shield must be less than the thickness of the dark space region, in order to sputter only from the target surface. However, some factors could affect this gap and the shield design such as:

♦ Increasing capacitive target-to-ground coupling, as the gap is decreased, in RF discharges.

♦ Sharp points, patches of dirt and non-metallic inclusions may cause local discharges or arcs, particularly with DC discharge and also non-metallic inclusions.

♦ The shield gap fixes an upper limit for the operating pressure because the thickness of the dark space decreases with pressure.

♦ The enhanced sputtering at the edge of the cathode can be minimised by increasing the length of the shield, particularly with longitudinal magnetic fields.

MASKS

Masking areas may be necessary when uncoated areas are required, or to preserve dimensional tolerances [69]. It is important that the mask material does not contaminate the vacuum chamber and the film.

SHUTTERS

Placing shutters between target and substrate is very helpful in achieving thermal and background pressure equilibrium conditions by pre-sputtering, whilst maintaining substrate protection. It is also possible to clean the target by removing the first few atomic layers that could otherwise contaminate the substrate [80].

FILM CONTAMINATION

The atom impurity conditions determine the effect of the contamination on the growth, structure and properties of the film. They can be incorporated at the substrate-film interface into the bulk film or onto the film surface. Furthermore, contamination reactions can occur at various stages of the overall deposition procedure [93,94].

Contaminant impurities at the film-substrate interface can arise from various sources, including [80,93]:

♦ Incomplete, or inefficient, or inadequate substrate cleaning.

♦ Deposition atmosphere contamination.

♦ In the time between cleaning and achieving a steady state to start deposition, in which some undesirable reactions can occur.

♦ In the act of sputter cleaning and deposition of the first layer the substrate is exposed to residual gases from the vacuum chamber or in the sputter gas atmosphere. For example, a partial gas pressure of only 10^{-4}Pa of O_2 or H_2O can cause oxidation rates of up to one monolayer per second.

♦ When the system is opened to be loaded or unloaded, the target is likely to become contaminated by either atmospheric pollution or handling.

Impurity incorporation inside the film is caused by reactions of residual gases during deposition; reactions in the gas phase between film atoms and impurity atoms; sputtering from a poisoned target and interaction of a film during deposition with the various species of a plasma [93]. The impurity concentration inside the film depends on the ratio of the sticking rates of impurity atoms (oxygen atoms for example) to sputtered atoms.

Film surface contamination occurs after film deposition. After deposition, the coating is first exposed to the vacuum chamber and then to the air. Consequently, oxide scales could be formed [93].

SUBSTRATE SURFACE PREPARATION

The surface substrate properties could influence the film formation stages of adatom nucleation, interface formation and film growth, which affects film structure and properties such as: adhesion, pinholes, density, porosity, film microstructure, morphology and mechanical properties [25,30,60,96].

As is evident from the foregoing, the substrate preparation is the first step in film deposition and is also a crucial part of the deposition process. The first goal of this step is a reproducible and economic surface preparation method that allows the fabrication of desirable film properties and good adhesion between coating and substrate[97].

Substrate preparation may involve the reduction or elimination of the contaminants, modification of the physical or mechanical properties of the substrate, activation of the surface species to enhance reaction or the addition of desirable species to the substrate to aid nucleation and adhesion of the film [96].

An important requirement in this step is that the substrate material conditions, and history, should be known and specified to help in selecting the surface preparation method. Monitoring the surface preparation method is difficult because the tests used in monitoring could contaminate the surface. The procedure relies on specifications and testing samples from each batch of substrates [96].

The recontamination of the substrate surface can come from a poor environment (processing gases, condensable vapour, fluids, contacting solid), poor handling or storage and in subsequent processes. This could be overcome by sputter cleaning the substrate immediately prior to deposition [82,96].

Plasma cleaning can be used in situ immediately prior to deposition. The substrate is bombarded by low energy ions and electrons. The bombardment energy depends on the substrate (insulate or conductive), the discharge (RF or DC) and the negative energetic particles from the target sheath. This method is effective for removing contamination without electronic damage, for example thin hydrocarbon or lubricant contaminations from aluminium plates [97]. However, it is ineffective in removing the native oxide layer or compounds.

The sputter cleaning, also known as backsputtering, may have the same drawbacks including [96]:

♦ Sputtering from the backing plate
♦ Contaminants in the plasma can react with the substrate
♦ Sputtered species can be returned to the surface by scattering
♦ The plasma may electronically damage semiconductor materials.

VACUUM SYSTEM

The sputtering requires an operating atmosphere which minimises the interaction between residual gases and the surface of growing film, i.e. a vacuum chamber that must be able to evacuate into the 1.3×10^{-5}Pa (10^{-7}Torr) range. Moreover, if throttling the pumping system is necessary, the working gas pressure must be sustained with the pump in operation. Industrial production coaters usually include a chamber with substrate-loading interlocks to protect the target from atmosphere pollution between deposition cycles and increase throughput [82].

A suitable vacuum system consists of a complete leak-tight vacuum chamber attached to a pump which operates at constant pumping speed, down to the lowest pressure required. Molecules or particles passing through the pump inlet port would be caught and not readmitted. The pump should not contribute to any contamination gases or vapour in the system atmosphere. Electric and magnetic fields and energetic particles should not interfere with the operating pumping system [74]. If a diffusion pump is introducing impurities, these can be minimised by throttling the system until the dynamic pressure at the diffusion pump itself drops to an acceptable value [90].

For applications that involve low vacuum, several types of pump are available such as: mechanical, rotary, vapour-stream pumps [98]. Diffusion and turbomolecular pumps are used with a high vacuum which must be backed continuously by mechanical pumps to exhaust the gases to the atmosphere. Cryo-pumps, sputter-ion pumps and turbomolecular pumps are used in ultra-high vacuum systems [74].

It is important to realise that inadequate sealing techniques are a major cause of problems in vacuum equipment. The greater expense of a strong, reliable seal is justified against the cost of leak detection, repair work, loss of experiments or process product [98]. A common problem met in the operation of high-vacuum systems is the inability to reach the ultimate pressure for which the system was designed, coupled with unusually long pump down times. These symptoms may be an indication of a leak somewhere in the

vacuum enclosure. Virtual leaks may also be observed, associated with ground shield and wall shield cleaning during the earlier part of the deposition process.

SPUTTERING POWER

In sputtering the power density and the rate at which power is inputted into the system contributes to heat in the target. When the power increases, the surface temperature also increases due to the bombarding action of the ions on the target. Excessive heating can lead to damage, as mentioned earlier, and set an upper power limit[77,80,92].

The RF systems are controlled either by the power input to the matching network or the target voltage. The DC voltage is normally obtained by filtering out the RF component with an LC circuit. At both electrodes the sheath voltage is determined by the difference between plasma potential and electrode potential [80]. The power supply must also be able to handle arcing without shutdown or causing damage, which may result from contamination or thin layers of nonconducting material onto the target [77].

SPUTTERING PRESSURE

In order to determine the effects of the vacuum environment on the sputtering process, it is important to consider the working gas pressure. On the other hand, metal-gas interactions at the substrate or the growing film depend strongly on process parameters such as: pressure, temperature [93].

Operating pressure limits are imposed either by the glow discharge or the film deposition. The glow discharge sets a lower pressure limit. The discharge is sustained by electrons that make ionising collisions in the gas. The degree of ionisation decreases when gas density decreases and consequently gas pressure. For very low gas pressures, the discharge current, for constant voltage, will also decrease and the sputtering rate will become very small [80].

For a constant power input the deposition rate increases linearly with pressure, due to the increased ion density and so the sputtering-current density increases. When still higher pressures are used, the deposition rate falls off rapidly with increasing pressure. In practice the optimum working pressure may be lower than the breakdown point. This is because the problem of backstreaming of the pump fluid occuring may lead to a local rise in chamber pressure.

Also, at high pressures the dark space is reduced, so making it more difficult to have an effective ground shield [68]. Furthermore, at high pressure the mean free path of the sputtered atoms and ions will be short, so the high collision probability will lead to lowering the energy of ions and neutrals. Consequently, the backscattering of the sputter atoms to the target is increased and also the charged particle density at the substrate[77,80,83].

One can envisage that an increase in inert gas pressure means an increase in the background impurity concentration that will be transferred to the growing film. Also,

argon may become entrapped in the film. The latter can be minimised either by increasing the substrate temperature or applying bias voltage [90].

SUBSTRATE TEMPERATURE

The substrate temperature affects the growing film, its final structure, the sticking coefficient, deposition rate, and gas incorporation into the film [77]. So it is an important parameter but often difficult to control [80].

The goal is to measure the temperature of the substrate surface rather than the bulk substrate. However, it is a difficult task due to the thermal barrier present, e.g. the electrical isolation between the substrate and thermocouple or due to thermal isolation between substrate and substrate platform. The problem is intensified by the power input to the substrate from the glow discharge, which is liable to make the surface temperature greater than that of its bulk. The absolute value of substrate surface temperature is therefore quite difficult to determine.

The use of a thin film thermocouple evaporated onto the surface of the substrate has been proposed, but this is not very convenient because it could contaminate the film[80]. Another option is to use an infra-red thermometer that measures the infra-red radiation emitted by the substrate, but this demands a knowledge of the transmission characteristics of the window through which observation is made, unless the detection system can be built into the vacuum system, and also a knowledge of the surface emmissivity[80].

Heating of the substrate platform can be achieved by circulating a hot liquid or by electrical resistance and radiant heating. While cooling of the substrate platform can be attained by circulating cooling water or liquid nitrogen [80].

DEPOSITION RATE

The main factors that influence the deposition rate are the current density, the voltage, substrate and target temperature [83,90,92]. The deposition rate can be increased until the target temperature starts to damage the sputtering system or produce undesirable film properties such as high stress [92].

At a given power, the current density is more efficient for determining the deposition rate rather than voltage owing to the fact that the sputtering yield increases slowly with increasing ion energy, while the sticking coefficient is proportional to the current density. On the other hand, increasing the discharge current by increasing the applied voltage is restricted because the ionisation decreases with increasing electron energy over 100eV [82]. Consequently, it is an advantage to sputter at high current and low voltage by using either thermionically or magnetically supported glow discharges or by increasing the pressure [90]. However, the sputtering rate can only be increased by increasing the argon pressure in a limited range [82].

The deposition rate, uniformity and consequently the film thickness distribution are determined not only by the sputtering source such as: design, area, its characteristics

emission behaviour (e.g. cosine or point source), but also by parameters such as: operating pressure, target-to-substrate distance and their relative orientation, substrate geometry [91,92].

To achieve better uniform film thickness may require repetitive experimentation, which is time consuming. Nevertheless, the homogeneity of the film thickness is of interest in the production of and development of thin films. The designers of sources and coating systems, must take account of the useable substrate size and overall process economics [83].

STEP COVERAGE

Components with vertical steps have been a problem to coat with the same deposition rate as for the whole component, i.e. conformal coverage. Cracks could develop as the film on the different surfaces grows together as illustrated in figure 1.33. Neither rotating the substrate table nor using planetary rotation offers a proper solution. Improvement to the step coverage and minimising the possibility of cracking can be achieved by increasing the substrate temperature or by substrate bias. The substrate bias level can be applied to make the film thickness of the wall the same as the plane surface by resputtering [77].
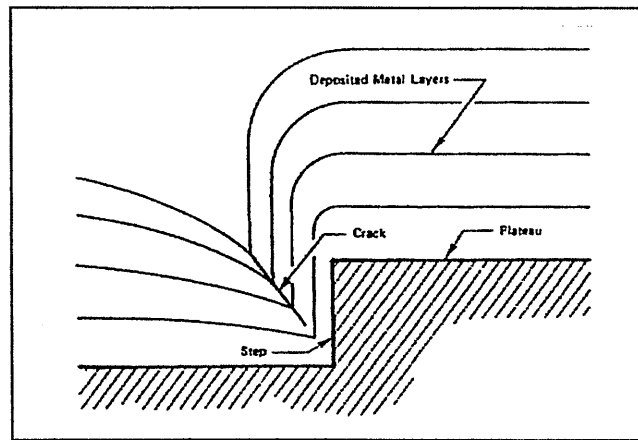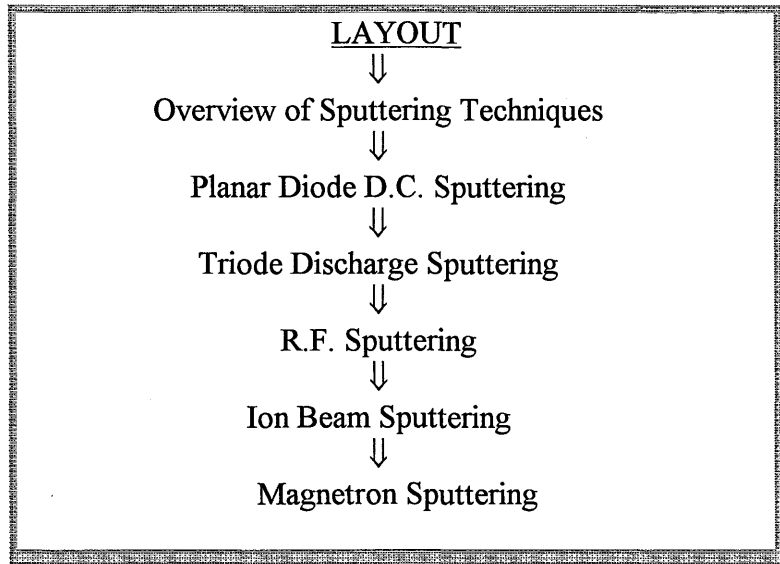

Figure 1.33. Conformal coverage configuration [77].

1.4.3. SPUTTERING TECHNIQUES

<div style="border:1px solid">

<u>LAYOUT</u>
⇓
Overview of Sputtering Techniques
⇓
Planar Diode D.C. Sputtering
⇓
Triode Discharge Sputtering
⇓
R.F. Sputtering
⇓
Ion Beam Sputtering
⇓
Magnetron Sputtering

</div>

The basic demands for commercial applications of thin film technology processes by sputtering methods include: high deposition rate, uniformity of the film thickness over a large area, good target utilisation and often low substrate heating [92].

A number of techniques have been developed to provide better control over film chemistry, microstructure and properties, and sputtering process demands, including: DC glow discharge, Triode discharge, RF discharge, Magnetron and Ion-beam sputtering. The sputter deposition techniques, in any configuration, could be operated in three modes: reactive sputtering, bias sputtering and ion irradiation [82].

All these techniques utilise a low pressure glow discharge that has been confirmed to be the most cost effective source of ions. Often it has proved difficult to achieve a uniform and sufficient supply of ions over the target surface. Also, the low deposition rate that may result can make the sputtering process uneconomic for most industrial applications. Consequently, a wide range of glow discharge apparatus geometries have been used in an attempt to [82,92]:

♦ Increase the ion supply and thus the sputtering rate
♦ Increase the target area and thus the available deposition area
♦ Reduce plasma heating of the substrate
♦ Permit low working-gas pressures
♦ Facilitate the coating of particular substrate shapes

The selection of a sputtering device for a given application depends on the substrate (size, shape, material, temperature sensitivity, resistance to plasma irradiation), nature of the coating (single or multilayer design, thickness, materials, critical properties, lifetime) and production volume. The main feature of each sputtering technique will be reviewed below:

1-PLANAR DIODE DC SPUTTERING

The planar diode is the simplest configuration of sputtering apparatus, as illustrated in figure 1.34. Nevertheless, a wide variety of thin, complex films, multicomponent films and refractory films have been deposited by this technique.
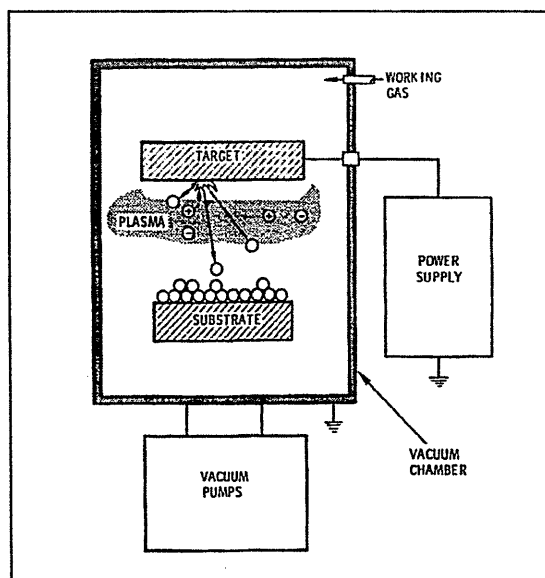

Figure 1.34. Scheme of a parallel-plate diode sputtering system [82].

In a DC diode the sputter source is a cathode of an electric circuit. A high negative voltage (DC) is applied to the cathode. Then a glow discharge of a type known as an abnormal negative glow, as described in chapter 1.4.1, is maintained between the electrodes with a suitable pressure. A ground shield is clamped around the target. The latter is water cooled unless it is to be operated at low deposition rate or for short runs.

The substrate is placed on a grounded anode (target). The two electrodes are housed in a vacuum chamber. The argon gas is introduced into the chamber, typically at pressures of 3.9-13.3Pa (30-100mTorr). The voltage required to maintain a glow discharge having a current density of 0.1-2.0mA/cm^2 is usually in the range 500-5000V[84,90]. The dark space thickness is typically between 1 and 4cm, depending on the pressure and the current density.

Several factors could decrease the deposition rate, which is one of the main limitations of this process, including [82]:

♦ The ions and fast neutrals that bombard the target have an energy that may be less than 10-20% of the potential drop across the CDS owing to the fact that, at typical operating pressures, the ion motion, is disrupted by collisions and charge exchange with gas atoms in the CDS.

♦ The high scatter level of sputtered atoms during transport from the target to the substrate.

♦ The collision-dominated transport of the sputtered atoms reduces their kinetic energy by the time they reach the substrate.

♦ Many of the energetic primary electrons and ions spend their energy by bombarding the substrate because they fail to transfer their energy into the plasma.

♦ Ions and electrons could be lost from the edges of the discharges.

The foregoing suggest the DC diode technique's main limitations are due to the lack of ionisation to sustain the glow discharge. This can be minimised by either increasing the probability of ionisation or increasing the number of electrons in the following ways [80]:

♦ Using a magnetic field to contain the primary electrons.

♦ Using the ionisation enhancement given by RF excitation.

♦ Injecting electrons into the discharge by using a hot filament electron source.

The planar diode can operate with both DC and RF power supply and also in two modes: reactive sputtering and bias sputtering. Substrate sputter cleaning and bias sputtering are easily attained by adding a negative bias to the substrate holder. Applying an axial magnetic field may lower the operating pressure or increase the ion current but could squeeze the discharge and cause non-uniform deposition onto the substrate.

The main advantages and some of the drawbacks of DC diode technique are illustrated in figure 1.35 [70,77,82].

ADVANTAGES

- The technique is suitable for research and small production volume.

- It is a widely used technique due to its simplicity.

- The target can be fabricated easily from a wide range of materials.

- Good film adhesion is assured for low temperature epitaxy.

DISADVANTAGES

•Substrate heating.
•Low deposition rates.

• Inability to sputter from an insulating target. An insulator surface in a plasma will cause negative charge build up to the plasma potential like a floating electrode.

•Arcing could be a problem due to patches, pockets of outgassing, or asperities This could lead either to the necessity of conditioning a target before usage, or by slowly increasing the applied power and sputtering away the arc forming effect.

•Inability to deposit on insulating substrates

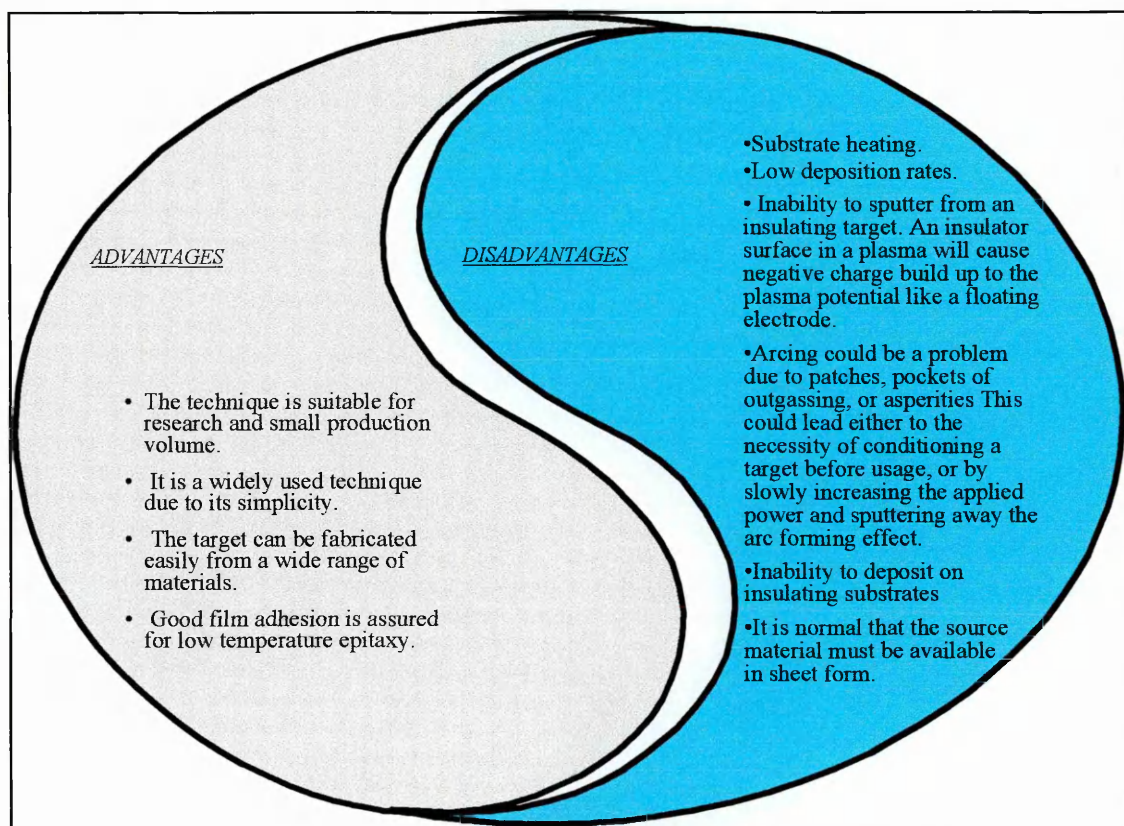•It is normal that the source material must be available in sheet form.

Figure 1.35. Advantages and disadvantages of DC diode technique.

2-TRIODE DISCHARGE SPUTTERING

Triode discharge devices use an additional electrode, independent of the target, as illustrated in figure 1.36. Consequently, additional electrons are injected into the glow discharge by thermionic emission rather than by impact ion bombardment. The purpose of the hot filament is to increase the ions at the target surface, so keeping the target bias voltage constant, which increases the ionisation that is required for sustaining the glow discharge [68].
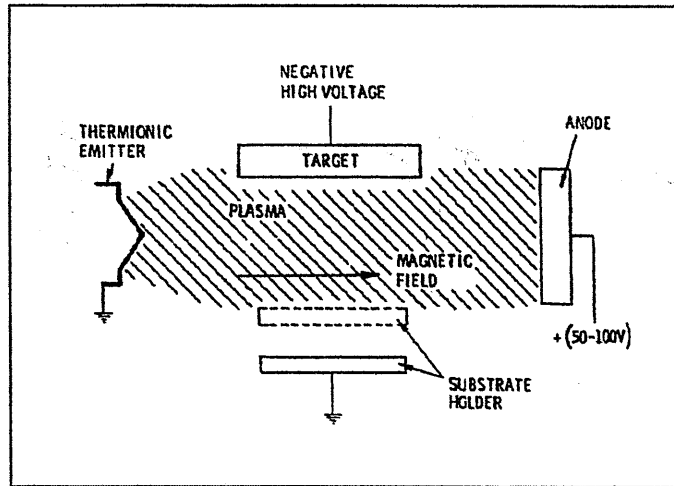

Figure 1.36. Scheme of a triode discharge device [82].

The hot-cathode triode can be operated at low pressures such as 6.6×10^{-2} - 1.3×10^{-1} Pa (0.5-1mTorr) and the driving voltage is only 50-100V, although the current may be several amperes from an AC or DC source. The filament is made of tungsten or another refractory metal. An adequate DC or RF potential could be applied to the target[70,77,80,82,90].

Applying an axial magnetic field could help in keeping electrons away from the chamber walls; interaction with the chamber walls reduces the electron velocity, permitting recombination and this removes primary electrons from the plasma. The magnetic field thus enhances ionisation and excitation by increasing the availability of primary electrons. But such a field could produce a distortion of the current distribution over the target surface [80,82,99].

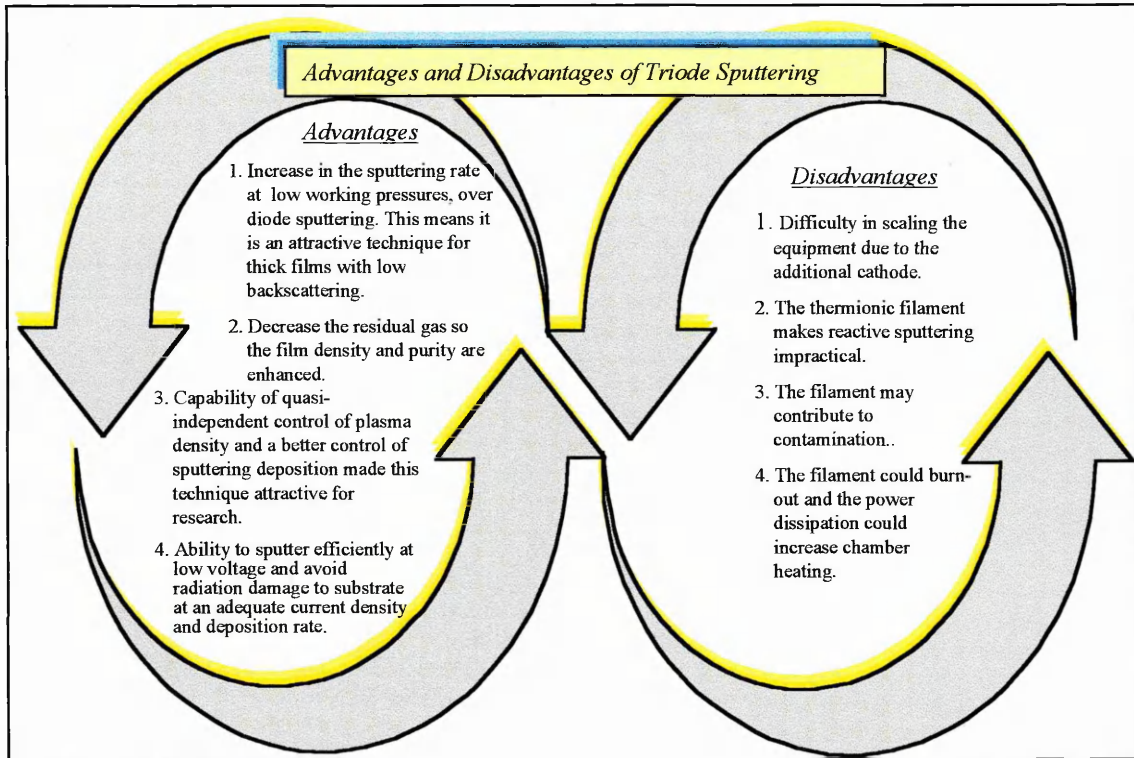The advantages of this technique as well as the main disadvantages are outlined in the figure 1.37 [68,70,77,80].

Advantages and Disadvantages of Triode Sputtering

Advantages

1. Increase in the sputtering rate at low working pressures, over diode sputtering. This means it is an attractive technique for thick films with low backscattering.

2. Decrease the residual gas so the film density and purity are enhanced.

3. Capability of quasi-independent control of plasma density and a better control of sputtering deposition made this technique attractive for research.

4. Ability to sputter efficiently at low voltage and avoid radiation damage to substrate at an adequate current density and deposition rate.

Disadvantages

1. Difficulty in scaling the equipment due to the additional cathode.

2. The thermionic filament makes reactive sputtering impractical.

3. The filament may contribute to contamination..

4. The filament could burn-out and the power dissipation could increase chamber heating.

Figure 1.37. Advantages and disadvantages of triode sputtering.

3-R.F. SPUTTERING

The RF sputtering device is illustrated in figure 1.38, where a non-conducting target is placed over one electrode and a substrate on the other one. An alternating voltage (AC) power supply is used at RF frequency. The operating frequency is generally 13.56MHz, since this is the frequency in the 10-20MHz range that has been allocated by the Federal Communication Commisson for Industrial-Scientific-Medical purposes [82,68]. This frequency does not allow accumulation of ion charge in a cathode during the RF cycle. If some positive charge is gathered during one half-cycle, then it can be neutralised by electron bombardment during the next half-cycle. Thus, the electrodes need no longer be electrical conductors.

The RF glow discharge forms with a CDS over each electrode. The electrons spend almost all their time near the centre position between the electrodes, and oscillate between cathode and anode on each half of RF cycle. When the electrons go toward one electrode, this uncovers ions at the other electrode to form a positive ion sheath. This sheath takes over nearly the total voltage in which the ions are accelerated and where they then bombard the electrodes. When the electrons go toward an electrode for only a small fraction of a half cycle, some of them can balance the ion flux through the cycle. Consequently, the electrodes approach or exceed the plasma potential for a very short part of RF cycle.

At RF frequency, only the electrons can follow the temporal variation in the applied potential because the ions are relatively immobile. Thus, the plasma can be

pictured as an electron gas, that moves back and forth, i.e. in an oscillating movement of electrons, in a sea of near stagnant ions [68].

Additional electrons are created as a result of this electron oscillation in an RF field. There they can pick up sufficient energy by making in-phase collisions with gas atoms to cause ionisation in the plasma. Additional ionisation could come from less energetic electrons that are repelled from the electrode toward the discharge. This variety of plasma excitation is very effective at high frequencies and can be maintained at lower gas pressure. This means that the secondary electron is no longer key to maintaining the RF discharge.

The RF current through the plasma is predominantly an electron current caused by electron motion instead of power transfer from the oscillating electrons into the gas. This current is out of phase with the applied voltage. Power transfer only occurs as the ion current passes through the sheaths, unless some ions and electrons are in phase with the voltage. The ion current and thus the sputtering rate at a given electrode, is determined by the difference in potential between the electrode and the plasma [68].

The electrical character of an RF discharge can be classified either as balanced or unbalanced or single-ended [68,82,95]. In a balanced system both electrodes are identical and their potential is 180° out of phase, as illustrated in figure 1.38A. The sputtering voltage is about equal to half the peak-to-peak RF potential and each electrode could be covered with a dark sheath and be sputtered. In an unbalanced system the electrode on which the substrate is placed is larger than the target electrode. So the drop in RF voltage across the substrate electrode is small, due to the large sheath capacitance, as illustrated in figure 1.38B.
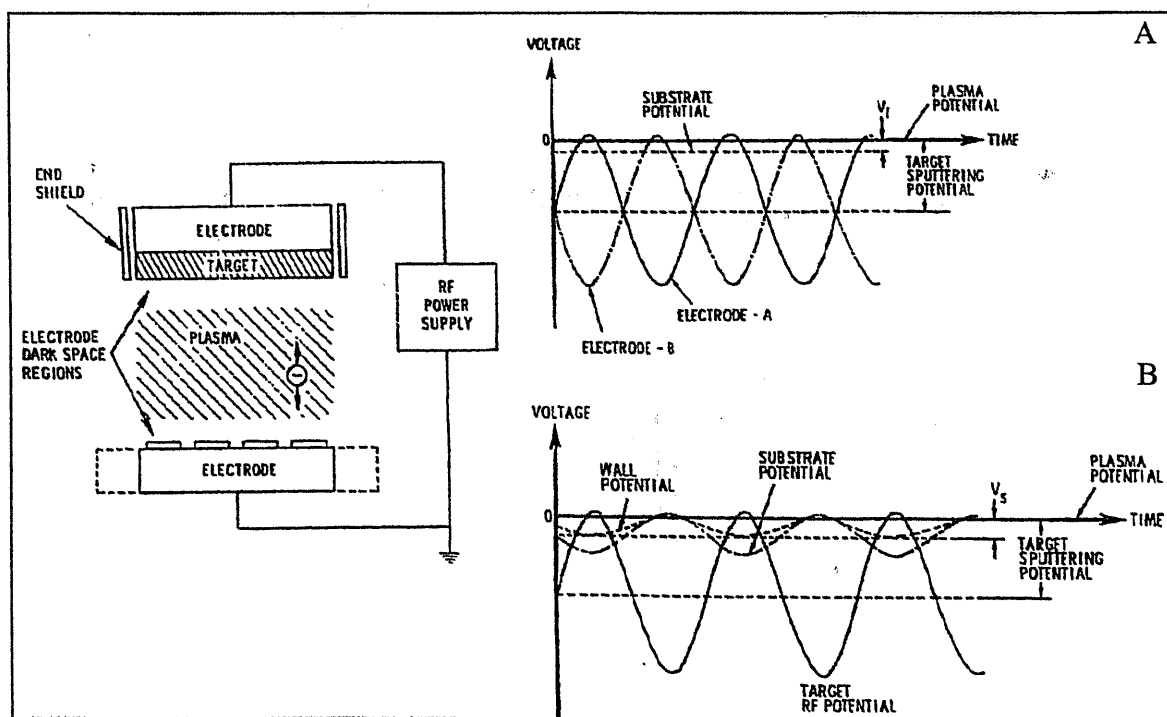

Figure 1.38. Scheme of a planar RF diode sputtering device and the target voltage versus the plasma potential for a balanced system (A) and for a single -ended system (B) [82].

The typical electrical circuit, in the RF sputtering technique, consists of: RF power supply, an inductive coupling to the load and a matching network. The RF system requires an impedance matching network between the power supply and the vacuum chamber. The purpose of this network is to increase the power dissipation in the discharge and to protect the generator.

Since both electrodes and chamber walls are in contact with the plasma, the impedance is dominated by the sheaths. The sheath capacitances result from the charge separation across the dark space. Long leads will exhibit inductance, while overhanging flanges and projections will exhibit capacitance. If the substrate is not properly grounded, undesirable RF voltages can develop on its surface. As a result, these power losses decrease efficiency [77,90,95]. Many commercial sputtering sources monitor the reflected power from the load as an index of how effectively the matching network is adjusted. The reflected power should be minimised.

The main advantages of this technique are outlined in figure 1.39 [82,95].

1. The RF technique allows films to be deposited from insulating targets.

2. The RF discharge uses electron ionisation more efficiently, so the operating pressures can be extended down to 1mTorr and the electrons lost from the plasma are also reduced.

3. RF discharges in planar diode systems can be operated at lower pressures such as 0.6-1.9Pa (5-15mTorr), compared to DC discharge 4-13.3Pa (30-100mTorr)

4. The RF system is more efficient, compared to DC in sustaining the glow discharge

5. Arcing rarely forms in RF discharges. The field is maintained in one direction for less than one cycle and reduces to zero twice in each cycle, making it difficult to sustain the arc

6· Reduced scatter of the sputtered atoms due to low operating pressure

7· Reactive sputtering can be used with RF discharges

Advantages of RF Technique

Figure 1.39. Advantages of RF technique.

The RF sputtering technique has a wide application in the electronics industry for nonconducting and semiconducting materials, insulating materials, compounds, refractory semiconductors, ferroelectric compounds, oxides, pure metals, alloys, nitrides, sulphides, chlorides, pyrex glass and plastic.

4-ION BEAM SPUTTERING

Ion beam sputtering techniques are arranged such that the target is held obliquely and intersects an ion beam that is created by an independent ion source, as illustrated in figure 1.40. The substrates are suitably placed to receive the film.
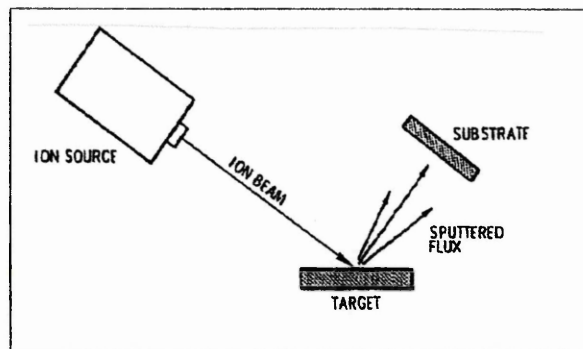

Figure 1.40. Scheme of ion-beam sputtering [82].

This method permits independent control over the energy and the current density of the ion bombardment. In addition, the ion beam source can deposit material at very low working gas pressures (<0.1mTorr) onto substrates that are not in contact with a plasma [70].

The method is ideal for collecting data at higher bombarding-ion energies. However, these devices are limited for industrial applications due to the small ion-beam sizes of about 1cm and so the deposited area. Recently, the ion thruster technology has been provided with an ion beam source with large diameter, between 10 and 30cm, while Kaufmann ion beam sources are now available up to 1m in diameter or more [82]. The main advantages of this technique are outlined in figure 1.41 [80].

Advantages of Ion Beam Sputtering

• The substrate is not part of the electrical circuit, so it is much easier to incorporate substrate heating, cooling and process control.

• The low operating pressures minimise gas incorporation into the growing film. Reduced sputter particle collision means the sputtered atoms keep their energy.

• An attractive method for ion beam etching, special deposition applications and research studies

• Ability to sputter under high-vacuum conditions

• Ability to maintain a field-free region between target and substrate which allows the sputtering of powder materials and minimises unwanted heating.

Figure 1.41. Advantages of Ion Beam Sputtering.

5-MAGNETRON SPUTTERING

The use of magnetron sputtering devices has grown swiftly in the past two decades due to the industrial deposition of refractory films, high temperature wear resistant films as well as microelectronics thin films [70,85]. Nevertheless, new magnetron designs have been continuously developed over this time span while relatively little work has been published on the fundamental aspects of the magnetron process [100]. The purpose of using a magnetic field in a sputtering system is to increase the sputtering rate, extend the operating conditions and reduce electron bombardment at the substrate. The magnetron systems also attempt to make the plasma more efficient by trapping the electrons near the target, increasing their ionising effect and reducing their losses [80].

The magnetron sputtering technique can be defined as a cold-cathode discharge, enhanced using a magnetic field. The $\bar{E} \times \bar{B}$ drift and cathode sheath are shaped to ensure that the secondary electrons emitted from the target are trapped within the negative glow region. Consequently the mean free path (m.f.p.) of the electrons in the discharge is decreased and the collision cross-sections are increased. More ions can then be produced for ionisation without increasing the gas pressure. Moreover, the loss of fast electrons going to the anode and walls is eliminated. The magnetic field also accelerates the ions to knock out the target particles [72,80,82,85,92].

How do the electrons behave in the magnetron discharge? The electrons in a magnetic field can be trapped and then collisional diffusion across the magnetic field lines makes the plasma more efficient. An applied electric field perpendicular to the magnetic field makes the electrons undergo a motion in a direction perpendicular to both fields. This motion is known as the $\bar{E} \times \bar{B}$ drift and has a cycloidal form if the initial electron energy is small compared to that gained from the electric field, as illustrated in figure 1.42A. However, if the initial electron energy is large compared to the electric field then the $\bar{E} \times \bar{B}$ drift becomes more circular, as illustrated in figure 1.42B. Magnetic field strengths between 50 and 100G are usually used with sputtering glow discharge devices[72,82].
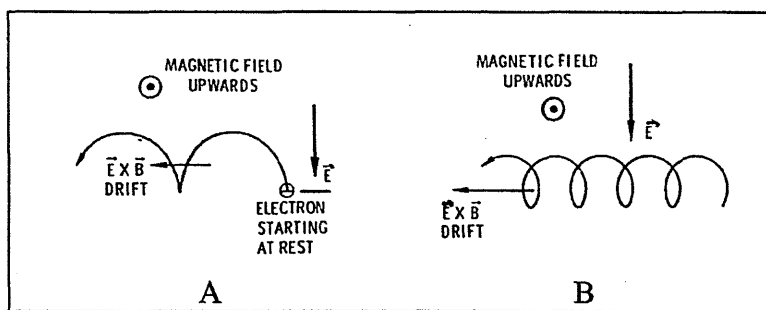

Figure 1.42. The electron paths in static magnetic and electric field [72,82].

The plasma only exists in the target areas where the magnetic field and electrical field are orthogonal to each other. Consequently, the maximum force is exerted on the particles in this area. Therefore, the etching zones of different shapes on the target can be identified in conformity with the plasma shape where the discharge occurs.

Magnetron sputtering can be configured in a variety of forms including: planar magnetron (circular or rectangular), S-gun type, cylindrical type (cylindrical-post

magnetron, hollow magnetron, magnetic end-confinement). The selection of a particular type of magnetron depends on the deposit material, substrate and target availability for a desired geometry. The cylindrical targets are difficult to manufacture and are more suitable for batch processes. The planar targets are easily machined or hot pressed and are more suitable for continuous process operation [77].

In the plasma-ring devices, some field lines could intersect the substrate which allows electron bombardment to the substrate. However, the electron bombardment intensity is much less over planar diodes and consequently the substrate heating is less. All plasma-ring magnetrons offer the advantage that a magnetic field can be produced by permanent magnets located within the cathode rather than by magnetic field coils located at or beyond the chamber walls for cylindrical magnetrons.

Magnetron sputtering can be undertaken using either DC or RF power supplies. DC magnetrons are typically operated at discharge currents in the range of 1 to 50A. A magnetic field parallel to the RF field can constrain the electrons and reduce their chance of being lost, mainly at lower pressure. The magnetic field is considerably more important for enhancing the RF discharge in terms of improving its efficiency, compared to the DC discharge.

When a magnetic target material is used, it must be magnetically saturated so that its magnetic behaviour is surpressed and a field of the desired shape can be maintained over its surface [70].

Typical current-voltage curves for various types of magnetron source compared to planar diode are shown in figure 1.43. These curves show the effect of ionisation processes in a plasma discharge [70,82]. A more efficient discharge requires lower voltage for a given cathode current density. Magnetron discharge obeys a relationship of the form I proportional V^n, where n is an index to the performance of the electron trap and is typically in the range 5 to 9.
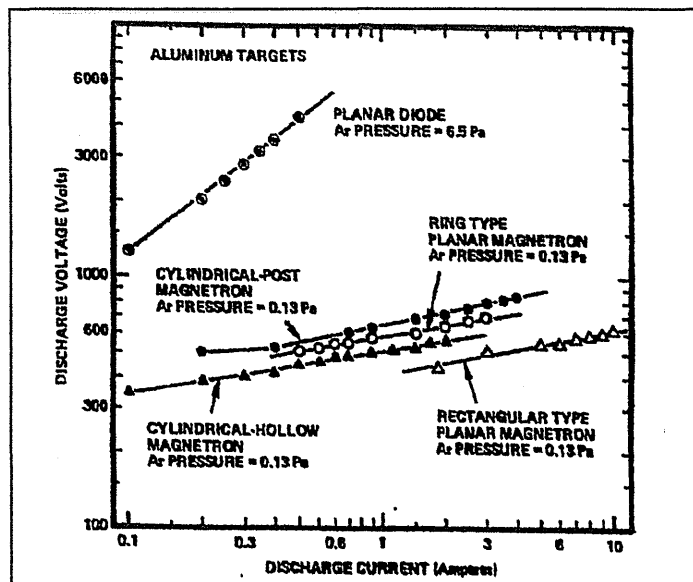

Figure 1.43. Typical current-voltage for several Al sputtering sources at Ar working gas [82].

Figure 1.44 shows a typical deposition profile for cylindrical-post magnetron (a), planar magnetron (b), ring-type planar magnetron (c). At typical operating pressures (1mTorr), the deposition flux can be predicted with reasonable accuracy by assuming a cosine emission of sputtered material from the erosion area and collisionless passage to the substrate. Simulation methods for determining the motion of sputtered atoms has been reported for unhomogeneous target erosion [101].
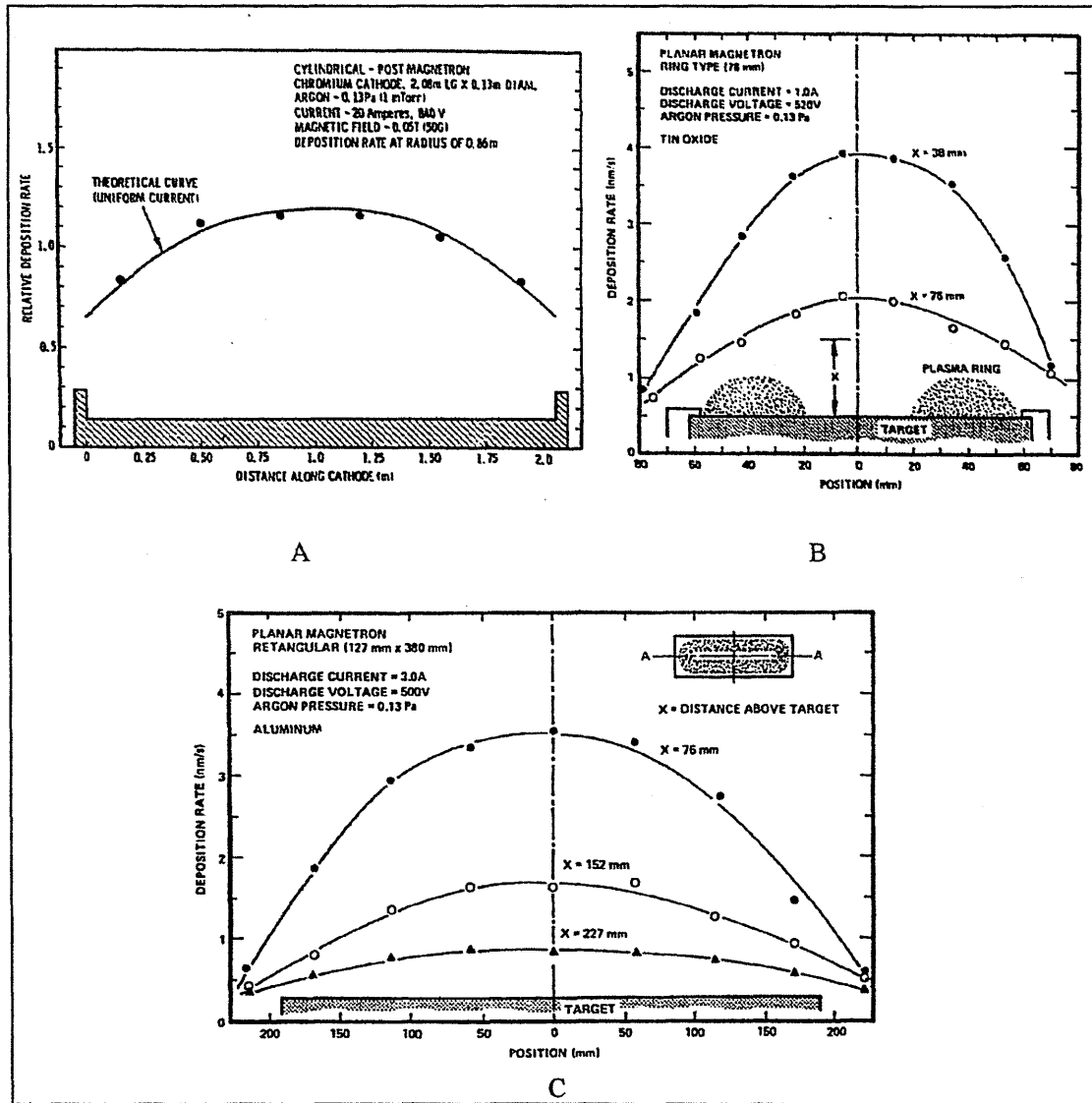

Figure 1.44. Typical deposition profiles for different types of magnetron.

The development of high performance magnetron sputtering has opened up new applications and has also provided the following advantages outlined in figure 1.45.[82,68,102,80,70,92,103,104,105,77,106]. The main disadvantages of this technique are also outlined in figure 1.45 [80,92].

Advantages

- Relatively high deposition rates (>1 μm/min) but this still may not be economic for some thick film applications.
- Large deposition area capability and large production volume.
- Reduced substrate heating, over diode sputtering, which expands the range of feasible applications, materials and thermally sensitive substrate applications.
- Proper cathode design, aided by minimal aperturing or by plasma control (unbalanced magnetron), can provide film thickness uniformity better than ±5%.
- Magnetron sputtering can coat complex substrate shapes.
- Co-sputtering magnetrons allow immobile metals such as electric conductors (Al,Cu,Ag,Au) and refractory metals (Nb,Mo,W,Ta) to be sputter deposited.
- Low sputtering pressure and therefore fewer electrons scattered out of the reaction area.
- Planar magnetron source has better step coverage, compared to planar diode.

Disadvantages

- Magnetrons seem to be more susceptible to arcing than other types of sputtering system, which can be exacerbated by the high current, low voltage power supplies which are required to drive the low impedance discharge.
- The power dissipated at the target by the large ion current involved causes considerable problems with target cooling.
- Low efficiency of the target utilisation due to the erosion area.

Figure 1.45. Advantages and disadvantages of magnetron sputtering.

PLANAR MAGNETRON

Nowadays, the planar magnetron devices are the most widely used form of magnetron sputtering. They have been configured either in a circular or rectangular form[77] as is illustrated in figure 1.46. They very often use planetary rotating substrates to provide good film uniformity [107].

The planar magnetron can be scaled to large sizes. The rectangular magnetron is particularly useful for coating a large substrate surface that is transported in a direction perpendicular to the long axis of the cathode. Large circular planar magnetrons of about 0.6m in diameter have also been reported [82].
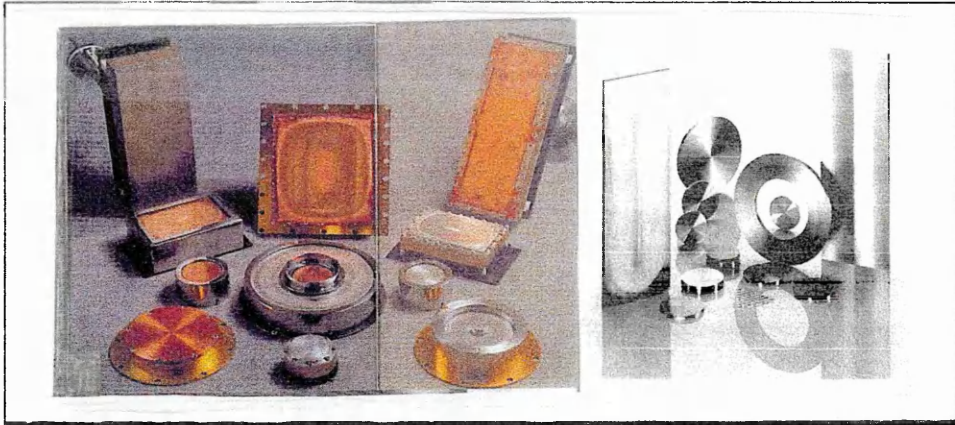
Figure 1.46. Several shapes of planar magnetron.

The electric and magnetic field configuration permits the electrons to be trapped and create ions by collisions between gas atom and electrons. Sustaining the glow discharge depends on the degree of ionisation. The conditions for trapping electrons are that $\overline{E} \times \overline{B}$ and the cross electric and magnetic fields form a closed loop. If B decreases or E increases or the energy of the particles increases, then the electrons may not be confined and will escape.

The more energetic the drift current, the more ionisation that will occur. This situation takes place in the glow discharge ring where the magnetic field is strong and parallel to the target surface. The glowing ring is located in front of the target and between the pole pieces of the cathode assembly. In this area a drift current of electrons with sufficient energy for ionisation exists. Consequently a narrow V-shaped erosion groove is formed and is related to the electron motion, magnetic field distribution and magnetic confinement of the electrons. The glow discharge shape between anode and cathode is a toroidal plasma band form as shown in figure 1.47[82,85,92,103,107,108].
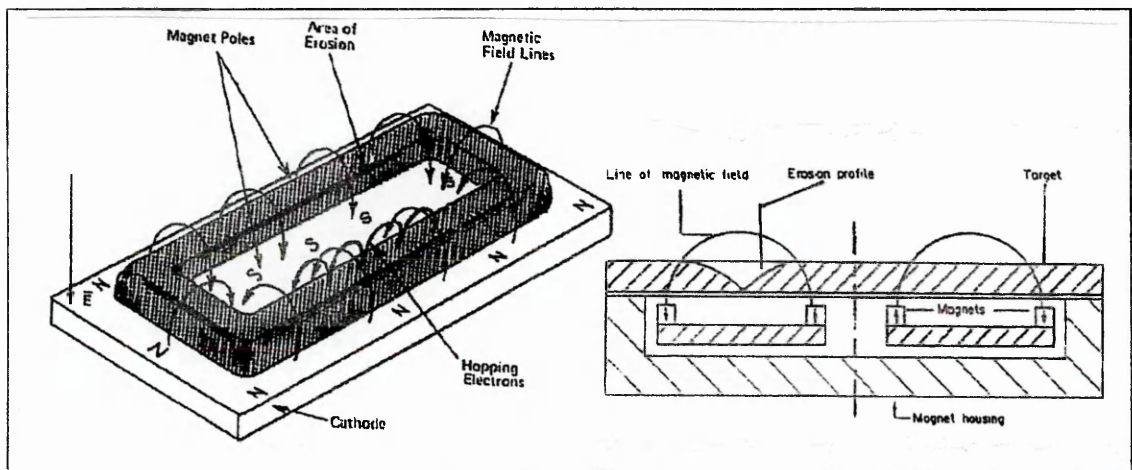
Figure 1.47. Planar magnetron sputtering configuration [80,105].

The groove erosion profile becomes deeper as the sputtering goes on. Then the voltage decreases by about 12% during the target life for maintaining the current, as the secondary electrons emitted from the sides of the groove go toward the centre, producing a high ionisation current [82,107].

The sputtered particles with direction normal to the substrate occur in front of the gully area. As the radial distance from the erosion zone centre increases, the angle of sputtered particles impinging on the substrate increases and this decreases their energy. This tendency could be enhanced for high pressures and results in a non-uniform film thickness. On the other hand, as the groove shape grows, the angle of the sputtered particles is reduced and the film thickness distribution deteriorates with time. The latter is an important aspect for extending target life [83,107]. The target utilisation is typically about 25-30% [103,105,108].

The ring erosion is independent of the material composition, surface finish and quality of the target [85,91]. The groove shape is mainly dependent on magnetic field strength, shape, and target material and is controlled by the magnetron design.

A multi-target magnetron system consists of several separate magnetrons operating independently of each other [109]. This system has several attractions that enables the development of new coatings, including: independent control of the individual target current and the material yield from each magnetron, e.g. TiAlN films produced by reactive DC unbalanced magnetron co-sputtering with individual pure Ti and Al targets; change in composition of the coating does not require shutdown of the coater unit to change the target for the production of multilayer coatings.

UNBALANCED MAGNETRON SYSTEMS

The localised erosion area in the conventional magnetron target under the plasma rings, except in cylindrical magnetrons, has several detrimental effects, related to its form and shape, including [91,103,108]: deposition rates varying with operating time, frequent target replacement, non-uniform distribution thickness, low efficiency of target utilisation. Nevertheless, this problem can be minimised with unbalanced magnetrons by changing the magnetron design, broadening the erosion area or flattening the magnetic field [80].

The magnetic field configuration can have notable effects on the magnitude and spatial distribution of the plasma properties and thus film properties. For example, a fully dense coating at low bias voltage seems to require ion current densities over $2mA/cm^2$, which is difficult to achieve with a conventional magnetron. The unbalanced magnetron offers the possibility to minimise the effects of the erosion target area, giving high density-low energy ion and electron bombardment and also increasing the ionisation density in the region near the substrate, i.e. extending the plasma to the substrate. The latter results in high ion current density on the biased substrate and thus increased reactivity of the process on the substrate surface, hence a lower operating pressure [110,102]. An unbalanced magnetron can also give coatings densification at high current density. Low bias voltage is necessary to produce this densification and this results in less damage to the film.

Recently, it has been possible to predict film uniformity for a range of source to substrate distances by design of mask shapes to intercept material between source and substrate and by a computer program to simulate the magnetron source using erosion target data [91,104].

The unbalanced magnetron has been designed in several configurations to improve magnetron performance and efficiency, as shown in figure 1.48. Some of these configurations are:

♦ Magnetron with a moving magnet assembly swinging behind the target increases the target life [103,108].

♦ The double-electromagnetic structure improves the uniformity of film thickness distribution within ±5%. The cathode consists of two electromagnet coils (inner and outer) coaxially on a magnetic yoke behind the target plate [107].

♦ Placing the poles of the magnetic circuit in front of the target surface could result in a flatter erosion profile [92].

♦ The interpoles target-hollow magnetron consists of soft magnetic pole pieces positioned on top of permanent magnets. This design allows a flat magnetic field and target utilisation of 64% and also the ability to run a self-sputtering mode without incorporation of argon gas, which is attractive for very pure layers [105].

♦ The facing target system consists of two target magnetrons placed opposite each other. The substrate is held on a plane perpendicular to the surface of the targets. This configuration gives a very high deposition rate at low substrate temperatures. Also, the geometrical parameters such as: inter-target distance, target-substrate distance and target size give a flexibility to coat thin films over larger areas [111,112].

♦ Cathode with poles above the annular target results in a relatively flat magnetic field [103,108].

♦ Symmetrical magnets of one inner annular magnetron and two outer annular magnets facing each other result in target utilisation about 64% [103,108].

♦ Magnetron with an auxiliary solenoid magnetic field results in target utilisation of 51% [103,108].

♦ Inverting the magnets in the unbalanced magnetron provides a continuous field across the chamber, resulting in higher ion current at the substrate. Also, the current density could be increased three times compared with a conventional magnetron [110].

♦ The combination of the two techniques, unbalanced magnetron plus cathodic arc, offers advantages for multilayer alloy deposition providing significantly higher ion fluxes to the substrate and growing film [113,114].

♦ An ultra high vacuum DC planar magnetron with an external variable axial magnetic field (B_{ext}) superimposed on the permanent magnetic field has been reported [82]. The sign of B_{ext} affects the plasma density near the substrate and hence the ion flux incident at the substrate [115].
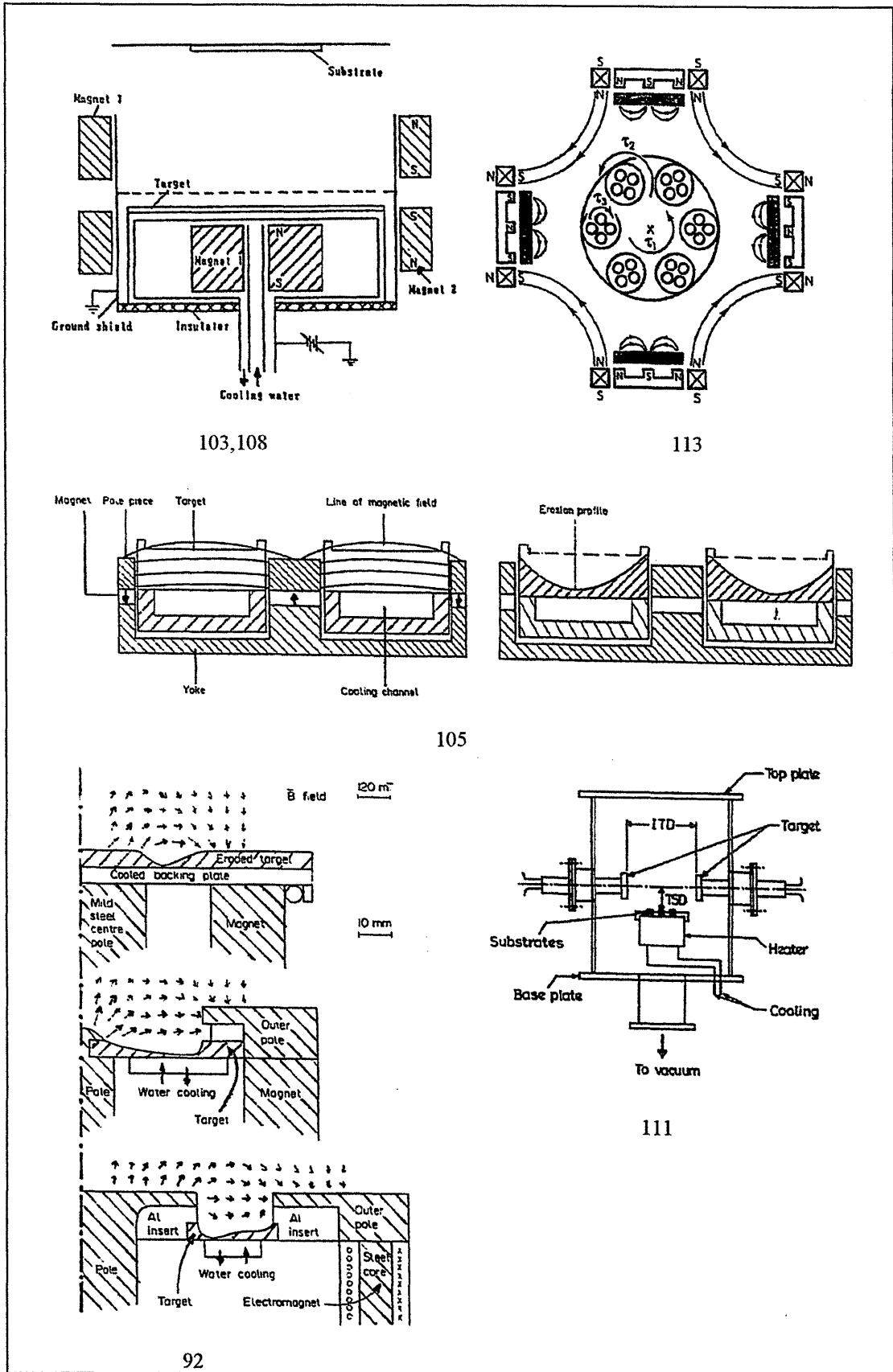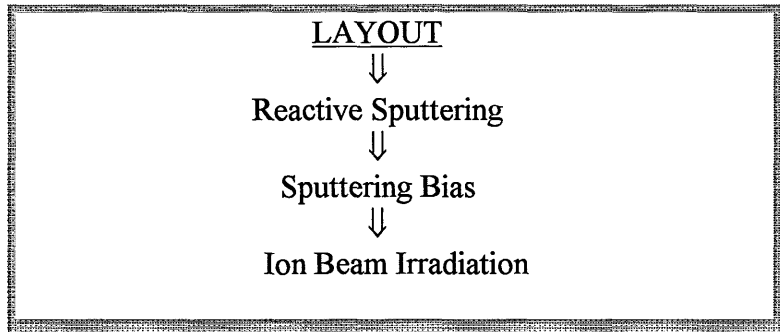
Figure 1.48. Several unbalanced magnetron configurations.

1.4.4. MODES OF SPUTTERING

<u>LAYOUT</u>
⇓
Reactive Sputtering
⇓
Sputtering Bias
⇓
Ion Beam Irradiation

REACTIVE SPUTTERING

Reactive sputtering is a widely used technique to deposit compound and alloy thin films. This method can be used either with magnetron or RF sputtering or DC sputtering.

It is a process in which a fraction of at least one of the depositing species enter in the deposition process in the gas phase. The target could be either a pure metal or alloy or a compound containing volatile species. In the pure metal or alloy target the high vapour-pressure species is provided entirely in the gas phase while in the case of compounds, a small partial pressure of the reactive gas is added to the discharge.

The working gas is a mixture of argon and reactive gas where argon is a buffer gas. A reactive gas may be intentionally added to produce a suitable film composition[36,116]. Chemical reactions could take place on the target, in the gas phase for high working pressure and on the substrate.

In sputtering with a reactive gas/argon mixture, the relationship between film properties and the reactive gas injection rate is generally very non-linear. The non linearity occurs due to the sticking coefficient on the condensing film which depends on the growth rate of the film, composition, film structure and temperature [80]. This means, that a condensing film works as a getter for the reactive gas and this effect falls quickly as stoichiometry is reached. Keeping high deposition rates for stoichiometric films requires an injection of the reactive gas near the substrate and argon gas near the target. This also minimises the chance that the target may be poisoned [70].

The main parameters of the reactive process are; target erosion rate, film deposition rate, target composition and reactive gas pressure, which may exhibit a hysteresis with the reactive gas flow. This latter requires dynamic flow control of the reactive gas to minimise this hysteresis effect. The contribution of the reactive gas ion in the total target erosion rate is up to 20% [116].

A compound layer forming on a cathode during reactive sputtering is referred to as cathode poisoning. This effect depends on the metal/reactive gas combination and the properties of the cathode surface layer. The poisoning effect introduces several practical problems, including: decrease in the target erosion rate and even termination of the

discharge current. Arcing on the target surface may cause a reduction in the deposition rate. If the material to be deposited passes abruptly from a metal to a nearly stoichiometric compound, then intermediate materials, such as suboxides, become difficult to deposit. The hot target in reactive sputtering operates at a high enough temperature to evaporate the surface layer and thus avoid the poisoning effect [117].

The reactive sputtering process is dependent on the system geometry, the accumulation of coating on walls and fixtures and the positions of gas injection and its composition. All these parameters must be carefully controlled in order to use effectively the reactive sputtering on industrial production and film optimisation [36,82].

The advantages of reactive sputtering are [70,80]:

- Compounds and alloys can be formed from metallic targets
- Insulating compounds can be deposited using DC power supplies
- Films with graded composition can be formed
- Can be used to restore the stoichiometry of the film

BIAS SPUTTERING

Applying a negative potential (Vb) to a substrate will establish a sheath potential (Vp-Vb) in front of the substrate. The sheath polarity accelerates positive ions onto the substrate, i.e. the substrate could become a sputtering target. For small bias voltage, the sheath at the substrate will be thin enough so there will be no collisions. However, increasing bias voltage, the sheath thickness grows so that collisions may become important and attenuate the ion energy. Consequently, the average energy of particles striking the substrate will increase slowly compared to the applied bias voltage. Moreover, the fast electrons from the target can bombard the substrate, increasing the bias on the substrate. This is true in the DC system but is restricted in RF [80].

Biased negatively, the substrate before deposition can be used to improve film adhesion to the substrate and remove contaminations. However, during deposition it can preferentially remove oxygen, reduce argon incorporation into the growing film, increase substrate temperature, provide low-energy ion bombardment of the growing film, increase film density, improve film purity and control film properties. The properties that can be modified are, for example: resistivity, hardness [77,80,118]; change crystallography orientation, for example AlN coatings, by reactive sputtering [119].

The growing film is also subject to resputtering by the incoming ions. However, at moderate bias voltage (about -50V) there will be little resputtering of the growing film. Negative substrate bias can be used to control film deposition and thus the conformal coverage of surface topography by resputtering. Consequently, to coat a perpendicular step is easier [120].

The process consists of resputtering deposited material and redepositing it on the side walls. This is facilitated by sputtering under a cosine law, i.e. there is a tendency for material to be ejected sideways rather than outward (cosine or overcosine) at high energy. As the bias voltage is increased and the deposition rate decreases, relatively more metal is resputtered onto the side walls. The process parameters must be chosen

cautiously due to gas scattering right back onto the target and the substrate backing plate will also be subjected to ion bombardment. Consequently, backing plate material could be incorporated into the growing film.

The basis for bias sputtering to produce high purity films is that during resputtering most impurities should be removed in preference to the atoms of the films [90].

A positive bias applied to the substrate attracts secondary electrons. The latter will be accelerated onto the substrate, heating the surface and reducing the sticking coefficient. Substrate temperature and electrical bias also have an effect on the crystal structure of the film [77]. The positive bias also raises the plasma potential and so will increase the energy of ion bombardment. This can be useful as a cleaning technique but can also be a source of contamination [80].

Selective deposition can be achieved by high bias sputtering, i.e. selective growth and erosion. Experimentally, this has been demonstrated. It has been shown that Al is selectively deposited on Si and not on W surfaces. Also, Ti is selectively deposited on Si and not on Pt surface. The high mass and high atomic density materials are likely candidates for growth-inhibiting materials while low mass and low density materials are likely candidates for growth-promoting materials during bias deposition of low to medium mass species [120,121,122].

ION BEAM IRRADIATION

Using a second ion gun to irradiate the substrate by an ion-beam has been shown to affect film nucleation, and growth kinetics, adhesion, film microstructure and chemistry and hence film properties [82].

1.5 CHARACTERIZATION OF THIN FILMS

LAYOUT
⇓
Overview of Film Characterization
⇓
Objectives
⇓
Types of Film Characterization
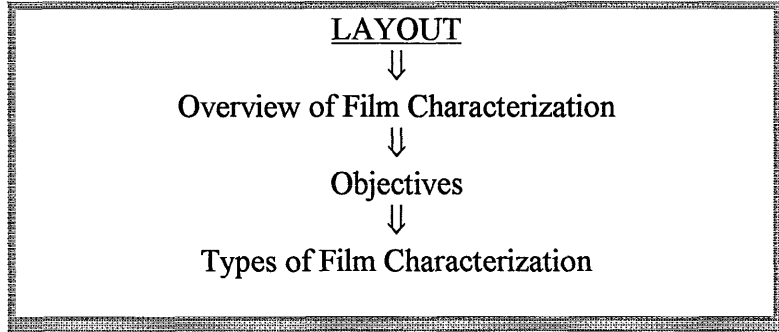
Coating deposition techniques can offer the possibility of modifying the surface properties of components through coating deposition to improve performance, reliability and lifetime and hence profitability. To achieve such benefits, it is important to understand the interrelationship between coating properties and their performance, and how these properties may be controlled either by choice of deposition process or control of microstructure, as mentioned earlier [123].

Thin films or coatings, in single or multilayer design have microstructures, physical and mechanical properties that could be different from either those of the identical bulk material or the substrate material [124,125,126]. Some unique film properties can come from the fabrication processes and the microstructure, due to the restricted grain size and thickness of the film, as illustrated in the figure 1.49. The same figure shows the main properties such as the chemical, physical and mechanical, for each system of the film/substrate composite including: surface, bulk coating and interfaces [123].

When a coating/substrate performance is well established, then it is worth optimising each part of the composite system and their inter-relationships. Moreover, understanding the relationship between microstructure and mechanical properties has been one of the targets in Materials Science mainly because this can be controlled by the selection of deposition technology and processing parameters. For example, knowing the mechanisms responsible for deformation and fracture of film material may allow the mechanical properties to be changed through the control of microstructure [123,127,128,129].

From figure 1.49 it is evident that many of the film properties are useful only in certain applications, so there is a need to characterise the film by measuring a few fundamental properties for specific applications [123]. This means that it is not sufficient to look for individual properties, such as hardness, when selecting a coating for a given engineering application. Other properties such as residual stresses or adhesion are equally important [129]. In the same way, the experimental study of mechanical properties of thin films requires the development and use of non-traditional mechanical techniques. In these chapters we shall be looking at the traditional as well as non-traditional mechanical measurement techniques that have been used in this area.
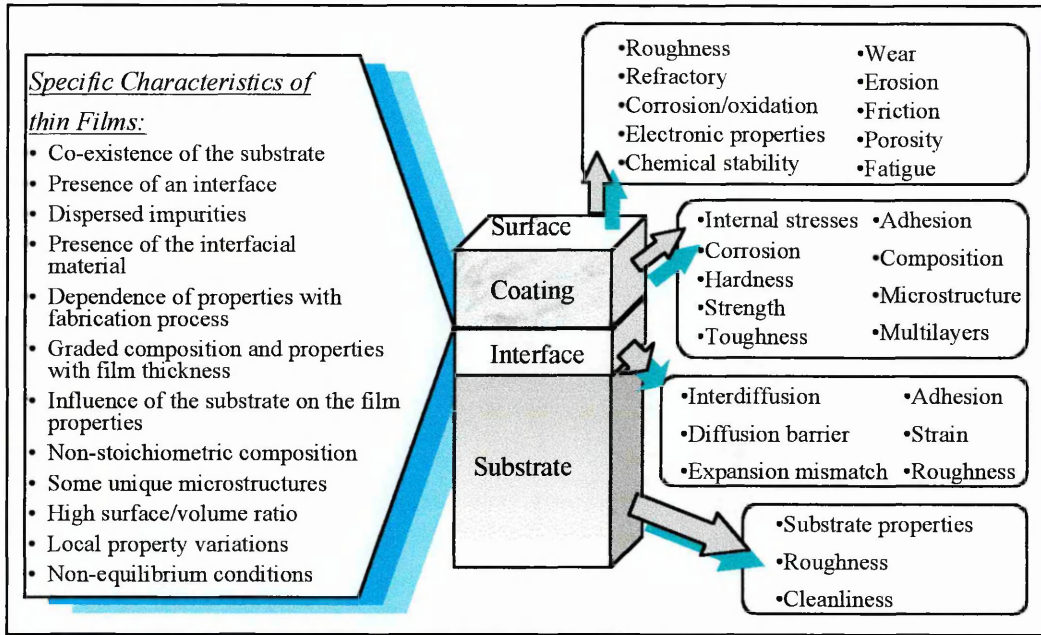
Figure 1.49. Specific characteristics and main properties of thin films.

It is clear from the foregoing that the characterization of thin films is essential and could include several targets such as [124]:

♦ Development of new material processing parameter optimisations.

♦ Set up process control, specifications and monitoring for making the process reproducible.

♦ Problem solving.

♦ Development of the processing variables to control the properties of the material.

♦ Determination of functionality and establishing performance limits for a specific application.

♦ Acceptance of products in terms of functionality and stability.

♦ Establishing the baseline for composition, structure or performance of the coating.

♦ Determining the stability and degradation conditions of the material in service.

♦ Aiding in analysis of failure.

Film characterization can be defined as absolute or relative. Absolute characterization can be achieved by a specific value. However, the absolute value usually requires accurate measuring techniques and standards and the comparison of the measured values to standards for the parameter of interest. The relative characterization is obtained by comparing to an acceptable value that need not be standardised. Relative characterization is easier to obtain and cheaper than absolute values [124].

Film characterization may also be classified according to certain objectives such as: functionality, behaviour, stability. Functional characterization relates to the final use of the material, e.g. hardness, wear. The behaviour is a function of processing parameters, mechanical properties and structure. The stability refers to the product variation during subsequent processes, handling, storage and use in service, e.g. corrosion resistance.

93

Property evaluation could be general or vary locally over the whole component. Moreover, the general properties may be non-uniform over a large area on the deposition fixtures. Such deviations could result either from the substrate conditions, or deposition parameters or the technique itself. Hence, when selecting methods for sample characterization one must consider such variations and incorporate them in appropriate statistical design methods. To identify each sample and its position in the fixture for future reference with respect to variations in properties may be a helpful policy in selecting the method of sampling.

In testing films, one differentiates between the properties of the films that are adherent to the substrate and those that are free-standing. This means, they have been separated from their substrate. In both cases the knowledge of the film thickness is essential [125].

1.5.1. STRUCTURAL CHARACTERIZATION

LAYOUT
⇓
Film Formation
⇓
Nucleation and Film Growth Modes
⇓
Computer Methods Simulation
⇓
Structural Models
⇓
Effects of Low Energy Ion Irradiation
⇓
Structural Characterization Techniques
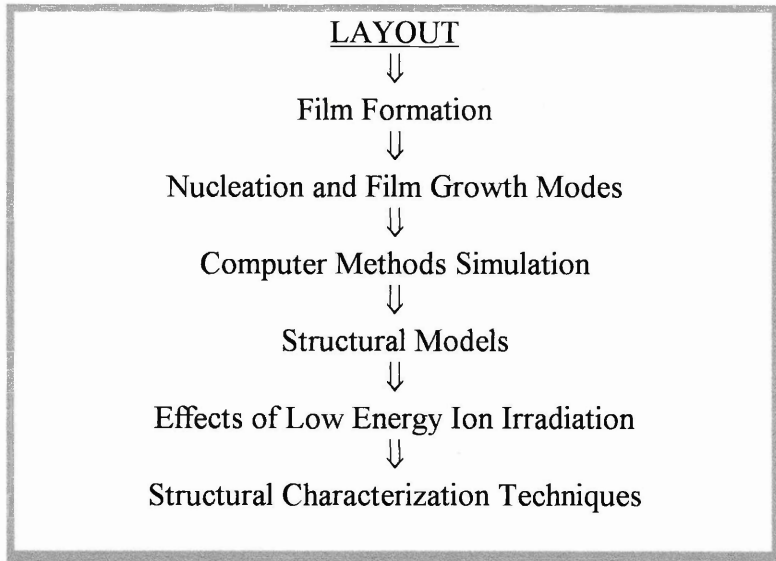
Understanding some of the unique film properties requires a detailed knowledge and understanding of the film formation with a specific fabrication process. The film formation stages due to atomistic processes are outlined in figure 1.50 [124].
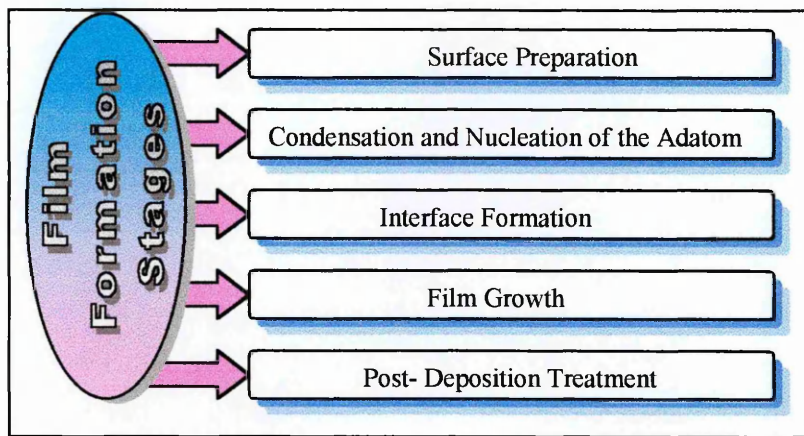
Figure 1.50. Film formation stages due to atomic process.

The film condensation processes start with the impingement of sputtered material on the substrate, mostly in an atomic or molecular form. Then they transfer their kinetic energy to the lattice and become freely bonded adatoms. The latter have some mobility on the surface so they diffuse over it. Thereafter they interchange energy with the lattice and other adsorbed species until they are either adsorbed, or reevaporate, or resputter, or become trapped at low-energy lattice sites. Finally, the incorporated atoms readjust their positions within the lattice by bulk diffusion processes [80,124,130,131].

The nucleation density depends upon the adatom kinetic energy, adatom surface mobility, chemical reaction, adsorbed surface species, and the nucleation sites available.

The atomic mobility across the surface depends on temperature, defects and impurities or physical barriers which impede the atom diffusion and available energy [124,132].

The nucleation density of adatoms on a substrate surface and the mode of growth determines the structure of the interface, such as: contact area, voids, restructuring of the interface layer. Interface formation starts during nucleation of the adatom on the surface and may continue through the deposition process and still continue during post-deposition processes, and perhaps even in service.

It is clear from the above that atomic travel includes four basic processes: shadowing, surface diffusion, bulk diffusion and desorption [130]. The factors that determine the nucleation and growth kinetics, microstructure evolution, and hence, physical properties of the film grown by PVD are outlined in figure 1.51 [77,124,131,133].

Factors Which Determine Physical Properties of the Film Growth

- The film material
- The incident film flux angle
- The kinetic energy of the incident species
- The film growth temperature and heating during deposition
- The flux of contaminants
- The substrate material such as: morphology, structure, chemistry and physical properties
- The surface cleanliness
- The surface crystallinity, and orientation
- The ion/surface interaction
- Deposition variables: film deposition rate

Figure 1.51. Factors that determine physical properties of the film growth by PVD.

The important structural features that affect the physical properties of multilayer coatings are interdiffusion, interface roughness, layer thickness homogeneity, the flatness of the layers and the repeatability of individual layers [134].

The contaminants present depend on the base pressure, pumping speed, and the design of the vacuum system. Moreover, substrate surface cleanliness depends upon pre-deposition methods, as mentioned in chapter 1.4.2.

Non-equilibrium thermodynamic deposition conditions could form several imperfections. The most important are those that arise at the interface caused by poor vacuum, impurities, resputtering and decomposition. The outcome is poorly bonded nucleation sites giving low density interface layers and thus weak bond strength. Stoichiometry variations, phase separation, complex precipitates, stress gradients, uncontrolled nucleation, columnar or grain boundary diffusion pathways, and poor stability are also observed [132].

Post-deposition treatment may be used to improve the film or interface properties, to lessen impurity problems and rectify composition. Some of these treatments include: burnishing or shot peening; rapid thermal processing; annealing; ion

beam mixing. The latter results in enhanced interface adhesion in several metals, insulators and organic-substrate composites. Nevertheless, each treatment can add new forms of defect interactions [124,132,135].

Thin films can grow with amorphous, polycrystalline textured and single crystalline structures depending on the substrate temperature, deposition rate, film material and processing parameters. Both polycrystalline and amorphous films produced by vapour deposition at low temperature ($T_s<0.3T_m$) are habitually formed with open columns with voids and pores along the column boundaries. Such structures are susceptible to environment contamination which can be incorporated in the voids. This results in poor mechanical and optical properties and also affects the magnetic and electric resistivity. Such films are also anisotropic. Metastable phases and special structures are often formed but with an increase in the film thickness they may disappear. Epitaxial deposition has a crystalline structure and a crystallographic orientation which follow that of the substrate. When a film grows on single crystal substrate under special conditions (epitaxy growth) it could also become a single crystal [135,136,137].

There are three models that describe the film growth on a substrate surface, which are discussed below:

1. Three-dimensional island (3-D) or Volmer-Weber [133,135,136,137].

2. Two-dimensional layer-by-layer (2-D) or Frank-van der Merwe [138,135,133,136,137]

3. Stranski-Krastanov model [135,133,136,137].

1. Three-Dimensional (3D) Island or Volmer-Weber

The main features of the 3-D nucleation and growth are illustrated in figure 1.52. An impinging flux of film species is thermally equilibrated on the substrate surface by a few vibrational periods. Then the adatoms can diffuse over the surface and interact with other adatoms or re-evaporate. Small clusters are nucleated directly on the substrate surface and then grow in size into islands with sequential coalescence to form a continuous film.
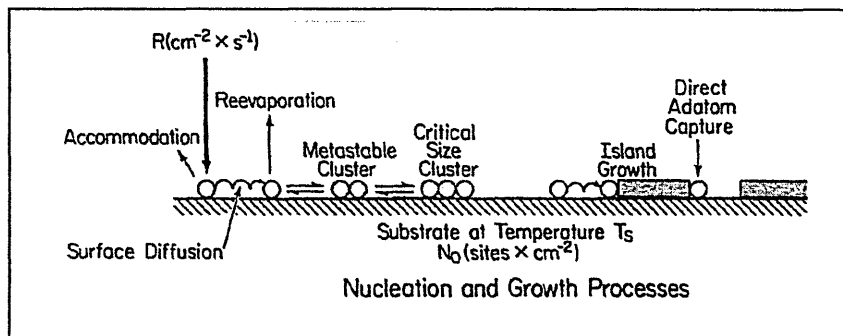

Figure 1.52. Main features of the 3-D nucleation and growth [135].

This type of growth occurs when the film atoms are more strongly bound to each other than to the substrate. A schematic illustration of the sequential steps during 3-D growth for island density versus the nominal film thickness is shown in figure 1.53.

The critical nucleus size can grow either by direct impingement or by catching the vapor-phase species or by the capture of condensed adatoms which are diffusing across the substrate surface. As the deposition goes ahead, the size and densities of the nuclei increase and so reach a maximum at typical values of 10^{10} to $10^{12} cm^{-2}$ which gives island sizes of 10 to 100nm. Over the maximum point, further deposition leads to a decrease in the nucleus density due to coalescence of adjacent clusters. However, the islands continue to grow by catching mobile adatoms and small clusters. Then the film becomes semi-continuous with channels and holes. These latter can be filled by secondary nucleation as the growing film becomes continuous.

The secondary nucleation is a result of the driving force for coalescence that reduces the surface energy by rounding the islands. Stresses may occur in continuous films due to film/substrate lattice constant and thermal expansion mismatch and can also be relieved by dislocations climbing. Nevertheless, recrystallization can also occur during coalescence, which tends to eliminate misorientation and increase the nucleus size.

Dense small islands during the initial stages of deposition will form continuous films at a relatively low film thickness, though a few large islands during the early stages of deposition will produce films with an island structure at relatively large film thickness. The thickness at which 3-D nucleated films become continuous depends upon the film material, substrate material, supersaturation (S) and growth temperature (T_s). This critical thickness decreases with an increase in the deposition rate at constant growth temperature.
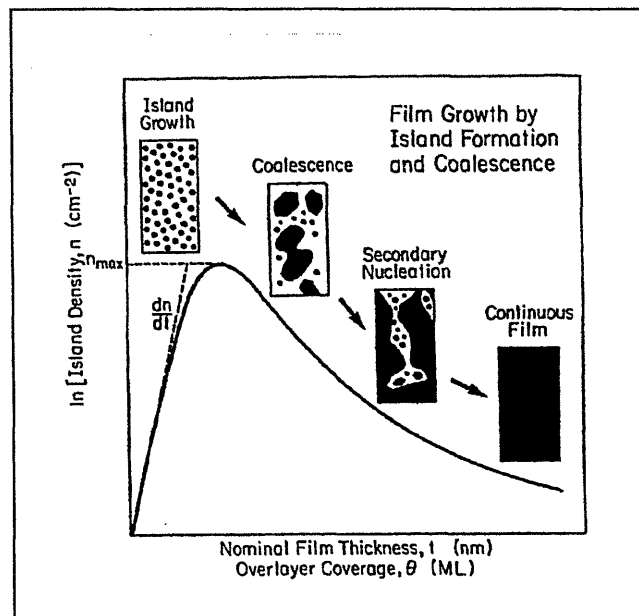

Figure 1.53. Steps during 3-D growth for island density versus nominal film thickness [135].

The minimum thermodynamic requirement to achieve net deposition is that the condensate pressure in the gas phase (p) should be equal to its equilibrium vapour pressure over the solid (p_s). Consequently, the supersaturation ratio must be larger than one, $S=(p/p_s)>1$, because the nuclei have a greater vapour pressure than that of the bulk material due to their high surface/volume ratio. Thus the clusters must be greater than a

certain minimum critical size to allow film growth. The critical cluster size decreases as the supersaturation increases, which will occur either by increasing the incident flux of condensing species (p), or decreasing p_s which depends exponentially on the growth temperature.

For high deposition rates (or low deposition temperature), higher than the surface site density multiplied by the adatom surface diffusivity, then the film is amorphous owing to the lack of time for adatoms to diffuse across the surface and sit at low energy positions before they are overlayered by subsequently deposited adatoms.

Covalent materials have low packing densities and strong directional bonding, and, therefore, easily form an amorphous state by deposition since the high metal diffusibility depositing them in an amorphous state is more difficult.

2. *Two-Dimensional Layer-by-Layer (2-D) or Frank-Van Der Merwe*

The 2-D layer-by-layer growth occurs when the desorption energy (no binding) of film atoms condensed on the substrate is equal to or larger than the desorption energy of film atoms condensed on other film atoms. Therefore, it is easier for the atoms depositing on an existing plane of atoms to desorb rather than those on the substrate. Atoms continually arrive and adsorb all over the surface. Those on existing deposits desorb more easily. The net result is that atoms will build up in two dimensional layers. This requisite can be performed by growing a film on a substrate of the same material under ultra high vacuum. In this case, no barrier exists to nucleation, in spite of coverage, and no supersaturation is essential. Consequently, the growth occurs in a quasi layer-by-layer manner by step motion as one monolayer across the surface.

There are numerous examples of this growth in metal-metal (Cd on W) and semiconductor-semiconductor systems ($YBa_2Cu_3O_7$ onto $SrTiO_3$). However, a small amount of oxygen can reduce the growth rate and then furnish a barrier to nucleation. As a result the nucleation mode changes to 3-D growth which then obstructs the epitaxial growth.

3. *Stranski-Krastanov Model*

This third growth mode is a mixed-mode in which the film initially nucleates by 2-D growth and then turns into 3-D growth. The change occurs after a few monolayers of the 2-D growth, because this mode of growth becomes unfavourable, and may be due to the release of elastic energy stored in the film as a result of the film/substrate lattice mismatch.

Computer simulation methods and molecular dynamic simulations have been very helpful in drawing some conclusions about the microstructure evolution, demonstrating that [133,135]:

♦ The open columnar structure may be caused by low adatom mobility combined with self-shadowing by previous deposited atoms.

♦ Increasing the growth temperature could result in a film with much higher density.

♦ The temperature range, in which a porous columnar microstructure moves to one that is densely packed, increases slowly with increasing deposition rate.

♦ The introduction of grains with low surface energy, i.e. crystrallographic texture in the early stages of the film deposition, tends to activate grain growth.

♦ Low energy ion bombardment can improve the film structure.

Movchan and Demchisin [129,130,135,139,140] were the first researchers to classify the film microstructure produced by vapour deposition, developing a structure-zone-diagram. The main features are illustrated in figure 1.54. Thick films (0.3-2mm) of Ti, Ni, W, ZrO_2, Al_2O_3 and Fe were deposited by electron beam evaporation. These authors concluded that the coating microstructure could be represented as a function of the normalised growth temperature (T_s/T_m) for three zones. Each zone has a specific characteristic structure and physical properties as mentioned below:

ZONE 1 (T_s/T_m<0.2-0.3): The microstructure consists of tapered crystals with domed tops which are separated by voided boundaries. The internal structure of the crystal is poorly defined with high dislocation density. The crystallite width increase with T_s/T_m and that dependence suggests an activation energy about 0.1-0.2eV which is too low to be explained by grain growth mechanisms. This zone is dominated by conditions of low adatom mobility.

ZONE 2 (0.3<T_s/T_m<0.5): The microstructure consists of columnar grains separated by dense intercrystalline boundaries. The boundaries had high dislocation densities. The surface exhibits a smoother matt aspect. The grain width was less than the film thickness. The grain width increases with T_s/T_m giving an activation energy about equal to that for surface diffusion.

ZONE 3 (0.5<T_s/T_m<1): The microstructure consists of equiaxed grains with a bright smooth surface. The grain diameter increases with T_s/T_m and yields an activation energy like that of bulk self-diffusion. The transition between zone 2 and 3 was gradual, thus the boundary had a positive slope.
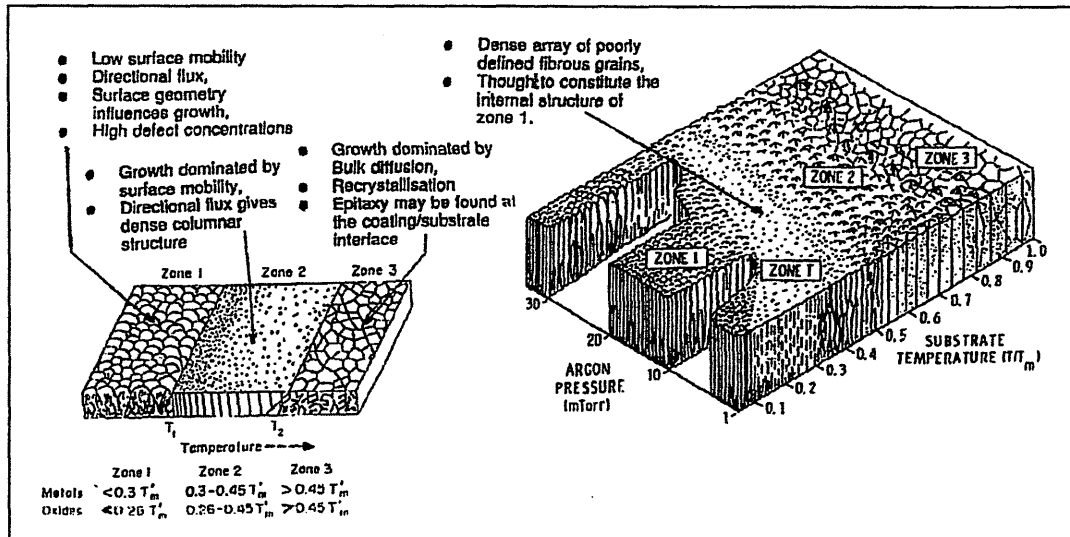
Figure 1.54. Movchan & Demchisin model on left hand side. Thornton's model on right.

Sanders's model [130] was based on a dominant physical process. The range 1 ($T_s/T_m<0.1$) was dominated by shadowing. The range 2 ($0.1<T_s/T_m<0.3$) was dominated by surface diffusion. The range 3 ($0.3<T_s/T_m<1$), the most significant process, was dominated by bulk diffusion. However, at high T_s/T_m Sander's inferred a new range based on liquid-like condensation.

Thornton's model [129,130,135,139,141] went one step further over the Movchan and Demchisin diagram by adding an additional axis to account for the sputtering pressures. He also added an additional region called the transition zone as illustrated in figure 1.54. The Ti, Cr, Fe, Cu, Mo and Al coatings onto glass, in the range of 25-250μm thickness were produced by post-cylindrical magnetron sputtering.

ZONE 1: The structure consists of columnar crystallites defined by open voided boundaries. This type of structure is aided by surface roughness, high argon pressure and an oblique flux deposition. The lack of adatom diffusion to overcome the shadowing effects depends upon the degree of surface roughness. The shadowing effect can occur in amorphous and crystalline films. Preferential growth on the surface peaks over the valleys increases with oblique deposited flux which brings about open boundaries. The surface roughness can result from the initial nuclei shape, preferential nucleation at substrate inhomogeneities, substrate roughness itself and preferential growth.

TRANSITION ZONE (T): The transition zone is defined as the limiting form of the zone 1 structure at zero T_s/T_m on infinitely smooth substrates. The structure consists of a dense matrix of poorly defined fibrous structure without voided boundaries and high dislocation density. The boundaries are sufficiently dense to produce acceptable mechanical properties. This transition zone, structure is believed to be the internal structure of the zone 1 crystallites. Films with this structure grow on smooth homogeneous substrates at T_s/T_m where the adatom diffusion overcomes the roughness of the substrates and the initial nucleation so that the shadowing effects are minimised.

ZONE 2: The columnar structure goes toward an equiaxed shape crystallite separated by dense intercrystalline boundaries. At high T_s/T_m the surface was smooth with grooved

grain boundaries. This growth structure is controlled by adatom diffusion. Incidentally, the growth takes a form of platelets or needles. The growth depends on the crystal face condensation, lattice adsorption, surface diffusion, T_s/T_m and residual gases.

ZONE 3: The structure consists of dense grain and twin boundaries. The grains could be either equiaxial or columnar, depending upon stresses at the initial deposition. This zone is controlled by bulk diffusion processes such as: recrystallization, grain growth.

Metal films in the transition zone exhibit high hardness and strength but low ductility. The densely packed structure in zone 1 has the same hardness as that produced in zone T but poorer strength. The ceramic compound films have low hardness at low T_s/T_m. The dislocation density and hardness of metals decreases rapidly with T_s/T_m until the zone 2 develops. Within the zones 2 and 3 the sizes of the columnar and equiaxed grains increase with T_s/T_m and the hardness and strength of metals decrease. Metals deposited in the low T_s/T_m range of zone 2 exhibit high strength and low ductility. However, those deposited in the high T_s/T_m range of zone 3 are similar to fully annealed bulk material.

The film microstructure is strongly affected by working pressure, surface roughness and ion bombardment:

♦ Increasing the pressure for values that increase the oblique deposited flux could result in a more open zone 1 structure. Using shields for limiting the oblique flux, can result in a dense zone T structure. Moreover, increasing pressure at low T_s/T_m may open intergrain boundaries and then the structure could change from zone T to zone 1. Also, residual gas adsorption promotes a zone 1 structure. On the other, hand, decreasing pressure could result in an increase in energetic particle bombardment and hence growing film densification.

♦ The zone 1 structure exhibits arrays of shadow growth boundaries associated with the substrate roughness. The most open boundaries are associated with severe surface irregularities. Substrates prepared by machining or polishing leaving grooves would produce the zone 1 structure. Oblique flux deposition and surface roughness are similar in producing shadowing. Increasing the T_s/T_m the shadow boundaries are overcome by adatom diffusion. Moreover, a smooth substrate is an effective way of promoting a dense coating at moderate T_s/T_m.

♦ The ion bombardment using bias sputtering can reduce the open structure at low T_s/T_m by creating nucleation sites for arriving atoms or by eroding surface roughness peaks and rearranging material into valleys [142]. A disadvantage is that inert gas entrapment may cause blisters during annealing.

Grovenor's model [135,143,144] is based on TEM analysis of Ni, Pt, Au, Cu, Al, Pb, Ti, Co, W, Cr, Ni and NiAl coatings produced by evaporation. A slightly different structure for the zone 1 and T compared with other models was reported where an activation energy for grain boundary formation is a function of their crystallography, even at low temperature. The zone 1 consists of bundles of small grains for $T_s/T_m < 0.1$ while the zone T consist of small grained structures of a bimodal distribution extended to $T_s/T_m = 0.3$. Above $T_s/T_m = 0.3$ small grain structures were concentrated near the

coating/substrate interface. These then gave rise to larger columnar of equiaxed grain structures, depending on substrate temperature.

J.R.Nicholls's model [143,144] was based on Al films for deposition pressure between 1.3×10^{-4} to 1.3×10^{-1} Pa (10^{-6} to 10^{-1} Torr) at growth temperatures up to 900K. The diagram is plotted on a gas pressure logarithmic scale. The structure can be predicted by a combination of existing models having linear boundaries. This model, as well as Grovenor's model, is illustrated in figure 1.55.
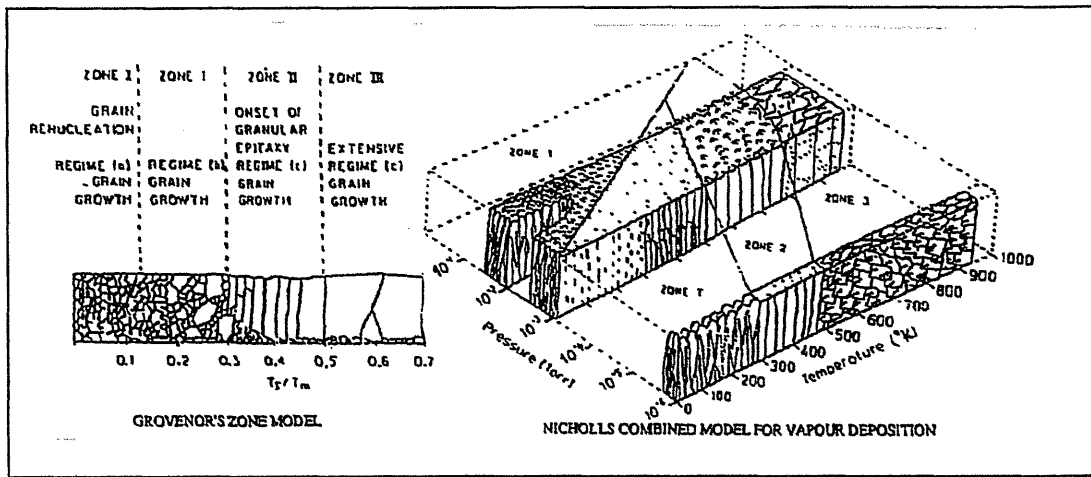
Figure 1.55. Grovenor's model and Nicholls's model [143,144].

The structural-zone-diagrams supply a useful method of classifying film microstructure qualitatively. The prediction of film microstructure and properties through these diagrams must take into account that film growth kinetics are strongly dependent on several factors, as mentioned before.

The kinetic energy of the incident species during film growth during plasma assisted deposition can be increased up to several hundred eV. However, the energetic particle bombardment before and during deposition may be used to modify the interface constitution and the stages of film formation. The low energy ion irradiation, often <100eV, during deposition offers a better control over film nucleation and growth kinetics and thus the microstructure, chemistry and physical properties of thin films which are included in figure 1.56 [80,133,135].
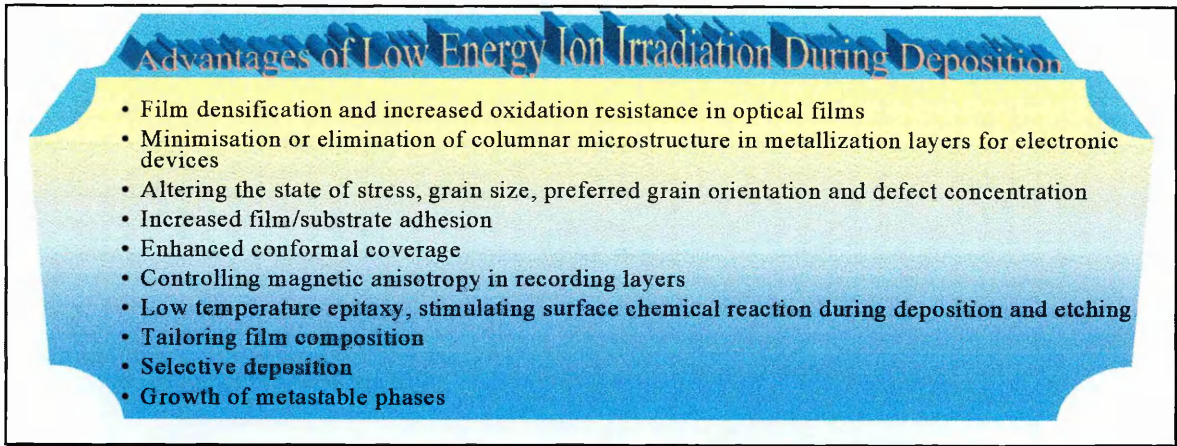
Figure 1.56. Advantages of low energy ion irradiation during dputtering.

To produce high quality films at low epitaxial temperatures requires a balance between the beneficial effects of ion irradiation enhanced diffusion that is supplied by atomic rearrangement into lower energy sites and the lowering of residual damage by annealing out bombardment induced defects during deposition. The literature suggests that the most favourable deposition conditions would seem to be: low ion energy, relatively high ion-to-neutral flux ratios, and provided that contamination from background impurities is not a problem, low deposition rate [133,135].

STRUCTURAL CHARACTERIZATION TECHNIQUES

The continuing development of advanced materials, quality control and failure analysis require ever closer control of properties such as: structural, chemical, mechanical, stability and electronic performance. These factors have placed new demands on analytical techniques which have been developed to characterise materials as thin films with less than 1µm thickness or multilayer films.

The adequate characterization of a material requires a combination of different methods to obtained the necessary depth of information which is nowadays required. Every method has specific advantages and adds its pieces to the puzzle to complete the required information about the sample. Some of the typical information and analytical techniques are pictured in the figure 1.57.
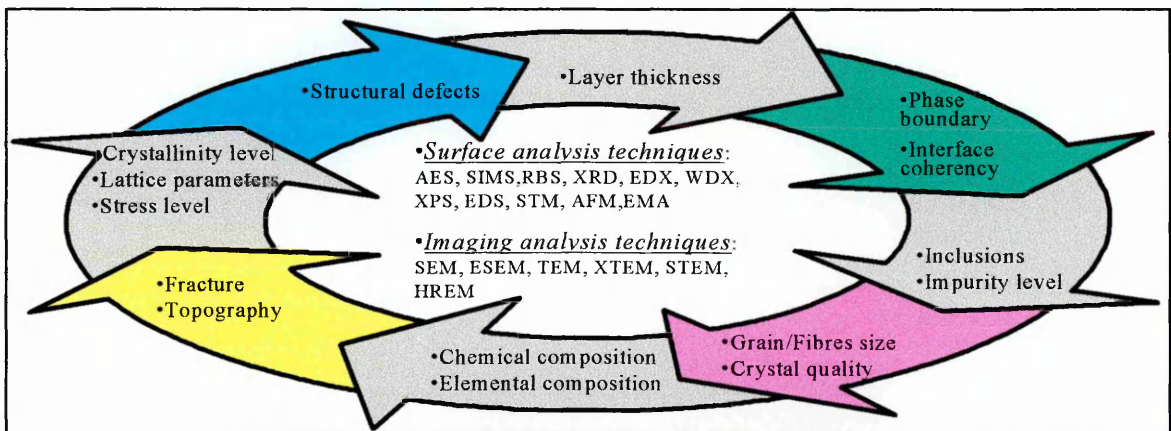

Figure 1.57. Some of the typical analytical techniques.

In this chapter we shall be looking at the main features of the most used analytical techniques:

1. Auger Electron Spectroscopy (AES) [145,146,147]

The evaluation of Auger electron energy provides surface chemical information. As a result, AES spectra are used to survey the surface composition of materials. Also, combining with ion beam milling (ion sputtering) enables a measurement of elemental composition as a function of the depth (so-called depth profiles). The electron beam used in AES techniques can be focused on a small spot and deflected to a region of interest on a sample. Spatial resolution of 25-50nm has been achieved by sacrificing the beam current and thus sensitivity.

2. X-Ray Photoelectron Spectroscopy (XPS) [145]

An X-ray source mounted near to the sample is used for excitation. The X-ray exposes a broad area of the sample, often a few millimetres. The XPS spectra is used to survey the surface composition of materials and can be combined with ion sputtering to generate a depth profile.

3. Secondary Ion Mass Spectroscopy (SIMS) [145]

SIMS is a mass analysis of secondary ions generated by ion sputtering. It has sensitivity 10^4-10^5 more than AES or XPS and the depth profile resolution is less than 5nm (50Å) depending on the analysis conditions. SIMS data is more difficult to quantify then other techniques such Rutherford Backscattering Spectroscopy (RBS) and these can be used to normalise the data.

4. X-Ray Diffraction (XRD) [145,146,148,149,150,151,152]

The principle of this technique is that crystallites within a sample located in a collimated X-ray beam diffract X-rays at specific angles and intensities as the chemical composition and crystallographic structure produce a unique angular distribution of diffracted intensity which allows information about crystallographic structure to be obtained. The analysis is based on comparison of the diffractometer scan with known standards. Crystalline materials lead to sharp diffraction peaks, whereas amorphous materials produce broad diffuse scattering of X-rays. Analysis of the width of reflections along a crystallographic axis provides data about crystallite size and the degree of disorder within the crystal. The type of information that is obtained by X-ray diffraction includes: phase identification and quantification, crystallinity, lattice constants crystal structure and size, preferred orientation. All these measurements may be influenced by the strain present in the thin film. By measuring changes in lattice constants as a result of this strain, residual stresses can be determined.

Conventional analyses assume the sample as a homogeneous set of crystals with random orientation. This assumption can lead to error for multilayer coatings with layer thickness less than the penetration depth of the X-rays. Moreover, the transparency of the layers can limit the diffracted intensity. However, the chemical modulation, structure

and strain in multilayer coatings have been analysed using dynamic X-ray diffraction theories.

5. Scanning Electron Microscopy (SEM) [145,146,151,147,153,154]

SEM provide scanning two dimensional images of solid surfaces using electron beam generated secondary electrons. The primary beam may be focused on a spot less than 5nm (50Å) in diameter, in the range of 2.5 to 50KV. For X-ray analytical purposes the probe size is typically 2μm diameter. SEM images at less than 2nm (20Å) resolution have been obtained with several hundred thousand times magnification. The operating parameters such as voltage, beam diameter, beam current, angle of incidence, time and frame speed could improve image quality. Insulator materials may be coated with a thin conductive layer to dissipate the surface charge.
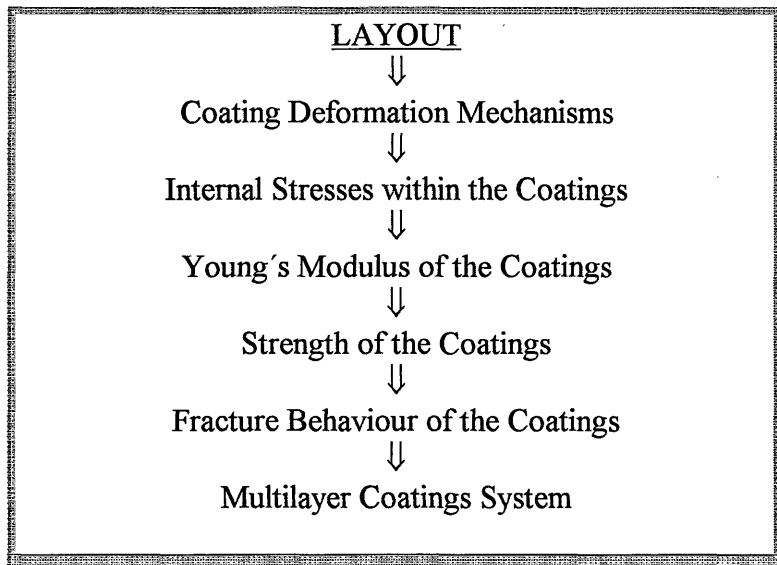
The environmental SEM, called the ESEM, operates with a gas pressure of up to 2.6×10^3(20Torr) in the specimen chamber. It therefore allows insulated materials to be examined without any coating. One of the most common analyses attached to the SEM is the energy dispersive x-ray spectroscopy (EDS). However, the useful range is from 1 to 220KeV, which limits the analysis to elements with Z>9 (when using a machine with Be window). In window fewer mode elements with Z between 6 and 9 can be detected.

6. Transmission Electron Microscopy (TEM) [145,146,147]

The TEM uses an electron beam at higher accelerating potential (100-400KV) to obtain information from samples which are thin enough (50-300nm) to transmit electrons. The samples are thinned by a combination of chemical, mechanical polishing and ion milling. The TEM resolution could be higher than 0.15nm. The transmitted electrons are used to form either an image or a diffraction pattern or for X-ray microanalysis composition.

The standard method for generating diffraction patterns is by selected area diffraction (SAD) where an aperture is used to limit the area of the specimen from which the diffraction pattern is obtained. The latter can be used to determine the crystal system and lattice constants of phases within the thin foil structure. Attachment of EDS detectors permits the identification of local elemental composition variations at a spatial resolution of about 0.1μm. The STEM is both a scanning and transmission microscope which operates between 100 to 200KV. The electron beam is focused on a small probe which is scanned across the specimen.

1.5.2. MECHANICAL PROPERTIES OF THIN FILMS BY TRADITIONAL METHODS

<u>LAYOUT</u>
⇓
Coating Deformation Mechanisms
⇓
Internal Stresses within the Coatings
⇓
Young's Modulus of the Coatings
⇓
Strength of the Coatings
⇓
Fracture Behaviour of the Coatings
⇓
Multilayer Coatings System

Nowadays, the characterization of thin films tends to be towards their functionality. However, features such as behaviour and stability in service could also be of importance. For example, the coating materials used for microelectronic integrated circuits and magnetic disks must perform their electronic and magnetic functions but corrosion, mechanical and wear failures should not occur. Such failures could be produced by residual stresses, substrate deformation, friction and erosion, or strain from thermal expansion coefficient mismatch [127].

The measurement of thin film mechanical properties has become of foremost importance in the last few years. The explanation can be found in the following examples, which also show that some failures in the component integrity could be attributed to its mechanical properties:

♦ Inorganic dielectric and passivation films, for microelectronics devices, have been reported to be dependent on mechanical strains resulting from coefficient of thermal expansion mismatch, mechanical deformation of the substrate and residual stresses in the film resulted [155,127].

♦ The ultimate strain has been reported to be an important property of inorganic passivation films when a microelectronics device heats up during service, because the coating could not be made stiff enough to resist dimensional changes caused by thermal expansion [155].

♦ The quality and reliability of SiH_4 and NH_3 passivation films used for semiconductor devices have been reported to be dependent on the stress, the modulus of elasticity and the thermal expansion coefficient [156].

♦ The control of industrial coatings technologies could be improved by mechanical properties measurement on-line [128].

107

♦ Thin films for microelectronic devices and wear and corrosion protection have caused increased interest in the mechanical properties of coatings. The films must withstand the stresses produced during the deposition process and thermal expansion mismatch during service and processing. They must also have the required properties for specific applications [125,157].

I. COATING DEFORMATION MECHANISMS

The interpretation of the mechanical properties of thin films on non-deformable substrates requires a knowledge of the film deformation mechanisms. The formation of misfit dislocations in epitaxial and heteroepitaxial thin films on single crystal substrates has been shown to provide a basis for understanding the dislocation processes responsible for plastic deformation within thin films [127].

Owing to the lattice mismatch between the film and substrate, the former must be elastically strained in order to establish an epitaxial relationship with the substrate. From the equilibrium theory of misfit dislocations, a thin film in an equilibrium state has homogeneous strain and contains no misfit dislocations. Such films are perfectly coherent with the substrate and the energy of the film is the lowest.

The associated energy due to uniform strain varies linearly with the film thickness, while the associated energy due to misfit dislocations varies logarithimically with the film thickness. As a result, a certain critical thickness needs to be exceeded for the free energy of the film to be reduced by the presence of misfit dislocations. The introduction of misfit dislocations leads to a relaxation of the homogeneous strain in the film and promotes plastic deformation. Consequently there is a critical thickness below which fully coherent epitaxial films are thermodynamically stable [127].

The mechanisms of misfit dislocation formation within the film can be explained by dislocations on the substrate surface which grow into the film and then reach the free surface of the film. These are called threading dislocations. The misfit dislocations are created by the movement of the threading dislocations, and also during annealing of the film. The multiplication of dislocations can be produced by the crossing of two misfit dislocations or by defects nucleating in the growing film. It is important to point out that inhomogeneous deformation can lead to fracture of the film, either by dislocation slip or by grain boundary sliding [127,158].

II. INTERNAL STRESSES IN THE COATINGS

Films prepared by PVD techniques often develop internal stresses, sometimes several times larger than the bulk yield strength of film material, both in tension and compression. Moreover, internal stresses can be related to the maximum coating thickness and control film spallation [123,159].

The internal stresses of thin films can have several effects on the integrity of the components and film behaviour, as illustrated in figure 1.58.
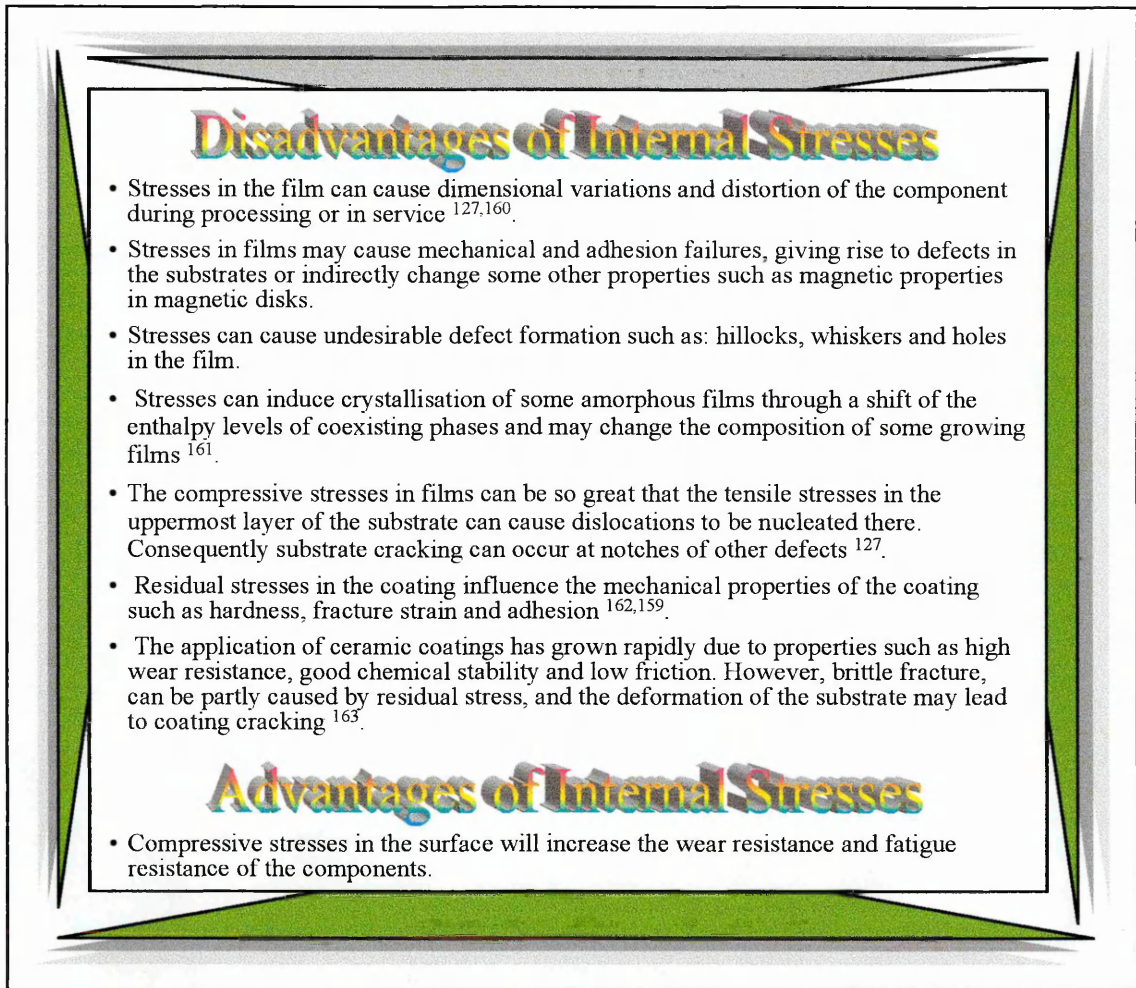
Disadvantages of Internal Stresses

- Stresses in the film can cause dimensional variations and distortion of the component during processing or in service [127,160].

- Stresses in films may cause mechanical and adhesion failures, giving rise to defects in the substrates or indirectly change some other properties such as magnetic properties in magnetic disks.

- Stresses can cause undesirable defect formation such as: hillocks, whiskers and holes in the film.

- Stresses can induce crystallisation of some amorphous films through a shift of the enthalpy levels of coexisting phases and may change the composition of some growing films [161].

- The compressive stresses in films can be so great that the tensile stresses in the uppermost layer of the substrate can cause dislocations to be nucleated there. Consequently substrate cracking can occur at notches of other defects [127].

- Residual stresses in the coating influence the mechanical properties of the coating such as hardness, fracture strain and adhesion [162,159].

- The application of ceramic coatings has grown rapidly due to properties such as high wear resistance, good chemical stability and low friction. However, brittle fracture, can be partly caused by residual stress, and the deformation of the substrate may lead to coating cracking [163].

Advantages of Internal Stresses

- Compressive stresses in the surface will increase the wear resistance and fatigue resistance of the components.

Figure 1.58. Disadvantages and advantages of internal stresses.

Film stresses have two origins [162]:

1. Thermal stresses (σ_{th}).

2. Intrinsic stresses (σ_g).

The thermal stresses [126,127,141,161] result from the thermal expansion or contraction coefficient mismatch between the substrate and film. They can be produced in the film materials after deposition, during manufacturing of the component, and associated with post-annealing processes and remain there during the subsequent use. If the thermal stresses exceed the fracture strength of the film, despite being restrained by a strong coating-to-substrate adhesion, fracture may occur. At high deposition temperature the differences in the coefficients of thermal expansion of the substrate and the film material can result in very high residual stresses either in tension or in compression, depending on which material has the higher coefficient of thermal expansion [56,141].

Assuming that the thickness of the substrate is much larger than that of the film and the film is elastically isotropic, then the thermal stress is given by the equation 1.3. A positive value of thermal stresses corresponds to tensile stresses.

$$\sigma_{th} = \left(\frac{E_f}{1-\upsilon_f}\right) \times \left(\alpha_f - \alpha_s\right) \times \left(T_s - T_m\right) \tag{1.3}$$

Where E_f is the Young's modulus of the film

α_f and α_s are the coefficient of thermal expansion for the film and substrate respectively

T_s and T_m are the substrate temperature during deposition and measurement temperature respectively

υ_f is the Poisson's ratio of the film

The elastic strain to fit the film onto the substrate is given by:

$$\varepsilon = -\left(1-\upsilon_f\right) \times \left(\alpha_f - \alpha_s\right) \times \left(T_s - T_m\right) = -\left(1-\upsilon_f\right)\Delta\alpha\Delta T \tag{1.4}$$

A general definition for intrinsic stresses covers all the stresses that are not directly related to thermal mismatch. However, a more specific definition referred to the stress developed during the film growth process. Consequently, intrinsic stresses depend on the deposition techniques and processing conditions. Most of the growth of film comes about far from thermodynamic equilibrium with the effect that non-equilibrium microstructures can be produced. Such microstructures and crystallographic defects can lead to extra stresses caused by the tendency of the film to shrink or expand as soon as it has been deposited onto the substrate [127,161].

There are some methods of modifying the stresses created in the growing film such as [56]:

- ♦ To limit the film thickness
- ♦ To use concurrent energetic particle bombardment during deposition to maintain a near stress free condition
- ♦ To alter the concurrent bombardment conditions periodically
- ♦ To add alloying or reacting material periodically
- ♦ To mix materials
- ♦ To generate an open columnar morphology that cannot transmit a stress

Films deposited by evaporation which do not have any external agency, such as: impurities or ion bombardment, often exhibit tensile stresses. This can be explained due to the differences in temperature between the arriving atoms at the film surface and substrate temperature and also the non-thermodynamic condition during film growth at low temperatures recognised by a high degree of disorder. As a result, any relaxation mechanism such as annihilation of structural defects in the film, towards a more ordered state, can cause tensile stresses. The incorporation of impurities in the vacuum deposited films can sometimes result in compressive stresses e.g. oxygen in Al films [126,161,164].

Films deposited by sputtering often exhibit compressive stresses. Such stresses can be caused by the bombardment of the film surface by energetic species such as: sputtered atoms, neutral atoms from sputtering gas, backscattered neutral ions from the cathode, i.e., the atomic peening process which increases the volume of the film. As a result, the stresses can be created by crystal lattice defects such as interstitials and

dislocations. However, the ion bombardment facilitates the formation of dense structures without grain boundary voids but increases the point defects in the structure due to implantation of energetic ions. The literature refers to the stopping power for incoming ions as nearly proportional to the square root of the incident flux energy (E). Then the stresses in the film should be proportional to $E^{1/2}$. The compressive stresses induced in the film decrease above a critical gas pressure and they can become tensile due to the energetic particle bombardment effect [161,165,141,162]. Hence, the film structure may become weakened, and the film structure becomes porous with more entrapped argon [166]. The AlN films prepared by reactive DC magnetron sputtering show a transition from compressive to tensile stress when the ratio of Ar/N_2 increases to more than 2 to 1 [167].

The deposition parameters in sputtering that could influence the coating stresses include: substrate temperature, working gas species, working gas pressure, deposition rate, angle of incident flux, apparatus geometry, distance between the substrate and the source, bias voltage, target power, etc. [168].

The working gas species and sputtering target purity are less important compared to the gas pressure. The deposition rate has only a small influence. High deposition rates can produce large compressive stresses and increase the critical pressure to develop tensile stresses. The critical pressure increases with the atomic mass of the coating material. Decreasing the working gas pressure below a predetermined value results in an increase in the residual stress due to decreasing the gas scattering because low gas pressure leads to more energetic ions with a higher kinetic energy [162].

Oblique substrate orientation such as: substrates of a complex shape, relative to the coating flux tend to produce tensile stress [141]. The total stresses were found to depend on the level of substrate bias during deposition because the use of substrate bias can control the porosity, grain size and defect densities in the film. For example, increasing the bias voltage on a TiN coating during deposition results in a large compressive stress due to the high kinetic energy of the bombarding Ar ions on the substrate [123,162].

The microstructure and thus the intrinsic stress in the film is strongly dependent on the deposition conditions, as shown by Thornton's model. The energy stored in a film by the stresses can be considered as a thermodynamic driving force which tends to relax the stresses by activation of vacancy, interstitial and dislocation movement. For deposition conditions in the zone 1 of Thornton's diagram the film structure has micropores and voids and the zone is not often highly stressed. High intrinsic stresses are often observed in the transition zone. At temperatures in zone 2 the recovery of the strained grains into new strain-free grains occurs. At temperatures in zone 3, the coexistence of recovery and recrystalisation relaxes the intrinsic stresses in a growing film by bulk diffusion [123,126,141].

The total stress originated in the film as a function of T/T_m is illustrated in figure 1.59. The substrate temperature is presupposed to be greater than room temperature and the film thermal expansion coefficient is also assumed to be greater than the substrate. As a result, the tensile thermal stress is produced on cooling the substrate. At a low ratio of T/T_m the intrinsic stress dominates over the thermal stress. However, for the ratio of T/T_m in zone 2 the recovery processes are effective and the intrinsic stress is reduced. At

higher ratio of T/T_m the thermal stress dominates. The total stress may have a minimum at some intermediate T/T_m as a result of the combined effects of the intrinsic and thermal stresses [141].
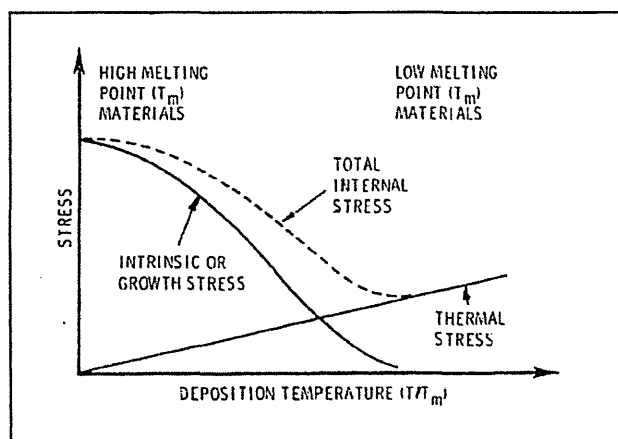

Figure 1.59. Representation of thermal and intrinsic stresses in a film [141].

The coating materials can be divided into two categories according to their melting point [141]:

1. *Low melting point materials ($T/T_m>0.25$):* They are soft with a high thermal expansion coefficient, low activation energy for self-diffusion and produce low intrinsic stresses such as: Al, Pb.

2. *High melting point material ($T/T_m\leq0.25$):* They are harder with a lower thermal expansion coefficient, high activation energy for self-diffusion and produce high intrinsic stresses such as: Cr, Mo.

In summary, the stresses in the films on substrates can arise from the misfit between the elastic and thermal properties of the film and substrate. Nevertheless, there are many ways in which the volume of the film may change over the substrate surface, including [127]:

♦ Variation in the thermal expansion coefficient between film and substrate

♦ Annihilation of excess vacancies, dislocations and grain boundaries that could produce densification of the film

♦ Phase transformation and composition changes can produce dilatation strains in the film

♦ Normal misfits between film and substrate in their stress free state exist for heteroepitaxial films.

Analytical models for predicting the internal stresses in a multilayer coating have been successfully developed from the stress of each layer with [165,169].

III. BALANCING INTRINSIC AND EXTRINSIC STRESSES

The stress distribution of the coating/substrate composite requires the sum of the normal forces and bending moment over the total cross-section to be zero. Consequently, stresses of an opposite sign are formed in the substrate to balance the film stresses and then the sign reverses at the interface. Moreover, the stresses in the substrate change sign at the neutral axis, so the substrate stresses on the surface opposite the coating have the same sign as in the coating. The substrate must bend to balance the bending moment which is produced by the stressed film. As the substrate is thicker compared to the film, so the stresses in the substrate are quite small compared to the film stresses. Consequently, the substrate bending is insignificant compared to the film stress.

Internal stresses in the film are often determined by measuring the curvature, or deflection, of the substrate [126]. The lattice mismatch between the film and the substrate must be accommodated by a uniform strain in the film, together with slight bending of the substrate, which leads to biaxial stresses in the film. Such stresses may be relaxed by plastic flow through dislocation nucleation and motion depending of the film thickness[127].

Considering a very thin film onto a thick substrate, the film and substrate thickness is much less than their lateral dimensions and the biaxial elastic modulus is isotropic in the plane of the substrate. In this case the biaxial stress in the film (σ_f) may cause the substrate to bend elastically, and can be expressed as a function of substrate curvature by Stoney's equation [127,126,158]:

$$\sigma_f = E_s \times \left(\frac{t_s^2}{6t_f} \right) \times \Delta K \qquad (1.5)$$

Where E_s is the biaxial elastic modulus of the substrate $E_s = \dfrac{E}{1-\upsilon}$

t_s and t_f are the thickness of the film and substrate respectively

ΔK is the change in the substrate curvature

The elastic strain in the film as a function of the biaxial elastic modulus of the film (E_f) is given by:

$$\varepsilon_f = \left(\frac{E_s}{E_f} \right) \times \left(\frac{t_s^2}{6t_f} \right) \times \Delta K \qquad (1.6)$$

The stresses in an epitaxial thin film can be determined without measuring the curvature of the bare substrate. This can be achieved by making two curvature measurements before and after thinning the substrate from its back. The equations are given in reference [158].

Small substrate deflections require an accurate measuring system. For large deflections Senderoff's equation can be used, which is based on the elastic beam theory. It is only applicable if the width-to-length ratio of the substrate is less than 0.07. The

determination of the total residual stress in the film by Senderoff's equation [162] is given by:

$$\sigma_f = \frac{\frac{E_s}{(1-\upsilon_s)}\left(t_s + \frac{E_f(1-\upsilon_s)}{E_s(1-\upsilon_f)}t_f\right)^3}{6Rt_st_f} \qquad (1.7)$$

Where σ_f is the total residual stress in the film (GPa)

E_s and E_f are the Young's modulus of the substrate and coating respectively

υ_f and υ_s are the Poisson's ratio of coating and substrate respectively

t_s and t_f are the thickness of substrate and film respectively (m)

R is the radius of curvature (m)

For single crystal or polycrystalline films with strong crystallography texture, the anisotropy of the elastic properties must be taken into account, as mentioned in reference 127 for measuring residual stresses. For films deposited sequentially, each film can cause a fixed amount of bending, so the curvature change is determined by the stress and thickness of each film. The total change of substrate curvature is the sum of the curvature change associated with the presence of each film. The sign of the curvature change caused by each film must also be taken into account.

Thin films of uniform thickness do not cause a significant stress in the underlying substrate. However, for patterned structures the interactions of stresses for different films can be significant and must be taken into account in stress calculation. If the plane of the substrate parallel to the plane of the film has non-isotropic elastic properties so the substrate is not elastically isotropic in that plane and does not bend symmetrically. In this case the beam theory is not applicable [127].

The experimental technique for measuring stresses in a thin film on a substrate fall into two classes [126,127,166,162,156,170,171] and some of these techniques are referred to below:

1. *Those based on direct measurement of the elastic strain in the film such as*: XRD, RBS

2. *Those based on the curvature of the substrate such as*: optical interferometry, laser scanning, optical microscopy, bulge technique.

X-Ray technique: The literature has reported that curvature of a single crystal substrate produces a strain in the crystal lattice that can be detected by XRD. The XRD technique is based on measurement of the change in the lattice plane distance of a set of planes (hkl) for different orientations of the specimen [127,162,172].

Several X-ray techniques have been used to measure stresses in polycrystalline thin films such as: glancing angle X-ray scattering (GIXS), the $\sin^2\psi$ method [173,174]. In both techniques the strain or the relative change of the lattice spacing d in the film is

114

related to the change in the diffraction angle ϕ through the Brägg law where d_0 and ϕ_0 are in the unstressed state. The strain is given by [175]:

$$\varepsilon = \frac{\Delta d}{d_0} = \frac{\sin\phi_0}{\sin\phi - 1} \qquad (1.8)$$

The $\sin^2\psi$ method is a traditional X-ray method applied to measuring strains at the surface of the bulk materials and films. According to this method the strain $\varepsilon(\phi,\psi)$ at a constant ϕ is a linear function of $\sin^2\psi$ and the stress can be found from the slope of this relationship from $\left(\frac{(1+\upsilon)}{E}\right) \times \sigma_\phi$. The strain $\varepsilon(\phi,\psi)$ is determined for several directions that are specified by the polar angles ϕ and ψ. Assuming the stress state within a coating is in biaxial stress, which requires that the measured value of strain is related to the principal stresses σ_{11} and σ_{22} given by:

$$\varepsilon_{\phi\psi} = \left(\frac{S_2}{2}\right) \times \left\{\sigma_{11}\cos^2\phi + \sigma_{22}\sin^2\phi\right\}\sin^2\psi + S_1\left(\sigma_{11} + \sigma_{22}\right) \qquad (1.9)$$

Where S_1 and $S_2/2$ are the X-ray elastic constants for a particular (hkl) reflection. For an elasticity isotropic film then

$$\frac{S_2}{2}(hkl) = \frac{(1+\upsilon)}{E} \qquad ; \qquad S_1(hkl) = -\frac{\upsilon}{E}$$

Where E is Young's modulus and υ is Poisson's ratio. In this method an interplanar spacing d serves as an internal strain gauge given by:

$$\varepsilon_{\phi\psi} = \frac{\left(d_{\phi\psi} - d_0\right)}{d_0}$$

$$\sigma_\phi = \sigma_{11}\cos^2\phi + \sigma_{22}\sin^2\phi$$

Where $d_{\phi\psi}$ is the interplanar spacing of crystal planes which are perpendicular to the ψ direction in the stressed condition and d_0 the interplanar spacing in the unstressed condition. The slope of $\sin^2\psi$ versus $\varepsilon_{\phi\psi}$ is proportional to σ_ϕ when a biaxial stress state is assumed. The compressive stress in the plane of the coating expands the planes parallel to the surface due to the Poisson's ratio effect.

$$\varepsilon_{\phi\psi} = \frac{\left\{a_{(hkl)} - a_0\right\}}{a_0} = S_1\left(\sigma_{11} + \sigma_{22}\right)$$

$$a_{(hkl)} = a_0 - \left(\frac{2\upsilon}{E}\right)\sigma_\phi a_0$$

Where a_0 is the lattice parameter of the unstressed film and σ_ϕ is the internal stress. The linear manner in the $\sin^2\psi$ versus $\varepsilon_{\phi\psi}$ plots is not always observed and plots often show ψ splitting and curvature due to the presence of shear stresses and stresses normal to the surface [123,175].

Optical Interferometry Technique: The optical interferometry technique is able to measure the substrate curvature changes by counting of interference fringes. This technique is advisable for quite large curvatures [127]. An optical displacement-detection apparatus has been able to measure in situ the stress of a film [171].

Laser Scanning Technique: The laser scanning technique is one the most popular techniques for measuring substrate curvature connected with film stresses. A beam of laser light reflects off the surface of a curved surface at an angle θ that depends on the orientation of the surface. After the laser beam scan, if the substrate is bent, then the light reflects at a different angle. A photodetector can be used to detect the change in angle of the reflected laser beam. Some laser scanning devices use a rotating mirror to scan the laser beam over the substrate. The substrate shape along the laser scan path needs to be found before deposition or after the film is removed in order to obtain the change in curvature associated with the presence of the film [127].

As a conclusion, the most sensitive technique for measuring strain in films involves RBS dechanneling and XRD. However, they do not measure continuous strain relaxation and also require a long time for measurement. The XRD technique gives a wide variety of information such as: measurement of all of the components of stress in the film; detection of spatial variations of stress within the film either from grain to grain or from one point in the film to another. It can be used at temperatures up to 1200°C. However, this technique is limited to crystalline films and cannot be used to determine stresses in nanocrystaline materials or amorphous films. For single films this technique gives absolute values [127,158].

The substrate curvature technique is often preferable due to its simplicity and can be applied to special conditions such as in situ heating or cooling or during film growth. Moreover, the average film stress can be easily calculated without the knowledge of elastic properties of the film. This technique allows strain and strain relaxation to be monitored in epitaxial films by using the laser scanning technique. If the stress varies through the thickness, then the substrate curvature technique gives only the average value of the stresses [126,127,158].

IV. HARDNESS

The hardness is usually the initial guide to knowing the applicability of the coating. Some investigators [177] have reported that some hardness values found in the literature or in manufacturers' specifications are often equivocal because they have been measured in a non-standard way. Some of the problems that could be pointed out in the determination of the hardness in coatings onto substrate are outlined in figure 1.60[123,154,156,176,177].

Factors to Be Considered in the Determination of Coating Hardness:

- The presence of the coating/substrate interface. The indentation size effect (ISE) should also not interfere with the film hardness measurement. To minimise this effect, a rule of thumb criterion is often applied. Such a criterion establishes that the indentation depth must be less than one tenth of the coating thickness. However, this rule is often difficult to achieve using standard microhardness equipment for coating thickness less than 5μm unless non-traditional methods are used.

- The accuracy of the hardness measurement is affected by: small indentation size, poor surface finishing and adsorbed surface layers such as: water, oxidation. To minimise these problems the literature recommends using a large load/indenter size range provided that reliable hardness measurement can still be achieved, which depends on film thickness.

- Some ceramic and metal coatings show increased hardness at low loads (<0.1Kgf). This is known as the indentation size effect (ISE). The load effect can be observed in single crystals, polycrystalline and aggregate materials. Several proposals have been made to explain this effect, including: surface work hardening, surface oxide films, non-continuous deformation, friction between the indenter and the indenter material

- Using spherical and conical indenters in crystallographic anisotropy hard materials could result in distorted indentations and circumferential tensile stresses around the contact area that could produce brittle fractures. To minimise these effects, pyramidal indenters are often used, such as: Vickers, Knoop or Berkovitch. However, the anisotropy effect is not completely overcome. For example, variation in hardness from one crystal to another, and changes with respect to a specific crystallographic orientation for a given material, have been observed. As a result, it is advisable to specify both the planes of indentation and the orientation of the indenter when comparing hardness values. The Knoop indenter is usually used for measuring hardness of hard materials. Owing to it being more likely to give crack free impressions the hardness value is determined on the basis of the length of the long diagonal. The alignment of this diagonal with a specific crystallographic direction may not be so critical because of its low penetration depth.

- The classical hardness methods limit the minimum depth of the indentation to less than 1-2 μm because the indentation is too small to be measured by conventional light microscopy. Some indentations measured on an optical microscope may have a 30% error when compared with SEM measurements.

- Increasing the dwell time in some hard materials leads to an increase in the size of the indentation for a given normal load and so an apparent reduction in the hardness. This means indentation creep can occur. This effect has been observed in ionic and covalent solids at room temperature and in some crystalline solids at temperatures up to $0.4T_m$.

Figure 1.60. Factors to be considered in the determination of coating hardness.

Nowadays, hardness models have become available which allow the hardness of the bulk coating to be determined independently of the substrate, for hard coatings onto soft substrate, soft coatings onto hard substrate and for multilayer coating systems [123].

The hardness model suggested by Sergent for coating thickness in the range of 1-10μm is based on the volume law of mixtures and has been extended by S. Bull and

D.Rickerby [123,177]. The latter considered the presence of the deforming volume shape of the coating and substrate, as shown in figure 1.61.
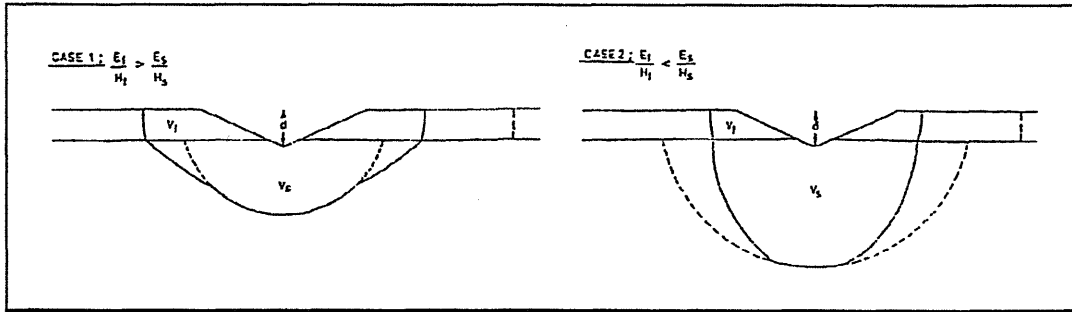

Figure 1.61. Rickerby's model for the hardness of the coating/substrate system [123].

According to Rickerby's model, the hardness of the coating/substrate system (H_c) is given by:

$$H_c = \frac{V_f}{V} H_f + \frac{V_s}{V} X^3 H_s \qquad \text{for } H_f > H_s \tag{1.10}$$

$$H_c = \frac{V_f}{V} X^3 H_f + \frac{V_s}{V} H_s \qquad \text{for } H_f < H_s \tag{1.11}$$

Where H_f and H_s are the hardness of the coating and substrate material respectively and they are determined as a function of the contact size. V_s and V_f are the deforming volumes in the substrate and coating and V is the total deforming volume given by

$$V = V_f + X^3 V_s \qquad \text{for } H_f > H_s$$

$$V = X^3 V_f + V_s \qquad \text{for } H_f < H_s$$

X is an empirical factor which relates to the modification of the deforming value of the softer strained component of the coating/substrate system and it is strongly dependent on the ratio of plastic zone radii of the coating and substrate. Using a spherical cavity model to describe the deforming volumes of the coating and substrate, then the radius of the volume deformed plastically (R_p) can be calculated. Hence the X can be based on the ratio of deforming volumes between the coating and substrate given by:

$$R_p \propto \left(\frac{E}{H}\right)^n \qquad ; \qquad X = \left(\frac{E_f H_s}{E_s H_f}\right)^n$$

Where E_f and E_s are the elastic modulus of the film and substrate. The exponent n is theoretically in the range 1/2 to 1/3 but in practice is determined by fitting to experimental results. When the load is increased, the coating is strongly pressed into the indentation so multiple cracking can occur. This means that the deforming volume in the coating will not be a slice through a hemispherical volume. In this case the hardness and ISE index of the coating should be determined from the low load data where cracking within the indent is not a problem. For this reason this model should be used for a minimum thickness of coating of around 1μm.

A recent hardness model has been developed to understand the hardness of the coated systems, considering the penetration depth of the indentation given by [178]:

$$H_c = H_s + \left(\frac{H_f - H_s}{1 + k\beta^2} \right)$$ (1.12)

Where K is a fitting parameter which describes indenter properties

$\beta = (\delta/t)$ is the indentation depth normalised with respect to the coating thickness

In summary, a reliable hardness model should be able to predict the hardness of a coating/substrate composite over a range of indentation sizes or loads and use parameters that reflect the hardness behaviour of either the substrate or coating without any ISE effect. The hardness models can be used in quality control for comparison of coatings from different manufacturing processes, comparison of coatings of different thickness on different substrates, evaluation and development of new coatings and studying of the effect of the processing parameters on mechanical properties [177].

V. YOUNG'S MODULUS

Several investigators [128,179] consider that the elastic modulus is the most important mechanical property for the characterization of coating performance. However, the most important mechanical property is the one which makes the component fail or reduces its lifetime. So why is elastic modulus so important? Figure 1.62 outlines some examples of the elastic modulus knowledge advantages[128,180,166,177,179,156].

Why is Elastic Modulus so Important ?

- The mechanical thermal shock resistance depends linearly on the elastic modulus.
- The elastic modulus is dependent on the bonding forces between atoms, so the elastic modulus can give information about the atomic co-ordination. For example, this has been used in the amorphous carbon structure to assess the degree of covalent bonding.
- The knowledge of elastic modulus is important in the analysis of the mechanical behaviour of coatings to improve their fatigue resistance.
- P-J.Burnett and D.Rickerby infer that the elastic modulus of the TiN unbiased coating would be dependent upon the ratio of voids to columns, thus coating morphology.
- The stress-strain behaviour, contact stress field, integrated surface hardness, cracking, spalling, bending and residual stress states of coating systems are all functions of the in plane elastic modulus.
- Poor adhesion impedes the stress transfer between the coating and the substrate. This decreases the integrated elastic stiffness and so the elastic modulus and so the component integrity.
- Wear-resistant coatings could be subjected to external loading conditions so adhesion and resistance to fracture are basic requirements. Coating/substrate interface failure may be increased by a stress discontinuity across the interface due to a Young's modulus mismatch between the coating and the substrate.

Figure 1.62. Advantages in knowledge of elastic modulus.

Several techniques have been performed to measure the elastic modulus of thin films, such as: resonant frequency, bending test, ultrasonic surface waves, bulge tester, vibration membrane, speed of bulk waves, strain gauge, surface wave, derivation from

XRD stress measurement [181]. But none of these methods is either universal or accurate enough for calculating Young's modulus of a sub 1μm thick layer deposited on a 200μm thick substrate [156]. As a result, to obtain meaningful elastic modulus results, the accuracy of the measurement and the homogeneity and stability of several geometrical and physical parameters must be extremely high. The accuracy of the elastic modulus of the coating is dependent on the geometrical conditions, substrate, properties and error in the measurement and the homogeneity of the elastic modulus [182]. Some of the mentioned techniques are referred to below:

Dynamic Resonance or Resonant Frequency Technique [125,179,184]

The resonant frequency allows the elastic properties of the coating to be determined. The technique consists of making a specimen vibrate either in bending or in tension mode and measuring its resonant frequency.

The specimen temperature can vary from 27°C to 1227°C. The applied frequency may vary between 1KHz and 1MHz. Conductive materials can be tested directly in the apparatus while non-conductive materials require a previous metallic plating. The elastic modulus of the coating (E_f) can be calculated by Berr's equation given by [185]:

$$\left(\frac{N + \Delta N}{2}\right)^2 = 1 + \varepsilon\left(3\frac{E_f}{E_s}\right) - \frac{\rho_f}{\rho_s} \tag{1.13}$$

Where N is the resonant frequency of an uncoated specimen

(N+ΔN) is the resonant frequency for specimen with coating

E_s is the Young's modulus of the substrate

ρ_s, ρ_f are the density of the substrate and the coating respectively

$\varepsilon = (h_f/h_s) < 1$ is the coating thickness over substrate thickness

A resonant frequency method was reported by P. Hancock [184] to calculate the coating modulus, in the range between 5-10μm, by measuring the resonant frequency of an oxidising rod with known scale growth rates. The system measured (E/1-υ) and an assumption had to be made for the value of Poisson's ratio. The author derives an alternative equation given in reference [184].

The advantage of this technique over others is that it is able to perform measurements without contact between the specimen and the exciting or detecting components. The uncertainty in Young's modulus value from equation 1.13 is about 10% for a film thickness of the order 1μm, but successful results have been reported for films in the range of 0.1 to 0.9 μm. This technique requires accurate measurements of thickness of the coating and substrate and temperature control during the experiments. P. Hancock and J. Nicholls in 1994 reviewed alternative methods to measuring the elastic modulus and stated that the only direct way of measuring the elastic modulus is by using depth-sensing microindentation.

A laser beam is used to produce ultrasonic waves. The method uses a cylindrical lens that guides the laser beam to be focussed on the specimen surface in a focal line. The wave propagates perpendicularly to the direction of the focal line with a frequency over 100MHz. After this, the beam is received by a piezoelectric transducer. Both specimen and transducer are fixed on a moving table relative to the laser beam and with an accuracy of x=1µm. The relative error of the wave velocity is less than ±10⁻³. The Young's modulus of the layer can be calculated according to Newlands' theory by:

$$\sum_i \left[C(f_i) - C\left[\frac{d}{\chi_i}, E_f, \upsilon_f, \rho_f, E_s, \upsilon_s, \rho_s \right]^2 \right]$$ (1.14)

Where $C(f_i)$ are the values of surface wave velocity measured for a series of frequencies f_i, E_f, υ_f, ρ_f and E_s, υ_s, ρ_s are the coating and substrate parameters respectively.

The measurement of the film elastic modulus is not influenced by changes in the sound path direction on the substrate. The values have a scatter of ±5GPa for several angles of the sound path. The film is bonded to the substrate and the specimen does not need either special form or dimensions. This method allows calculation of the shear, biaxial and flexural modulus.

The bulge test applies gas at pressure to make a circular mounted free-standing film deflect. The height (h) of the bulge is measured as a function of the applied gas pressure (p). Typical maximum pressure values are 65KPa±40Pa and the maximum bulge height is 0.5mm±2.5µm. Two methods can be employed to measure bulge deflection:

1. Using a bourdon gauge to measure pressure to about ±0.04KPa and a micrometer to measure the total bulge deflection (±2.5µm).

2. Using an electrical transducer to monitor pressure to about ±0.04KPa and a laser interferometer to provide a precise measure of the total deflection. This is less precise than the micrometer because it does not provide a measurement of the total deflection including the initial bulge height (h_o) associated with p_o

The biaxial stress σ and strain ε at the centre of the bulge foil when the thickness t_f of the foil is small over radius r of the hole is given by:

$$\sigma = \alpha \left(\frac{P \times r^2}{h \times t_f} \right) \qquad ; \qquad \varepsilon = \beta \left(\frac{h^2}{r^2} \right)$$ (1.15)

Where α and β are constant for a spherical bulge (assuming a Poisson's ratio of 0.33) so α=0.28 and β=0.69. The total height of the bulge deflection should be corrected for the initial height (h_o). An initial pressure (p_o) is used to remove slack in the foil. The elastic modulus is determined from the initial slope of σ versus ε curve. The accuracy is no better than 5-10% for film thickness from 0.5 to 2µm. This test eliminates the risks of

edge defects. Moreover, a fluid such as glycerol can be used to smooth wrinkles by wetting the bottom of the film and holding it flat.

Bending Test [128,156,179,181]

The measurement of the in-plane elastic modulus of the coatings onto substrates by a bending test has been performed with different configurations. Some of them are mentioned below.

Andre Rouzaud et al [128] produced a three point bending design that was applied to a flat rectangular coated beam ranging from 0.5 to 10μm thickness. The load was applied at the central point of the sample. A programmable displacement was imposed by the end points in order to keep the central specimen fixed. A piezoelectric force system for a nominal range of 0-50N was placed below the central bending point. An optical microscope coupled with a video camera allowed the sample area under test to be monitored. An acoustic emission detector is fixed in the central point in order to detect acoustic noise from the beginning of the cracks. The elastic modulus measurements are performed by computing the S_1 and S_2 slopes obtained from the uncoated and coated beams of the force versus displacement curve. The scatter in standard deviation that was found for E_f may be related to low adhesion. The uncertainty range of the modulus is about ±10%. This technique allows the stress field to be monitored together with the onset of cracks and an estimate of the adhesion of the coating.

A. G. Van Nie [156] determined the elastic modulus of the coatings by placing a beam in a three-point bending test. The curvature caused by the central load was measured with a standard laser (Hewlett Packard). The relationship between the curvature of the coated beam, stresses and elastic modulus is based on the plane strain model and Timoshenko's relations for pure bending of plates. Some conclusions were drawn from these experiments such as: the elastic modulus of the substrate is independent of the applied load; the E_f values are different from sample to sample, this may be due to either the geometric dimensions of the beam varying or to the scatter in E_s due to surface imperfections; the elastic modulus of the film (E_f) is independent of the applied load but it increases with the stress in the coating.

Chin-Chen Chiu et al [179] determined the elastic modulus of a coated beam from a pure bending that could be performed in a four-point bend test. The elastic modulus of the coating (E_f) and the beam (E_s) can be calculated from the surface strain detected by a strain gauge attached to a specimen loaded using the equation:

$$E_f = E_s R\left(\frac{KR + 2K - R}{2R - K + 1}\right) \qquad (1.16)$$

where R is the relative thickness given by $R = \dfrac{t_s}{t_f}$

K is the relative strain given by $K = -\dfrac{\varepsilon_s}{\varepsilon_f}$

The relationship between relative strain, relative thickness and elastic modulus is shown in figure 1.63. For a coating/substrate system at E_s/E_f constant ratio, the relative strain goes toward a unit value when the relative thickness is increased. Constant experimental error due to the strain measurement gives an increase in the uncertainty of the measured modulus data when R is increased. It is advisable to use small values of R for measuring the elastic modulus of the coating. The test requires accurate dimensions of the specimen and coating thickness.
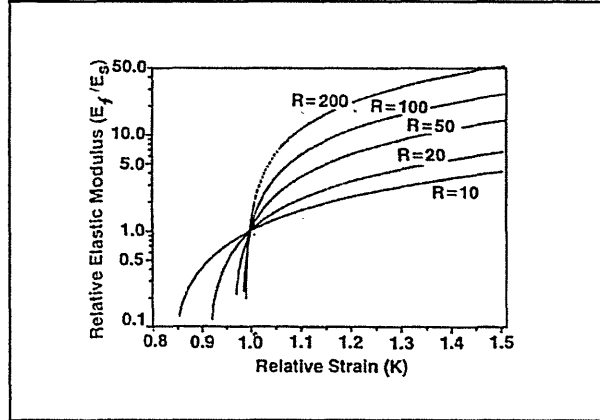
Figure 1.63. Relationship between relative strain, relative thickness and elastic modulus [179].

H. Ascada [181] designed a four-point bend test to measure the Young's modulus of TiC and TiN films. The deflection of the beams was measured by a laser device. The elastic modulus was calculated from the deflection versus force curve of the substrate or the coated specimen. The Young's modulus of the coating and for each layer was given by:

$$E_{fi}I_{fi} = E_s I_s + 2\Sigma\left(E_{fi}I_{fi}\right) \tag{1.17}$$

Where E_{ft} and E_s are the elastic modulus of the coated specimen and substrate respectively.

E_{fi} is the elastic modulus of the layers

I is the moment of inertia.

As is evident from the foregoing, the in-plane elastic modulus of the film does not depend on the mechanical properties of the film but the thickness and biaxial elastic modulus of the substrate and its dimensions. The flexural modulus of the film/substrate composite is dominated by the properties of the substrate.

VI. STRENGTH OF THIN FILMS

Some films exhibit high strength that can be due to the following effects: [127]

♦ The fine microstructure. Moreover, after annealing, the grain size cannot exceed the thickness of the film so notable grain size strengthening can occur in the film

♦ The dislocation density in the film could be quite high, which contributes to the high strength of the film

♦ The apparent strength of thin films can be caused by constraints from the substrate. For example, the strength of an Al film onto silicon substrate is much higher compared to the free standing film strength.

♦ The yield strength of thin films is often higher than that of the bulk materials. For example, the constraint effect of the substrate produces Al films that are stronger than bulk Al of comparable grain size.

There are two main factors that determine the strength of thin films:

1. The grain size effect
2. The influence of the substrate.

The grain size effect can be described by the Hall-Petch relation given by:

$$\sigma_y = \sigma_i + Kd^{-\frac{1}{2}} \tag{1.18}$$

Where σ_y is the yield strength of the polycrystalline sample

σ_I is the overall resistance of the lattice to dislocation movement

K is the Hall-Petch coefficient

d is the grain size

The substrate effect can be explained by the film/substrate interface constraint on dislocation motion in the film. The literature suggests that decreasing the film thickness, increases the constraint of dislocation motion. Moreover, a non-deformable layer on the film surface can cause a constraint of the dislocation motion. As a result, the yield strength of polycrystalline films has been shown to have a strong inverse dependence on the film thickness, owing to the fact that the grain size of the film is restricted by the film thickness [126].

The evaluation of the plastic deformation properties of a thin film attached to the substrate requires the stress and strain variations in the film to be measured. Such a requirement cannot be fulfilled with mechanical tests for bulk materials. Using the difference in the thermal expansion coefficient mismatch between the film and the substrate enables the biaxial yield strength of the film to be determined by heating or cooling. The curvature technique allows the stress changes in the film to be measured. This method permits a study of the yielding and plastic flow of the film [126,127].

The plastic flow occurs when the thermal stress exceeds the yield strength of the film, which can be measured by a stress-temperature curve. The time-dependent plastic flow can be evaluated by keeping the temperature constant and measuring the kinetics of stress relaxation. It is important to point out that the mechanism of stress relaxation in the first heating cycle does not contain plastic deformation of the film but it is a result of a structure transformation associated with grain growth of the as-deposited structure state [126,127].

VII. FRACTURE BEHAVIOUR OF THE COATINGS

Cracking in the coatings and their debonding from the substrate has been evaluated by indentation, scratch methods and bending tests. The elastic-plastic stress field around an indenter or the stylus tip makes this analysis very complex. However, bending tests have been shown to offer a simple alternative method.

Different bending test designs have been reported in the literature, such as:

♦ A four-point bend jig design was built to fit into the SEM chamber. Applying an increased load makes the tensile stress in the specimen surface increase to fracture or debond the coating. This method allows a direct observation of crack population and also allows estimates of the interfacial shear strength of the system. The main disadvantage is the effect of edges [163].

♦ A controlled strain was applied to a specimen in a four-point bend test. The cracking was detected by an electrochemical method. The ultimate strain as a sum of the residual strain and the material's intrinsic ultimate strain could not be determined. This method enables the fracture behaviour of insulating films to be evaluated. Moreover, this method gives reproducible results, providing the ultimate strain of the film is less than the limit of tensile elastic strain of the substrate [155].

VIII. MULTILAYER COATING SYSTEMS

Multilayer coatings or films consist of alternating layers of two different materials, generally in a well-proportioned or periodic manner. The layer thickness can be produced as small as 1nm or less. The characteristic microstructural scale is the wavelength or superlattice periodicity (λ) which is the sum of two layer thicknesses. Amorphous and polycrystalline multilayer structures have been designed with metallic, ionic and covalent materials often up to 1000 layers [189].

Two specific procedures have been used to produce multilayer coatings such as: the vapour source is interrupted by shutters or the sample is moved through independent sources in a controlled manner. The time sequence is of importance because contamination of the multilayer from the system ambient can affect the properties of the coating [190,191]. The deposition conditions (deposition rate fluctuations, shutter rotation speed) can affect the layer thickness control and interface sharpness. The latter can also be affected by the thermodynamics of the material system.

The mechanical properties of multilayer systems can be controlled by different mechanisms, depending on the layer thickness. The bulk properties and microstructure growth process dominate the thick single layers, while the interface mechanisms dominate when the number of layers increases and the single layer thickness decreases[189].

The stresses in multilayer coatings can result from the mismatch in thermal expansion of coating and substrate and between layers, and from the existence of microdefects within coating layers and loading in service. The stresses may cause failure of the weak layer or peeling off, either of the coating or one or more layers. The peeling

effect can be caused either by crack propagation along a layer interface, or start through a scratch, or by buckling over an area of imperfect adhesion. A mathematical model for stress analysis and failure probability of multilayer PVD coating was developed by V.U.Lyubimov et al[165]. The model gives the possibility of determining stresses as a function of layer composition and thickness, deposition temperature and substrate bias voltage.

Several reports in the literature [192] have mentioned the effect of λ on the elastic and plastic properties of multilayer coatings for values lower than 5nm. The most important effect is the so called supermodulus effect. This means an enhancement in the elastic modulus for $\lambda \cong 2$nm in multilayer thin films such as Cu-Pb, Cu-Ni, Ag-Pb [187,192]. Such elastic modulus enhancement was stated to be above 100% over the rule of mixtures. When these reports were published some researchers became very excited and tried to produce the same coatings and characterise them by different techniques. However, they could not get the same values and since then the supermodulus effect has been questioned and may be a result of measurement errors.

Testardi et al [125] had observed that the Young's modulus on Cu/Ni films of modulated composition of λ=0.8+0.8nm was twice as large as that of analogous CuNi alloy by using beam resonance methods. While Berry and Pritchet produced Cu/Ni films with a modulation length of 0.9-3.5nm they could not find any modulus enhancement by using a vibrating cantilever beam technique. T. E. Schlesinger et al [193] produced nanoindentation measurements on Cu/Ni thin film and stated that no supermodulus were observed but enhancements in the hardness were observed. Baker et al [125] employed both indentation and microbeam deflection methods to measure Young's modulus in Au/Ni films for λ ranging from 0.8 to 4.5nm and could not detect any supermodulus effect although a considerable modulus enhancement had been found in these films when the bulge test technique had been used by Yang et al. Moreover, an apparent 500% enhancement in elastic modulus for 1.47nm Cu/Pb foil in a bulge test was reduced to 12% using an initial height (h_o) correction to produce a linear elastic response to 0.10% offset strain [187].

The elastic modulus values for single homogeneous coatings determined by different techniques are in good conformity but it is clear from the foregoing that widely divergent values have been found for composition modulated films. Moreover, from the analysis of the bulge test, using an initial height correction shows that modulus enhancement could exist in metallic multilayers but not to the degree reported without such correction. As a result of such a controversy about the extent of the modulus variations, it is nowadays agreed to be much lower than was originally reported. As a result, considerable effort has been made to improve elastic modulus measurement techniques in thin films such as: ultrasonic wavespeed techniques [125,192,187].
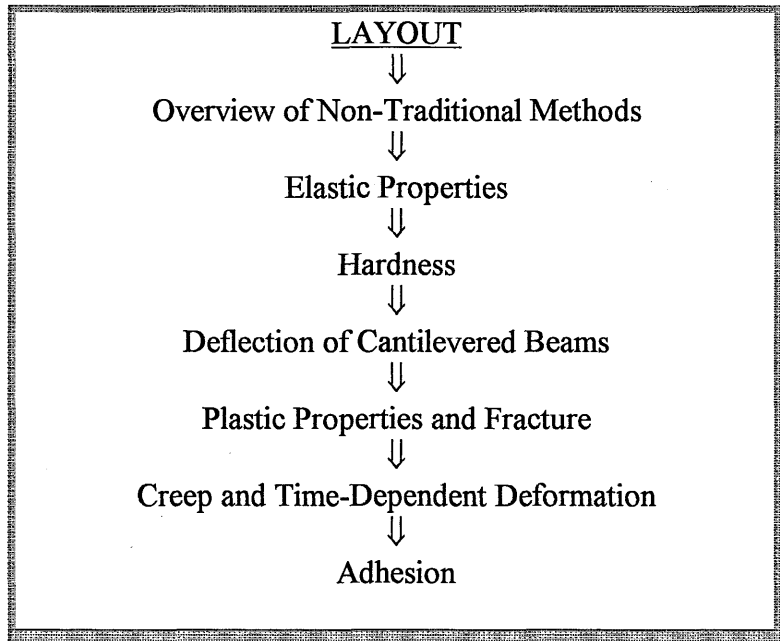
Several theories have been proposed to explain the supermodulus effect based on the effects of coherency strain or based on a high density of interfaces or based on electronic effects caused by the superlattice periodicity. As the latter have not been observed, it is doubtful that the electronic behaviour affects the elastic properties. Moreover, computer simulations suggest that modulus variations occur in films where the misfit strain is accommodated by interfacial dislocations rather than by coherency

strains, so the coherency strain may have some effect in the elastic modulus of certain systems. The computer simulation has also confirmed that elastic property variations in multilayer thin films could result from the high density of interfaces. This can be explained by the intrinsic interface stress associated with any interfaces that can produce elastic strains of the order of 1% in multilayer films. These strains were predicted to be inversely proportional to the bilayer repeat length. Such elastic strains are large enough to produce elastic order effects that could be responsible for modulus variation depending on the sign of the interface stress [191,192].

Köhler [189] in 1970 proposed that when two materials with significantly different shear modulus are used as ultrathin layer materials in a laminated composite, the strength of this composite material could be over the rule of mixtures, due to the forces of opposite sign inhibiting dislocation formation and mobility. This theory was able to be confirmed only after the development of low load indentation methods. For example, the microhardness of TiN/VN(100) superlattice thin films as a function of superlattice period (λ) shows significant enhancements above the microhardness of both layer materials with the hardness reaching a maximum value, at a superlattice period of about 5nm ($\cong$5500HV). Fe(001)/Pt(001) multilayer films show hardness above that expected from a rule of mixtures by a factor of approximately 2.5 in the composition wavelength range of 2-10nm. These results for microhardness can be explained by Köhler theory and the high density of interface characteristics of these materials [191,192,193,195]. Recent models based on XRD techniques provide strength/hardness predictions of superlattice structure. These models predicted that the hardness is dependent on the interface width [194].

Cu/Ni multilayered films have shown an uncommonly large damping capacity up to an order of magnitude larger than that of bulk metals using resonant frequency techniques on small samples. This effect may result from energy dissociation mechanisms associated with grain boundaries and interfaces. This study suggests that more research should be done in this area, i.e. damping properties of multilayer films [192]. To sum up the multilayer coating design is able to provide several properties for the same component, such as: running-in, wear resistance, damping and adhesion to the substrate for piston rings of internal combustion engines [180]. Other sliding wear applications could also benefit from these combined properties achieved by using multilayer coatings.

1.5.3. MECHANICAL PROPERTIES OF THIN FILMS BY NON-TRADITIONAL METHODS

<div style="border:1px solid">

LAYOUT
⇓
Overview of Non-Traditional Methods
⇓
Elastic Properties
⇓
Hardness
⇓
Deflection of Cantilevered Beams
⇓
Plastic Properties and Fracture
⇓
Creep and Time-Dependent Deformation
⇓
Adhesion

</div>

Traditional techniques such as microhardness are not able to evaluate mechanical properties in the submicron range with layers of less than 5μm. Several attempts have been made in the last decade to overcome this situation by developing so-called non-traditional techniques.

Li and Wu [127] have developed microindentation equipment that allows the displacement of the indenter into the material to be imposed and measurement of the load. Such equipment is suitable for measuring stress relaxation by indentation.

Yu et al [127] have studied the mechanical properties by impression tests. This technique is based on the projected contact area, which does not change as the indenter is pushed into the material. The indenter is flat ended with the shape of a right circular cylinder.

Nishiboni and Kinosita [196] have developed a Vickers type ultra-microhardness tester for thin films. The penetration depth under a given load can be determined to ±10nm (100Å).

In the last few years, such depth-sensing instruments have become available for continuously measuring force and displacement during indentation. Such instruments are called nanoindentors and they allow mechanical properties of thin films to be determined. It has become the most popular technique used in this area [127,197].

The basis for the nanoindentation technique consists of driving a hard indenter into the specimen. As the load is increased, the material deforms first elastically and then plastically. The elastic deformation is recovered during the unloading process. When the test begins, the contact area is very small and there is no distinction between elastic and

plastic displacement. However, as the indenter is driven into and withdrawn from the specimen, the contact area is changing continuously. During the indentation process a load-displacement curve provides information about several properties of the film including: hardness, elastic, plastic and creep properties [125,198].

The nanoindenter equipment usually applies the load either by an electromagnetic coil or by a piezoelectric device. In the former case the load is determined from the current that flows in the coil, while in the latter case a load cell is required and a capacitive sensor measures the displacement. The force and displacement resolutions are in the range of 10nN and 0.1nm respectively, for some instruments[125,198,199].

Nanoindentation experiments are performed with either a Berkovitch three-sided pyramidal indenter or a four-sided Vickers indenter or spherical indenters. The most commonly used and suitable indenter shape for small contact areas are the Berkovitch indenters, which have three non-parallel planes intercepting at a single point. They have the same depth-to-area relation as the standard Vickers square pyramid indenters. This means that the cross-section area varies as the square of the depth of the indenter. The Vickers indenter is more resistant to damage under load. The spherical indenters allow a more uniform stress distribution and the elastic/plastic transition is better defined but is more difficult to manufacture reliably [125,127,198,199,200].

The nanoindenter tests allow mechanical properties to be measured and quantified in different ways, such as: by standard indentation, by deflection of cantilevered microbeams or membranes, by scratch tests or by pin-on-disk wear tests. Surface topography can also be measured in the same instrument.

Topographical information has become more important in recent years for the characterization of surface deformation in and around the indentation area. Various methods have been proposed including: SEM, TEM, STM/SFM with scanning probe. The latter technique is able to measure qualitatively interfacial effects such as: material pile-up around indentation with three dimensional images, to allow correlation between hardness and imprint size [199].

A further development of the nanoindentation method permits an analysis at extremely low loads and shallow depths. This technique adds to a DC load AC modulation of about 10^{-8}N at a frequency of 60-70Hz. The signal from the capacitance transducer results from displacements as small as 0.1nm which are measured with a lock-in amplifier. This technique also minimises the thermal drift effect during indentation[125,201]. The ultra-low load indentation minimises the contribution of the substrate material to be incorporated in the film properties measurements [203].

The main advantages of nanoindentation which make this technique so popular and widespread are illustrated in figure 1.64 [125,183,199,198,127,202,203] The same figure also points out some drawbacks of the nanoindentation technique [125,127]. These are general observations and work on the way to overcome the many disadvantages.
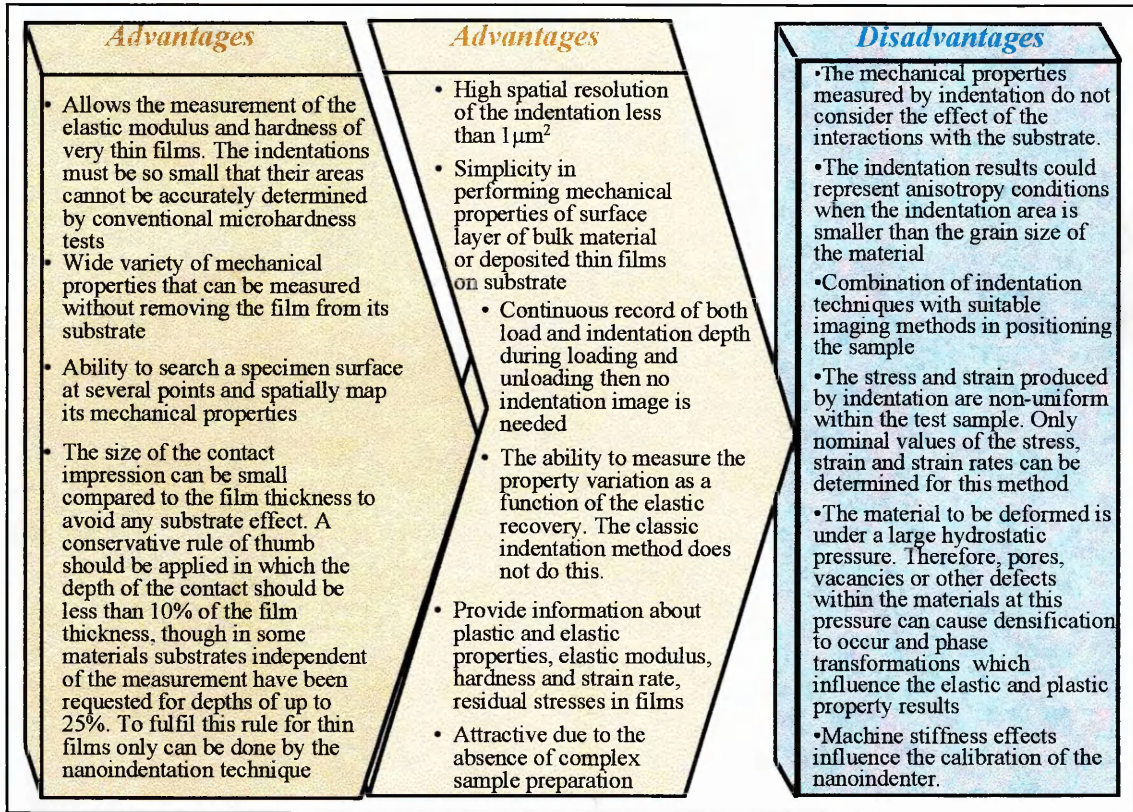
Advantages	Advantages	Disadvantages

Advantages

- Allows the measurement of the elastic modulus and hardness of very thin films. The indentations must be so small that their areas cannot be accurately determined by conventional microhardness tests
- Wide variety of mechanical properties that can be measured without removing the film from its substrate
- Ability to search a specimen surface at several points and spatially map its mechanical properties
- The size of the contact impression can be small compared to the film thickness to avoid any substrate effect. A conservative rule of thumb should be applied in which the depth of the contact should be less than 10% of the film thickness, though in some materials substrates independent of the measurement have been requested for depths of up to 25%. To fulfil this rule for thin films only can be done by the nanoindentation technique

Advantages

- High spatial resolution of the indentation less than $1\,\mu m^2$
- Simplicity in performing mechanical properties of surface layer of bulk material or deposited thin films on substrate
  - Continuous record of both load and indentation depth during loading and unloading then no indentation image is needed
  - The ability to measure the property variation as a function of the elastic recovery. The classic indentation method does not do this.
- Provide information about plastic and elastic properties, elastic modulus, hardness and strain rate, residual stresses in films
- Attractive due to the absence of complex sample preparation

Disadvantages

- The mechanical properties measured by indentation do not consider the effect of the interactions with the substrate.
- The indentation results could represent anisotropy conditions when the indentation area is smaller than the grain size of the material
- Combination of indentation techniques with suitable imaging methods in positioning the sample
- The stress and strain produced by indentation are non-uniform within the test sample. Only nominal values of the stress, strain and strain rates can be determined for this method
- The material to be deformed is under a large hydrostatic pressure. Therefore, pores, vacancies or other defects within the materials at this pressure can cause densification to occur and phase transformations which influence the elastic and plastic property results
- Machine stiffness effects influence the calibration of the nanoindenter.

Figure 1.64. Nanoindentation technique advantages and disadvantages.

The nanoindentation technique has proved effective in the mechanical properties study of several materials such as: optical coatings, hard coatings and materials with surfaces modified by ion implantation and laser treatment.

I. ELASTIC PROPERTIES

The elastic and plastic deformation that occurs during indentation is shown in the load versus displacement curve in figure 1.65. The slope of the loading curve increases with depth of the indentation because the contact area increases during indentation so it is not possible to determine the elastic modulus from this curve. However, this is possible from the unloading curve if the contact area and the elastic properties of the indenter are known [125,127].

Tabor [125,197] showed that the shape of the unloading curve and the recovery deformation can be related to the elastic modulus and the size of the contact area. As the indenter is not perfectly rigid, an effective modulus (E_r) can be calculated from the slope (S) of the unloading curve and defined by [125,197,198]:

$$\frac{1}{E_r} = \frac{\left(1 - \upsilon^2\right)}{E} + \frac{\left(1 - \upsilon_i^2\right)}{E_i} \tag{1.19}$$

$$S = \frac{dP}{dh} = \frac{2}{\sqrt{\pi}} \beta \sqrt{A} E_r \tag{1.20}$$

Where E and υ are the elastic modulus and Poisson ratio of the material

E$_i$ and υ_i are the elastic modulus and Poisson ratio of the indenter

P is the applying load

h is the indentation depth

A is the contact area of the indenter

β is a dimensionless parameter that depends on the geometry of the indenter
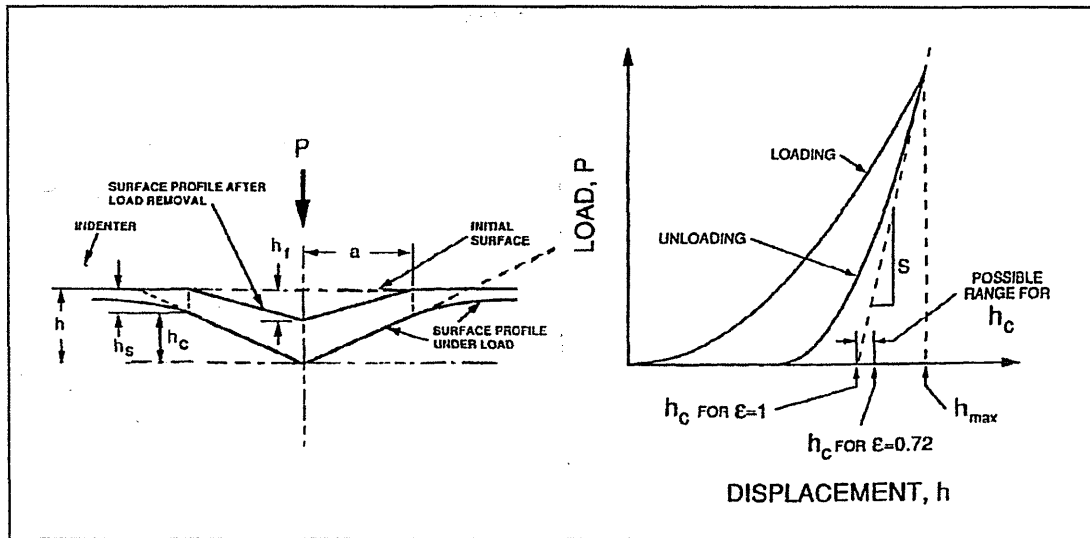
Figure 1.65. Scheme of a section through an indentation on left hand side and the load versus indenter displacement on the right hand side [197].

The indenter shape effect is more pronounced for deposited films on substrate[205]. R.B. King [124,125,127] showed that the value of β varies slightly for different indenter shapes such as:

♦ Circular symmetry β=1.000

♦ Triangular symmetry β=1.034

♦ Square symmetry β=1.012

The non-linearity of any unloading curve indicates a decrease in the contact area. On the other hand, the slope of the unloading curve and the projected contact area at the maximum load must be known for the calculation of hardness and Young's modulus values.

The contact area could be obtained from an area function of the cross-section of the indentation depth F(h) measured from the tip of the indenter. Such an area function for an ideal sharp Berkovitch indenter is F(h)=24.5h^2 but it is difficult to achieve an ideal tip sharpness.

Several models have been proposed for the determination of the depth of the indentation for a given area function [125,197,205]. Doerner and Nix proposed a simple linear extrapolation of the linear region of the unloading curve at maximum load. This model needs to remove elastic deformation from the measured displacement due to machine compliance due to machine compliance.

131

Oliver and Pharr [125,197,206] suggested that the unloading curve should be expressed by a power law because the unloading curve is often non-linear in the initial stage. This model also suggests a fitting tangent to a power law fit to determine the slope of the unloading curve. The question is: "Which portion of the unloading curve should be fitted since at low loads there are uncertainties associated with loss of contact and at high loads there may be time dependent effects such as creep". The power law of the unloading curve is given by:

$$P = \alpha\left(h - h_f\right)^n \tag{1.21}$$

Where h is the elastic displacement of the indenter
α, h_f and n are constants to be determined by least square fitting procedure
n usually ranges from 1.2 to 1.6

Oliver and Pharr also suggested that the contact area at peak load should be calculated by the contact depth h_c given by:

$$h_c = h_{max.} - \varepsilon\left(\frac{P_{max.}}{dP/dh}\right) \tag{1.22}$$

The value of ε depends on indentation geometry such as:

♦ ε=1.00 for flat punch

♦ ε=0.75 for a paraboloid of revolution

♦ ε=0.72 for a conical indenter

A scheme of the cross-section through an indentation is given in figure 1.65. At peak load, the load and displacement are $P_{máx}$ and $h_{máx}$. The final depth of residual hardness impression (h_f) is observed when the indenter is withdrawn. Experimental work suggested that ε is independent of the specimen material and the unloading curve is close to the parabolic geometry so ε=0.75. Consequently, the contact area can be calculated from the area function as A=F(h_c).

Another parameter that should be taken into account is the compliance of the system, mainly for large indentations. Any elastic deformation of the instrument at a particular load must be subtracted from the apparent diamond displacement at that load. There are several factors which influence the instrument compliance including the specimen and diamond mounting adhesives. The equipment frame and the indentation can be designed as two springs in series $C=C_f+C_s$, where C is the total compliance, C_f is the frame compliance and C_s is the specimen compliance. The total compliance is the inverse of contact stiffness. The specimen compliance and the total compliance are given by [156].

$$C_s = \left(\frac{\sqrt{\pi}}{2E_r\sqrt{A_c}}\right) \tag{1.23}$$

$$C = C_f + \left(\frac{\sqrt{\pi}}{2E_r \sqrt{A_c}} \right) \qquad (1.24)$$

Where E_r is calculated from equation 1.19, considering the elastic modulus of the diamond indenter 1141GPa and the Poisson's ratio 0.07. The plot of C versus $\left(\frac{1}{\sqrt{A_c}} \right)$ is linear for E_r constant and intersects the compliance axis at the frame compliance C_f. The most suitable value for C_f is achieved when C_s is very small, i.e. for large stiff indentations [156]. The contact area at different contact depths can be calculated by:

$$A = \frac{\pi}{4E_r^2 (C - C_f)^2} \qquad (1.25)$$

The area function for the Berkovitch indenter as a deviation from the ideal geometry can be given as $A(h_c) = 24.5h_c^2 + C_1 h_c^1 + C_2 h_c^{1/2} + C_3 h_c^{1/4} + \ldots + C_8 h_c^{1/128}$. Two procedures have been developed for the determination of the area function. These procedures include a series of indentations in a calibrated material over a range of indentation sizes. The first method uses a soft calibrant metal. Both the indentation sizes measured by TEM replication and the indentation load-displacement data establish the area function. The second method indents a material with well-known isotropic elastic properties such as quartz and the area function is inferred from the load-displacement data by assuming the elastic constants are independent of the depth. This method does not require any other equipment [198,206].

The total compliance is determined from the unloading slope. Two methods are referred to in the literature. In one method a linear extrapolation of the upper portion of the unloading curve was proposed by Doerner and Nix. In the other method the tangent at maximum load to a power law fit of the unloading curve was proposed by Oliver and Pharr. Using Al as a calibrant material has given rise to considerable scatter in results, so it is advisable to use fused silica or tungsten [156].

To summarise, the key parameters for the determination of hardness and elastic modulus are: the peak load ($P_{máx}$), the displacement at peak load ($h_{máx}$), the load frame compliance, the area function of the diamond, the unloading contact stiffness [197,198].

The uncertainties in the calibration of load (δ_p) and displacement (δ_h) measurement of the area function (δ_{Ac}) of the indenter and determination of the frame compliance (δ_{Cf}) produces uncertainties in the hardness and modulus measurement. The effect of uncertainties in individual parameters can be calculated analytically. Consequently, the total uncertainty of the measurement (δ_{total}) can then be estimated by:

$$\delta_{total} = \sqrt{\delta_p^2 + \delta_h^2 + \delta_{Cf}^2 + \delta_{Ac}^2} \qquad (1.26)$$

Assuming the uncertainty in frame compliance is independent of other measurement uncertainties, because it is doubtful if it is due to uncertainties in the

measured load and displacement, then measurement uncertainly tended to increase when the load decreases, mainly for hard and stiff materials [206].

For indentation depths of about 10-25% of the film thickness the substrate may affect the hardness and modulus measurement of the film. In this case the following equation takes into account the substrate effect [198].

$$S = \left(\beta E_r \sqrt{A}\right) \frac{\left[\left(1 - \upsilon_s^2\right)\Big/ E_s\right] + \left[\left(1 - \upsilon_i^2\right)\Big/ E_i\right]}{\left[\dfrac{\left(1 - \upsilon_f^2\right)}{E_f\left(1 - e^{-\alpha t_s/\sqrt{A}}\right)}\right] + \left[\dfrac{\left(1 - \upsilon_s^2\right)}{E_s e^{-\alpha t_f/\sqrt{A}}}\right] + \left[\dfrac{\left(1 - \upsilon_i^2\right)}{E_i}\right]} \tag{1.27}$$

Where S is the stiffness of the unloading curve

A is the contact area

E_f is the elastic modulus of the film

t_f is the film thickness

E_s and υ_s are the elastic constants of the substrate

E_i and υ_i are the elastic constants of the indenter

υ_f is the Poisson's ratio of the film

β is constant, dependent of the geometry of indenter

α is constant, dependent on the geometry of the indenter and the size parameter $\left(\sqrt{A}\Big/ h_f\right)$

II. HARDNESS

The nanoindentation microhardness is a measure of resistance to local deformation [125] or the mean pressure that the material will support under load [198] and can be given by the ratio:

$$H = \frac{P_{max}}{A(h_c)} \tag{1.28}$$

Where P_{max} is the peak load applied to a given indenter

$A(h_c)$ is the project area of contact at peak load based on the Oliver and Pharr model

The conventional hardness is based on the area left by the indentation and may be less than the area at peak load produced by the nanoindenter. This is because some materials may not fully deform plastically under the contact area load, thus elastic recovery may occur on unloading [125,198].

To overcome the substrate effect in very thin films extremely shallow indentation techniques have been developed as mentioned before. The effect of the substrate on the measurement of hardness has been treated by finite element simulation with limited success [198]. Also, it is possible that pressure under the indenter can induce phase transformations during the test. Such transformations would affect the load-

displacement curves and so the hardness and modulus measurement [125]. The indentation response of the coated system may be affected by the mechanical properties of the substrate, different residual stress states and the microstructure of the coating and the nature of the coating/substrate interface [207].

III. DEFLECTION OF CANTILEVERED BEAMS

A nanoindenter tester can be used to apply the load to a free-standing cantilevered microbeam to measure the associated deflection as shown in figure 1.66. The beams are prepared either by lithographic patterning and anisotropic etching or by chemical micromachining techniques. The elastic modulus, yield strength and residual stress of the films are determined from the load-deflection curve [125,127,160,198,208,209,210].
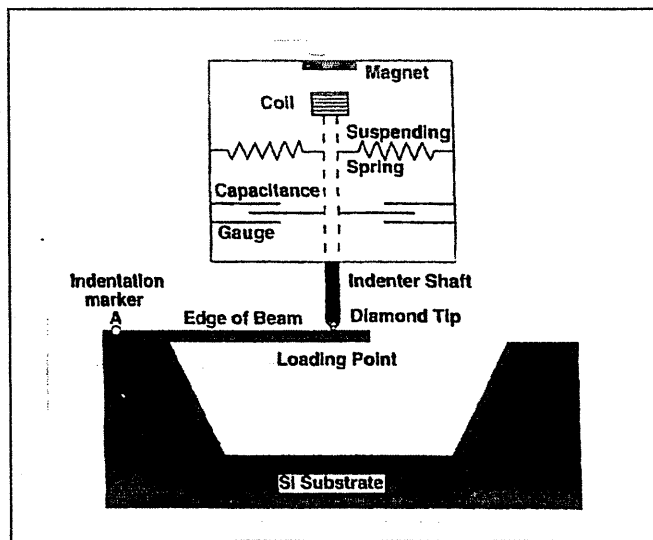
Figure 1.66. Loading device on microcantilever beam [210].

When the beam is bent in a cantilever device, one side of a longitudinal neutral plane is strained in tension while the other side of the plane is strained in compression. As the main deformation occurs at the fixed side of the beam, then the pressure under the indenter should not be important [127]. The beam deflection under a load P applied to the free end of the beam of length L, width b, thickness h_f, Poisson's ratio υ and b>>L is given by:

$$\delta = \frac{4\left(1-\upsilon^2\right)PL^3}{bEh_f^2} \qquad (1.29)$$

The Young's modulus is deduced from the slope of δ versus P. The yield strength and the strain hardening properties of the beam can be found by calculating the stresses in the beam during non-elastic bending from the same curve [127,125,198].

Some uncertainties associated with geometry and deformation in the model should be pointed out in order to make additional corrections including [127,125,198]:

♦ Beam geometry data, mainly thickness of the film are very important
♦ Angle between beam and supporting walls

♦ Undercutting or insufficient etching at the beam support
♦ Compliance of the system, mainly the spring constant
♦ Non-linearity of the load-deflection curve at large deflection
♦ Sideways bucking of the beam due to the use of a sharp indenter
♦ Shear stress at high thickness/length ratio
♦ Penetration of the pointed indenter into the beam material
♦ Slippage between the indenter and the beam

This technique is useful for the determination of elastic and plastic properties of thin films and the results obtained show a good agreement in the literature. The main disadvantages are the difficulty in preparing samples, precision of geometric measurement and the use of free-standing specimens [198].

IV. PLASTIC PROPERTIES AND FRACTURE

Tabor [125] related the ultimate tensile strength (σ_{ut}) to a Vickers hardness for materials with work hardening exponent (n) given by:

$$\frac{\delta_{UT}}{HV} = \left(\frac{1-n}{2.9}\right) \times \left(\frac{12.5n}{1-n}\right)^{n} \tag{1.30}$$

Bell et al [125] produced stress-strain curves for 1μm thick gold and Al-Cu deposited onto Si by indentation measurements with a spherical diamond indenter. The stress was proposed to be related exponentially to the strain, $\sigma \propto \varepsilon^{n}$, and n is related to the Meyer index by m=n+2.

The fracture toughness is a measure of the resistance of a material to withstand crack propagation. In most brittle materials such as ceramics these are visible radial cracks from the indentation. The length of these cracks can be connected with the fracture toughness. Lawn et al [125], using the expanding cavity concept of Yoffe, determined the fracture toughness by indentation given by:

$$K_{cr} = \alpha \left(\frac{E}{H}\right)^{1/2} \times \left(\frac{P}{c^{3/2}}\right) \tag{1.31}$$

Where E is the young's modulus,
H is the hardness,
P is the load on the indenter
c is the crack length
α is a constant dependent on the geometry of the indenter

Pharr et al [125] by replacing the Berkovitch indenter with a cubic-corner indenter made the threshold load for the crack formation, found by Lawn, lower and were then able to produce meaningful results for the fracture toughness for ceramics by this nanoindentation method.

136

V. CREEP AND TIME-DEPENDENT DEFORMATION

The nanoindentation methods allow the displacement of the indenter under a given load to be monitored as a function of time and thus evaluation of indentation creep is possible [211]. However, the creep effect evaluated by nanoindentation is more complex compared to classic methods [125,198,212].

As the rate of indenter movement can be measured, so it is also possible to correlate the effect of strain rate on deformation. The stress and strain associated with indentation are non-uniform, as the strain-rate varies with radial distance from the contact point, hence only nominal values can be calculated for the stress and strain rate effects, but such strain rate effects and normal loading conditions have minimal effect[127,198]. The change in load at a fixed depth of penetration allows the stress relaxation to be evaluated [125]. The time-dependent properties can also be evaluated using contact loading rate tests, load rate change tests and load relaxation tests [198].

VI. ADHESION

The net hardness of a composite coating/substrate system is a complex function of thickness of the coating, hardness of the coating and of the substrate. The adhesion between coating and substrate is also important. The nanoindentation method may be able to help in the determination, either qualitative or quantitative, of these parameters[214].

The hardness measurement can be used to provide a qualitative analysis of film adhesion. For example, if the adhesion of a soft film to a hard substrate is poor, the resulting hardness decreases because the constraint is lower [198,206].

A more quantitative measure of thin film adhesion to substrate can be achieved by a scratch test where the load-displacement curve allows the critical load for film detachment to be determined. Scratch testing consists of moving a spherical stylus across the film surface under constant or increasing load until interfacial failure occurs. This gives a critical value when the film is unable to follow the elastic-plastic deformation of the substrate. Loads for adhesion show abrupt changes at failure. Scratch testing results depend strongly on the elastic and plastic properties of the film and substrate and the interface properties [198,205].

If a polished cross-section is indented by a Vickers indender at the interface of the composite, the adhesion behaviour can be determined qualitatively from measurements of the film and substrate hardness, their elastic modulus and from the interfacial crack length [215]. B.Fabes and W. Oliver developed a qualitative model for the composite hardness of a soft film on a hard substrate, the aim of which is understanding the factors such as: coating hardness, substrate hardness and interfacial bonding on the mechanical properties of the composite. The indentation process through the substrate was divided into three stages: plastic zone confined to coating, interaction of the plastic zone with the substrate and penetration of the indenter into the substrate. From an understanding of the interfacial bonding information about film adhesion can be deduced[216].

EXPERIMENTAL PROCEDURE

2. EXPERIMENTAL PROCEDURE

2.1. MULTI-TARGET SPUTTERING SYSTEM

```
                    LAYOUT
                      ⇓
       Overview of Multi-Target Sputtering System
                      ⇓
               Vacuum Chamber
                      ⇓
               Vacuum System
```
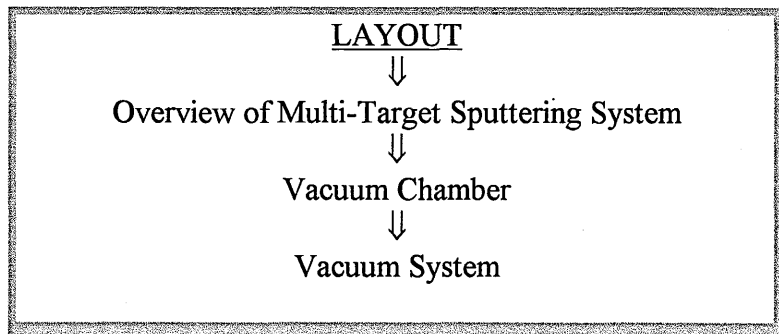
A description of the multi-target sputtering system used in this project will be given. This sputtering system consists of a pumping station, a vacuum chamber with a rotating work table, three planar magnetron targets, an RF generator with bi-RF-switch and two manually operated matching networks as in sketch in the figure 2.1.

Vacuum Chamber

1-Rotating table
2-Three substrate holders
3-Three target ports
4-Baffle plate
5-Pumping system
6-Ar MFC
7-Two matching networks
8-RF generator

Sputtering Apparatus

1-Vacuum chamber
2-Chevron baffle
3-Diffusion pump
4-Rotary pump
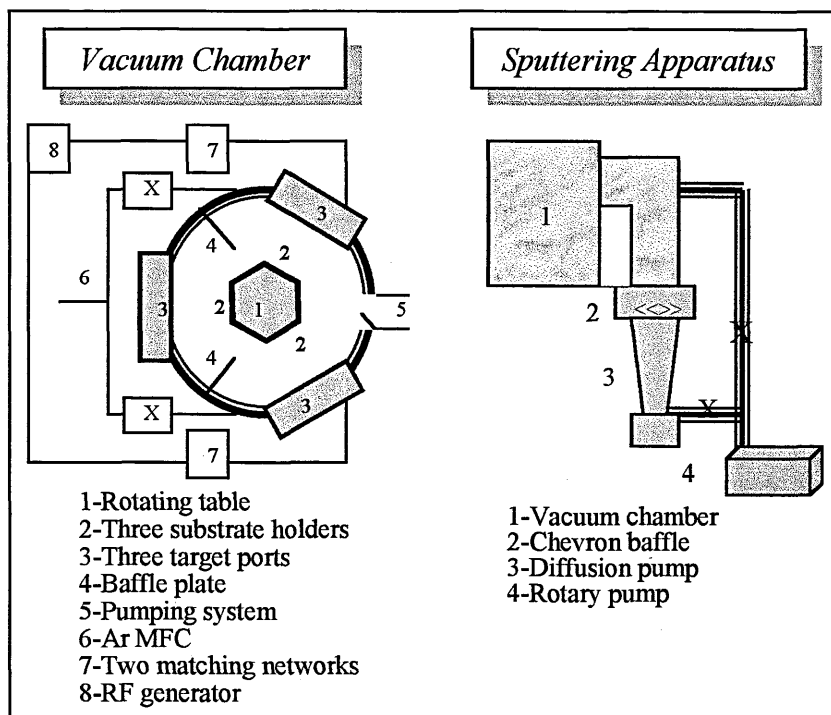
Figure 2.1. Sketch of Vacuum Chamber and Sputtering Apparatus [109].

The vacuum chamber is stainless steel, double walled with water-cooling facilities. It has eighteen apertures: three small viewing ports, a pressure gauge port, three target ports, the substrate holder port, two gas inlet ports, the pumping port, five entry facilities, the air admittance port and a motor drive port.

A three faced rotating substrate holder work table is used on which the substrates are clamped (100mm×130mm). The specimens are held using small stainless

steel screws and washers in an arrangement shown in figure 2.2 which also shows the target being bonded to a backing plate.

The system has been equipped with three conventional rectangular magnetron cathodes (100mm×200mm) placed around the chamber wall in a triangular arrangement. However, only two cathodes were used in this research. The third position was used either for loading the chamber or for protecting the substrates during sputter cleaning of the target. In the chamber the targets are separated by baffle plates in order to avoid cross contamination during deposition. A water cooling system is used to avoid cracking of the target due to temperature differences, as previously described in chapter 1.4.2.
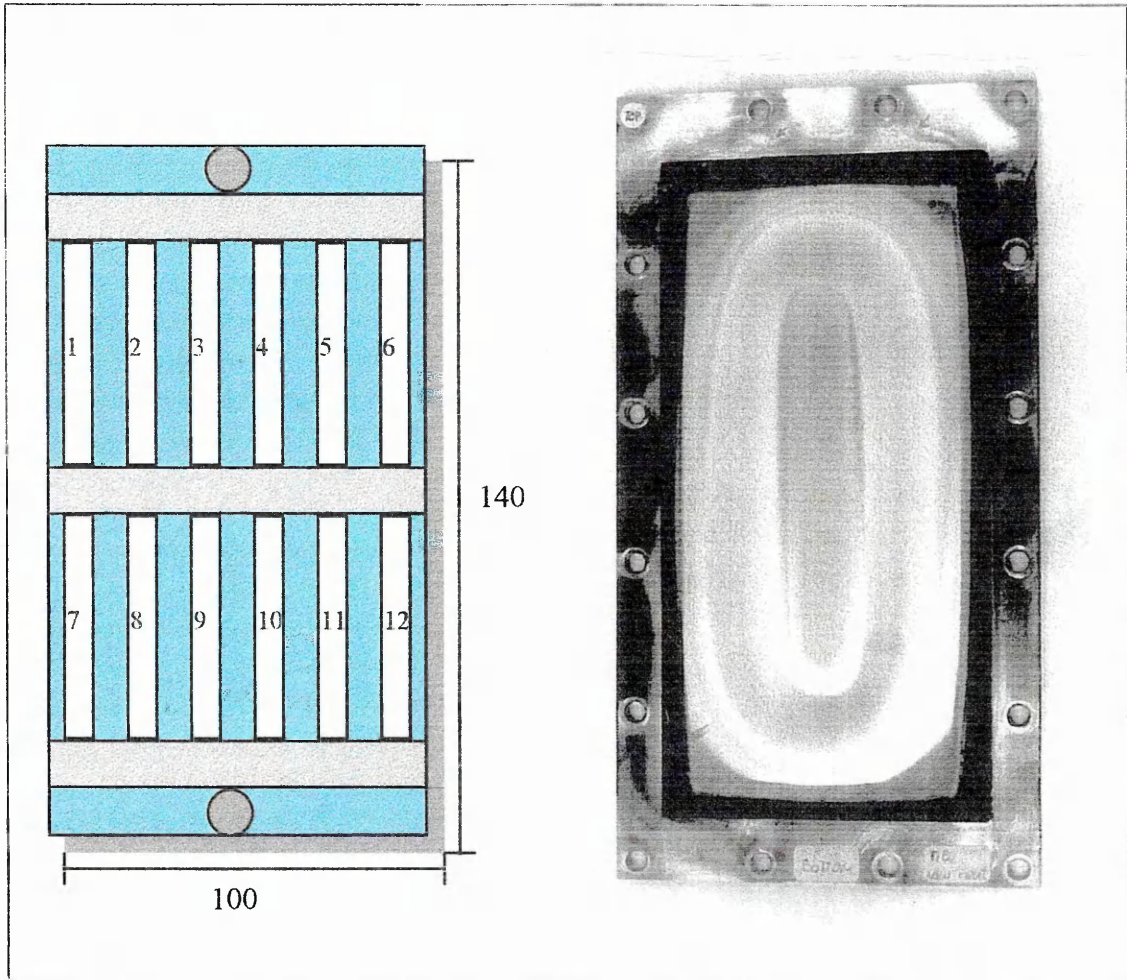
Figure 2.2. Substrate holder with samples on the left and sputtering target on the right.

The distance between each target surface and the work table is approximately 70mm. Each cathode is connected, through a commercial matching network unit, to an individual 1KWRF generator working at a frequency of 13.56MHz. A voltage meter is also connected to the output of the matching network to monitor each cathode's potential. During the deposition, target, substrate, chamber and plasma conditions can be changed and the matching network can be used to make the necessary adjustments.

The vacuum pressure inside the chamber is measured by traditional vacuum devices. A Pirani gauge manufactured by Edwards Ltd. Ref.M6A can measure the soft

139

vacuum down to 0.1Pa (10^{-3}Torr). Technical information of the Pirani gauge is in references [74,75,98,143,144]. The Penning gauge is manufactured by Edwards Ltd. Ref.D145-33-000 and it is used to measure the high vacuum down to 1.3×10^{-5}Pa (10^{-7}Torr). Technical information can be found in reference [74,143]. A Baratron gauge with a low-impedance capacitance manometer type absolute vacuum gauge is used to monitor the total pressure during the deposition. It gives a highly accurate value of the pressure at different stages of the sputtering process [143].

The flow of the working gas is controlled and regulated by Tylan Mass Flow Controllers (MFC). To remove possible oxygen and mist contamination, the gas is gettered by passing through titanium chips in an electrically heated oven at 700°C before being introduced into the MFC. A getter is a highly reactive substance which reacts with the molecules to remove and trap them in a solid phase. If the oven is overheating, the titanium chips could melt and cause pressure fluctuations and promote coating oxidation. If the oven is underheating, the contaminant gas can be injected into the chamber.

The deposition pressure depends on the degree of pumping, the throttling conditions and the amount of gas bled into the system. The total pressure is set by using a variable degree throttling operation after fixing the flow of argon. This procedure avoids the influence of the efficiency of the pumping station on deposition and it is the best way to guarantee a constant total pressure. The efficiency of the pumping station may decrease due to natural wear and tear. Moreover, the effect of oil changing, temperature of the cooling water, or a change in the pumping station will not be noticed as the constant gas flow will be guaranteed with this operating technique. The gases used are fed by means of stainless steel piping.

The pumping station consists of an Edwards Ref. ISC4-50R rotary pump and an Edwards Ref. E603 diffusion pump. These pumps are isolated from the vacuum chamber by an Edwards Ref. QSB6 butterfly valve which can be water cooled to prevent oil vapour entering into the chamber. A schematic cross-section of a rotary pump and difusion pump is illustrated in figure 2.3.

The Rotary pump is a mechanical pump that runs immersed in oil and it produces pressures down 1 to 0.1Pa (10^{-2} to 10^{-3}mbar). During operation the gases enter from the work chamber into the volume created by the eccentric mounting of the rotor in the stator. The blade mounted in the rotor moves the gas volume so then it can be trapped and compressed just above one atmosphere and forces the exhaust valve open for discharging the gas. The pressure in the network linked to the rotary pump is measured by a Pirani gauge [75,143,74].

The diffusion pump is one of the most widely used pumps for obtaining high vacuum owing to its high pumping speed for all gases and low cost per unit pumping speed and it can also produce pressures about 10^{-8}Pa (10^{-10}mbar). The diffusion pump cannot exhaust gas directly to the atmosphere and so requires a backing pump, often a rotary pump, to be operated continuously in series with it.

These pumps start to operate with the inlet closed by a valve, then a rotary pump is switched on and left running for exhausting inside the diffusion pump at least to 10Pa (0.1mbar) pressure. The water supply is turned on. The oil placed in the pump base

(where there is a heater) begins to boil and evaporate within 20 minutes. The oil vapour flows up through the jet chimneys and emerges from the jet nozzles at supersonic velocity. Then the oil molecules condense on the pump wall which is water cooled and flow back down to the boiler as an oil film, where the oil is reboiled and evaporated. Gas molecules present in the vessel above diffuse into the jet and are forced by jet action into a region of high pressure in a lower area of the pump. They will subsequently be removed from the diffusion pump by the rotary pump [74,75,217].
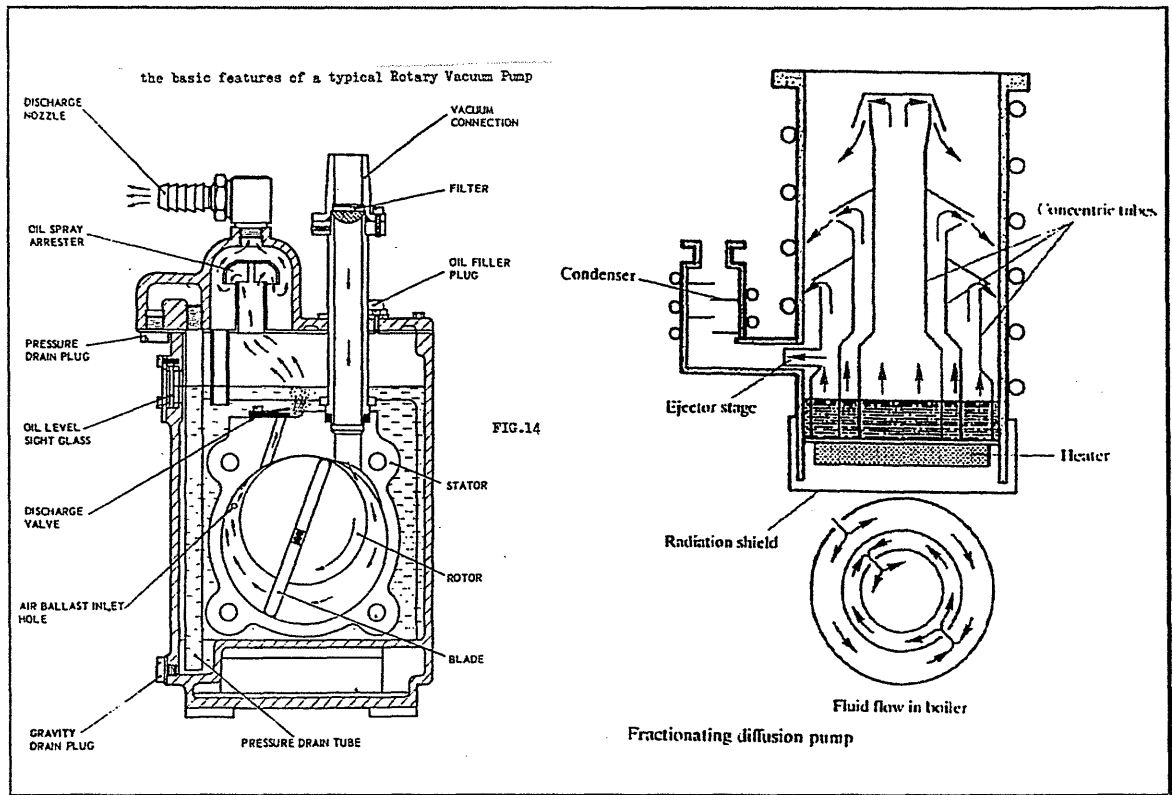
Figure 2.3. Representation of the rotary pump on left and diffusion pump on right [75].

The overall view of multi-target sputtering system is in the photograph 2.1.
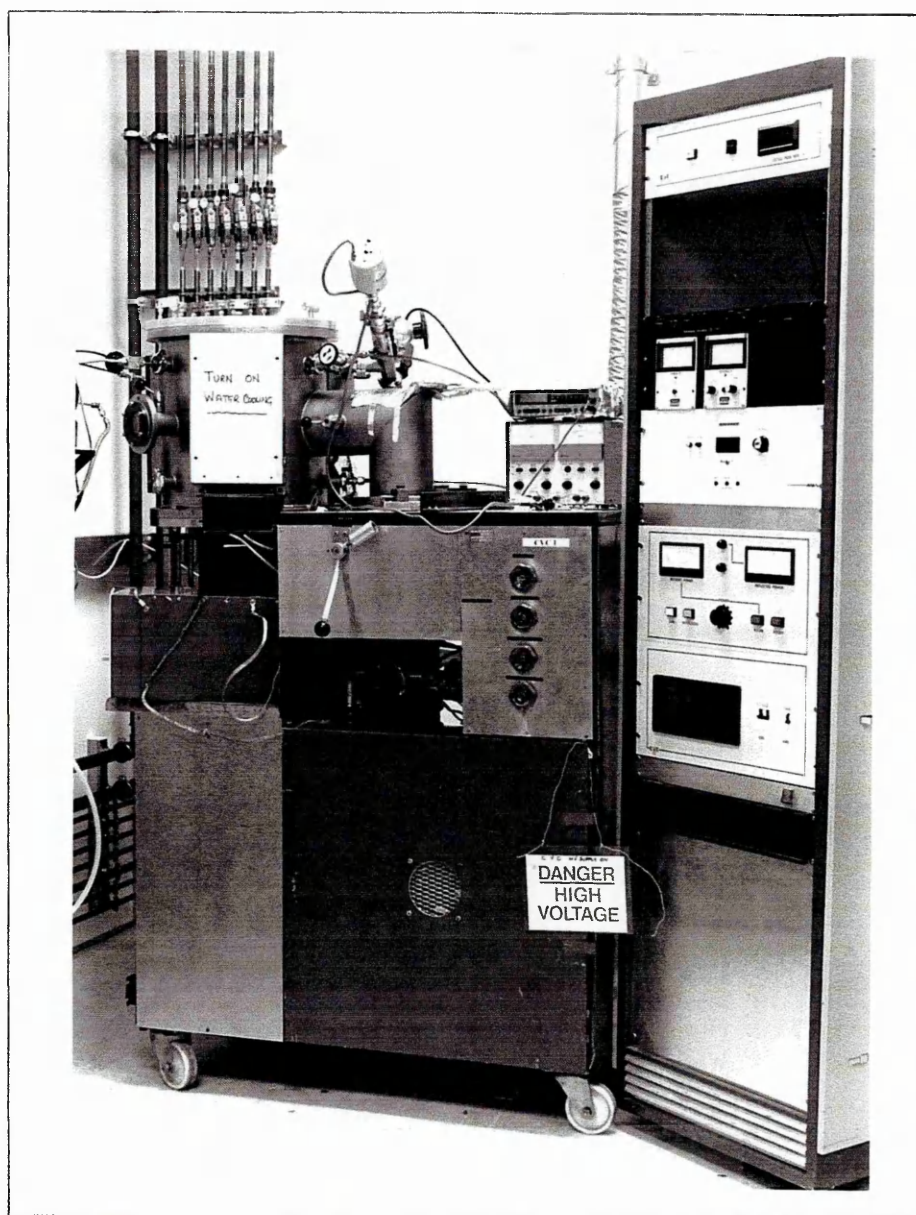
Photograph 2.1. Multi-target sputtering system.

2.2. EXPERIMENTAL SET UP

```
┌─────────────────────────────────────────────┐
│                   LAYOUT                       │
│                     ⇓                          │
│       Stages of the Deposition Procedure       │
│                     ⇓                          │
│   Main Features of the Working Gas, Specimen   │
│        Substrate and Sputtering Target         │
└─────────────────────────────────────────────┘
```
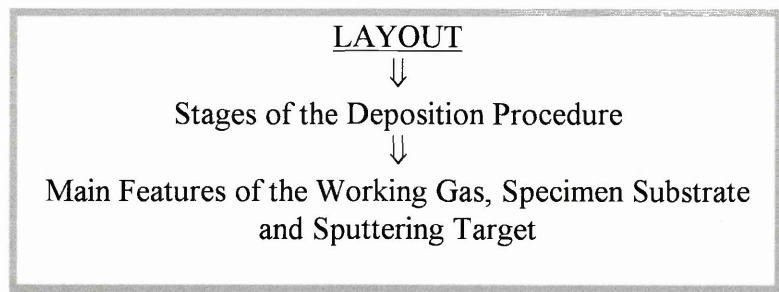
The sputter deposition procedure used in this research follows the normal routine in this kind of deposition technique with the stages shown in figure 2.4. For all the experiments the deposition procedure must always be the same. All the additional variables that may be introduced by operating in different ways must be immediately eliminated to keep the process under control.
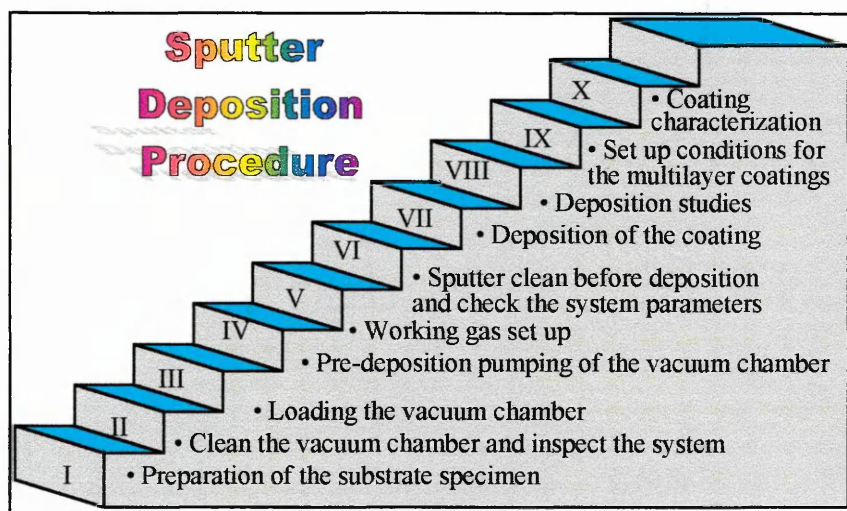
Figure 2.4. Sputter deposition procedure.

I- Preparation of the substrate specimen: The preparation of the substrate occurred sequentially in three steps:

1. Specimen polishing to 1μm diamond.
2. Ultrasonic clean in two baths: First commercial purity IPA followed by the Analar IPA (Isopropyl alcohol) baths. Each bath duration of 15 minutes.
3. Vapour degreasing clean with Analar IPA in a Soxhlet extractor heated by an evaporator Mantle.

After cleaning, all the specimens were kept in a vacuum desiccator until they were loaded into the vacuum chamber.

II-Clean the vacuum chamber and inspect the system: Clean chamber contaminations from previous runs and check the system, namely: targets, rotating table position, seals, water cooling pumping system.

III-Loading the vacuum chamber: Clamp the substrate holder onto the work table after attachment of the specimens to it. The substrate holder was made of aluminium.

IV-Pre-deposition pumping of the vacuum chamber: The vacuum chamber was pumped down continuously to reduce the outgassing flux from the chamber walls and specimens because the final pressure affects the growth and properties of the coating. The vacuum was pumped down to a final pressure of 1.3×10^{-4}Pa (10^{-6} Torr).

V-Working gas set up: The working gas was injected into the chamber for the desired flow. The pumping system was throttled with the butterfly valve, so that the required total pressure within the chamber could be sustained with the pumps operating. At this stage, the getter temperature should be at 700°C to eliminate argon contamination.

VI-Sputter clean before deposition and check the system parameters: Firstly establish the plasma at low power below the threshold value ($\cong$40WRF) for cleaning the target. No deposition will be noticed and the contaminants are removed by the pumping station. Secondly, sputter clean the substrate by applying DC bias voltage. Before starting the deposition it is advisable to make sure that no cycling of the pressure occurs in the chamber at the required value, the water cooling target system is at the required temperature and there is no sign of leakage, the plasma is stable and the voltage produced is kept constant.

VII-Deposition of the coatings: Start deposition by increasing the RF power to a required value and deposit for a given pre-set time. Multilayer coatings can be produced by alternately positioning the substrate in front of each target. Using the RF-bi-switch the plasma is not broken and the pressure is kept constant in the vacuum chamber. During deposition verify regularly the operating parameters, keep a constant control of the matching network with the RF generator and take the required parameter readings. When the deposition is ended, cool down the system for about 45 minutes in argon flow and inspect the system.

VIII-Deposition studies: The pre-selection of deposition conditions is partially determined empirically and is largely dependent of the sputtering apparatus. Preliminary single-layer coatings were produced to study the deposition conditions such as: deposition rate, sputtering power, sputtering pressure, target voltage, substrate position inside the vacuum chamber and their interrelationship.

IX-Set up of the Conditions for the Multilayer Coatings: The coating/substrate composite design is performed as metal/ceramic multilayer coatings using sequential sputtering. The two varying parameters for the multilayer coatings are the composition wavelength (λ) and the relative volume fraction of the ceramic (V_c) as illustrated in figure 2.5. They are given by the equations:

$$\lambda = t_c + t_m$$

$$V_c = \frac{t_c}{\left(t_c + t_m\right)}$$

Where t_c is the thickness of the ceramic layer
t_m is the thickness of the metal layer

144
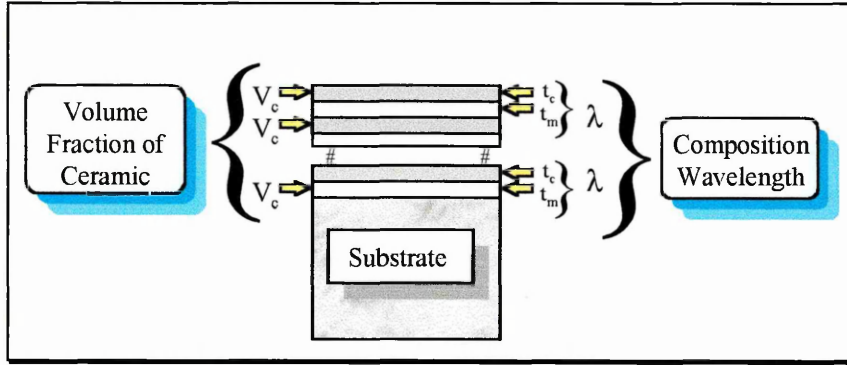
Figure 2.5. Varying parameters for multilayer coatings.

The composition wavelength defines the periodicity of the repeated multilayer structure and the thickness of the ceramic layer must be less than the critical defect size for fracture. The coatings were performed for three values of composition wavelength of 50nm, 100nm and 200nm and five values of the volume of ceramic of 0%, 25%, 50%, 75% and 100%.

The thickness of individual layers varied between 12.5nm and 150nm, for the total thickness of the coatings (t_f) of 5µm. The thickness variations of the ceramic and metal layers for each composition wavelength are described in the table 2.1.

λ (nm)	V_c (%)	t_c (nm)	t_m (nm)	t_f (μm)	$N°$ of Layers
-	100	5000	-	5	1
50	75	37.5	**12.5**	5	200
	50	25.0	25.0		
	25	**12.5**	37.5		
100	75	75	25	5	100
	50	50	50		
	25	25	75		
200	75	150	50	5	50
	50	100	100		
	25	50	150		
-	0	-	5000	5	1

Table 2.1. Thickness variations of the ceramic and metal layers for each composition wavelength.

X-Film characterization: The coatings characterization in this research consists essentially of structural characterization and mechanical properties evaluation using different techniques, as mentioned later in this chapter.

Some the main features of working gas, specimen substrates and sputtering targets used in this project will now be given:

WORKING GAS

High purity argon was used during deposition for all deposited coatings as a working gas. The purity of the argon was 99.998%.

SPECIMEN SUBSTRATES

The specimens were made of copper, aluminium and steel. The main properties of the substrate materials are summarised in table 2.2. The position of each substrate during deposition was chosen to give uniform and reproducible deposition conditions for each specimen of each substrate material. According to the arrangement in figure 2.2 the substrate positions are:

◆ Positions 1, 6, 7 and 12 were filled with copper substrates

◆ Positions 2, 5, 8, and 11 were filled with aluminium substrates

◆ Positions 3, 4, 9 and 10 were filled with steel substrates

Substrate Material	Al	Cu	Steel (AISI1095)
Length (mm)	50	50	50
Width (mm)	10	10	10
Thickness (mm)	0.25	0.20	0.20
Purity (%)	99.5	99.9	
Chemical Analysis *ppm **(%)	* Si<2500; Fe<4000 Cu<500; Mn<500 Mg<500; Zn<700 Ti<500	* Ag=500 Bi<10 Pb<50 O=500	** 0.95-1.05C 0.15-0.35Si 0.4-0.6Mn; S<0.025 0.1-0.3Cr; P<0.030
Material Condition	Temper half hard	Temper half hard	
Tensile Modulus (GPa)	70.6	129.8	206.9 (30×10⁶psi)
Thermal Conductivity (Wm⁻¹K⁻¹)	237	401	
Melting Point (°C)	660.4	1083	
Poisson's Ratio	0.345		0.293
Hardness (HV)			400-600
Tensile Strength (N.mm⁻²)			1900
Thermal Expansion Coefficient 10⁻⁶K⁻¹	23.6	17	12.1

Table 2.2. Main properties of the substrate material [213,218].

SPUTTERING TARGET

In each experiment one metal and a ceramic target were mounted in opposite positions to produce multilayer coatings. Al, NiCr, Ti and Mo metal targets were used in this project. The ceramic target was titanium diboride. The main properties of each target are given in table 2.3.

Target Material	TiB_2	Al	Ti	NiCr (Nimonic 75)	Mo
Chemical Analysis *ppm **(%)	*Co<1500 Fe<1500 Ni<1500			** 18-21Cr 0.2-0.6Ti 0.08-0.15C Si<1.0; Cu<0.5 Fe<5.0; Mn<1.0	* Al<20; Ca<20 Fe=50; K<2 Mg<20; Pb<30 Si<50; Ti<30 W=10; C=40 H=5; N<10 O<30
Purity (%)	99.5				
Dimensions	203×102×6				
Material Conditions				Annealed	Annealed
Atomic radium (nm)		0.143	0.147		0.14
Crystal Structure	HCP	FCC	HCP		BCC
Density @ 20°C (g.cm^{-3})		2.7	4.5	8.37	10.22
Melting Point (°C)		660.4	1660	1340-1380	2617
Electrical Resistivity @ 20°C ($\mu\Omega$m)		2.67	54	109	5.7
Linear Expansion Coefficient @ 0-100C ($10^{-6}K^{-1}$)		23.5	8.9		5.1
Thermal Conductivity @ 0-100°C (W.m^{-1}K^{-1})		237	21.9	11.7	138
Hardness (HV)					200
Poisson's Ratio		0.345	0.361		0.393
Bulk Modulus (GPa)		75.2	108.4		261.2
Tensile Modulus (GPa)		70.6	120.2		324.8
Tensile Strength (MPa)					485-550
Yield Strength (MPa)					415-450

Table 2.3. Main properties of target material [218].

Bonding the sputtering targets onto the backing plate is an important aspect to point out because unsuccessful bonding could involve costs and be time consuming. The debonding of targets from the backing plate when sputtering from ceramic targets like borides, nitrides or carbides is caused by the brittleness of these materials. The bonding material, therefore, has to overcome the mismatch between the different thermal expansion coefficients of the backing plate and the target. In addition, it has to be stable at elevated temperatures and at low pressures.

In sputtering, there are three different methods to fix a target to a backing plate made either of copper or austenitic stainless steel or molybdenum. These are:

♦ Clamping: this may be used for metals but not for intermetallics or even ceramic.
♦ Gluing using epoxy resin adhesives, sometimes with metallic additions to ensure a suitable electrical conductivity.
♦ Brazing using liquid metals, or diffusion bonding processes.

Gluing as well as brazing are suitable to sputter ceramic materials at least at moderate sputtering power. The literature [18] refers to a bonding technique with indium to

bond boride or nitride targets to backing plates made of copper or austenitic stainless steel for target diameter about 75, 150 and 200mm. Before bonding, the target as well as the backing plate were coated with nickel or nickel alloy, e.g. Inconel, to a thickness of about 5μm and silver with a thickness of about 2μm. Nickel is used to hinder diffusion of indium into the target, silver is used to ensure sufficient wetability for indium. Both coatings were deposited by sputtering. Indium is used as foil with a thickness of 0.5mm. Bonding is done using a simple heating plate. Care must be taken, to avoid cracking of the target during bonding, i.e., allow the system (heating plate, coated target, indium, coated backing plate, weight) about 15 minutes to reach the bonding temperature of about 250 to 355°C. Another 15 minutes at bonding temperature has been reported for diffusion processes and at least 1hour for cooling down, depending on target size. This bonding technique has been used for DC sputtering targets at power densities in the range between 2.5 to 5W/cm^2 target area (400 to 600W). The bonding quality was reported to be good enough to obtain a suitable lifetime of the target/backing plate system.

An important factor for all bonding methods is the stability of the backing plate. There should be no bending of the plate caused by the pressure of the coolant in the sputtering system. Bonding of ceramics like Ti-Borides is critical because of the differences in thermal expansion of ceramics versus copper.

Bonding with epoxy cermet is very easy because there is no necessity to heat the target and backing plate. To increase the thermal conductivity the epoxy cermet could be filled with silver powder. Nevertheless, the thermal conductivity is still lower than with metallic bonding. Metallic bonding needs metallization of the target so the target and backing plate have to be heated up to the melting point of the soldering material. Mostly InSn alloys are used and the melting point is around 150°C. Metallic bonding allows sputtering at high power, but if the temperature of the target gets too high the metallic bond will fail.

After considerable research to find a suitable bonding technique, the titanium diboride target was brazed to the copper backing plate, which was shown to be a successful technique at moderate sputtering power. The cooling efficiency was calculated according to the procedure indicated in chapter 1.4.2 for a water flow of 2 l/min and water temperature rise of about 3°C. The nomograph, figure 1.32, gives a power of about 425Watts which is in good agreement with the obtained value of the following equation:

$$Q = M \times S \times (\theta_1 - \theta_2) \times 4.2 = 33.3 \times 1 \times 4.2 = 416 \text{ Watts}$$

where M is the mass in gm/s
$\Delta\theta = 3°C$
S is the specific heat of the water

The sputtering system used has been working with a ceramic target at power higher than 400WRF without causing damage. The calculated power should be considered with a safety coefficient. However, the cooling system needs to be improved to allow more confidence at the top end of the moderate sputtering power range.

2.3. CHARACTERIZATION OF THE COATINGS

LAYOUT
⇓
Coating Thickness Measurements
⇓
Structural Characterization:
♦ XRD, SEM, TEM, Auger, XPS
⇓
Mechanical Property Measurements:
♦ Residual Stresses
♦ Modulus of Elasticity
◊ Models of Deformation of Coated Beam
◊ Analysis of the Margin of Error
◊ Elastic Modulus by Three-Point Bend test
◊ Elastic Modulus by Nanoindentation
♦ Hardness by Nanoindentation
♦ Nanoindentation Tester
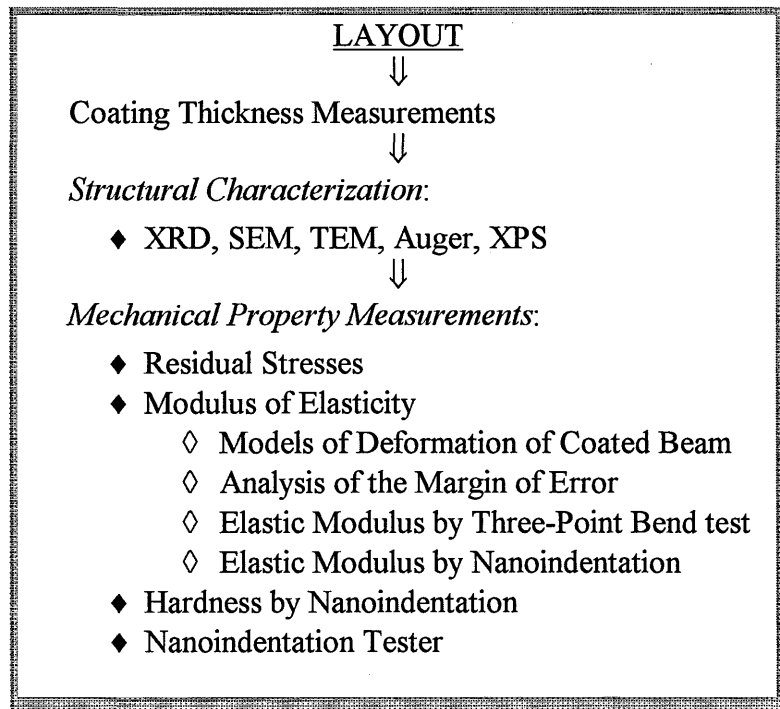
The characterisation of the coatings used in this research was made essentially by structural and mechanical property evaluation, as shown below:

I. COATING THICKNESS MEASUREMENTS

It is important to know the thickness of the coatings or layers in multilayer coating design. Some methods suitable to give this information include:

♦ Surface profiles using a stylus (Talysurf). This method consists of producing a step in the coating during deposition by masking part of the specimen. The step measurement was performed by Talysurf equipment. Several ways can be used to mask the specimen such as [38]:

1. A clamp washer is used to shield the substrate, which leaves a step in the coated specimen. The accuracy of the step can be poor using this method, due to field effects.

2. An aluminium tape is used to shield the substrate, which produces a sharper step. However, the tape glue could melt and could contaminate the coating unless used at low deposition temperature.

3. A water-soluble pen is drawn on a selected area on the substrate. After the deposition the specimen is bathed in water, which leads to peeling of the coating over the ink marked region, leaving a clear step.

♦ SEM and TEM techniques. The latter mainly for layers within the coating.

149

♦ Ball crater technique. This method uses three body abrasive wear, namely: a steel ball, slurry and the sample surface. A steel ball is rolled on the test sample and a slurry falls continuously onto the ball at the contact region. The slurry increases the wear rate in a controlled manner and gives reproducible results. The normal force between the sphere and the specimen derives from the weight of the sphere. The rotational motion of the sphere is achieved by contact with a variable speed rotating shaft. The rotation of the sphere against the specimen in the presence of the abrasive particles generates a ball wear crater. By comparing the geometry of the crater for different periods of wear time, the thickness of the crater and the wear rate of the coating and the substrate can be determined. A schematic representation of this technique is shown in figure 2.6.
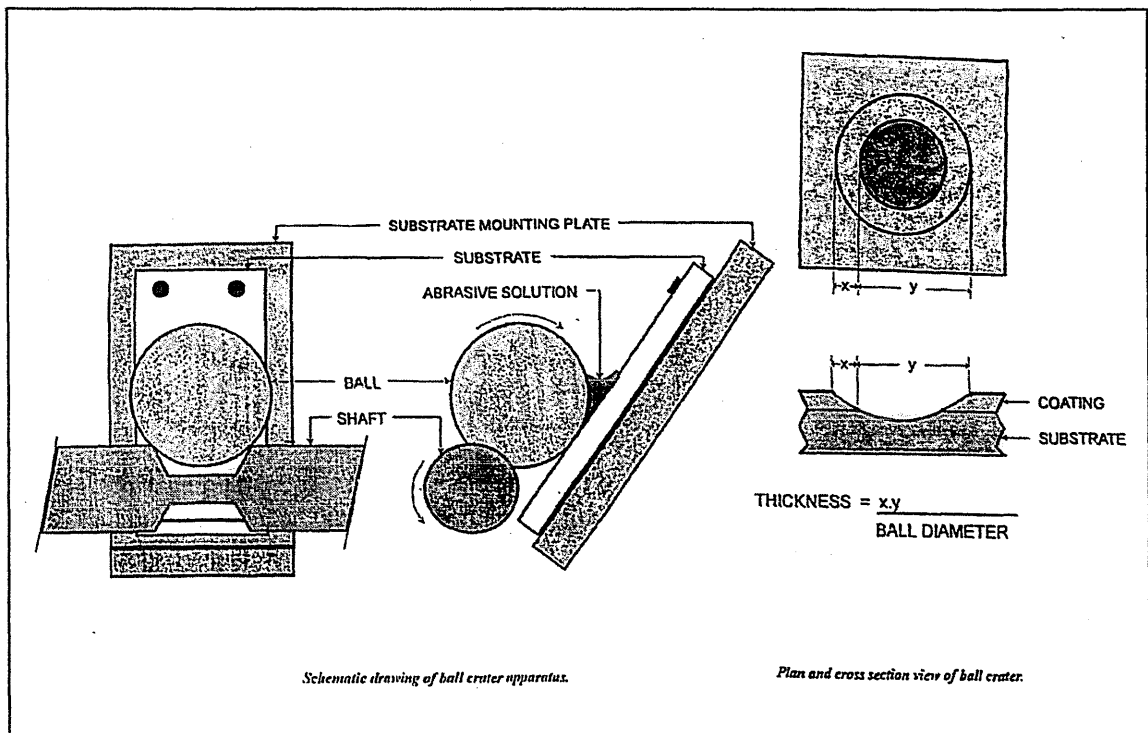
Figure 2.6. Representation of Ball Crater Technique [219].

II. STRUCTURAL CHARACTERIZATION

The structural characterization techniques used with single and multilayer coating designs include: XRD, Auger, XPS, SEM, TEM.

1. X-RAY DIFFRACTION TECHNIQUE

The X-Ray diffraction analysis was performed using a Philips PW1840 diffractometer. The XRD spectrum was performed with CoKα (1.788965Å) radiation and the cathode voltage was 20KV and the tube current 10mA. The range of 2θ scan was between 20° and 100° at speeds of 0.05°/min. with an incremental step of 0.01° held for 12 seconds. These test conditions were set up in order to give the best resolution and this was kept constant for all experiments. The coated specimens were sitting on the

specimen holder at the centre of the diffractometer chamber and rotated in synchronisation with the detector. Consequently the diffracting planes are parallel to the plane of the deposit. The X-ray spectrum is recorded by computer. The X-ray plot results are analysed by comparison between the spectrum obtained and the ASTM data cards available. The XRD analyses generate information about chemical composition of the coating as well as the structure in terms of degree of crystallinity.

2. SEM AND TEM TECHNIQUES

The SEM equipment used was a Cambridge 250SEM, with backscatter detector and Link EDS facility. The Backscatter detector and EDS was used to give the following information:

♦ Morphology observed by fractography of the coating

♦ Thickness of the coating and layers of multilayer coatings

♦ Microstructure of the coating

♦ Chemical composition of the coating

Some analysis was performed using TEM equipment and Link EDS system to give information about chemical composition, analysis of the interfaces and microstructure. The main drawback of this technique is the difficulty in the preparation of the samples. The samples were prepared by microtome, which involves cutting thin (<2000Å) slices through the coating using a diamond knife. These thin slices are then mounted on Cu grids for analysis.

3. AUGER AND XPS

The Auger and XPS technique were used to give information about chemical composition at the surface of the coating and through a few layers by depth profiling. An ESCALAB 200D was used in this study. The operating conditions were 5KV, 10nA at 100 times magnification in spot mode. Etching conditions were standardised on a stainless steel stub to be $20\mu A/cm^2$ current density. The results are analysed by comparison between the spectrum from the samples and the standards that were considered within a degree of reliability.

III. MECHANICAL PROPERTY MEASUREMENTS

The mechanical properties that were measured in the deposited coatings include: microhardness, residual stresses and elastic modulus. The techniques that were used to measure these properties are described below:

1. RESIDUAL STRESSES:

A qualitative demonstration of internal stresses of the coatings was made by comparing the substrate curvature by photography.

The experimental technique for measuring the residual stresses in the coating on the substrate was based on the curvature of deflection of the substrate by optical

microscopy at 5 times magnification, using a Joyce-Loebel Image Analyser. Stoney's equation (equation 1.5) was used for the calculations and is given by:

$$\sigma_f = E_s \times \left(\frac{t_s^2}{6t_f} \right) \times \Delta K$$

Where E_s is the biaxial elastic modulus of the substrate $E_s = \dfrac{E}{1-\upsilon}$

t_s and t_f are the thickness of the film and substrate respectively

ΔK is the the substrate curvature change

2. IN-PLANE ELASTIC MODULUS

Two approaches were developed for the calculation of the elastic modulus of the coating by using a three point bending test. The first model was developed by J.R.Nicholls and myself and the second one by P.Hancock. Both of them are described as follow:

1st model: Deformation of coated beam

Consider the pure bending of a rectangular cross-section beam. Assume the material is isotropic and follows Hooke's law and that the stress distribution is not disrupted by irregularities in the shape of the beam or by discontinuities in loading. Otherwise this theory cannot be used, since the stress concentration produced by these irregularities could overcome the stresses produced from the bending theory.
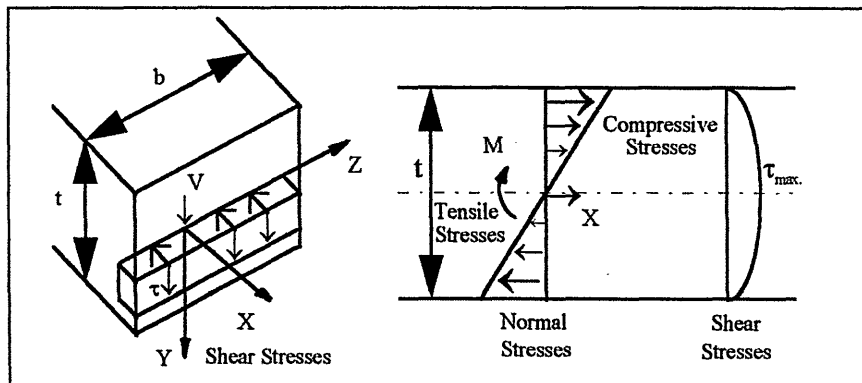
Figure 2.7. Representation of the normal and shear stresses in a bending beam.

When the beam is bent, the outer fibres go from tension on one side to compression on the other side. Then there must be a section on which there is zero strain called neutral axis, as illustrated in figure 2.7. The maximum tensile and compressive stresses in the beam occur at points located at the edges of the beam. As the beam is loaded by external forces, then internal stresses and strains are created within the beam. The normal stress σ_x is uniaxial to the cross-section and can be obtained from the normal strains ε_x. The normal stresses and the bending moment are given by [220]:

$$\sigma_x = E\varepsilon_x = \frac{Ey}{R} \tag{2.1}$$

$$M = \sqrt{\sigma_x} y \, da = \frac{E}{R} \sqrt{y^2} \, da = \frac{EI}{R} \qquad (2.2)$$

Where R is the radius of curvature and I is the moment of inertia of the cross-section area relative to the z axis. The normal stresses in the beam vary linearly with the distance y from the neutral axis and bending moment, but inversely proportional to the moment of inertia and are given by [221]:

$$\sigma_x = \frac{M_y}{I}$$

Assuming that the shear stresses τ act parallel to the shear force V, that is parallel to the vertical sides of the cross-section, the distribution of shear stresses is uniform across the width of the beam. The shear stress in a rectangular beam varies quadratically with the distance y from the neutral axis and is given by [220,221]:

$$\tau = \frac{V}{2I}\left(\frac{t^2}{4} - y^2\right)$$

That shear stress is zero when $y = \pm\, t\, /\, 2$ but the maximum value occurs at the neutral axis where y = 0. Because the shear stress τ varies parabolically from top to bottom of the beam, it follows that the shear strain $\gamma = \tau\, /\, G$ varies in the same manner. As a result, cross-sections of the beam that were originally plane surfaces become warped. The lines will not remain straight but will become curves with the maximum shear strain occurring at the neutral surface.

For slender beams it is usually assumed that any deflection due to shearing is negligible and thus is all due to bending, owing to the shear stress being very much less than the normal stresses. Although near the supports where M is small, it is the dominant factor but its influence on the total deflection is negligible.
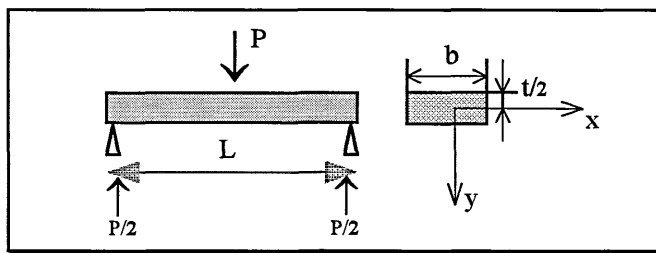
Figure 2.8. A central loaded beam with its dimensions.

For an uncoated beam of rectangular cross-section with width (b) constant and thickness t, the neutral axis is at the middle of the section, as illustrated in figure 2.8. The moment of inertia of the beam by using a simple elastic bend theory is given by [222]:

$$I_s = \frac{bt_s^3}{12} \qquad (2.3)$$

The deflection for x = L/2 by applying force P is given by:

$$\delta_s = \frac{PL^3}{48E_s I_s} = \frac{PL^3}{4E_s bt_s^3} \tag{2.4}$$

Considering the weight of a beam (P_1) it is necessary to add $5/8P_1$ to the load at the centre. Then the total deflection is given by:

$$\delta_s' = \left(P + \frac{5}{8}P_1\right)\left(\frac{L^3}{48EI}\right) \tag{2.5}$$

Hence the slope (γ_s) of the graph δ versus P without the weight of beam correction is given by:

$$\gamma_s = \frac{L^3}{4E_s bt_s^3} = \frac{\delta_s}{P} \tag{2.6}$$

Then the elastic modulus of the uncoated beam or substrate is given by:

$$E_s = \frac{L^3}{4\gamma_s bt_s^3} \tag{2.6}$$

Considering the correction for weight of the beam, then the slope is given by:

$$\gamma_s' = \frac{L^3}{4E_s bt_s^3} = \frac{\delta_s}{P + \frac{5}{8}P_1} \tag{2.7}$$

We then assume that a coated beam is a sandwich beam which consists of a composite beam made with two thin layers with a high modulus on either side of a thick core. We also assume the cross-sections of the beam remain plane during bending. In this case the normal strain (ε_x) varies linearly with the distance y from the neutral axis of the sections $\varepsilon_x = K y$. Both materials of the beam are assumed to obey Hooke's law.
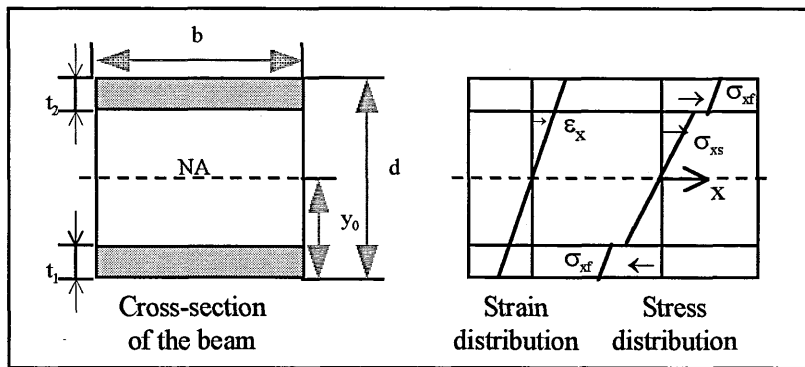
Figure 2.9. Cross-section of the beam with strain and stress distribution.

Consider a cross-section of width b and depth d with a bottom skin of thickness t_1 and a top skin of thickness t_2, as illustrated in figure 2.9. The modulus is E_f for the skin and E_s for the core. The stress distribution is now discontinuous and the equilibrium equations and the bending moment are given by:

$$\int_0^{t1} \sigma_{xx}^f dy + \int_{t1}^{d-t2} \sigma_{xx}^s dy + \int_{d-t2}^{d} \sigma_{xx}^f dy = 0$$

$$M = \frac{bE_f}{R} \int_0^{t1} (y - y_0) y dy + \frac{bE_s}{R} \int_{t1}^{d-t2} (y - y_0) y dy + \frac{bE_f}{R} \int_{d-t2}^{d} (y - y_0) y dy$$

Where R is the radius of curvature and y_0 is the distance from the neutral axis to the surface, the expressions for y_0, σ_{xx}^s, and σ_{xx}^f are given by:

$$y_0 = \frac{1}{2} \left[\frac{E_f d^2 - (E_f - E_s)\{(d - t_2)^2 - t_1^2\}}{E_f d - (E_f - E_s)\{d - (t_1 + t_2)\}} \right]$$

$$\sigma_{xx}^f = \left(\frac{E_f(y - y_0)}{R} \right) \quad ; \quad \sigma_{xx}^s = \left(\frac{E_s(y - y_0)}{R} \right)$$

According to beam bending theory the bending moment is given by:

$$M = \frac{IE}{R} = \frac{bd^3 E}{12R} = \frac{S}{R}$$

Where S is an equivalent stiffness and given by:

$$S = \left(\frac{bd^3 E_f}{12} \right) \left[4 - 4 \left(\frac{E_f - E_s}{E_f} \right) \left\{ \left(1 - \frac{t_2}{d}\right)^3 - \left(\frac{t_1}{d}\right)^3 \right\} - 3 \left\{ \frac{\left[1 - \left(\frac{E_f - E_s}{E_f} \right) \left\{ \left(1 - \frac{t_2}{d}\right)^2 - \left(\frac{t_1}{d}\right)^2 \right\} \right]^2}{\left[1 - \left(\frac{E_f - E_s}{E_f} \right) \left\{ 1 - \left(\frac{t_1}{d} + \frac{t_2}{d}\right) \right\} \right]} \right\} \right] \quad (2.8)$$

Assuming the beam is coated only on one side as is the situation in this project, so the thickness $t_1 = t_f$, $t_2 = 0$ and $d = t_f + t_s$. We also assume the neutral axis will not move because the film is very thin (<5μm). Then the stiffness is given by:

$$S = \left(\frac{b}{12} \right) (t_f + t_s)^3 E_f \left[4 - 4 \left(\frac{E_f - E_s}{E_f} \right) \left(1 - \frac{t_f^3}{(t_f + t_s)^3}\right) - 3 \left\{ \frac{\left\{ 1 - \left(\frac{E_f - E_s}{E_f} \right) \left(1 - \frac{t_f^2}{(t_f + t_s)^2}\right) \right\}^2}{\left\{ 1 - \left(\frac{E_f - E_s}{E_f} \right) \left(1 - \frac{t_f}{(t_f + t_s)}\right) \right\}} \right\} \right] \quad (2.9)$$

Hence the slope for the composite for the graph δ versus P is given by:

$$\gamma_c = \frac{d\delta}{dP} = \frac{L^3}{48EI} = \frac{L^3}{48S} \quad (2.10)$$

Considering that $A = (t_f - t_s)^3$; $B = \frac{t_f}{t_f + t_s}$ and $\mu = \left(\frac{E_f - E_s}{E_f} \right)$, then the stiffness is given by:

$$S = \frac{b}{12} AE_f \left[\mu(B-1)^3 + 1 + 3B^2 + \frac{3B^3}{(1-\mu+\mu B)} \right]$$

Ignoring the term $\left(\frac{3B^2}{1-\mu+\mu B} \right)$ the error for $E_f = E_s$ is only 0.18% and for $E_f = 10E_s$ is 1.2%, so the term to a first approximation may be ignored and then S is replaced by $\left(\frac{L^3}{48\gamma} \right)$. Consequently, the modulus of the film that should be used in further calculations is given by:

$$E_f = \frac{\left[\frac{L^3}{4b\gamma_c} - E_s t_s^3 \right]}{\left[4t_f^3 + 6t_f^2 t_s + 3t_f t_s^2 \right]} \tag{2.11}$$

To correct for the weight of beam requires equation 2.7 to be used.

2nd Model: Deformation of coated beam

If the coating has a different modulus, then the neutral axis will move away from the centroid. The new position can be calculated by using the transformed section method whereby the transformed beam is modified to have the same neutral axis as the composite beam, as shown in cross section in figure 2.10. Where E_s is the modulus of the substrate and E_f is the modulus of the coating.
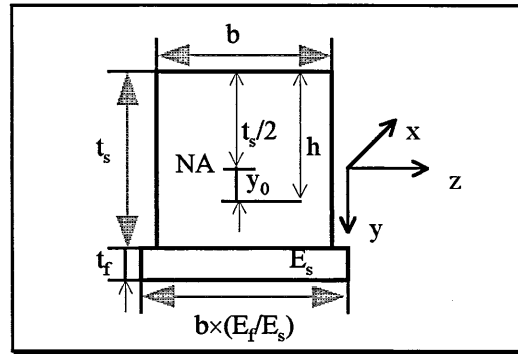
Figure 2.10. Transformed beam with dimensions.

The resulting force equation becomes,

$$E_s \int_s y_s dA_s + E_f \int_f \alpha y_f dA_f = 0 \tag{2.12}$$

Where $\alpha = E_f/E_s$ and,

$$E_s \int_s y_s dA_s = E_s \left[\frac{(t_s - h)}{2} (t_s - h)b - \frac{h}{2} (hb) \right]$$

156

$$E_s \int_f \alpha y_f dA_f = E_s \left[\alpha \left(t_s - h + \frac{t_f}{2} \right) t_f b \right]$$

Substitution in equation 2.12 gives:

$$h = \frac{2t_s t_f + t_f^2 \alpha + t_s^2}{2 \left(t_s + \alpha t_f \right)}$$ (2.13)

If $y_0 = h - (t_s/2)$. Then,

$$y_0 = \left[\left(\frac{\alpha t_f}{2} \right) \frac{\left(1 + \frac{t_f}{t_s} \right)}{\left(1 + \alpha \frac{t_f}{t_s} \right)} \right]$$ (2.14)

To calculate the moment of inertia of the total composite beam, the parallel axis theorem is used whereby the moment of inertia I with respect to any axis is equal to I related to the centroid plus the product of area and the square of the distance between the centroid and the new axis. Hence,

$$I_s = \frac{bt_s^3}{12} + bt_s y_0^2 \qquad ; \qquad I_f = \frac{b\alpha t_f^3}{12} + b\alpha t_f \left(\frac{t_f}{2} + \frac{t_s}{2} - y_0 \right)^2$$

$$I_t = I_s + I_f = \frac{b \left(t_s^3 + \alpha t_f^3 \right)}{12} + b\alpha t_f \left(\frac{t_f}{2} + \frac{t_s}{2} - y_0 \right)^2 + bt_s y_0^2$$ (2.15)

The central beam deflection for a simply supported beam for $y_0 = t_f/2$, is given by:

$$\delta = \frac{Pl^3}{48 I_t E} = \left(\frac{Pl^3}{48 E_s b} \right) \left(\frac{12}{t_s^3 + \alpha t_f^3 + 12 t_s y_0^2 + 12 \alpha t_f \left(\frac{t_f}{2} + \frac{t_s}{2} - y_0 \right)^2} \right)$$ (2.16)

The slope of the plot δ versus P for the composite (γ_c) and uncoated beam (γ_s) and the ratio γ_s / γ_c are given by:

$$\gamma_c = \left(\frac{l^3}{4 E_s b} \right) \left(\frac{1}{\left[t_s^3 + \alpha t_t^3 + 12 t_s \delta^2 + 12 \alpha t_f \left(\frac{t_f}{2} + \frac{t_s}{2} - y_0 \right)^2 \right]} \right)$$ (2.17)

$$\gamma_s = \frac{l^3}{4 E_s b t_s^3}$$ (2.18)

$$\frac{\gamma_s}{\gamma_c} = 1 + \alpha\left(\frac{t_f}{t_s}\right)^3 + 12\left(\frac{\delta}{t_s}\right)^2 + 12\alpha\left(\frac{t_f}{t_s^3}\right)\left(\frac{t_f}{2} + \frac{t_s}{2} - y_o\right)^2 \tag{2.19}$$

Expanding equation 2.19 and putting the terms in descending importance gives:

$$\frac{\gamma_s}{\gamma_c} = 1 + 3\alpha\left(\frac{t_f}{t_s}\right) - \left(\frac{12\alpha t_f \delta}{t_s^2}\right) + 12\left(\frac{\delta}{t_s}\right)^2 - \left(\frac{12\alpha t_f^2 \delta}{t_s^3}\right) - \left(\frac{12\alpha t_f^2 \delta}{t_s^3}\right) + 4\alpha\left(\frac{t_f}{t_s}\right)^3 + \left(\frac{12\alpha t_f \delta^2}{t_s^3}\right) \tag{2.20}$$

Inserting realistic values for α and t_f over the range of interest shows that this equation is accurate to within ±4% when only the first two terms are used. Hence,

$$\frac{\gamma_s}{\gamma_c} \approx 1 + 3\alpha\left(\frac{t_f}{t_s}\right) = 1 + 3\left(\frac{E_f}{E_s}\right)\left(\frac{t_f}{t_s}\right) \tag{2.21}$$

The change in slope which is equivalent to the compliance for a coated beam compared to an uncoated beam ($\Delta\gamma$) is given by:

$$\Delta\gamma(\%) \cong 3\left(\frac{E_f}{E_s}\right)\left(\frac{t_f}{t_s}\right) \times 100 \tag{2.22}$$

Then the elastic modulus of the film is given by:

$$E_f = \left(\frac{E_s t_s}{3t_f}\right)\left(\frac{\gamma_s}{\gamma_c} - 1\right) \tag{2.23}$$

Analysis of the Margin of Error

The margin of error of mechanical properties is related to the geometrical conditions, substrate properties, error of the measurement and homogeneity and stability of the parameter [182]. The analysis of the relative errors was performed for parameters that involve the equations 2.6, 2.11 and 2.23.

$$E_s = \frac{L^3}{4\gamma_s b t_s^3},$$

$$E_f = \left(\frac{E_s t_s}{3t_f}\right) \times \left(\frac{\gamma_s}{\gamma_c} - 1\right),$$

$$E_f = \frac{\left[\dfrac{L^3}{4b\gamma_c} - E_s t_s^3\right]}{\left[4t_f^3 + 6t_f^2 t_s + 3t_f t_s^2\right]}$$

Where $\gamma_s = \gamma_1$ and $\gamma_c = \gamma_2$ are the slope of the uncoated and coated beam respectively

b is the width of the beam

L is the length between the supports

t_f is the film thickness

t_s is the uncoated beam thickness

δ is the deflection

P is the applied load

E_s is the elastic modulus of the uncoated beam

The figures 2.11, 2.12 and 2.13 show the dependence of the error of the elastic modulus determined by the equations 2.6, 2.11 and 2.23 respectively on the various parameters. The most restrictive demand concerning the elastic modulus on the uncoated beam is the thickness. For an coated beam the less stringent command for both models is the thickness of the film measurement. However, the effect of the equipment compliance is more significant for the 2nd model than other parameters. The 1st model depends strongly on the compliance of the system, substrate dimensions and substrate elastic modulus.
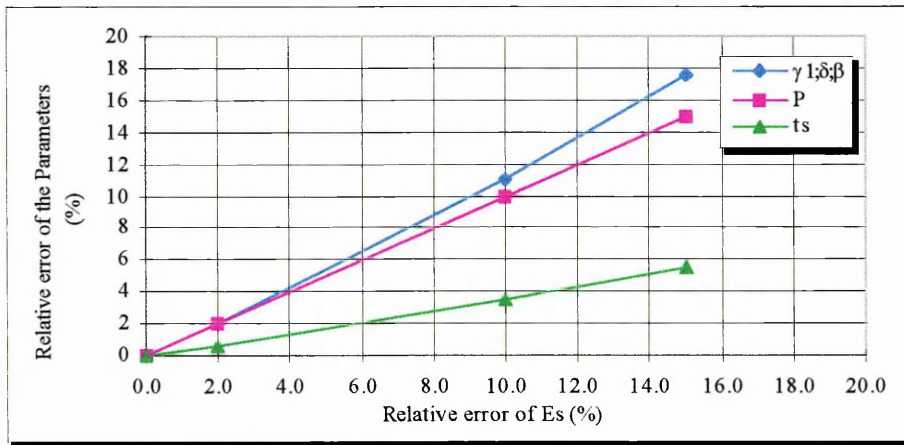
Figure 2.11. Relative error of E_s versus Relative error of the parameters, from equation 2.6.
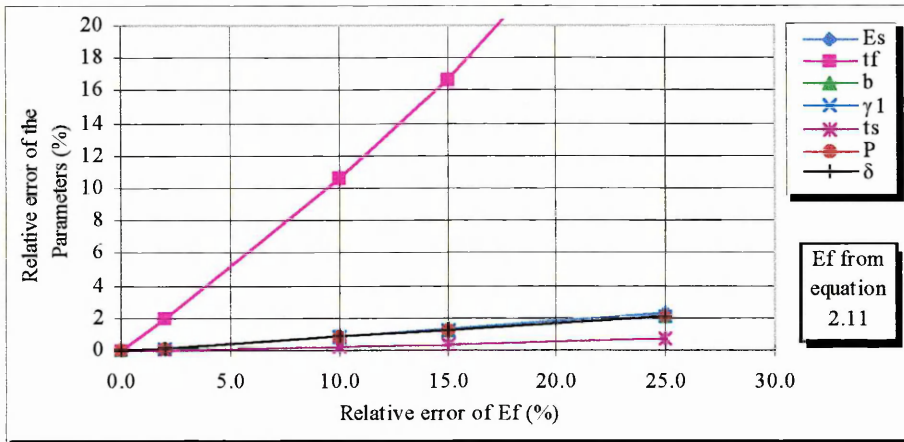
Figure 2.12. Relative error of E_f versus relative error of the parameters from equation 2.11.

159
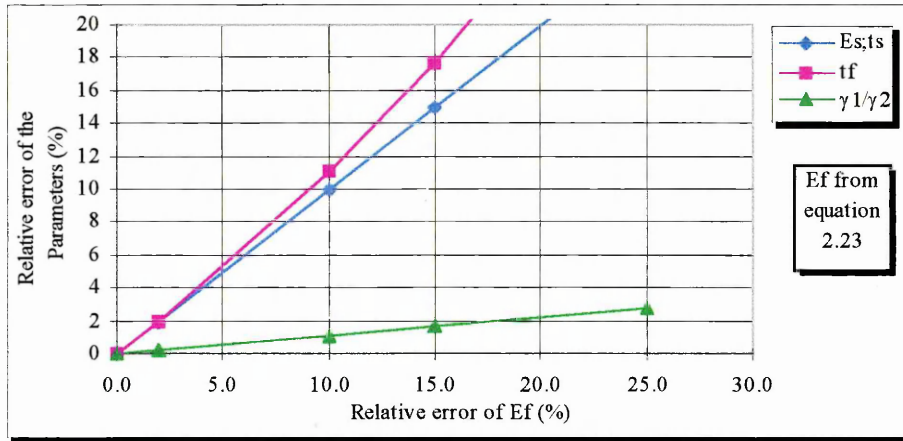
Figure 2.13 Relative error of E_f versus relative error of the parameters from equation 2.23.

The in-plane elastic modulus of the coatings was measured by traditional methods such as: three-point bending tests. The elastic modulus of the coatings was also measured by nanoindentation technique. The description of both of these techniques (traditional and non-traditional methods) is given in this section.

Elastic Modulus by Three-Point Bending Test

A small three point bending apparatus was designed and built to fit in the optical microscope working table. The deflection of the specimen was measured by a micrometer on the optical microscope with an accuracy of 2μm. Owing to the compliance effect of the bending apparatus in the elastic modulus measurement, four different methods for applying the load were designed, including: mechanical loading using weights, using a hydraulic system, electromagnetic system and mechanical loading using water as a weight. The sequence of these designs follows an attempt to improve the accuracy of the measurements. The last three point bend test designs used the nanoindentation instrument. A description of all these designs is given below:

♦ The mechanical loading using a weights method consisted of applying the load by changing the number of fixed weight washers for a required weight, as shown in figure 2.14. The main disadvantage of this method is the way the load is applied, which depends upon the skill of the operator and the system vibration. Both of these affect the compliance of the system.

160
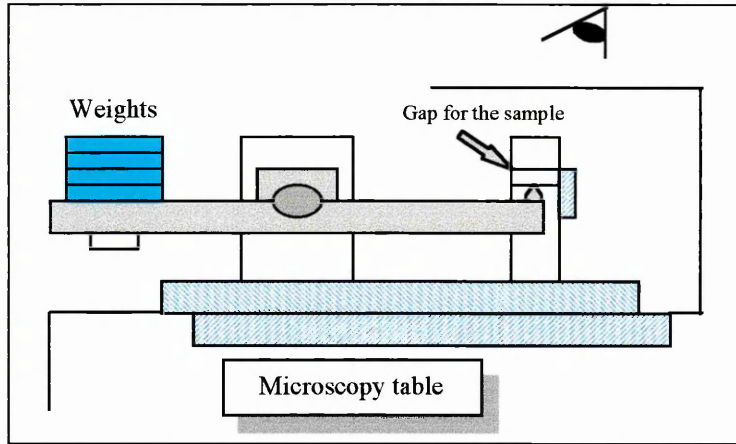
Figure 2.14. The three point bend test by mechanical loading using weights.

◆ The electromagnetic method consists of applying the load by a solenoid device. Varying the current through the solenoid, using a Variac, changes the applied force. The room between the microscope working table and its base was too small to install a sufficiently large solenoid device for a required load. As a result a lower capacity solenoid was used, but as the current increased in the solenoid it caused the solenoid to become very hot and then the values were very unstable.

◆ The hydraulic method consists of applying the load by a piston that was controlled by the pressure inside a cylindrical chamber, as shown in figure 2.15. The difficulty of the method was in keeping the alignment of the piston at a constant speed. The speed of the piston was found to be strongly dependent of the friction between the piston and seal, air in the oils and oil viscosity. Different oils with different viscosities and different types of seal were used but the unstable results could not be overcome.
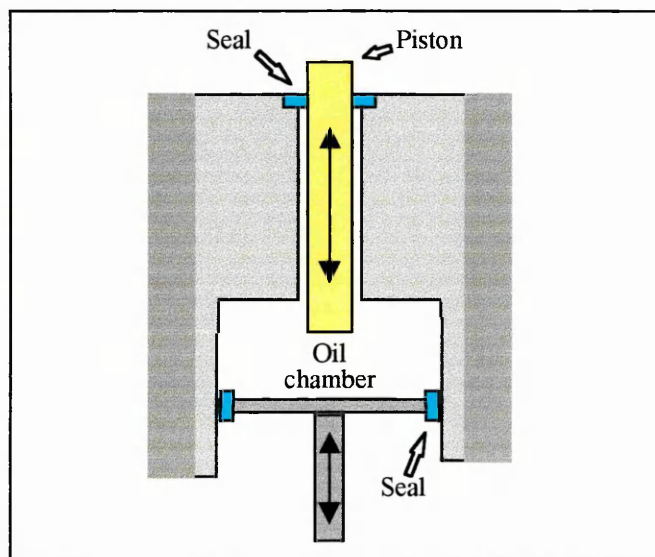
Figure 2.15. The three-point bend test by hydraulic method.

♦ The mechanical weight method using water consists of applying the load by dropping water from a pipette into a reservoir, as shown in figure 2.16. The method gave more accurate values than the mechanical weight using washers but required much more time to control the speed of the water and avoid vibrations.
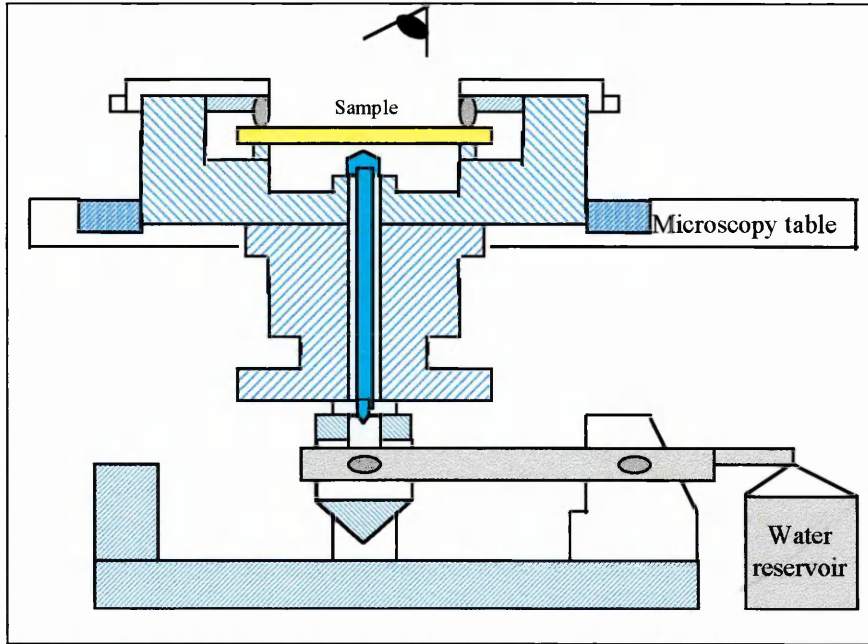
Figure 2.16. The three point bend test by mechanical weight method using water.

♦ The measurement of elastic modulus by three-point bending test using a nanoindentation tester was performed by a small jig fixed to the support specimen holder. The load was applied in the horizontal direction, as shown in figure 2.17 instead of the vertical as in the classical methods.
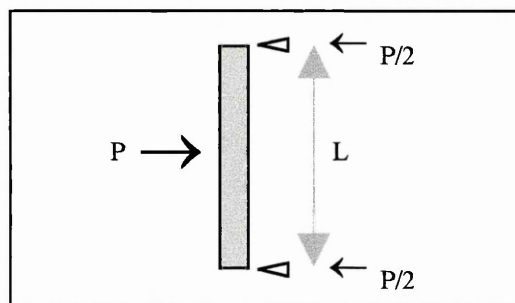
Figure 2.17. A central loaded beam for three-point bend test by nanoindentation tester.

3. ELASTIC MODULUS BY NANOINDENTATION

The elastic modulus was measured by a nanoindentation test either by indentation or by three-point bending test, as mentioned earlier. The measurement of elastic modulus by indentation was performed according to Oliver and Pharr's model

162

described in chapter 1.5.3. The description of the indentation tester is given later in this section.

4. HARDNESS

The hardness of single and multilayer coatings was performed by a nanoindentation test according to Oliver and Pharr's model described in section 1.5.3. For each sample seven indentations were performed, as recommended in many hardness measurement standards. The contact depth was chosen in order to be less than 10% of the film thickness.

5. NANOINDENTATION TESTER

The nanointentation experiments were performed using Nanotest 550 equipment in Micro Materials Ltd. laboratory [215]. The operating basis consists of measurement of the stylus movement in contact with a specimen surface. The penetration depth resolution of the indenter is better than 1nm and the spatial resolution can be performed to position accuracy of less than 50nm. The overview of the equipment is shown in figure 2.18.

The equipment can operate essentially in two ways:

1-Indentation measurement: An increasing load is applied and the indenter is impressed into the specimen surface. After reaching a pre-determined value, the load is reduced and the penetration depth decreases due to elastic recovery of the deformed material. The depth versus load is monitored continuously, which allows both Young's modulus and hardness data to be deduced from these curves, as mentioned in chapter 1.5.3.

2-Scanning measurement: a static or increasing load is applied and the specimen is moved perpendicular to the stylus axis and the probe displacement into or out of the surface is monitored. Properties such as: topography, profilometry, scratch resistance or frictional forces can be measured by this process. The parameters that can be recorded are load, depth, transverse displacement, frictional force, acoustic emission and time.

Figure 2.18. Nanotest 550 equipment.

The equipment is placed in a cabinet to reduce draughts, to control the atmosphere temperature and to reduce acoustic vibrations because they affect the measurement precision. Control of the temperature can reduce the electronic drift and mechanical changes. The temperature was set up about 2°C above the maximum room temperature. It is advisable to leave the instrument at least half an hour to thermally stabilise after the cabinet has been opened and before doing any measurement. Two small heaters are sited at the front of the cabinet, while the probe controller temperature is placed on the metal-work at the height of the pendulum in order to give an average temperature of the cabinet. The cabinet sits either on a concrete and pneumatic passive damping table or on an active air table for isolating possible vibrations.

The nanotest pendulum can be performed at low load up to 500mN and at high load up to 20N. An axled pendulum on frictionless bearings is designed to be a light-stiff-cylindrical shaft made of ceramic, as shown in figure 2.19. The load is applied from a voltage across the coil mounted at the top of the pendulum. The coil is attracted towards a permanent magnet producing motion of the indenter either toward or into the specimen surface.

When the pendulum coil is energised, the rotation of the pendulum is limited by a mechanical limit stop located above the hinge. The limit stop not only defines the maximum outward movement of the indenter but also the operating orientation of the pendulum. The latter can also be positioned manually by a micrometer adjustment. The hinge is a friction-free design and consists of four steel foils clamped in an X pattern. These foils are very stiff in the direction of the indenter movement but very fragile in other directions; the pendulum should be handled with care.

The displacement of the indenter is measured by a capacitor located below the hinge and consists of two circular parallel plates. One plate is attached to the indenter holder which makes the capacitance change as the indenter moves and it is measured by a capacitance bridge unit. The latter is located near the capacitor for minimising stray capacitance effects which might affect the readings. The two plates could be set for a maximum measurement depth of 1-1.5μm but the system is at full sensitivity at about 0.3

164

to 0.5mm separation of the capacitance plates (depth resolution and capacitance plate separation are related).

The pendulum without voltage across the coil tends to fall clockwise. The equilibrium position could be achieved by adjusting with balance weights. This set of weights is below the plates and also counters the mass of the coil. The electronic control unit receives an AC signal from the capacitance bridge which is then amplified, rectified, digitised and transferred to the computer. The control unit contains a ramp generator which supplies the coil current. The voltage across the coil is measured, amplified, digitised and transferred to the computer.
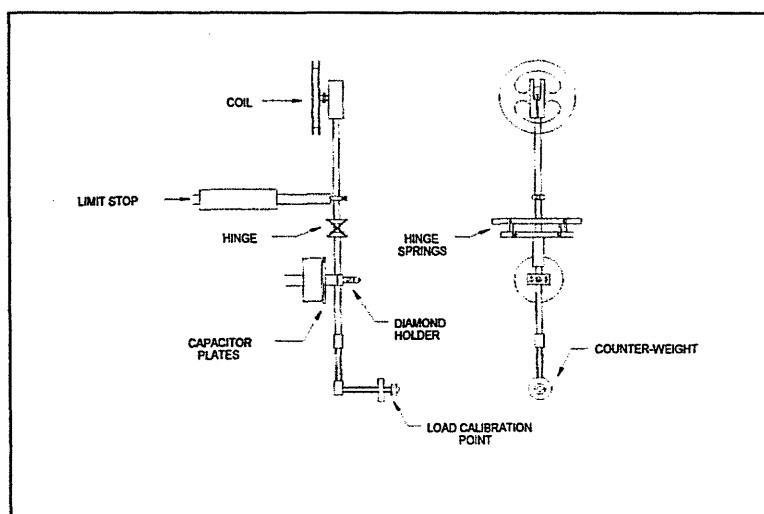
Figure 2.19. The nanotest pendulum [215].

The high load pendulum is a lot heavier and more robust. The stiffness comes from three ceramic rods placed between the hinge and the coil assembly. The magnet is much bigger over the low load pendulum with the coil winding placed directly in the air gap. The hinge is a friction free design that allows the diamond to be placed underneath its vertical axis. The plate spacing under normal conditions is about 1.2-1.5mm to allow a measurement depth of $\cong$7-8μm at full system sensitivity.

There are several calibrations to be carried out at different stages, which are essential to perform, including the following measurements: load, depth, frame compliance, indenter tip area function, pendulum test and zero load calibration. The main features of these calibrations are mentioned below [206,215,224].

Pendulum Test: The purpose of this test is to set a vertical operating orientation for the pendulum and hence an indentation axis normal to the specimen surface, parallel and correctly spaced capacitor plates, correct mechanical balance of the pendulum and a correct electrical balance of the capacitance bridge. The pendulum test also sets the signal to go between two reference levels from 0 volts to 7.0±0.1 volts and the depth amplifier sensitivity to a maximum. Moreover, it applies a voltage across the coil to bring the pendulum against the limit stop. A typical pendulum test curve is shown in figure 2.20.
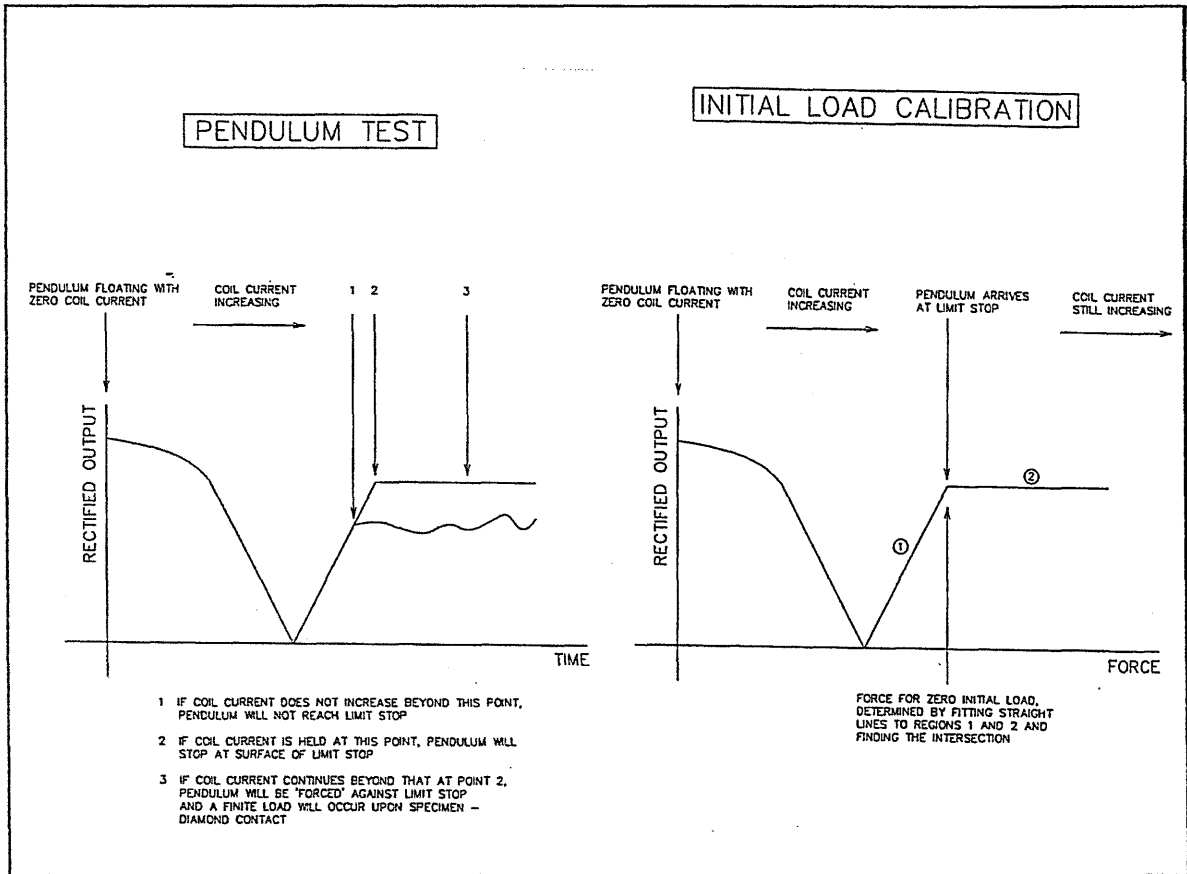
Figure 2.20. Representation of initial load calibration and pendulum test [215].

Zero load calibration: The zero load calibration supplies a minimum coil voltage to bring the pendulum into contact with the limit stop. A limit stop with contamination can lead to notable errors in the initial load measurement. The general rule for this test is to carry out a minimum number of calibrations, often three, before measurement and other calibrations. The calibration is performed using a plot of rectified output versus force, as shown in figure 2.20.

Load calibration: The load calibration is a straight forward procedure and it consists of hanging a series of masses often between 0-10gf from a set point at the bottom of the pendulum while the coil applies a countering force equating to a known voltage for each mass. The principle is that the clockwise moment due to the applied mass W must be balanced by anticlockwise moment due to the coil current. The mechanical balance point is defined as the equilibrium pendulum position corresponding to limit stop contact, as shown in figure 2.21. It is a very stable calibration and hence only needs to be repeated once every two months.
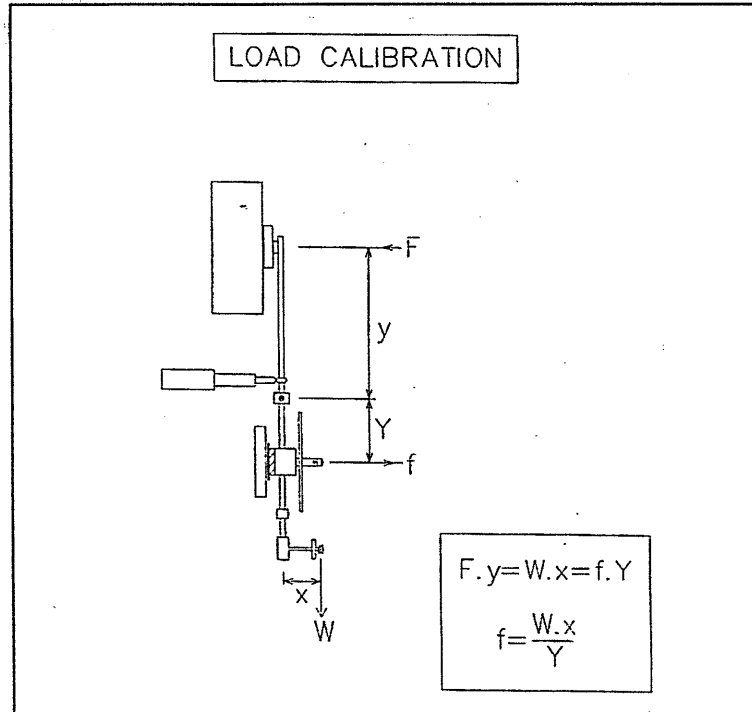
Figure 2.21. Representation of load calibration [215].

Depth calibration: This calibration determines the relationship of measuring plate sensitivity to a known distance moved by the x motor while it is in contact with the pendulum. This sensitivity and hence the depth range can be altered by changing the value of amplifier gain with maximum sensitivity at 100 and minimum at 15, typical standard deviation of about 1 to 5×10^{-4} is observed, over 5-10 depth calibrations, at full sensitivity. The depth calibration is very sensitive to operating conditions and should be performed frequently.

Diamond area function calibration: The Berkovitch indenter shape changes with time as the tip becomes rounded. The unsharpness of the diamond affects the results of the measurements, mainly at shallow depths up to 300nm. The indenter area calibration can offset this effect. The diamond area calibration procedure involves performing a series of indentation experiments on a quartz sample where the diamond contact area as a function of contact depth is determined from the elastic recovery of the indentations. The largest indentation in the series of experiments should not be more than 1μm and the measurements should be performed with the depth amplifier at full gain. A wide range of indentations from 0.5mN to 80mN is performed to ensure that both the tip defect and the ideal region are included. In practice a scheduled indentation is performed for 5 runs at each of 0.5, 1, 3, 5, 10, 20, 40 and 80mN. Using the correct value for the instrument compliance, the contact areas are calculated from the equation 1.24, using the literature value for E (1141GPa) and υ (0.07) for the diamond indenter.

The values of C_f, C_s can be obtained from the equations 1.19 and 1.23. A fitting procedure is applied to the area and contact depth data to find the following area function $A = ah_c^2 + bh_c$. Where a and b are constants and h_c is the contact depth. The data is analysed by the Oliver and Pharr method.

Compliance calibration: The instrument compliance is required to determine the elastic properties of materials, as mentioned in chapter 1.5.3. The compliance calibration procedure requires several indentation experiments to be performed on a quartz sample. The complete procedure is based on the Oliver and Pharr model and is as follows:

1-Raw data: Using fused quartz and Berkovitch indenter, 10 depth versus load curves are produced with a maximum load of 80mN. Using an ideal diamond area function given by $A=24.5h_c^2$ and with h_c obtained from Oliver and Pharr analysis of the raw data, an initial estimate of the frame compliance is obtained from equation 1.24, where C_t is measured by obtaining the tangent at maximum load to a power law fit of the unloading curve, as proposed by Oliver and Pharr.

2-Correct raw data for frame compliance: the first estimate of C_f is used to correct the raw data and produce a new value of h_c again using the method of Oliver and Pharr.

3-The procedure is repeated for convergence. The method assumes that the modulus is constant and independent of depth. A typical value for compliance, at low pendulum load is about 1nm/mN.

A typical indentation measurement involves the following stages:

1-Positioning the specimen: the specimen should be within 0.5mm of the indenter by direct control from the computer keyboard.

2-Indentation system parameters set up: definition of all measurement parameters. A set of measurement parameters is defined either for one indentation or a series of indentations at the same location or at different locations. The maximum load can be maintained for a dwell period. The screen in figure 2.22 shows the parameters relative to the full range available.
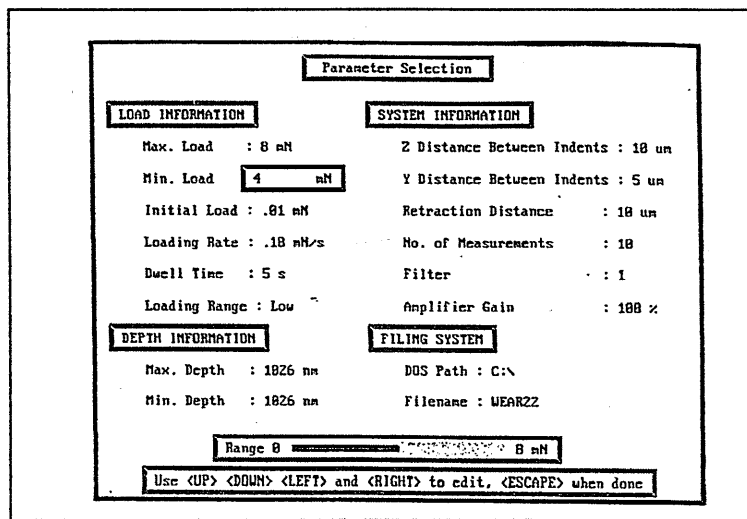

Figure 2.22. Screen of the indentation system parameters set up [215].

◆ Maximum and minimum load: It is possible to set an experiment to have all measurements ending at the same load or to set the first measurement to the maximum load and then set minimum load as the lowest maximum in a series.

♦ Initial load: This is a load applied to bring the pendulum into contact with the limit stop. It is often set to 0.05mN unless the environment is too noisy.

♦ Filter: Four depth amplifier filters are available. It is set to 1 for all measurements unless the environment is to be noisy.

♦ Amplifier gain: The amplifier gain sets the maximum depth measurement sensitivity at 100 (matching to maximum resolution) and minimum at 15 ($\cong 6.66$ times less resolution, which matches greater available measurement depth). Low values of gain would be used for depth measurement of the order of 10μm, while high values would be used for depth measurement of the order of 1μm.

♦ Maximum and minimum depth: They can be set either to run a series of measurements to a pre-determined depth or a range between maximum and minimum depth as for the load.

♦ Dwell time: The dwell time allows the time at maximum load to be set for a given period, usually for 15 sec, but this depends on the indenter material.

♦ Retraction distance: This is the distance that makes the sample move away from the surface when the measurement is complete. Hence, stopping the diamond from remaining in contact, while the sample is moved to the next indent location. Such a distance is often 10μm for a smooth sample with a short distance between indentations.

3-Perform an Indentation: The measurement starts by a slow movement of the specimen towards the indenter. This is detected by a change in capacitance as the pendulum is slightly moved away from the limit stop.

4-Collect the Data: Collecting load versus depth data for each indentation, the following information must be included: maximum penetration depth, plastic depth, local hardness, reduced modulus, plastic work, elastic work.

5-Analysis and saving of data

6-Move to the next programmed analysis position

This technique includes: Corrections, specimen preparation and diamond handling. Those aspects are referred to below [206,215,224]:

Corrections

The main concern in the use of the indentation instrument is stability of the environment with respect to thermal drift and mechanical vibrations. Both affect the displacement determination and applying the load can cause heating which changes displacement values. It is quite difficult to keep a stable environment during an indentation experiment so that some estimated corrections must be made of the thermal drift. A simple linear correction has been made and incorporated in the instrument software. This correction consists of monitoring drift by imposing a hold period load at about 10% of the maximum load, periodically.

Specimen Preparation

A smooth surface specimen gives a more consistent result. It is worth spending some time on specimen preparation but care must be taken not to change the microstructure of the material. The specimen is fixed to an aluminium stub by a suitable adhesive such as: superglue, silver paint or Indian wax. The adhesives should allow the sample to be removed once the testing is complete. Moreover, the adhesive should be stiff enough to not contribute to the system compliance.

Diamond Handling

The most common indentation diamond is the Berkovitch. Its dimensions are shown in figure 2.23. It was used in the nanoindentation measurement in this project. The diamond indenter is attached to a stainless steel stub and clamped in front of the moving capacitor plates. The diamond should wear and its shape may change, mainly due to debris sticking to it. This means that the diamond should be checked and cleaned regularly.
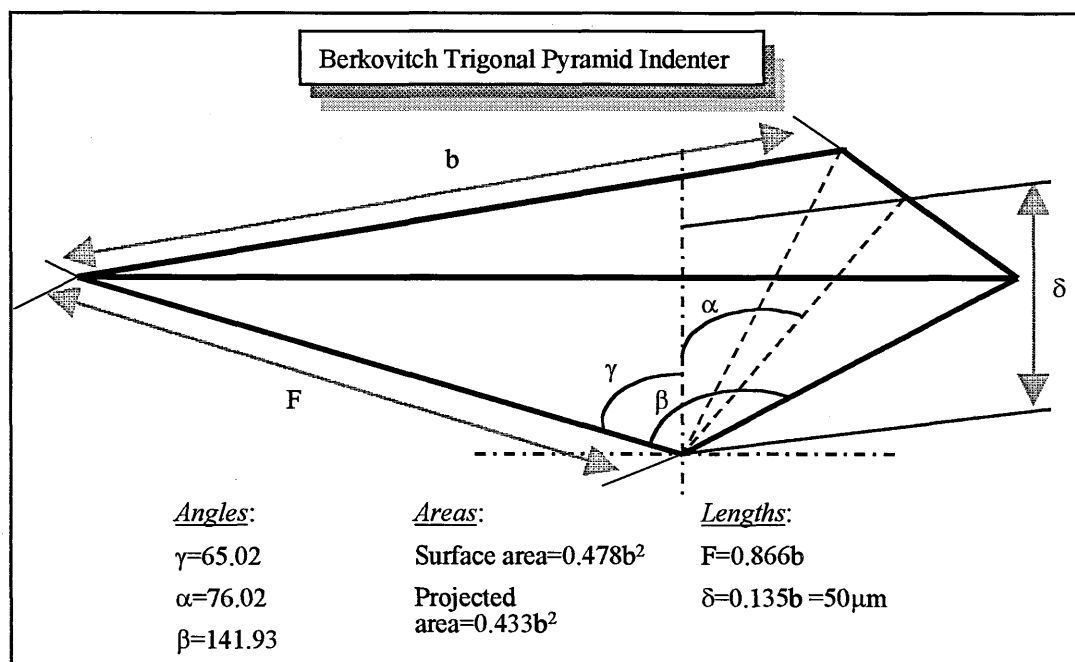
Figure 2.23. Representation of the Berkovitch indenter [215,225].

RESULTS AND DISCUSSION

3. RESULTS AND DISCUSSION

3.1. DEPOSITION STUDIES OF PRELIMINARY SINGLE-LAYER COATINGS

LAYOUT
⇓
Effect of the Sputtering Pressure and Power on the Deposition Rate
⇓
Effect of the Sputtering Pressure and Power on the Bias Voltage of the Plasma
⇓
Effect of the Temperature on the Deposition Conditions
⇓
Effect of the Substrate Position inside the Vacuum Chamber on the Deposition Rate
⇓
Effect of the Deposition Conditions on the Coating Microstructure
⇓
Summing up
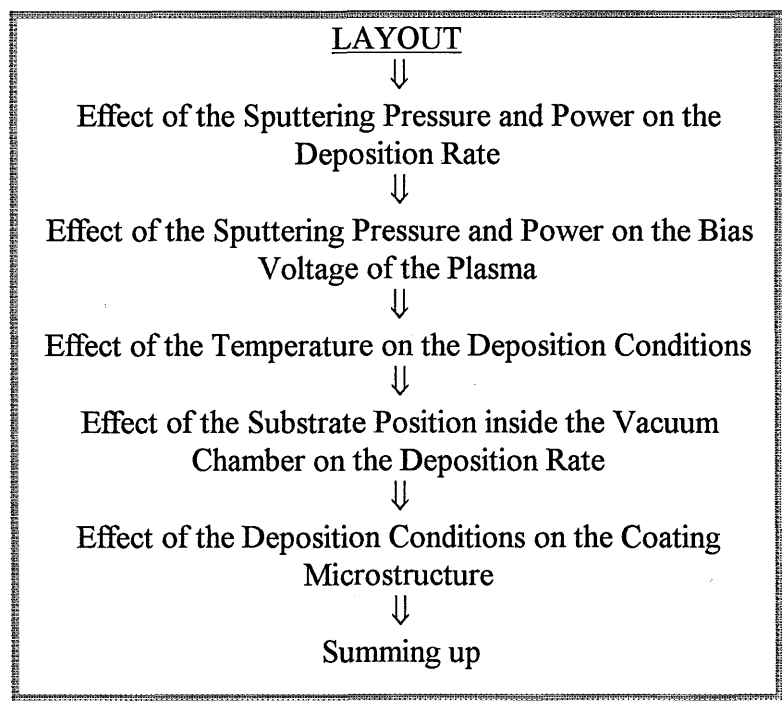
3.1.1. EFFECT OF THE SPUTTERING PRESSURE AND POWER ON THE DEPOSITION RATE

The dependence of the sputtering pressure on the deposition rate for Al films is shown in figure 3.1 at 300 and 400WRF sputtering power. These curves are typical of the sputtering process, as mentioned in section 1.4.2, whereby, the deposition rate increases with a sputtering pressure up to a maximum value and then has an abrupt decrease. The peak curve is a balanced value between high ionisation and lost ion energy due to the mean free path reduction.

Increasing the sputtering power shows an increase in deposition rate for the studied range of pressure, figure 3.2, as expected. This is due to the increased efficiency of the ion bombardment of the target, due to the increased velocity of the bombarding ions.

For Ti, NiCr, Mo and TiB_2 films, the dependence of the deposition rate on sputtering pressure is not so nicely shown as for the Al films, as represented in figure 3.3. At a given chamber pressure the deposition rate shows an increase together with the sputtering yield for the following elements: Al (S=1.0), Mo (S=0.7), Ti (S=0.5). The deposition rate seems to be insensitive to sputtering pressure for TiB_2 and Ti films.

Figure 3.4 shows the deposition rate at 0.6Pa (4.5×10^{-3}Torr) sputtering pressure versus sputtering yield for Ti and Al at 300WRF, Mo at 250WRF and NiCr at 200WRF. The deposition rate increases with the sputtering yield for Ti, Mo and Al. Considering

the sputtering yield for NiCr of 1.2 atoms/ion, the deposition rate does not appear to follow the pattern of other elements. However the NiCr was deposited at 200WRF power. Assuming that above the sputtering threshold (40V) the deposition rate increases with RF power (confirmed for aluminium in figure 3.2), then the deposition rate at 300WRF power for NiCr can be estimated at 2.2μm/h. This latter point agrees with the sputtering yield criterion that has been observed to apply for Ti, Mo and Al deposition due to the backward scattering.

The thickness of the coatings was measured using the SEM technique from fractography samples. It was found difficult to measure the film thickness by this technique for ductile materials such as Al and NiCr because the fracture edges were not sharp. It is worth pointing out that the deposition rate values quoted are representative values. Absolute thickness on a given sample depends upon various factors such as: sample position inside the vacuum chamber, measurement technique, erosion target area, thickness uniformity within the sample, etc.
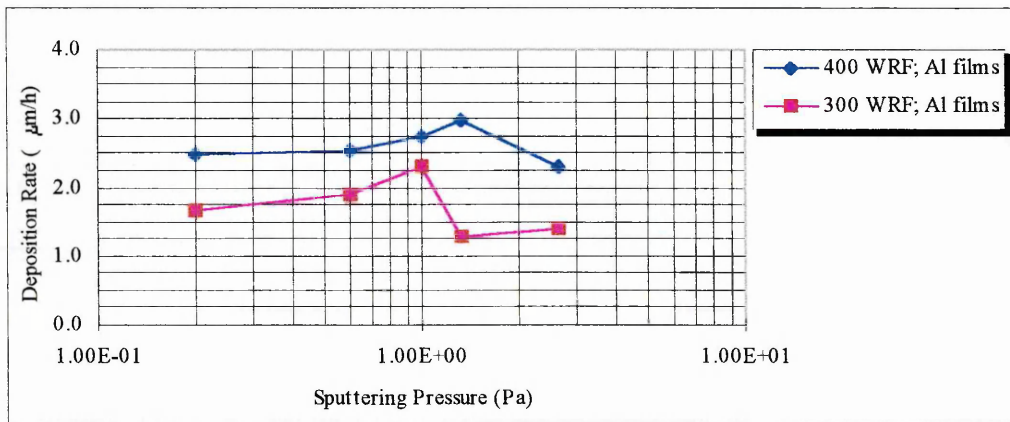

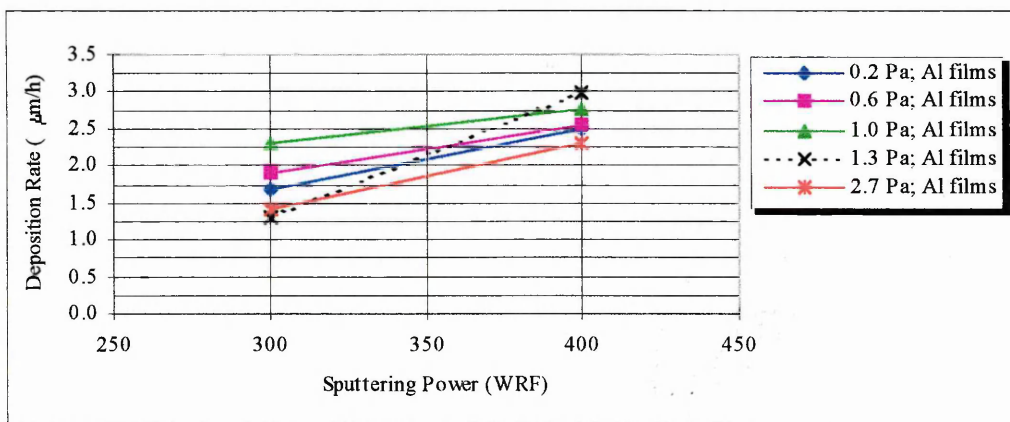Figure 3.1. Deposition rate versus Sputtering pressure for Al film onto copper substrate.

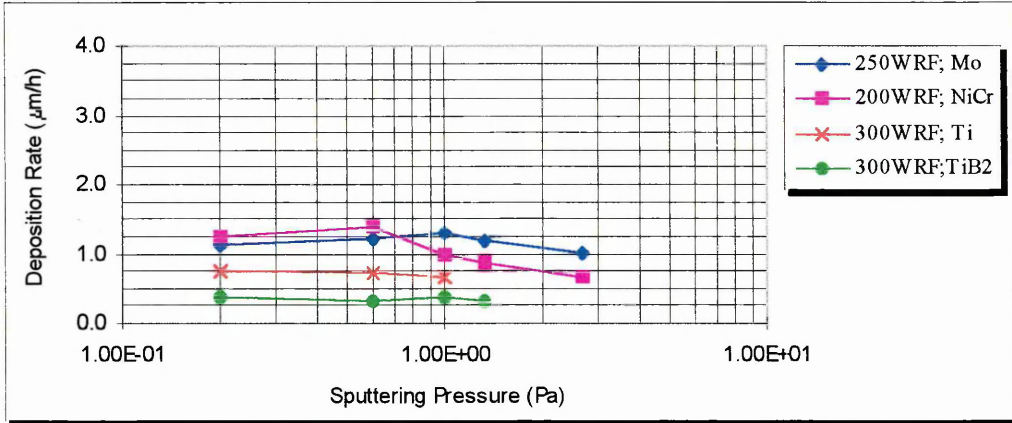Figure 3.2. Deposition rate versus sputtering power for Al film onto copper substrate.

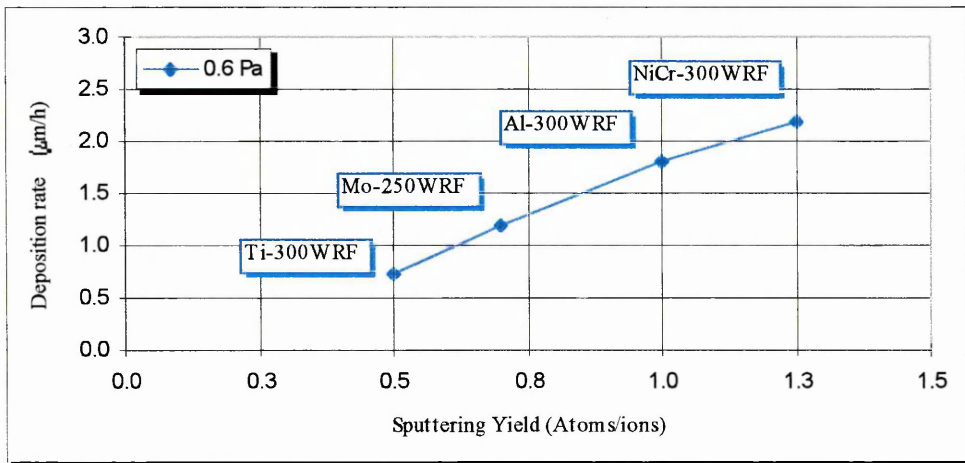Figure 3.3. Deposition rate versus sputtering pressure for Mo, Ti, NiCr and TiB$_2$ films onto copper substrate.

Figure 3.4. Deposition rate at 0.6Pa (4.5×10^{-3}Torr) sputtering pressure versus sputtering yield for Ti, Al, Mo and NiCr films.

3.1.2. EFFECT OF THE SPUTTERING PRESSURE AND POWER ON THE BIAS VOLTAGE OF THE PLASMA

A voltage probe gives the target potential during deposition. The coatings were produced by RF sputtering, with a blocking capacitor, thus the voltage is the mean D.C. voltage generated on the target. This is a balance between the ion flux and electron flux impacting the target. The bias voltage increases until charge transfer from electron and ion bombardment is equal. Increasing the sputtering pressure should increase the ion flux. Increasing the RF power will increase the peak-to-peak RF voltage. Hence, increasing either the sputtering pressure or sputtering power increases the voltage measured on this probe, as shown in figures 3.5, 3.6 and 3.8. However, the latter is more effective. Figure 3.7 shows that the measured deposition rate and bias voltage are directly related, when depositing aluminium. Similar behaviour would be expected for the other metals/alloys (Mo, Ti, NiCr), although this is less well shown (figure 3.9) other than for Mo at sputtering pressures below 1Pa.

Al films at low sputtering pressure, figure 3.7, show a value about -30V probe voltage when no deposition was observed, which is in good agreement with the sputtering threshold for Al indicated in figure 1.25 in section 1.4.1. The same observation can be made for Mo films in the figure 3.9 for low sputtering pressures. At high sputtering pressures for Al films, this value increases to about -75V. This may be due to the incorporation of impurities in the sputtering environment such as oxygen, implying that Al-O clusters may be sputtered at high pressures.
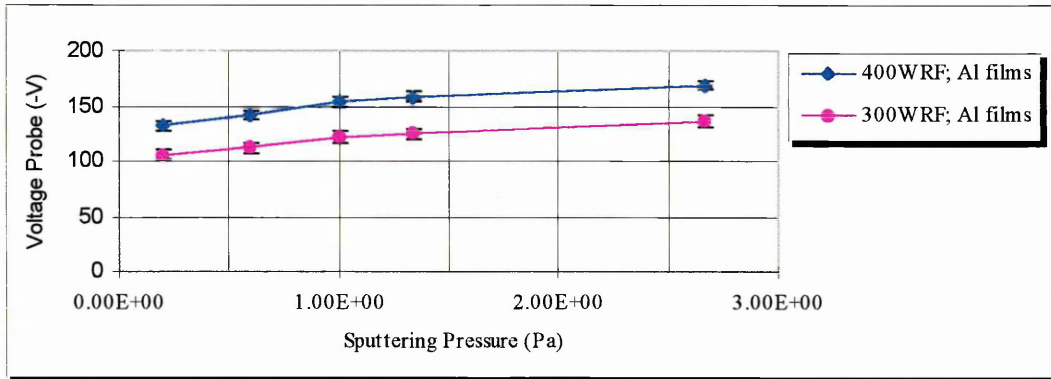

Figure 3.5. Voltage probe versus sputtering pressure for Al film onto copper substrate.
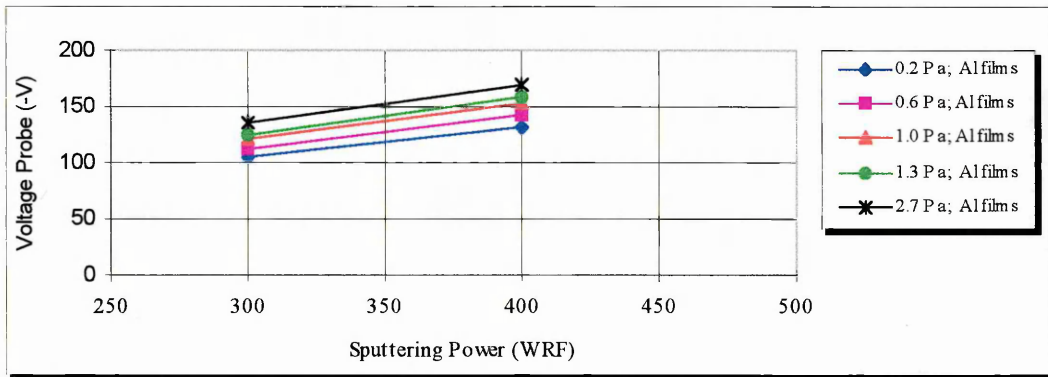

Figure 3.6. Voltage probe versus sputtering power for Al film onto copper substrate.
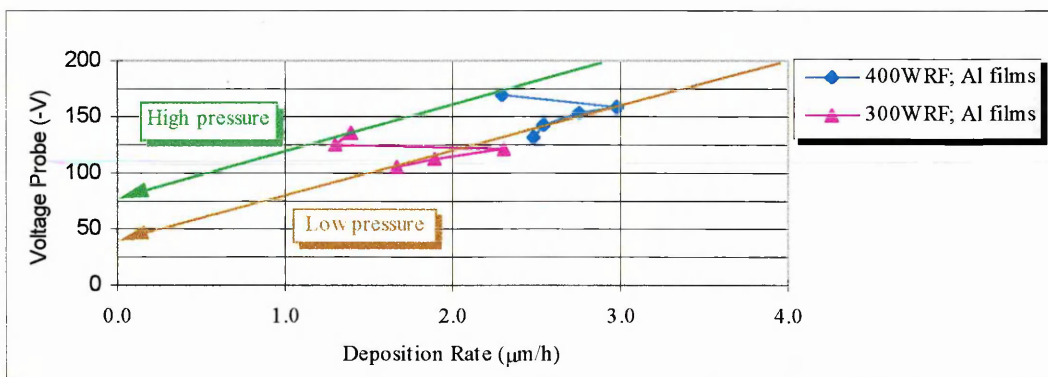

Figure 3.7. Voltage probe versus deposition rate for Al film onto copper substrate.
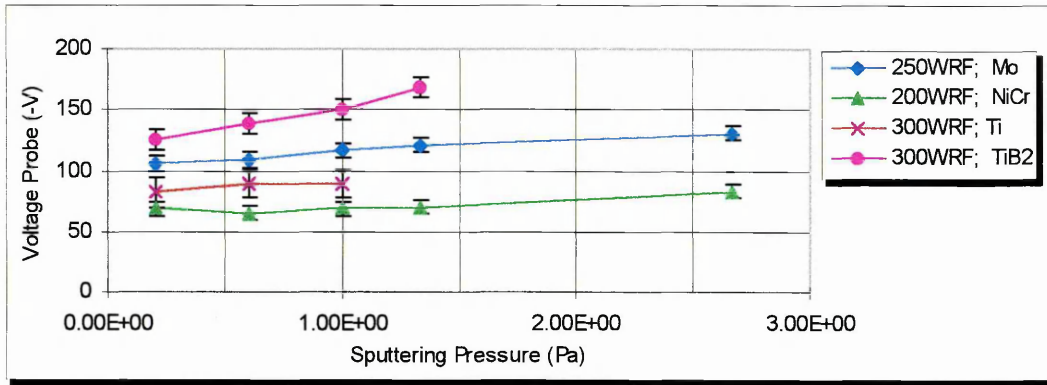
174

Figure 3.8. Voltage probe versus sputtering pressure for Mo, NiCr, Ti and TiB₂ films onto copper.
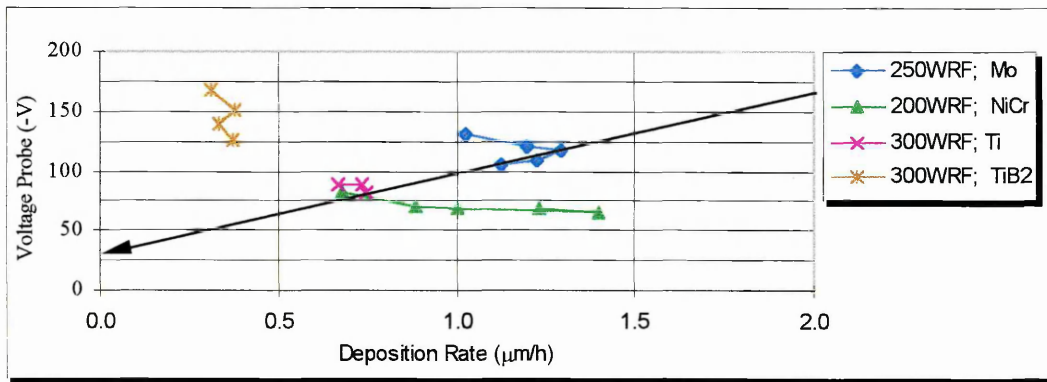

Figure 3.9. Voltage probe versus deposition rate for Mo, NiCr, Ti and TiB₂ films onto copper.

3.1.3. EFFECT OF THE TEMPERATURE ON THE DEPOSITION CONDITIONS

The substrate temperature during deposition, in all experiments, was dependent on the sputtering conditions for each material, because the substrate was neither water cooled nor heated.

As mentioned in chapter 1.4.2., it is quite difficult to measure the substrate temperature. Therefore, there may be some errors in the measured substrate temperature compared to the actual substrate temperature. A thermocouple was placed between the substrate holder and under the substrate to avoid coating the thermocouple [152]. The readings were taken before starting deposition (T_i) and immediately ending deposition (T_f) to avoid interference from the RF electric field (this means the reflected power). However, figure 3.10 shows that the RF effect was not completely eliminated because it was expected that the Al films for 300WRF and 400WRF should have higher temperatures, as the deposition time in each run was similar.

Figure 3.11 shows the average temperature for the range of pressure studied for all single films. As a conclusion, the temperature was lower than 200°C for all coatings. The initial temperature was measured after sputter cleaning the target and substrate. This

175

is the reason for such temperatures being higher than the room temperature. Sputter cleaning was at 40WRF for one hour.
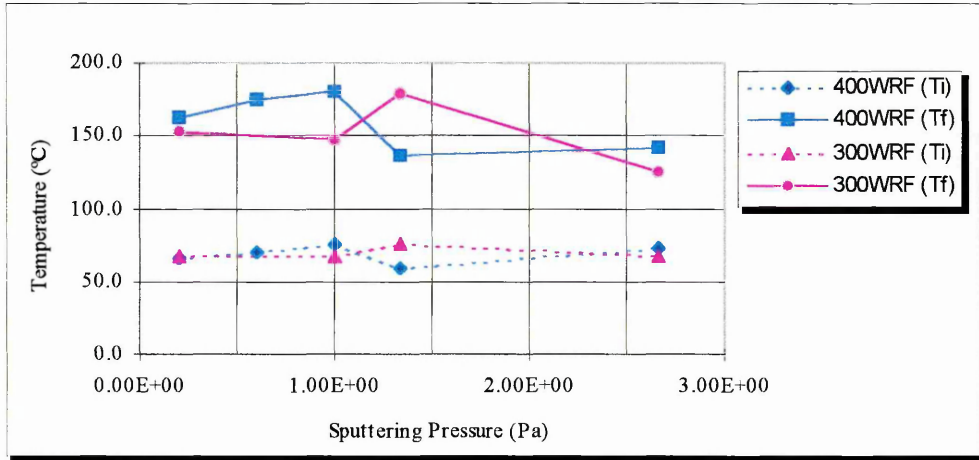
Figure 3.10. Substrate Temperature versus sputtering pressure for Al film onto copper substrate.
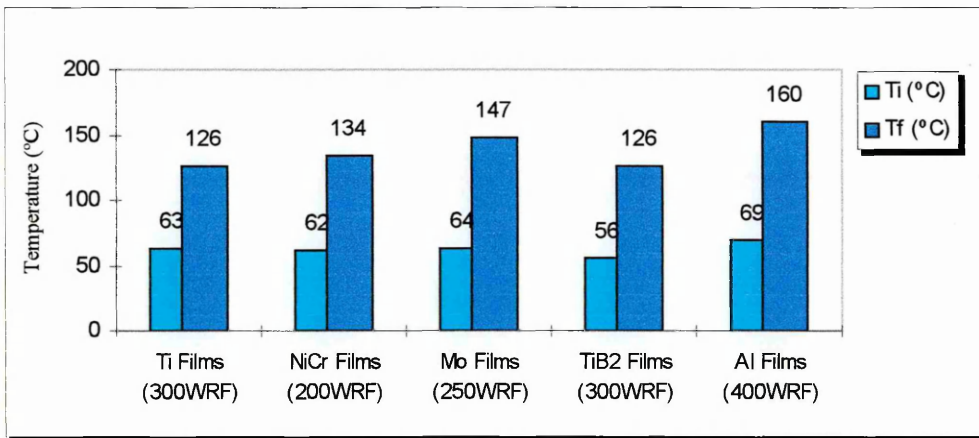
Figure 3.11. Average substrate temperature for Ti, NiCr, Mo, TiB$_2$ and Al films.

3.1.4. EFFECT OF THE SUBSTRATE POSITION INSIDE THE VACUUM CHAMBER ON THE DEPOSITION RATE

The figures 3.12 to 3.15 show the effect of the deposition rate as a function of different sample positions inside the vacuum chamber. The relationship between target size, substrate holder and sample position arrangement inside the chamber is shown in figure 2.2 of the section 2.1. The Al and TiB$_2$ films for this study were deposited onto a glass substrate and the thickness measurements were made using the Talysurf.

Two main factors affect the deposition rate in these experiments; the flux of argon (and its entry position) and the erosion area of the target. As the Al has a higher sputtering yield than TiB$_2$, so the argon flux position prevails over the erosion area and

high deposition rate values are observed next to the argon source. The Al seems to be more influenced by the pressure gradient from the argon inlet to the pumping station than TiB$_2$. The position of the argon inlet and outlet is shown in figure 2.1 of the section 2.1. All the experiments were carried out with the two inlet argon valves opened. For TiB$_2$ films the erosion area dominates the deposition rate, and hence film thickness uniformity.

Modelling was performed to confirm the variation of TiB$_2$ film thickness as a function of the erosion area of the target, by considering the erosion area of the target as two vapour sources, as illustrated in figure 3.16. The deposition rate can be described by cosine evaporation law:

$$d = d_0 (\cos\theta)^n \cos\phi \left(\frac{R_0^2}{R^2}\right)$$

Where R$_0$ is the distance between target and substrate

d_0 is the deposition rate in front of the source

$\phi = \theta$ because the distance between target and substrate is constant and therefore the source and substrate planes are parallel.

The geometry of this configuration is illustrated in figure 3.16. The deposition rate at the point D (=B), is a combination of the sputtering rates from source 1 and source 2 and is given by:

$$d_D = d_0 + d_0 \left[\cos(\theta_D)^n\right] \cos\theta_D \left(\frac{R_0^2}{R_D^2}\right) \qquad (3.1)$$

Where R$_0$ = 70mm

R$_D$ = 86.02mm

θ_D = 35.54°

d_D = 1.72μm (measured value)

The deposition rate at the point C is twice the deposition either from the source 1 or source 2 given by:

Where R$_0$ = 70mm

R$_C$ = 74.33mm

θ_C = 19.65°

d_C = 1.80μm (measured value)

Solving the two equations should give the values of n and d$_0$ so

$$\frac{1}{d_0} = \frac{\left(1 + \left[\cos(\theta_D)^{n+1}\right]\right) \times \left(\frac{R_0^2}{R_D^2}\right)}{d_D} \qquad (3.2)$$

$$\frac{1}{d_0} = \frac{2}{d_C \left[\cos(\theta_C)^{n+1}\right] \times \left(\frac{R_0^2}{R_C^2}\right)} \qquad (3.3)$$

Considering the two equations (3.2 and 3.3) as a function of $f_1(n,d_o)=f_2(n,d_o)$ then,

$$\frac{\left(1+\left[\cos(\theta_D)^{n+1}\right]\right)\times\left(\dfrac{R_0^2}{R_D^2}\right)}{d_D}=\frac{2}{d_C\left[\cos(\theta_C)^{n+1}\right]\times\left(\dfrac{R_0^2}{R_C^2}\right)} \tag{3.4}$$

By giving values to n to equalise these two terms of the equation 3.4 it was possible to find a value of n=4.65 and then d_o=1.425, for this sputtering geometry. To confirm this model the deposition rate at the point A was calculated giving a value of 1.33μm which is in good agreement with the measured value of 1.35μm.

Figure 3.12. Substrate position inside the chamber versus film thickness for Al films onto glass substrate.

Figure 3.13. Film thickness versus substrate position inside the chamber and target erosion area for Al films onto glass substrate.
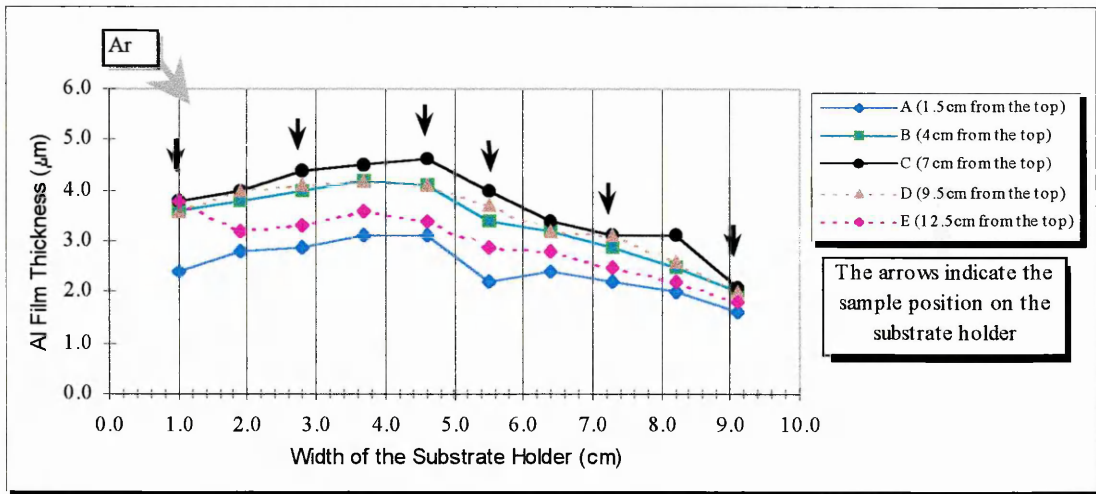
178

Figure 3.14. Substrate position inside the chamber versus film thickness for TiB$_2$ films onto glass substrate.
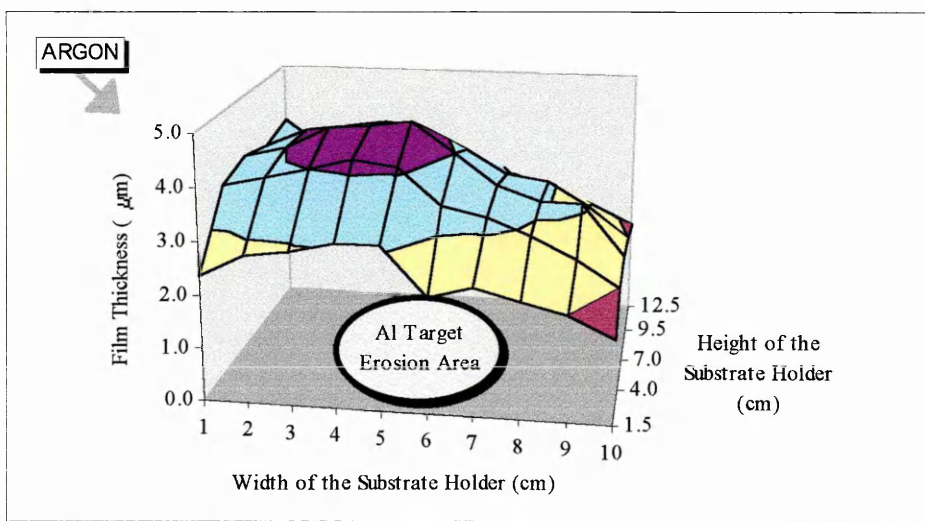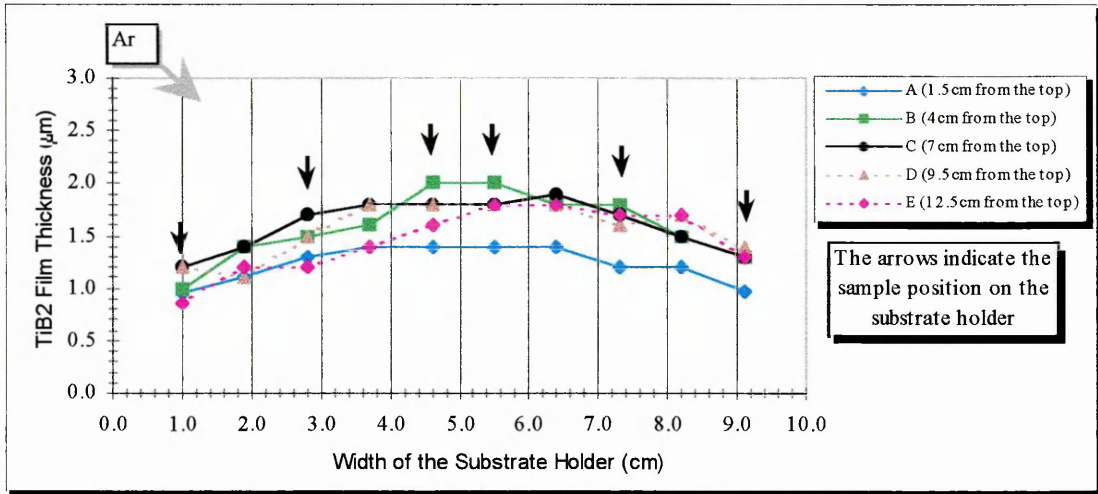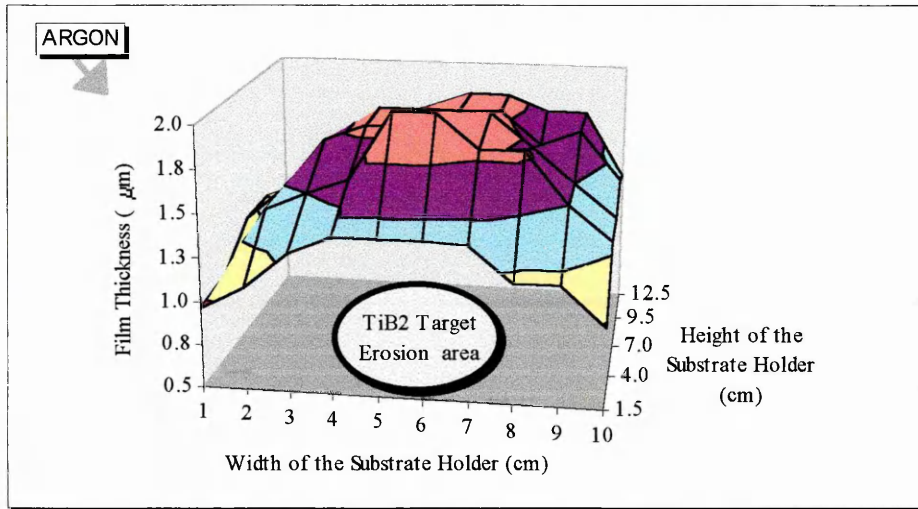

Figure 3.15. Film thickness versus substrate position inside the chamber and target erosion area for TiB$_2$ films onto glass substrate.
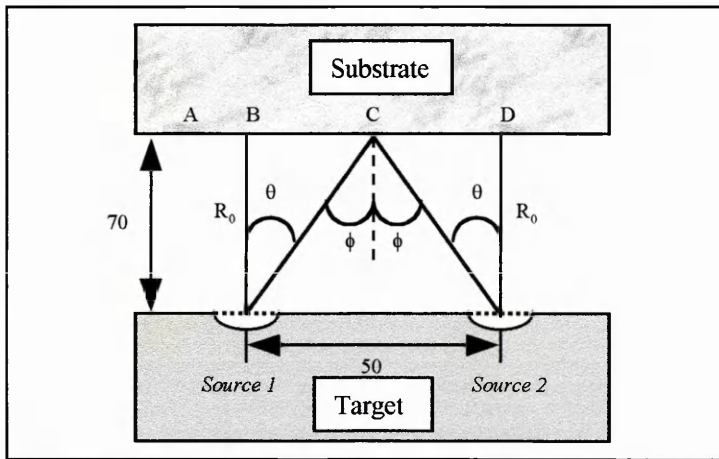
Figure 3.16. Cross-section of the target in front of the substrate.

179

3.1.5. EFFECT OF THE DEPOSITION CONDITIONS ON THE COATING MICROSTRUCTURE

The microstructural analysis of the single coatings was performed by SEM examination and XRD spectra. Samples of impact-fracture cross-section were prepared for SEM surface topography. The XRD was performed with CoKα radiation (1.788965Å) and the cathode voltage was 20KV and the tube current 10mA. The range of 2θ scan was between 20° and 100° at a speed of 0.05°/min with an incremental step of 0.01° held for 12 seconds.

The topography of the Al coatings is shown in photograph 3.1 for 300 and 400WRF sputtering power at 0.6Pa (4.5×10^{-3}Torr) sputtering pressure. According to Thornton's model, for the Al coating microstructure for T_s/T_m in the range of 0.26 to 0.3, for the sputter conditions used, the microstructure should be placed between the transition zone and zone 2. However, the photographs do not show this expected microstructure, particularly the coating produced at 300WRF power. This is thought to be due to plastic deformation of the coating during the impact fracture process.
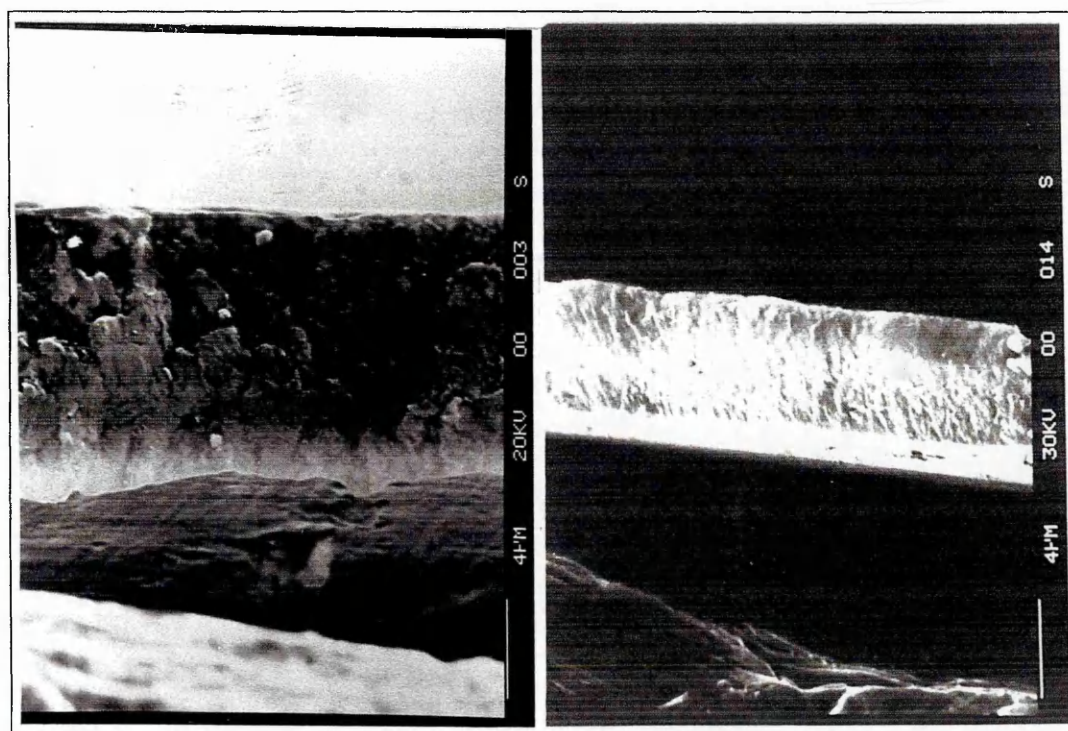
Photograph 3.1. Al film microstructure onto copper for 0.6Pa (4.5×10^{-3}Torr) at 300WRF on the left and at 400WRF on the right.

According to Thornton's model, the NiCr, Ti, Mo and TiB_2 film microstructures should be placed in zone 1. The surface topography for these coatings is shown in photographs 3.2 to 3.4. As the TiB_2 films do not show XRD peaks (only a very small peak for the coating deposited at 0.20Pa (1.5×10^{-3}Torr)) the TiB_2 films may be amorphous, which agrees with some research [49,51,63] mentioned in chapter 1.2.1 in this range of sputtering conditions.

Table 3.1 gives an indication that the films at 0.60Pa (4.5×10^{-3}Torr) sputtering pressure have a high degree of crystallinity in each series. As the film thickness in each series is not uniform, some care should be taken with this conclusion. Some difficulties were found in identifying NiCr film structures because the copper and nickel-chrome peaks overlap in the same position. The Ti film at 1.3Pa (1.0×10^{-2}Torr) shows a small peak that seems to be titanium oxide. This may be due to the possibility of oxygen incorporation in the film, when the argon pressure is increased.

Film Material	*Sputtering Conditions*		*Film Thickness*	*XRD Peaks (counts)*			
Al	Pressure (Pa)	Power (WRF)	*(μm)*	(111) Al	(200) Al	(220) Al	(311) Al
System cubic	0.2		2.5	171	184	-	-
(FCC)	0.6		7.1	245	141	135	-
a=4.0494Å	1.0	300	7.9	360	114	81	110
Slip plane (111)	1.3		3.5	334	146	-	-
	2.7		3.5	262	-	129	-
	0.2		5.4	365	105	-	123
	0.6		5.1	282	130	-	-
	1.0	400	6.2	388	157	-	107
	1.3		6.7	283	111	127	137
	2.7		4.6	393	157	143	-
NiCr				(111) Ni	(220) Ni		
System cubic (FCC)	0.2		3.6	918	140		
	0.6		5.0	2462	-		
	1.0	200	3.0	663	-		
	1.3		2.8	659	-		
	2.7		2.0	878	-		
Ti				(010)Ti	(002) Ti	(011)Ti	(200)TiO$_2$
System hexagonal	0.6		2.7	365	295	190	-
a=2.9509Å : c=4.6788Å	1.0	300	2.2	167	225	119	-
Slip plane (001)	1.3		2.5	-	279	112	109
Mo				(110)Mo	(200)Mo		
System cubic (BCC)	0.2		4.7	2075	-		
a=3.1472Å	0.6		3.8	954	95		
Slip plane (112)	1.0	250	4.8	218	-		
	1.3		3.6	314	-		
	2.7		3.6	109	-		
TiB$_2$				(001)TiB$_2$			
System hexagonal	0.2	300	1.6	192			
a=3.028Å	0.6	300	1.5	-			
c=3.228Å	1.0	300	1.7	-			
Slip plane (001)	2.7	300	1.4	-			

Table 3.1. X-ray diffraction peaks and preferential growth plane for Al, Ti, NiCr, Mo and TiB$_2$ films in function of the sputtering conditions.
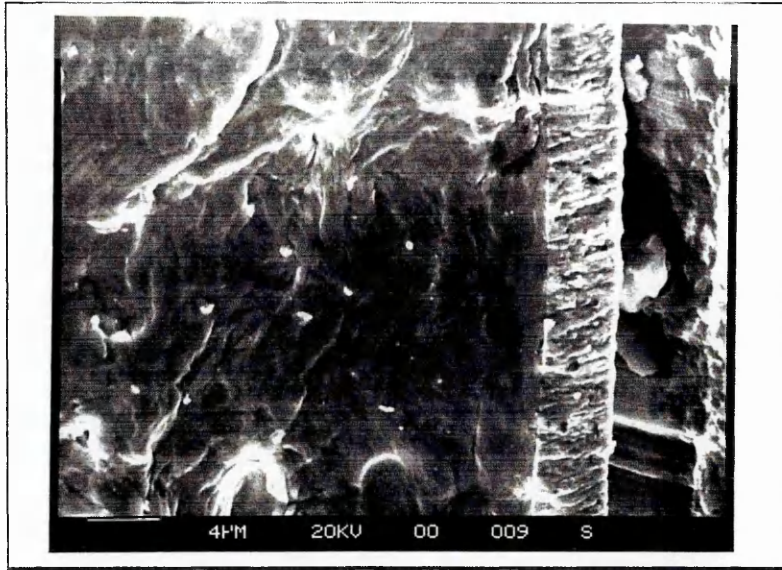
Photograph 3.2. Mo film microstructure onto copper for 0.6Pa at 250WRF.
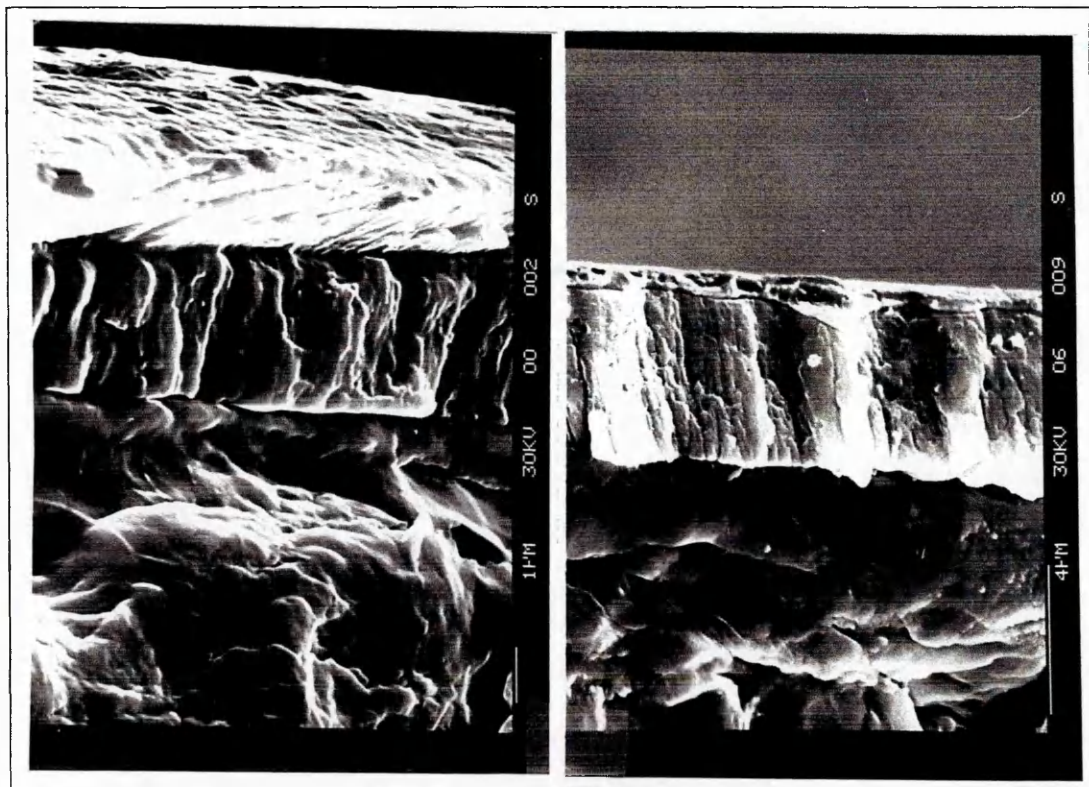
Photograph 3.3. Ti film microstructure onto copper for 0.6Pa at 300WRF on the left. NiCr film onto copper for 0.6Pa at 200WRF on the right.
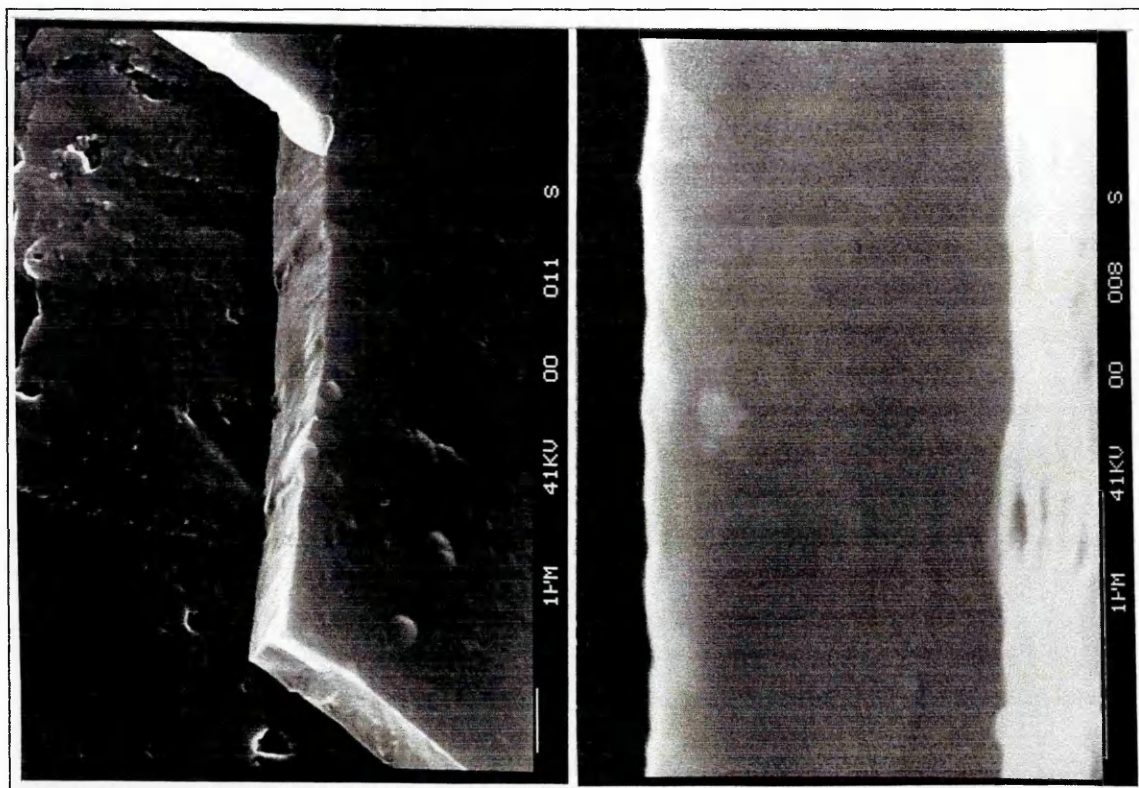
Photograph 3.4. TiB$_2$ film microstructure onto copper for 0.6Pa sputtering pressure at 300WRF sputtering power.

The chemical analysis of the TiB$_2$ films was performed by XPS for Ti 2p, B 1s and O 1s spectra, as shown in figures 3.17 to 3.19. The sputter conditions of the analysed samples are:

- ♦ TB5: TiB$_2$ onto Cu for 300WRF power and 0.2Pa (1.5×10^{-3}Torr) Ar pressure
- ♦ TB3: TiB$_2$ onto Cu for 300WRF power and 1.0Pa (7.5×10^{-3}Torr) Ar pressure
- ♦ TB6a: TiB$_2$ onto Al for 300WRF power and 1.3Pa (1.0×10^{-2}Torr) Ar pressure

The Ti 2p spectrum shows that the samples TB5 and TB3 have similar bonding behaviour, while the TB6a bonding was slightly different. Moreover, all samples follow the TiB$_2$ standard spectrum. Similar behaviour was observed for the B 1s spectrum. The O 1s spectrum shows that the samples TB5 and TB3 have similar bonding behaviour but the TB6a peak is shifted slightly to the left. This latter sample may have a higher fraction of oxygen atoms, consistent with it being deposited at high pressure. The stoichiometry of TiB$_2$ onto copper for 300WRF sputtering power and 1.0Pa (7.5×10^{-3} Torr) sputtering pressure was found to be TiB$_{\cong 1.6}$, i.e. below stoichiometry.

The TiB$_2$ deposited on an Al substrate, sputtered at 1.0Pa (7.5×10^{-3}Torr) argon pressure with 300WRF sputtering power, was analysed by the TEM technique. The TEM sample was prepared by the microtome technique. The photograph 3.5 shows a small piece of the coating bonded to the Al substrate grains. The chemical analysis trace at the interface found an AlB compound, while in the coating a TiB$_x$ compound dominated, as illustrated in figure 3.20.
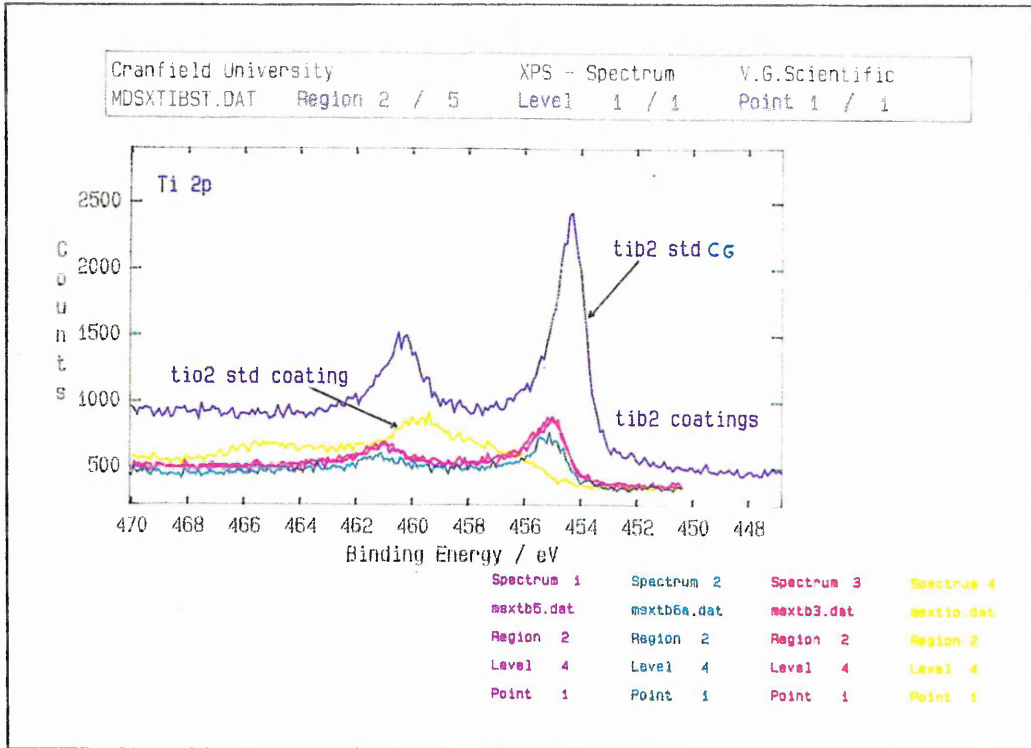
Figure 3.17. XPS spectrum for Ti 2p of the TiB_2 coatings.
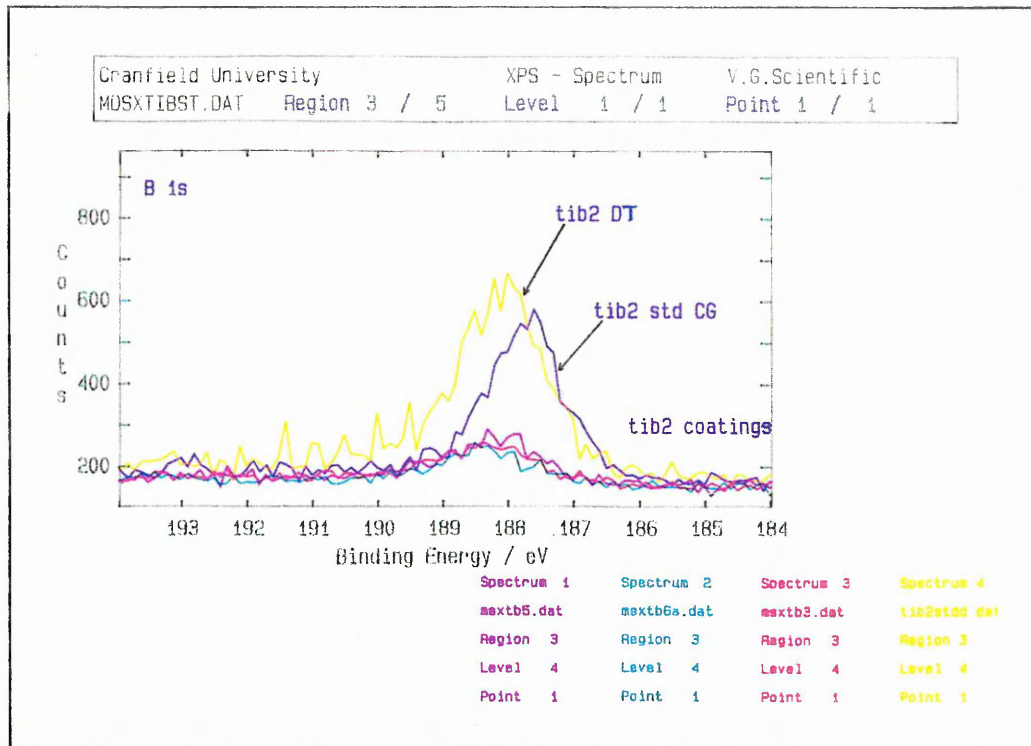
Figure 3.18. XPS spectrum for B 1s of the TiB_2 coatings.
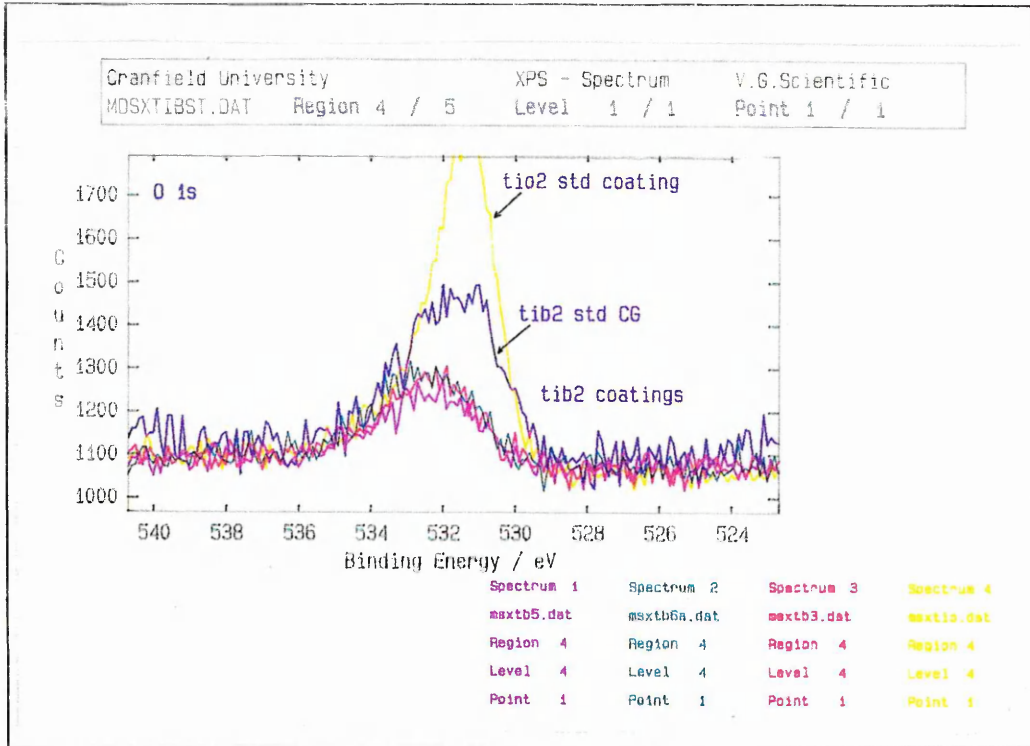
Figure 3.19. XPS spectrum for O 1s of the TiB$_2$ coatings.
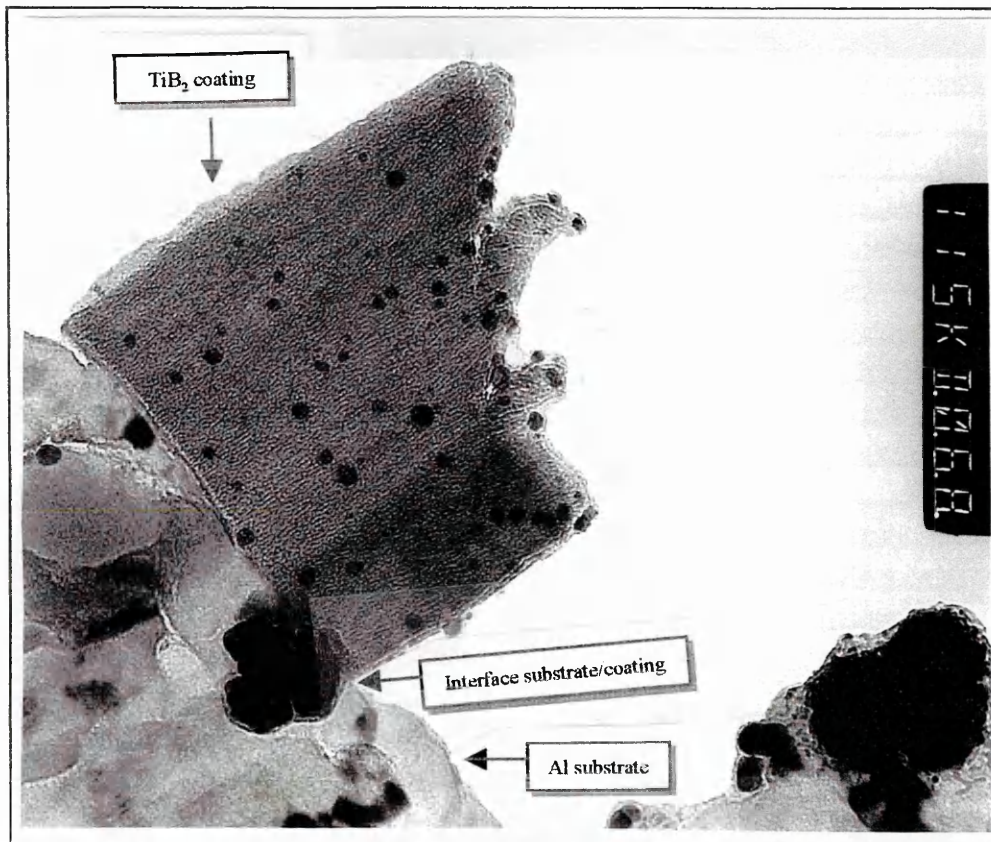
Photograph 3.5. TiB$_2$ film microstructure onto Al for 1.0Pa sputtering pressure at 300WRF sputtering power.
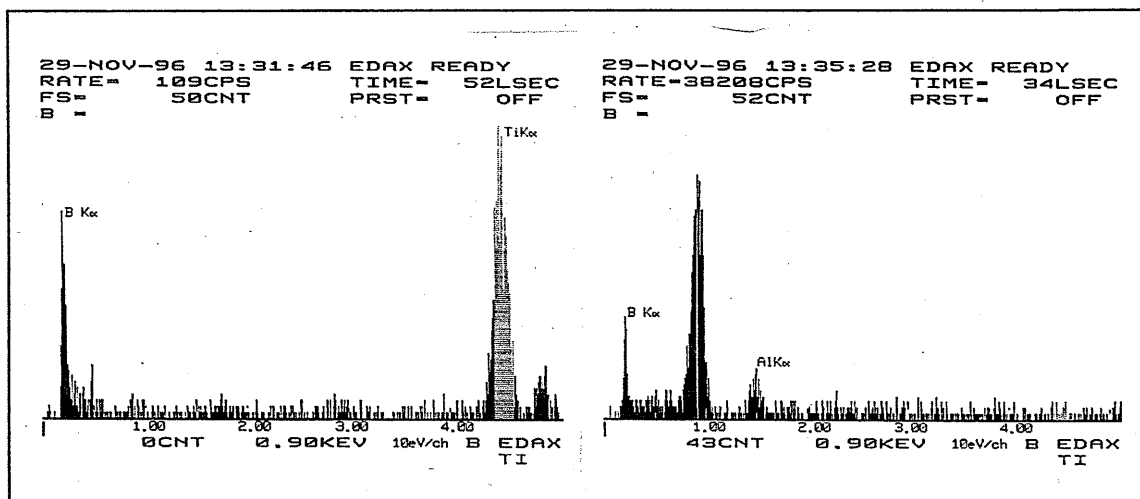
Figure 3.20. EDAX analysis for TiB_2 film onto Al for 1.0Pa sputtering pressure at 300WRF sputtering power.

3.16. SUMMING UP

The preliminary deposition studies of single coatings such as: Al, NiCr, Ti, Mo, TiB_2 were performed giving the following information:

♦ Al, NiCr and Mo films show typical sputtering deposition curves of deposition rate versus the sputtering pressure, while the deposition rate for TiB_2 and Ti seems not to be affected by the sputtering pressure. The Ti films may reflect some sputtering parameter effects because this would not be expected for metal systems such as titanium.

♦ For a given sputtering pressure of 0.6Pa the deposition rate increases with the sputtering yield for Ti, Mo, and Al films

♦ Considering the sputtering conditions studied, increasing either the sputtering pressure or RF power increases the DC offset voltage measured on Al, Mo, NiCr, Ti and TiB_2 target voltage.

♦ The substrate temperature was found to be lower than 200°C for all single-layer coatings in the range of sputtering conditions studied.

♦ The two main parameters that affect the thickness of the Al and TiB_2 coating uniformity are the argon flux position and the target erosion area. The former was found to prevail over the erosion area for Al coatings. Hence, high deposition rate values are found next to the argon source. The target erosion area was found to dominate the deposition rate of the TiB_2 coatings, positioning the high values at the centre of the target. The film thickness uniformity would be expected to affect the mechanical properties of the film, as referred to in the literature (section 1.4.3).

♦ The specimen position arrangement inside the vacuum chamber (figure 2.2) was chosen according to the study of the substrate position effect within the vacuum chamber on the deposition rate. The TiB_2 film thickness uniformity was modelled

by considering the target erosion area as two vapour sources that confirm the measured thickness of the coatings.

♦ The stoichiometry of the TiB_2 films at 1.0Pa sputtering pressure for 300WRF sputtering power was found to be $TiB_{\cong1.6}$. The AlB compound formed at the interface between coating and Al substrate, while within the coating the TiB_x compound prevails. The TiB_2 coatings between 1.4 to 1.6μm thickness were found to be amorphous.

These deposition studies of the preliminary single coatings indicate that the optimum sputtering conditions to produce the multilayer coatings should be as follows:

♦ *Aluminium deposition:* 0.6Pa (4.5×10^{-3}Torr) argon pressure at 400WRF power

♦ *Titanium deposition:* 0.6Pa (4.5×10^{-3}Torr) argon pressure at 300WRF power

♦ *Nimonic 75 alloy (NiCr) deposition:* 0.6Pa (4.5×10^{-3}Torr) Ar pressure at 200WRF power

♦ *Molybdenum deposition:* 0.6Pa (4.5×10^{-3}Torr) argon pressure at 250WRF power

♦ *TiB_2 deposition:* 0.6Pa (4.5×10^{-3}Torr) argon pressure at 300WRF power

All the substrate was sputtered clean with a negative D.C. bias of 40V for one hour to improve adhesion to the substrate. Hence, all the films produced under these sputter conditions were adherent to the steel, copper and aluminium substrates

The two main limitations of the deposition studied are:

♦ The deposition temperature was limited by the ceramic target temperature

♦ The film thickness uniformity depends on the argon source position and the target erosion area and also on the target material.

The former influences the degree of crystallinity achieved in the TiB_2 layers, while the later may affect the reproducibility of the multilayer coatings from one substrate position to another.

3.2. BI-LAYERS COATINGS DEPOSITION

LAYOUT
⇓
Sputtering Deposition Conditions
⇓
Characterization of the Coating Microstructure
⇓
Mechanical Properties Measurements: Hardness and
Elastic Modulus by Nanoindentation
⇓
Summing up
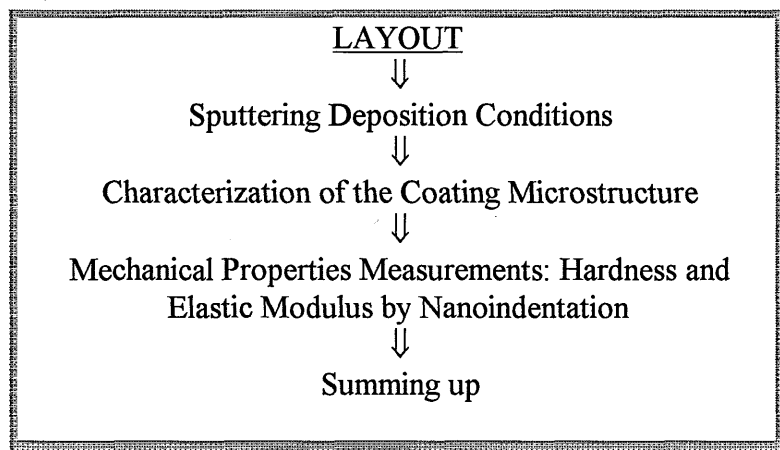
3.2.1. SPUTTERING DEPOSITION CONDITIONS

Following the study on single-layer coatings, the deposition conditions for the two-layer coatings, were selected for different metal layers such as Al, NiCr, Ti, Mo, as the underlay with TiB_2 on top. These are given in table 3.2. The total thickness of the coatings was designed to be 5μm for 50% of the volume fraction of ceramic.

Coating System	Substrate	Sputtering pressure (Pa)	Sputtering power of metal layer (WRF)	Sputtering power of ceramic layer (WRF)
Al/TiB$_2$	Steel, Al, Cu	0.6	400	300
Al/TiB$_2$	Steel, Al, Cu	1.0	400	300
NiCr/TiB$_2$	Steel, Al, Cu	0.6	200	300
Ti/TiB$_2$	Steel, Al, Cu	0.6	300	300
Ti/TiB$_2$	Steel, Al, Cu	0.6	250	300
Mo/TiB$_2$	Steel, Al, Cu	0.6	250	300

Table 3.2. Sputtering conditions of the bi-layer coatings.

3.2.2. CHARACTERIZATION OF THE COATING MICROSTRUCTURE

The microstructure characterization was performed by impact-fracture cross-section samples, as shown in photographs 3.6 to 3.11. The TiB_2 layer on top of the two-layer coatings shows either a crystalline or amorphous structure which is also observed to vary with the metal layer topography. The Al layer structure is deformed by the fracturing method. The NiCr layer structure was consistent with the transition zone of Thornton's model. The Mo intermediate layer onto aluminium and steel substrate seems to be placed in zone 1. These films deform during fracturing and may alter the apparent thickness ratio, as can be seen in figures 3.10 and 3.11. The actually thickness ratio is given in table 3.3.
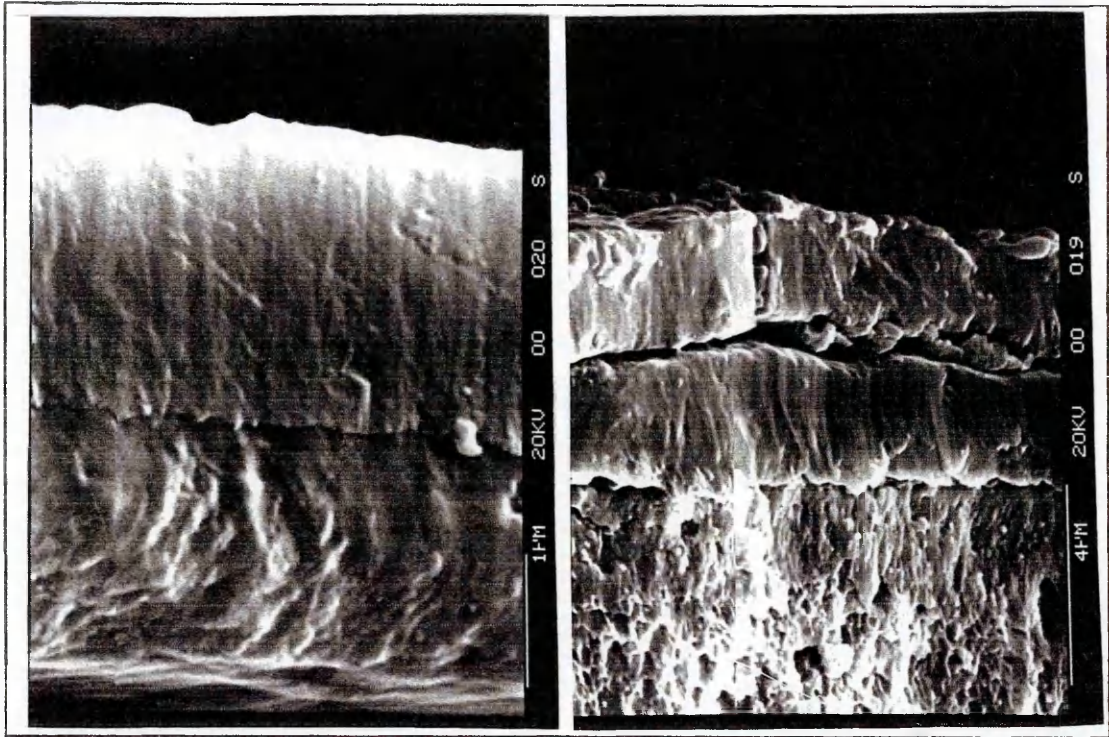
Photograph 3.6. Al/TiB$_2$ two-layer microstructure at 1.0Pa (7.5×10^{-3}Torr) pressure on copper substrate on the left and on steel substrate on the right.
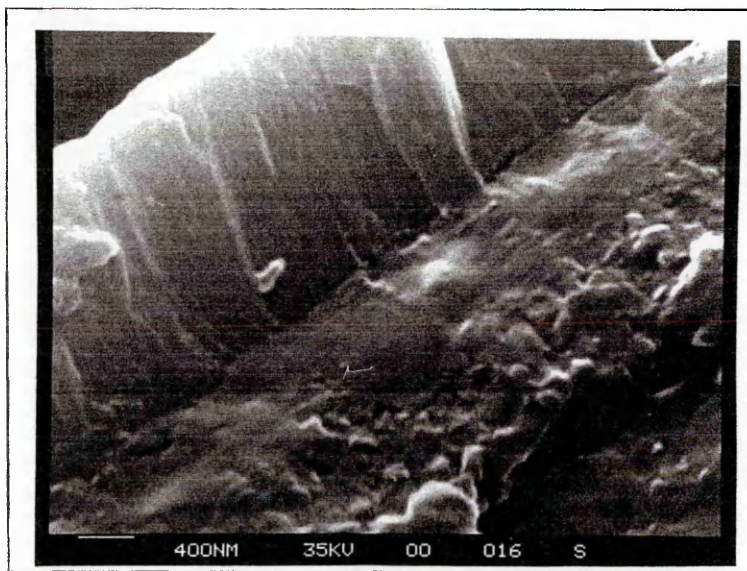
Photograph 3.7. Al/TiB$_2$ two-layer microstructure on Al substrate at 1.0Pa (7.5×10^{-3}Torr) sputtering pressure.

189
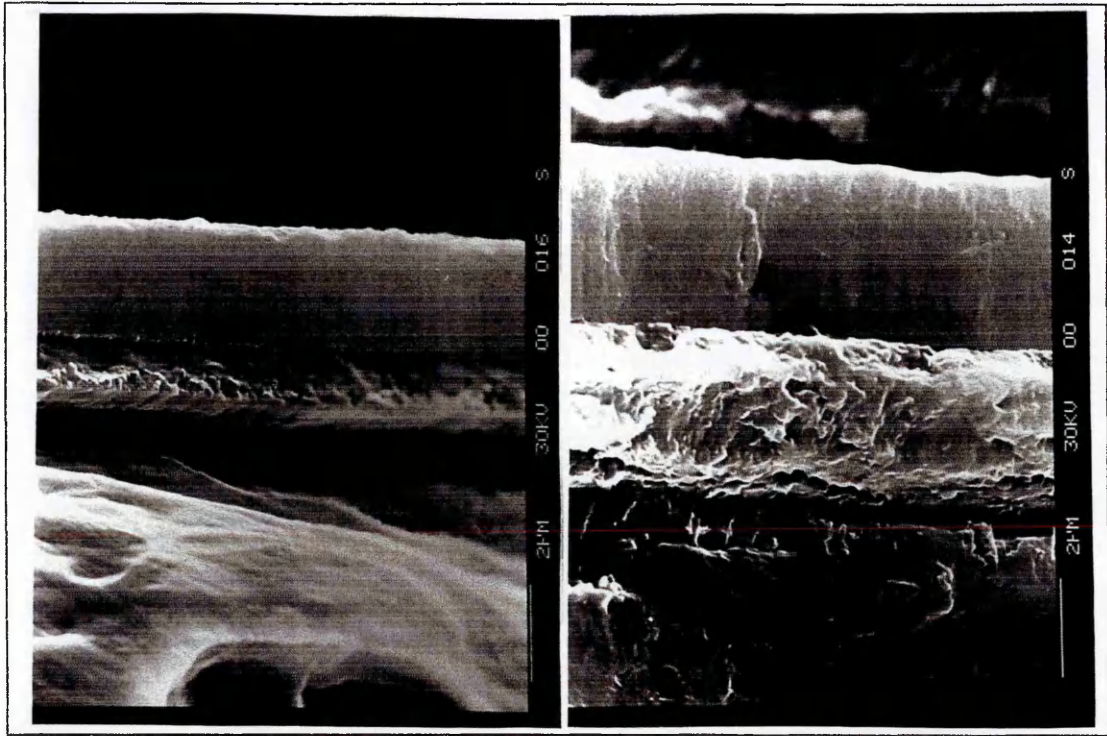
Photograph 3.8. Al/TiB$_2$ two-layer microstructure at 0.6Pa (4.5×10^{-3}Torr) pressure on copper substrate on the left and on Al substrate on the right.
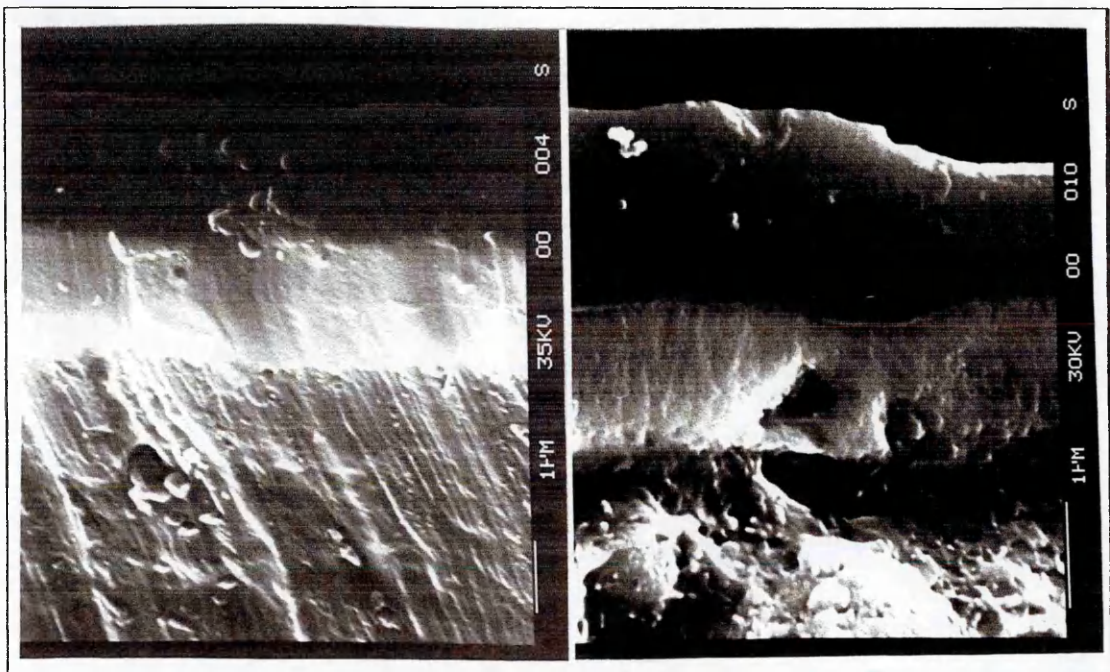
Photograph 3.9. NiCr/TiB$_2$ two-layer microstructure on copper substrate on the left and on steel substrate on the right.

190
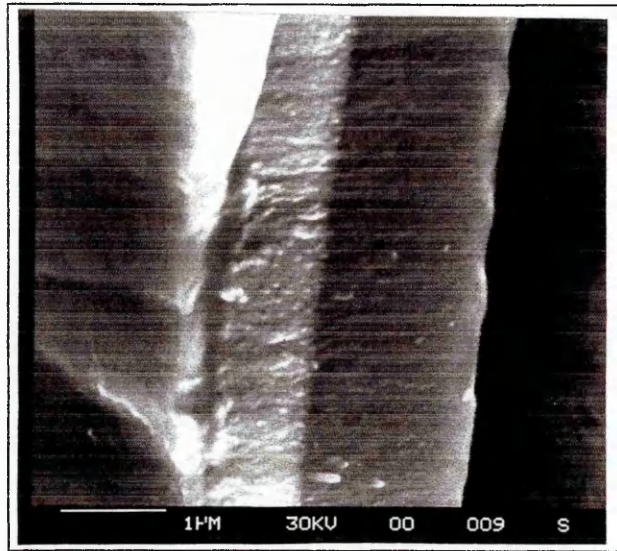
Photograph 3.10. NiCr/TiB$_2$ two-layer microstructure on Al substrate.
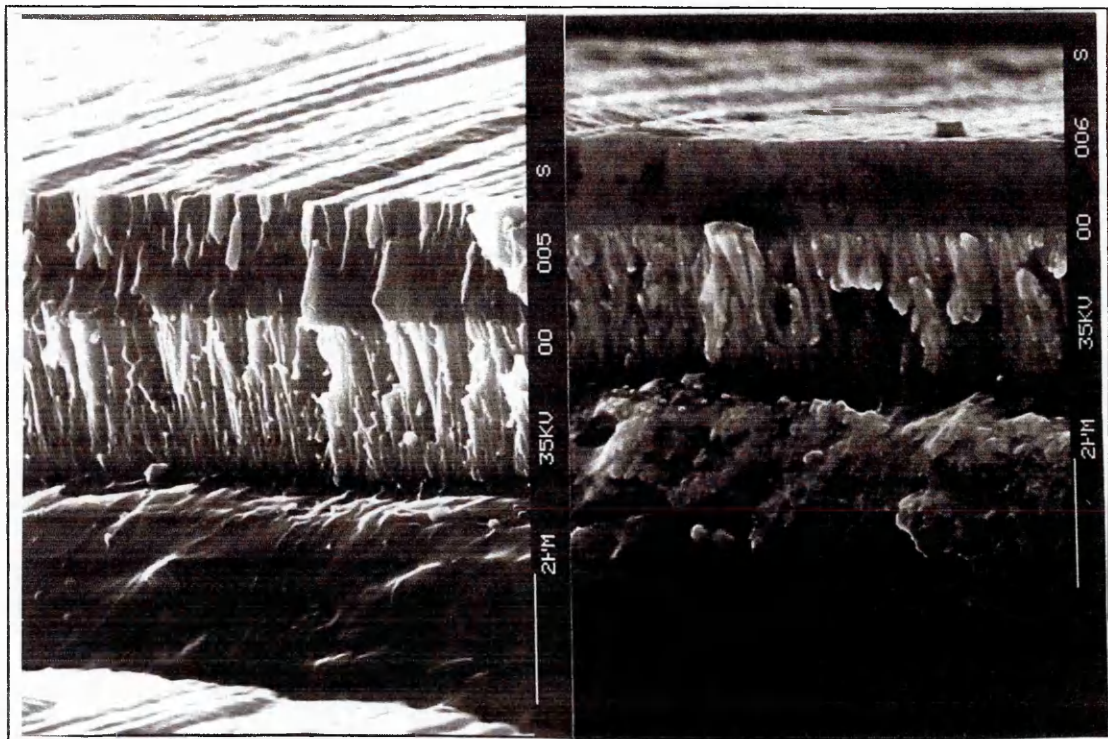
Photograph 3.11. Mo/TiB$_2$ two-layer microstructure on Al substrate on the left and on steel on the right.

The degree of crystallinity of the bi-layer coatings was evaluated by XRD spectra, as shown in table 3.3. The XRD spectrum was performed with the same operating conditions as the single-layer coatings described in section 3.1.

The TiB$_2$ layer onto Al shows a very fine columnar structure with preferential reflections of (001) and (002) which correspond to the close packed planes of TiB$_2$ (001) in all of the bi-layer coating systems. The apparent degree of crystallinity depends on the

thickness of the TiB_2 layer, as shown in table 3.3. The Al layer seems to have a very ductile structure, as apparent from the fracture technique, and this has hidden the real coating structure. At 0.6Pa (4.5×10^{-3}Torr) the Al layer shows very small and broad peaks. The XRD spectrum values for the bi-layer coatings in table 3.3 are in the appendix.

The TiB_2 structure on NiCr is similar to that of the Al/TiB_2 system. The $NiCr/TiB_2$ coatings do not show any detectable NiCr peaks through the TiB_2 layer, unless they overlap with Al, Cu, Fe peaks (from the substrate) for the interplanar spacing between 2.02 to 2.04Å. The TiB_2 structure onto Mo shows a very fine column structure on steel substrate, and a coarse column structure on the Al substrate. The XRD spectrum shows the preferential reflections (001) and (002) for the TiB_2 layer and crystalline peaks for the Mo layer.

Film Material	Substrate Material	Sputtering Conditions		Layer Thickness (μm)		X-Ray Diffraction Peaks (counts)				
		Pressure (Pa)	Power (WRF) Metal/TiB₂	Metal	TiB₂	(001) TiB₂	(002) TiB₂	(111) Al	(110) Mo	(211) Mo
Al/TiB₂	Steel (4)	0.6		-	-	812	-	-		
	Al (1)	0.6		3.1	3.5	2408	1101	-		
	Cu	0.6	400/300	1.5	2.0	117	-	-		
	Steel	1.0		2.5	2.5	1084	460	420		
	Al (1)	1.0		1.7	2.0	196	-	-		
	Cu	1.0		2.0	2.3	1666	838	-		
NiCr/TiB₂	Steel	0.6		1.3	2.0	2161	1323			
	Al	0.6	200/300	1.5	1.7	529	360			
	Cu	0.6		1.3	1.7	2060	1083			
Mo/TiB₂	Steel	0.6	250/300	2.0	1.3	1796 (2)	1000		2343	269
	Cu	0.6	250/300	-	-	292 (2)	215		348	358 (3)
(1) The Al peaks can be the same for the film and substrate										
(2) These peaks are shifted from 3.21Å to 3.4Å										
(3) This peak can overlap with Cu peak										
(4) The Al peak can overlap with Fe peak										

Table 3.3. X-ray diffraction peaks and preferential growth plane for Al/TiB_2, $NiCr/TiB_2$ and Mo/TiB_2 two-layer coatings.

Chemical analysis was performed by Auger depth profile, as shown in figures 3.21 to 3.23 for the Al/TiB_2 system at 1.0Pa (7.5×10^{-3}Torr) sputtering pressure. The figures 3.21 and 3.22 were obtained by ion etching through the coating and then doing a linear scan across the interface to analyse the elements. Ti and B were found in the TiB_2 layer and Al in the Al layer. The Oxygen peak was practically non-existent. The slope at the interfaces could be due to either the interdiffusion between the two phases, suggesting an AlB_x phase or a result of the ion etching. To investigate the diffusion effect it is necessary to compare the slope of the etch ion crater with the spectrum. The Auger depth profile gives a good topography of the analysed area with distinction of the two layers.

To reduce the duration of the analysis the same samples were dimpled, rather than ion etched. The figure 3.23 shows the Auger results of the linear scan across the interface of the wall of the crater. This method reduces the duration of the analysis but introduces, oxygen contamination. This oxygen could come from either Al oxidation under atmospheric conditions or oxidation during the dimpling process.
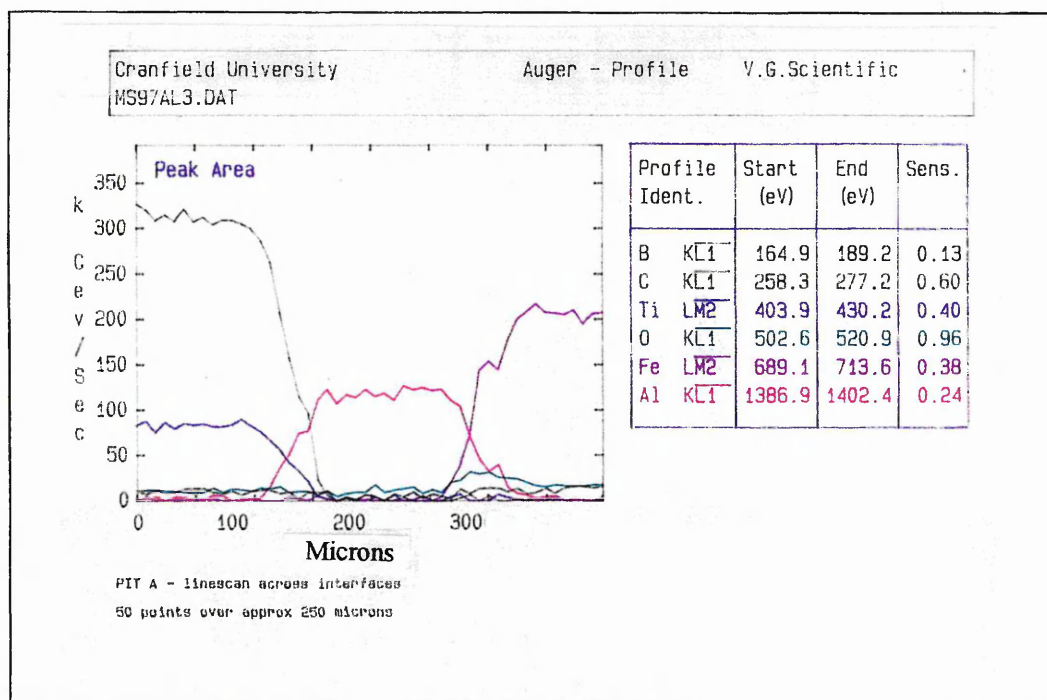
Figure 3.21. Auger depth profile for Al/TiB$_2$ coatings by ion etching for 50 points over 250 μm.
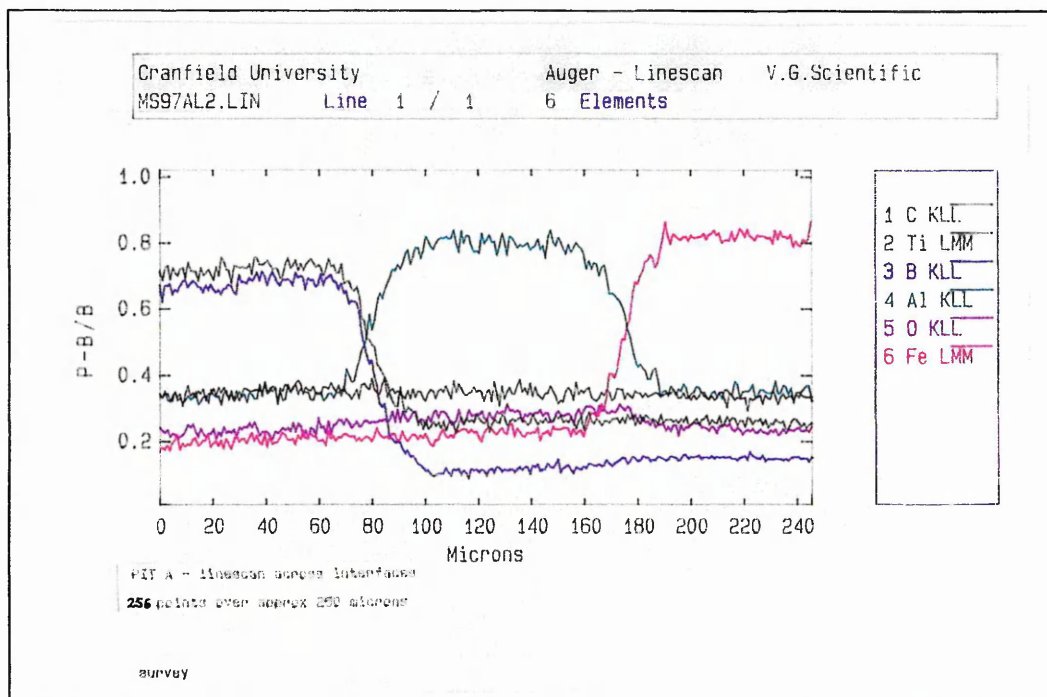
Figure 3.22. Auger depth profile for Al/TiB$_2$ coatings by ion etching for 256 points over 250 μm.
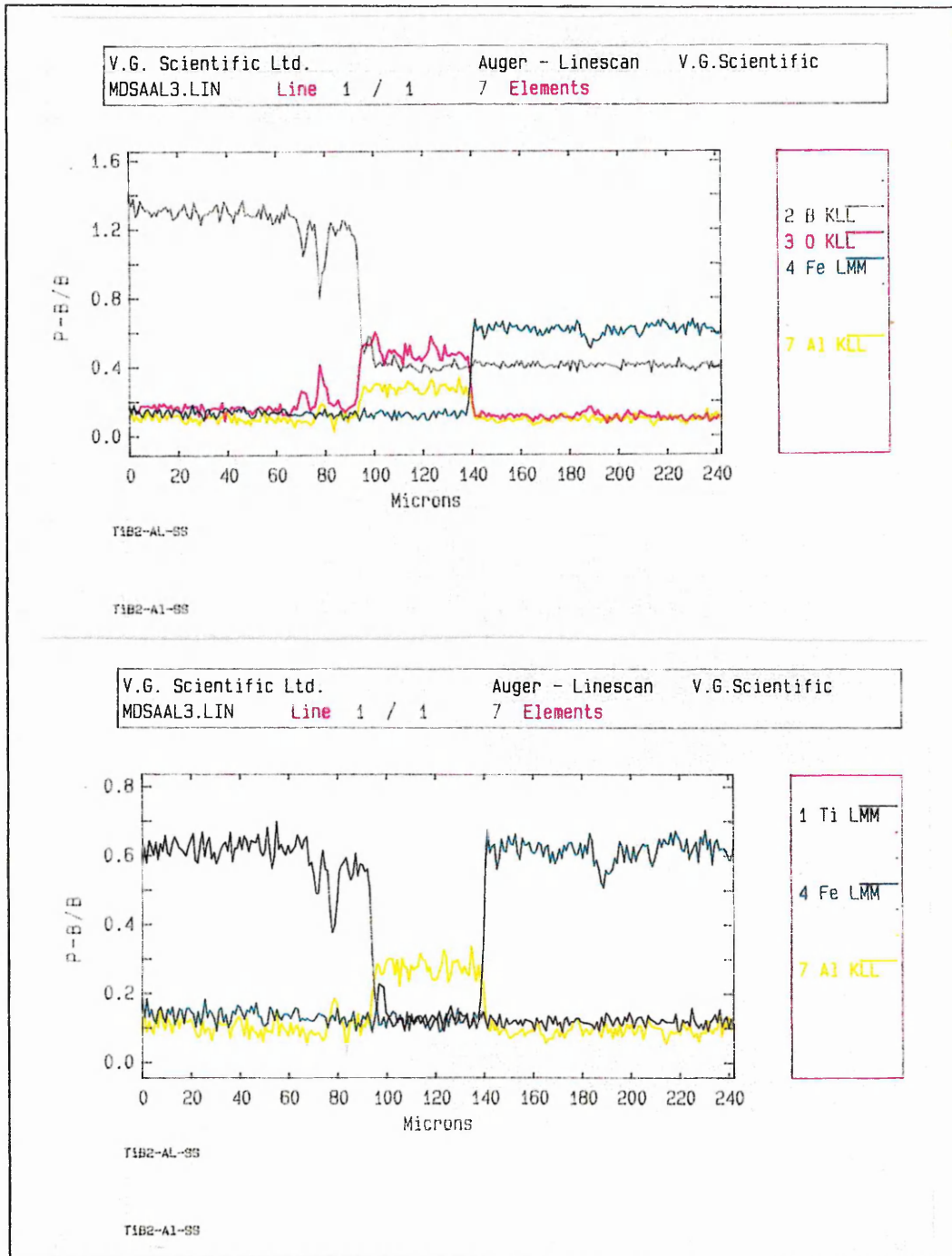
Figure 3.23. Auger depth profile for Al/TiB$_2$ coatings by dimpling process.

3.2.3. MECHANICAL PROPERTIES MEASUREMENTS

The hardness and elastic modulus measurements of the two-layer coatings were performed by nanoindentation, using a nanoindenter 550. Analysis was based on the Oliver and Pharr model with a Berkovitch indenter. The samples were mounted on aluminium stubs by means of a cyanoacrylate adhesive. All sample surfaces were cleaned by rinsing with ethanol and blowing off with an air duster. The parameters set up for the experiments and the sputtering conditions of the bi-layer coatings on steel and aluminium

substrate are shown in table 3.4 and 3.5 respectively. A dwell time at maximum load of 10 seconds was applied to all experiments, allowing for possible time dependent plastic deformation. The amplifier gain of 100 was applied to all experiments. Figure 3.24 shows an example of parameters set up and analysis information about the experiment.
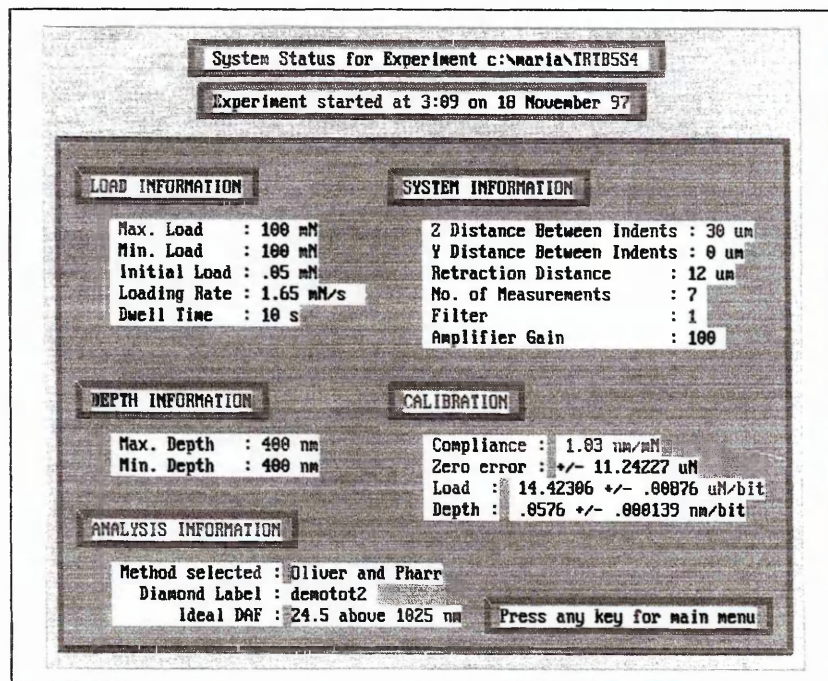
Figure 3.24. An example of parameters set up for nanoindentation.

Coating System (Steel substrate)	Sputtering Power (WRF) (metal / ceramic)	Sputtering Pressure (Pa)	Max. Load (mN)	Initial Load (mN)	Rate (mN/s)	Max. Depth (nm)	Complaince C(nm/mN)	Zero Error (±µN)	Calibration Load (µN/bit)	Calibration depth (nm/bit)	Drift Correction
Al/TiB$_2$	400/300	1.0	64	0.05	0.45	200	1.03	1.09	2.1±0.002	0.058±0.0001	y
Al/TiB$_2$	400/300	1.0	100	0.05	1.65	400	1.03	2.91	14.4±0.009	0.058±0.0001	y
Al/TiB$_2$	400/300	0.6	66	0.1	0.13	200	1.08	-	2.1±0.002	0.052±0.0002	n
Al/TiB$_2$	400/300	0.6	66	0.1	0.46	400	1.08	-	2.1±0.002	0.052±0.0002	n
NiCr/TiB$_2$	200/300	0.6	66	0.1	0.13	200	1.08	-	2.1±0.002	0.052±0.0002	n
NiCr/TiB$_2$	200/300	0.6	66	0.1	0.46	400	1.08	-	2.1±0.002	0.052±0.0002	n
Mo/TiB$_2$	250/300	0.6	66	0.05	0.45	200	1.03	-	2.1±0.002	0.058±0.0001	y
Mo/TiB$_2$	250/300	0.6	100	0.05	1.65	400	1.03	-	14.4±0.009	0.058±0.0001	y
Ti/TiB$_2$-1st read.	300/300	0.6	66	0.1	0.46	200	1.08	-	2.1±0.002	0.052±0.0002	n
Ti/TiB$_2$-2nd read.	300/300	0.6	66	0.05	0.45	200	1.03	1.57	2.1±0.002	0.058±0.0001	y
Ti/TiB$_2$-1st read.	300/300	0.6	66	0.1	1.03	400	1.08	-	2.1±0.002	0.052±0.0002	n
Ti/TiB$_2$-2nd read.	300/300	0.6	100	0.05	1.65	400	1.03	11.24	14.4±0.009	0.058±0.0001	y
Ti/TiB$_2$	250/300	0.6	66	0.1	0.46	200	1.08	-	2.1±0.002	0.052±0.0002	n
Ti/TiB$_2$-1st read.	250/300	0.6	66	0.1	1.03	400	1.08	-	2.1±0.002	0.052±0.0002	n
Ti/TiB$_2$-2nd read.	250/300	0.6	100	0.05	1.65	400	1.03	3.78	14.4±0.009	0.058±0.0001	y

Table 3.4. Parameters set up of the nanoindentation experiments for bi-layer coatings on steel.

Coating System (Al substrate)	Sputtering Power (WRF) (metal / ceramic)	Sputtering Pressure (Pa)	Max. Load (mN)	Initial Load (mN)	Rate (mN/s)	Max. Depth (nm)	Complaince C(nm/mN)	Zero Error (±µN)	Calibration Load (µN/bit)	Calibration depth (nm/bit)	Drift Correction
Al/TiB$_2$	400/300	1.0	64	0.05	0.45	200	1.03	2.82	2.1±0.002	0.058±0.0001	y
Al/TiB$_2$	400/300	1.0	100	0.05	1.65	400	1.03	-	14.4±0.009	0.058±0.0001	y
Al/TiB$_2$	400/300	0.6	66	0.1	0.13	200	1.08	-	2.1±0.002	0.052±0.0002	n
Al/TiB$_2$	400/300	0.6	66	0.1	0.46	400	1.08	-	2.1±0.002	0.052±0.0002	n
NiCr/TiB$_2$	200/300	0.6	66	0.1	0.13	200	1.08	-	2.1±0.002	0.052±0.0002	n
NiCr/TiB$_2$	200/300	0.6	66	0.1	0.46	400	1.08	-	2.1±0.002	0.052±0.0002	n
Mo/TiB$_2$	250/300	0.6	66	0.05	0.45	200	1.03	-	2.1±0.002	0.058±0.0001	y
Mo/TiB$_2$	250/300	0.6	100	0.05	1.65	400	1.03	6.29	14.4±0.009	0.058±0.0001	y
Ti/TiB$_2$-1st read.	300/300	0.6	66	0.1	0.46	200	1.08	-	2.1±0.002	0.052±0.0002	n
Ti/TiB$_2$-2nd read.	300/300	0.6	66	0.05	0.45	200	1.03	3.43	2.1±0.002	0.058±0.0001	y
Ti/TiB$_2$-1st read.	300/300	0.6	66	0.1	0.46	400	1.08	-	2.1±0.002	0.052±0.0002	n
Ti/TiB$_2$-2nd read.	300/300	0.6	100	0.05	1.65	400	1.03	8.63	14.4±0.009	0.058±0.0001	y
Ti/TiB$_2$-1st read.	250/300	0.6	66	0.1	0.46	200	1.08	-	2.1±0.002	0.052±0.0002	n
Ti/TiB$_2$-2nd read.	250/300	0.6	66	0.05	0.45	200	1.03	1.09	2.1±0.002	0.058±0.0001	y
Ti/TiB$_2$-1st read.	250/300	0.6	66	0.1	1.03	400	1.08	-	2.1±0.002	0.052±0.0002	n
Ti/TiB$_2$-2nd read.	250/300	0.6	100	0.05	1.65	400	1.03	3.84	14.4±0.009	0.058±0.0001	y

Table 3.5. Parameters set up of the nanoindentation experiments for bi-layer coatings on aluminium.

The raw data of the force-displacement curves recorded at each indentation depth were processed based on the Oliver and Pharr method. A correction was made for the previously calibrated machine compliance (C_s), diamond area function (A_c) and contact depth (h_c), with 80% unloading data used for the power law curve fitting and ε being taken as 0.75. The calculation of hardness (H) and elastic modulus (E) values of the tested samples used equations 1.18, 1.23 and 1.19 in the section 1.5.3. These are reproduced below:

$$H = \frac{P_{max.}}{A_c}$$

$$E_r = \left(\frac{\sqrt{\pi}}{2}\right) \times \left(\frac{1}{\sqrt{A_c}}\right) \times \left(\frac{1}{C_s}\right)$$

$$\left(\frac{1}{E_r}\right) = \left[\frac{\left(1 - \upsilon_s^2\right)}{E_s}\right] + \left[\frac{\left(1 - \upsilon_i^2\right)}{E_i}\right]$$

Where E_i and υ_i are the Young's modulus and Poisson's ratio for the diamond indenter, which were taken as 1141GPa and 0.07 respectively. E_s and υ_s are the Young's modulus and Poisson's ratio for the tested samples. E_s was unknown and to be measured, υ_s was assumed to be 0.11 [12,17] for TiB$_2$ and the bi-layer coatings. The latter is due to the fact that the indentation only penetrates the outer layer (TiB$_2$) and so avoids the substrate effect. E_r is the reduced modulus from the raw data.

On each sample seven indentations were made at two different depths (200nm, 400nm). The elastic modulus and hardness results quoted are the average of five measurements, as shown in tables 3.6 and 3.7 for the steel and aluminium substrate respectively. The highest and lowest values were rejected as extremes. For example, the curves in figure 3.25A are due to variations in surface roughness, measured on the Mo/TiB$_2$ bi-layer. Also, the typical, unusual curves due to vibration or cracks were rejected, for example the curves of the figures 3.25B and 3.26.
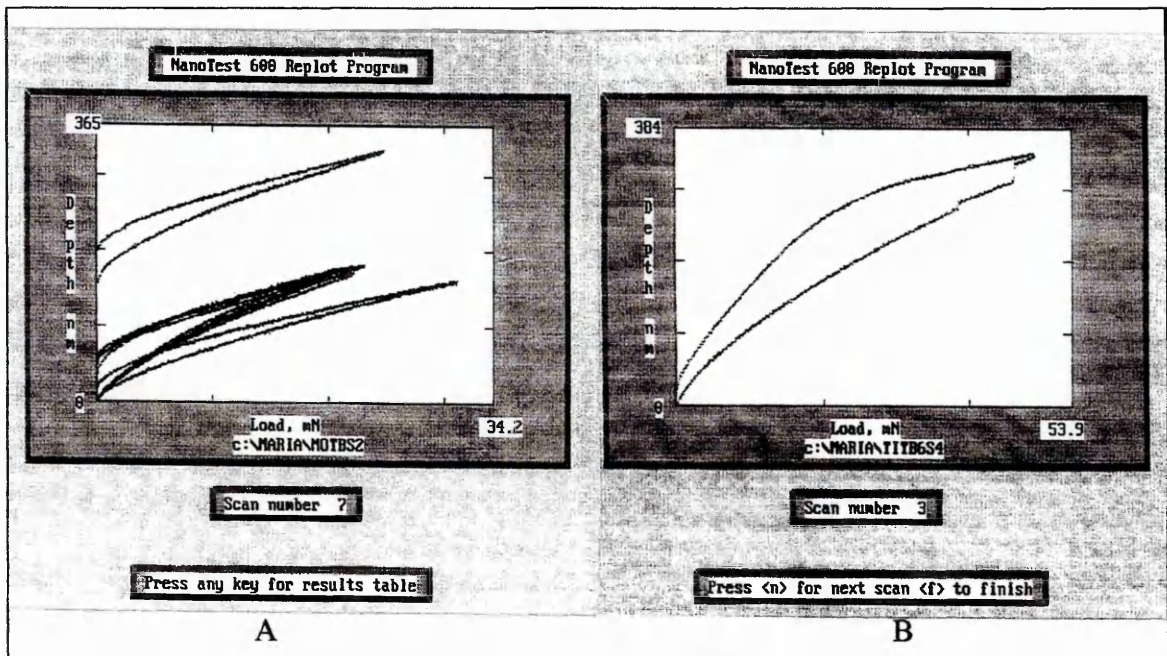
Figure 3.25. Nanoindentation curves due to surface roughness (A) and vibration or cracks (B).
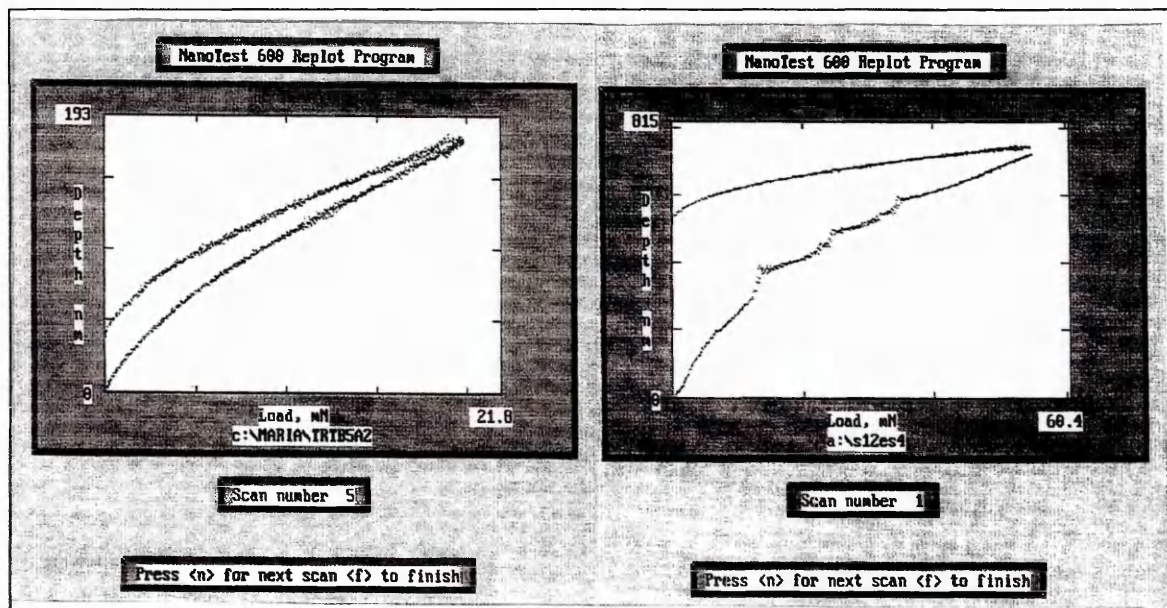
Figure 3.26. Nanoindentation curves due to vibration.

197

Coating System (Steel Substrate)	Sample Reference	Sputtering Power (WRF) (metal / ceramic)	Sputtering Pressure (Pa)	Poisson's Ratio (ν_s)	Plastic Depth (nm)	STDEV	Hardness (GPa)	STDEV	Elastic Modulus (GPa)	STDEV
Al/TiB$_2$	ALTB1S2	400/300	1.0	0.11	*121*	7	27.04	5.86	306.0	44.2
Al/TiB$_2$	ALTB1S4	400/300	1.0	0.11	255	8	21.70	1.30	237.9	12.0
Al/TiB$_2$	ALTB2S2	400/300	0.6	0.11	*98*	5	45.89	4.71	367.9	58.4
Al/TiB$_2$	ALTB2S4	400/300	0.6	0.11	212	13	39.66	4.19	341.5	17.7
NiCr/TiB$_2$	NCTBS2	200/300	0.6	0.11	*106*	6	46.33	7.52	493.2	117.8
NiCr/TiB$_2$	NCTBS4	200/300	0.6	0.11	186	34	31.14	13.21	305.8	74.7
Mo/TiB$_2$	MoTBS2	250/300	0.6	0.11	*112*	3	34.12	1.58	362.9	16.3
Mo/TiB$_2$	MoTBS4	250/300	0.6	0.11	222	6	34.79	2.79	342.6	19.7
Ti/TiB$_2$-1st read.	TITB5S2	300/300	0.6	0.11	*110*	5	37.39	3.19	370.4	21.8
Ti/TiB$_2$-2nd read.	TRTB5S2	300/300	0.6	0.11	*118*	6	28.65	2.75	326.7	34.4
Ti/TiB$_2$-1st read.	TITB5S4	300/300	0.6	0.11	219	7	37.19	4.05	339.8	26.1
Ti/TiB$_2$-2nd read.	TRTB5S4	300/300	0.6	0.11	231	11	28.27	3.26	261.9	11.6
Ti/TiB$_2$	TITB6S2	250/300	0.6	0.11	*105*	9	51.45	10.24	564.9	119.8
Ti/TiB$_2$-1st read.	TITB6S4	250/300	0.6	0.11	211	19	42.29	8.15	447.0	124.1
Ti/TiB$_2$-2nd read.	TRTB6S4	250/300	0.6	0.11	228	14	31.04	7.62	301.7	66.3

Table 3.6. Hardness and elastic modulus results for bi-layer coatings on steel substrate at two different depths (200nm, 400nm).

Coating System (Al Substrate)	Sample Reference	Sputtering Power (WRF) (metal / ceramic)	Sputtering Pressure (Pa)	Poisson's Ratio (ν_s)	Plastic Depth (nm)	STDEV	Hardness (GPa)	STDEV	Elastic Modulus (GPa)	STDEV
Al/TiB$_2$	ALTB1A2	400/300	1.0	0.11	*111*	6	28.27	1.89	241.1	5.1
Al/TiB$_2$	ALTB1A4	400/300	1.0	0.11	241	8	19.22	1.60	158.4	1.8
Al/TiB$_2$	ALTB2A2	400/300	0.6	0.11	*96*	10	33.78	5.62	210.6	10.7
Al/TiB$_2$	ALTB2A4	400/300	0.6	0.11	207	14	25.06	3.07	143.3	3.1
NiCr/TiB$_2$	NCTBA2	200/300	0.6	0.11	*111*	9	25.87	3.98	207.0	22.9
NiCr/TiB$_2$	NCTBA4	200/300	0.6	0.11	228	11	20.29	2.20	140.8	4.1
Mo/TiB$_2$	MoTBA2	250/300	0.6	0.11	*113*	5	29.17	2.07	283.9	12.2
Mo/TiB$_2$	MoTBA4	250/300	0.6	0.11	222	6	29.22	1.68	239.6	8.6
Ti/TiB$_2$-1st read.	TITB5A2	300/300	0.6	0.11	*112*	2	31.86	2.24	291.8	28.0
Ti/TiB$_2$-2nd read.	TRTB5A2	300/300	0.6	0.11	*113*	6	27.26	2.92	252.4	19.7
Ti/TiB$_2$-1st read.	TITB5A4	300/300	0.6	0.11	232	7	23.58	2.07	190.4	12.7
Ti/TiB$_2$-2nd read.	TRTB5A4	300/300	0.6	0.11	247	7	18.05	1.44	155.8	3.6
Ti/TiB$_2$-1st read.	TITB6A2	250/300	0.6	0.11	*113*	7	29.36	4.96	264.5	13.9
Ti/TiB$_2$-2nd read.	TRTB6A2	250/300	0.6	0.11	*114*	7	28.66	4.42	255.6	33.0
Ti/TiB$_2$-1st read.	TITB6A4	250/300	0.6	0.11	248	3	19.61	0.69	177.5	2.8
Ti/TiB$_2$-2nd read.	TRTB6A4	250/300	0.6	0.11	249	13	18.30	2.57	163.4	4.8

Table 3.7. Hardness and elastic modulus results for bi-layer coatings on Al substrate at two different depths (200nm, 400nm).

1. ANALYSIS OF THE HARDNESS RESULTS

Figures 3.27 to 3.29 show the hardness values for different bi-layer coating systems on steel substrates, while figures 3.30 to 3.32 show the hardness values for different bi-layer coating systems on aluminium substrates. The number below the coating system on the x-axis corresponds to the plastic depth. The number 1 or 2 next to the plastic depth corresponds to the first or second set of measurements. The label in each coating system gives information about either sputtering power or pressure or compliance of the nanoindentation measurements.

Figure 3.27 shows the hardness of the bi-layer coatings on steel substrates at 0.6Pa sputtering pressure for two indentation depths (200nm, 400nm). The effects of both the intermediate layer and the substrate give different values for the same coatings, at two different depths. The apparent hardness shows a tendency to drop with the plastic depth. Hence, the greater depth may have the interlayer or substrate effects incorporated in the results. However, it is more likely to be an intermediate layer effect because the thickness of each layer is about 2μm, as shown in table 3.3. The measurement at low plastic depth gives the more realistic value for the TiB_2 top layer.

Figure 3.28 shows the hardness results for Al/TiB_2 coatings on steel at different sputtering pressures (0.6Pa, 1.0Pa) and Ti/TiB_2 coatings on steel for two sets of measurements on the same sample. The Al/TiB_2 coating at 0.6Pa sputtering pressure shows much greater hardness than Al/TiB_2 coatings at 1.0Pa sputtering pressure. Moreover, the Ti/TiB_2 coatings show a great difference in hardness between the two sets of measurements, which is not expected. A statistical Anova analysis was, therefore, performed for Ti/TiB_2 coatings on steel substrate for two different sputtering powers of Ti layer (250WRF, 300WRF) and two sets of measurements in the same sample, as shown in table 3.8.

The Anova analysis, table 3.8, shows that the major source of error is between repeat measurements on the same sample (29.1%). The error of the reproducibility between samples (11.2%) reflects variations in sputtering conditions and overall measurement accuracy (3.3%) is less significant. The error between repeat measurements on the same sample reflects various measurement uncertainties (for example surface roughness, intrinsic point to point variation in the growth of the film) which were introduced during the experiments, as shown in table 3.4, such as: using two different indenters; replacing the spring of the equipment; thermal drift correction not performed for all experiments; load and depth calibration not kept constant for all experiments; the initial load calibration not done for many of the experiments. Hence, the high hardness values for the Al/TiB_2 coatings on steel compared to Mo/TiB_2 on steel (figure 3.27) may be due to these uncertainties in measurements.

Figure 3.30 shows the hardness values for different bi-layer coating systems on Al substrate at 0.6Pa sputtering pressure for two indentation depths. The apparent hardness value shows a tendency to drop with the plastic depth, as observed for the bi-layer coatings on steel substrate (figure 3.27). The variation in the hardness value is less significant for the $NiCr/TiB_2$ coatings on Al substrate compared to those on steel substrate.

Figure 3.31 is equivalent to figure 3.28 but for coatings on Al substrates. The variation in the hardness values for two sets of measurements on Ti/TiB$_2$ coatings is also observed for coatings on Al substrate. Similarly, the Al/TiB$_2$ coatings for different sputtering pressures show different hardness values but not so significant, as is shown by the Al/TiB$_2$ coatings on steel.

A statistical Anova analysis was also performed for Ti/TiB$_2$ coatings on Al substrates for two different sputtering conditions and two sets of measurements, considering two penetration depths, as shown in tables 3.9 and 3.10.

Tables 3.9 and 3.10 show that the major source of error is between repeat measurements on the same sample with 9.1% for 200nm depth and 17.2% for 400nm depth. This error reflects the measurement uncertainties mentioned before in this section. The error in reproducibility between samples is 1.9% for 200nm and 9.4% for 400nm depth. This error reflects the effect of sputtering conditions and also the intermediate layer for the two penetration depths. The overall measurement accuracy is 6.7% for 200nm depth and 10.6% for 400nm depth, which is significant compared to the variation within the samples.

To overcome some of the measurement uncertainties, before each schedule the nanoindentation machine was calibrated against quartz to give a value of 70GPa for the elastic modulus compared with a real value of 72GPa of elastic modulus. The figure 3.29 shows the hardness values for Al/TiB$_2$, Ti/TiB$_2$ and Mo/TiB$_2$ coatings on steel after this calibration of the nanoindenter. The hardness values of these coating systems for 200nm penetration depth were close to the TiB$_2$ monolayer coating with a value of 33.90GPa on the steel substrate (see table 3.33). On the other hand, the hardness values increase on going from Al/TiB$_2$ (27.04±5.86GPa) to Ti/TiB$_2$ (28.65±2.75GPa) and then Mo/TiB$_2$ coatings (34.12±1.58GPa). This must be due to an underlay (metal coating) effect as the hardness of this metal layer increases from Al to Ti to Mo.

The hardness values for Al/TiB$_2$, Ti/TiB$_2$ and Mo/TiB$_2$ coatings on Al substrate are shown in figure 3.32. The hardness values of these coatings at 200nm depth are slightly higher compared to the TiB$_2$ monolayer coatings with a value of 26.96GPa on Al substrate (see table 3.34). The hardness values for Al/TiB$_2$ coatings (28.27±1.89GPa), Ti/TiB$_2$ coatings (27.26±2.92GPa) and Mo/TiB$_2$ coatings (29.17±2.07GPa) are very close to each other.
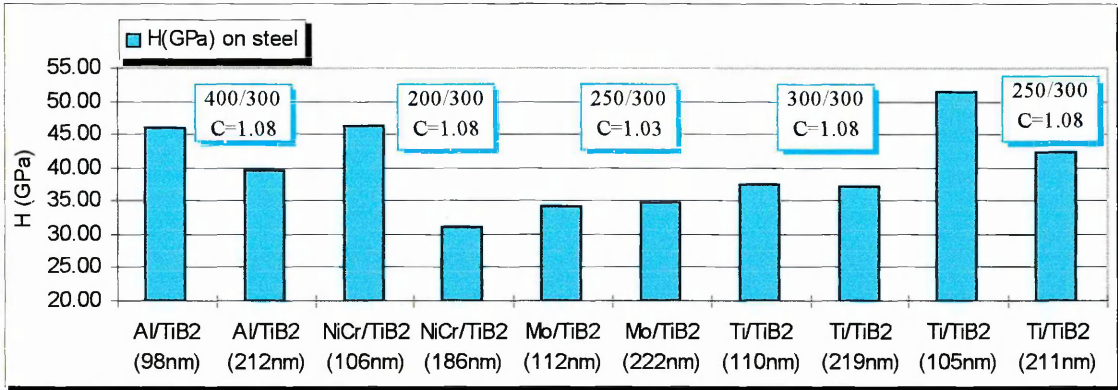
Figure 3.27. Hardness values for the Al/TiB$_2$, NiCr/TiB$_2$, Mo/TiB$_2$ and Ti/TiB$_2$ two-layer coatings on steel substrate, at 0.6Pa sputtering pressure, for two indentation depths (200nm,400nm).

Figure 3.28. Hardness values for Al/TiB$_2$ bi-layer coatings on steel at different sputtering pressure and Ti/TiB$_2$ bi-layer coatings on steel for two sets of measurements in the same sample.

Figure 3.29. Hardness values for Al/TiB$_2$, Ti/TiB$_2$ and Mo/TiB$_2$ bi-layer coatings on steel substrate after nanoindenter calibration with quartz sample.

Hardness (GPa) on Steel Substrate for 400nm Indentation Depth					
Sample Reference	*1ˢᵗ read*	*STDEV*	*2ⁿᵈ read*	*STDEV*	*Mean H for two readings*
TiTB5S2	37.19	4.05	28.27	3.26	32.73
TiTB6S2	42.29	8.15	31.04	7.32	36.67
Mean per series	39.74		29.66		34.70

Anova: Two-Factor Without Replication

SUMMARY	*Count*	*Sum*	*Average*	*Variance*			
Row 1	2	65.46	32.73	39.78			
Row 2	2	73.33	36.67	63.28			
Column 1	2	79.48	39.74	13.01			
Column 2	2	59.31	29.66	3.84			
Source of Variation	*SS*	*df*	*MS*	*F*	*STDEV*	*P-value*	*F crit*
Rows	15.48	1	15.48	11.41	3.93	0.18	161.45
Columns	101.71	1	101.71	74.94	10.09	0.07	161.45
Error	1.36	1	1.36		1.16		
Total	118.55	3					

Conclusion	
Overall Relative Error	3.3%
Relative Error Between Samples Measurement	11.2%
Measurement Relative Error for Repeat Readings	29.1%

Table 3.8. Anova analysis of hardness results, for Ti/TiB$_2$ bi-layer coatings on steel substrate for two different sputtering conditions and two measurement readings in the same sample.
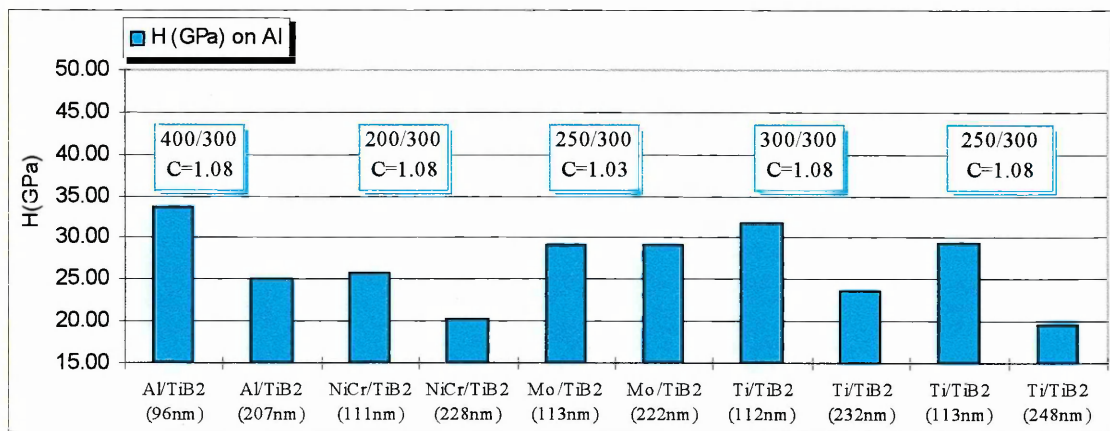
Figure 3.30. Hardness values for the Al/TiB$_2$, NiCr/TiB$_2$, Mo/TiB$_2$ and Ti/TiB$_2$ two-layer coatings on Al substrate, at 0.6Pa sputtering pressure, for two indentation depths (200nm,400nm).

202
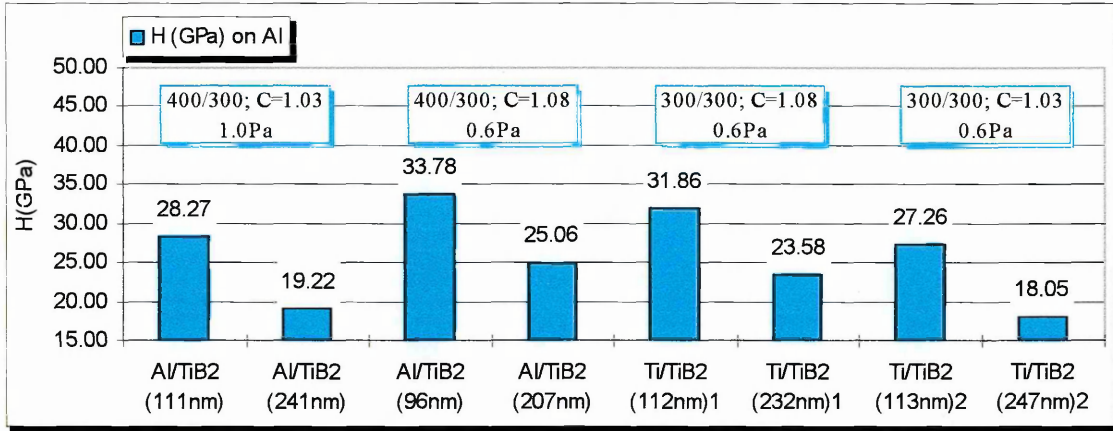
Figure 3.31. Hardness values for Al/TiB$_2$ bi-layer coatings on Al substrate at different sputtering pressure and Ti/TiB$_2$ bi-layer coatings on Al substrate for two sets of measurements in the same sample.
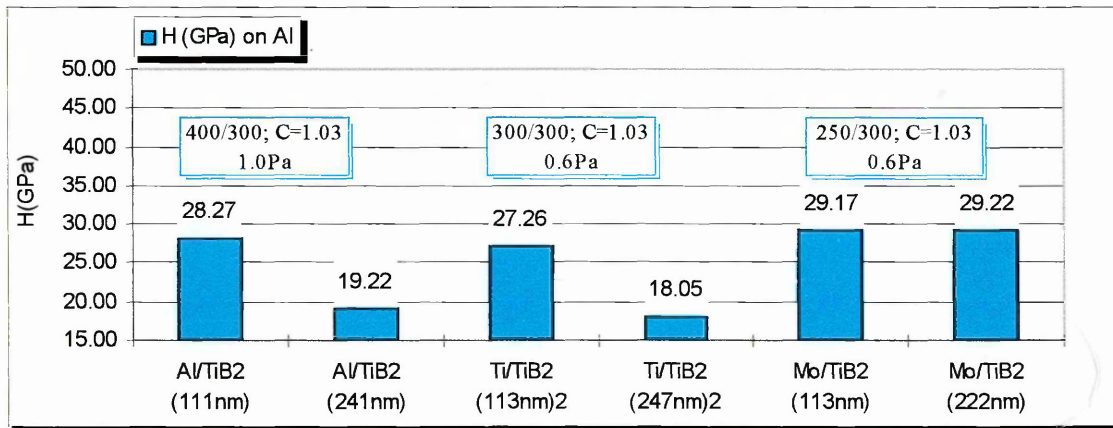
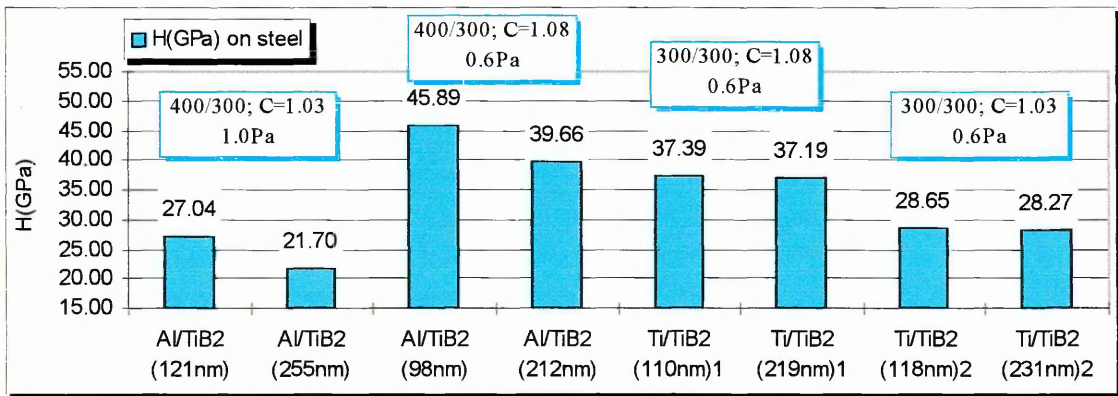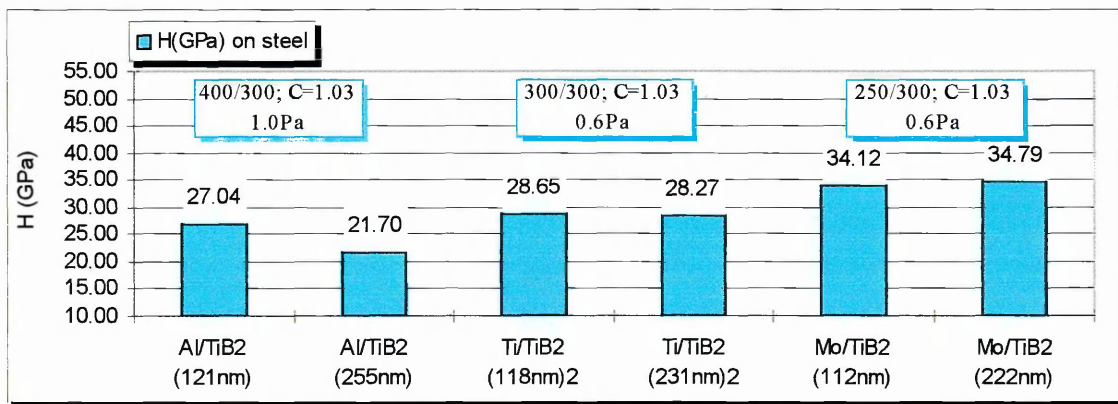

Figure 3.32. Hardness values for Al/TiB$_2$, Ti/TiB$_2$ and Mo/TiB$_2$ bi-layer coatings on Al substrate after nanoindenter calibration with quartz sample.

Hardness (GPa) on Al Substrate for 200nm Indentation Depth					
Sample Reference	*1st read*	*STDEV*	*2nd read*	*STDEV*	*Mean H for two readings*
TiTB5A2	31.86	2.24	27.26	3.92	29.56
TiTB6A2	29.36	4.96	28.66	4.42	29.01
Mean per series	30.61		27.96		29.29
Anova: Two-Factor Without Replication					
SUMMARY	*Count*	*Sum*	*Average*	*Variance*	
Row 1	2	59.12	29.56	10.58	
Row 2	2	58.02	29.01	0.25	
Column 1	2	61.22	30.61	3.13	
Column 2	2	55.92	27.96	0.98	

Source of Variation	*SS*	*df*	*MS*	*F*	*STDEV*	*P-value*	*F crit*
Rows	0.30	1	0.30	0.08	0.55	0.82	161.45
Columns	7.02	1	7.02	1.85	2.65	0.40	161.45
Error	3.80	1	3.80		1.95		
Total	11.13	3					

Conclusion	
Overall Relative Error	6.7%
Relative Error Between Samples Measurement	1.9%
Measurement Relative Error for Repeat Readings	9.1%

Table 3.9. Anova analysis of hardness results for Ti/TiB$_2$ bi-layer coatings on Al substrate for two different sputtering conditions and two measurement readings in the same sample.

Hardness (GPa) on Al Substrate for 400nm Indentation Depth					
Sample Reference	*1st read*	*STDEV*	*2nd read*	*STDEV*	*Mean H for two readings*
TiTB5A4	23.58	2.07	18.05	1.44	20.82
TiTB6A4	19.61	0.69	18.30	2.57	18.96
Mean per series	21.60		18.18		19.89
Anova: Two-Factor Without Replication					
SUMMARY	*Count*	*Sum*	*Average*	*Variance*	
Row 1	2	41.63	20.82	15.29	
Row 2	2	37.91	18.96	0.86	
Column 1	2	43.19	21.60	7.88	
Column 2	2	36.35	18.18	0.03	

Source of Variation	*SS*	*df*	*MS*	*F*	*STDEV*	*P-value*	*F crit*
Rows	3.46	1	3.46	0.78	1.86	0.54	161.45
Columns	11.70	1	11.70	2.63	3.42	0.35	161.45
Error	4.45	1	4.45		2.11		
Total	19.61	3					

Conclusion	
Overall Relative Error	10.6%
Relative Error Between Samples Measurement	9.4%
Measurement Relative Error for Repeat Readings	17.2%

Table 3.10. Anova analysis of hardness results for Ti/TiB$_2$ bi-layer coatings on Al for two different sputtering conditions and two measurement readings in the same sample.

2. ANALYSIS OF THE ELASTIC MODULUS RESULTS

Figures 3.33 to 3.35 show the elastic modulus values for different bi-layer coating systems on steel substrates while the figures 3.36 to 3.38 show the elastic modulus values for the same two-layer coating systems but onto Al substrates. These figures are presented in the same manner as the hardness value figures to facilitate the comparison between hardness and elastic modulus of the coatings.

Figure 3.33 shows the elastic modulus of the bi-layer coating systems on the steel substrate at 0.6Pa sputtering pressure for two indentation depths (200nm, 400nm). The elastic modulus of $NiCr/TiB_2$ coatings and Ti/TiB_2 coatings at 250WRF sputtering power for the Ti layer drop significantly with the plastic depth. The other coating systems do not show such significant variation in the elastic modulus with the plastic depth as the two systems do. However, the elastic modulus of the bi-layer coating systems onto the Al substrate shows a more uniform variation with the penetration depth compared to those on steel substrate, as shown in figure 3.36.

Figure 3.34 shows the elastic modulus results for Al/TiB_2 coatings on the steel substrate at two different sputtering pressures and Ti/TiB_2 coatings onto the steel substrate for two sets of measurements on the same sample. A variation in the elastic modulus values is observed either for Al/TiB_2 coatings or Ti/TiB_2 coatings. The same behaviour appears for the same coating systems onto the Al substrate, as shown in figure 3.37.

A statistical Anova analysis was performed for Ti/TiB_2 coatings onto the steel substrate for two different sputtering powers of the Ti layer (250WRF, 300WRF), and two sets of measurements on the same sample, as shown in table 3.11. This analysis shows that the major source of error is between repeat measurements on the same sample (33.1%). This error reflects various measurement uncertainties, as mentioned before. The error in the reproducibility between samples (21.8%) reflects variation in sputtering conditions. The overall measurement accuracy is 10%.

An Anova analysis was also performed for the same coatings system but onto the Al substrate for two penetration depths (200nm, 400nm) as shown in tables 3.12 and 3.13. The major source of error is also between repeat measurements on the same sample with 9.1% for 200nm depth and 14.2% for 400nm depth. This error reflects the measurement uncertainties mentioned earlier. The error in the reproducibility between samples is 4.5% for 200nm and 1.5% for 400nm depth. This error reflects the effect of sputtering conditions and the intermediate layer stiffness effect. The overall measurement accuracy is 5.7% for 200nm depth and 6.0% for 400nm depth, which is significant compared to the variation within the samples.

Figure 3.35 shows the elastic modulus value for Al/TiB_2, Ti/TiB_2 and Mo/TiB_2 coatings onto the steel substrate after calibration of the nanoindenter with quartz sample, as mentioned earlier. The elastic modulus of these coatings systems for 200nm depth increases on going from Al/TiB_2 (306.0±44.2GPa) to Ti/TiB_2 coatings (326.7±34.4GPa) and then Mo/TiB_2 coatings (362.9±16.3GPa). The tendency is to approach the modulus of the TiB_2 monolayer coatings on the steel substrate which have a value of 379.4GPa

(see table 3.33). The elastic modulus of these coatings shows a tendency to drop with the plastic depth. The same behaviour appears for the same coating system onto Al substrate (see figure 3.38). The elastic modulus value increases on going from Al/TiB_2 (241.1±5.1GPa) to Ti/TiB_2 coatings (252.4±19.7GPa) and then Mo/TiB_2 coatings (283.9±12.2GPa) on the Al substrate. The elastic modulus of Mo/TiB_2 coatings on Al substrate is higher compared to the reference value of 273.9GPa for the TiB_2 monolayer coating onto Al substrate (see table 3.34) but they do not follow the rule of mixtures.
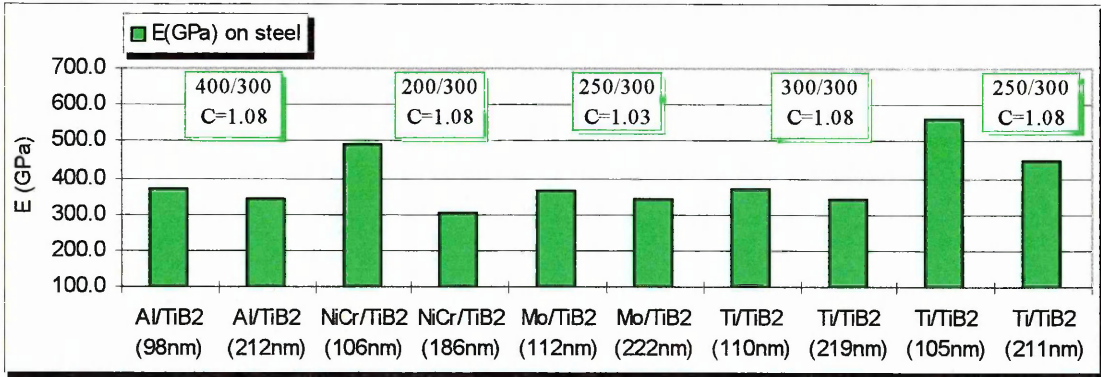
Figure 3.33. Elastic modulus values for the Al/TiB_2, $NiCr/TiB_2$, Mo/TiB_2 and Ti/TiB_2 two-layer coatings on steel substrate, at 0.6Pa sputtering pressure, for two indentation depths (200nm,400nm).

Figure 3.34. Elastic modulus values for Al/TiB_2 bi-layer coatings on steel substrate at different sputtering pressure and Ti/TiB_2 bi-layer coatings on steel substrate for two sets of measurements in the same sample.

Figure 3.35. Elastic modulus values for Al/TiB_2, Ti/TiB_2 and Mo/TiB_2 bi-layer coatings on steel substrate after nanoindenter calibration with quartz sample.

Elastic Modulus of the film on Steel Substrate for 400nm Depth (GPa)					
Sample Reference	1st read	STDEV	2nd read	STDEV	Mean E_f for two readings
TiTB5S4	339.8	26	261.9	11.00	300.85
TiTB6S4	447.0	124	301.7	66.30	374.35
Mean per series	393.4		281.8		337.60
Anova: Two-Factor Without Replication					

SUMMARY	Count	Sum	Average	Variance
Row 1	2	601.7	300.9	3034.20
Row 2	2	748.7	374.4	10556.05
Column 1	2	786.8	393.4	5745.92
Column 2	2	563.6	281.8	792.02

Source of Variation	SS	df	MS	F	STDEV	P-value	F crit
Rows	5402.25	1	5402.25	4.757	73.50	0.274	161.446
Columns	12454.56	1	12454.56	10.967	111.60	0.187	161.446
Error	1135.69	1	1135.69		33.70		
Total	18992.5	3					

Conclusion	
Overall Relative Error	10.0%
Relative Error Between Samples Measurement	21.8%
Measurement Relative Error for Repeat Readings	33.1%

Table 3.11. Anova analysis of elastic modulus results for Ti/TiB_2 bi-layer coatings on steel substrate for two different sputtering conditions and two measurement readings in the same sample.
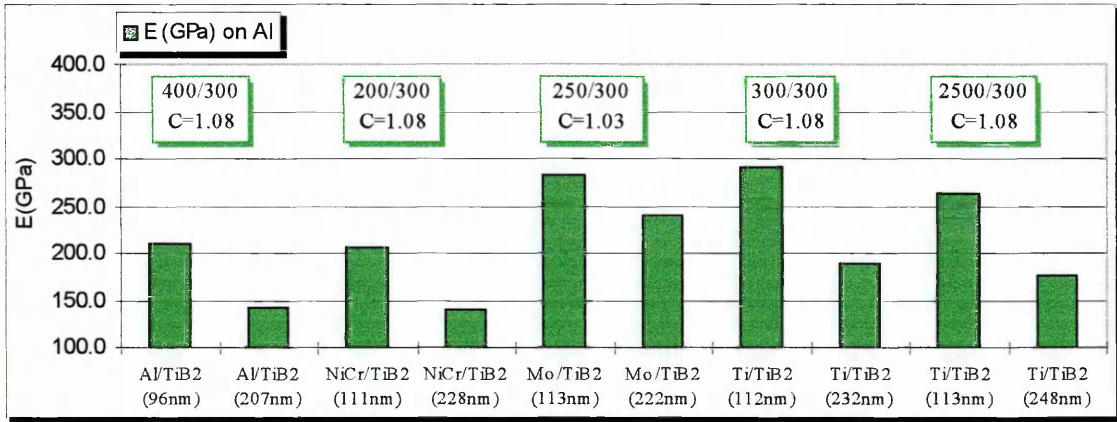
Figure 3.36. Elastic modulus values for the Al/TiB$_2$, NiCr/TiB$_2$, Mo/TiB$_2$ and Ti/TiB$_2$ two-layer coatings on Al substrate, at 0.6Pa sputtering pressure, for two indentation depths (200nm, 400nm).
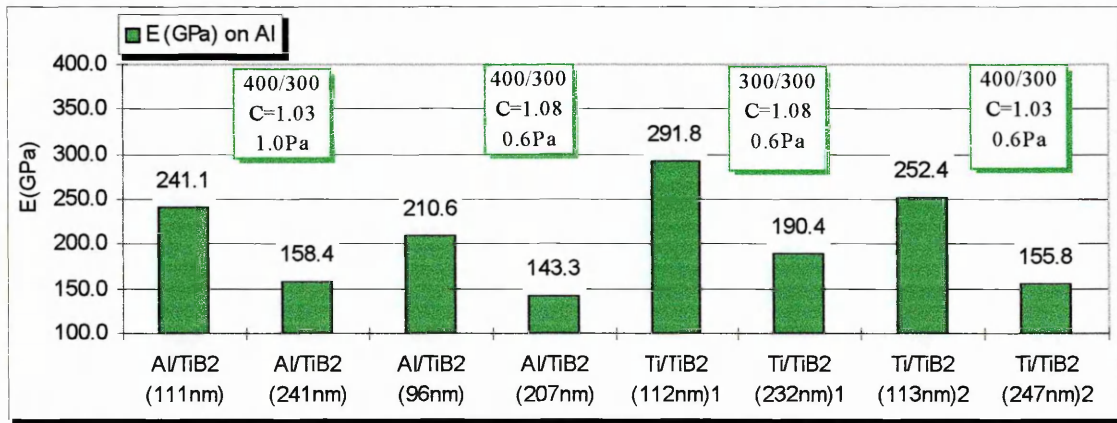
Figure 3.37. Elastic modulus values for Al/TiB$_2$ bi-layer coatings on Al substrate at different sputtering pressure and Ti/TiB$_2$ bi-layer coatings on Al substrate for two sets of measurements in the same sample.
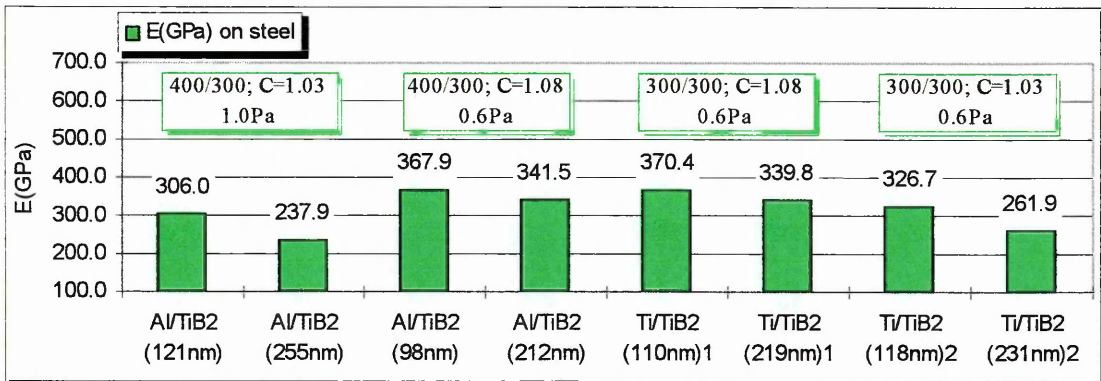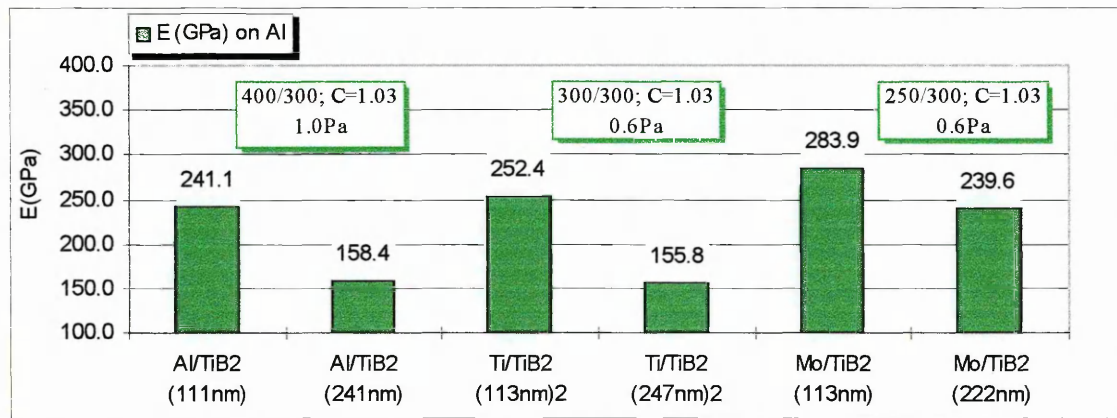

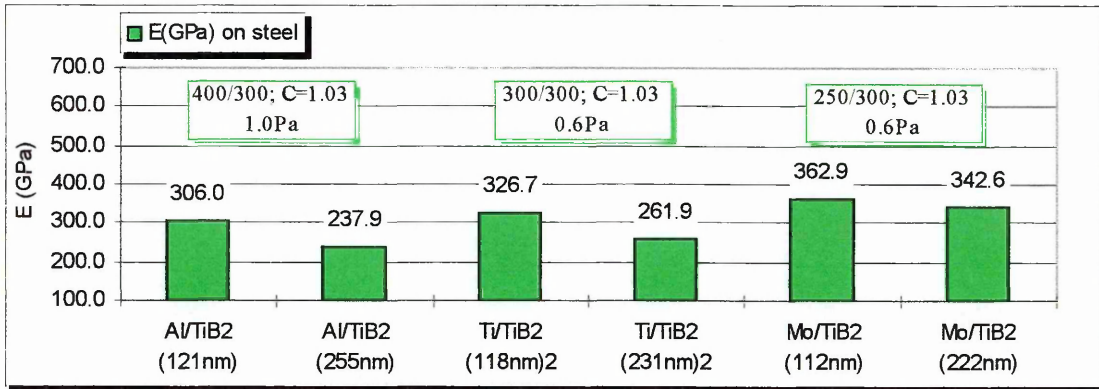Figure 3.38. Elastic modulus values for Al/TiB$_2$, Ti/TiB$_2$ and Mo/TiB$_2$ bi-layer coatings on Al substrate after nanoindenter calibration with quartz sample.

Elastic modulus of the film on Al substrate for 200nm Indentatio depth (GPa)					
Sample Reference	*1ˢᵗ read*	*STDEV*	*2ⁿᵈ read*	*STDEV*	*Mean E_f for two readings*
TiTB5A2	291.8	28.0	252.4	19.7	272.1
TiTB6A2	264.5	13.9	255.6	33.0	260.1
Mean per series	278.2		254.0		266.1

Anova: Two-Factor Without Replication

SUMMARY	Count	Sum	Average	Variance
Row 1	2	544.20	272.10	776.18
Row 2	2	520.10	260.05	39.60
Column 1	2	556.30	278.15	372.65
Column 2	2	508.00	254.00	5.12

Source of Variation	SS	df	MS	F	STDEV	P-value	F crit
Rows	145.20	1	145.20	0.62	12.05	0.57	161.45
Columns	583.22	1	583.22	2.51	24.15	0.36	161.45
Error	232.56	1	232.56		15.25		
Total	960.99	3					

Conclusion	
Overall Relative Error	5.7%
Relative Error Between Samples Measurement	4.5%
Measurement Relative Error for Repeat Readings	9.1%

Table 3.12. Anova analysis of elastic modulus results, for Ti/TiB$_2$ bi-layers on Al for two different sputtering conditions and two measurements in the same sample.

Elastic modulus of the film on Al substrate for 400nm Indentation depth (GPa)					
Sample Reference	*1ˢᵗ read*	*STDEV*	*2ⁿᵈ read*	*STDEV*	*Mean E_f for two readings*
TiTB5A4	190.4	12.7	155.8	3.6	173.1
TiTB6A4	177.5	2.8	163.4	4.8	170.5
Mean per series	184.0		159.6		171.8

Anova: Two-Factor Without Replication

SUMMARY	Count	Sum	Average	Variance
Row 1	2	346.2	173.10	598.58
Row 2	2	340.9	170.45	99.41
Column 1	2	367.9	183.95	83.21
Column 2	2	319.2	159.60	28.88

Source of Variation	SS	df	MS	F	STDEV	P-value	F crit
Rows	7.02	1	7.02	0.07	2.65	0.84	161.45
Columns	592.92	1	592.92	5.64	24.35	0.25	161.45
Error	105.06	1	105.06		10.25		
Total	705.01	3					

Conclusion	
Overall Relative Error	6.0%
Relative Error Between Samples Measurement	1.5%
Measurement Relative Error for Repeat Readings	14.2%

Table 3.13. Anova analysis of elastic modulus results, for Ti/TiB$_2$ bi-layer coatings on Al substrate for two different sputtering conditions and two measurement readings in the same sample.

3.2.3. SUMMING UP

The TiB_2 structure in these two-layer coating designs is crystalline and the degree of crystallinity depends both on the film thickness (table 3.3) and the roughness of the metal layer, as shown in photograph 3.11.

The stoichiometry of the TiB_2 top layer was not determined but is believed to be similar to that of the monolayer TiB_2 coating for the same sputtering conditions.

The apparent hardness of the different coating systems is greater on the steel substrate than on the Al substrate, except for Al/TiB_2 coatings onto the Al substrate at 200nm depth at 1.0Pa sputtering pressure (table 3.4 and 3.5).

The apparent hardness of the different coatings systems drops with plastic depth, except for Mo/TiB_2 coating onto Al and steel substrates and Ti/TiB_2 onto steel at 300WRF sputtering power for Ti layer (table 3.4 and 3.5). These coatings systems may not show the intermediate layer effect incorporated during measurements.

A statistical Anova analysis referred to in table 3.14 shows that the hardness and elastic modulus values measured before the nanoindenter machine was calibrated with a quartz sample had significant relative errors for repeat measurements of the same sample. This error reflects the measurement uncertainties and is not constant for different sets of measurements. The Ti/TiB_2 coating onto Al substrate shows overall the lowest relative error of the measurement and is more significant compared to the relative error within the samples. The overall relative error of the measurements is less than 11% but this is not constant for all measurements.

Hence the results quoted before quartz calibration of the machine cannot be considered as absolute and reflect various measurement uncertainties which were introduced during these measurements.

The more confident results are shown in figure 3.39 and 3.40 for hardness and elastic modulus values respectively because, before undertaking this schedule, the nanoindenter was calibrated with a quartz reference sample. The hardness increases on going from the system with the Al metal layer to a Ti layer and then a Mo layer on steel substrates. The hardness of the coating system with the Mo metal layer is very close to the TiB_2 monolayer coating for the same sputtering conditions. The hardness value of Al/TiB_2 coatings is slightly higher on Al substrates compared to those on steel substrates. For 200nm indentation depth the elastic modulus values of the two-layer coatings increased on going from the Al layer to Ti layer and then Mo metal layer either on a steel substrate or on an Al substrate. The Mo/TiB_2 coating on Al substrates gives an elastic modulus that is slightly higher than for a TiB_2 monolayer coating, while for a steel substrate it is very close to the elastic modulus of the monolayer coating. These three coating systems show a high elastic modulus on steel substrates compared to those on Al substrates. This may be due to the added compliance of the stiffer substrate. The three two-layer coating systems show values of elastic modulus above the rule of mixtures as shown in figure 3.41,when considering the coating with 50% of volume fraction of ceramic.

The intermediate metal layer results in a TiB_2 top layer on a steel substrate that tends to reach the hardness and elastic modulus of a TiB_2 monolayer, for the same sputtering conditions, but without its brittleness. Because of this, the two-layer coatings did not show microcracks compared with TiB_2 monolayer coatings as shown in photograph 3.13.

Hardness results on Ti/TiB$_2$ two-layer coatings			
	Ti/TiB$_2$ coatings onto Al for 200nm depth	*Ti/TiB$_2$ coatings onto Al for 400nm depth*	*Ti/TiB$_2$ coatings onto steel for 400nm depth*
Overall relative error	6.7%	10.6%	3.3%
Relative error between samples measurements	1.9%	9.4%	11.2%
Measurement relative error for repeat readings	9.1%	17.2%	29.1%
Elastic modulus results on Ti/TiB$_2$ two-layer coatings			
	Ti/TiB$_2$ coatings onto Al for 200nm depth	*Ti/TiB$_2$ coatings onto Al for 400nm depth*	*Ti/TiB$_2$ coatings onto steel for 400nm depth*
Overall relative error	5.7%	6.0%	10.0%
Relative error between samples measurements	4.5%	1.5%	21.8%
Measurement relative error for repeat readings	9.1%	14.2%	33.1%

Table 3.14. Relative error of the hardness and elastic modulus results from Anova analysis for Ti/TiB$_2$ bi-layer coatings.
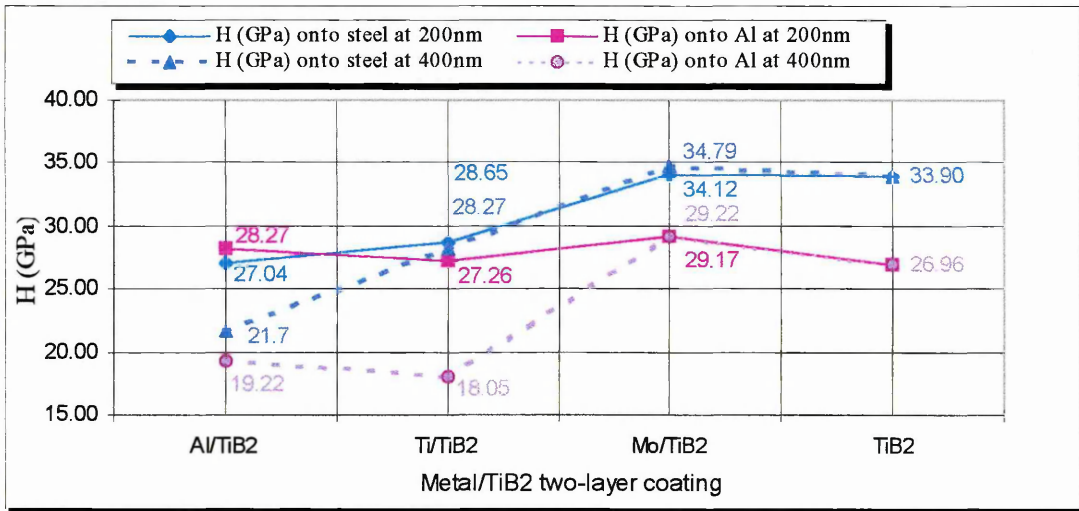
Figure 3.39. Hardness versus metal/TiB$_2$ bi-layer coating system on steel and Al substrate, for 200nm and 400nm indentation depth.
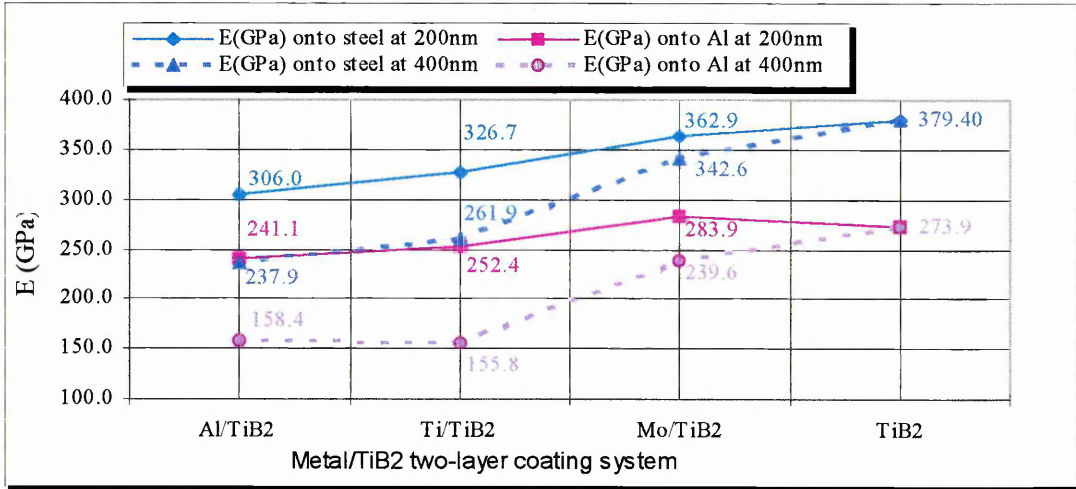
Figure 3.40. Elastic modulus versus metal/TiB$_2$ bi-layer coating system on steel and Al substrate, for 200nm and 400nm indentation depth.
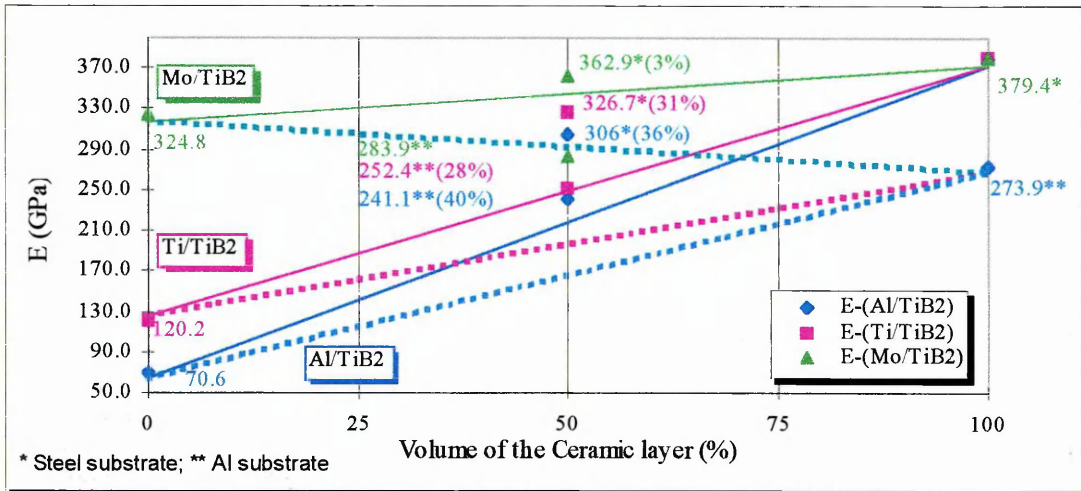
Figure 3.41. Elastic modulus of the X/TiB$_2$ bi-layer coating system on steel and Al substrate in function of the volume of ceramic layer TiB$_2$.

212

3.3. MULTILAYER COATING DEPOSITION

LAYOUT
⇓
Sputtering Deposition Conditions
⇓
In-Plane Elastic Modulus Measurements:

♦ Three-Point Bend Test by Mechanical
   Loading Using Weights
♦ Three-Point Bend Test by Mechanical
   Loading Using Water as a Weight
♦ Three-Point Bend Test by Nanoindentation
⇓
Elastic Modulus and hardness measurements by
Nanoindentation
⇓
Structural Characterization
⇓
Analysis of the Internal Stresses
⇓
Summing up

3.3.1. DEPOSITION CONDITIONS

Two preliminary series of multilayer coatings (series A and C) were produced before producing the set with controlled wavelengths (λ) and volume fractions of ceramic (V_c) for the multilayer coatings defined in table 2.1 (series E).

The first series in this set, series A, was deposited at 1.0Pa (7.5×10^{-3}Torr), because these coatings were deposited before the optimised sputtering conditions had been established.

Five runs of the third series in this set, series E, were produced to improve the multilayer coating by varying either the TiB_2 sputtering power or metal layer type.

The total thickness of the coating design was 5µm and the sputtering conditions of the series are given in table 3.15.

Series	Sample Reference	System	λ (nm)/ Vc (%)	Working Gas	Sputtering Pressure (Pa)	Sputtering Power metal/TiB$_2$ (WRF)
A (5 runs)	4A	Al/TiB$_2$	200/75	Ar	1.0	400/300
	1A	Al/TiB$_2$	200/50	Ar	1.0	400/300
	5A	Al/TiB$_2$	200/25	Ar	1.0	400/300
	2A	Al/TiB$_2$	100/50	Ar	1.0	400/300
	3A	Al/TiB$_2$	50/50	Ar	1.0	400/300
C (3 runs)		TiB$_2$	-	Ar	0.6	300
	1C	Al/TiB$_2$	200/75	Ar	0.6	400/300
	4C	(Al/TiB$_2$)N$_2$	200/75	Ar+30%N$_2$	0.6	400/300
E (15 runs)		TiB$_2$	-	Ar	0.6	300
	7E	Al/TiB$_2$	200/75	Ar	0.6	400/300
	2E	Al/TiB$_2$	200/50	Ar	0.6	400/300
	3E	Al/TiB$_2$	200/25	Ar	0.6	400/300
	9E	Al/TiB$_2$	100/75	Ar	0.6	400/300
	6E	Al/TiB$_2$	100/50	Ar	0.6	400/300
	5E	Al/TiB$_2$	100/25	Ar	0.6	400/300
	11E	Al/TiB$_2$	50/75	Ar	0.6	400/300
	14E	Al/TiB$_2$	50/50	Ar	0.6	400/300
	12E	Al/TiB$_2$	50/25	Ar	0.6	400/300
	17E	Al/TiB$_2$	50/75	Ar	0.6	400/400
	16E	Al/TiB$_2$	50/75	Ar	0.6	400/440
	8E	NiCr/TiB$_2$	50/75	Ar	0.6	200/300
	15E	NiCr/TiB$_2$	50/75	Ar	0.6	200/400

Table 3.15. Sputtering conditions of multilayer coatings.

3.3.2. IN-PLANE ELASTIC MODULUS MEASUREMENTS

A comparison of three different methods for measuring the in-plane elastic modulus is given in the following sections for the uncoated beam and coated beam. The three approaches are compared based on the mathematical analysis of errors referred to in the section 2.3. The in-plane elastic modulus of the uncoated beam was calculated using the equation 2.6 (E_s), while the in-plane elastic modulus of the coated beam was calculated using the equation 2.11 ((E_f)$_1$) and 2.23 ((E_f)$_2$) of the section 2.3. The maximum relative error was calculated between the maximum and mean values of the population of two or more values.

I-THREE POINT BEND TEST BY MECHANICAL LOADING USING WEIGHTS

Eight steel uncoated beams and twenty steel coated beams were tested by a three point bending test with mechanical loading, using washer shaped weights. Three measurements were performed for each sample. Loads 9.9g, 15.2g, 20.5g, 25.8g, 31.1g, 36.4g, 41.7g, 47.0g and 49.3g were used. Loads below 9g gave unreliable results.

1. In-Plane Elastic Modulus Results of the uncoated Beam

The in-plane elastic modulus values of the eight beams are shown in table 3.16. These values were calculated taking the width (12.6998mm) and thickness (0.1982mm) of the beams as constant values. These values are a mean of the measuring beams' dimensions of table 3.19. The elastic modulus was calculated from equation 2.6 (E_s). The average deflection was corrected for a zero point error from the fitted curve. The average slope was calculated from the ratio of the δ/P for each load. The relative error was calculated between the maximum and mean value of the slope. The method of elastic modulus calculation was the same for all samples.

In-Plane Elastic Modulus of Steel Beams			
Steel Substrate	E_s *(GPa)*	*Relative Error (%)*	*STDEV*
S1	213.6	1.5	2.2
S2	214.3	1.0	1.2
S3	214.0	1.0	1.7
S4	220.2	2.8	3.6
S5	218.6	3.3	3.5
S6	232.3	1.9	4.2
S7	225.0	1.8	3.8
S8	223.0	1.6	3.8
Mean	220.1	1.9	3.0
E_s calculation was based on the slope from δ/P for each load			

Table 3.16. In-plane elastic modulus of the uncoated beams by mechanical loading using weights.

The mean value of the elastic modulus of the steel beam is 220GPa, as shown in table 3.16, which is high compared to the book value of 207GPa (table 2.2). The mean relative error was found to be 1.9% for the eight series of measurements. This may be due to the variations in the beam dimensions and measurement uncertainties. According to the mathematical analysis of the relative error referred to in section 2.3, this value may give a relative error of the elastic modulus of the film up to 25%. Hence, analysis of the slope (γ_s) of the deflection (δ) versus load (P) curve was performed to investigate the measurement accuracy, as shown in table 3.17. This analysis consists of calculating the slope (γ_s) in two different ways:

1. From the ratio of the δ/P for each load, which takes into account any deflection and load effect measurement $(\gamma_s)_1$. In this method, the average slope and the STDEV were calculated for loads between 9.9g and 49.3g.

2. From a linear curve fit (Least square, denoted L.S.) of the mean deflection for different loads, considering the slope is constant over the full range of loads $(\gamma_s)_2$.

215

Steel substrate	Slope from d/P $(\gamma_s)_1$	Relative Error (%)	STDEV	Slope from L.S. $(\gamma_s)_2$	Correlation factor (R^2)	STDEV between $(\gamma_s)_1$ and $(\gamma_s)_2$
S1	7.4316	1.8	0.075	7.4356	0.9998	0.0028
S2	7.4061	0.9	0.043	7.4043	0.9999	0.0013
S3	7.4168	1.7	0.060	7.4118	0.9999	0.0035
S4	7.2112	3.0	0.118	7.2132	0.9999	0.0014
S5	7.2643	2.7	0.117	7.2704	0.9997	0.0043
S6	6.8365	4.6	0.129	6.8333	0.9994	0.0023
S7	7.0577	3.9	0.123	7.0532	0.9994	0.0032
S8	7.1197	4.1	0.126	7.1108	0.9993	0.0063
Mean	*7.2180*	*2.8*	*0.099*	*7.2166*		

Table 3.17. Slope values of the curve deflection versus load.

Table 3.17 shows the values of the slopes $(\gamma_s)_1$ and $(\gamma_s)_2$; relative errors and STDEV of $(\gamma_s)_1$; correlation factors of the fitting curves (R^2) and the STDEV between $(\gamma_s)_1$ and $(\gamma_s)_2$. According to the mathematical analysis of errors in section 2.3, the average relative error of the slope (2.8%) corresponds to a relative error of 2.7% for E_s, without taking into account the dimension measurement of the samples. The variation of the STDEV between $(\gamma_s)_1$ and $(\gamma_s)_2$ reflects the repeatability of the measured deflection and load because the slope $(\gamma_s)_2$ was considered constant over the whole range of loads.

A statistical Anova analysis was performed for the slopes referred to in table 3.17, as shown in table 3.18. This analysis shows that the major source of errors is the reproducibility between samples (4.09%). This error reflects variations in the sample dimensions because they were considered as a constant value. The error between the two slopes of the same sample is 0.04%. This error reflects the repeatability of the measured compliance of the system. The overall measurement accuracy is 0.05%. The two latter errors are much less significant than the dimensions of the beam, which agrees with the mathematical error analysis in the section 2.3.

Analysis of the Slope from the Curve Deflection versus Load for Uncoated Beams			
Sample Reference	Slope from δ/P $(\gamma_s)_1$	Slope from L.S. $(\gamma_s)_2$	Mean of $(\gamma_s)_1$ and $(\gamma_s)_2$
S1	7.4316	7.4356	7.4336
S2	7.4061	7.4043	7.4052
S3	7.4168	7.4118	7.4143
S4	7.2112	7.2132	7.2122
S5	7.2643	7.2704	7.2674
S6	6.8365	6.8333	6.8349
S7	7.0577	7.0532	7.0555
S8	7.1197	7.1108	7.1153
Mean per series	7.2180	7.2166	7.2173

Anova: Two-Factor Without Replication

SUMMARY	Count	Sum	Average	Variance			
Row 1	2	14.8672	7.4336	8.00E-06			
Row 2	2	14.8104	7.4052	1.62E-06			
Row 3	2	14.8286	7.4143	1.25E-05			
Row 4	2	14.4244	7.2122	2.00E-06			
Row 5	2	14.5347	7.2674	1.86E-05			
Row 6	2	13.6698	6.8349	5.12E-06			
Row 7	2	14.1109	7.0555	1.01E-05			
Row 8	2	14.2305	7.1153	3.96E-05			
Column 1	8	57.7439	7.2180	4.34E-02			
Column 2	8	57.7326	7.2166	4.41E-02			
Source of Variation	SS	df	MS	F	STDEV	P-value	F crit
Rows	6.13E-01	7	8.75E-02	6836.847	0.296	7.04E-13	3.787
Columns	7.98E-06	1	7.98E-06	0.624	0.003	4.56E-01	5.591
Error	8.96E-05	7	1.28E-05		0.004		
Total	6.13E-01	15					
Conclusion							
Overall relative error							0.05%
Relative error between samples measurement							4.09%
Relative error for the two slopes $(\gamma_s)_1$ and $(\gamma_s)_2$							0.04%

Table 3.18. Anova analysis of the slope from the curve deflection versus load.

2. In-Plane Elastic Modulus Results of the Coated Beam

Twenty steel coated beams of the series A (see table 3.15 for sputtering conditions) were tested by three-point bend test using washers as weighs.

The indices of S4, S5, S10 and S11 of the sample reference correspond to different sample positions within the vacuum chamber. For the positions S4 and S5 both the width and substrate thickness were measured. These values were assumed to apply for samples S10 and S11 as they were manufactured from the same steel at the same time. Hence, a mean value of the measuring beams from table 3.19 was used. This

assumption may explain in part the big scatter of E_f for S10 and S11 positions as shown in Figure 3.42 and table 3.19. The beam thickness was measured by weighing and can be calculated using:

$$t_s = \frac{M}{\rho l b}$$

Where M is the mass of the beam
      ρ is the density of the beam material
      l is the length of the beam
      b is the width of the beam

The beam mass was weighed using a digital balance with accuracy of $\pm 10 \mu g$. The beam width was measured by profile projector at 20 times magnification with micrometer heads with a resolution of $0.1 \mu m$. The length of the beam was measured by using a Joyce-Loebel Image Analyser. For all coated beams the thickness of the coatings was not measured so a constant value of $5 \mu m$ was used. It is not expected that the actual film thickness will differ from this value by more than 25% based on the previously calibrated deposition rate.

The elastic modulus was calculated for the coated beam from equation 2.11 $(E_f)_1$. As the elastic moludus of the uncoated beams was not measured by three-point bend testing, a constant book value of 207GPa (table 2.2) was used to calculate the elastic modulus of the coatings. The average deflection was corrected for a zero point error from the fitted curve. The relative error was calculated between the maximum and mean values of the slope. The slopes of the composite (coating+substrate), $(\gamma_c)_1$ and $(\gamma_c)_2$, were calculated from the analysis used for the uncoated beams. The method of elastic modulus calculation was the same for all samples and it was the same as for the uncoated beams.

The in-plane elastic modulus results of the coatings and the slopes of the composites are tabulated in table 3.19. The STDEV between the slope from $\delta/P, (\gamma_c)_1$ and L.S., $(\gamma_c)_2$ for the same sample for the coated beam can be attributed to the repeatability of the measured compliance of the system. The STDEV of the E_f values using the two different methods of the composite slope $((\gamma_c)_1, (\gamma_c)_2)$ calculations are low, confirming the agreement between these two methods and reflecting the applied load and deflection measurement accuracy. The elastic modulus of the sample 1AS11 was calculated considering the designed value of dimensions for the sample (b=12.7mm; t_s=0.2mm) and a mean value of a set of samples measurements (b=12.6998; t_s=0.1982mm), giving a value of -14.7GPa and 56.7GPa respectively. This shows that the accuracy of the sample dimension measurements is very significant in the E_f calculation.

Sample Reference (Al/TiB$_2$ films onto steel)	Width (mm)	Substrate thickness (t_s) (mm)	Slope from δ/P (γ_c)$_1$	Relative Error (%)	STDEV	Slope from L.S. (γ_c)$_2$	Correlation factor (R^2)	STDEV between (γ_c)$_1$ and (γ_c)$_2$	Elastic modulus from (γ_c)$_1$; (E_f)a (GPa)	Relative error of (E_f)a between readings (%)	Elastic modulus from (γ_c)$_2$; (E_f)b (GPa)	STDEV between (E_f)a and (E_f)b
1AS4	12.7035	0.1969	7.1127	0.5	0.034	7.1158	0.9999	0.0022	256.9	-	255.8	0.79
2AS4	12.7170	0.1978	6.8390	0.7	0.033	6.8425	0.9999	0.0025	328.6	-	327.1	1.06
3AS4	12.6899	0.1985	7.0221	2.0	0.098	7.0364	0.9993	0.0101	227.6	-	221.8	4.10
4AS4	12.6953	0.1957	7.0756	1.6	0.062	7.0840	0.9998	0.0059	326.1	-	322.8	2.31
5AS4	12.7003	0.1995	7.0010	0.8	0.028	7.0007	0.9999	0.0002	193.9	-	194.0	0.09
1AS5 (1)	12.6921	0.1995	6.9452	0.9	0.035	6.9451	0.9999	0.0001	218.0		218.0	0.03
1AS5 (2)	12.6921	0.1995	7.0068	1.8	0.059	7.0019	0.9999	0.0035	192.9	6.1	195.0	1.45
2AS5 (1)	12.6868	0.1943	7.6590	0.9	0.052	7.6539	0.9998	0.0036	161.8		163.6	1.28
2AS5 (2)	12.6868	0.1943	7.7442	3.6	0.21	7.7213	0.9972	0.0162	132.1	10.1	140.0	5.57
3AS5 (1)	12.6991	0.2008	6.8547	1.0	0.05	6.8612	0.9998	0.0046	199.2		196.6	1.81
3AS5 (2)	12.6991	0.2008	6.8734	1.4	0.06	6.8695	0.9997	0.0028	191.8	1.9	193.2	1.02
4AS5 (1)	12.7143	0.2008	6.8368	1.0	0.06	6.8392	0.9997	0.0017	204.1		203.2	0.65
4AS5 (2)	12.7143	0.2008	6.8134	1.3	0.06	6.8217	0.9998	0.0059	214.1	2.4	210.5	2.57
5AS5 (1)	12.6994	0.1969	7.3377	1.1	0.04	7.3361	0.9999	0.0011	169.9		170.6	0.50
5AS5 (2)	12.6994	0.1969	7.2727	0.8	0.06	7.2750	0.9995	0.0016	194.5	6.8	193.7	0.54
1AS10	12.6998	0.1982	6.6473	1.3	0.068	6.6538	0.9995	0.0046	399.8	-	396.8	2.17
2AS10	12.6998	0.1982	6.4960	1.2	0.050	6.4996	0.9998	0.0025	469.6	-	467.9	1.20
3AS10	12.6998	0.1982	7.3224	1.8	0.074	7.3178	0.9997	0.0033	123.1	-	124.7	1.11
4AS10	12.6998	0.1982	6.8014	1.0	0.036	6.8043	0.9999	0.0021	331.9	-	330.4	1.01
5AS10	12.6998	0.1982	6.9065	1.0	0.045	6.9057	0.9998	0.0006	286.8	-	287.4	0.38
1AS11	12.6998	0.1982	7.5048	1.4	0.086	7.4934	0.9995	0.0081	56.7	-	60.8	2.91
2AS11	12.6998	0.1982	7.3238	0.9	0.076	7.3155	0.9995	0.0059	122.4	-	125.5	2.24
3AS11	12.6998	0.1982	7.1900	1.3	0.064	7.1896	0.9998	0.0003	173.1	-	173.3	0.11
4AS11	12.6998	0.1982	7.0399	1.4	0.049	7.0345	0.9999	0.0038	232.3	-	234.5	1.57
5AS11	12.6998	0.1982	7.0490	0.8	0.062	7.0569	0.9999	0.0056	228.7	-	225.5	2.24
1AS11	12.7	0.2	7.5048	1.4	0.086	7.4934	0.9995	0.0081	-14.6		-10.6	2.86
Mean				*1.3*						*5.5*		

(1)- Refer to the first reading; (2)- Refer to the second reading

Table 3.19. In-plane elastic modulus of the coated samples and the associated composite slopes.

According to the mathematical analysis of error in section 2.3, the average relative error of the slope of 1.3% (table 3.19) corresponds to a relative error of 15.4% in E_f from equation 2.11. The scatter of the relative error of the composite slope results in wide limits for the estimated elastic modulus of the coatings, average values of which are tabulated in table 3.20 for the sample position S5. To further assess this reproducibility, repeat tests of a subset of samples were analysed by an Anova statistical method on repeat readings, as shown in the same table (table 3.20).

This Anova analysis shows that the major source of error is the reproducibility between samples (18.9%) which will most likely reflect variations in coating thickness

and the variables used in coating manufacture (λ, V_c). The errors between repeat measurements (4.7%) on the same sample and the overall measurement accuracy (8.7%) are less significant.

Elastic Modulus of Al/TiB$_2$ Coatings on Steel Subatrate (Series A)			
Sample Reference	$(E_f)a$ 1st read. (GPa)	$(E_f)a$ 2nd read. (GPa)	Mean of the two readings
1AS5	218.0	192.9	205.5
2AS5	161.8	132.1	147.0
3AS5	199.2	191.8	195.5
4AS5	204.1	214.1	209.1
5AS5	169.9	194.5	182.2
Mean per series	190.6	185.1	187.8

Anova: Two-Factor Without Replication

SUMMARY	Count	Sum	Average	Variance
Row 1	2	410.90	205.45	315.01
Row 2	2	293.90	146.95	441.05
Row 3	2	391.00	195.50	27.38
Row 4	2	418.20	209.10	50.00
Row 5	2	364.40	182.20	302.58
Column 1	5	953.00	190.60	566.23
Column 2	5	925.40	185.08	961.02

Source of Variati	SS	df	MS	F	STDEV	P-value	F crit
Rows	5049.2	4	1262.29	4.76	35.53	0.08	6.39
Columns	76.2	1	76.18	0.29	8.73	0.62	7.71
Error	1059.8	4	264.96		16.28		
Total	6185.2	9					

Conclusion	
Overall relative error	8.7%
Relative error between samples measurement	18.9%
Relative error for the two slopes $(\gamma_s)_1$ and $(\gamma_s)_2$	4.7%

Table 3.20. Anova analysis for Al/TiB$_2$ coatings in position S5 for two measurements in the same sample.

The wide scatter in the elastic modulus of the films is a function of sample position inside the vacuum chamber (figure 3.42) and gives only apparent conclusions about the varying parameters of the coating (λ, V_c). The position S5 shows less scatter because the elastic modulus values are the average of two readings.

Figure 3.43 shows the elastic modulus of the coatings S5 and S4 as a function of the composition wavelength and volume of ceramic layer. Both samples S4 and S5 show an increase in elastic modulus with volume of ceramic layer. The highest values of in-plane elastic modulus were found for 50% at 100nm for sample S4 and 75% at 200nm for sample S5. Both samples have a high value for 75% at 200nm.
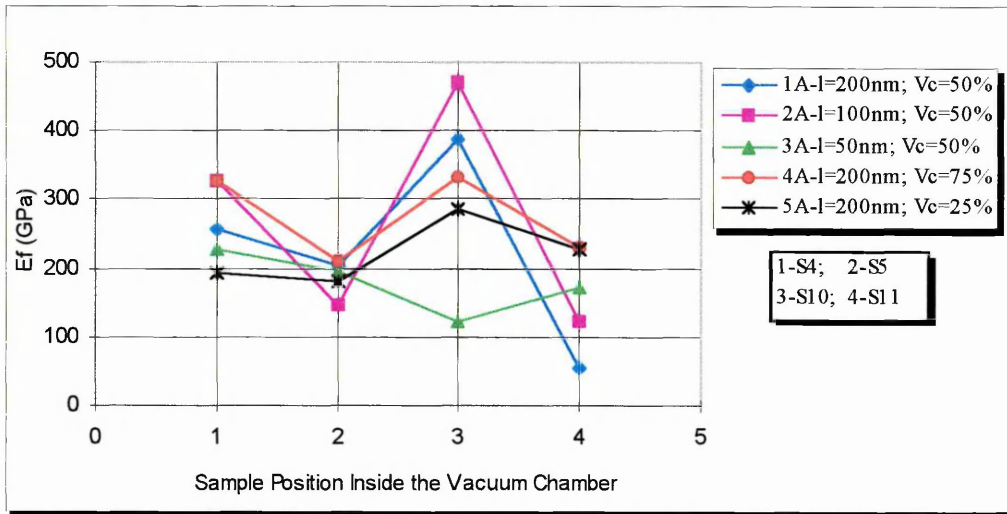
Figure 3.42. In-plane elastic modulus in function of the Al/TiB$_2$ coatings position inside the vacuum chamber.
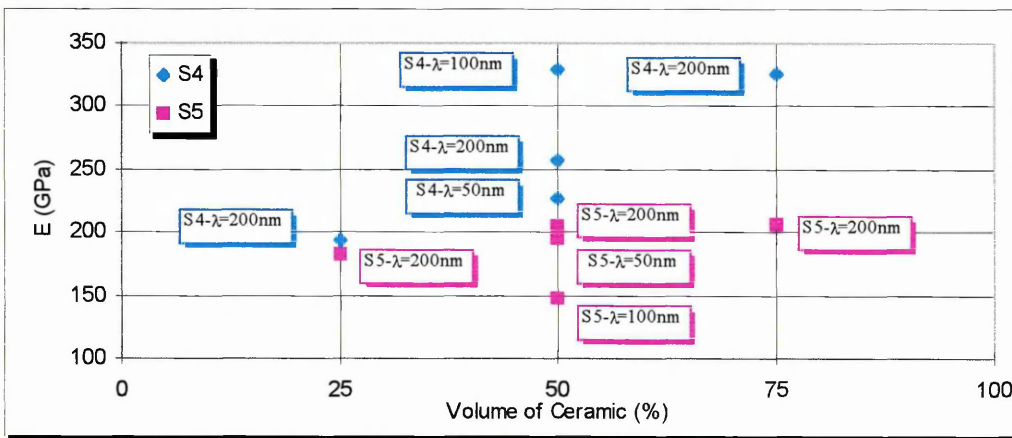
Figure 3.43. In-plane elastic modulus of Al/TiB$_2$ coatings in function of the volume of ceramic layer and composition wavelength.

II-*THREE POINT BEND TEST BY MECHANICAL LOADING USING WATER AS A WEIGHT*

Four steel, four aluminium and four copper uncoated beams and three steel and two aluminium coated beams were tested with a three point bending test by using water as the loading method. Seven measurements were performed for each sample. Loads of 11.6g, 15.4g, 19.3g, 23.1g, 27.0g, 30.8g, 34.7g, and 38.5g were used. Loads below 11g gave unreliable results. The two measurements with the highest STDEV of the slope from the ratio δ/P were rejected so the results are the average of five measurements.

1. *In-Plane Elastic Modulus Results of the uncoated Beams*

The in-plane elastic modulus was calculated, for the uncoated beam, from equation 2.6. The dimensions of the beams (b, t$_s$) were measured by the same method

referred to in the mechanical loading using washers. On each sample two sets of measurements were performed (first reading and second reading). The procedure of elastic modulus calculation was the same for all samples and it was the same as for the mechanical loading using washers as weights method. Table 3.21 shows values of the elastic modulus for the substrates (steel, Cu, Al) together with the values of the relative error and STDEV, for the two readings.

In-Plane Elastic Modulus of Steel, Al and Cu Beams														
Substrate Material	E_s (GPa)	Relative Error (%)	STDEV	Relative error for the two readings (%)	Substrate Material	E_s (GPa)	Relative Error (%)	STDEV	Relative error for the two readings (%)	Substrate Material	E_s (GPa)	Relative Error (%)	STDEV	Relative error for the two readings (%)
Steel	207.0				*Al*	70.0				*Cu*	129.8			
S1(1)	206.9	5.4	5.60		A1(1)	72.8	2.1	0.80		C1(1)	129.5	1.7	0.99	
S1(2)	202.9	0.8	1.16	1.0	A1(2)	73.5	0.4	0.24	0.5	C1(2)	129.1	0.9	0.73	0.2
S2(1)	209.7	4.2	4.71		A2(1)	74.5	0.9	0.55		C2(1)	133.5	1.5	1.02	
S2(2)	210.3	1.9	2.48	0.1	A2(2)	72.5	0.4	0.28	1.4	C2(2)	131.3	0.5	0.46	0.8
S3(1)	211.7	2.9	3.87		A3(1)	75.6	1.2	0.47		C3(1)	138.0	4.7	2.89	
S3(2)	208.8	2.7	2.7	0.7	A3(2)	73.9	0.8	0.53	1.1	C3(2)	127.7	1.1	0.74	3.9
S4(1)	214.4	7.9	7.86		A4(1)	75.7	0.9	0.46		C4(1)	141.6	2.8	2.82	
S4(2)	212.5	3.6	3.48	0.4	A4(2)	73.3	1.1	0.48	1.6	C4(2)	131.7	0.4	0.32	3.6
Mean	209.7	3.7	4.0	0.6	*Mean*	74.0	1.0	0.5	1.1	*Mean*	132.8	1.7	1.2	2.1

E_s calculation was based on γ_s from δ/P for each load $(\gamma_s)_1$; (1)-1st reading; (2)-2nd reading

Table 3.21. In-plane elastic modulus for steel, Al and Cu for uncoated beams.

Table 3.21 shows that the average value of the elastic modulus for steel beams is 209.7GPa, for Al beams 74GPa and for Cu beams 132.8GPa compared with the book values of 207GPa, 70GPa and 129.8GPa respectively. The mean relative error between the two sets of measurements is 0.6% for steel beams, 1.1% for Al beams and 2.1% for Cu beams. This error reflects the repeatability of the measurements.

Figure 3.44 shows the variation of the E_s for steel, Al and Cu beams for two sets of measurements and the book values of these materials. The steel and Al beams show less variation between any two readings over the copper beam.

Table 3.22 shows values of the slope for the steel, Al and Cu substrate together with the values of the relative error and STDEV of the slope from δ/P and the correlation factor of the fitting curves. The relative error of the slope is higher for steel (2.2%) over Cu (1.2%) and the Al (0.9%). The mean STDEV of the $(\gamma_s)_1$ for the two readings is 0.03 for steel beams, 0.08 for Al beams and 0.17 for Cu beams. However, they are higher compared to those between $(\gamma_s)_1$ and $(\gamma_s)_2$. This reflects the fact that the repeatability of the measurements is more significant than the repeatability of the load and deflection measurement in the same test, confirming that the method depends on the water speed between sets of measurements, as referred to in section 2.3.
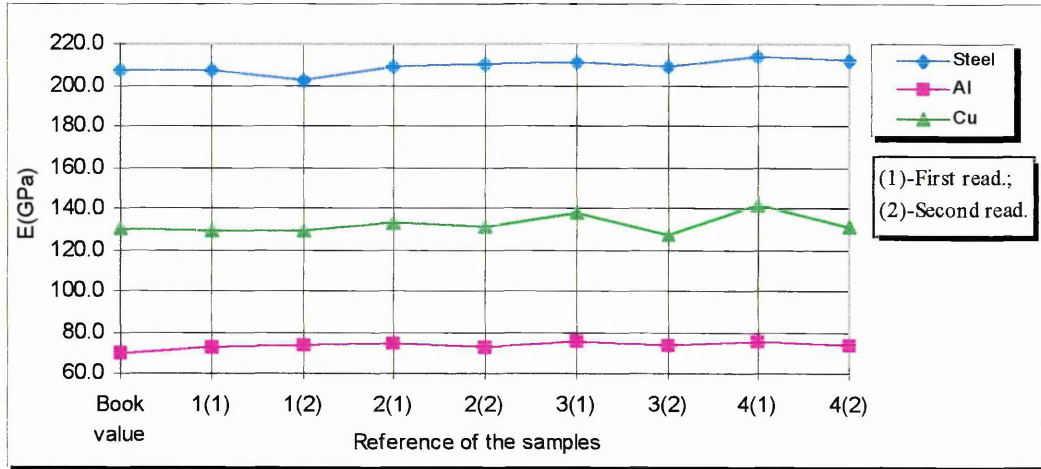
Figure 3.44. In-plane elastic modulus for steel, Al and Cu beams for two sets of measurements.

Slope of the Curve Deflection versus Load for Steel Al and Cu Beams							
Substrate Material	Slope from $(\gamma_s)_1$	Relative Error (%)	STDEV	STDEV of the $(\gamma_s)_1$ for two readings	Slope from $(\gamma_s)_2$	Correlation factor (R^2)	STDEV between $(\gamma_s)_1$ and $(\gamma_s)_2$
Steel							
S1(1st reading)	3.7784	3.0	0.102		3.7886	0.9972	0.0072
S1(2nd reading)	3.8511	0.9	0.022	0.0514	3.8519	0.9998	0.0006
S2(1st reading)	3.8743	3.0	0.086		3.8834	0.9974	0.0064
S2(2nd reading)	3.8616	1.3	0.045	0.0090	3.8653	0.9993	0.0026
S3(1st reading)	3.8388	2.3	0.070		3.8456	0.9976	0.0048
S3(2nd reading)	3.8924	1.3	0.050	0.0379	3.8977	0.9993	0.0037
S4(1st reading)	4.0459	3.9	0.143		4.0603	0.9958	0.0102
S4(2nd reading)	4.0791	1.7	0.065	0.0235	4.0850	0.9993	0.0042
Mean		*2.2*	*0.073*	*0.030*			*0.005*
Al							
A1(1st reading)	5.1346	1.2	0.056		5.1304	0.9994	0.0030
A1(2nd reading)	5.0836	0.6	0.016	0.0361	5.083	0.9999	0.0004
A2(1st reading)	5.2325	1.0	0.039		5.2331	0.9996	0.0004
A2(2nd reading)	5.3752	0.8	0.021	0.1009	5.3757	0.9999	0.0004
A3(1st reading)	5.1476	0.7	0.032		5.1472	0.9997	0.0003
A3(2nd reading)	5.2642	1.2	0.038	0.0824	5.2668	0.9996	0.0018
A4(1st reading)	5.0765	1.0	0.031		5.0781	0.9998	0.0011
A4(2nd reading)	5.2431	0.6	0.034	0.1178	5.2466	0.9998	0.0025
Mean		*0.9*	*0.033*	*0.084*			*0.001*
Cu							
C1(1st reading)	5.8345	0.9	0.044		5.8334	0.9996	0.0008
C1(2nd reading)	5.8514	0.9	0.033	0.0120	5.854	0.9998	0.0018
C2(1st reading)	5.6319	1.2	0.043		5.634	0.9998	0.0015
C2(2nd reading)	5.7281	0.5	0.020	0.0680	5.729	0.9999	0.0006
C3(1st reading)	5.5638	2.2	0.113		5.5721	0.9990	0.0059
C3(2nd reading)	6.0100	0.8	0.035	0.3155	6.0095	0.9996	0.0004
C4(1st reading)	5.3692	2.6	0.106		5.3607	0.9980	0.0060
C4(2nd reading)	5.7692	0.5	0.014	0.2828	5.7683	1.0000	0.0006
Mean		*1.2*	*0.051*	*0.170*			*0.002*

Table 3.22. Slope values for the steel, Al and Cu substrate of uncoated beams.

A statistical Anova analysis was performed for the elastic modulus of steel, Al and Cu beams for two sets of readings, as shown in table 3.23. This analysis shows that the significant factor is the E_s between different beams (steel, Al, Cu). The variation between samples is not significant.

In-Plane Elastic Modulus of Steel, Al and Cu Beams					
	E_s for Steel (GPa)	E_s for Al (GPa)	E_s for Cu (GPa)		
1.1 (1st reading)	206.9	72.8	129.5		
1.2 (2nd reading)	202.9	73.5	129.1		
2.1 (1st reading)	209.7	74.5	133.5		
2.2 (2nd reading)	210.3	72.5	131.3		
3.1 (1st reading)	211.7	75.6	138.0		
3.2 (2nd reading)	208.8	73.9	127.7		
4.1 (1st reading)	214.4	75.7	141.6		
4.2 (2nd reading)	212.5	73.3	131.7		

Anova: Two-Factor With Replication

SUMMARY	Steel	Al	Cu	Total	
1.1					
Count	2	2	2	6	
Sum	409.8	146.3	258.6	814.7	
Average	204.9	73.2	129.3	135.8	
Variance	8.0	0.2	0.1	3498.5	
2.1					
Count	2	2	2	6	
Sum	420.0	147.0	264.8	831.8	
Average	210.0	73.5	132.4	138.6	
Variance	0.2	2.0	2.4	3750.7	
3.1					
Count	2	2	2	6	
Sum	420.5	149.5	265.7	835.7	
Average	210.3	74.8	132.9	139.3	
Variance	4.2	1.4	53.0	3708.6	
4.1					
Count	2	2	2	6	
Sum	426.9	149.0	273.3	849.2	
Average	213.5	74.5	136.7	141.5	
Variance	1.8	2.9	49.0	3886.5	
Total					
Count	8	8	8		
Sum	1677.2	591.8	1062.4		
Average	209.7	74.0	132.8		
Variance	12.7	1.4	22.7		

Source of Variation	SS	df	MS	F	STDEV	P-value	F crit
Sample	100.99	3	33.66	3.22	5.80	6.11E-02	3.49
Columns	74064.02	2	37032.01	3546.28	192.44	2.32E-17	3.89
Interaction	32.01	6	5.34	0.51	2.31	7.89E-01	3.00
Within	125.31	12	10.44		3.23		
Total	74322.34	23					

Conclusion	
Relative error of E_s for steel substrate	1.7%
Relative error of E_s for Al substrate	1.6%
Relative error of E_s for Cu substrate	3.6%
Relative error of the measurements	3.2GPa

Table 3.23. Anova analysis for the in-plane elastic modulus for steel, Al and Cu uncoated beams.

2. In-Plane Elastic Modulus Results of the Coated Beams

The coated beams used for calculating the in-plane elastic modulus, by mechanical load using water as a loading method, are the series 1C and 4C on steel and Al substrate respectively. The sputter conditions are in table 3.15. The index of S3, S4, A2 and A8 corresponds to different sample positions within the vacuum chamber.

The in-plane elastic modulus was calculated for the coated beam from equation 2.11 (1st mathematical model) and 2.23 (2nd mathematical model). The width and substrate thickness were measured for all samples by the same method referred to in the mechanical loading using washers. The film thickness was measured by ball cratering described in section 2.3. The photograph 3.12 shows the layers within the coating at 400 times magnification by this method for Al/TiB_2 coating on the steel substrate. The procedure of elastic modulus calculation was the same for all samples and it was the same as for the mechanical loading using washers as weights method. Table 3.24 shows values of the elastic modulus for the substrates (steel, Cu, Al) together with the values of the relative error and STDEV. The relative error for the steel samples is 2.8% while for Al samples it is 0.8%. They are in the range found in table 3.21 of 3.7% for steel and 1.0% for Al beams and also for the STDEV.

E_s for Al and Steel Uncoated Beams			
Composite beam material	E_s *(GPa)*	*Relative error (%)*	*STDEV*
Steel substrate			
Al/TiB_2 (S3)	212.2	2.6	3.04
Al/TiB_2 (S4)	202.8	3.8	3.78
$(Al/TiB_2)N_2$ (S3)	212.9	2.0	2.48
Mean	*209.3*	*2.8*	*3.10*
Al substrate			
Al/TiB_2 (A2)	71.20	0.6	0.26
$(Al/TiB_2)N_2$ (A8)	71.10	0.9	0.50
Mean	*71.15*	*0.8*	*0.38*
E_s calculation was based on $(\gamma_s)_1$ from δ/P			

Table 3.24. In-plane elastic modulus for uncoated beams.

Table 3.25 shows values of the elastic modulus for the coated beams (steel, Cu, Al) together with the values of the relative error and STDEV. This table gives the following information:

♦ From the relative error value of $(E_f)_{1b}$ based on $(\gamma_c)_1$, and $(\gamma_s)_1$, for example 14.5% for Al/TiB_2(S3), when compared with the $(E_f)_{1a}$ value based on a "E_s book value" and $(\gamma_c)_1$, for example 9.6% for Al/TiB_2(S3), from the equation 2.11, we see that the compliance of the steel substrate through the γ_s is a significant factor. This effect is not significant for Al substrate.

♦ The accuracy of γ_s, which is strongly influenced by the frame compliance of the system and beam thickness, strongly affects the E_f results. This is shown by comparing the relative error of $(E_f)_{1a}$ with $(E_f)_{1b}$.

♦ The relative errors of E_f calculated from the equation 2.23 when considering either a "book value of E_s", $(E_f)_{2a}$ or the measured substrate value, $(E_f)_{2b}$ shows that the values of E_s only affect slightly the E_f values (16.3%, 16.7%). This is due to the mathematical model considering the ratio of the compliance (γ_s/γ_c).

♦ The STDEV in the film elastic modulus based on the second mathematical model (equation 2.23) between $((E_f)_{2a},(E_f)_{2b})$ is much less than that obtained with the first mathematical model (equation 2.11) between $((E_f)_{1a},(E_f)_{1b})$. This is thought to be due to the better repeatability obtained by measuring the ratio of the compliance (γ_s/γ_c) rather than using the value of compliance.

♦ The relative error in the elastic modulus based on the equation 2.23 is higher than that obtained with equation 2.11. This may reflect the fact that the measured compliance of the system is not constant for different measurements and the thickness of the beam and coating varies.

E_f for Al and Steel Coated Beams													
Composite beams material	$(E_f)_{1a}$ (GPa)	Relative error (%)	STDEV	$(E_f)_{1b}$ (GPa)	Relative error (%)	STDEV	STDEV between $(E_f)_{1a}$ and $(E_f)_{1b}$	$(E_f)_{2a}$ (GPa)	Relative error (%)	STDEV	$(E_f)_{2b}$ (GPa)	Relative error (%)	STDEV	STDEV between $(E_f)_{2a}$ and $(E_f)_{2b}$
Steel substrate													
Al/TiB$_2$ (S3)(1)	409.2	8.3	28.1	356.5	16.1	50.7	37.3	370.4	18.5	57	379.7	18.5	58.5	6.6
Al/TiB$_2$ (S3)(2)	400.1	10.8	22.5	347.5	12.8	31.3	37.2	360.7	14.0	36.4	369.8	14.8	37.3	6.4
Mean of two read.	*404.65*	*9.6*	*25.3*	*352.0*	*14.45*	*41.0*	*37.2*	*365.6*	*16.3*	*46.7*	*374.8*	*16.7*	*47.9*	*6.5*
Al/TiB$_2$(S4)	503.7	3.6	13.6	557.4	9.1	46.1	38.0	582.4	10.8	57.9	597.0	10.8	59.3	10.3
(Al/TiB$_2$)N$_2$ (S3)	315.5	3.6	13.1	211.1	32.2	47.1	73.8	213.2	34.1	49.1	219.3	34.1	51.1	4.3
Al substrate													
Al/TiB$_2$ (A2)	235.8	9.1	17.4	228.9	7.1	13.6	4.9	258.2	21.5	33.7	259.3	21.5	33.9	0.8
(Al/TiB$_2$)N$_2$ (A8)	682.0	6.3	34.6	678.0	6.5	33.0	2.8	693.9	6.5	34.1	695.9	6.5	34.2	1.4

$(E_f)_{1a}$ calculation was based on $(\gamma_c)_1$, for Es=207GPa, from equation 2.11
$(E_f)_{1b}$ calculation was based on $(\gamma_c)_1$ and $(\gamma_s)_1$, from equation 2.11
$(E_f)_{2a}$ calculation was based on $(\gamma_c)_1$, for Es=207GPa, from equation 2.23
$(E_f)_{2b}$ calculation was based on $(\gamma_c)_1$ and $(\gamma_s)_1$, from equation 2.23

Table 3.25. In-plane elastic modulus for steel and Al coated beams.

Table 3.26 shows the slope of the deflection versus load curve for Al and steel substrate with the values of relative error and STDEV. This table gives the following information:

♦ The mean relative error of the slope for Al and steel uncoated beams is in the range found in table 3.22. The relative error of the substrate slope, $(\gamma_s)_1$ is higher for steel than for Al beams.

♦ The STDEV between γ_1 and γ_2 for uncoated and coated beams reflects the repeatability of the load and deflection measurements in the same test. The STDEV between γ_1 and γ_2 for uncoated and coated beams are very similar, confirming that the repeatability of the load and deflection measurements in the same test is less significant compared to the repeatability of the measurement, sample dimensions and film thickness, as shown in the STDEV for each sample.

♦ The variation of the STDEV between γ_1 and γ_2 for coated beams reflects the film thickness accuracy

Slope of the curve deflection versus load for Al and steel coated beams														
Composite Beam Material	t_f (mm)	Slope from $(\gamma_s)_1$	Relative error (%)	STDEV	Slope from $(\gamma_s)_2$	Correlation factor (R^2)	STDEV between $(\gamma_s)_1$ and $(\gamma_s)_2$	Slope from $(\gamma_c)_1$	Relative error (%)	STDEV	Slope from $(\gamma_c)_2$	Correlation factor (R^2)	STDEV between $(\gamma_c)_1$ and $(\gamma_c)_2$
Steel substrate													
Al/TiB$_2$ (S3)	6.04	4.0200	2.2	0.057	4.0247	0.9991	0.003	3.4467	2.1	0.039	3.4531	0.9995	0.0045
Al/TiB$_2$ (S4)	5.00	3.8673	1.9	0.071	3.8744	0.9988	0.005	3.1784	0.6	0.014	3.1784	0.9999	0.0000
(Al/TiB$_2$)N$_2$ (S3)	3.60	3.7407	1.7	0.043	3.7452	0.9993	0.003	3.5426	0.7	0.012	3.5425	0.9999	0.0001
Mean			*1.9*	*0.06*			*0.004*		*1.1*	*0.02*			*0.002*
Al substrate													
Al/TiB$_2$ (A2)	3.50	5.4721	0.4	0.020	5.4704	0.9999	0.001	4.8130	1.2	0.044	4.8089	0.9996	0.0029
(Al/TiB$_2$)N$_2$ (A8)	3.20	5.5511	1.2	0.035	5.5565	0.9999	0.004	4.0441	2.3	0.056	4.0385	0.9989	0.0040
Mean			*0.8*	*0.03*			*0.003*		*1.8*	*0.05*			*0.003*

γ_1 is the slope from the ratio of the δ/P for each load
γ_2 is the slope from the fitted curve L.S.

Table 3.26. Slope of the deflection versus load curve for Al and steel coated beams.

III-*THREE POINT BEND TEST BY NANOINDENTER*

Two uncoated beams made of steel and Al were tested in a three point bending test devised for the nanoindenter. Four measurements were performed for each sample with the load range from 0 to 20g. The measurements with highest STDEV of the slope from the ratio δ/P were rejected, so the results are the average of three measurements. The first 8g data point was also ignored to avoid including the effect of sample set up.

The in-plane elastic modulus (E_s) was calculated for the uncoated beam from equation 2.6. The procedure of elastic modulus calculation for the two samples was the same as that used for the previous methods. The parameter set up and calibration of the nanotester 550 is shown in table 3.27.

Parameter Set Up						Calibration		
Beam Material	Max. Load (mN)	Initial Load (mN)	Loading Rate (mN/s)	Filter	Amplifier Gain (%)	Initial Load (μN)	Load (μN/bit)	Depth (nm/bit)
S1 (1)	200	0.5	3.8	1	15	±4.4191	14.7662±0.0205	1.6657±0.0047
S1 (2)	200	0.5	3.52	1	15	±1.6680	13.6352±0.1211	1.5631±0.0026
A1 (1)	200	0.5	3.8	1	15	±4.0414	14.7662±0.0207	1.6657±0.0049
A1 (2)	200	0.5	3.52	1	15	±5.9577	13.6352±0.1211	1.5631±0.0026
(1)- Refer to the first reading; (2)- Refer to the second reading								

Table 3.27. Parameter set up for three point bend test by nanoindenter.

The experiments were performed with a cylinder indenter reproduced with diameter of 2mm. The in-plane elastic modulus for the steel and aluminium beams is in table 3.28 and 3.29 respectively. These tables of results were obtained without applying a correction for the compliance of the nanoindenter. As the E_s values were found to be much lower than the values indicated in the literature, this is believed to be due to the compliance of the nanoindenter modifying the results, which was not calibrated for this case. Using the raw data for the steel and aluminium samples it was possible to calculate the fitting curve of the elastic modulus versus compliance, which obeys a power law with the correlation factor of 0.9987 and 0.9984, as shown in figure 3.45 and 3.46.
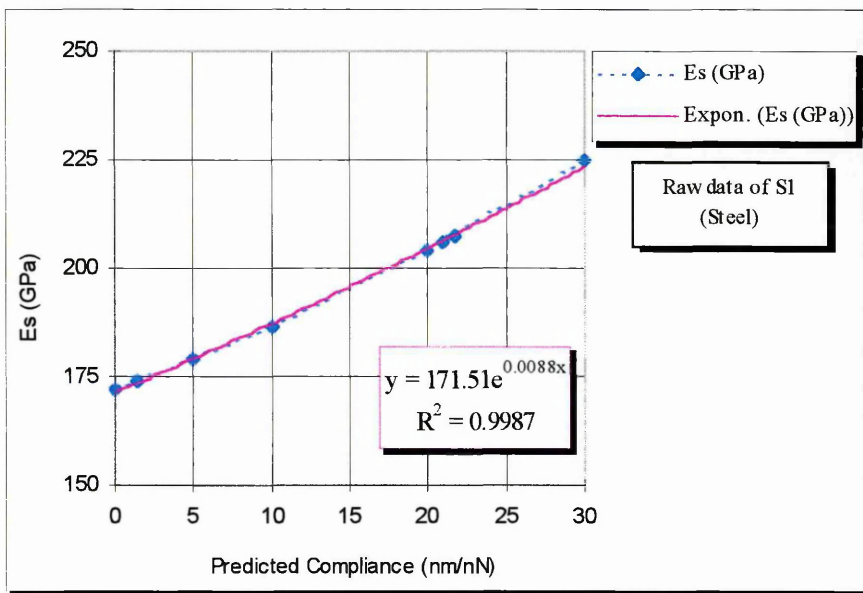

Figure 3.45. Predicted compliance (C) of the nanoindenter as a function of the E_s for steel sample.
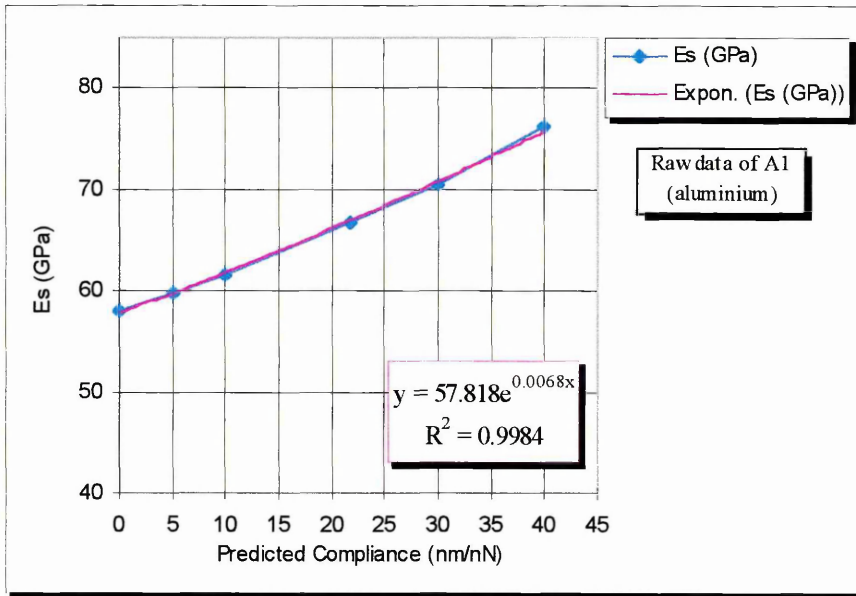
Figure 3.46. Predicted compliance (C) of the nanoindenter as a function of the E_s for aluminium sample.

The predicted compliance was used to correct the E_s values to those recommended in the literature, as shown in table 3.28. The predicted compliance based on steel raw data is 21.75nm/nN, while the predicted compliance based on Al raw data is 30nm/nN. For no compliance correction, the average relative error of the slope is 0.35%, the STDEV of the slope is 0.004 and the relative error for two readings is 0.5% for the steel beams. The values for the Al beams are not as promising as shown in table 3.29, with no compliance correction, the average relative error of the slope is 0.7%, the STDEV of the slope is 0.01 and the relative error for two readings is 1.8%.

The predicted compliance based on steel raw data gives a more realistic E_s value for the steel beam than that based on the Al raw data. This may be thought to be because the steel beam results are more reliable.

The load and depth calibration for this method are independent of the compliance of the system. The springs of the equipment were replaced between the two readings of the beams. This added another uncertainty to the compliance and may increase the error between the two readings.

Three Point Bend Test by Nanoindenter for Steel Beam								
No Compliance Correction								
Steel Beam	Slope from d/P $(\gamma_s)_1$	Relative error (%)	STDEV	R^2 of fitting curve for each measurement	Mean E_s (GPa)	Relative error (%)	STDEV	Relative error of E_s for two readings (%)
S1(1)	1.2530	0.31	0.003	0.9998; 0.9999; 1.0000	171.9	0.38	0.39	
S1(2)	1.2668	0.39	0.004	0.9999; 0.9999; 0.9999	170.1	0.51	0.51	0.5
Mean		*0.35*	*0.004*		*171.0*	*0.4*	*0.45*	
Predicted Compliance based on raw data (C) =21.75nm/nN								
Steel Beam	Slope from d/P $(\gamma_s)_1$	Relative error (%)	STDEV	R^2 of fitting curve for each measurement	Mean E_s (GPa)	Relative error (%)	STDEV	Relative error of E_s for two readings (%)
S1(1)	1.0396	0.36	0.003	0.9998; 0.9999; 0.9999	207.2	0.45	0.57	
S1(2)	1.0536	0.46	0.004	0.9999; 0.9998; 0.9999	204.5	0.61	0.74	0.7
Mean		*0.41*	*0.004*		*205.8*	*0.53*	*0.66*	
Predicted Compliance based on raw data (C) =30nm/nN								
Steel Beam	Slope from d/P $(\gamma_s)_1$	Relative error (%)	STDEV	R^2 of fitting curve for each measurement	Mean E_s (GPa)	Relative error (%)	STDEV	Relative error of E_s for two readings (%)
S1(1)	0.9588	0.40	0.003	0.9997; 0.9999; 0.9999	224.7	0.49	0.67	
S1(2)	0.9718	0.58	0.005	0.9999; 0.9998; 0.9989	221.7	1.39	1.27	0.7
Mean		*0.49*	*0.004*		*223.2*	*0.94*	*0.97*	
(1)-Refer to first reading; (2)- Refer to second reading								

Table. 3.28. In-plane elastic modulus results for steel beams.

Three Point Bend Test by Nanoindenter for Aluminium Beam								
No Compliance Correction								
Al Beam	Slope from d/P $(\gamma_s)_1$	Relative error (%)	STDEV	R^2 of fitting curve for each measurement	Mean E_s (GPa)	Relative error (%)	STDEV	Relative error of E_s for two readings (%)
Al(1)	1.6486	0.7	0.01	0.9997; 0.9998; 0.9996	58.1	1.59	0.33	
Al(2)	1.7100	0.7	0.01	0.9999; 0.9995; 0.9993	56.0	1.61	0.37	1.8
Mean		0.7	0.01		57.1	1.6	0.35	
Predicted compliance based on raw data (C)=21.75 nm/nN								
Al Beam	Slope from d/P $(\gamma_s)_1$	Relative error (%)	STDEV	R^2 of fitting curve for each measurement	Mean E_s (GPa)	Relative error (%)	STDEV	Relative error of E_s for two readings (%)
Al(1)	1.4352	0.81	0.01	0.9997; 0.9997; 0.9996	66.8	1.83	0.43	
Al(2)	1.4968	0.85	0.01	0.9999; 0.9993; 0.999	64.0	1.85	0.49	2.1
Mean		0.8	0.01		65.4	1.8	0.46	
Predicted compliance based on raw data (C)=30nm/nN								
Al Beam	Slope from d/P $(\gamma_s)_1$	Relative error (%)	STDEV	R^2 of fitting curve for each measurement	Mean E_s (GPa)	Relative error (%)	STDEV	Relative error of E_s for two readings (%)
Al(1)	1.3547	0.85	0.01	0.9996; 0.9996; 0.9995	70.8	1.93	0.48	
Al(2)	1.4159	0.89	0.01	0.9999; 0.9993; 0.9989	67.7	1.96	0.55	2.2
Mean		0.9	0.01		69.3	1.9	0.52	
(1)- Refer to first reading; (2)- Refer to second reading								

Table. 3.29. In-plane elastic modulus results for aluminium beams.

3.3.3. ELASTIC MODULUS AND HARDNESS BY NANOINDENTATION

The hardness and elastic modulus of multilayer coatings, series A, C and E, were performed by nanoindentation, using a nanoindenter 550. The sputter conditions of these series are in table 3.15. The elastic modulus and hardness calculations and measurement procedures were the same as described for the bi-layer coatings. However, the Poisson's ratio was assumed to be 0.11 [12,17] for TiB_2 and was rationed as a function of the volume of the ceramic layer for the multilayer coatings.

I-SERIES A

Seven coated samples made of steel were tested by nanoindentation. The experiments were performed for four indentation depth ranges, for each sample. They were selected corresponding to 1/5, 1/10, 1/20 and 1/50 of the total coating thickness of 5μm. A dwell time at maximum load, holding period, of 10 seconds was applied to all experiments, allowing for possible time dependent plastic deformation. The amplifier gain of 100 was applied to all experiments. The parameters set up for each sample are shown in table 3.30.

On each sample seven indentations were made for the four indentation depth ranges. The elastic modulus and hardness results quoted are the average of five measurements, as shown in table 3.31 for the steel substrate. The highest and lowest values were rejected as extremes.

Sample Reference (steel substrate)	Varying parameters of the TiB₂ (λ nm; Vc%)	Max. Load (mN)	Initial Load (mN)	Rate (mN/s)	Max. Depth (nm)	Complaince C(nm/mN)	Zero error (± μN)	Calibration Load (μ N/bit)	Calibration depth (nm/bit)
1AS4		24	0.05	0.15	130	1.25	-	0.8121±0.00704	0.041±0.00209
1AS4	200/50	24	0.05	0.53	300	1.25	-	0.8121±0.00704	0.041±0.00209
1AS4		190	0.05	1.22	600	1.25	-	8.0006±0.06671	0.041±0.00209
1AS4		194	0.05	5.53	1200	1.25	-	8.0006±0.06671	0.041±0.00209
2AS4		24	0.05	0.15	130	1.25	-	0.8121±0.00704	0.041±0.00209
2AS4	100/50	24	0.05	0.53	300	1.25	-	0.8121±0.00704	0.041±0.00209
2AS4		190	0.05	1.22	600	1.25	-	8.0006±0.06671	0.041±0.00209
2AS4		190	0.05	5.53	1200	1.25	-	8.0006±0.06671	0.041±0.00209
3AS4		24	0.05	0.15	130	1.25	-	0.8121±0.00704	0.041±0.00209
3AS4	50/50	24	0.05	0.53	300	1.25	-	0.8121±0.00704	0.041±0.00209
3AS4		190	0.05	1.22	600	1.25	-	8.0006±0.06671	0.041±0.00209
3AS4		190	0.05	5.53	1200	1.25	-	8.0006±0.06671	0.041±0.00209
4AS4		24	0.05	0.15	130	1.25	-	0.8121±0.00704	0.041±0.00209
4AS4	200/75	24	0.05	0.53	300	1.25	-	0.8121±0.00704	0.041±0.00209
4AS4		190	0.05	1.22	600	1.25	-	8.0006±0.06671	0.041±0.00209
4AS4		190	0.05	5.53	1200	1.25	-	8.0006±0.06671	0.041±0.00209
5AS4		24	0.05	0.15	130	1.25	-	0.8121±0.00704	0.041±0.00209
5AS4	200/25	24	0.05	0.53	300	1.25	-	0.8121±0.00704	0.041±0.00209
5AS4		190	0.05	1.22	600	1.25	-	8.0006±0.06671	0.041±0.00209
5AS4		190	0.05	5.53	1200	1.25	-	8.0006±0.06671	0.041±0.00209
2AS11		24	0.05	0.15	130	1.49	-	0.8121±0.00704	0.041±0.00013
2AS11	100/50	24	0.05	0.53	300	1.49	-	0.8121±0.00704	0.041±0.00013
2AS11		194	0.05	1.22	600	1.49	-	8.0006±0.06671	0.041±0.00013
2AS11		194	0.05	5.53	1200	1.49	-	8.0006±0.06671	0.041±0.00013
4AS11		24	0.05	0.15	130	1.49	-	0.8121±0.00704	0.041±0.00013
4AS11	200/75	24	0.05	0.53	300	1.49	-	0.8121±0.00704	0.041±0.00013
4AS11		194	0.05	1.22	600	1.49	-	8.0006±0.06671	0.041±0.00013
4AS11		194	0.05	5.53	1200	1.49	-	8.0006±0.06671	0.041±0.00013

Table 3.30. Parameters set up of the nanoindentation experiments for multilayer coatings, series A.

Sample Reference (Steel substrate)	Varying Parameters of the Al/TiB₂ (λ nm; Vc %)	Possoin's Ratio (vₓ)	Plastic depth (nm)	H (GPa)	STDEV	E (GPa)	STDEV
1AS4	200/50		118.6	5.93	1.11	140.1	21.1
	200/50	0.21	263.0	5.52	0.78	138.6	9.3
	200/50		521.0	4.30	0.49	119.6	8.5
	200/50		1016.0	3.46	0.50	106.4	10.5
2AS4	100/50		120.0	6.51	1.17	163.7	20.8
	100/50	0.21	264.0	5.85	0.98	158.0	13.5
	100/50		521.0	4.62	0.20	133.2	8.2
	100/50		1022.0	3.54	0.21	117.4	4.3
3AS4	50/50		113.0	9.39	0.80	198.9	26.7
	50/50	0.21	268.0	5.10	0.31	137.8	10.4
	50/50		520.0	4.43	0.26	123.4	7.3
	50/50		1007.0	3.87	0.22	110.6	3.3
4AS4	200/75		106.0	12.99	1.66	216.4	32.0
	200/75	0.16	253.0	8.05	0.76	182.0	25.7
	200/75		503.0	5.62	0.57	140.4	16.2
	200/75		955.0	5.34	0.12	140.7	7.9
5AS4	200/25		120.0	5.69	0.44	140.9	9.5
	200/25	0.25	275.0	3.57	0.09	110.6	10.2
	200/25		538.0	3.25	0.95	101.9	9.1
	200/25		1060.0	2.66	0.37	92.8	7.9
2AS5	100/50		120	5.69	0.44	143.7	9.7
	100/50	0.21	275	3.57	0.09	112.8	10.4
	100/50		552	4.56	0.37	126.1	9.2
	100/50		1000	3.6	0.27	108.9	5.6
4AS5	200/75		110	12.17	3.03	265.9	68.5
	200/75	0.16	302	5.91	0.73	160.5	25
	200/75		530.6	6.18	0.41	165.7	16.9
	200/75		934	5.69	0.25	167.7	10.1

Table 3.31. Hardness and elastic modulus result for multilayer coatings, series A.

1-Analysis of the Hardness Results

Figure 3.47 shows an increase in hardness for low depth plastic deformation. This has been reported in the literature, see section 1.5.2. The volume of ceramic has a strong effect on the hardness, a much greater effect than the composition wavelength. The highest value was found for the 200nm/75% and the lowest for the 200nm/25%.

Figure 3.48 shows a plot of the hardness against composition wavelength. For intermediate penetration depths (±300nm), maximum hardness is observed for the 100nm composition wavelength at 50% volume fraction of ceramic. However, it can be seen that the hardness increases as the composition wavelength decreases particularly for the lowest indent penetration depth (figure 3.47).

Figure 3.49 shows a plot of hardness against plastic depth for two samples (S4,S11) with the same composition wavelength and volume fraction. Both samples have

232

the same behaviour, except sample S11 for approximately 300nm indenter depth. This may be due to this coating having a thick aluminium layer.
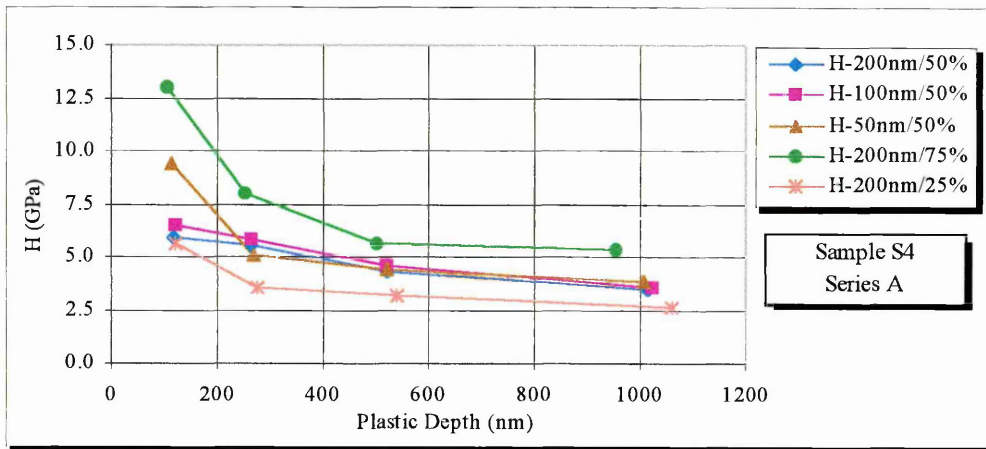

Figure 3.47. Hardness in function of the penetration depth for coatings of the series A.
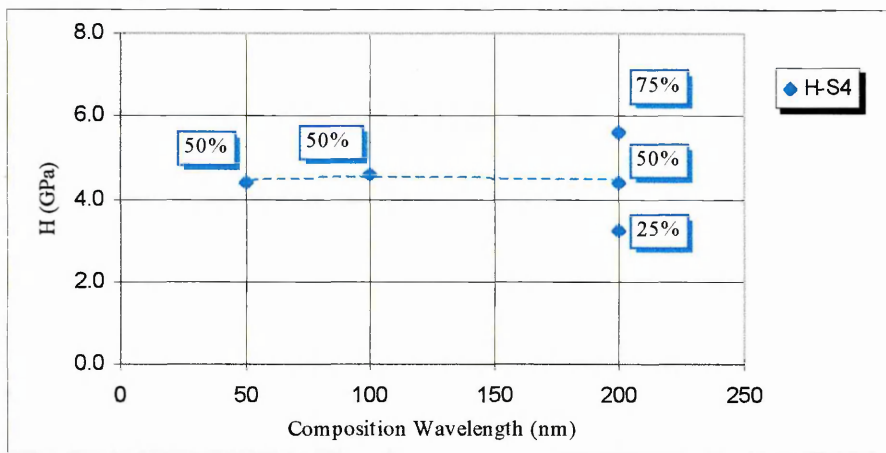

Figure 3.48. Hardness versus composition wavelength and volume fraction for approximately 300nm plastic depth.
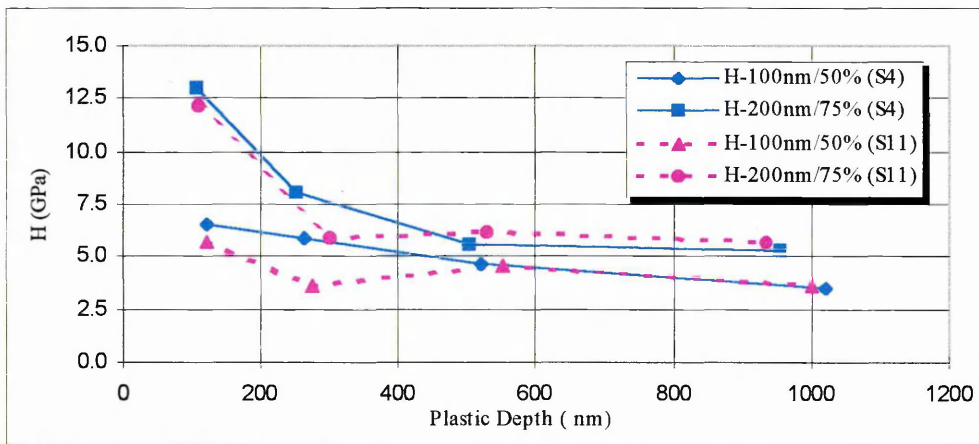

Figure 3.49. Hardness in function of the penetration depth for samples S4 and S11.

2-Analysis of the Elastic Modulus Results

The elastic modulus against plastic depth curves are shown in graph 3.50. The elastic modulus behaves very similarly to the hardness. The elastic modulus shows a similar relationship to the hardness related to the penetration depth.

Figure 3.51 shows a plot of the elastic modulus against composition wavelength and volume of ceramic fraction. The behaviour of the composite modulus is similar to hardness, a maximum for the 50nm composition wavelength when measured at small indentation depth (figure 3.50), whilst on increasing the indentation depth, the maximum elastic modulus is observed for the 100nm layers at 50% volume fraction. Similar to the hardness, results for the elastic modulus increase with volume fraction of ceramic layer.

Figure 3.52 shows a plot of the elastic modulus against plastic depth for two samples with the same composition wavelength and volume fraction of ceramic. For intermediate penetration depths the samples do not show the same behaviour. This may be due either to a different layer thickness or vibrations during the indentation experiment.

Nanoindentation measurements were undertaken using different machine operating conditions, such that the following uncontrolled variables may contribute to the measurement accuracy: using two different frame compliance values; thermal drift correction was not performed for all experiments; depth calibration was not kept constant for all experiments; the initial load calibration was not done for all experiments; some vibration was evident in some curves.
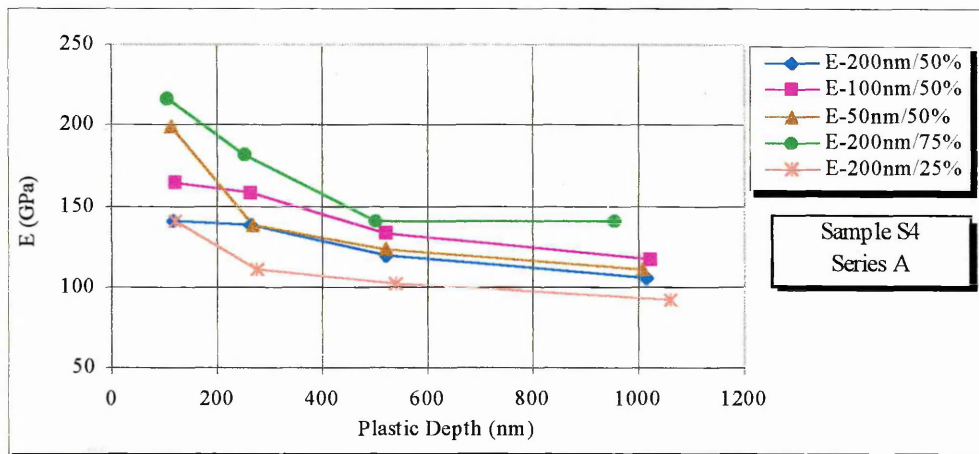

Figure 3.50. Elastic modulus in function of the penetration depth for coatings of the series A.
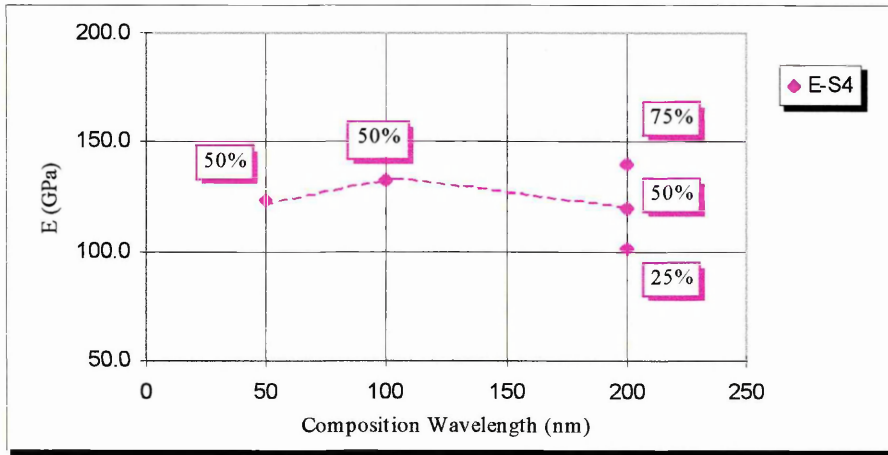
Figure 3.51. Elastic modulus versus composition wavelength and volume fraction for approximately 300nm plastic depth.
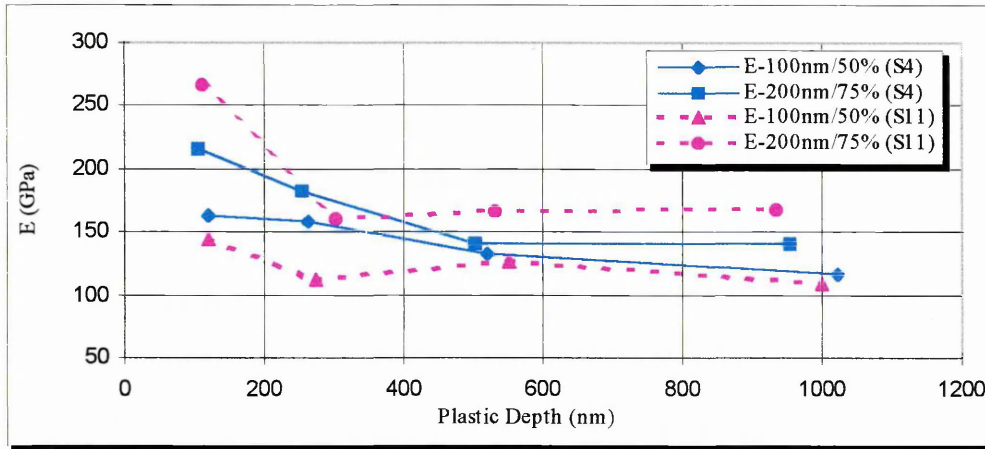

Figure 3.52. Elastic modulus versus penetration depth for samples S4 and S11.

II-SERIES C

Eight steel and seven aluminium coated samples were tested by nanoindentation (see table 3.15 for sputter conditions). The experiments were performed for two indentation depth ranges, for each sample. The depth range was selected as 200nm and 600nm for the Al and steel substrate respectively. A dwell time at maximum load of 10 seconds was applied to all experiments, allowing for possible time dependent plastic deformation. The amplifier gain of 100 was applied to all experiments. The parameters set up for each sample are shown in table 3.32.

On each sample seven indentations were made for two indentation depths. The highest and lowest values were rejected as extremes. Hence the elastic modulus and hardness quoted are the average of five measurements, as shown in tables 3.33 and 3.34 for steel and aluminium substrate respectively.

Coating System	Max. load (mN)	Initial load (mN)	Loading Rate (mN/s)	Max. Depth (nm)	Compliance (nm/mN)	Zero error (± µN)	Calibration load (µN/bit)	Calibration depth (nm/bit)	Drift correction
Al/TiB$_2$(S4)	64	0.05	0.45	200	1.03	±2.4199	2.0998±0.00242	0.0576±0.00014	y
Al/TiB$_2$(S4)	150	0.05	3.71	500	1.03	-	14.4231±0.00876	0.0576±0.00014	y
Al/TiB$_2$(S4)	100	0.10	1.20	600	1.52	-	7.8993±0.0399	0.049±0.00039	n
Al/TiB$_2$(S3)	150	0.10	1.20	600	1.42	-	7.8995±0.0399	0.0476±0.0002	n
Al/TiB$_2$(S9)	150	0.10	1.20	600	1.52	-	7.8993±0.0399	0.049±0.00039	n
Al/TiB$_2$(S10)	150	0.10	1.20	600	1.52	-	7.8993±0.0399	0.049±0.00039	n
Al/TiB$_2$(A2)	22	0.10	0.26	200	1.52	-	0.8072±0.00195	0.049±0.00039	n
Al/TiB$_2$(A5)	22	0.10	0.26	200	1.52	-	0.8072±0.00195	0.049±0.00039	n
Al/TiB$_2$(A8)	64	0.05	0.45	200	1.03	±4.1193	2.0998±0.00242	0.0576±0.00014	y
Al/TiB$_2$(A11)	22	0.10	0.26	200	1.52	-	0.8072±0.00195	0.049±0.00039	n
TiB$_2$(S3)	150	0.10	1.20	600	1.42	-	7.8995±0.0399	0.0476±0.0002	n
TiB$_2$(S9)	64	0.05	0.45	200	1.03	±1.6448	2.0998±0.00242	0.0576±0.00014	y
TiB$_2$(S9)	150	0.05	3.71	500	1.03	±5.7331	14.4231±0.00876	0.0576±0.00014	y
TiB$_2$(A2)	22	0.10	0.26	200	1.52	-	0.8072±0.00195	0.049±0.00039	n
TiB$_2$(A2)	150	0.10	1.20	600	1.42	-	7.8995±0.0399	0.0476±0.0002	n
TiB$_2$(A8)	64	0.05	0.45	200	1.03	±3.0116	2.0998±0.00242	0.0576±0.00014	y
TiB$_2$(A8)	150	0.05	3.71	500	1.03	±3.8342	14.4231±0.00876	0.0576±0.00014	y
(Al/TiB$_2$)N(S3)	150	0.10	1.20	600	1.42	-	7.8995±0.0399	0.0476±0.0002	n
(Al/TiB$_2$)N(S4)	64	0.05	0.45	200	1.03	±3.7916	2.0998±0.00242	0.0576±0.00014	y
(Al/TiB$_2$)N(S4)	150	0.05	3.71	500	1.03	±7.1752	14.4231±0.00876	0.0576±0.00014	y
(Al/TiB$_2$)N(A8)	64	0.05	0.45	200	1.03	±4.3820	2.0998±0.00242	0.0576±0.00014	y
(Al/TiB$_2$)N(A8)	150	0.05	3.71	500	1.03	±0.0000	14.4231±0.00876	0.0576±0.00014	y

(S3),(S4),(S9)-Reference of the sample position inside the vacuum chamber on steel substrate
(A2),(A5),(A11),(A8)-Reference of the sample position inside the vacuum chamber on Al substrate

Table 3.32. Parameters set up of the nanoindentation experiments for multilayer coatings, series C.

Coating System (Steel substrate)	Poisson's ratio (v_s)	Plastic depth (nm)	H (GPa)	STDEV	E (GPa)	STDEV
Al/TiB$_2$(S4)	0.16	163	8.93	1.40	216.2	32.1
Al/TiB$_2$(S4)(2)	0.16	406	8.84	0.34	208.9	6.3
Al/TiB$_2$(S4)(1)	0.16	461	8.72	0.69	206.7	9.5
Al/TiB$_2$(S3)	0.16	462	8.93	0.27	211.1	6.4
Al/TiB$_2$(S9)	0.16	463	8.67	0.20	215.1	17.4
Al/TiB$_2$(S10)	0.16	461	8.52	0.12	197.8	4.5
TiB$_2$(S3)	0.11	322	33.92	4.45	379.4	34.1
TiB$_2$(S9)	0.11	118	29.12	0.96	335.5	8.7
TiB$_2$(S9)	0.11	291	29.11	0.68	303.2	4.2
(Al/TiB$_2$)N(S3)	0.16	422	10.96	0.48	160.0	8.7
(Al/TiB$_2$)N(S4)	0.16	155	9.13	1.48	153.5	15.7
(Al/TiB$_2$)N(S4)	0.16	369	10.23	0.26	146.2	4.0

(1)-1st reading; (2)-2nd reading

Table 3.33. Hardness and elastic modulus result for multilayer coatings onto steel, series C.

Coating System (Al substrate)	Poisson's ratio (υ_s)	Plastic depth (nm)	H (GPa)	STDEV	E (GPa)	STDEV
Al/TiB$_2$(A2)	0.16	156	8.50	0.59	171.2	16.0
Al/TiB$_2$(A5)	0.16	151	10.14	0.60	183.2	6.9
Al/TiB$_2$(A8)	0.16	164	7.91	0.69	179.9	5.4
Al/TiB$_2$(A11)	0.16	151	10.18	0.74	189.3	26.3
TiB$_2$(A2)	0.11	114	26.96	3.21	273.9	25.9
TiB$_2$(A2)	0.11	320	18.17	1.60	105.1	1.9
TiB$_2$(A8)	0.11	127	22.33	4.00	244.9	15.4
TiB$_2$(A8)	0.11	274	25.12	1.60	178.9	4.5
(Al/TiB$_2$)N(A8)	0.16	151	9.31	1.94	141.7	15.8
(Al/TiB$_2$)N(A8)	0.16	376	8.48	0.54	111.6	3.5

Table 3.34. Hardness and elastic modulus result for multilayer coatings onto Al, series C.

1-Analysis of the Hardness Results

Figures 3.53 to 3.56 show the hardness values of the Al/TiB$_2$, (Al/TiB$_2$)N$_2$ and TiB$_2$ coating systems either on steel or aluminium substrates, as a function of the sample position inside the vacuum chamber. The number below the coatings system on the x-axis corresponds to the sample position inside the vacuum chamber. The label in each coating system gives information about either plastic depth or compliance of the nanoindentation measurements.

Figures 3.53 and 3.54 show that the hardness variation versus sample position inside the chamber is more stable for steel substrates, compared to an Al substrate. However, this inference could be in doubt due to the uncertainties of the measurements, for example sample S4 for the same plastic depth with two different compliances of the indenter (1.03, 1.45nm/mN). An addition of 30%N$_2$ shows an increase in hardness of the Al/TiB$_2$ system as shown in figure 3.55. This may be due to the lattice distortion by the nitrogen atoms.

The figure 3.56 shows that the hardness values for TiB$_2$ coatings is higher for steel over Al substrates. The hardness values of 33.92GPa for TiB$_2$ on a steel and 26.96GPa for TiB$_2$ on an Al substrate will be considered as reference values for multilayer coatings series C and bi-layer coatings. This increase in hardness on steel when compared with aluminium substrate is considered to be due to the stress field from indentation interacting with the underlying substrate.

A statistical Anova analysis was performed on two samples of (Al/TiB$_2$)N$_2$ coatings on Al (A8) and steel (S4) substrates respectively, for a total depth of 200nm and 500nm, as shown in table 3.35. The relative error between samples is 8.5%. This error reflects the different substrate stiffness and variations in the layer thickness as a function of the sample position inside the vacuum chamber. The error for the two depths is much less significant (1.5%). The overall relative error in the measurement is 10.4%. As the nanoindentation conditions were the same for both samples, this error may reflect the accuracy of the machine calibration.

An Anova analysis was performed on two samples of TiB_2 coatings onto the Al substrate for investigating the effect of the indentation parameters such as: compliance, thermal drift correction, zero load calibration, see table 3.36. The relative error between sample measurements is 5%. The error for two depths is 13%. This error may reflect some substrate effect incorporated in the measurements. Both errors are much less significant compared to the accuracy of the measurements (25%). The overall relative error reflects the effect of the indentation parameters in this study.
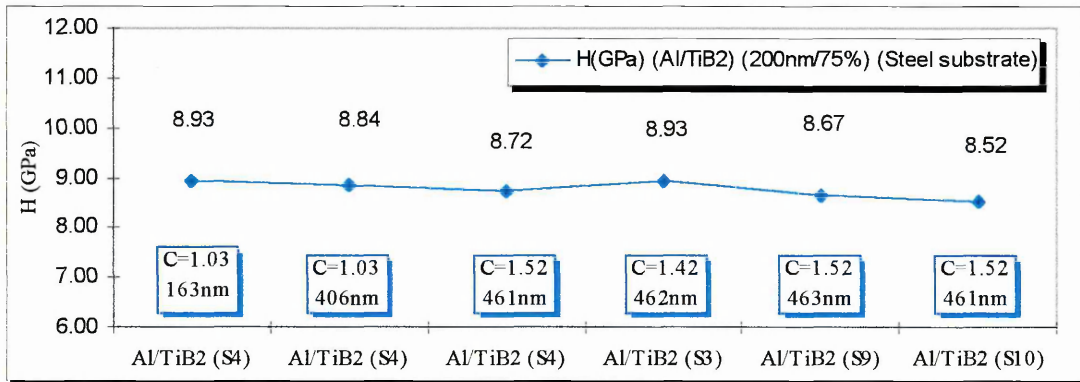
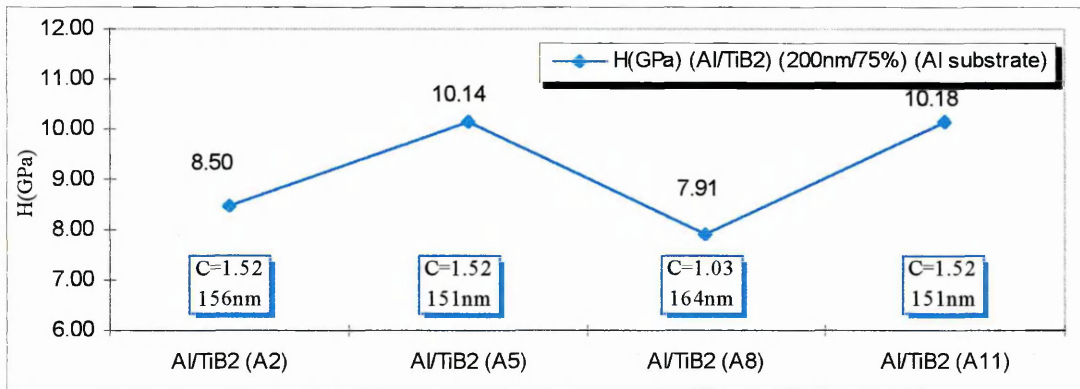Figure 3.53. Hardness for Al/TiB$_2$ coatings onto steel substrate, series C.

Figure 3.54. Hardness for Al/TiB$_2$ coatings onto aluminium substrate, series C.
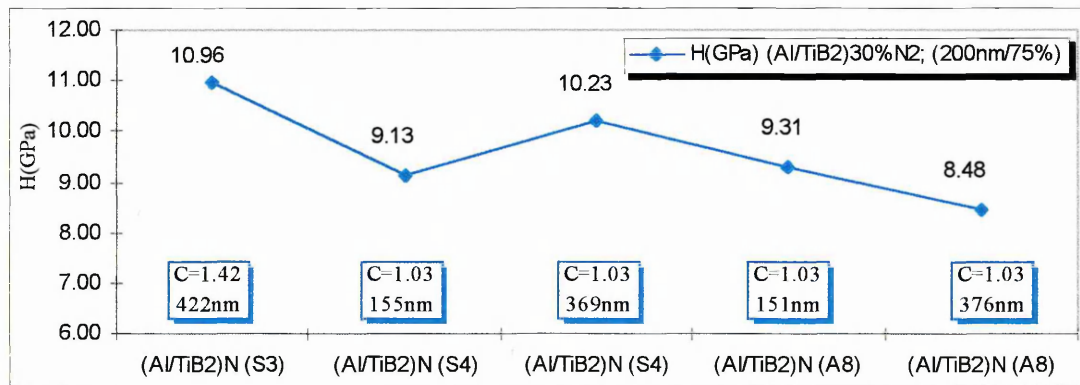

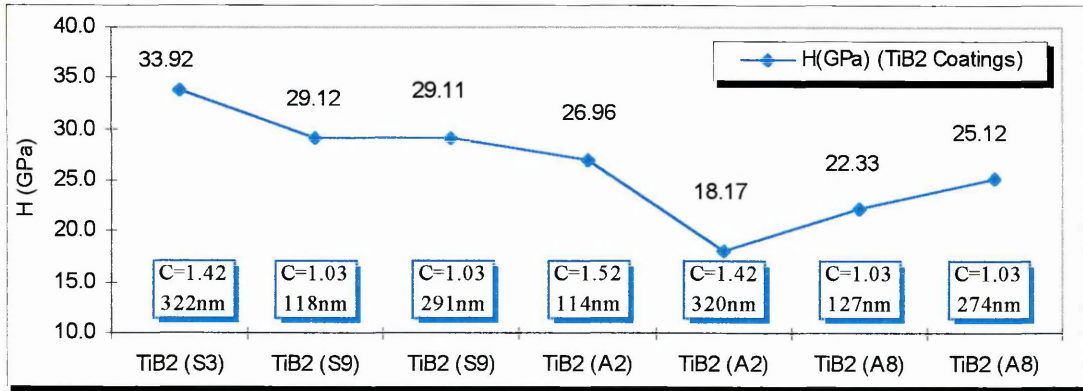Figure 3.55. Hardness for (Al/TiB$_2$)30%N$_2$ coatings onto aluminium (A8) and steel (S3, S4) substrates.

Figure 3.56. Hardness for TiB_2 coatings onto aluminium (A8, A2) and steel (S3, S9) substrates.

Sample Reference	Total depth of 200nm	Total depth of 500nm	Mean H of two depths				
$(Al/TiB_2)N(S4)$	9.13	10.23	9.68				
$(Al/TiB_2)N(A8)$	9.31	8.48	8.90				
Mean per series	9.22	9.36	9.29				
Anova: Two-Factor Without Replication							
SUMMARY	*Count*	*Sum*	*Average*	*Variance*			
Row 1	2	19.36	9.68	0.61			
Row 2	2	17.79	8.90	0.34			
Column 1	2	18.44	9.22	0.02			
Column 2	2	18.71	9.36	1.53			
Source of Variation	*SS*	*df*	*MS*	*F*	*STDEV*	*P-value*	*F crit*
Rows	0.62	1	0.62	0.66	0.78	0.57	161.45
Columns	0.02	1	0.02	0.02	0.13	0.91	161.45
Error	0.93	1	0.93		0.97		
Total	1.57	3					
Conclusion							
Overall relative error							10.4%
Relative error between samples measurement							8.5%
Relative error for two depths							1.5%

Table 3.35. Anova analysis of the hardness for $(Al/TiB_2)N_2$ coatings on Al (A8) and steel (S4) substrates.

Sample Reference	Total depth of 200nm	Total depth of 500nm	Mean H of two depths				
TiB_2(A2)	26.96	18.17	22.57				
TiB_2(A8)	22.33	25.12	23.73				
Mean per series	24.65	21.65	23.15				
Anova: Two-Factor Without Replication							
SUMMARY	Count	Sum	Average	Variance			
Row 1	2	45.13	22.57	38.63			
Row 2	2	47.45	23.73	3.89			
Column 1	2	49.29	24.65	10.72			
Column 2	2	43.29	21.65	24.15			
Source of Variation	SS	df	MS	F	STDEV	P-value	F crit
Rows	1.35	1	1.35	0.04	1.16	0.87	161.45
Columns	9.00	1	9.00	0.27	3.00	0.70	161.45
Error	33.52	1	33.52		5.79		
Total	43.87	3					
Conclusion							
Overall relative error							25.0%
Relative error between samples measurement							5.0%
Relative error for two depths							13.0%

Table 3.36. Anova analysis of the hardness for TiB_2 coatings on Al (A8,A2) substrates.

11-Analysis of the Elastic Modulus Results

Figures 3.57 to 3.60 show the elastic modulus of the Al/TiB_2, $(Al/TiB_2)N_2$ and TiB_2 coating systems either on steel or aluminium substrates. These figures are presented in the same manner as the hardness figures, to facilitate the comparison between hardness and elastic modulus of the coatings.

The elastic modulus seems to be uniform for different sample positions inside the vacuum chamber, see figures 3.57 and 3.58. An addition of 30%N_2 gave rise to a decrease in elastic modulus of the Al/TiB_2 system as shown in figure 3.59. This effect is believed to be related to the nitrogen atoms' ability to deform the lattice. The elastic modulus values of the composites are less than the values predicted from the rule of mixtures, as can be seen in figure 3.61. Figure 3.60 shows the elastic modulus values for TiB_2 coatings are higher for steel compared to Al substrates. The elastic modulus value of 379.4GPa for TiB_2 on a steel and 273.9GPa for TiB_2 on an Al substrate will be considered as reference values for multilayer coatings series C and bi-layer coatings.

A statistical Anova analysis was performed on two samples of $(Al/TiB_2)N_2$ coatings on Al (A8) and steel (S4) substrates respectively, for a total depth of 200nm and 500nm, as shown in table 3.37. This analysis shows that the major source of error is the repeatability between samples (16.8%). This error reflects the different substrate stiffness and variations in layer thickness. Both effects are more significant to elastic modulus compared to the hardness, see table 3.35. The relative error of the two depths is 13.5% and the overall relative error is 8.2%.

An Anova analysis was performed on two samples of TiB_2 coatings onto Al substrate for investigating the effect of the indentation parameters such as: compliance, thermal drift correction, zero load calibration, see table 3.38. This analysis shows that the major source of error is the effect of the penetration depth (58.9%) when tested on Al substrates. This error reflects the substrate effect incorporated in the measurements, as confirmed in figure 3.60. The overall relative error (25.6%) is due to the effect of the indentation parameters. The relative error between samples is less significant (11.2%).

Indentation studies were undertaken on two different machines and this resulted in the following contribution to measurement error: using two different frame compliances; thermal drift correction was not performed for all experiments; depth calibration was not kept constant for all experiments; the initial load calibration was not done for all experiments.
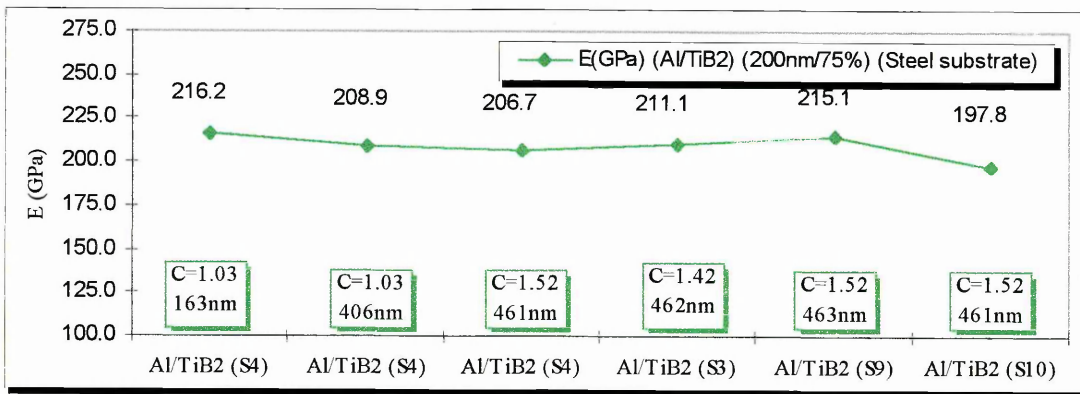

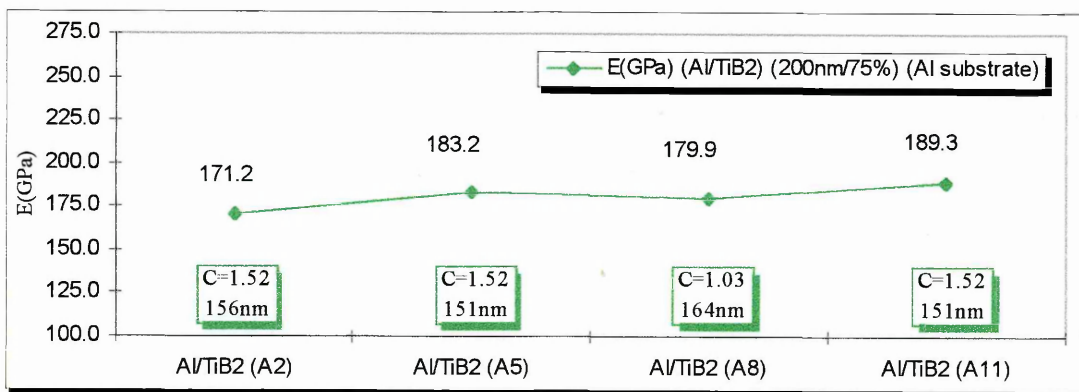Figure 3.57. Elastic modulus for Al/TiB_2 coatings onto steel substrate.

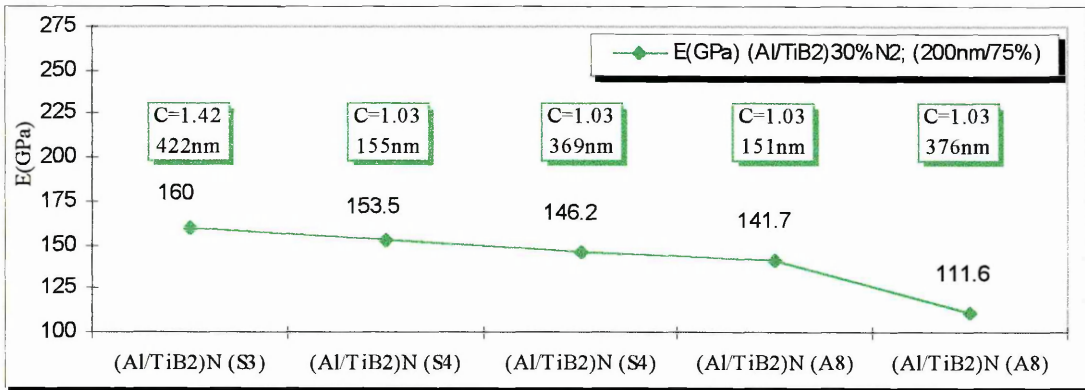Figure 3.58. Elastic modulus for Al/TiB_2 coatings onto aluminium substrate.

Figure 3.59. Elastic modulus for (Al/TiB$_2$)30%N$_2$ coatings onto aluminium (A8) and steel (S3,S4) substrates.
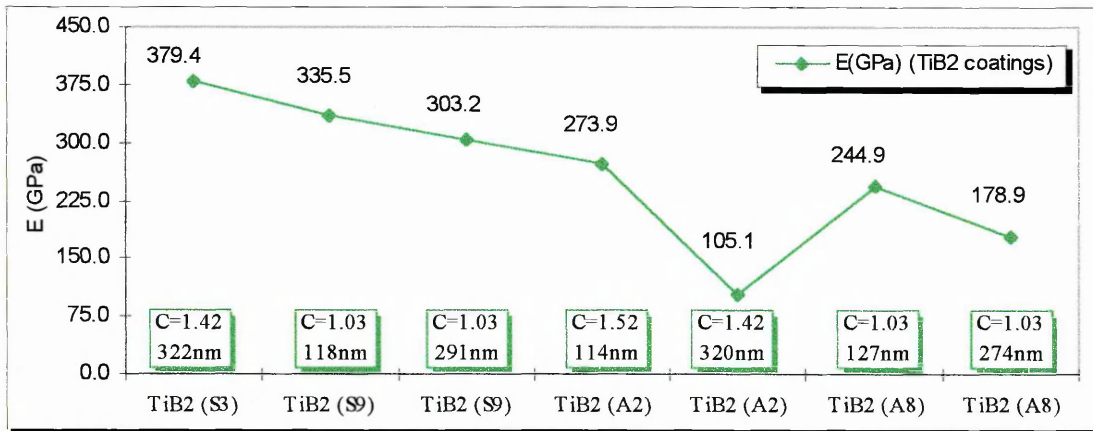

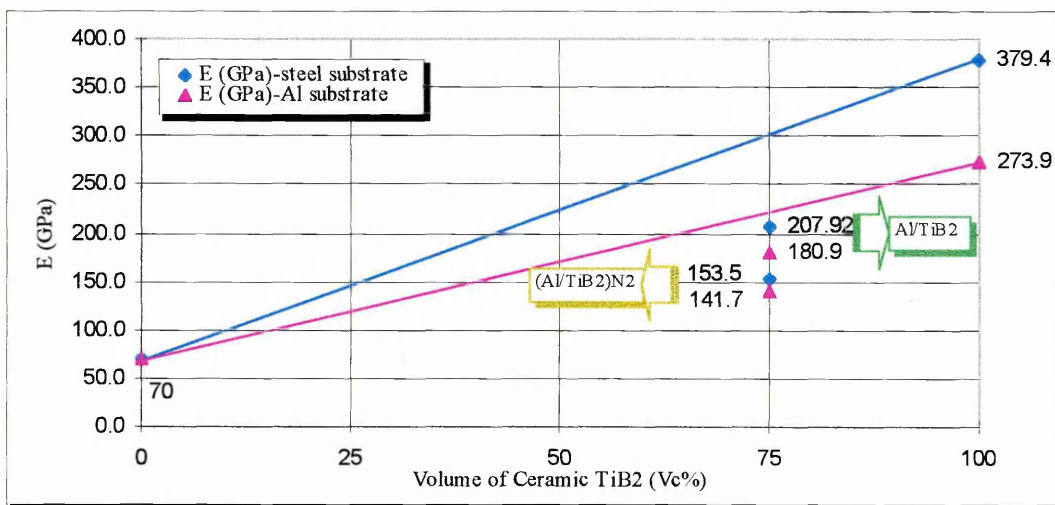Figure 3.60. Elastic modulus for TiB$_2$ coatings on Al (A8,A2) and steel (S3,S9).

Figure 3.61. Rule of mixtures for the elastic modulus of the composites Al/TiB$_2$ and (Al/TiB$_2$)/N$_2$.

Sample Reference	Total depth of 200nm	Total depth of 500nm	Mean E of two depths				
(Al/TiB$_2$)N(S4)	153.5	146.2	149.9				
(Al/TiB$_2$)N(A8)	141.7	111.6	126.7				
Mean per series	147.6	128.9	138.3				

Anova: Two-Factor Without Replication

SUMMARY	Count	Sum	Average	Variance			
Row 1	2	299.7	149.85	26.64			
Row 2	2	253.3	126.65	453.01			
Column 1	2	295.2	147.60	69.62			
Column 2	2	257.8	128.90	598.58			

Source of Variation	SS	df	MS	F	STDEV	P-value	F crit
Rows	538.24	1	538.24	4.14	23.2	0.29	161.45
Columns	349.69	1	349.69	2.69	18.7	0.35	161.45
Error	129.96	1	129.96		11.4		
Total	1017.89	3					

Conclusion							
Overall relative error							8.2%
Relative error between samples measurement							16.8%
Relative error for two depths							13.5%

Table 3.37. Anova analysis of the E_f for (Al/TiB$_2$)N$_2$ coatings on Al (A8) and steel (S4).

	Total depth of 200nm	Total depth of 500nm	Mean E of two depths				
TiB$_2$(A2)	273.9	105.1	189.5				
TiB$_2$(A8)	244.9	178.9	211.9				
Mean per series	259.4	142.0	200.7				

Anova: Two-Factor Without Replication

SUMMARY	Count	Sum	Average	Variance			
Row 1	2	379.0	189.5	14246.7			
Row 2	2	423.8	211.9	2178.0			
Column 1	2	518.8	259.4	420.5			
Column 2	2	284.0	142.0	2723.2			

Source of Variation	SS	df	MS	F	STDEV	P-value	F crit
Rows	501.76	1	501.76	0.19	22.4	0.74	161.45
Columns	13782.76	1	13782.76	5.22	117.4	0.26	161.45
Error	2641.96	1	2641.96		51.4		
Total	16926.48	3					

Conclusion							
Overall relative error							25.6%
Relative error between samples measurement							11.2%
Relative error for two depths							58.9%

Table 3.38. Anova analysis of the hardness for TiB$_2$ coatings on Al (A8,A2) substrates.

III-SERIES E

Thirteen steel and eleven aluminium coated samples were tested by nanoindentation. For each sample, the experiments were performed for measuring the

elastic modulus and the hardness of the coatings. The indentation depth ranges were selected to follow the $t_f/10$ rule of thumb, based on a total film thickness (t_f) of 5μm. A dwell time at maximum load of 10 seconds was applied to all experiments allowing for possible time dependent plastic deformation. The amplifier gain of 100 was applied to all experiments. The parameters set up for each sample are shown in table 3.39 and 3.40 for steel and aluminium substrates respectively.

Sample Reference	Coating System on Steel	Sputtering Power (WRF) (metal/ceramic)	Varying Parameters (λ nm / V%)	Max.load (mN)	Initial load (mN)	Loading Rate (mN/s)	Max. depth (nm)	Compliance (nm/mN)	Zero error (± μN)	Calibration load (μN/bit)	Calibration depth (nm/bit)	Drift correction
7ES4	Al/TiB₂	400/300	200/75	150	0.05	3.71	500	1.03	-	14.4231±0.00876	0.0576±0.0001	yes
2ES4	Al/TiB₂	400/300	200/50	66	0.1	1.03	650	1.08	-	2.1207±0.00165	0.522±0.0002	no
3ES4	Al/TiB₂	400/300	200/25	66	0.1	1.03	650	1.08	-	2.1207±0.00165	0.522±0.0002	no
9ES4	Al/TiB₂	400/300	100/75	66	0.1	1.03	650	1.08	-	2.1207±0.00165	0.522±0.0002	no
6ES4	Al/TiB₂	400/300	100/50	66	0.1	1.03	650	1.08	-	2.1207±0.00165	0.522±0.0002	no
5ES4	Al/TiB₂	400/300	100/25	66	0.1	1.03	600	1.08	-	2.1207±0.00165	0.522±0.0002	no
11ES4	Al/TiB₂	400/300	50/75	66	0.1	1.03	700	1.08	-	2.1207±0.00165	0.522±0.0002	no
14ES4	Al/TiB₂	400/300	50/50	66	0.1	1.03	650	1.08	-	2.1207±0.00165	0.522±0.0002	no
4ES10	TiB₂	300	-	200	0.5	1.65	400	1.03	±6.5905	14.4231±0.00876	0.576±0.00014	no
4ES10	TiB₂	300	-	66	0.5	0.45	200	1.03	±1.0855	2.0998±0.00242	0.576±0.00014	no
8ES4	NiCr/TiB₂	200/300	50/75	200	0.1	1.68	700	1.08	-	14.7105±0.01597	0.522±0.0002	no
15ES4	NiCr/TiB₂	200/400	50/75	200	0.1	1.68	700	1.08	-	14.7105±0.01597	0.522±0.0002	no
17ES4	Al/TiB₂	400/400	50/75	200	0.1	1.68	700	1.08	-	14.7105±0.01597	0.522±0.0002	no
16ES4	Al/TiB₂	400/440	50/75	200	0.1	1.68	700	1.08	-	14.7105±0.01597	0.522±0.0002	no

Table 3.39. Parameters set up of the nanoindentation experiments for Al/TiB₂, NiCr/TiB₂ and TiB₂ coating systems onto steel substrate at 0.6Pa sputtering pressure, of the series E.

Sample Reference	Coating System on Aluminium	Sputtering Power (WRF) (metal / ceramic)	Varying Parameters (λ nm / V%)	Max.load (mN)	Initial load (mN)	Loading Rate (mN/s)	Max. depth (nm)	Compliance (nm/mN)	Zero error (± μN)	Calibration load (μN/bit)	Calibration depth (nm/bit)	Drift correction
7EA8	Al/TiB₂	400/300	200/75	66	0.1	1.03	700	1.08	-	2.1207±0.00165	0.522±0.0002	no
2EA8	Al/TiB₂	400/300	200/50	66	0.1	1.03	650	1.08	-	2.1207±0.00165	0.522±0.0002	no
3EA8	Al/TiB₂	400/300	200/25	66	0.1	1.03	600	1.08	-	2.1207±0.00165	0.522±0.0002	no
9EA8	Al/TiB₂	400/300	100/75	66	0.1	1.03	650	1.08	-	2.1207±0.00165	0.522±0.0002	no
6EA8	Al/TiB₂	400/300	100/50	66	0.1	1.03	650	1.08	-	2.1207±0.00165	0.522±0.0002	no
5EA8	Al/TiB₂	400/300	100/25	66	0.1	1.03	600	1.08	-	2.1207±0.00165	0.522±0.0002	no
11EA8	Al/TiB₂	400/300	50/75	66	0.1	1.03	650	1.08	-	2.1207±0.00165	0.522±0.0002	no
4EA8	TiB₂	300		66	0.1	1.03	600	1.08	-	2.1207±0.00165	0.522±0.0002	no
8EA8	NiCr/TiB₂	200/300	50/75	66	0.1	1.03	700	1.08	-	2.1207±0.00165	0.522±0.0002	no
15EA8	NiCr/TiB₂	200/400	50/75	66	0.1	1.03	700	1.08	-	2.1207±0.00165	0.522±0.0002	no
16EA8	Al/TiB₂	400/440	50/75	66	0.1	1.03	700	1.08	-	2.1207±0.00165	0.522±0.0002	no

Table 3.40. Parameters set up of the nanoindentation experiments for Al/TiB₂, NiCr/TiB₂ and TiB₂ coating systems onto aluminium substrate at 0.6Pa sputtering pressure, of the series E.

On each sample seven indentations were made for one indentation depth. The highest and lowest values were rejected as extremes. Hence the elastic modulus and hardness values are the average of five measurements, as shown in table 3.41 and 3.42 for steel and aluminium substrates respectively.

Sample Reference	Coating System on Steel	Sputtering Power (WRF) (metal/ceramic)	Varying Parameters (λ nm / V%)	Poisson's Ratio (v_s)	Plastic depth (nm)	H (GPa)	STDEV	E (GPa)	STDEV
7ES4	Al/TiB$_2$	400/300	200/75	0.16	406	8.84	0.34	208.9	6.3
2ES4	Al/TiB$_2$	400/300	200/50	0.21	549	5.83	0.60	173.3	12.0
3ES4	Al/TiB$_2$	400/300	200/25	0.23	538	3.74	0.64	152.7	16.3
9ES4	Al/TiB$_2$	400/300	100/75	0.16	472	9.71	0.95	132.4	4.2
6ES4	Al/TiB$_2$	400/300	100/50	0.21	536	6.54	1.37	164.9	10.5
5ES4	Al/TiB$_2$	400/300	100/25	0.23	528	4.26	0.27	149.5	6.1
11ES4	Al/TiB$_2$	400/300	50/75	0.16	489	10.63	0.42	222.2	2.5
14ES4	Al/TiB$_2$	400/300	50/50	0.21	532	7.79	0.94	211.3	18.9
4ES10	TiB$_2$	300	-	0.11	245	27.31	2.29	314.2	15.8
8ES4	NiCr/TiB$_2$	200/300	50/75	0.16	473	17.95	0.75	304.5	6.3
15ES4	NiCr/TiB$_2$	200/400	50/75	0.16	465	18.81	0.76	302.3	8.6
17ES4	Al/TiB$_2$	400/400	50/75	0.16	534	10.23	0.15	216.0	5.0
16ES4	Al/TiB$_2$	400/440	50/75	0.16	531	10.81	0.41	231.0	6.2

Table 3.41. Hardness and elastic modulus results for multilayer coatings onto steel, series E.

Sample Reference	Coating System on Aluminium	Sputtering Power (WRF) (metal/ceramic)	Varying Parameters (λ nm / V%)	Poisson's Ratio (v_s)	Plastic depth (nm)	H (GPa)	STDEV	E (GPa)	STDEV
7EA8	Al/TiB$_2$	400/300	200/75	0.16	573	6.63	0.32	140.5	8.0
2EA8	Al/TiB$_2$	400/300	200/50	0.21	554	5.27	0.63	134.8	9.6
3EA8	Al/TiB$_2$	400/300	200/25	0.23	548	2.87	0.46	118.6	6.7
5EA8	Al/TiB$_2$	400/300	100/25	0.23	527	4.05	0.25	128.6	3.0
9EA8	Al/TiB$_2$	400/300	100/75	0.16	521	7.53	0.39	162.3	3.8
6EA8	Al/TiB$_2$	400/300	100/50	0.21	547	5.54	0.15	138.5	5.7
11EA8	Al/TiB$_2$	400/300	50/75	0.16	552	8.06	0.33	171.3	6.8
4EA8	TiB$_2$	300	-	0.11	291	26.00	2.74	249.9	24.1
8EA8	NiCr/TiB$_2$	200/300	50/75	0.16	392	15.72	1.55	191.1	5.4
15EA8	NiCr/TiB$_2$	200/400	50/75	0.16	417	14.03	0.40	155.4	3.9
16EA8	Al/TiB$_2$	400/450	50/75	0.16	537	8.66	0.23	157.0	3.3

Table 3.42. Hardness and elastic modulus results for multilayer coatings onto aluminium, series E.

1-Analysis of the Hardness Results

The hardness values of 27.31GPa for TiB$_2$ coating onto steel and 26GPa for TiB$_2$ coating onto Al substrates will be considered as a reference value for the multilayer coatings series E, see table 3.41 and 3.42.

Figure 3.62 shows the plot of the hardness values in function of the composition wavelength and volume fraction of ceramic for steel and Al substrates. The coating hardness increases when the composition wavelength decrease, as well as when the volume of ceramic increases. The volume of ceramic layer is more significant compared to the composition wavelength.

Figure 3.63 shows the hardness values for TiB$_2$, Al/TiB$_2$ and NiCr/TiB$_2$ coatings at 0.6Pa (4.5×10^{-3}Torr) sputtering pressure for different sputtering power. The composition wavelength and volume fraction of ceramic for these coatings are 50nm and

75% respectively. The number below the coatings system on the x-axis corresponds to the sputtering power. Changing the Al layer for the NiCr layer in multilayer coatings increases the hardness of the coating for the same sputtering conditions of the ceramic layer. Changes to the TiB_2 sputtering power do not have a great significance on the hardness of the coatings. Only a slight increase for $NiCr/TiB_2$ on steel and a slight decrease on the Al substrate was observed and that could be due to different substrate stiffness.

Table 3.43 shows an Anova statistical analysis of the hardness values for the Al/TiB_2 coatings onto steel and Al substrates for 200nm and 100nm composition wavelength at 25, 50, 75% volume fraction respectively. This analysis shows that the relative error of the two substrates is 33.6%. This error reflects the different substrate stiffness and variations on the layer thickness as a function of the sample position inside the chamber. This variation of the hardness on the two substrates is very clear in the figure 3.62. The relative error between sample measurements is 48.5%, which is the major source of error in this analysis. This error reflects the effect of the composition wavelength and volume of ceramic fraction. Both errors are more significant compared to the overall relative error in the measurements (9.6%). Thus, both coating layer structure (composition wavelength, volume fraction of ceramic) and substrate material are significant factors in determining the measured coating hardness. Because of these the coating structure is the more significant.

Table 3.44 shows an Anova statistical analysis for the $NiCr/TiB_2$ coatings onto steel and Al substrates at 0.6Pa (4.5×10^{-3}Torr) sputtering pressure for two sputtering power values. The measurement relative error for two substrates is 21%, which is the major source of error. This error reflects the different stiffness of the substrates and the layer thickness, as mentioned above. The relative error between samples is 2.5%. This error reflects the effect of the TiB_2 sputtering power which it is not very significant in the range between 300 to 400WRF. The overall relative error in the measurement is 7.7%.
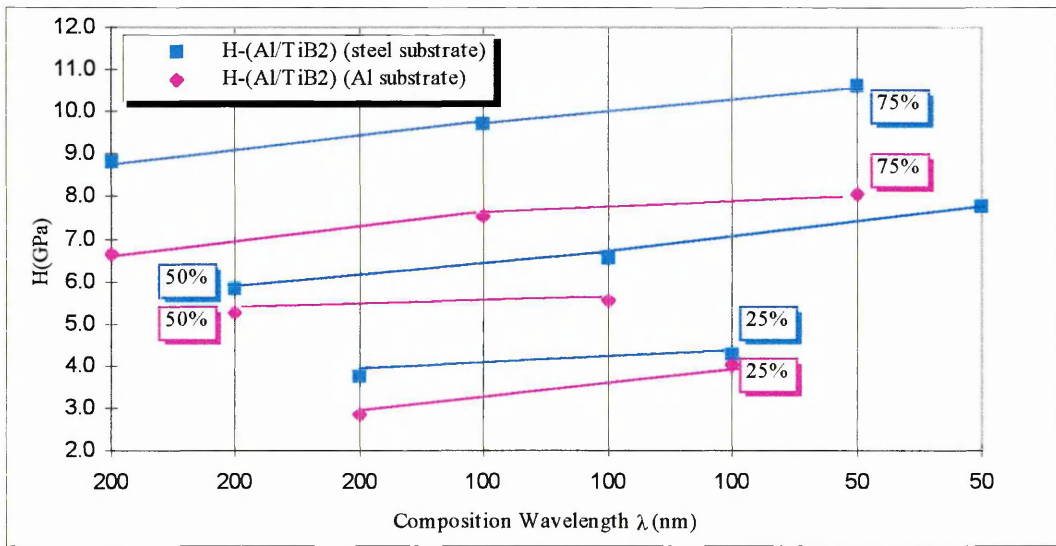

Figure 3.62. Hardness in function of composition wavelength and volume fraction for Al/TiB_2 coatings onto steel and Al substrates.
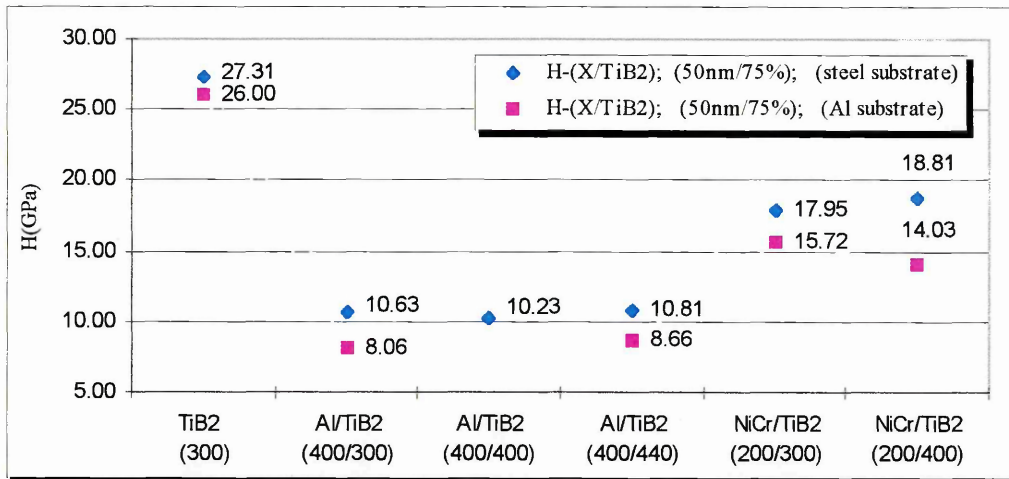
Figure 3.63. Hardness for Al/TiB$_2$, NiCr/TiB$_2$ and TiB$_2$ coating systems onto steel and Al substrate at 0.6Pa sputtering pressure.

Sample Reference	Steel Substrate	Aluminium Substrate	Mean for two Substrates					
7E	8.84	6.63	7.74					
2E	5.83	5.27	5.55					
3E	3.74	2.87	3.31					
9E	9.71	7.53	8.62					
6E	6.54	5.54	6.04					
5E	4.26	4.05	4.16					
Mean per series	6.49	5.32	5.90					
Anova: Two-Factor Without Replication								
SUMMARY	Count	Sum	Average	Variance				
Row 1	2	15.30	7.65	2.08				
Row 2	2	11.10	5.55	0.16				
Row 3	2	6.61	3.31	0.38				
Row 4	2	17.24	8.62	2.38				
Row 5	2	12.08	6.04	0.50				
Row 6	2	8.31	4.16	0.02				
Column 1	6	38.75	6.46	5.62				
Column 2	6	31.89	5.32	2.85				
Source of Variation	SS	df	MS	F	STDEV	P-value	F crit	
Rows	40.76	5	8.15	25.59	2.86	0.001	5.05	
Columns	3.92	1	3.92	12.31	1.98	0.017	6.61	
Error	1.59	5	0.32		0.56			
Total	46.28	11						
Conclusion								
Overall Relative Error								9.6%
Relative Error Between Samples Measurement								48.5%
Measurement Relative Error for two Substrates								33.6%

Table 3.43. Anova analysis of the hardness for Al/TiB$_2$ coatings onto steel and Al substrates.

Sample Reference	Steel Substrate	Aluminium Substrate	Mean H of two substrates				
NiCr/TiB$_2$(200/300)	17.95	15.72	16.84				
NiCr/TiB$_2$(200/400)	18.81	14.03	16.42				
Mean per series	*18.38*	*14.88*	*16.63*				

Anova: Two-Factor Without Replication

SUMMARY	Count	Sum	Average	Variance			
Row 1	2	33.67	16.84	2.49			
Row 2	2	32.84	16.42	11.42			
Column 1	2	36.76	18.38	0.37			
Column 2	2	29.75	14.88	1.43			

Source of Variation	SS	df	MS	F	STDEV	P-value	F crit
Rows	0.17	1	0.17	0.11	0.41	0.80	161.45
Columns	12.29	1	12.29	7.56	3.50	0.22	161.45
Error	1.63	1	1.63		1.28		
Total	14.08	3					

Conclusion	
Overall Relative Error	7.7%
Relative Error Between Samples Measurement	2.5%
Measurement Relative Error for two substrates	21.0%

Table 3.44. Anova analysis of the hardness for NiCr/TiB$_2$ coatings onto steel and Al substrates.

2-Analysis of the Elastic Modulus Results

The elastic modulus value of 314.2GPa for TiB$_2$ onto steel and 249.9GPa for TiB$_2$ onto Al substrate is going to be considered as a reference value for the multilayer coatings series E, see table 3.41 and 3.42.

Figure 3.64 shows the plot of the elastic modulus values as a function of the composition wavelength and volume fraction for steel and Al substrates. The highest elastic modulus in this set was obtained with λ=50nm and V$_c$=75% either on steel or aluminium substrates. However, they are marginally lower than predicted by the rule of mixtures, as shown in figure 3.66. The elastic modulus of the composite for 200nm composition wavelength increases with the volume of ceramic either on steel or Al substrates. However, the elastic modulus of the composites onto steel for λ=100nm tends to be lower compared to those for λ=200nm. The lower value (100nm,75%) is believed to be due to the measurement errors because of the shape of the nanoindentation curves. These samples were displaced from the zero axis and this has an influence on the elastic modulus calculation. The elastic modulus of the composite onto the Al substrate for λ=100nm is higher compared to that for λ=200nm and also follows the same pattern of the λ=200nm composite related to the volume of ceramic.

Changing the Al layer for the NiCr layer in multilayer coatings increases the elastic modulus of the coating for the same sputtering conditions of the ceramic layer, as shown in figure 3.65. The dependence on the TiB$_2$ sputtering power is not very significant over the range used. However, by changing the Al layer for a NiCr metal layer, the elastic

modulus of the coating is slightly above that predicted by the rule of mixtures for a steel substrate, as shown in figure 3.66.

For Al substrates the elastic modulus values of the composites are lower than for the steel, which may be due to the different stiffness of the substrate, see figures 3.64 and 3.65.

Table 3.46 shows an Anova statistical analysis of the elastic modulus values for the Al/TiB$_2$ coatings onto steel and Al substrates for λ=200nm and λ=100nm at 25, 50, 75% volume fraction of ceramic respectively. This analysis shows that the major source of error is the variation between the two substrate measurements (30.4%). This error reflects the stiffness of the substrate, the layer thickness and indentation experiment conditions. Hence, this may be explained in part by the different behaviour of the coating onto the two different substrates, as a function of the volume fraction of ceramic. The relative error between samples is 13.0%. This error reflects the effect of the composition wavelength and volume fraction of ceramic. The overall relative error of the measurements is 15.1 %. The results were measured with depth calibration kept constant for all experiments, the initial load calibration was not done for all experiments and without thermal drift correction and this may influence the measured results. However, the variations in layer structure and substrate type are much less significant for the elastic modulus than for the hardness.

Table 3.45 shows an Anova statistical analysis of the elastic modulus for the NiCr/TiB$_2$ coatings onto steel and Al substrates at 0.6Pa (4.5×10^{-3}Torr) sputtering pressure for two sputtering power values. The major source of error is that for the measurement for two substrates (54.6%) which agrees with the Anova analysis of the hardness values. The relative error between samples (7.8%) and the overall relative error (7.1%) are much less significant compared with the measurements for different substrates.
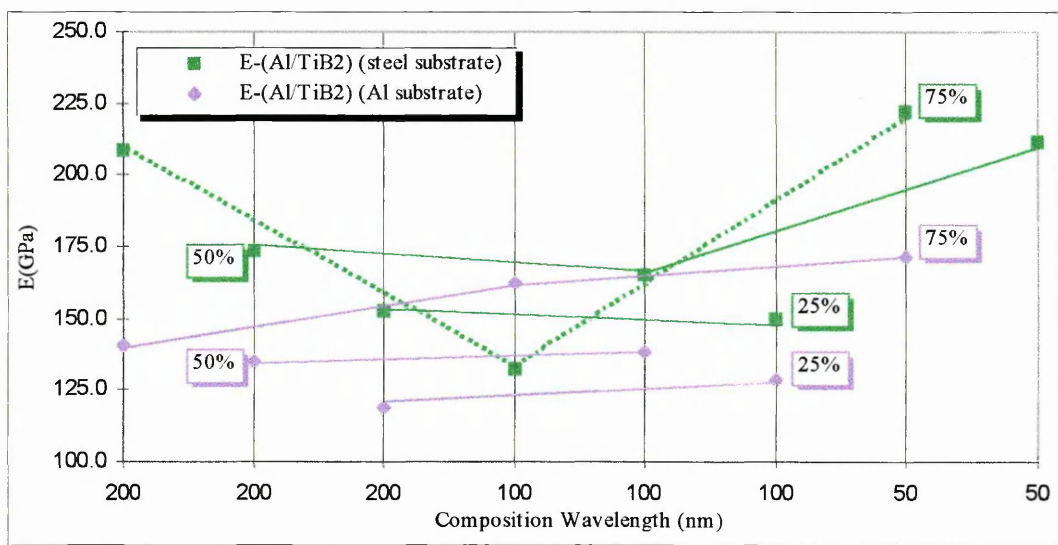
Figure 3.64. Elastic modulus in function of composition wavelength and volume fraction for Al/TiB$_2$ coatings onto steel and Al substrates.
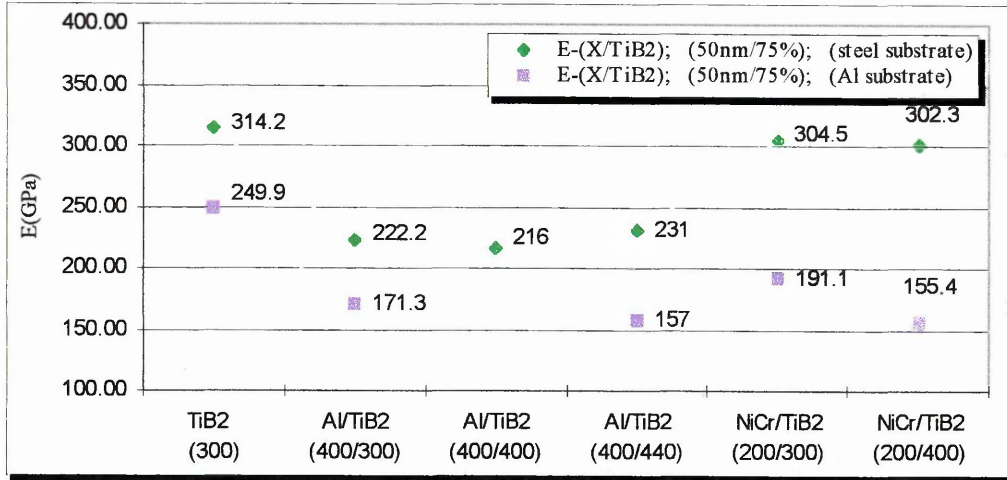
Figure 3.65. Elastic modulus for Al/TiB$_2$, NiCr/TiB$_2$ and TiB$_2$ coating systems onto steel and Al substrate at 0.6Pa (4.5×10^{-3}Torr) sputtering pressure.
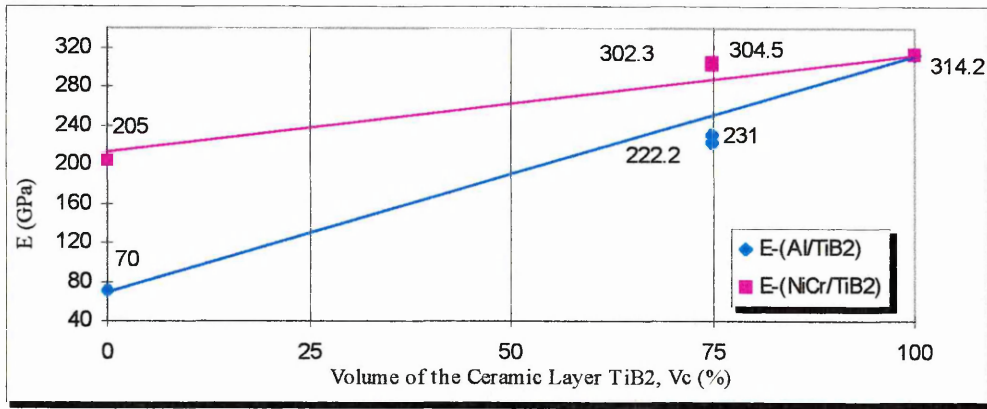

Figure 3.66. Elastic modulus of the Al/TiB$_2$ and NiCr/TiB$_2$ coatings onto steel in function of the volume of ceramic layer TiB$_2$.

Sample Reference	Steel substrate	Aluminium substrate	Mean E for two substrates				
NiCr/TiB$_2$(200/300)	304.5	191.1	247.80				
NiCr/TiB$_2$(200/400)	302.3	155.4	228.85				
Mean per series	*303.40*	*173.25*	*238.33*				
Anova: Two-Factor Without Replication							
SUMMARY	*Count*	*Sum*	*Average*	*Variance*			
Row 1	2	495.6	247.80	6429.78			
Row 2	2	457.7	228.85	10789.81			
Column 1	2	606.8	303.40	2.42			
Column 2	2	346.5	173.25	637.25			
Source of Variation	*SS*	*df*	*MS*	*F*	*STDEV*	*P-value*	*F crit*
Rows	359.1	1	359.102	1.280	18.950	0.461	161.446
Columns	16939.0	1	16939.02	60.38	130.15	0.08	161.45
Error	280.6	1	280.56		16.75		
Total	17578.7	3					
Overall Relative Error							7.1%
Relative Error Between Samples Measurement							7.8%
Measurement Relative Error of two Substrates							54.6%

Table 3.45. Anova analysis of the elastic modulus for NiCr/TiB$_2$ coatings onto steel and Al substrates

Sample Reference	Steel Substrate	Aluminium Substrate	Mean E for two Substrates				
7E	208.9	140.5	174.70				
2E	173.3	134.8	154.05				
3E	152.7	118.6	135.65				
9E	132.4	162.3	147.35				
6E	164.9	138.5	151.70				
5E	149.5	128.6	139.05				
Mean per series	*163.62*	*137.22*	*150.42*				
Anova: Two-Factor Without Replication							
SUMMARY	*Count*	*Sum*	*Average*	*Variance*			
Row 1	2	349.40	174.70	2339.28			
Row 2	2	308.10	154.05	741.13			
Row 3	2	271.30	135.65	581.41			
Row 4	2	294.70	147.35	447.00			
Row 5	2	303.40	151.70	348.48			
Row 6	2	278.10	139.05	218.40			
Column 1	6	981.70	163.62	687.79			
Column 2	6	823.30	137.22	213.65			
Source of Variation	*SS*	*df*	*MS*	*F*	*STDEV*	*P-value*	*F crit*
Rows	1922.38	5	384.48	0.74	19.61	0.62	5.05
Columns	2090.88	1	2090.88	4.04	45.73	0.10	6.61
Error	2584.82	5	516.96		22.74		
Total	6598.08	11					
Conclusion							
Overall Relative Error							15.1%
Relative Error Between Samples Measurement							13.0%
Measurement Relative Error for the two Substrate							30.4%

Table 3.46. Anova analysis of the elastic modulus for Al/TiB_2 coatings onto steel and Al substrates

3.3.4. STRUCTURAL CHARACTERIZATION

Multilayer coatings involve alternating layers of two different materials in a periodic manner. The microstructure characteristic is the composition wavelength or periodicity (λ). This is a sum of the two layer thicknesses. The composition wavelength must be less than the critical size for fracture in the ceramic layer. The relative volume fraction of ceramic within the composite imposes the hardness and elastic properties of the coating.

In this project the varying parameters of the multilayer coatings are the composition wavelength and the relative volume fraction of ceramic, as mentioned in section 2.2. The structural characterization in the multilayer coatings section gives information about the composition wavelength, volume of ceramic layers, total coating thickness, chemical composition and structure. The structural characterization includes optical examination, SEM analysis, XRD characterization and Auger analysis.

Photograph 3.12 shows the layers within the Al/TiB_2 coatings onto steel at λ=200nm and V_c=75%, at 400 times magnification by ball cratering. This film is abraded at a shadow incline angle (the coating is approximately 5µm thick but appears 75µm thick in the picture).

Photograph 3.13 shows the topography of the TiB_2 coating onto steel by optical microscope at 100 times magnification. The coating of 5μm thickness was micro-cracked due to the brittleness of the TiB_2 ceramic.

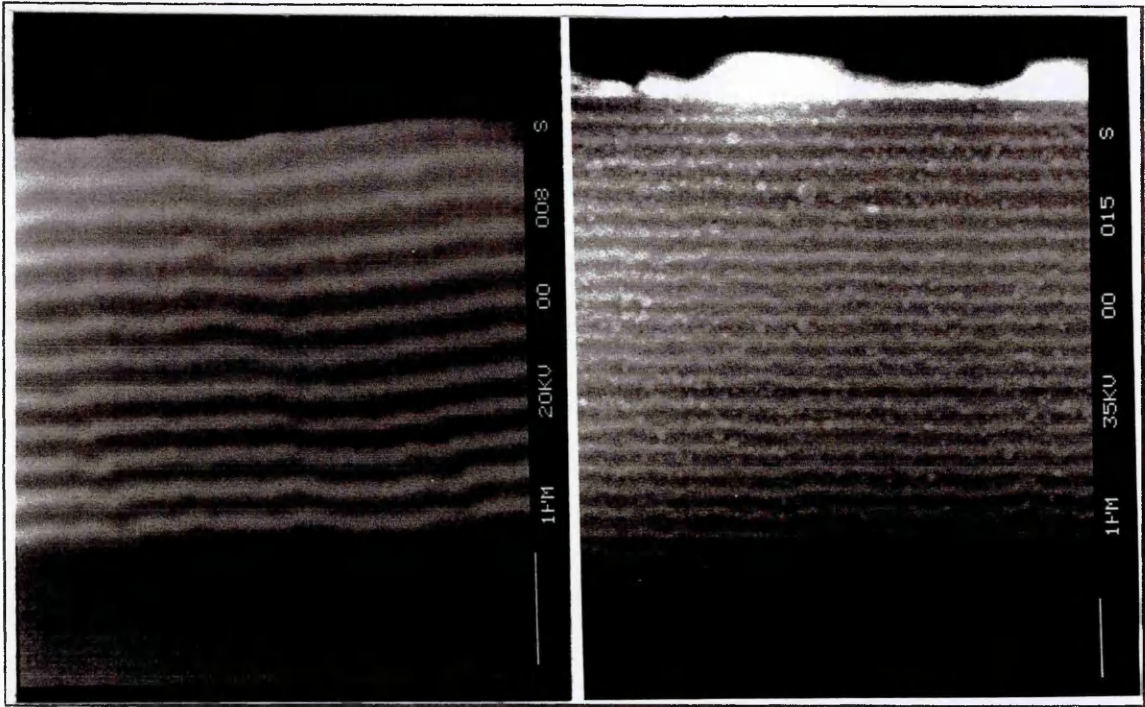Photograph 3.14 shows Al/TiB_2 coating onto Aluminium at λ=300nm on the left and λ=200nm on the right by SEM image.
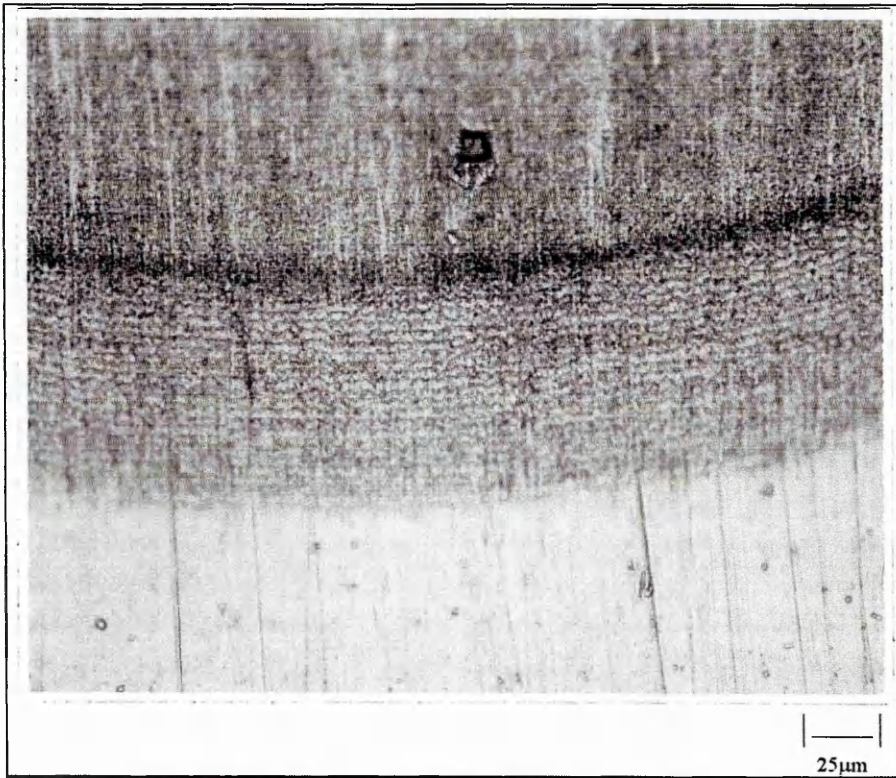
Photograph 3.12. Al/TiB_2 coating by ball cratering.
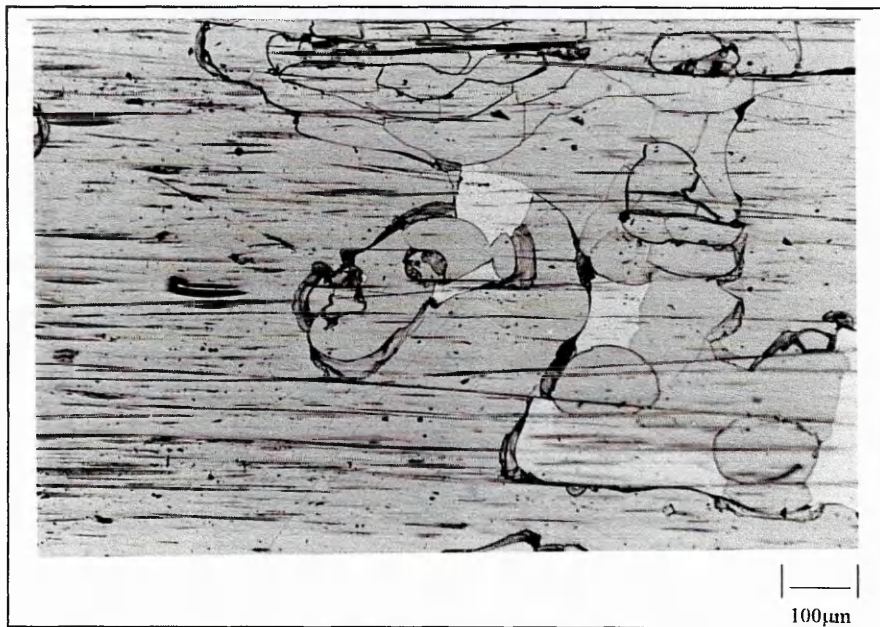
Photograph 3.13. Topography of TiB_2 coating onto steel by optical microscope.

Photograph 3.14. Al/TiB$_2$ multilayer coating onto aluminium at λ=300nm on the left and λ=200nm on the right by SEM image.

XRD analysis was carried out for the series C specimens for studying the effect of the substrate position inside the vacuum chamber as shown in table 3.47. The positions 2 and 8 are most favourable for TiB$_2$ peaks on the Al substrates, while for steel substrates all positions have the same counts. The TiB$_2$ coatings onto steel substrate have micro-cracks, see photograph 3.13. Overall, the Al/TiB$_2$ coatings seem not to have significant TiB$_2$ peaks. However, peaks of the coating could overlap with Fe peaks and Al peaks from the substrate respectively, so identification of them on the coating is difficult.

Coating System	X-Ray Diffraction TiB$_2$ Peaks for Steel Substrate (counts)				X-Ray Diffraction TiB$_2$ Peaks for Al Substrate (counts)			
Substrate position*	3	4	9	10	2	5	8	11
TiB$_2$**	191	196	189	***	169	102	301	113
Al/TiB$_2$**	-	112	106	-	-	-	123	-
*** The coating come apart by spallation								
** All TiB$_2$ peaks are for the preferential plane (001)								
*Substrate position inside the vacuum chamber								

Table 3.47. X-Ray diffraction peaks for TiB$_2$ and Al/TiB$_2$ coatings, series C.

An Auger study was carried out with Al/TiB$_2$ coatings from the series A for a λ=200nm and V_c=50% sample. Figure 3.67 shows a depth profile through the outer two layers for an ion etch speed of 20μA/cm^2. This corresponds to an etching rate of $\cong$0.03nm/sec. for the TiB$_2$ layer. To reduce the duration of the analysis, the etch speed

253

was increased to $30\mu A/cm^2$. This corresponds to an etching rate of $\cong 0.05nm/sec.$, which gives the same spectrum information as shown in figure 3.68.

Figure 3.69 shows a depth profile through a few outer layers. The slope of the elements at the interface between these layers could be due either to interdiffusion or ion etching effects. The presence of the oxygen is not significant as it decreases to negligible proportions after a first layer and only the main elements were analysed. The repeatability of the composition wavelength is given by the ratio of the composition wavelength for the two pairs of layers that was found to be 0.92. The stoichiometry of the TiB_X was found to be between 1.72 and 1.74.
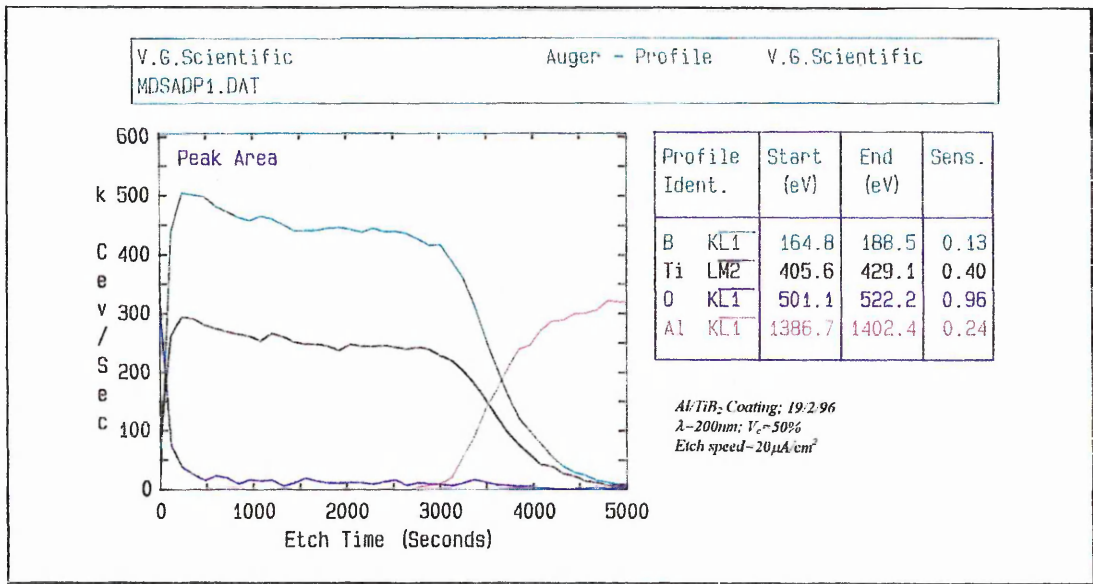
Figure 3.67. Auger depth profile for Al/TiB$_2$ coatings for a outer layer at ion etch speed of $20\mu\text{Å/cm}^2$.
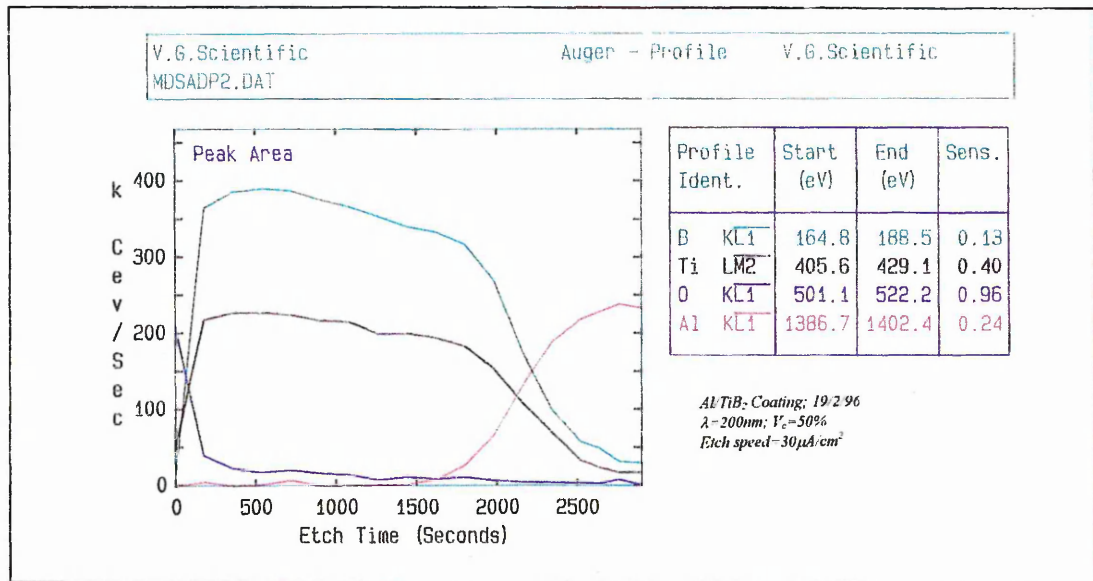
Figure 3.68. Auger depth profile for Al/TiB$_2$ coatings for the outer layer at ion etch speed of $30\mu\text{Å/cm}^2$.
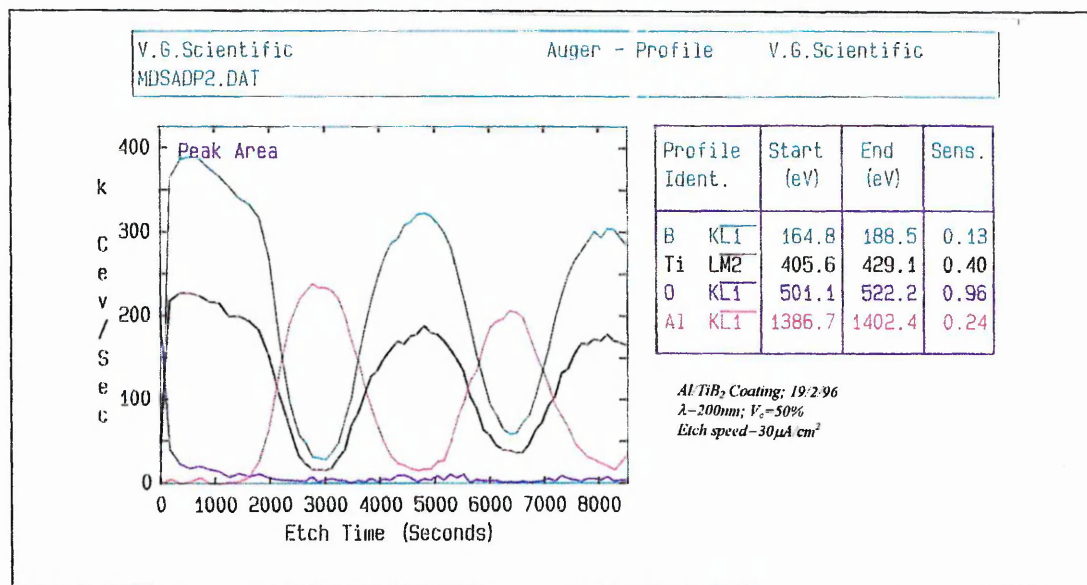
Figure 3.69. Auger depth profile for Al/TiB$_2$ coatings for a few outer layers at ion etch speed of 30μÅ/cm^2.

An Auger depth profile analysis was performed on some samples of the series E specimens, as shown in figures 3.70 to 3.75. Table 3.48 shows the repeatability of the composition wavelength, volume fraction and ceramic stoichiometry.

The repeatability of the composition wavelength for the analysed coatings is at worst ±10% on thickness but is often better than ±3%. The volume fraction of ceramic varies between 65% and 73% for a nominal 75% ceramic volume fraction, and between 57% and 64% for a nominal 50% ceramic volume fraction. The actual volume fraction deposited varies with the composition wavelength. All were deposited to a nominal 50% volume fraction, but for λ=50nm it is 50% ceramic, λ=100nm it is 55% ceramic and at λ=200nm it is 60% volume fraction. The repeatability of the TiB$_x$ stoichiometry is in good agreement and varies between 1 and 1.93 for copper substrate and 2.03 for steel substrate. The different stoichiometry data for 2EC1 and 2ES4 samples from the same sputtered deposition must be due to B:Ti calibration.

Sample Reference	Substrate	Varying Parameters (λ nm;Vc%)	λ$_1$	λ$_2$	λ$_1$/λ$_2$	X$_1$	X$_2$	V$_{c1}$ (%)	V$_{c2}$ (%)
1EC1	Cu	200/75	7790	7019	0.90	1.29	1.23	73	65
2EC1	Cu	200/50	6883	6921	1.01	1.00	1.01	61	62
6EC1	Cu	100/50	3781	3661	1.03	1.28	1.35	56	54
2ES4	steel	200/50	3726	3663	1.02	2.03	2.03	64	57
2EC1	Cu	200/50	6731	7366	0.91	1.79	1.93	62	59
13EC1	Cu	50/50	1264*	1169**	1.08	1.82*	1.65**	50	49
* Second pair of layers; ** Third pair of layers									

Table 3.48. Composition wavelength, volume fraction and ceramic stoichoimetry for Al/TiB$_2$ coatings, series E.
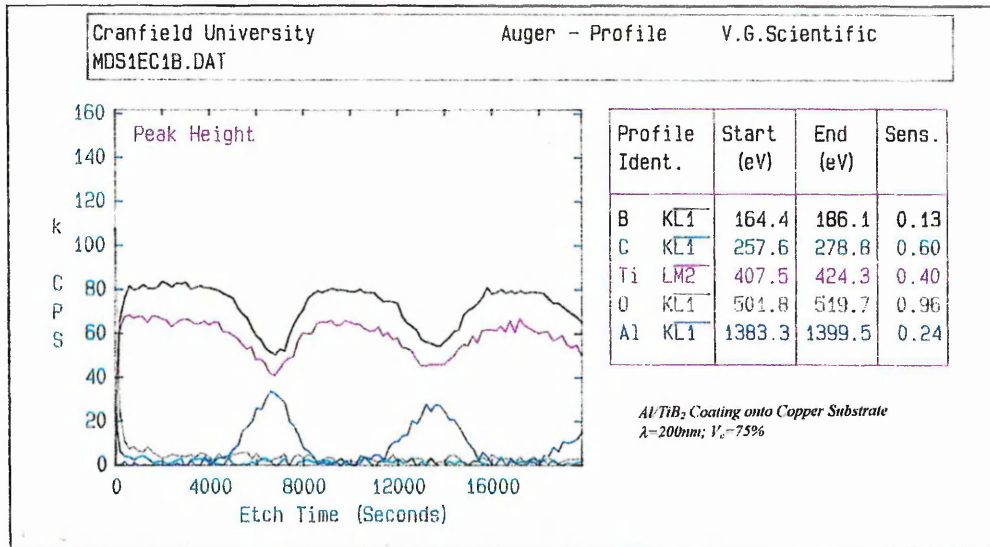
Figure 3.70. Auger depth profile for Al/TiB$_2$ coatings onto Cu for λ=200nm; V$_c$=75%.

Figure 3.71. Auger depth profile for Al/TiB$_2$ coatings onto Cu for λ=200nm; V$_c$=50%.

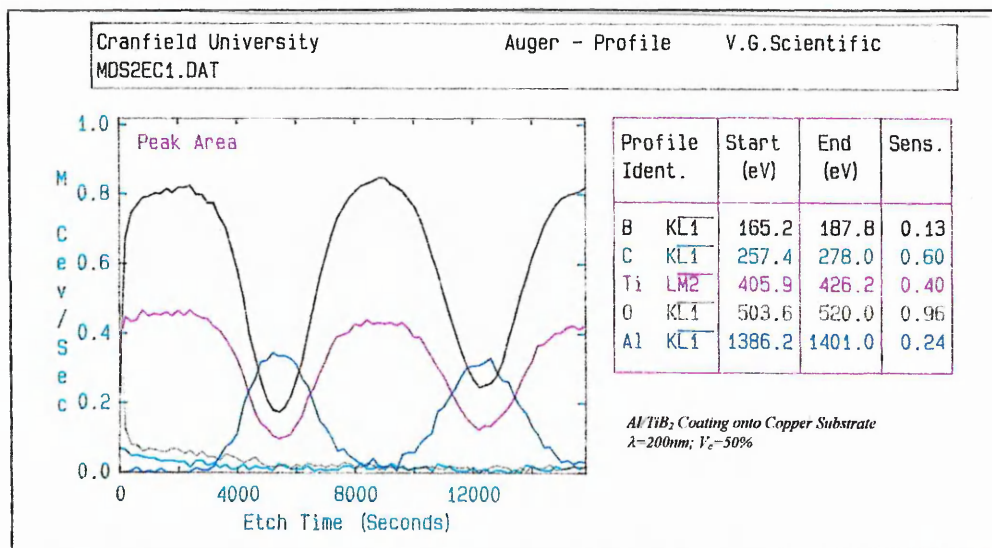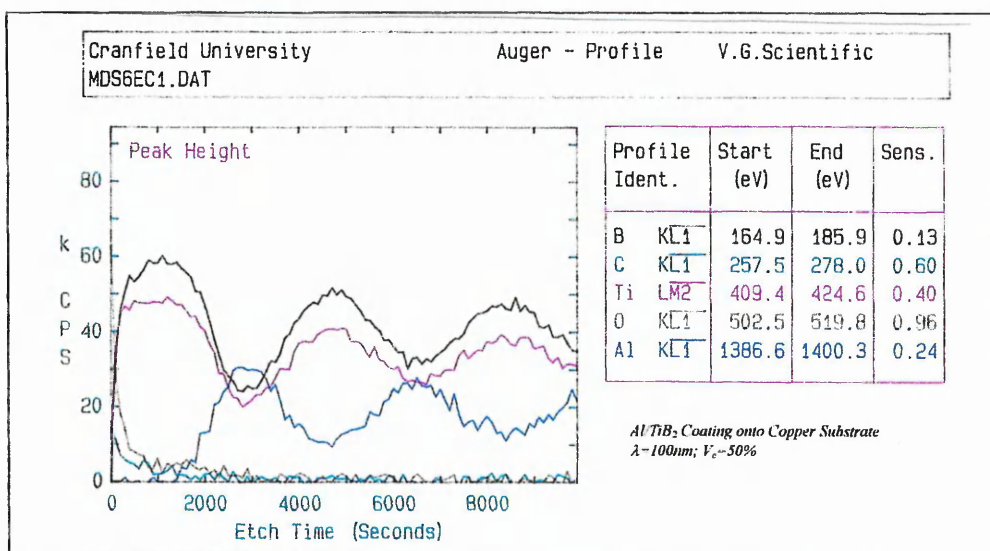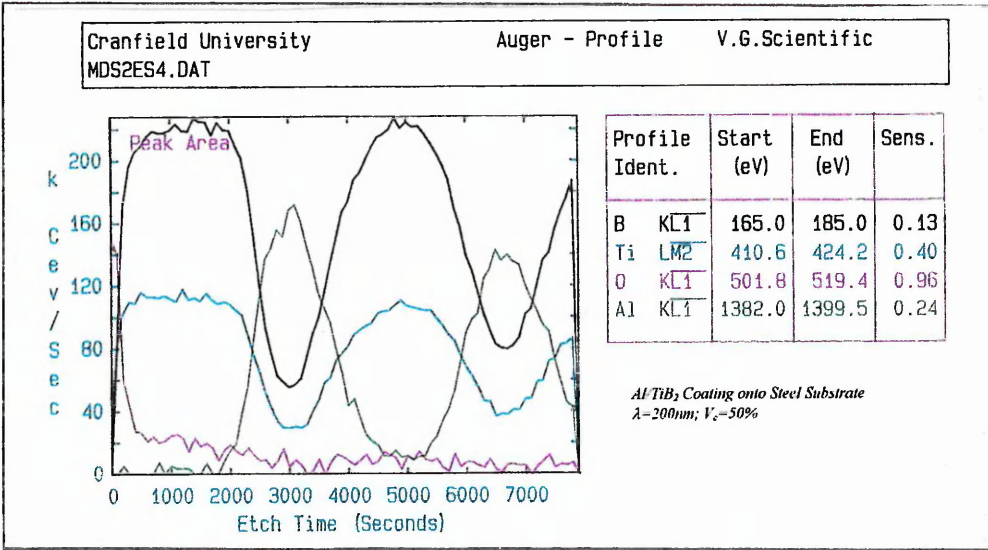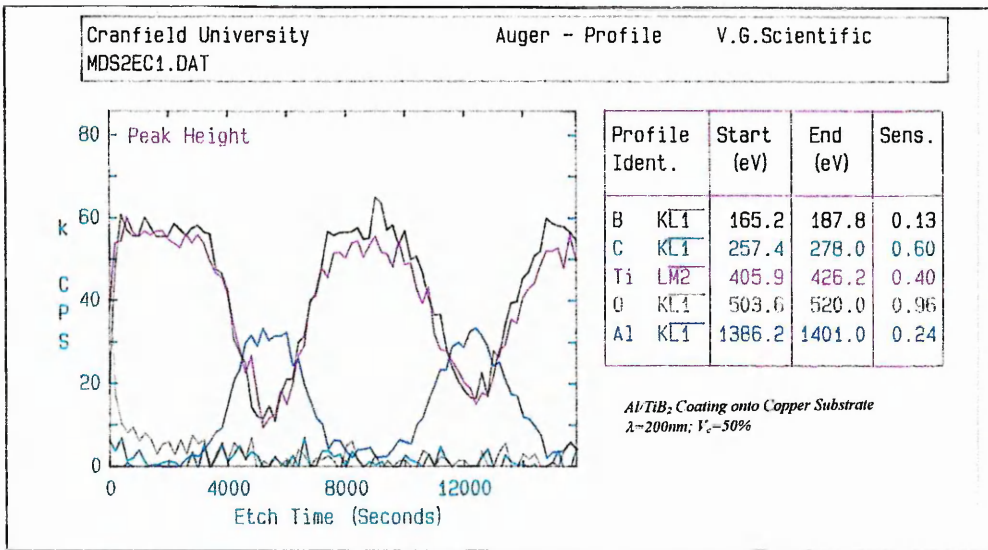Figure 3.72. Auger depth profile for Al/TiB$_2$ coatings onto Cu for λ=100nm; V$_c$=50%.

256

Figure 3.73. Auger depth profile for Al/TiB₂ coatings onto Steel for λ=200nm; V_c=50%.

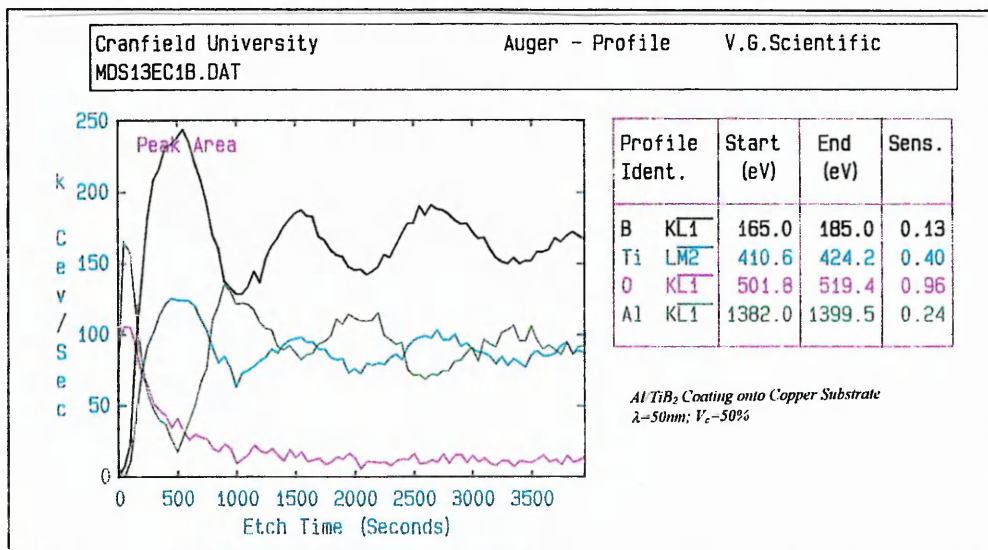Figure 3.74. Auger depth profile for Al/TiB₂ coatings onto Cu for λ=200nm; V_c=50%.

Figure 3.75. Auger depth profile for Al/TiB₂ coatings onto Cu for λ=50nm; V_c=50%.

3.3.5. ANALYSIS OF INTERNAL STRESSES

The evaluation of the internal stress was performed in two ways: qualitative demonstration and by measuring the curvature of the substrate.

1. Qualitative Demonstration:

An internal stresses demonstration of the coating is given qualitatively by comparing the substrate curvature by photography. This assumes the curvature of the coated substrate is due to the internal stresses in the film and not the possible curvature of the bare substrate, before coating.

Photographs 3.15 to 3.18 show the samples from the series C depositions. The TiB_2 coatings have the highest curvature compared to the Al/TiB_2 and $(Al/TiB_2)N_2$ coating systems, either on steel or aluminium substrates. The constraint between coating and steel substrate can result in stress capable of cracking and spalling of the coating, as shown for TiB_2 coatings onto steel. However, the TiB_2 coatings on Al substrates did not crack. Instead, the substrate showed deformation in two directions. An addition of $30\%N_2$ to the Al/TiB_2 system decreases the curvature of the composite onto Al substrate, except for position 5. This means that the internal stresses may be higher for Al/TiB_2 coatings compared to the $(Al/TiB_2)N_2$ coatings. The stresses within coatings can result from the mismatch in thermal expansion of the coating and substrate and between layers (multilayer coatings). This may explain the higher curvatures for aluminium substrate compared to steel substrate.

Photograph 3.19 shows the curvature of single layer TiB_2 coatings onto Cu, Al and steel, series E. The least curvature is seen for the steel samples, then copper, then aluminium because of the coefficient of thermal expansion increase on going from steel then Cu and then Al (see table 2.2). Hence, the thermal stresses are expected to be higher on Al substrate.

Photographs 3.20 to 3.22 show the Al/TiB_2 multilayer coatings, series E, for the set of composition wavelength and volume fraction of ceramic. These coatings onto steel are adherent to the substrate and the substrate curvature is lower compared to the TiB_2 coatings. The multilayer coatings with 75% of volume of ceramic show higher curvature than the 50% and 25% of volume of ceramic. These coatings onto Al are adherent to the substrate and they do not deform in two directions like TiB_2 coatings. The coating with $\lambda=50nm$ seems to have less substrate curvature compared to $\lambda=200nm$ and $\lambda=100nm$. Also, increasing the V_c of ceramic increases the substrate curvature, hence the internal stresses in the coating.

Photographs 3.23 and 3.24 show that the $NiCr/TiB_2$ coatings have high substrate curvature on steel and Al substrate compared to the Al/TiB_2 system for the same TiB_2 sputtering power. Hence, the internal stresses may be higher in the first coating system.
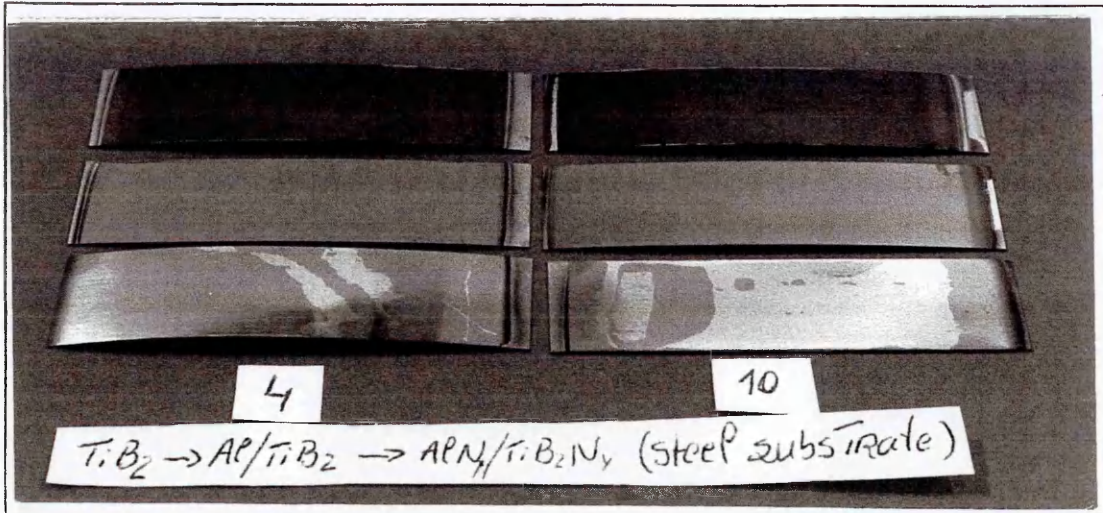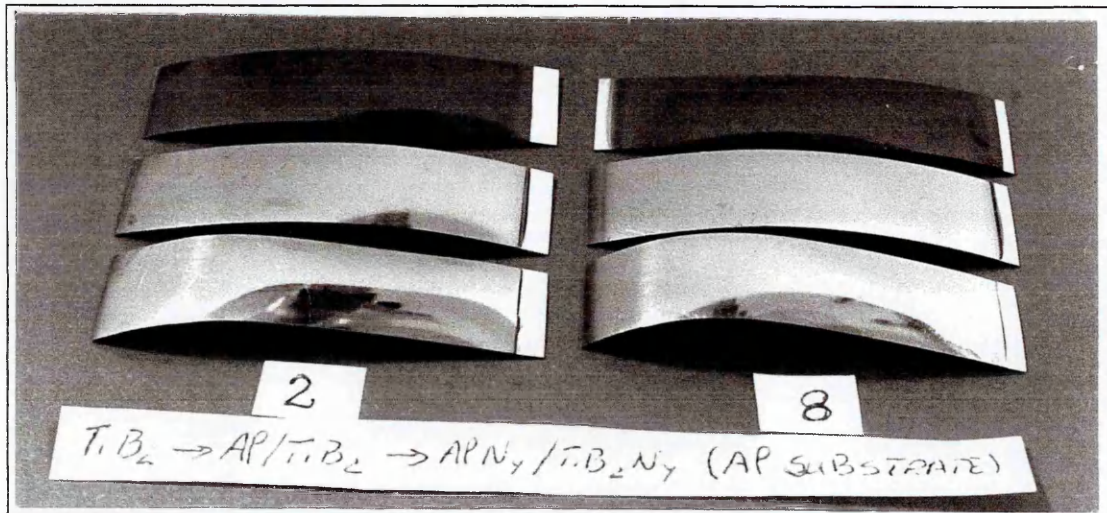
Photograph 3.15. TiB$_2$, Al/TiB$_2$ and (Al/TiB$_2$)N$_2$ coatings onto steel for positions 4 and 10 inside the vacuum chamber, series C.
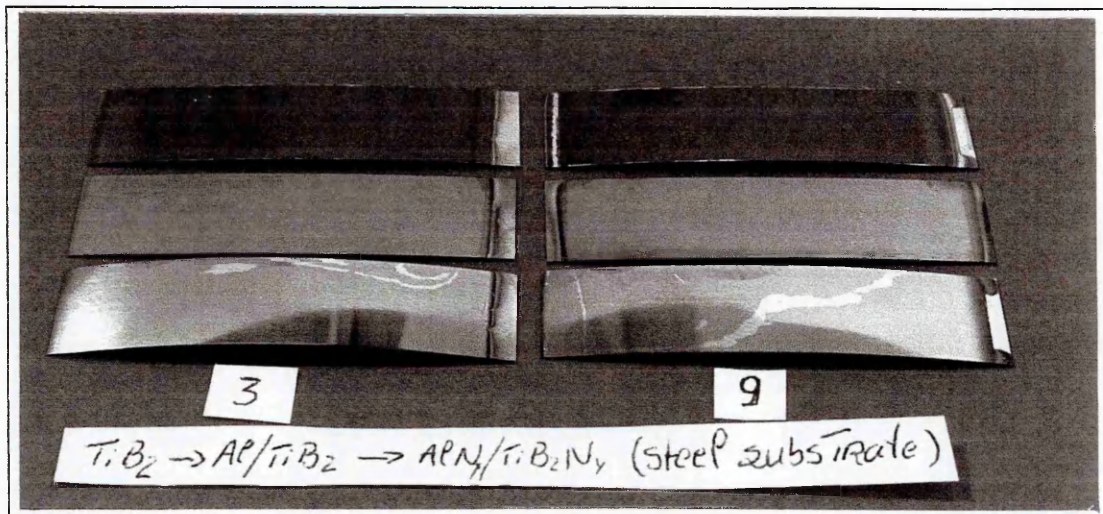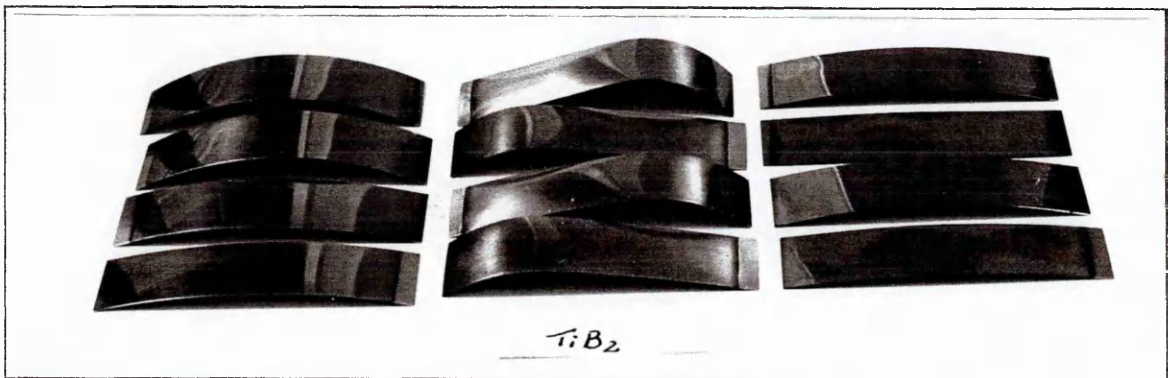

Photograph 3.16. TiB$_2$, Al/TiB$_2$ and (Al/TiB$_2$)N$_2$ coatings onto steel for positions 3 and 9 inside the vacuum chamber, series C.
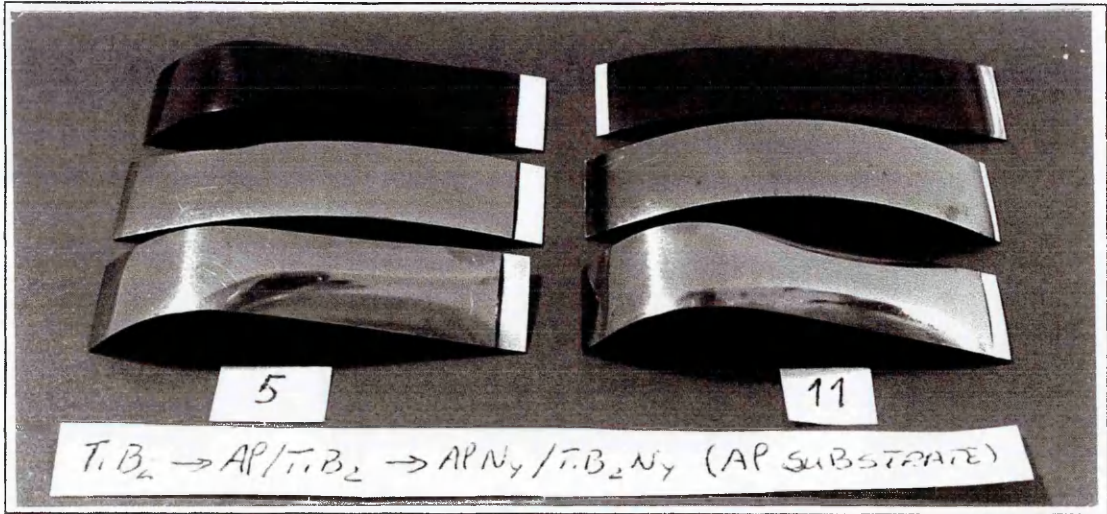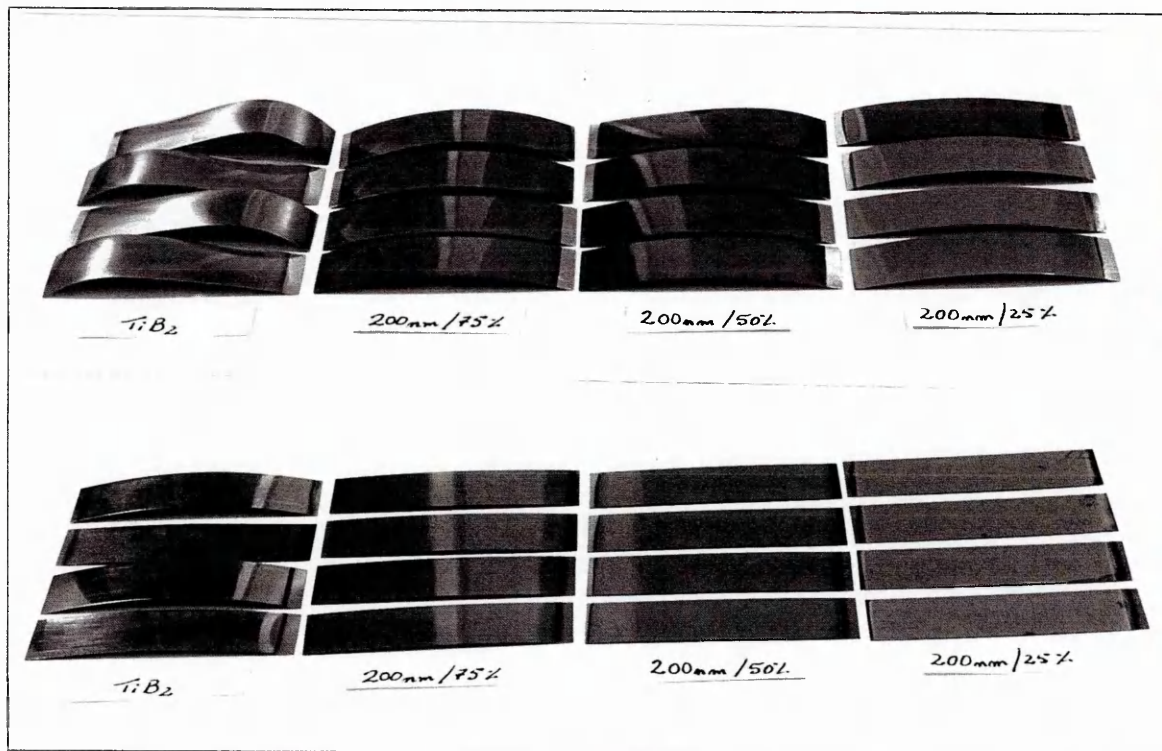
Photograph 3.17. TiB$_2$, Al/TiB$_2$ and (Al/TiB$_2$)N$_2$ coatings onto aluminium for positions 5 and 11 inside the vacuum chamber, series C.
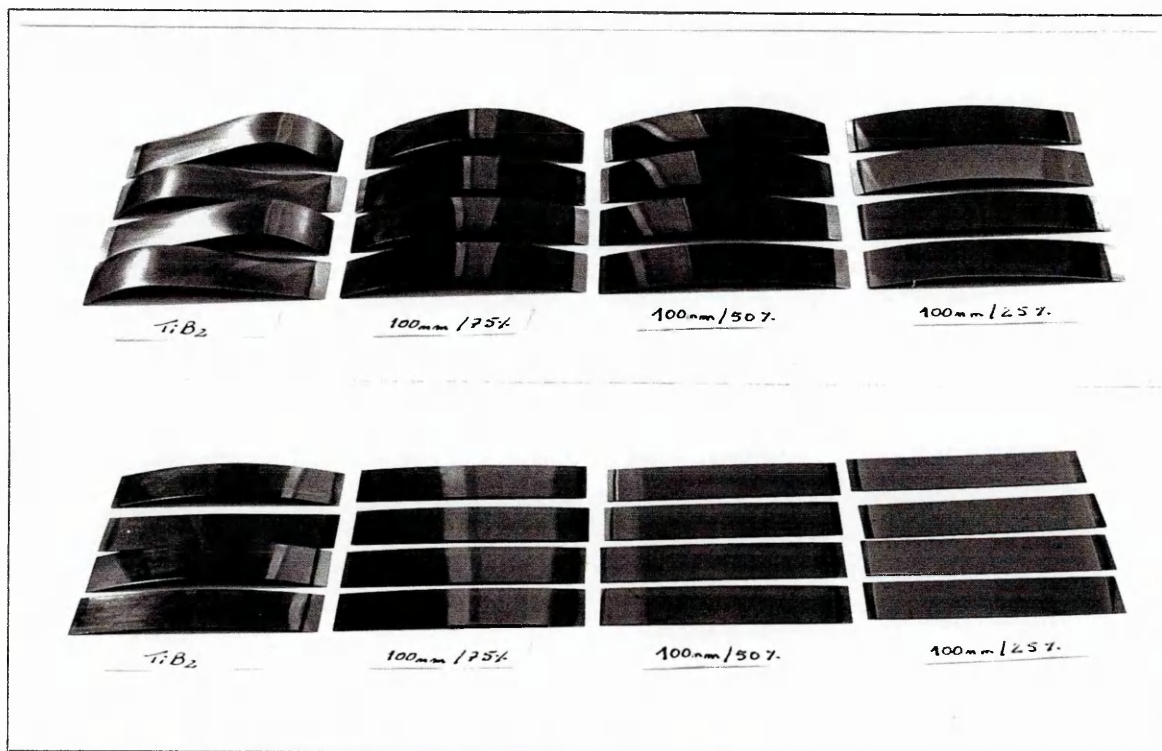

Photograph 3.18. TiB$_2$, Al/TiB$_2$ and (Al/TiB$_2$)N$_2$ coatings onto aluminium for positions 2 and 8 inside the vacuum chamber, series C.
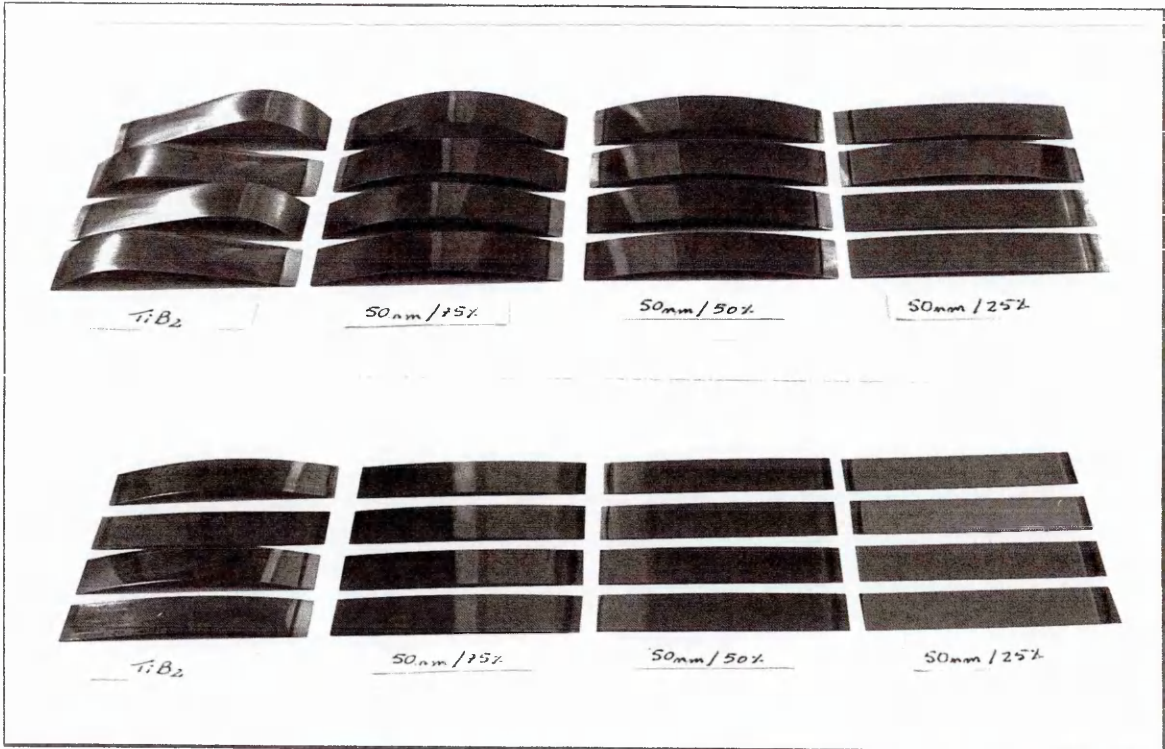

Photograph 3.19. TiB$_2$, coatings onto steel (left), aluminium (middle) and copper (right) for different positions inside the vacuum chamber, series E.

Photograph 3.20. TiB$_2$, and Al/TiB$_2$, coatings onto steel (bottom) and aluminium (top) at λ=200nm and V$_c$=75%, 50%, 25%, for different positions inside the vacuum chamber, series E.

Photograph 3.21. TiB$_2$, and Al/TiB$_2$, coatings onto steel (bottom) and aluminium (top) at λ=100nm and V$_c$=75%, 50%, 25%, for different positions inside the vacuum chamber, series E
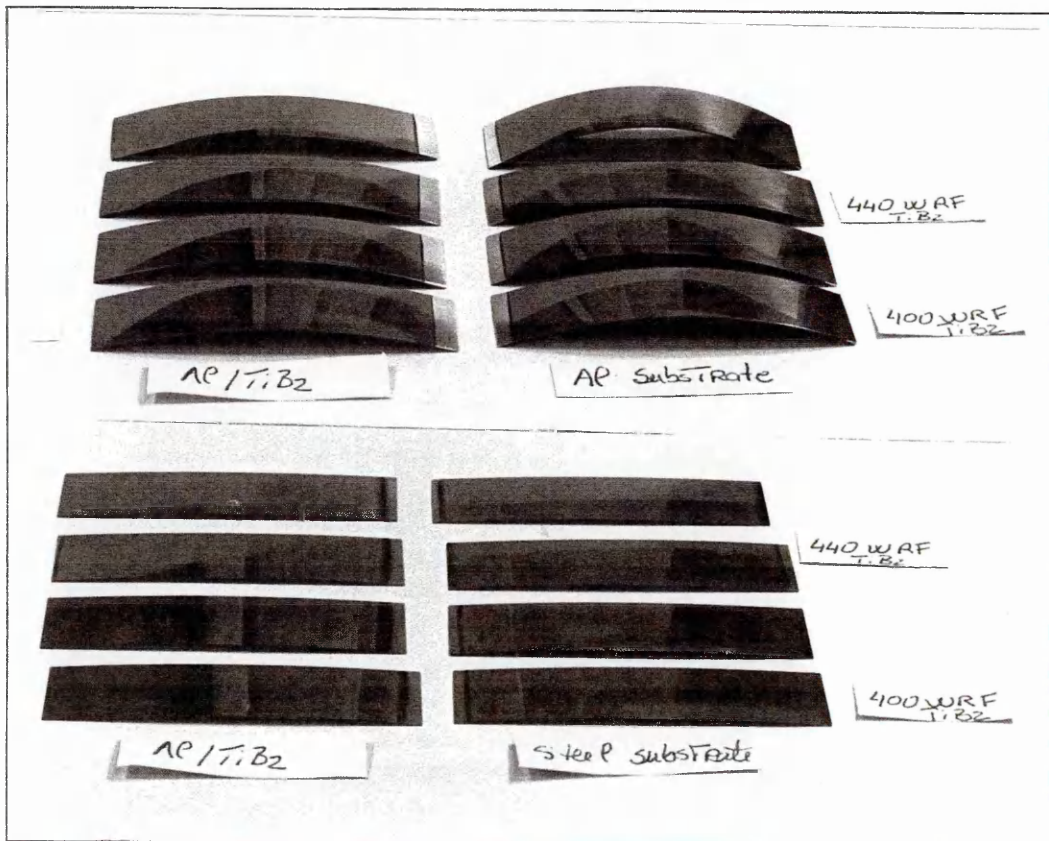
261

Photograph 3.22. TiB_2, and Al/TiB_2, coatings onto steel (bottom) and aluminium (top) at $\lambda=50$nm and $V_c=75\%$, 50%, 25%, for different positions inside the vacuum chamber, series E.
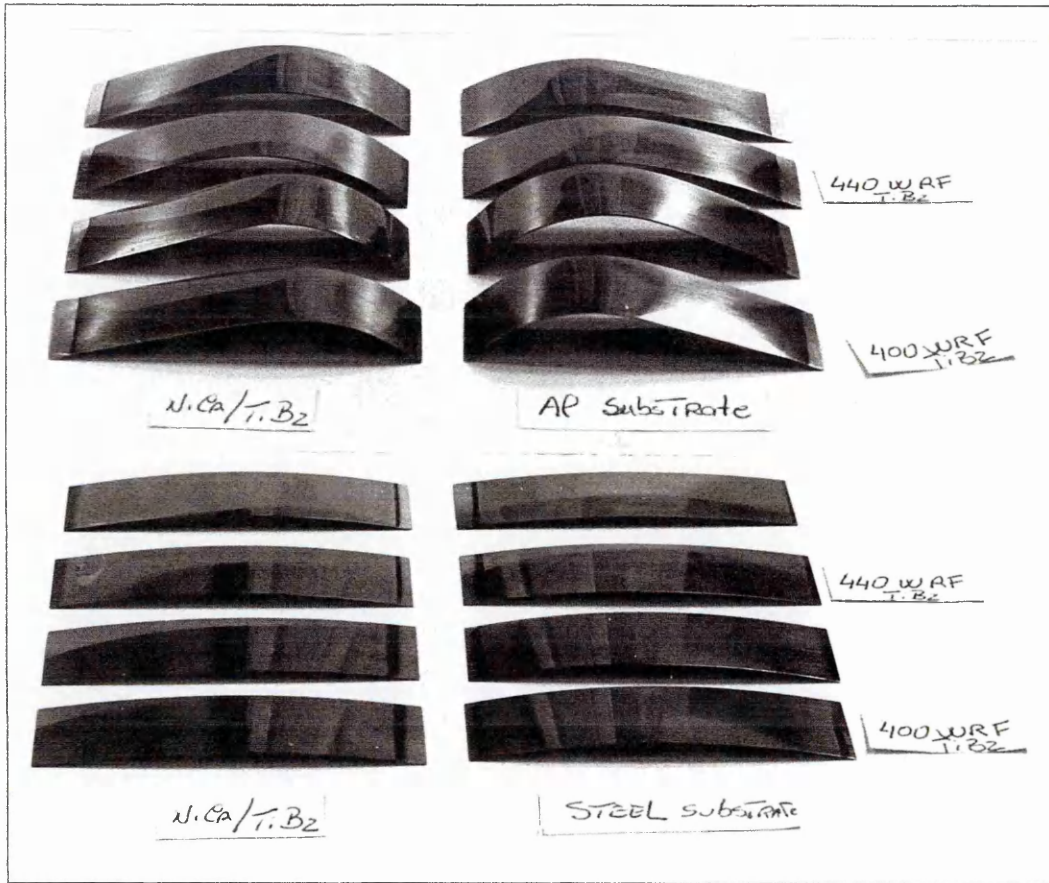

Photograph 3.23. Al/TiB_2, coatings onto steel (bottom) and aluminium (top) at two TiB_2, powers, series E.

Photograph 3.24. NiCr/TiB$_2$ coatings onto steel (bottom) and aluminium (top) at two TiB$_2$. powers, series E.

2. Quantitative Analysis

The quantitative analysis of the internal stresses was performed for Al/TiB$_2$ and (Al/TiB$_2$)N$_2$ coatings of the series C, used in three-point bend test with water as a loading method. The procedure for measuring the internal stresses in these coatings was described in section 2.3 and by using Stoney's equation 1.6. Measuring the curvature gives the following estimates of the stresses in these coatings as shown in table 3.49.

Coating system	Substrate	t_s (mm)	t_f (μm)	υ_s	E_s (GPa)	δ (μm)	σ_f (GPa)
Al/TiB$_2$ (S3)	Steel	0.1947	6.04	0.30	206.7	539.9	-0.14
Al/TiB$_2$ (S4)	Steel	0.2002	5.00	0.30	206.7	669.4	-0.21
(Al/TiB$_2$)N$_2$ (S3)	Steel	0.1990	3.60	0.30	206.7	969.9	-0.43
Al/TiB$_2$ (A2)	Aluminium	0.2533	3.50	0.35	70.6	3530.5	-0.99
(Al/TiB$_2$)N$_2$ (A8)	Aluminium	0.2520	3.20	0.35	70.6	2015.2	-0.55

δ- Refer to the deflection variation of the beam

(S3),(S4),(A2),(A8)-Refer to sample positon inside the vacuum chamber

Table 3.49. Estimation of internal stresses for Al/TiB$_2$ and (Al/TiB$_2$)N$_2$ coating systems, series C.

3.3.6. SUMMING UP

1. Mechanical Three Point Bend Methods

The in-plane elastic modulus of the film depends strongly on the dimensions and the in-plane elastic modulus of the substrate. Moreover, the elastic modulus is nearly independent of the thickness of the film, as mentioned in section 1.5.2. The effect of the beam dimensions on measurement accuracy can be shown either by mechanical loading using washers as weights (table 3.18 and 3.19) or by mechanical loading using water as a weight method (table 3.25). This effect has been demonstrated by using two different methods of slope calculation and by using an Anova analysis.

The relative error of E_s for steel beams is higher compared to those for aluminium and copper beams under mechanical loading using water as a weight. This may reflect the fact that the compliance of the steel substrate is more significant compared to the aluminium substrate for the E_f calculations (table 3.25).

Measuring the ratio of the compliance (γ_s/γ_c) rather than using the handbook value of the compliance gives better repeatability of the measurements, as shown by the mechanical loading using water as a weight.

Table 3.50 shows the maximum relative error of the slope and elastic modulus for the three point bend test approaches for measuring the in-plane elastic modulus of uncoated and coated steel beams. The high value of E_s and E_f relative errors for mechanical loading using water as weight reflects either the accuracy of the applied load for low deflection between sets of experiments or the samples' dimensional accuracy. The relative error for mechanical loading using washers as weights (1.9%) is less compared to mechanical loading by using water as a weight (3.7%). However, the elastic modulus of steel beam for the last method (209.7GPa) is much closer to the "book value" of 207GPa compared to those by mechanical loading using washers as a weight (220.1Gpa). This last method shows that the elastic modulus variation from one reading to another (5.5%) is higher than the mean relative error of the elastic modulus (1.9%), so the measurement repeatability is very significant for this method. The repeatability of the load for each experiment is more significant for the mechanical loading using washers method.

For the three approaches developed in this project for measuring the in-plane elastic modulus, the measurement repeatability increases from the washer method, to the water method, and then to the indenter method. Thus, the reliability of the methods increases with measurement accuracy, making the three point bend test by nanoindenter candidates the best of these for measuring the in-plane elastic modulus very accurately (see table 3.50).

The compliance of the equipment, mainly the frame compliance, and load and deflection calibration have a strong effect on the measured elastic modulus of the film. The system measurement accuracy for three-point bend tests using both the washer and water methods depends on the accuracy of the applied load, deflection measurement, frame compliance, vibration sample compliance and slipping between sample and support. While the three-point bend test by nanoindenter depends on the load and depth

calibration, the compliance of the system is a function of the cylinder indenter, the vibration sample compliance and slipping between sample and support.

Three Point Bending Test on Steel Beams			
Methods	*Mechanical loading using washers as weights*	*Mechanical loading using water as weights*	*Nanoindenter*
Mean relative error of the slope γ_s (%)	2.8	2.2	0.35
Mean relative error of the slope γ_c (%)	1.3	1.1	-
Mean relative error of the E_s (%)	1.9	3.7	0.40
Mean relative error of the E_f (%)	-	5.6	0.40
Mean relative error of E_s between readings (%)	-	0.6	0.50
Mean relative error of E_f between readings (%)	5.5	1.1	-
Disadvantages	The applying load depends either the operator or system vibration.	The water speed and vibration control require more time.	The load is applied in the horizontal direction.
Advantages	Easy to operate.		Easy to operate, load and deflection monitoring.

Table 3.50. Comparison between the three-point bending test approaches for steel beams.

2. Nanoindentation Method

The hardness and elastic modulus of Al/TiB_2 coatings, series A, show an increase for low plastic depth of indentation, or low loads, as shown in figure 3.47 and 3.50. This effect on hardness is well documented in the literature as an ISE for monolayer coatings.

The Al/TiB_2 coatings series A for different positions inside the chamber show the same behaviour as a function of the penetration depth for the same λ and V_c, either for elastic modulus values or hardness values (figures 3.49 and 3.52).

The elastic modulus and hardness values of the TiB_2 single-layer coating of the series C are higher compared to those for series E. This may be because sputtering conditions of the system differ.

Some coatings of the system Al/TiB_2, $(Al/TiB_2)N_2$, $NiCr/TiB_2$ and TiB_2 show high hardness and elastic modulus when deposited onto steel substrates rather then on aluminium substrates. This may be due either to the different stiffness on the substrates or the possible formation of the AlB compound at the aluminium substrate/coating interface.

The Al/TiB_2, $(Al/TiB_2)N_2$ and TiB_2 coatings, series C, show that the hardness variation with sample position inside the chamber is more reproducible for steel substrates compared to Al. This can be explained in terms of the effect of thickness uniformity of the Al and TiB_2 coatings as a function of the argon flux position and the target erosion area, as shown in figures 3.13 and 3.15. This effect is not shown for the elastic modulus.

An addition of $30\%N_2$ to the Al/TiB_2 system increases the hardness but decreases the elastic modulus of the multilayer coating. This can be explained by the distortion of the boron sublattice by nitrogen atoms (figure 3.55).

The hardness and elastic modulus values of the Al/TiB_2 coatings, series A, at $\lambda=200nm$ and V_c of 75%, 50%, 25% are lower compared to those of the series E. This may be because the process conditions differ. However, both series follow the same pattern related to the volume fraction of ceramic. Increasing the volume of ceramic in Al/TiB_2 multilayer coating increases the hardness and elastic modulus of the coating. The same effect was found when decreasing the composition wavelength. The volume fraction has a strong effect on the hardness and elastic modulus of these coatings, much greater than the composition wavelength. The highest elastic modulus and hardness values for the coatings of series A were found to be at $\lambda=200nm$ and $V_c=75\%$ and for the series E at $\lambda=50nm$ and $V_c=75\%$. Both series do not follow the rule of mixtures.

The Al/TiB_2 systems give values of elastic modulus below those predicted by the rule of mixtures when measured using nanoindentation. However, on changing the Al for a NiCr metal layer, the elastic modulus improves to give values above the rule of mixtures predictions on steel substrates (304.5GPa), when compared with TiB_2 coatings (314.2GPa) deposited under the same sputtering conditions (figure 3.66).

The X/TiB_2 multilayer protective-coatings (X=Al or NiCr) improves the hardness of the aluminium substrates, reaching the hardness value of 15.72GPa for the $NiCr/TiB_2$ system and 8.66GPa for the Al/TiB_2 system. The hardness of steel is improved with Al/TiB_2 coatings (series E) for a combination of 200nm/75%, 100nm/75%, and 50nm/75%, for composition wavelength and volume of ceramic. However, on changing Al for NiCr on a steel substrate, the hardness further increases reaching a value of 18.81GPa. The elastic modulus of the coating on steel is only slightly improved with the Al/TiB_2 system for a combination of 200nm/75%, 50nm/75%, and 50nm/50%, for composition wavelength and volume of ceramic, giving a maximum value of 222.2GPa. The elastic modulus increases to 304.5GPa for the $NiCr/TiB_2$ system compared with a steel "book value" of 206.7GPa. The elastic modulus of the aluminium is improved either by the Al/TiB_2 coatings or $NiCr/TiB_2$ coatings, for all ranges of λ and V_c studied, compared to an aluminium "book value" of 70.6GPa.

The nanoindentation measurement accuracy depends strongly on the calibration of the nanoindenter parameters such as: frame compliance, thermal drift correction, zero load calibration, and penetration depth, as shown in table 3.32. The experimental results of hardness and elastic modulus measured using the nanoindenter cannot be considered as absolute values but as relative values because of the uncertainties found during their analysis and shown through this section.

3. Structural Characterization

The TiB_2 single-layer coating with about $5\mu m$ is very fragile because the coating has cracking (photograph 3.13). The XRD spectrum of the TiB_2 coatings shows some peaks for the close packed plane while the Al/TiB_2 multilayer coatings XRD spectrum does not have significant peaks. This means that the TiB_2 layer within the composite

coating is amorphous. Moreover, the TiB_2 layer is sub-stoichiometric, as shown in table 3.47. Both structure and stoichiometry of the TiB_2 layers could be the explanation for the low hardness and elastic modulus of the Al/TiB_2 multilayer coatings.

4. Analysis of the internal stresses

The qualitative analyses of the stress show the multilayer coating has less internal stresses compared to the TiB_2 coatings either onto aluminium or steel substrates. This is believed to be due to the individual layers. The intrinsic stresses in the TiB_2 film, produced during the deposition process, are relieved by the stress relaxation of the Al layer of the multilayer coating. Measured values of internal stress are in the range -0.1 to 1GPa.

In table 3.49 it can be seen that the stress levels on the Al substrate are higher than on the steel. This is to be expected as the Al has a higher thermal expansion coefficient than the steel and then generates higher thermal stresses.

On changing the Al for NiCr metal layer within the coatings, for the same λ and V_c, this seems to increase the internal stresses of the multilayer coatings. This increases intrinsic stresses when using NiCr multilayer because stress relaxation within the NiCr is less easy than from Al (it is a higher melting point film).

The TiB_2 coatings on steel substrate showed spallation and cracks which do not happen with multilayer coatings. The TiB_2 coatings onto aluminium substrates show higher substrate curvature than the multilayer coatings.

CONCLUSION AND FURTHER WORK

OUTLINED

⇓

4.1. General Conclusion

4.2. Further Work

4. CONCLUSIONS AND FURTHER WORK

4.1. GENERAL CONCLUSIONS .

At the end of each technical section the main results have been identified and discussed, for example the deposition conditions for all coatings were discussed in section 3.1.6, the mechanical properties of bilayers in sections 3.2.4. and for multilayers in section 3.3.6. The following pages identify and bring together the more important findings.

1. Monolayer Coating Design

For single layer coatings the optimum sputtering conditions have been identified so that these conditions could be used to produce multilayer coatings, for example:

♦ *For Aluminium deposition:* 0.6Pa (4.5×10^{-3}Torr) argon pressure at 400WRF power
♦ *For Titanium deposition*: 0.6Pa (4.5×10^{-3}Torr) argon pressure at 300WRF power
♦ *For Nimonic 75 alloy (NiCr) deposition*: 0.6Pa (4.5×10^{-3}Torr) argon pressure at 200WRF power
♦ *For Molybdenum deposition*: 0.6Pa (4.5×10^{-3}Torr) argon pressure at 250WRF power
♦ *For TiB$_2$ deposition*: 0.6Pa (4.5×10^{-3}Torr) argon pressure at 300WRF power

Al, NiCr and Mo films show typical sputtering deposition curves of deposition rate versus the sputtering pressure, while the deposition rate for TiB$_2$ and Ti seems not to be affected by the sputtering pressure. TiB$_2$ coatings would not be expected to be influenced by these factors as they are ceramic, but the unusual behaviour of titanium requires further investigation. However, as this coating was not used in the multilayer coatings, this problem was left to later workers. The suggestion is that, as titanium is highly avaricious for oxygen it may be contaminant related but this requires to be substantiated.

For a given sputtering pressure of 0.6Pa the deposition rate increases with the sputtering yield for Ti, Mo, and Al. This is in agreement with generally accepted theories of coatings, as discussed in section 1.4.1.

Considering the sputtering conditions studied, increasing either the sputtering pressure or RF power leads to increased deposition rates as observed. This is due to an increase in the DC offset target voltage which increases the ion bombardment.

The conditions were chosen to ensure that the substrate temperature was lower than 200°C for all single-layer coatings in the range of sputtering pressure and power studied. This is particularly important as it was necessary to coat aluminium substrates which cannot withstand high temperatures.

As referred to in the literature, the uniformity of the deposition rate has been one the main concerns in planar magnetron sputtering because this affects either the

properties of the coatings or the profitability of the process. The two main parameters that affect the thickness of the Al and TiB_2 coating uniformity are the argon flux position and the target erosion area. The former was found to prevail over the erosion area for Al coatings. Hence, the high deposition rate values are found next to the argon source. The target erosion area was found to dominate the deposition rate of the TiB_2 coatings, positioning the high values at the centre of the target. This has been modelled using a cosine evaporation law, discussed in detail in section 3.1.4. where the predicted results are found to fit the experimental observations.

The stoichiometry of the TiB_2 films at 1.0Pa sputtering pressure and 300WRF sputtering power was found to be $TiB_{\cong 1.6}$. An AlB compound was found at the interface between the TiB_2 coating and Al substrate. The TiB_2 coatings of between 1.4 to 1.6µm thickness were found to be amorphous whilst thicker films were crystalline. These differences in structure are found to be important when comparing localised (nanoindentation) and in-plane elastic modulus measurements, as shown later.

2. Two-layer Coating Design

When the above coating conditions were used to produce the bilayers (section 3.2.) some important results were identified. For example, the TiB_2 coatings were thicker than the multilayer and monolayer coatings and hence these coatings were mainly crystalline as opposed to the thin multilayer TiB_2 coatings, which were found to be amorphous. This is an important factor for, as the crystalline materials were only observed in this section, it suggests that the interface and epitaxial problems can exert an appreciable influence on early coating growth.

The stoichiometry of the TiB_2 top layer was not determined but is believed to be similar to that of the monolayer TiB_2 coatings which are sub stoichiometric at $TiB_{1.6}$ for the same sputtering conditions.

It is important to note that bi-layer coatings were adherent to the substrate without cracks, whilst monolayer TiB_2 coatings on steel showed extensive microcracks due to their brittleness (photograph 3.13). This demonstrates the importance of the presence of a metallic interface which is produced in the chamber as it is likely to have a much cleaner surface for adhesive bonding of the TiB_2.

The apparent hardness of the different coating systems produced in this study shows that the hardness is mainly greater on the steel substrates than on the Al substrate. This may be due to either the different stiffness of the substrates or the possible formation of the AlB compound at the aluminium substrate/coating interface. However, it is considered that it is more likely to be due to the interaction of the elastic stress field with the underlying substrates. This is confirmed by the fact that the apparent hardness of the different coating systems decreases with plastic depth (except for Mo/TiB_2 coating onto Al and steel substrates and Ti/TiB_2 onto steel where the intermediate layers are of high modulus, which will reduce this effect).

The more reliable results for hardness and elastic modulus values respectively are shown in figures 3.39 and 3.40 because, before undertaking this schedule the nanoindenter was calibrated with a quartz reference sample.

The two-layer coating systems, (Al/TiB_2, Ti/TiB_2 on steel and aluminium and Mo/TiB_2 on steel), show values of elastic modulus above the rule of mixtures, as shown in figure 3.41. The elastic modulus improvements are: 36.2% for Al/TiB_2 onto steel, 30.8% for Ti/TiB_2 onto steel, 3.1% for Mo/TiB_2 onto steel, 40.2% for Al/TiB_2 onto Al and 28% for Ti/TiB_2 onto aluminium. This analysis was based on TiB_2 coatings for the same sputtering conditions and assuming that the two-layer coatings have 50% of the volume of ceramic. The highest improvement in the elastic modulus of the two-layer coatings was found to be for Al/TiB_2 either onto Al or steel substrates. The reason is because the top TiB_2 coating has high hardness and elastic modulus and this is the dominant factor in the indentation system to give values that are based on towards the ceramic properties.

Similarly, the hardness values on the bilayer coatings gave values very similar to the hardness of the bulk TiB_2 (33.7GPa). This is shown in figure 3.39 where the hardness values of the coatings on steel substrates, for 200nm or 400nm indentation depth, increases on going from Al/TiB_2 (27.04GPa) to Ti/TiB_2 (28.65GPa) and then Mo/TiB_2 (34.12GPa). This last system has a hardness very close to the TiB_2 monolayer coating for the same sputtering conditions. For the aluminium substrate the hardness values, for Al/TiB_2, Ti/TiB_2, Mo/TiB_2 and TiB_2 for 200nm indentation depth are very close to TiB_2 coating for the same sputtering conditions. The hardness value of Al/TiB_2 coatings at 200nm plastic depth is slightly higher on steel substrates compared to those on Al substrates. These results again show the effect of the interaction of the stress field with the underlying material, but as the bilayer TiB_2 thickness is large ($\cong 2.5\mu m$) the effect is only limited.

It should be remembered that the high modulus and hardness values for these materials reflect both the increased thickness of the TiB_2 layers and may also be influenced by the fact that in these layers the structure of the TiB_2 is crystalline.

3. Multilayer Coating Design

The results of the multilayer coatings were discussed in section 3.3 and the results summarised in section 3.3.6. It should be noted that there is a significant difference between the TiB_2 formed on the two layer coatings and on the multilayer coatings. As discussed earlier, in the two-layer ones thicker TiB_2 coatings are found and the material is crystalline, whereas with the thinner multilayer TiB_2 coating the structure was amorphous and non-stoichiometric, approximating to formula $TiB_{(1-x)}$ as shown in table 3.48. This structural change has a significant influence on the mechanical properties because tests such as nanoindentation are sensitive to detailed local structure and in particular are sensitive to through thickness structure, whereas tests such as the three point bend tests give overall, average, in plane values.

The hardness and elastic modulus of the Al/TiB_2 coatings measured on the nanoindenter show an increase for low plastic depth of the indentation, or low loads

(figures 3.47 and 3.50). Different sample positions inside the vacuum chamber show the same behaviour as a function of the penetration depth for the same λ and V_c (figures 3.49 and 3.52). The increased hardness for low loads has been referred to in the literature for monolayer coatings and discussed earlier for bilayer coatings and the effect is considered to be due to the stress field interaction with the underlying structure eg. some coatings of the systems Al/TiB_2, $(Al/TiB_2)N_2$, $NiCr/TiB_2$ and TiB_2 show high hardness and elastic modulus when deposited onto steel substrates and rather lower when on aluminium substrates.

The hardness variation with the sample position inside the chamber is more reproducible for coatings onto steel substrates rather then for coatings on Al substrates, for the systems Al/TiB_2, $(Al/TiB_2)N_2$, and TiB_2. This can be explained by the thickness uniformity of the Al and TiB_2 coating as a function of the argon flux position related to the relative positions of the steel and aluminium samples and the target erosion area (figures 3.13 and 3.15). The effect can be predicted by the cosine rule as described in section 3.1.4.

An addition of 30%N_2 to the Al/TiB_2 system increases the hardness but decreases the elastic modulus of the multilayer coating. This can be explained by the distortion of the lattice by nitrogen atoms (figure 3.55).

Increasing the volume of ceramic in Al/TiB_2 multilayer coating increases the hardness and elastic modulus of the composite coating. The same effect was found when decreasing the composition wavelength. The volume fraction of ceramic has a strong effect on the hardness and elastic modulus of these coatings, much greater than the composition wavelength. The highest elastic modulus and hardness values for the coatings of series A were found to be at $\lambda=200nm$ and $V_c=75\%$ and for the series E at $\lambda=50nm$ and $V_c=75\%$. Both series do not follow the rule of mixtures. The reason for these changes is that the values obtained are determined by the thickness of the outer TiB_2 layer. The greater this thickness the higher the value of apparent hardness and modulus that is recorded for the coating.

On changing the Al for a NiCr metal layer at $\lambda=50nm$ and $V_c=75\%$ the elastic modulus improves to give values above the rule of mixtures predictions on steel substrates (304.5GPa), when compared with TiB_2 coatings (314.2GPa) deposited under the same sputtering conditions (figure 3.66). This is because the modulus of the NiCr layer is similar to the steel underlayer and the TiB_2 modulus is higher.

The X/TiB_2 multilayer protective-coatings (X=Al or NiCr) improve the hardness of the aluminium substrates, reaching the hardness value of 15.72GPa for $NiCr/TiB_2$ system and 8.66GPa for Al/TiB_2 system. The hardness of steel is improved with Al/TiB_2 coatings (series E) for a combination of λ and V_c for 200nm/75%, 100nm/75%, and 50nm/75%. However, on changing Al for NiCr on steel substrates, the hardness further increases, reaching a value of 18.81GPa. The elastic modulus of the steel is only slightly improved with the Al/TiB_2 system for a combination of λ and V_c for 200nm/75%, 50nm/75%, and 50nm/50%, giving a maximum value of 222.2GPa. The elastic modulus increases to 304.5GPa for the $NiCr/TiB_2$ system compared with a steel "book value" of 206.7GPa. The elastic modulus of the aluminium is improved either by

the Al/TiB$_2$ coatings or NiCr/TiB$_2$ coatings, for all ranges of λ and V$_c$ studied compared to an aluminium "book value" of 70.6GPa.

These results again show that the hardness and elastic modulus values depend upon the layered structures measured and dominated by the amount of TiB$_2$ in the total coating.

4. Comparison Between Elastic Modulus by Mechanical Three-Point Bend Methods and Nanoindentation Method

The nanoindentation measurement accuracy depends strongly on the calibration of the nanoindenter parameters such as: frame compliance, thermal drift correction, zero load calibration and penetration depth, as shown in table 3.32. The experimental results of hardness and elastic modulus measured using the nanoindenter cannot be considered as absolute values but as relative values because of the uncertainties found during their analysis and shown through this section.

An additional calibration of the nanoindenter with quartz as a standard between schedules seems to be a good way forward to control the repeatability of the measurements because the machine can become non-calibrated easily.

A comparison between the elastic modulus from three-point bend tests and nanoindentation techniques shows an increase in the in-plane elastic modulus from 1.3 to 2.7 over the nanoindentation values depending on the coating system, as shown in table 3.51. The explanation could be found in several factors:

- Deflection of the beam in two directions, shown in photograph 3.18, gives a very high apparent value for the in-plane elastic modulus for the sample (Al/TiB$_2$)N$_2$(A2) compared with the sample in position (A8). This is due to the added stiffness from bending in two directions.

- The uncertainties of the experimental technique either by three point bend test or nanoindentation.

- Adding to the uncertainties of the measurement technique, the equivalent stiffness could affect the in-plane elastic modulus through the dimensions and elastic modulus of the uncoated beam and film thickness, as shown for the different values of sample Al/TiB$_2$(S4) and Al/TiB$_2$(S3) of the same run. The stiffness is a function of S $= f$ (b, E$_f$, E$_s$, t$_s$, t$_f$) as referred to in equation 2.9. The table 3.24 shows the relative error for sample S4 (3.8%) is higher compared with sample S3 (2.6%) and the film thickness differs by 1 μm between both samples.

- The three point bend test measured the in-plane elastic modulus of the film, i.e., the elastic modulus of the whole composite beam (coating+coating), while the nanoindentation method is largely influenced by the elastic modulus at the location of the coating indenter.

Sample Reference	In-plane Elastic Modulus $(E_f)i$; (GPa)	Elastic Modulus by Nanoindentation $(E_f)n$; (GPa)	Ratio of $(E_f)i / (E_f)n$
1AS4	256.9	119.6 (521nm)	2.1
2AS4	328.6	133.2 (521nm)	2.4
3AS4	227.6	123.4 (520nm)	1.8
4AS4	326.1	140.4 (503nm)	2.3
5AS4	193.9	101.9 (538nm)	1.9
Al/TiB$_2$ (S3)	557.4	208.9 (461nm)	2.7
(Al/TiB$_2$)(S4)	352.0	211.1 (462nm)	1.7
(Al/TiB$_2$)N$_2$ (S3)	211.1	160.0 (422nm)	1.3
(Al/TiB$_2$)(A2)	228.9	171.2 (156nm)	1.3
(Al/TiB$_2$)N$_2$ (A2)	678.0	141.7 (151nm)*	-
The values in brackets correspond to the plastic depth			
* Sample in position (A8)			

Table 3.51. Comparison between elastic modulus of the film by three-point bend test and nanoindentation.

It is instructive to compare the size of the Berkovitch diamond shown in figure 2.23 with the size of the columnar structure of the coating shown in photographs 3.5 to 3.11. These show that the diamond indenter will be forced on to the top of the columnar grains. This will cause collapse and shear along the column boundary and will lead to apparently lower values for the measured modulus. It is possible that this explains the reason for the difference in modulus measured by the two methods. Further work is required, with particular reference to observing the microstructure of the indentations to resolve this problem.

In an attempt to address this problem the nanoindentation technique was modified to give a three point bend test by replacing the central indenter with a simple cylindrical contact. Initial tests have been done using this technique with aluminium and steel uncoated beams. This technique was used to estimate the compliance of the nanoindenter system and the results are shown in table 3.28 and 3.29. It would be particularly useful to use this technique to calculate the in-plane modulus of the coated specimens to compare with the earlier crude three point bend tests using either washers or water as the loading medium. However, time did not allow these tests to be done and it is suggested that this is an area for further investigation.

4.1. FURTHER WORK

The present investigation has developed a method for producing multilayer coatings of ceramic and metal interlayers. It has been shown that both the hardness and the modulus of the samples can be improved by this technique and, in particular, it has demonstrated that the brittleness of TiB_2 can be accommodated by using a ductile interlayer to prevent microcracking.

The following investigations are suggested to take this research to the next stage:

1. The work has shown that the properties that have been investigated, namely hardness and Young's modulus may be dependent upon the structure of layers produced. It has been shown that TiB_2 is amorphous at low thickness and crystalline at higher values. An investigation into the metallography of the coatings allied with inspection of the indents produced by nanoindentation should help to explain many of the effects identified.

2. As the properties of the composite depend on the TiB_2 layer coating properties, so an improvement of TiB_2 layer structure could be brought about, for example by ion bombardment using either bias sputtering or low energy ion irradiation.

3. As the stoichoimetry of TiB_2 affects the composite properties, a study of the TiB_2 stoichiometry either for two layer coatings or multilayer coatings as a function of the sputtering conditions could help to improve the composite properties

4. A knowledge of the composition of the phase boundaries and interdiffusion is important for the interpretation of the mechanical properties. This study could be done by Auger depth profile rather by TEM analysis, as referred to in the literature.

5. Studying the effect of the thickness of the intermediate metal layer for the two-layer design on the TiB_2 top layer properties may improve performance. As referred to in the literature, the supermodulus effect only appears for a narrow range of composition wavelengths. Hence, lowering the composition wavelength for the coating systems studied may improve the elastic modulus of the composites.

6. The target temperature was one of the limitations in this project on the deposition temperature. Heating the substrate may help in changing the TiB_2 layer structure.

7. Annealing treatments of the coatings deposited at low temperatures may improve the strength and resistance to crack propagation of the layered material, improve interface properties and rectify composition anomalies.

8. Finally, the modification proposed for the nanoindentation technique by using a cylindrical contact rather than Berkovitch diamond to measure three point bend test results should be continued and the results compared to the indentation modulus values. This should give information which would help to explain the apparently different properties which are currently measured by the different techniques.

REFERENCES

1. Holleck, H. *Constitutional aspects in the development of new hard materials*, IN: R.K. Viswanadhan, D.J.Rowcliffe, J.Gurland (ed), Science of hard materials, Plenum Press, 1983, New York and London, 849-859.

2. Holleck, H.; Kühl, Ch.; Schulz, H. *Summary abstract: Wear resistant carbide-boride composite coatings*, Journal Vacuum Science Technology, A3(6), 1985 2345-2347.

3. Richerson, D.W. *Ceramics: Applications in manufacturing*, 1988.

4. Holleck, H.; Leiste, H.; Schneider, W. *Significance of phase boundaries in wear resistant TiC/TiB₂ materials*, IN: P. Vincenzini (ed), High. Tech. Ceramics, 1987, 2609-2622.

5. Sundgren, J.-E.; Hentzell, H.T.G. *Critical review: A review of the present state of the art in hard coatings grown from the vapor phase*, Journal Vacuum Science Technology, A4(5), 1986, 2256-2279.

6. Almond, E.A. *Deformation characteristics and mechanical properties of hardmetals*, IN: R.K. Viswanadhan, D.J.Rowcliffe, J.Gurland (ed), Science of hard materials, Plenum Press, 1983, New York and London, 517-557.

7. Holleck, H. *Material selection for hard coatings*, Journal Vacuum Science Technology, A4(6), 1986, 2661-2669.

8. Toth, L.E. *Transition metal carbides and nitrides*, Academic Press, New York and London, 1971, 1-260.

9. Andrievskii, R.A. *The synthesis and properties of interstitial phase films*, Russian Chemical Reviews, 66(1), 1997, 53-72.

10. Lynch, J.F.; Ruderer, C.G.; Duckworth, W.H. *Engineering properties of selected ceramic materials*, The American Ceramic Society, Inc., 1966, 4.1-5.10.

11. McColm, I.J. *Ceramic science for materials technologists*, 1983, 311-345.

12. Schneider, S.J. *Engineered Materials Handbook: Ceramics and glasses*, 4, 1991, 787-803.

13. Matkovich, V.I. *Boron and refractory borides*, New York, 1977, 351-406.

14. Goldschmidt, H.J. *Interstitial alloys*, 1967, 255-291.

15. Hove, J.E.; Riley, W.C. *Modern ceramics: Some principles and concepts"*, 1965, 9-23.

16. Lay, L. *Corrosion resistance of technical ceramics*, 1991, 81-91.

17. Viswanadham, R.K.; Mannan, S.K.; Kumar, K.S.; Wolfenden, A. *Elastic modulus of NiAl-TiB₂ composites in the temperature range 300 to 1273K*, Journal of Materials Science Letters, 8, 1989, 409-410.

18. Mitterer, C.; Rauter, M.; Rödhammer, P. *Sputter deposition of ultrahard coatings within the system Ti-B-C-N*, Surface and Coatings Technology, 41, 1990, 351-363.

19. Matsubara, E.; Waseda, Y.; Takeda, S.; Taga, Y. *Structural study of TiB₂ film by grazing incidence X-ray diffraction*, Thin Solid Films, 186, 1990, L33-L37.

20. Ananthapadmanabhan, P.V.; Sreekumar, K.P.; Ravindran, P.V.; Venkatramani, N. *Effect of oxygen pick-up on the properties of plasma sprayed titanium diboride coatings*, Thin Solid Films, 224, 1993, 148-152.

21. Tennery, V.J.; Finch, C.B.; Yust, C.S.; Clark, G.W. *Structure-property correlation for TiB₂-based ceramics densified using active liquid metals*, IN: R.K. Viswanadhan, D.J.Rowcliffe, J.Gurland (ed), Science of hard materials, Plenum Press, 1983, New York and London, 891-909.

22. Segal, D. *Chemical synthesis of advanced ceramic materials*, 1991, 1-155.

23. Platonov, G.L.; Savelév, B.A.; Toropchenov, V.S.; Anikin, V.N.; Anikeev, A.I. *Structure and composition of titanium diboride coatings*, Soc. Powder Metall. Met. Ceram., UDC 022.346.3, 24(6), 1985, 464-467.

24. Subramanian, C; Strafford, K.N.; Wilks, T.P.; Ward, L.P. *On the design of coating systems: Metallurgical and other considerations*, Journal of Materials Processing Technology, 56, 1996, 385-397.

25. Wert, J.J.; Oppliger, S.J. *Influence of composition and processing parameters on mechanical properties and erosion response of Ni-TiB₂ coatings*, Materials Science and Technology, 8, 1992, 825-835.

26. Committee on Coatings of High-Temperature Structural Material. *Coatings for high-temperature structural materials: Trends and opportunities*, National Academy Press, Washington, D.C., 1996, 1-33.

27. Holleck, H.; Schulz, H. *Advanced layer material constitution*, Thin Solid Films, 153, 1987, 11-17.

28. Andrievski, R.A. *Review: Films of interstitial phases: Synthesis and properties*, Journal of Material Science, 32, 1997, 4463-4484.

29. Gupta, V.; Argon, A.S. *Measurement of interface strength by laser pulse induced spallation*, Mat. Res. Soc. Symp. Proc., 188, 1990, 245-250.

30. Parrish, R.H.; Wert, J.J.; Oliver, W.C.; Sklad, P.S. *The effect of varying sputtering parameters on the microstructure and mechanical properties of 10%Ni+TiB₂ thin films*, Proceedings of the 7th International Conference on Erosion by liquid and solid impact, 1987, 18.1-18.7.

31. Basu, S.N.; Hubbard, K.M.; Hirvonen, J-P.; Mitchell, T.E.; Nastasi, M. *Microstructure and stability of TiB₂ and Cu multilayers*, Materials Research Society Symp. Proc., 187, 1990, 157-160.

32. Hubbard, K.M.; Basu, S.N.; Hirvonen, J-P.; Jervis, T.R.; Nastasi, M. *The mechanical property of Cu/TiB₂ multilayer structures*, Mat. Res. Soc. Symp. Proc., 188, 1990, 307-311.

33. Lehoczky, S.L. *Strength enhancement in thin-layered Al-Cu laminates*, Journal Applied Physics., 49(11), 1978, 5479-5485.

34. Tanaka, Y; Gür, T.M.; Kelly, M.; Hagstrom, S.B.; Ikeda, T. *Structure and properties of (Ti$_{1-x}$A$_x$)N films prepared by reactive sputtering*, Thin Solid Films, 228, 1993, 238-241.

35. Wuhrer, R.; Yeung, W.Y.; Phillips, M.R.; McCredie, G. *Study on DC magnetron sputter deposition of titanium aluminium nitride thin films: Effect of aluminium content on coating,* Thin Solid Films, 290/291, 1996, 339-342.

36. Shew, B-Y.; Hung, J-L.; Lu, D-F. *Effects of RF bias and nitrogen flow rates on the reactive sputtering of TiAlN films,* Thin Solid Films, 293, 1997, 212-219.

37. Kirk, J.A.; Flinn, D.R.; Lynch, M.J. *Wear of TiB₂ coatings,* Wear, 72, 1981, 315-323.

38. Tomé Ribeiro, A. *A study of the i-transition in rf-sputtered titanium nitride films,* PhD Thesis, Cranfield University, U.K., 1990.

39. Kaminsky, M.; Nielsen, R.; Zschack, P. *Preferential sputtering of TiC and TiB₂ coatings under D^+ and $^4He^+$ bombardment: Partial yields,* Journal Vacuum Science Technology, 20(4), 1982, 1304-1308.

40. Williams, L.M. *Plasma enhanced vapor deposition of titanium diboride films,* Appl. Phys. Lett., 46(11), 1985, 43-45.

41. Deng, H.; Chen, J.; Inturi, R.B.; Barnard, J.A. *Structure, mechanical and tribological properties of DC magnetron sputtered TiB₂ and TiB₂(N) thin films,* Surface and Coatings Technology, 76/77, 1995, 609-614.

42. Riviere, J.P.; Guesdon, P.H.; Delafond, J.; Denanot, M.F.; Farges, G.; Degout, D. *Crystalline TiB₂ coatings prepared by ion-beam-assisted deposition,* Thin Solid Films, 204, 1991, 157-161.

43. Bunshah, R.F.; Nimmagadda, R.; Dunford, W.; Movchan, B.A.; Demchishin, A.V.; Chursanov, N.A. *Structure and properties of refractory compounds deposited by electron beam evaporation,* Thin Solid Films, 54, 1978, 85-106.

44. Feldman, C.; Satkiewicz, F.G.; Jones, G. *Preparation and electrical properties of stoichiometric TiB₂ thin films,* Journal of the Less-Common Metals, 79, 1981, 221-235.

45. Yang, Y.; Zheng, Z.; Wang, X.; Liu, X.; Han, J.; Yoon, J. *Microstructure and tribology of TiB₂ and TiB₂/TiN double/layer coating,* Surface and Coatings Technology, 84, 1996, 404-408.

46. Nenadovic, T,; Gokovic, B.; Todorovic, B.; Jokic, T. *Sputtering yield and morphological changes of TiB₂ coatings induced by different incident beams,* Nuclear Instruments and Methods in Physics Research, B115, 1996, 523-527.

47. Padmanabham, K.R.; Sørensen, G. *The effect of the ion implantation on RF-sputtered TiB₂ films,* Thin Solid Films, 81, 1981, 13-19.

48. Ryan, J.G.; Roberts, S.; Slusser, G.J.; Adams, E.D. *The preparation and characterization of titanium boride films,* Thin Solid Films, 153, 1987, 329-339.

49. Shikama, T.; Sakai, Y.; Fukutomi, M.; Okada, M. *Deposition of TiB₂ films by a co-sputtering method,* Thin Solid Films, 156, 1988, 287-293.

50. Blom, H.-O.; Larsson, T.; Berg, S.; Östling, M. *Reactively sputtered titanium boride thin films,* Journal Vacuum Science Technology, A7(2), 1989, 162-165.

51. Lohmann, R.; Österschulze, E.; Thoma, K.; Gärtner, H.; Herr, W.; Matthes, B.; Broszeit, E.; Kloos, K.-H. *Analysis of RF-sputtered TiB₂ hard coatings by means of X-ray diffractometry and Auger electron spectroscopy,* Materials Science and Engineering, A139, 1991, 259-263.

52. Sade, G.; Pelleg, J. *Co-sputtered TiB₂ as a diffusion barrier for advanced microelectronics with Cu metallization,* Applied Surface Science, 91, 1995, 263-268.

53. Chen, J.; Barnard, J.A. *Growth, structure and stress of sputtered TiB₂ thin films,* Materials Science and Engineering, A191, 1995, 233-238.

54. Mitterer, C.; Rödhammer, P.;Störi, M.; Jeglitsch, F. *Radio-frequency sputter deposition of boron nitride based thin films,* Journal Vacuum Science Technology, A7(4), 1989, 2646-2651

55. Friesen, T.; Haupt, J.; Gissler, W.; Barna, A.; Barna, P.B. *Ultrahard coatings from Ti-BN Multilayers and by co-sputtering.* Surface and Coatings Technology, 48, 1991, 169-174.

56. Cotell, C.M.; Spague, S.A.; Smidt Jr., F.A. *Surface Engineering,* ASM Handbook, 5, 1994, 470-907.

57. Holleck, H.; Schulz, H. *Preparation and behaviour of wear-resistant TiC/TiB₂, TiN/TiB₂ and TiC/TiN coatings with high amounts of phase boundaries,* Surface and Coatings Technology, 36, 1988, 707-714.

58. Hilz, G.; Holleck, H. *"Characterization of microstructure and interfaces in TiC-TiB₂ coatings,* Materials Science and Engineering, A139, 1991, 268-275.

59. Hilz, G.; Holleck, H. *Structure and Effects of Interfaces in TiC-TiB₂-B₄C-SiC nanosize multilayer systems,* International. Journal. of Refractory Metals & Hard Materials, 14, 1996, 97-104.

60. Wert, J.J.; Oppliger, S.J. *The influence of composition and processing parameters on the mechanical properties and erosion response of Ni+TiB₂ coatings,* Journal of Materials Engineering and Performance, 1(1), 1992, 129-142.

61. Chambers, D.L.; Taylor, K.A.; Wan, C.T.; Susi, G.T. *Stresses in multilayer combinations of sputter deposited coatings of Ni, Ti, TiC+Ni, and TiB₂+Ni on carbon steel substrates,* Journal Vacuum Science Technology, A9(3), 1991, 1104-1108.

62. Taylor, K.A.; Emrick, A.J. *Comparison of stress and structural composition of sputter deposited thick coatings of TiB₂+Ni on polymeric composites,* Journal Vacuum Science Technology, A10(4), 1992, 1734-1739.

63. Rivière, J.P.; Guesdon, Ph.; Delafond, J. *Structure and properties of TiB₂ coatings produced by dynamic ion mixing,* Nuclear Instruments and Methods in Physics Research, North-Holland, B59/60, 1991, 237-240.

64. Chartier, P.; Rivière, J.P.; Mimault, J.; Girardeau, T. *A TEM and EXAFS study of TiB₂ coatings produced by dynamic ion mixing,* Nuclear Instruments and Methods in Physics Research, B95, 1995, 327-333.

65. Rivière, J.P.; Miguet, S.; Cahoreau, M.; Chaumont, J.; Delafond, J.; *"Formation of TiB₂ coatings at room temperature by dynamic ion mixing";* Surface and Coatings Technology, 84, 1996, 398-403.

66. Bunshah, R.F. *Handbook of deposition technologies for films and coatings,* 1994, 1-25.

67. Strafford, K.N.; Datta, P.K.; Googan, C.G. *Coatings and surface treatment for corrosion and wear resistance,* 1984, 181-209.

68. Maissel, L.I.; Glang, R. *Handbook of Thin Film Technology,* 1983, 3.1-3.33.

69. Strafford, K.N.; Datta, P.K.; Googan, C.G. *Coatings and surface treatment for corrosion and wear resistance,* 1984, 14-27.

70. Hocking, M.G.; Vasantasree, V.; Sidky, P.S. *Metallic & Ceramic coatings,* 1989, 49-102.

71. Chapman, B. *Glow discharge processes,* J. Wiley & Sons, Inc.; 1980, 1-17.

72. Bunshah, R.F. *Handbook of deposition technologies for films and coatings,* 1994, 29-74.

73. Freller, H. *Vapour-phase coating processes for hard coatings,* Vacuum, 45(10/11), 1994, 997-1000.

74. Harris, N.S. *Modern vacuum practice,* McGraw-Hill, 1989, 1-30

75. Spinks, W.S. *Vacuum technology,* Chapman & Hall Ltd., London, 1966, 14-23

76. Bunshah, R.F. *Handbook of deposition technologies for films and coatings,* 1994, 131-215.

77. Hill, R.J. *Physical vapour deposition,* Airco Temescal; 1976, 1-148.

78. Thomsen-Schmidt, P.; Schäfer, D.; Steiger, B.; Brauβe, H.; Johansen, H.; Martini, T. *Laser-assisted deposition of optical coatings,* Thin Solid Films, 253, 1994, 28-32.

79. Maissel, L.I.; Glang, R. *Handbook of thin film technology,* 1983, 1.1-1.120.

80. Chapman, B. *Glow discharge processes,* J. Wiley & Sons, Inc.; 1980, 177-341.

81. Bunshah, R.F. *Handbook of deposition technologies for films and coatings,* 1994, 320-358.

82. Bunshah, R.F. *Handbook of deposition technologies for films and coatings,* 1994, 249-306.

83. Heberlein, T.; Krautheim, G.; Wuttke, W. *The sputter deposition process: A Monte-Carlo study,* Vacuum, 42(1/2), 1991, 47-51.

84. Chapman, B. *Glow discharge processes,* J. Wiley & Sons, Inc.; 1980, 77-128.

85. Golan, G.; Axelevitch, A. *Ring etching zones on magnetron sputtering targets,* Thin Solid Films, 300, 1997, 72-77.

86. Taga, Y.; Gotoh, Y. *Role of kinetic energy of sputtered particles in thin film formation,* Thin Solid Films, 193/194, 1990, 164-170.

279

87. Gnaser, H.; Oechsner, H. *Preferential sputtering of isotopes: Fluence and emission-angle dependence,* Physical Review Letters, 63(24), 1989, 2673-2676.

88. Coburn, J.W. *Mass spectrometric studies of positive ions in R.F. glow discharges,* Thin Solid Films, 171, 1989, 65-80.

89. Fancey, K. S.; Matthews, A. *An investigation into the variation in bombardment intensity from ion plating discharges by sputter weight loss experiments,* Thin Solid Films, 193/194, 1990, 171-180.

90. Maissel, L.I.; Glang, R. *Handbook of thin film technology,* 1983, 4.1-4.41.

91. Swann, S. *Film thickness distribution in magnetron sputtering,* Vacuum, 38(8/10), 1988, 791-794.

92. Spencer, A.G.; Bishop, C.A.; Howson, R.P. *The design and performance of planar magnetron sputtering cathodes,* Vacuum, 37(3-4), 1987, 363-366.

93. Grajewski, V.; Uchida, H.H.; Fromm, E. *Oxygen contamination of metal films produced by vacuum deposition,* Thin Solid Films, 193/194, 1990, 990-998.

94. Cavaleiro, A.; Vieira, M.T.; Ramos, F.; Dias, J.P. *The ultimate vacuum pressure and the characteristics of sputtered coatings,* Thin Solid Films, 290/291, 1996, 238-242.

95. Chapman, B. *Glow discharge processes,* J. Wiley & Sons, Inc.; 1980, 139-172.

96. Bunshah, R.F. *Handbook of deposition technologies for films and coatings,* 1994, 82-125.

97. Steffen, H.; Schwarz, J.; Kersten, H.; Behnke, J.F.; Eggs, C. *Process control of RF plasma assisted surface cleaning,* Thin Solid Films, 283, 1996, 158-164.

98. Maissel, L.I.; Glang, R. *Handbook of thin film technology,* 1983, 2.1-2.132.

99. Golan, G.; Axelevitch, A.; Rabinovich, E. *Modified magnetic controlled plasma sputtering method,* Vacuum, 47(9), 1996, 1081-1083.

100. Rossnagel, S.M. *Magnetron plasma deposition processes,* Thin Solid Films, 171, 1989, 125-142.

101. Nanbu, K.; Uchida, S.; Yoshida, H. *Computer simulation of growth of thin films fabricated by the sputtering method: comparison with experiment,* Thin Solid Films, 228, 1993, 330-332.

102. Howson, R.P.; J'Afer, H.A.; Spencer, A.G. *Substrate effects from an unbalanced magnetron,* Thin Solid Films, 193/194, 1990, 127-137.

103. Fan, Q.-H; Chen, H.-Y. *Effects of magnetic field on the target erosion in the symmetrical magnets magnetron sputtering method,* Thin Solid Films, 229, 1993, 143-145.

104. Car, T.; Radic, N. *Film thickness variation in a cylindrical magnetron deposition device,* Thin Solid Films, 293, 1997, 78-82.

105. Kukla, R.; Krug, T.; Ludwig, R.; Wilmes, K. *A highest rate self-sputtering magnetron source,* Vacuum, 41(7/9), 1990, 1968-1970.

106. Hofmann, D.; Rost, A.; Schüßler, H. *A new sputter process for hard coating of large machine parts at low temperatures,* Materials Science and Engineering, A139, 1991, 290-293.

107. Abe, K.; Kobayashi, S.; Kamel, I.; Shimizu, I.; Tateishi, H.; Aiuchi, S. *Planar magnetron sputtering cathode with deposition rate distribution controllability,* Thin Solid Films, 96(3),1982, 225-233

108. Fan, Q.; Hong, Y.; Chen, H.; Chen, X. *A symmetrical magnet magnetron-sputtering method for film deposition,* Thin Solid Films, 229, 1993, 51-53.

109. Vales Silva, M.F.O. *Multilayer TiB_2/X wear resistant coatings: Analysis of the project,* Second Year Report on Research Toward a PhD, Cranfield University, 1995.

110. Rohde, S.L.; Petrov, I.; Sproul, W.D.; Barnett, S.A.; Rudnik, P.J.; Graham, M.E. *Effects of an unbalanced magnetron in a unique dual-cathode high rate reactive sputtering system,* Thin Solid Films, 193/194, 1990, 117-126.

111. Nathan, S.S.; Muralidhar, G.K.; Rao, G.M.; Mohan, S. *Effect of process parameters on glow discharge and film thickness uniformity in facing target sputtering,* Thin Solid Films, 292, 1997, 20-25.

112. Tominaga, K.; Kataoka, M.; Ueda T.; Chong, M.; Shintani, Y.; Mori, I. *Preparation of conductive ZnO:Al films by a facing target system with a strong magnetic field,* Thin Solid Films, 253, 1994, 9-13.

113. Petrov, I.; Losbichler, P.; Bergstrom, D.; Greene, J.E.; Münz, W.-D.; Hurkmans, T.; Trinh, T. *Ion-Assisted growth of $Ti_{1-x}Al_xN/Ti_{1-y}NbN$ multilayers by combined cathodic-arc/magnetron-sputter deposition,* Thin Solid Films, 302, 1997, 179-192.

114. Monaghan, D.P.; Teer, D.G.; Logan, P.A.; Laing, K.C.; Bates, R.I.; Arnell, R.D. *An improved method for the deposition of corrosion-resistant aluminium coatings for aerospace applications,* Surface and Coatings Technology, 60, 1993, 592-596

115. Petrov, I.; Adibi, F.; Greene, J.E.; Sproul, W.D.; Münz, W.-D. *Use of an externally applied axial magnetic field to control ion/neutral flux ratios incident at the substrate during magnetron sputter deposition,* Journal Vacuum Science Technology, A10(4), 1992, 3283-3287.

116. Ershov, A.; Pekker, L. *Model of D.C. magnetron reactive sputtering in $Ar-O_2$ gas mixtures,* Thin Solid Films, 289, 1996, 140-146.

117. Chau, R.Y.; Ho, W-S; Wolfe, J.C.; Licon, D.L. *Effect of target temperature on the reactive D.C.sputtering of silicon and niobium oxides,* Thin Solid Films, 287, 1996, 57-64.

118. Müller, D; Fromm, E. *Mechanical properties and adhesion strength of TiN and Al coatings on HSS, steel, aluminium and copper characterised by four testing methods,* Thin Solid Films, 270, 1995, 411-416.

119. Lee, H-C; Lee, J-Y; Ahn, H-J. *Effect of the substrate bias voltage on crystallographic orientation of reactivity sputtered AlN thin films,* Thin Solid Films, 251, 1994, 136-140.

120. Gelin, B.; Barklund, A.M.; Nender, C.; Berg, S. *Patterning with the use of ion-assisted selective deposition,* Vacuum, 41(4/6), 1990, 1074-1076.

121. Nender, C.; Berg, S. *Monte Carlo simulations of ion-assisted selective deposition,* Thin Solid Films, 193/194, 1990, 13-17.

122. Berg, S.; Katardjiev, I.V.; Nender, C.; Carlsson, P. *Large-area selective thin film deposition by bias sputtering,* Thin Solid Films, 241, 1994, 1-8.

123. Bull, S.J.; Rickerby, D.S. *Evaluation of coatings,* Br. Ceram. Trans. J., 88, 1989, 177-183.

124. Bunshah, R.F. *Handbook of deposition technologies for films and coatings,* 1994, 643-675.

125. Brotzen, F.R. *Mechanical testing of thin films,* International Materials Reviews, 39(1), 1994, 24-45.

126. Shirakawa, Y. *Mechanical properties of single and multilayer ceramics thin films,* M.Phil Thesis, Cranfield University, U.K., 1991.

127. Nix, W.D. *Mechanical properties of thin films,* Metallurgical Transactions, 20A, 1989, 2217-2245.

128. Rouzaud, A.; Barbier, E.; Ernould, J.; Quesnel, E. *A method for elastic modulus measurements of magnetron sputtered thin films dedicated to mechanical applications,* Thin Solid Films, 270, 1995, 270-274.

129. Bull, S.J., Rickerby, D.S. *Hard coatings,* Mat. Res. Soc. Symp. Proc., 188, 1990, 337-348.

130. Thornton, J.A. *High rate thick film growth,* Ann. Rev. Mater. Sci., 7, 1977, 239-260.

131. Maissel, L.I.; Glang, R. *Handbook of thin film technology,* 1983, 8.1-8.42.

132. Townsend, P.D. *Defects in coatings,* Thin Solid Films, 193/194, 1990, 342-349.

133. Greene, J.E.; Barnett, S.A.; Sundren, J.-E.; Rockett, A. *Low-energy ion/surface interactions during film growth from the vapor phase: Effects on nucleation and growth kinetics, defect structure and elemental incorporation probabilities,* Plasma-Surface Interactions and Processing of Materials, 1990, 281-311.

134. Schuhrke, T.; Zweck, J.; Hoffmann, H. *Quantitative analysis of electron microscopic micrographs of multilayers,* Thin Solid Films, 292, 1997, 118-123.

135. Bunshah, R.F. *Handbook of deposition technologies for films and coatings,* 1994, 682-724.

136. Reichelt, K. *Nucleation and growth of thin film,* Vacuum, 38(12), 1988, 1083-1099.

137. Lewis, B.; Anderson, J.C. *Nucleation and growth of thin films,* Academic Press, 1978, 287-488.

138. Bai, C.L.; Zhu, C.F.; Wang, X.W.; Zhang, P.C.; Li, Q.; Wang, C.; Zhao, B.R.; Zheng, L.Z.; Li, L. *Atomic force microscopy study of the growth mechanism of ultrathin YBa₂Cu₃O₇ (YBCO) films*, Thin Solid Films, 289, 1996, 70-73.

139. Thornton, J.A. *Influence of apparatus geometry and deposition conditions on the structure and topography of thick sputtered coatings*, Journal Vacuum Science Technology, 11(4), 1974, 666-670.

140. Movchan, B.A.; Demchishin, A.V.; "Study of the structure and properties of thick vacuum condensates of nickel, titanium, tungsten, aluminium oxide and zirconium dioxide"; Fiz. Metal. Metalloved, 28(4), 1969, 83-90.

141. Thornton, J.A.; Hoffman, D.W. *Stress-related effects in thin films*, Thin Solid Films, 171, 1989, 5-31.

142. Mawella, K.J.A.; Sheward, J.A. *Sputtered alloy coatings by codeposition: Effects of bias voltage*, Thin Solid Films, 193/194, 1990, 27-33.

143. Cannizzaro, A. *Mechanical properties of metal/ceramic multilayered coatings*, MSc Thesis, Cranfield University, U.K., 1993.

144. Bracq, F. *Multilayered Al/SiC coatings*, MSc Thesis, Cranfield University, U.K., 1992.

145. Bunshah, R.F. *Handbook of deposition technologies for films and coatings*, 1994, 763-815.

146. Hetherington, A.V.; Skinner, D.K. *Coordinated analysis for materials problems*, Microscopy and Analysis, 1993, 17-19.

147. Loretto, M.H. *Analysis of materials*, 1984, 65-177.

148. Maissel, L.I.; Glang, R. *Handbook of thin film technology*, 1983, 9.1-9.31.

149. Cullity, B.D. *Elements of X-ray diffraction*, 1956, 81-92.

150. Scardi, P.; Lutterotti, L.; Tomasi, A. *XRD characterization of multilayered systems*, Thin Solid Films, 236, 1993, 130-134.

151. Chaudhuri, J.; Alyan, S.M.; Jankowski, A.F. *Analysis of Ni/Ti multilayers by X-ray diffraction*, Thin Solid Films, 239, 1994, 79-84.

152. Vales Silva, M.F.O. *Multilayer TiB₂/X wear resistant coatings*, First year report on research toward a PhD, Cranfield University, 1994.

153. Prasad, K.V.R.; Shankar, M.V.; Subbanna, G.N.; Varna, K.B.R. *Principles of SEM for structural characterisation*, IN: N. P. Cheremisinoff, P.N. Cheremisionoff (ed.), Handbook of Advanced Materials Testing, 1995, 51-64.

154. Appel, C.C.; Bilde-Sorensen; Horsewell, A. *Characterization of materials by environmental SEM*, Royal Microscopical Society, 33(2), 1998, 98-100.

155. Ulrich, R.K.; Zhao, G. *A new apparatus for measuring the ultimate strain of thin films*, Thin Solid Films, 224, 1993, 63-68.

156. Van Nie, A.G. *A method for the determination of the stress in, and Young's modulus of silicon nitride passivation layers,* Solid State Technology, 1980, 81-84.

157. Rosenmayer, C.T.; Brotzen, F.R.; Gale, R.J. *Mechanical testing of thin films,* Mat. Res. Soc. Symp. Proc., 130, 1989, 77-86.

158. Nix, W.D.; Noble, D.B.; Turlo, J.F. *Mechanisms and kinetics of misfit dislocation formation in heteroepitaxial thin films,* Mat. Res. Soc. Symp. Proc., 188, 1990, 315-330.

159. Ignat, M.; Chouaf, A.; Normandon, Ph.; "Internal stresses and adhesion properties of film/substrate interfaces"; Mat. Res. Soc. Symp. Proc., 188, 1990, 97-102.

160. Cardinale, G.F.; Howit, D.G.; Clift, W.M.; McCarty, K.F.; Medlin, D.L.; Mirkarimi, P.B.; Moody, N.R. *Micromachined silicon cantilever beams for thin-film stress measurement";* Thin Solid Films, 287, 1996, 214-219.

161. D'Heurle, F.M.; Harper, J.M.E. *Note on the origin of intrinsic stresses in films deposited via evaporation and sputtering,* Thin Solid Films, 171, 1987, 81-92

162. Vijgen, R.O.E.; Dautzenberg, J.H. *Mechanical measurement of the residual stress in thin PVD films,* Thin Solid Films, 270, 1995, 264-269.

163. Ramsey, P.M.; Chandler, H.W.; Page, T.F. *Bending tests to estimate the through-thickness strength and interfacial shear strength in coated systems,* Thin Solid Films, 201, 1991, 81-89.

164. Nir, D. *Summary abstract: Energy dependence of the stress in diamondlike carbon films,* Journal Vacuum Science Technology, A4(6), 1986, 2954-2955.

165. Lyubimov, V.V.; Voevodin, A.A.; Spassky, S.E.; Yerokhin, A.L. *Stress analysis and failure possibility assessment of multilayer physically vapour deposited coatings,* Thin Solid Films, 207, 1992, 117-125.

166. Zhou, Z.-F.; Zhou, Q.-G.; Fan, Y.-D. *Stresses in amorphous Gd-Fe alloy thin films deposited by magnetron sputtering,* Mat. Res. Soc. Symp. Proc., 188, 1990, 91-96.

167. Rille, E.; Zarwasch, R.; Pulker, H.K. *Properties of reactivity DC-magnetron-sputtered AlN thin films,* Thin Solid Films, 228, 1993, 215-217.

168. Chinmulgund, M.; Inturi, R.B.; Barnard, J.A. *Effect of Ar gas pressure on growth, structure and mechanical properties of sputtered Ti, Al, TiAl and Ti_3Al films,* Thin Solid Films, 270, 1995, 260-263.

169. Juliet, P.; Rouzaud, A.; Aabadi, K.; Monge-Cadet, P.; Pauleau, Y. *Mechanical properties of hard W-C physically vapour deposited coatings in monolayer and multilayer configuration,* Thin Solid Films, 290/291, 1996, 232-237.

170. Griffin Jr., A.J.; Brotzen, F.R. *Mechanical properties and microstructures of Al-1%Si thin film metallizations,* Thin Solid Films, 150, 1987, 237-244.

171. Kim, Y-S; Shin, S-C. *In situ stress measurements of Co/Pd multilayer films using an optical non-contact displacement detector,* Thin Solid Films, 258, 1995, 128-131.

172. Rickerby, D.S.; Jones, A.M.; Bellamy, B.A. *X-ray diffraction studies of physically vapour-deposited coatings,* Surface and Coatings Technology, 37, 1989, 111-137.

173. Cohen, J.B. *Residual strsses: Measurement by diffraction and interpretation,* 1987, 122-125.

174. Perry, A.J.; Chollet, L. *States of residual stress both in films and in their substrates,* Journal Vacuum Science Technology, A4(6), 1986, 2801-2808.

175. Korhonen, M.A.; LaFontaine, W.R.; Paszkiet, C.A.; Black, R.D.; Li, C.-Y. *Measurement of stress relaxation in thin aluminium metallization by continuous indentation and X-ray techniques,* Mat. Res. Soc. Symp. Proc., 188, 1990.

176. Brookes, C.A. *Hardness measurements in the evaluation of hard materials,* IN: R.K. Viswanadhan, D.J.Rowcliffe, J.Gurland (ed), <u>Science of hard materials</u>, Plenum Press, 1983, New York and London , 181-199.

177. Burnett, P.J.; Rickerby, D.S. *Assessment of coating hardness,* Surface Engineering, 3(1), 1987, 69-79.

178. Korsunsky, A.M.; McGurk, M.R.; Bull, S.J.; Page, T.F. *On the hardness of coated systems,* Surface and Coating Technology, 99, 1998, 171-183.

179. Chiv, C.-C.; Case, E.D. *Elastic modulus determination of coating layers as applied to layered ceramic composites,* Materials Science and Engineering, A132, 1991, 39-47.

180. Lyubimov, V.V.; Voevodin, A.A.; Erokhin, A.L.; Timopheev, Yu.S.; *Application of multilayer ion-plasma coatings to increase service life of engine piston pairs,* Soviet Journal of Friction and Wear, 13(5), 145-148.

181. Asada, H.; Kishi, Y.; Hirose, Y. *Measurements of Young's moduli of TiC-coated film by the X-ray method,* Thin Solid Films, 236, 1993, 247-252.

182. Schwarzer, N.; Richter, F.; Hecht, G. *Determination of mechanical properties of thin films: A theoretical feasibility study,* Surface and Coatings Technology, 60, 1993, 396-400.

183. Vancoille, E.; Celis, J.P.; Roos, J.R. *Mechanical properties of heat treated and worn PVD TiN, (Ti,Al)N, (Ti,Nb)N and Ti(C,N) coatings as measured by nanoindentation,* Thin Solid Films, 224, 1993, 168-176.

184. Nicholls, J.R.; Mendes, C.; Hancock, P. *Measurement methods to determine the elastic properties of oxides at elevated temperatures,* Materials at High Temperatures, 12(2/3), 1994, 85-94.

185. Peraud, S.; Pautrot, S.; Villechaise, P.; Mazot, P.; Mendez, J. *Determination of Young's modulus by a resonant technique applied to two dynamically ion mixed thin films,* Thin Solid Films, 292, 1997, 55-60.

186. Schneider, D.; Scheibe, H.J.; Schwarz, Th. *Characterization of thin diamond-like carbon films by ultrasonic surface waves,* Diamond and related materials, 2, 1993, 1396-1401.

187. Jankowski, A.F.; Tsakalakos, T. *Effects of deflection on bulge test measurements of enhanced modulus in multilayered films,* Thin Solid Films, 290/291, 1996, 243-247.

188. Yang, W.M.C.; Tsakalakos, T.; Hilliard, J.E. *Enhanced elastic modulus in composition-modulated gold-nickel and copper-palladium foils,* Journal of Applied Physics, 48(3), 1977, 876-879.

189. Barzen, I.; Edinger, M.; Scherer, J.; Ulrich, S.; Jung, K.; Ehrhardt, H. *Mechanical properties of amorphous and polycrystalline multilayer systems,* Surface and Coatings Technology, 60, 1993, 454-457.

190. Dhez, P.; Weisbuch, C. *Physics, Fabrication and Applications of multilayered structures,* IN: Barbee, T.W. (ed.), Physics, Fabrication and Applications of multilayered structures, Plenum press, 1987, New York and London, 17-32.

191. Sundgren, J.-E.; Birch, J.; Håkansson, G.; Hultman, L.; Helmersson, U. *Growth, structure and properties of hard and wear-protective layered materials,* Thin Solid Films, 193/194, 1990, 818-831.

192. Cammarata, R.C. *Mechanical properties of nanocomposite thin films,* Thin Solid Films, 240, 1994, 82-87.

193. Schlesinger, T.E.; Cammarata, R.C.; Kim, C.; Qadri, S.B.; Edelstein, A.S. *Mechanical properties of multilayered Cu-Ni thin films measured by indentation techniques,* Mat. Res. Soc. Symp. Proc., 188, 1990, 295-300.

194. Madan, A.; Yashar, P.; Shinn, M.; Barnett, S.A; *"An X-ray diffraction study of epitaxial TiN/NbN superlattices"*; Thin Solid Films, 302, 1997, 147-154.

195. Daniels, B.J.; Nix, W.D.; Clemens, B.M. *Enhanced mechanical hardness in compositionally modulated Fe(001)/Pt(001) and Fe(001)/Cr(001) epitaxial thin films,* Thin Solid Films, 253, 1994, 218-222.

196. Kinosita, K. *Recent developments in the study of mechanical properties of thin films,* Thin Solid Films, 12, 1972, 17-28.

197. Oliver, W.C.; Pharr, G.M. *An improved technique for determining hardness and elastic modulus using load and displacement sensing indentation experiments,* Journal Mater. Res., 7(6), 1992, 1564-1583.

198. Pharr, G.M.; Oliver, W.C. *Measurement of thin film mechanical properties using nanoindentation,* M.R.S. Bulletin, 17(7), 1992, 28-33.

199. Randall, N.X.; Christoph, P.; Droz, S.; Julia-Schmutz, C. *Localised micro-hardness measurements with a combined scanning force microscope-nanoindentation system,* Thin Solid Films, 290/291, 1996, 348-354.

200. Swain, M.V.; Mencik, J. *Mechanical property characterization of thin films using spherical tipped indenters,* Thin Solid Films, 253, 1994, 204-211.
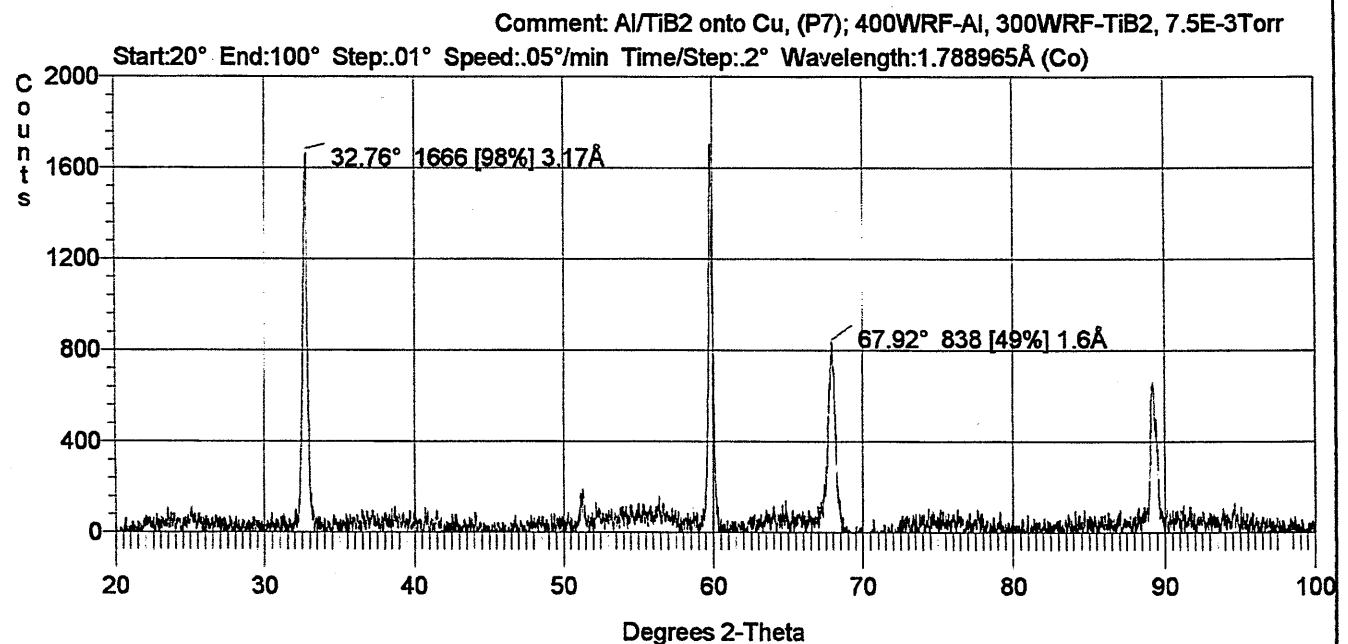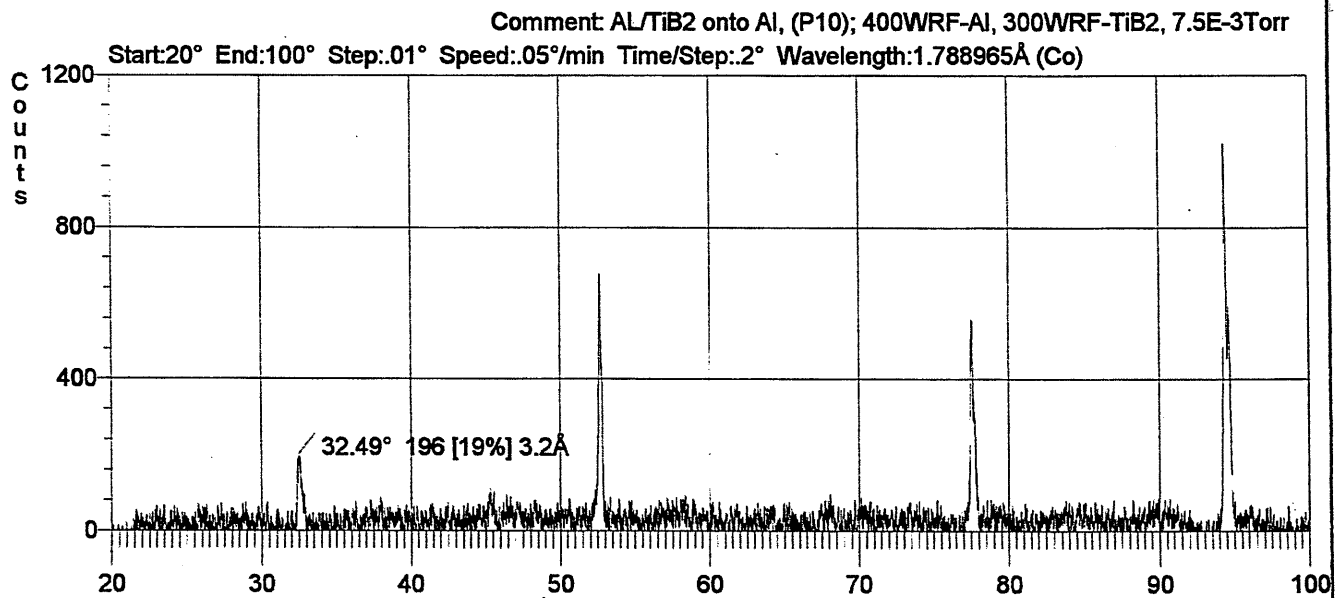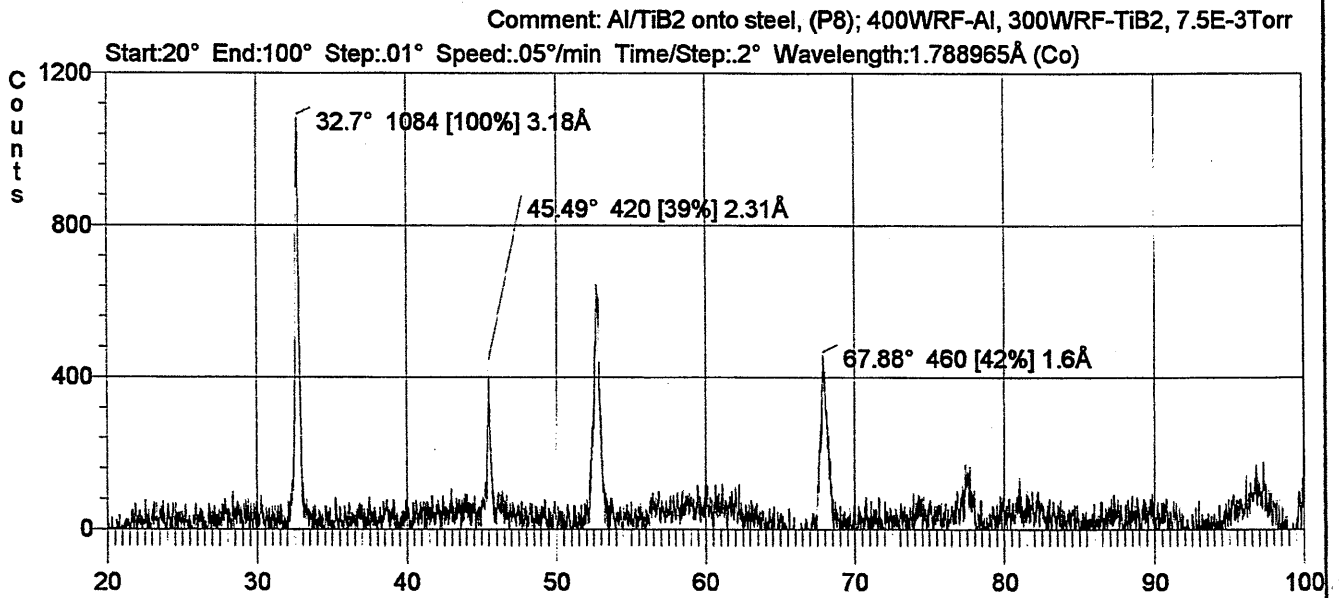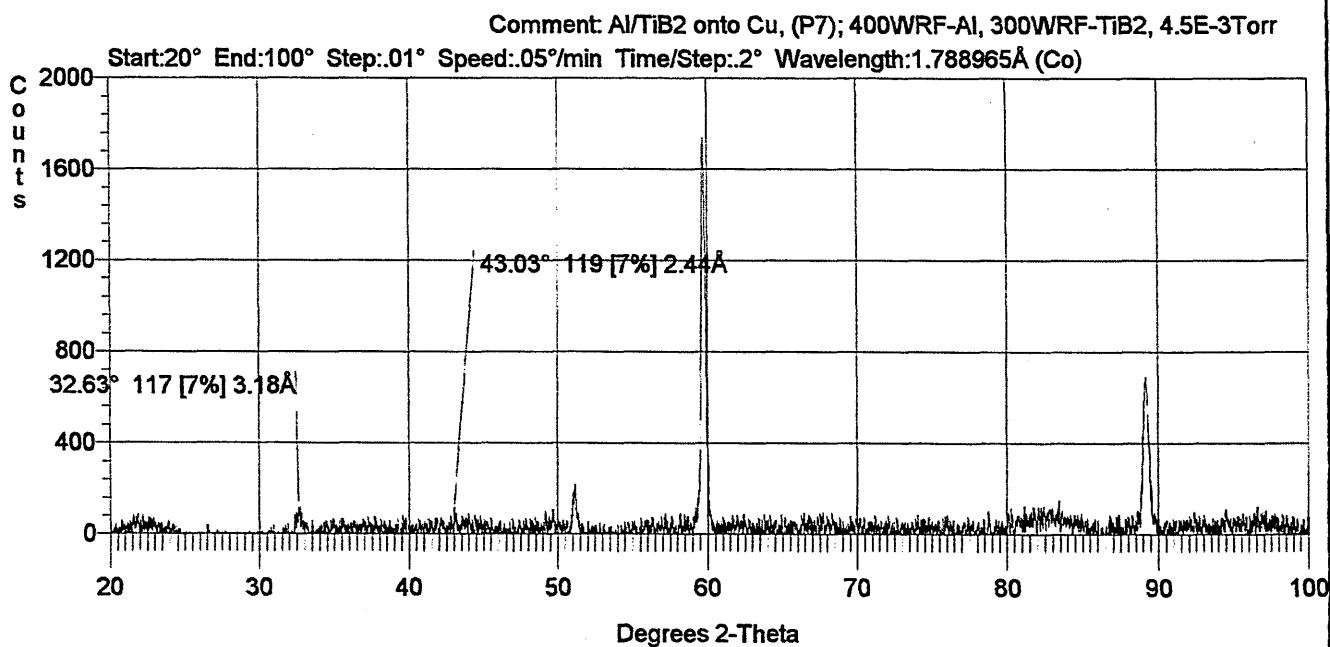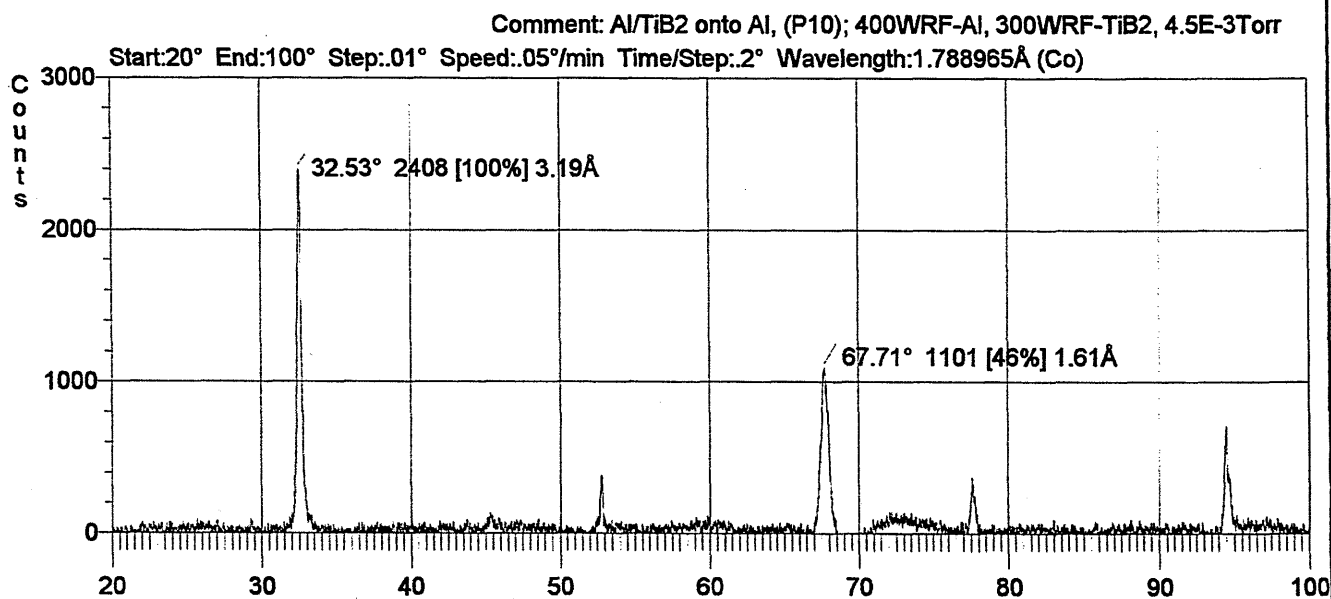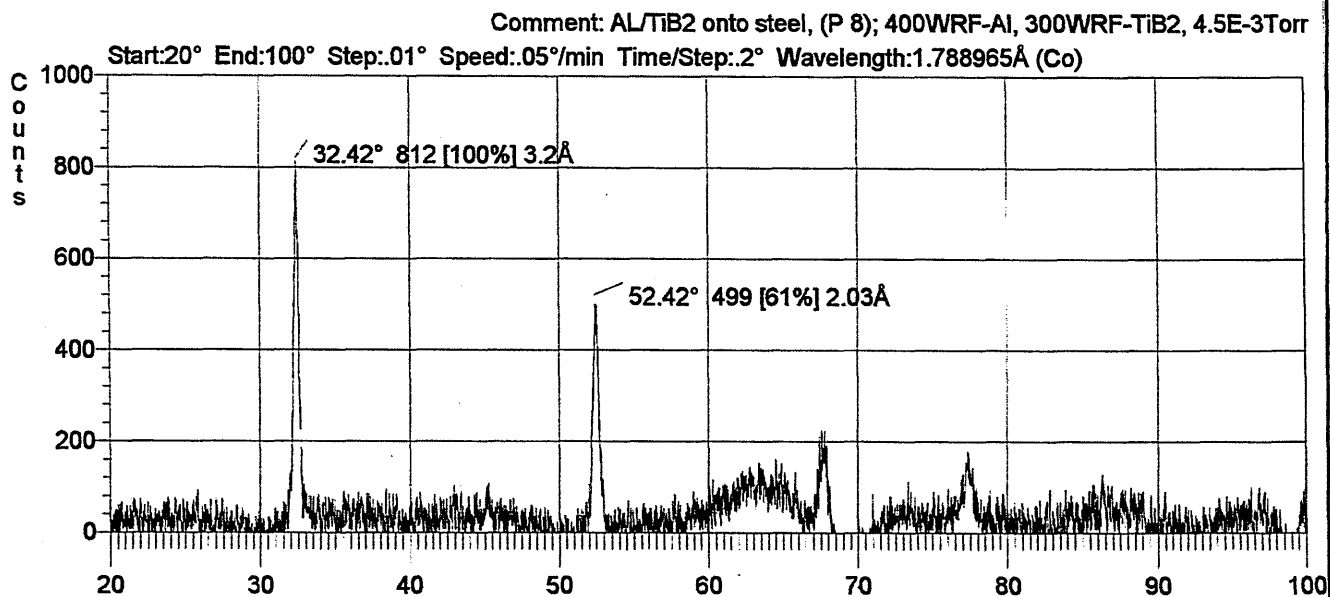
201. Pethica, J.B.; Oliver, W.C. *Mechanical properties of nanometer volumes of material: use of the elastic response of small area indentations*, Mat. Res. Soc. Symp. Proc., 130, 1989, 13-23.

202. Sun, Y.; Bell, T.; Zheng, S. *Finite element analysis of the critical ratio of coating thickness to indentation depth for coating property measurements by nanoindentation*, Thin Solid Films, 258, 1995, 198-204.

203. O'Hern, M.E.; Oliver, W.C.; McHargue, C.J.; Rickerby, D.S.; Bull, S.J. *The hardness and elastic modulus of TiN films as determined by ultra-low load indentation*, Mat. Res. Soc. Symp. Proc., 188, 1990, 139-143.

204. King, R.B. *Elastic analysis of some punch problems for a layered medium*, International Journal Solids structures, 23(12), 1987, 1657-1664.

205. Sneddon, I.N. *The relation between load and penetration in the axisymmetric Boussinesq problem for a punch of arbitrary profile*, Int. Journal Eng. Sci., 3, 1965, 47-57.

206. Saunders, S.R.J.; Shafirstein, G.; Jennett, N.M; Osgerby, S.; Meneve, J.; Smith, J.F.; Vetters, H.; Matlhaei-Schulz, E.; Haupt, J. *Synthesis report Round-Robin experiments with displacement sensing indentation instruments*, NPL report CMMT (D)8, 1995.

207. Hainsworth, S.V.; Bartlett, T.; Page, T.F. *The nanoindentation response of systems with thin hard carbon coatings*, Thin Solid Films, 236, 1993, 214-218.

208. Hong, S.; Weihs, T.P.; Bravman, J.C.; Nix, W.D. *Measuring stiffness and residual stresses of silicon nitride thin films*, Journal of Electronic Materials, 19(9), 1990, 903-909.

209. Baker, S.P.; Jankowski, A.F.; Hong, S. *Mechanical properties of compositionally modulated Au-Ni thin films using indentation and microbeam deflection techniques*, Mat. Res. Soc. Symp. Proc., 188, 1990, 289-295.

210. Weihs, T.P.; Hong, S.; Bravman, J.C.; Nix, W.D. *Mechanical deflection of cantilever microbeams: A new technique for testing the mechanical properties of thin films*, J. Mater. Res., 3(5), 1988, 931-942.

211. Raman, V.; Berriche, R. An investigation of the creep processes in tin and aluminium using a depth-sensing indentation technique, Journal Mater. Res., 7(3), 1992, 627-638.

212. Lucas, B.N.; Oliver, W.C. *The elastic, plastic and time dependent properties of thin films as determined by ultra low load indentation*, Mat. Res. Soc. Symp. Proc., 239, 1992, 337-341.

213. ASM, *Metals Handbook: Properties and selection-nonferrous alloys and special-purpose materials*, 2, 1990.

214. Rother, B; Dietrich, D.A. Evaluation of coating-substrate interface strength by differential load feed analysis of load-indentation measurements, Thin Solid Films, 250, 1994, 181-186.

215. *Nanotest 550: Operation Manual*, Micro Material Ldt., 1997.

216. Fabes, B.D.; Oliver, W.C. *Mechanical properties of coatings and interfaces,* Mat. Res. Soc. Symp. Proc.,188, 1990, 127-132.

217. Laurenson, L. *Diffusion pumps and associated fluids,* Vacuum, 37(8/9), 1987, 609-614.

218. *GoodFellow Cambridge limited Catalogue,* 1996/1997.

219. Rutherford, K.L.; Hutchings, I.M. *A Micro-abrasive test, with particular application to coated systems,* Surface and Coating Technology , 79, 1996, 231-239.

220. Gere, Timoshenko, *Mechanics of materials,* Chapman & Hall, 1995, 250-341.

221. Ugural, A.C.; Fenster, S.K. *Advanced strength and applied elasticity,* 1987, 134-186.

222. Williams, J.G. *Fracture mechanics of polymers,* 1984, 129-171.

223. Echigoya, J.-I. *Principles of adhesion testing,* IN: N. P. Cheremisinoff, P.N. Cheremisionoff (ed.), Handbook of Advanced Materials Testing, 1995, 449-829

224. Saunders, S.R.J.; Hall, D.J.; McCormick, N.J.; Shafirstein, G.; Jennett, N.M.; Meneve, J.; Smith, J.F.; Vetters, H.; Matlhaei-Schulz, E.; Haupt, J. *Calibration guidelines for load displacement indentation, Instruments and Procedures for Round-Robin Experiments,* NPL Report CMMT(D)10, 1995.

225. McGurk, M.R. *An exploration of contact deformation mechanisms in thin hard coated systems,* PhD thesis, Newcastle University, 1997.

APPENDIX

Start:20° End:100° Step:.01° Speed:.05°/min Time/Step:.2° Wavelength:1.788965Å (Co)

Counts

1200

32.7° 1084 [100%] 3.18Å

800

45.49° 420 [39%] 2.31Å

400

67.88° 460 [42%] 1.6Å

0

20   30   40   50   60   70   80   90   100

Start:20° End:100° Step:.01° Speed:.05°/min Time/Step:.2° Wavelength:1.788965Å (Co)

Counts

1200

800

400

32.49° 196 [19%] 3.2Å

0

20   30   40   50   60   70   80   90   100

Start:20° End:100° Step:.01° Speed:.05°/min Time/Step:.2° Wavelength:1.788965Å (Co)

Counts

2000

1600

32.76° 1666 [98%] 3.17Å

1200

800

67.92° 838 [49%] 1.6Å

400

0

20   30   40   50   60   70   80   90   100

Degrees 2-Theta

Comment: AL/TiB2 onto steel, (P 8); 400WRF-Al, 300WRF-TiB2, 4.5E-3Torr
Start:20° End:100° Step:.01° Speed:.05°/min Time/Step:.2° Wavelength:1.788965Å (Co)

32.42° 812 [100%] 3.2Å
52.42° 499 [61%] 2.03Å

Comment: Al/TiB2 onto Al, (P10); 400WRF-Al, 300WRF-TiB2, 4.5E-3Torr
Start:20° End:100° Step:.01° Speed:.05°/min Time/Step:.2° Wavelength:1.788965Å (Co)

32.53° 2408 [100%] 3.19Å
67.71° 1101 [46%] 1.61Å

Comment: Al/TiB2 onto Cu, (P7); 400WRF-Al, 300WRF-TiB2, 4.5E-3Torr
Start:20° End:100° Step:.01° Speed:.05°/min Time/Step:.2° Wavelength:1.788965Å (Co)

43.03° 119 [7%] 2.44Å
32.63° 117 [7%] 3.18Å

Degrees 2-Theta

Comment: NiCr/TiB2 onto steel (P8); 200WRF-NiCr,300WRF-TiB2, 4.5E-3Torr
Start:20° End:100° Step:.01° Speed:.05°/min Time/Step:.2° Wavelength:1.788965Å (Co)

31.25° 2161 [100%] 3.32Å

66.57° 1323 [61%] 1.63Å
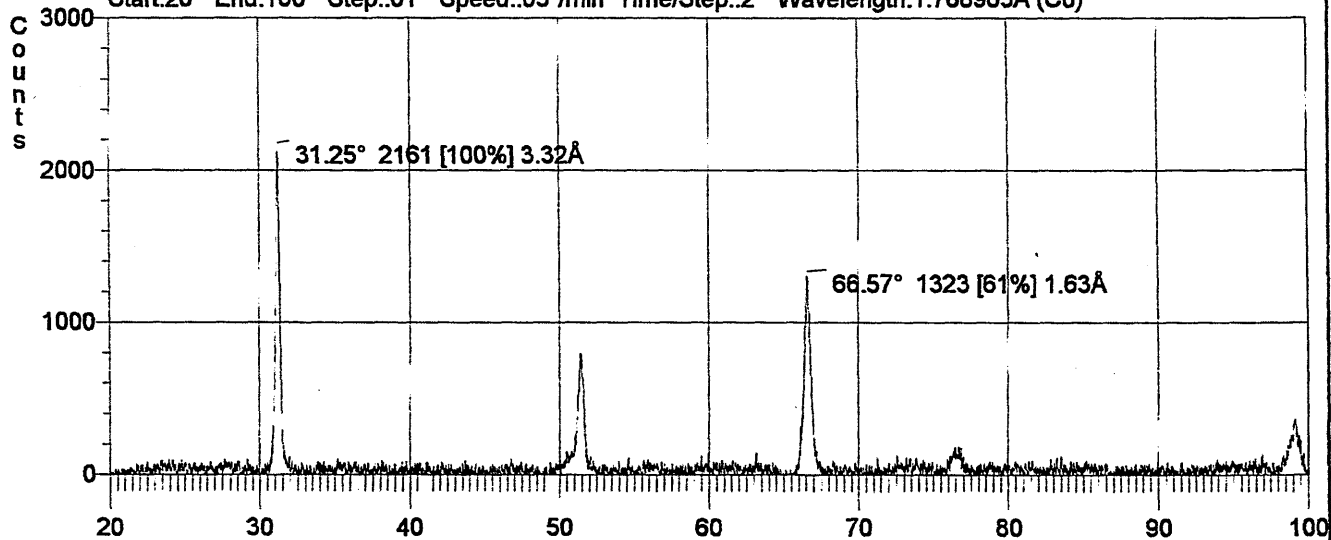
Comment: NiCr/TiB2 onto Al (P10); 200WRF-NiCr,300WRF-TiB2, 4.5E-3Torr
Start:20° End:100° Step:.01° Speed:.05°/min Time/Step:.2° Wavelength:1.788965Å (Co)

31.43° 529 [19%] 3.3Å

66.7° 360 [13%] 1.63Å
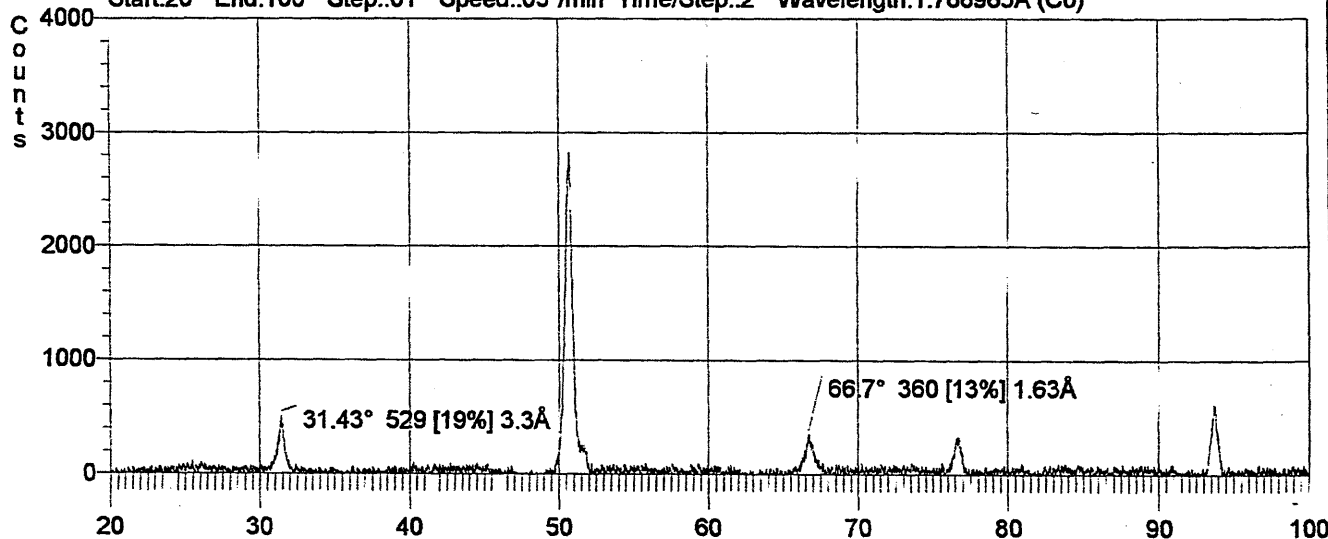
Comment: NiCr/TiB2 onto Cu (P7);200WRF-NiCr,300WRF-TiB2,4.5E-3Torr
Start:20° End:100° Step:.01° Speed:.05°/min Time/Step:.2° Wavelength:1.788965Å (Co)

31.43° 2060 [100%] 3.3Å

92.02° 168 [8%] 1.24Å

66.68° 1083 [53%] 1.63Å

Degrees 2-Theta

Comment: Mo/TiB2-3 onto Steel (Conditions:300WRF-TiB2; 250WRF-Mo; 4.5E-3Torr)
Start:20° End:100° Step:.01° Speed:.05°/min Time/Step:.2° Wavelength:1.788965Å (Co)

2343 [100%] 2.27Å

1796 [77%] 3.31Å

1000 [43%] 1.63Å

140 [6%] 1.17Å

269 [11%] 1.29Å

141 [6%] 2.06Å

Degrees 2-Theta

Comment: Mo/ TiB2-3 on Cu
Start:20° End:100° Step:.01° Speed:.05°/min Time/Step:.2° Wavelength:1.788965Å (Co)

358 [100%] 1.3Å

345 [97%] 2.3Å

292 [82%] 3.4Å

215 [60%] 1.64Å

Degrees 2-Theta